On the Influence of Cations in Non-Aqueous Electrochemistry

Dissertation

zur

Erlangung des Doktorgrades (Dr. rer. nat.)

der

Mathematisch-Naturwissenschaftlichen Fakultät

der

Rheinischen Friedrich-Wilhelms-Universität Bonn

vorgelegt von

Philip Heinrich Reinsberg

aus Bonn

–2019–

Angefertigt mit Genehmigung der Mathematisch-Naturwissenschaftlichen Fakultät
der
Rheinischen Friedrich-Wilhelms-Universität Bonn

Promotionskommission

Betreuer/Erstgutachter: Prof. Dr. Helmut Baltruschat

Zweitgutachter: Prof Dr. Thomas Bredow

Tag der mündlichen Prüfung: 12.07.2019
Erscheinungsjahr: 2019

Selbstständigkeitserklärung gemäß Promotionsordnung der Mathematisch-Naturwissenschaftlichen Fakultät (§6, Absatz 2)

Ich versichere, dass ich die vorliegende Arbeit unter Einhaltung der Regeln guter wissenschaftlicher Praxis selbstständig verfasst, keine anderen als die angegebenen Quellen und Hilfsmittel benutzt und die Zitate kenntlich gemacht habe. Ich habe weder vor noch während meiner Promotion oder bei der Anfertigung dieser Dissertation entgeltliche oder nicht-entgeltliche Beratungs- oder Vermittlungsdienstleistungen in Anspruch genommen.

Publications

Parts of this thesis have already been published in international, peer-reviewed journals.

(6) Reinsberg, P. H.; Koellisch, A.; Bawol, P. P.; Baltruschat, H.; *K–O_2 Electrochemistry: Achieving Highly Reversible Peroxide Formation*, Phys. Chem. Chem. Phys., **2019**, *21*, 4286–4294.

(5) Reinsberg, P. H.; Bawol, P. P.; Baltruschat, H.; *Fast and Simultaneous Determination of Gas Diffusivities and Solubilities in Liquids Employing a Thin-Layer Cell Coupled to a Mass Spectrometer, Part II: Proof of Concept and Experimental Results*. Anal. Chem. **2018**, *90*, 14150–14155.

(4) Reinsberg, P.; Abd-El-Latif, A. A.; Baltruschat, H., *Investigation of the Complex Influence of Divalent Cations on the Oxygen Reduction Reaction in Aprotic Solvents*. Electrochim. Acta **2018**, 273, 424–431.

(3) Reinsberg, P.; Weiss, A.; Bawol, P. P.; Baltruschat, H., *Electrochemical Reaction Order of the Oxygen Reduction Reaction in Li^+-Containing DMSO*. J. Phys. Chem. C **2017**, *121*, 7677–7688.

(2) Reinsberg, P.; Bondue, C. J.; Baltruschat, H., *Calcium–Oxygen Batteries as a Promising Alternative to Sodium–Oxygen Batteries*. J. Phys. Chem. C **2016**, *120*, 22179-22185.

(1) Reinsberg, P.; Bondue, C.; Baltruschat, H., *Mechanistic Investigation of the Oxygen Reduction in Magnesium Ion-Containing Dimethyl Sulfoxide*. Electrochim. Acta **2016**, *200*, 214-221.

Abstract

In this thesis, different aspects of the electrochemistry in non-aqueous electrolytes are presented. Electrochemistry in non-aqueous electrolytes plays a key role in the transition from conventional to renewable energy sources. Compact electrochemical energy storage systems, such as the non-aqueous lithium-ion battery, are indispensable for application in mobile devices, such as smartphones or laptops, and their further development is essential for the inevitable replacement of the conventional combustion engine by electrical engines. To overcome the limitations of the state-of-the-art-lithium-ion batteries, electrochemists all around the world seek for new technologies, enabling higher energy densities and a longer lifetime. One key technology currently discussed are so-called metal–air batteries, in which a metal-anode is combined with an oxygen cathode. However, while electrochemistry in aqueous electrolytes has a very long tradition and is well understood, we know much less about reaction mechanisms and the interface between electrode and electrolyte in non-aqueous electrolytes.

The main focus of this work lies on the oxygen reduction reaction (ORR) and evolution reaction (OER) in dimethyl sulfoxide (DMSO)-based electrolytes. Employing *operando* mass spectrometry and classical electrochemical measurements, various mechanistic aspects have been elucidated. By comparison between the ORR in presence of different alkali and alkaline earth metal ions it was shown that the cation significantly affects the product distribution and the mechanism of the ORR. The extensive interaction and ion pair formation between the cation of the conducting salt and reduced oxygen species has been exemplarily studied in the $K–O_2$ system. For all the cations under investigation, the main products are superoxide and peroxide species, while the oxide has not been found. Comparing the results for different alkali cations, it appears that a higher charge density of the cation fosters the formation of the corresponding, insoluble alkali peroxide. However, if the alkaline earth metals are also included the relation between charge density and product distribution is more complex. For instance, calcium mainly fosters superoxide formation at platinum or glassy carbon electrodes despite its relatively high charge density. Introducing another descriptor of the cation's effect, namely its acceptor number, a better correlation was obtained, although reasons for this behaviour remain elusive.

Another important aspect of the electrochemistry in non-aqueous electrolyte apart from the effect of the conducting salt is the effect of the electrode material. While the special behaviour of gold electrodes towards the ORR and OER in non-aqueous electrolytes has already been highlighted, in the present work mechanistic aspect have been further elucidated and the overall mechanistic picture has been refined. For example, in Li^+-containing electrolytes a direct, surface-confined reduction step from oxygen to peroxide has been identified at gold electrodes via the use of the rotating ring-disk electrode. Regarding divalent cations, gold seems to foster the peroxide formation regardless of the cation, while in the case of alkali

cations a distinct, potential-dependent transition from the one- to the two-electron process was observed. This transition again was correlated with the charge density of the monovalent cations. Interestingly, this transition from superoxide to peroxide formation is followed by a second transition, where the product distribution changes back from peroxide to superoxide due to the deactivation of the surface. This second transition has also been observed in the presence of the divalent cations and shows that the main difference between the cations is their ability to foster peroxide formation.

The effect of the partial pressure of oxygen on the ORR has also been investigated as it is an important parameter of a future, real-world battery, which will either be fed with air or with pure oxygen at variable pressures. While in Li^+-containing electrolytes the expected electrochemical reaction order of 1 with respect to the oxygen concentration was obtained, the reaction order was significantly lower in the presence of Mg^{2+}, implying the contribution of an adsorption process. Employing K^+-containing electrolyte we were able to show that an increase of the oxygen pressure also changes the product distribution from superoxide to peroxide, which we attributed to the pronounced precipitation of the sparingly soluble superoxide. A further essential issue which is addressed in this work it the influence of water on the non-aqueous electrochemistry, as it is a nearly ubiquitous “contaminant” and difficult to remove quantitatively. In principle, two different trends are observable. In the case of the rather irreversible reduction of oxygen in presence of Li^+, water leads to a shift of the peroxide formation to larger overpotentials. However, for the largely reversible $K–O_2$ and $Cs–O_2$ systems, addition of water leads to the pronounced formation of the peroxide, probably due to an irreversible follow-up reaction of the peroxide.

The importance of electromobility and storage systems for renewable energies has attracted not only electrochemists, who are interested in non-aqueous electrochemistry, but researchers from various fields of science. Scientists nowadays make great use of simulation techniques to predict the performance of electrical storage systems rather than testing every possible electrolyte combination. However, modelling of electrochemical cells requires knowledge of different parameters, one of which are the transport properties of oxygen. As state-of-the art methods of determining the transport properties were either too slow, too inaccurate or too expensive, we developed a new, non-electrochemical measurement cell which enables simultaneous measurement of the gas diffusivities and solubilities without external knowledge. Interestingly, the solubility of oxygen in DMSO increases for increasing temperatures. Moreover, a significant salting-in effect has been observed in the presence of lithium bis(trifluoromethane)sulfonimide, while the usual salting-out effect has been identified in the presence of the perchlorate salts of different cations. From the temperature-dependent diffusivities we were able to evaluate the activation barrier for the diffusion of oxygen in DMSO-based electrolyte, which will certainly be of great help for modelling electrochemical cells at different temperatures (think of cold winter and hot summer days).

While battery-related research usually focuses on the reversibility of the reaction and the energy density of a potential energy storage system, we aimed at elucidating more fundamental properties in this work and there is nothing more fundamental for an electrochemist than the interface between electrode and electrolyte. Therefore, the final section of this work deals with the investigation of the electrode–electrolyte interface via surface-enhanced infrared spectroscopy. The adsorption of cyanide and carbon monoxide from propylene carbonate have been studied and it was found that the observed shift of the vibrational bands are similar to the aqueous system, indicating similar adsorption geometries. Careful analysis of the adsorption of acetonitrile from acetonitrile-based electrolytes revealed that the solvent is adsorbed via the methyl-group for potential negative of the point of zero charge and that the solvent is electrochemically decomposed to cyanide. Moreover, there is a strong interaction between the cation of the conducting salt and acetonitrile, which shows up as a significant shift of the vibration bands of the methyl- and cyanide-groups.

In the present work we could give some deeper insights in the course of reactions in non-aqueous electrolytes as well as in the importance of the cation of the conducting-salt, the electrode material, the partial pressure of oxygen and the presence of water. Using a newly developed measurement cell for simultaneous determination of the gas diffusivities and solubilities new data concerning diffusivities and solubilities of oxygen in DMSO-based electrolytes could be collected. Moreover, further insights in the adsorption processes at the electrode electrolyte interface could be given by investigations using the surface-enhanced infrared spectroscopy. The presented results describe fundamental aspects of the electrochemistry in non-aqueous electrolytes and thus contribute to a better understanding of the underlying mechanisms, which will possibly help to improve the development of new batteries in practice.

Danksagung

Mein herzlicher Dank gilt all jenen, die während der letzten dreieinhalb Jahre sowohl im privaten als auch im beruflichen Umfeld unterstützt haben. Mein besonderer Dank gilt Professor Dr. Helmut Baltruschat, der die Betreuung dieser Arbeit übernommen hat. Es war immer wieder erstaunlich, wie viel Zeit sich Herr Baltruschat genommen hat, um mit mir wissenschaftliche Problemstellungen zu erörtern oder sogar bei praktischen Problemen zu helfen. Darüber hinaus ließ er mir sehr viel Freiheit, eigene wissenschaftliche Fragestellungen aufzustellen und zu bearbeiten, obwohl sie teilweise nicht mit seinen persönlichen Vorlieben übereinstimmten. Nur dank dieser großen Freiheit konnte ich mich so breitgefächert während meiner Promotion weiterbilden, wie ich es getan habe.

Mein besonderer Dank gilt auch den Kolleginnen und Kollegen des Arbeitskreises Elektrochemie, welche die Zeit während meiner Promotion so bereichert haben. Allen voran möchte ich Pawel P. Bawol und Martina Hegeman danken, diemich durch den größten Teil meiner Promotion begleitet haben und sowohl intellektuell als auch menschlich eine große Bereicherung waren. Auch Siegfried Ernst möchte ich hervorheben, der stets zur Stelle war, wenn sich intellektuelle Probleme anbahnten und sie in meist ausschweifender Form mit mir diskutierte. Mein herzlicher Dank gilt auch Carole Rossignol und Elke Thome, welche mir immer wieder bei Problemen rund um die Forschung halfen.

Ebenfalls möchte ich den Werkstätten der Chemischen Institute danken, wobei ich insbesondere Herrn Heinz-Peter Königshoven und Herrn Tobias Schönberg hervorheben möchte. Herr Königshoven stand mir immer mit Tat und Rat zu Seite und verzagte auch nicht, wenn ich dasselbe Werkstück zum zehnten Mal zu ihm mit einem Änderungswunsch brachte.

Schließlich möchte ich all den Menschen danken, die mich im privaten Umfeld unterstützt haben und mir durch Phasen des Zweifelns oder der Frustration geholfen haben oder mein Leben anderweitig bereichert haben. Ganz besonders möchte ich dabei meiner Verlobten, Jule, und meiner Familie danken, die immer für mich da waren. Danke, dass ihr stets an mich geglaubt habt und mich bei der Verwirklichung meiner Träume unterstützt habt, was nicht immer selbstverständlich war. Ein großer Dank geht auch an alle anderen Freunde, die die letzten Jahre meines Lebens so sehr bereichert haben und mir stets zur Seite standen.

Table of Contents

List of Figures

List of Tables

1 Introduction

In this introduction, a general overview about the hitherto existing mechanistic understanding of the oxygen reduction in aprotic electrolytes is given, establishing a link between the different publications included in this work. Subsequently each publication is presented in a separate chapter introduced by a short section putting the paper into context.

1.1 Motivation

Climate change poses new challenges to mankind[1]. Since the beginning of 1990s, it has been generally accepted that carbon dioxide (CO_2) emissions are a major reason for global warming[2,3]. A severe problem regarding the personal perception of the climate change is the significantly delayed "response" of the climate system[4], meaning that the full impact of the anthropogenic CO_2 emissions during the 20th century on climate change is not even visible yet. The major goal to mitigate climate change is to reduce CO_2 emissions, which already started to be effective[5]. The importance of science to achieve this goal has been highlighted[6]. While CO_2-neutral energy conversion using renewable energy sources is already well established, energy storage remains to be the bottleneck[7]. Regarding large-scale energy storage, pumped-storage hydroelectricity appears to be the most promising candidate due to its large efficiency of up to 80% and low costs[8,9]. However, despite its superior efficiency, hydroelectricity cannot be used as a universal solution for energy storage because of the minimum size and weight associated with a pumped-storage plant. Thus, the quest for energy storage solutions for electromobility and mobile devices remains challenging.

One approach to store energy for electromobility applications is to utilize rechargeable batteries, although interest in fuel cells celebrates its revival in 2018 due to the efforts of Japanese car manufacturers[10]. A major drawback of battery technologies available so far are their shortcomings in specific energies as compared to gasoline[11], although their power densities exceed that one of gasoline[12]. However, the resulting, decreased distance, which can be travelled per "refuelling unit", seems to lower customer's interest in vehicles driven by electromobility. A possible solution to this problem has been presented by Abraham in 1996[13], who proposed a secondary battery comprising of lithium metal as anode and oxygen as cathode with a non-aqueous electrolyte, promising superior energy densities of 3460 Wh kg^{-1} (calculated from thermodynamic data, referred to the mass of Li_2O_2[14]). Since then, a lot of effort has been put into research and alternatives to lithium as anode material have been proposed, such as sodium[15], potassium[16], magnesium[17] or calcium[18]. Besides approaches relying on non-aqueous electrolytes, also aqueous electrolytes have been proposed for post-lithium-ion batteries[19,20].

A problem related to the emergence of new battery technologies is that many researchers start with the investigation of "full-cells", meaning that they assemble an anode and a cathode

and investigate cycle life and capacity fading of the system. While this approach provides information on crucial parameters, which might be relevant to practical application, it does not even give information on the reactions relevant to the charging/discharging process. An important example from the field of metal–air batteries is the Li–air battery based on ethylene carbonate electrolytes as originally proposed by Abraham[13]. From the voltage-profiles and thermodynamic considerations, Abraham and co-workers concluded that their battery actually based on the reaction between lithium and oxygen with Li_2O_2 as a product. It took around 15 years until researchers showed using several analytical approach such as differential electrochemical mass spectrometry (DEMS) that the solvent used by Abraham was not stable towards the reactive oxygen species produced during reduction[21-23] and the battery proposed in 1996 was basically a non-aqueous fuel cell. This example shows, how important preceding fundamental studies are for constructing a battery, which is supposed to solve real-world problems.

The present work aims at elucidating the oxygen reduction (ORR) and evolution reaction (OER) in an aprotic environment on a fundamental level. To separate the ORR and OER from the reaction at the metal–anode, classical three-electrode set-ups have been employed. Moreover, well-defined hydrodynamic conditions

1.2 Mechanistic Insights: A historical overview

While the oxygen reduction and evolution in aqueous electrolytes is understood to an astonishing degree of detail[24-28], the situation is different for aprotic electrolytes. One of the first reports on oxygen reduction in an aprotic solvent dates back to 1957, when Kolthoff, a pioneer in analytical chemistry, started to investigate the polarography of different acetonitrile-based electrolytes and noted that oxygen is reduced in two reduction waves[29], in which the first reduction wave was attributed to a two-electron transfer based on an estimated diffusion coefficient. The presence of two reduction waves has also been shown in dimethyl sulfoxide (DMSO)[30] and N-methylacetamide[31], but Kolthoff and co-workers did not identify the reaction products.

Following up the work of Kolthoff and co-workers, Maricle and Hodgson were the first to identify superoxide as the main product in tetrabutylammonium perchlorate ($TBAClO_4$) containing DMSO and dimethylformamide (DMF) via *ex situ* electron spin resonance spectroscopy[32]. Thus, the authors described the ORR in DMF and DMSO via eq. (1.1):

$$O_2 + e^- \rightleftharpoons O_2^- \tag{1.1}$$

By adding phenol, the authors could also show that the reduction waves are shifted to more positive potentials in presence of proton sources and they hypothesized that this is due to the reaction of phenol with superoxide:

$$O_2 + Ph - OH + 2\,e^- \rightleftharpoons HO_2^- + Ph - O^- \tag{1.2}$$

These results were confirmed by alternating current voltammetry and extended to other solvents by Peover and White[33,34]. For alkaline earth metals, Hamm and co-workers proposed the formation of a di-superoxide in presence of alkaline earth metals[35,36]:

$$2\,O_2 + M^{2+} + 2\,e^- \rightleftharpoons M(O_2)_2 \tag{1.3}$$

Due to the unexpectedly large currents observed, the authors argued that a decomposition of the metal superoxide to the metal peroxide might occur upon which oxygen is released, which subsequently is reduced again.

$$M(O_2)_2 \rightarrow MO_2 + O_2 \tag{1.4}$$

Systematic investigation of the effect of the cation by Hamm and co-workers revealed that the second reduction wave, which represents the peroxide, is shifting to more positive potentials in the presence of the alkaline earth and alkali metal cations[35,36]. Parallel to that, Sawyer and co-workers systematically investigated the electrochemistry of oxygen in aprotic solvents by varying the electrolyte and the electrocatalyst and further investigating the role of water [37,38]. While previous authors had already mentioned a second reduction wave, it were Sawyer and co-workers who explicitly noted that there is a second, one-electron reduction step for the reduction of superoxide to peroxide, which occurred at potentials −1.3 V negative of the first reduction wave[37]:

$$O_2^- + e^- \rightarrow O_2^{2-} \tag{1.5}$$

Fujinaga *et al*. continued research on the effect of water[39] and thoroughly investigated the role of alkali cations as well as different tetraalkylammonium salts. Using a mercury electrode, the authors identified a third reduction wave (prior to metal deposition) in presence of the alkali cations, which they attributed to the formation of the oxide[40]:

$$O_2^{2-} + 2\,e^- \rightarrow 2\,O^{2-} \tag{1.6}$$

Until 1980, the scientific community believed that the electrochemistry of O_2 is only affected by the presence or absence of protons, but not by the solvent itself[41,42]. In a systematic study, Sawyer *et al*. showed that there is indeed an effect of the solvent and related the shift of the oxygen–superoxide couple as well as the further reduction to peroxide to the solvent's ability to solvate superoxide[43]. Later on in 1990, Aurbach and co-workers continued to investigate the ORR in aprotic solvents alongside with metal deposition. They showed that the addition of $5x10^{-4}$ M $LiClO_4$ to a dimethoxyethane $TBAClO_4$ solution leads to a highly irreversible behaviour of the system[44]. Aurbach also pointed out that propylene carbonate is prone to be attacked by superoxide and emphasized the possibility of disproportionation of superoxide to insoluble Li_2O_2 in the presence of Li^+, which has been confirmed in the meantime [45,46]. In a fundamental study, Ohsaka *et al*. evaluated the standard reaction entropy of the reduction of

oxygen in the non-aqueous electrolytes in the presence of tetraethylammonium perchlorate on glassy carbon electrode and found a value of 130 J $mol^{-1}K^{-1}$[47].

Although Aurbach in 1991 had already noted that the oxygen reduction in propylene carbonate is not reversible and attributed the absence of an anodic wave to a chemical reaction between propylene carbonate and superoxide[44], Abraham, five years later, proposed a lithium–air battery based on a propylene carbonate electrolyte[13]. While Abraham's article initially did not receive much attention, a report by Bruce and co-workers on the oxidation of Li_2O_2[48] led to an increase in interest in lithium–air batteries[49-57]. Research on lithium–air batteries was further intensified from 2009 on, when IBM started the Battery 500 Project[11] (the interest in Abraham's and Ogasawara's papers is shown as an example in Figure 1.1). It was about that time, when studies from different countries and working group proved via a variety of spectroscopic methods that organic carbonates are not stable in presence of superoxide [21-23,58-60]. Since 2011 different electrolytes have been investigated as potential candidates for lithium–air batteries, such as acetonitrile [61], ethers[21,62-64], dimethyl sulfoxide [62,65,66], ionic liquids [67,68] and others [69-73]. Further important improvement was achieved when in 2013 soluble redox mediators were introduced to reduce the overpotential for the oxidation of solid Li_2O_2 [74,75]. Parallel to that, research on alternatives to lithium–air batteries began to emerge, such as Na–air[15,76,77], K–air[16,78] and Mg–air[17,79,80].

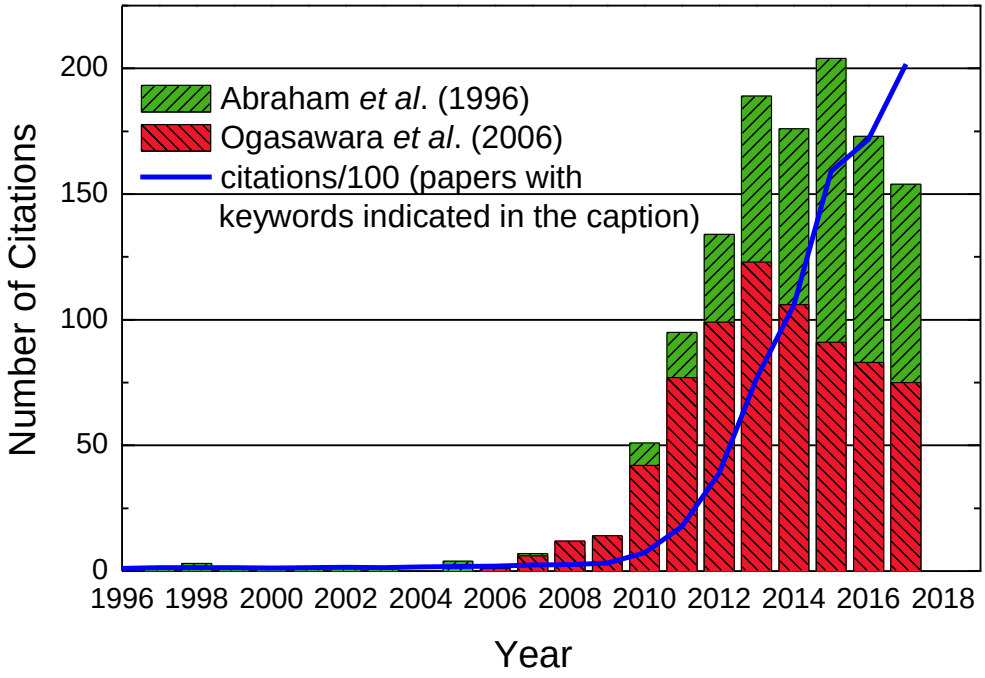

Figure 1.1. Citation report retrieved from Web of Science.[81] The red bar shows the citation for Abraham's paper[13] and the green is related to Ogasawara's[48] (green). The blue line shows the overall number of citations for papers with the keywords "lithium" + "air", "lithium" + "oxygen" and "Li-O_2" + "Li-air" in the title. The number has been divided by 100 to fit the scale.

Recently, inspired by the work of Matsuda *et al*.[82], Bruce and co-workers began to utilize quinones as mediators for the oxygen reduction [83] and finally presented a lithium–oxygen cell,

in which ORR and OER were mediated via organic molecules [84]. Further important approaches for enhancing the ORR mechanism rely on the addition of other cations [85,86] or the use of so-called hydrate-melt electrolytes [73].

Although research on alternative metal–air batteries had already started prior to the beginning of this PhD-project, thorough understanding of the mechanism of the ORR in aprotic solvents and the cation's influence remained elusive. Early systematic attempts of elucidating the effect of the cation were restricted to mercury as an electrode [35,36,40] as outlined above. More recent attempts, mainly relied on classical electrochemical methods [61,62,87] and use of *operando*[1] methods for identification of the products, like DEMS, was scarce. Furthermore, the scientific community was markedly influenced by Abraham and co-workers, who applied Pearson's Hard And Soft Acids and Bases (HSAB) concept [91] to predict the dependence of the ORR's product distribution on solvents and electrolytes [62,87,92]. However, Abraham and co-workers apparently misconceived[93] the concept and claimed that tetraalkyl-cations, due to their *soft* nature, would stabilize the *soft* base superoxide in form of a contact ion-pair complex [62] despite tetraalkylammonium salts being *weak* bases.

Summarizing, significant progress had been made in understanding and improving the ORR and OER in the presence of lithium at the beginning of this project. However, systematic and detailed studies of the effect of the cations present in the electrolyte were scarce. Unified mechanisms for the ORR/OER had been proposed, but they had not been thoroughly verified or falsified. Therefore, the aim of this project was to expand the mechanistic picture of the ORR/OER in aprotic electrolytes by varying the conducting salts, electrocatalyst, oxygen saturation, water contents and further parameters. The main goal was to systematically elucidate the role of the cation of the conducting salt, which is presented in chapter 3–8 for different cations. Chapter 3 is devoted to the role of Mg^{2+}, chapter 4 is devoted to Ca^{2+} and chapter 5 represents a general comparison between divalent alkaline earth metals. As a comparison to monovalent cations, the reaction mechanism in Li^{+}-containing DMSO is elucidated in detail in chapter 6. An investigation of the peroxide formation in presence of K^{+}-ion is shown in chapter 7, while the importance of ion pair formation in non-aqueous electrolytes is discussed in chapter 8 using K^{+}-containing DMSO as a model system. The mechanistic discussion is continued by an investigation of the effect of the electrolyte on the oxygen solubility and diffusivity in chapter 9. Finally, preliminary results on the electrochemical double-layer in selected non-aqueous electrolytes are shown in chapter 10.

[1] There is some ambiguity between the use of *operando* and *in operando*. Both terms origin from the Latin ablative of the gerund of the verb *operare* and mean something like "during working". However, in its original form as introduced by Bañares *et al*. it is *operando*[88]. The term *in operando* probably is derived from the term *in situ*. Nonetheless, both terms would be correct from a grammatical point of view as the word *in* is usually used to emphasize the temporal connotation, while the absence of *in* indicates a modal function of the gerund. Both connotations seem to be suitable in this context[89,90].

2 Experimental Techniques

In this part, some general considerations on the experimental techniques employed during this work are presented. Practical aspects and details can be found in the experimental section of each paper and articles cited therein.

2.1 Rotating Ring-Disk[2] Electrodes

An omnipresent problem for the determination of rate constants for electrochemical reactions (and heterogeneous reactions in general) is the fact that the measurable current usually is significantly affected by the rate of diffusion of species toward the electrode. For instance, for a truly reversible reaction, the current is exclusively determined by the rate of diffusion [96]. Therefore, it is important to work under well-defined hydrodynamic conditions, which allow for the exact calculation of the diffusion in order to obtain reliable, kinetic data. One of the most famous approaches to solve this issue is the rotating disk electrode (RDE) and its successor, the rotating ring-disk electrode (RRDE), which shall be discussed in this section.

2.1.1 History of the RRDE

The development of the RDE in the USSR dates back to the early 1950's[94,97]. One of the names which is strongly associated with the RDE is the name of Levich, who developed the theoretical framework for the convective-diffusive problem present at the RDE based on the works of von Kármán and Cochran[98-100]. Together with Koutecký, Levich succeeded to derive an equation which also takes into account the finite rate of the electrochemical reaction [101]. Later, Frumkin encouraged Levich to use a second electrode as a concentric ring around the disk electrode, which can be understood as the birth of the rotating ring-disk electrode (RRDE)[102]. While the development of the RRDE had only taken place in the USSR so far, Bruckenstein and Albery pioneered in adapting the RRDE-technique in the Western world[103,104] and enhanced the theoretical framework significantly by including further heterogeneous and homogeneous reactions[95,105-108].

2.1.2 Theoretical Background

A schematic drawing of an RRDE is shown in Figure 2.1. The RRDE comprises a disk electrode, which is separated by an insulating O-ring from the ring electrode. Both, disk and ring electrode are mounted into a chemically inert shroud. The coordinate y is defined orthogonal to the surface and is zero at the surface, while *r* denotes the radial coordinate.

[2] In the original articles published by Levich[94] and Albery[95] the spelling *disc* instead of *disk* was used. However, although there is no exact rule, today the spelling *dis*k appears to be more common.

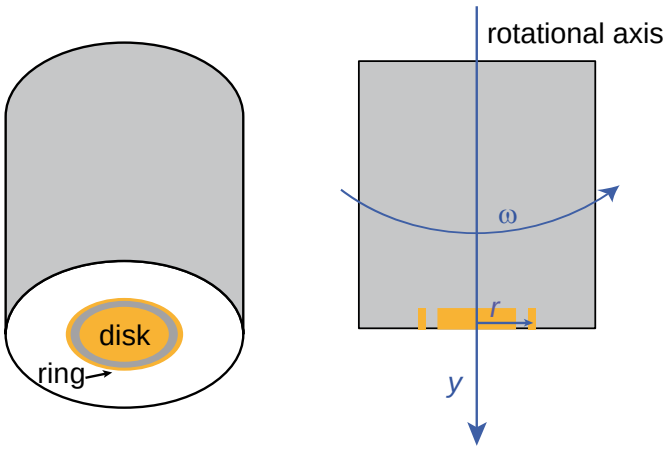

Figure 2.1. Schematic drawing of a rotating ring-disk electrode . The disk and ring electrode are mounted into non-conducting, chemically inert polytetrafluoroethylene.

During an experiment, the whole assembly including the shroud rotates at a rotational frequency ω. The rotational movement of the disk drags the fluid toward its surface and pushes it away from the centre in radial direction due to the centrifugal force. To illustrate the hydrodynamic conditions, the corresponding streamlines are shown in Figure 2.2. It is important to note that close to surface of the rotating disk, the velocity of the fluid perpendicular to the surface vanishes and there is a thin layer of electrolyte, in which no convection but only diffusion is active.

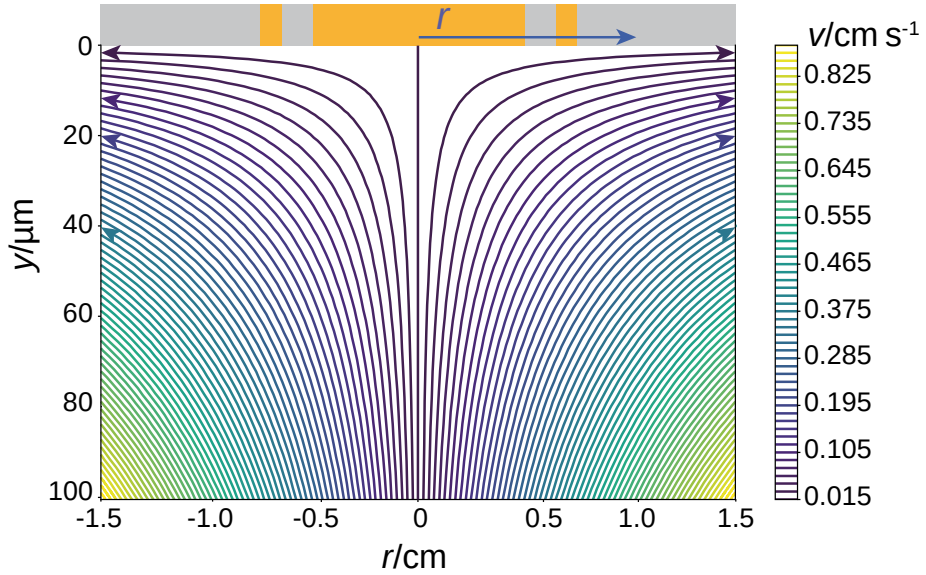

Figure 2.2. Streamlines in front of the electrode in a DMSO-based solution. The streamlines represent areas of constant velocity. The velocity v has been calculated from the axial and radial components of the velocity. Simulation of the streamlines by courtesy of Pawel P. Bawol, based on the first element of the infinite series given by von Kármán and Cochran [98,99].

The mathematical treatment of the convective-diffusive problem was carried out by Cochran[98] based on the works of von Kármán[99]. Taking advantage of the symmetry of the RRDE, the different components of the fluid velocity are defined in cylindrical coordinates rather than in Cartesian coordinates. The velocity component perpendicular to the surface is

v_y, the radial component is v_r and the azimuthal component is v_φ. Due to the complexity of the convective problem, the components of velocity cannot be represented in a closed form, but are represented by infinite series expansion. Moreover, the boundary conditions of the problem make it necessary to define two different sets of series, one which is valid close to the surface and one which is valid far away from the surface.

The different velocity components and their dependence on *y*, *r*, and *ω* for distances far away from the surface as well as close to the surface are given in the following set of equations [98,100] and displayed in Figure 2.3 a. The velocity component perpendicular to the surface (v_y) for large distances *y* is given by eq. (2.1), with *A*, *B* and α as constants and $\xi = (\omega/\nu)^{1/2} \cdot y$, where ν is the kinematic viscosity:

$$v_y = (\omega\nu)^{1/2}\left(-\alpha + \frac{2\cdot A}{\alpha}e^{-\alpha\xi} - \frac{A^2+B^2}{2\alpha^3}e^{-2\alpha\xi} - \frac{A\left(A^2+B^2\right)}{6\alpha^5}e^{-3\alpha\xi} + \ldots\right) \tag{2.1}$$

For small distances the velocity is given by eq. (2.2), where *a* and *b* are constants:

$$v_y = (\omega\nu)^{1/2}\left(-a\xi^2 + \frac{\xi^3}{3} + \frac{b\xi^4}{6} + \ldots\right) \tag{2.2}$$

For large distances the radial component is given by, where *c* is a constant:

$$v_r = r\omega\left(Ae^{-c\xi} - \frac{A^2+B^2}{2c^2}e^{-2c\xi} + \frac{A\left(A^2+B^2\right)}{4c^4}e^{-3c\xi} + \ldots\right) \tag{2.3}$$

The radial component v_r of the velocity for small distances from the surface is given by:

$$v_r = r\omega\left(a\xi - \frac{\xi^2}{2} - \frac{b\xi^3}{3} + \ldots\right) \tag{2.4}$$

For large distances the azimuthal velocity component is given by eq. (2.5):

$$v_\phi = r\omega\left(Be^{-c\xi} - \frac{B\left(A^2+B^2\right)}{12c^4}e^{-3c\xi} + \frac{AB\left(A^2+B^2\right)}{18c^6}e^{-4c\xi} + \ldots\right) \tag{2.5}$$

Finally, the azimuthal velocity for small distances from the surface is defined as:

$$v_\phi = r\omega\left(1 + b\xi + \frac{1}{3}a\xi^3 + \ldots\right) \tag{2.6}$$

The dashed line in Figure 2.3 a indicates the value of v_y which is close to $0.8v_{max}$. The corresponding distance δ_P equals 3.6 ξ and can be expressed in terms of the kinematic viscosity and the rotation rate:

$$\delta_P = 3.6(\omega\nu)^{1/2} \tag{2.7}$$

At this distance, the radial and azimuthal components of velocity vanish und only axial drag is present in the solution (Figure 2.3 a). Therefore, the distance δ_p is considered as the thickness of the hydrodynamic boundary layer (or the Prandtl layer).

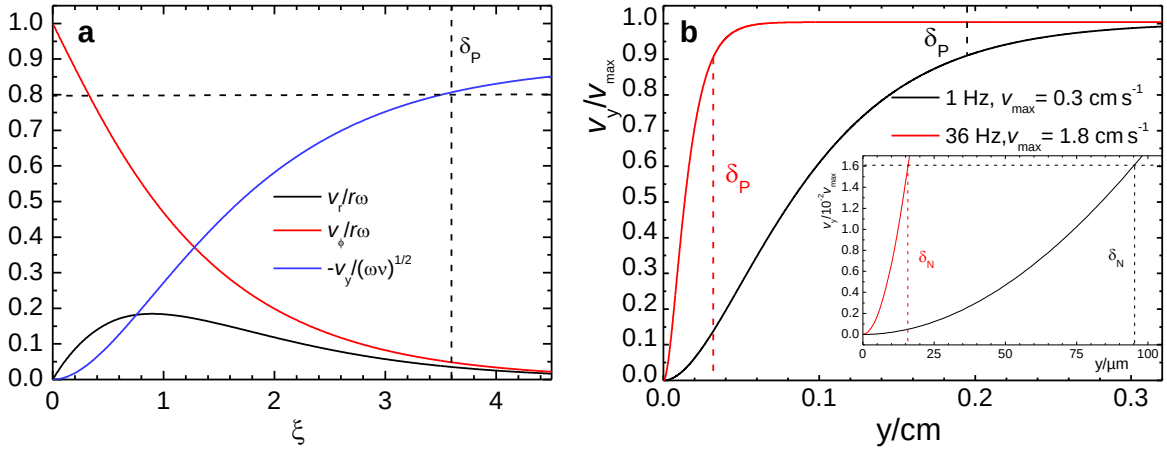

Figure 2.3. Velocity profile at the rotating electrode. **a**. Normalized axial (v_y), radial (v_r) and azimuthal (v_ϕ) components of the velocity with respect to the dimensionless distance from the electrode calculated according to [98]. δ_p represents the thickness of the hydrodynamic boundary. Courtesy of J. Fuhrmann. **b.** Axial velocity in DMSO normalized to the maximum velocity at different *y* distances from the electrode for a rotation rate of 1 Hz (black) and 36 Hz (red). The inset shows a magnification for distances close to the surface of the electrode. δ_N is the thickness of the Nernstian diffusion layer.

The normalized velocity profile in terms of the real distance *y* perpendicular to the surface is shown in Figure 2.3 b for two extreme values of the rotation rate used in this work. As can be seen, the thickness of the hydrodynamic boundary layer in DMSO varies from 0.03 cm at 36 Hz to up to 0.19 cm at 1 Hz. Even for rotation rates of 1 Hz, δ_p is much smaller than the radius of the disk electrode ($r = 0.25$ cm), which is essential for the approximations used in the derivation of the equations to be valid.

Having developed equations describing the velocity profile in the fluid, the equations relevant to the practical evaluation of experimental data shall be briefly introduced. The flux of a species *i* is given by Fick's first law of diffusion, where *j* is the flux density towards the electrode, D_i is the diffusion coefficient and c_i denotes the concentration of the species of interest:

$$j_i = -D_i\left(\frac{\partial c_i}{\partial y}\right) \tag{2.8}$$

For the steady-state diffusion limited current, the concentration of the reactant at $y = 0$ (c_s) equals 0, implying that the reactant is immediately reduced or oxidized when it reaches the surface. Assuming a linear concentration gradient, the limiting flux is given by eq. (2.9):

$$j_{i,\mathrm{lim}} = -D_i \left(\frac{\partial c_i}{\partial y} \right)_{y=0}$$
$$\approx D_i \frac{c_0 - c_s}{\delta_N} \qquad (2.9)$$
$$\approx D_i \frac{c_0}{\delta_N}$$

c_0 denotes the bulk concentration of the reactant and δ_N is the thickness of the diffusion layer, which is called Nernstian diffusion layer. The gradients of the concentration in front of the electrode are shown in Figure 2.4, where also the graphical definition of the Nernstian diffusion layer as the tangential gradient for $y = 0$ is given. Mathematically, the diffusion layer is given by eq. (2.10):

$$\delta_N = \left(\left(\frac{\partial c_i}{\partial y} \right)_{y=0} \right)^{-1} \cdot c_0 \qquad (2.10)$$

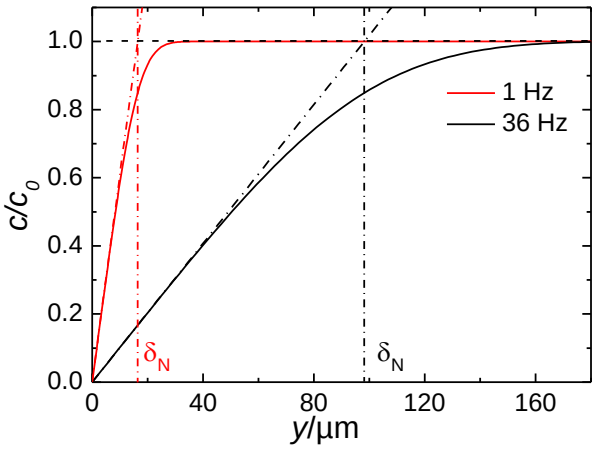

Figure 2.4. Concentration gradients in front of the electrode. The gradients have been simulated by P. P. Bawol based on the equations derived by von Kármán and Cochran [98-100]. The diffusion layer thickness at the RDE has been derived by Levich[100], using the first element of the infinite series given in eq. (2.2) with D as the diffusion coefficient:

$$\delta_N = 1.61 \cdot D^{1/3} \nu^{1/6} \omega^{-1/2} \qquad (2.11)$$

Substituting eq. (2.11) in eq. (2.9) and multiplication with the charge transferred per mole of reactant (zF) finally yields the expression for the diffusion-limited current:

$$i_{Diff} = 0.62 \cdot zFD^{2/3} \nu^{-1/6} \omega^{1/2} c_0 \qquad (2.12)$$

Inclusion of more terms of the velocity by Newman[109] results in a more accurate equation, giving slightly higher limiting currents (3% for a Schmidt number of 760 ($\mathrm{Sc} = \nu / D$) as in the case of O_2 in DMSO).

$$i_{Diff} = zF\omega^{1/2}c_0 \frac{0.62048\left(\frac{\nu}{D}\right)^{-2/3}}{1+0.2980\left(\frac{\nu}{D}\right)^{-1/3}+0.14514\left(\frac{\nu}{D}\right)^{-2/3}} \tag{2.13}$$

However, due to the relatively small error of eq. (2.11) and the complexity of eq. (2.13) by Newman[109], the equation by Levich is usually invoked for practical analysis. While eq. (2.12) defines the diffusion-limited current, the effect of the potential on the current is not included. For a totally irreversible one-electron step, the current at each potential is described by the Koutecký-Levich equation(eq. (2.14)), assuming Butler-Volmer like behaviour[110]:

$$\begin{aligned}\frac{1}{i} &= \frac{1}{i_{Diff}} + \frac{1}{i_K} \\ &= \frac{1}{Fc_0k_0\exp\left(-\alpha F\left(E-E_0\right)/RT\right)} + \frac{1}{0.62zFD^{2/3}\nu^{-1/6}\omega^{1/2}c_0}\end{aligned} \tag{2.14}$$

In eq. (2.14), k_0 is the standard rate constant for $E = E°$, α is the transfer coefficient and E is the potential. As can be seen from eq. (2.14), the potential dependence of the rate constant, which yields insights into the reaction mechanism, can be evaluated from RDE-data.

Another aspect, which shall be briefly discussed here is the transfer of species from the disk to the ring electrode. The transition time t_S has been defined in different ways by Bard [96] and Bruckenstein and Feldman [111]. Calculation of an average transit time ($t_{s,av}$, eq. (2.15)) assumes that species are produced at a $r_0/2$ with r_0 as the radius of the disk and react at the middle of the ring electrode defined by its inner radius r_1 and its outer radius r_2 ($(r_1+r_2)/2$):

$$t_{s,av} = 4.51\cdot\left(\frac{\nu}{D}\right)^{1/3}\left(\log\left(\frac{r_1+r_2}{r_0}\right)\right)^{2/3}\cdot\omega^{-1} \tag{2.15}$$

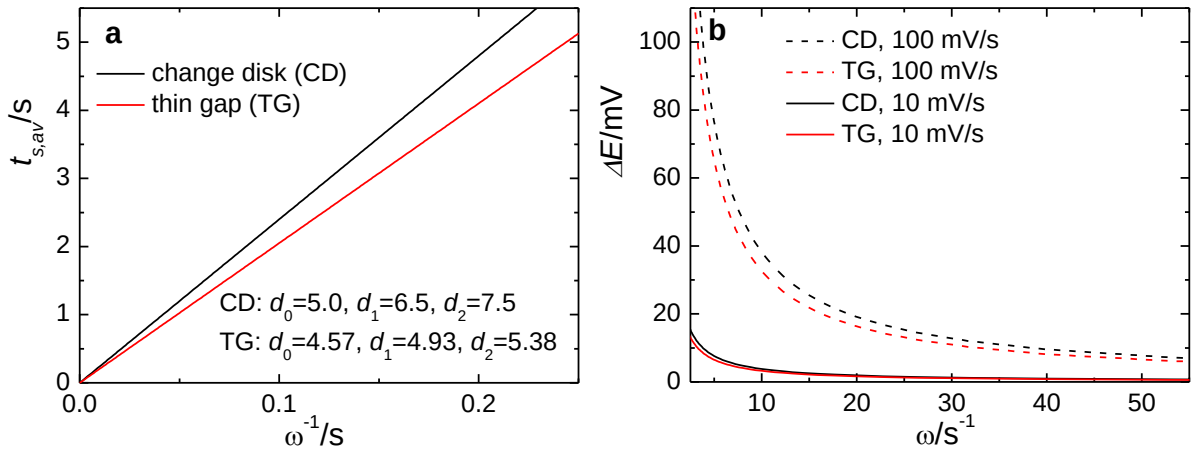

Figure 2.5. Average Transfer Time at the Rotating Ring-Disk Electrode. **a**. Average transfer time $t_{s,av}$ with respect to the inverse angular velocity for the change disk electrode (black) and the thin-gap electrode (red). **b**. Potential delay between disk and ring electrode for different sweep rates.

The average transition time for the different RRDEs utilized in this work is shown in Figure 2.5 a. The resulting delay between the potential at the disk and the detection at the ring is shown in Figure 2.5 b for a sweep rate of 10 mV/s (dashed) and 100 mV/s (solid). At a rotation rate of 4 Hz and a sweep rate of 100 mV/s, which represent the most extreme combination used in this work, the delay is in the order of 100 mV, acerbating the evaluation of the collection efficiency.

2.2 Differential Electrochemical Mass Spectrometry

With standard electrochemical techniques, reactants and products, in principle, have to be identified via their characteristic redox potentials. Even if the redox potentials of all possible redox reactions are known, significant kinetic limitations, which may depend on the electrode material, electrode structure, solvent, conducting salt and so on, shift the apparent redox potential and thus, make identification purely based on potential nearly impossible. Therefore, electrochemists often try to combine purely electrochemical methods with spectroscopic or other techniques. For the study of reactions involving volatile reactants and/or products, such as investigated in this work, differential electrochemical mass spectrometry (DEMS) has proven as an invaluable tool [112,113]. In a typical DEMS experiment, the consumption or evolution of volatile species during an electrochemical experiment is detected via a mass spectrometer. While it is not the goal of this work to give an exhaustive description of DEMS, the following paragraphs will focus on some critical aspects of the DEMS system from a practical point of view.

2.2.1 History of DEMS

One of the major practical problems of combining electrochemistry and mass spectrometry *in situ* is that the ion source typically operates at a maximum pressure of 10^{-3} mbar[114], which is significantly lower than the vapour pressure of most commonly employed electrolytes at room temperature. The first approach to overcome this issue dates back to the year 1971 [115]. Bruckenstein and Gadde used a porous electrode comprising Teflon, platinum and a glass frit as the interface to the vacuum system, in which the largest part of the pressure drop occurred. The technique was further refined in 1984 by Wolter and Heitbaum [114,116]. Improving the vacuum system by the use of a thin, porous Teflon-membrane covering the electrocatalyst, Wolter and Heitbaum were able to significantly decrease the delay between the detection in the mass spectrometer and the electrochemical reaction. While Bruckenstein and Gadde's system had a significant delay of 20 s [114] between the electrochemical generation and the mass spectrometric detection of species, Wolter and Heitbaum's approach enabled them to study dynamic processes. To differentiate between the experimental approaches, Wolter and Heitbaum named their method differential electrochemical mass spectrometry (DEMS) as opposed to the electrochemical mass spectrometry (EMS).

2.2.2 Dual thin-layer cell

Several different cell designs are available for use in a DEMS-system and have been reviewed in detail in the literature [112,113]. There are cells employing solid electrodes [117-120] or porous electrodes [114,121-123]. The dual thin-layer cell developed by Jusys and Baltruschat [119], which is mostly used during this work, shall briefly be discussed. While the working principle has not changed since 1999, several improvements have been made, such as the number of capillaries has been increased from four to six to optimize the flow conditions. A schematic drawing of the dual thin-layer cell used in this work is given in Figure 2.6. The electrolyte enters the cell at the inlet and flows to the upper compartment, where the working electrode (WE) is situated. The volume of the upper compartment is defined by the number and thickness of the Teflon O-rings. The electrolyte then leaves the upper compartment through six, centro-symmetrically aligned capillaries and enters the lower compartment, where a connection to the vacuum of the mass spectrometer (MS) is established via a porous Teflon membrane and volatile species can evaporate. Finally, the electrolyte leaves the cell via a channel connected to the lower compartment. To avoid electronic oscillations, which are related to the high electrolyte resistance due to the thin-layer geometry, a set of two counter electrodes (CE) is used. One is situated at the electrolyte outlet (CE1), the other close to the inlet (CE2), where also the reference electrode (RE) is placed. CE2 is connected to a high resistance (usually 1.1 MΩ), while CE1 is directly contacted by the potentiostat to minimize the Ohmic potential drop between WE and RE.

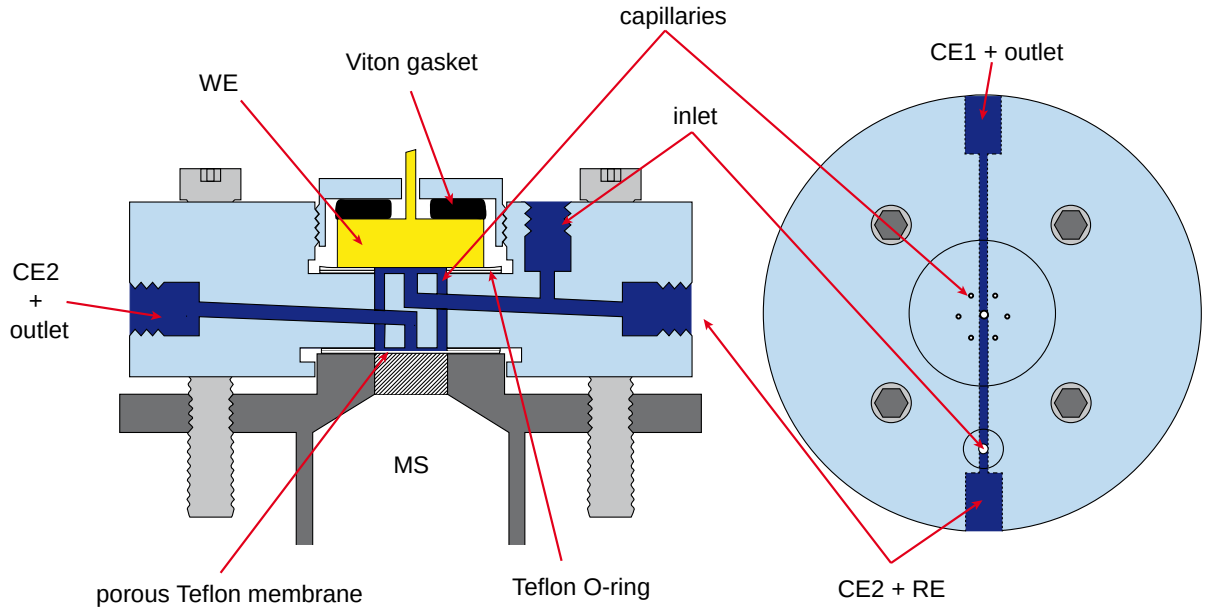

Figure 2.6. Dual thin-layer flow through cell. The left part shows a side view of the cell, while in the right part a top view is shown. For a detailed description of the cell, refer to the text. Modified after Bondue *et al.* [120].

2.2.3 Interface between Electrolyte and Vacuum: Capillarity

The key element in the cell described above, as well as most other *in situ* mass spectrometry set-ups [113,114] is a non-wetting membrane, which serves as an interface between liquid phase and the vacuum. The membrane has to be non-wetting in order to prevent electrolyte leaking into the vacuum. Moreover, the membrane needs to be porous and the pores must not be flooded to ensure sufficient mass transport. If the membrane was non-porous, the volatile species had to diffuse through the polymer of the membrane. On the other hand, if the pores were flooded, the volatile species had to diffuse through the liquid layer, which is also a quite slow process as compared to the diffusion of species in the gas phase. Unfortunately, the criterion of non-wettability greatly reduces the number of electrolytes, which can be used in a classical DEMS-experiment employing a porous Teflon-membrane as an interface.

The phenomenon of capillarity is usually described in terms of the Young-Laplace equation:

$$\Delta p = \gamma \left(\frac{1}{R_1} + \frac{1}{R_2} \right) \tag{2.16}$$

In eq. (2.16), Δp is the pressure difference across the interface (p_{inside}-$p_{outside}$), γ is the surface tension and R_1 and R_2 denote the principal radii which describe the shape of the curved meniscus, which are equal for spherical geometry. In the case of non-complete wetting, the liquid meets the capillary wall at an angle θ (Figure 2.7). From simple geometric considerations it follows that $R = r/\cos(\theta)$. Inserting this relation into eq. (2.16) and considering that $R_1 = R_2$ leads to:

$$\Delta p = \frac{2\gamma \cos(\theta)}{r} \tag{2.17}$$

For contact angles of θ>90°, the cosine becomes negative and thus, the pressure difference across the interface becomes negative. In the classical experiment, where the capillary is pointing upwards (Figure 2.7, left), this leads to a capillary depression. However, in the case of the DEMS-interface the situation is slightly different, as the capillaries point downwards. For a wetting electrolyte this would mean that the capillary force and the gravitational force act in the same direction and thus, the capillary is completely flooded.

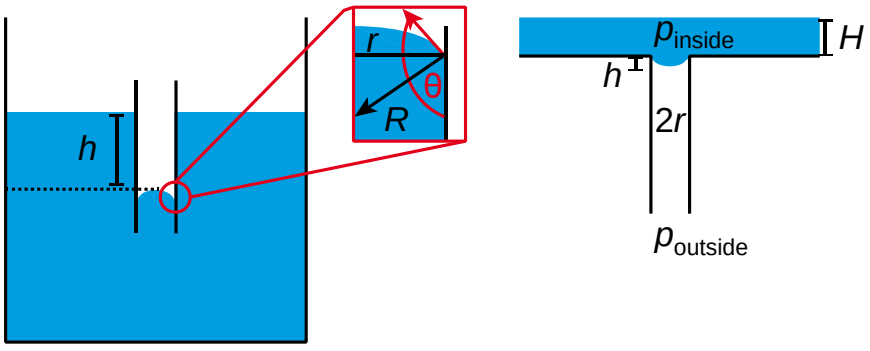

Figure 2.7. Illustration of the capillarity effect.

The pressure difference across the interface in the DEMS-system can be expressed as follows: The pressure outside is the pressure within the vacuum system and can be approximated as zero. The pressure inside of the liquid in the capillary is constituted as follows:

$$p_{outside} = p_{atm} + (h + H)\rho g \tag{2.18}$$

In eq. (2.18), p_{atm} denotes the atmospheric pressure which rests on top of the liquid layer, h is the height of the liquid within the capillary, H is the height of the liquid layer above the capillary, ρ is the density and g is the gravitational constant. Typically, the total height $h + H$ is of the order of some mm (or only µm for thin-layer geometries). Taking g as 10 $m^2 s^{-1}$ and using a typical density of 1000 kg m^{-3}, the hydrostatic pressure at the bottom of a 10 mm column equals 100 Pa or 10^{-3} bar, which is only one thousandth of the atmospheric pressure and thus, can be neglected. With these assumptions, Wolter and Heitbaum estimated the maximum allowable pore radius as 0.8 µm for an aqueous electrolyte (γ = 72 mN/m[124]).

2.2.4 Interface between Electrolyte and Vacuum: Evaporation

A second important aspect regarding the choice of electrolyte is its vapour pressure. Even if the liquid does not leak into the pores, substantial evaporation at the interface has to be avoided to maintain a low pressure in the analyser. The evaporation rate is mainly determined by the flux through the thin pores, which usually have a diameter of d = 0.02 µm[120,125] and a length of l = 50 µm[120,125]. To determine the flow conditions in the capillary the mean free path of the molecules Λ has to be considered, which is given by eq. (2.19) [126], where d_{mol} is the diameter of the molecule and the other parameters have the usual meaning:

$$\Lambda = \frac{k_B T}{\pi \sqrt{2} d_{mol}^2 p} \tag{2.19}$$

Assuming a vapour pressure of 3170 Pa at 298 K [127] and a diameter of the water molecule of d_{mol}= 0.3 nm, a mean free path of 3.2 µm is calculated, which is significantly larger than the pore diameter. Therefore, molecular flow can be assumed[114]. The flux of species from the cell to the vacuum for the conditions of molecular flow can be written as follows, where L is the conductance of the pore and p_1 is the vapour pressure of the solvent, which is usually large as compared to the pressure in the vacuum system:

$$\begin{aligned} j &= L \frac{\Delta p}{RT} \\ &\approx L \frac{p_1}{RT} \end{aligned} \tag{2.20}$$

As the pores can be described as long, narrow tubes, their conductance is given by eq. (2.21) [126] with A as then cross-section of the one pore, which is also known as the Knudsen-Dushman equation:

$$L = \frac{4}{3}\frac{d}{l} \cdot L_{short} = \frac{4}{3}\frac{d}{l} \cdot A \cdot \sqrt{\frac{RT}{2\pi M}} \tag{2.21}$$

Thus, the final equation for the flow is:

$$j = \frac{p}{RT} \cdot \frac{4}{3}\frac{d}{l} \cdot A \cdot \sqrt{\frac{RT}{2\pi M}} \; . \tag{2.22}$$

Substituting the relevant parameters (T = 298 K, p = 3170 Pa [127], M = 18 g mol^{-1}, d = 0.02 µm, l = 50 µm), a total flux of 3.2x10^{-17} m^{3}s^{-1} per pore is calculated. The total number of pores N_p is directly related to the surface area of the membrane A_M via $N_p = \varphi \bullet A_M/A$, where φ represents the porosity (φ = 0.5 in this case). Multiplying eq. (2.22) with this expression and assuming a membrane area of 0.3 cm^2, the total flux J is 1.5 µL s^{-1} or 0.1 mL h^{-1}. Interestingly, the same result is obtained if Knudsen diffusion within the pores is assumed [128]. In the case of Knudsen diffusion, usually Fick's first law for gases is invoked (again assuming that the pressure at the vacuum site is negligible):

$$j = -D\frac{p}{RT} \cdot \frac{1}{l} \tag{2.23}$$

The diffusion coefficient is readily obtained from Kinetic Gas theory:

$$D = \frac{d}{3} \cdot \sqrt{\frac{8RT}{\pi M}} \tag{2.24}$$

Substituting eq. (2.23) in eq. (2.24) and rearrangement gives the following expression:

$$j = -\frac{p}{RT} \cdot \frac{1}{l}\frac{d}{3} \cdot \sqrt{\frac{8RT}{\pi M}}$$

$$= \frac{p}{RT} \cdot \frac{1}{l} \cdot \frac{d}{3} \cdot \sqrt{\frac{16RT}{2\pi M}} \tag{2.25}$$

$$= \frac{p}{RT} \cdot \frac{d}{l} \cdot \frac{4}{3} \cdot \sqrt{\frac{RT}{2\pi M}}$$

Equation (2.25) is exactly the same equation as eq. (2.22). To maintain a low pressure in the ionization chamber a large fraction of the evaporating species have to be removed via a vacuum pump. The general relationship between the pumping speed of a vacuum S, the vapour pressure (p_V) and the total flux of species normalized to the surface area of the membrane (J_M) under stationary conditions is shown in eq. (2.26):

$$p_V \cdot S = \varphi \cdot J_M \cdot A_M \cdot \frac{RT}{p} \tag{2.26}$$

If a pressure of 10^{-3} mbar is to be maintained, a minimum pumping speed of 38 L s^{-1} is needed, substituting the values from above. However, with the usual pumping speed of 200 L s^{-1} also larger surface areas of 1 cm^2 are accessible [114]. Alternatively, one can calculate the maximum allowable product of the vapour pressure and molar mass for a given pump speed and surface area:

$$\frac{p_V}{\sqrt{M}} = \frac{p \cdot S}{A_M} \cdot \frac{3}{4} \cdot \frac{l}{d} \sqrt{\frac{2\pi}{RT}} \qquad (2.27)$$

$$p_V = 63 \cdot \frac{\text{Pa mol}^{1/2}}{\text{kg}^{1/2}} \sqrt{M}$$

The relation given in eq. (2.27) is displayed in Figure 2.8 for different solvents typically used in our laboratory.

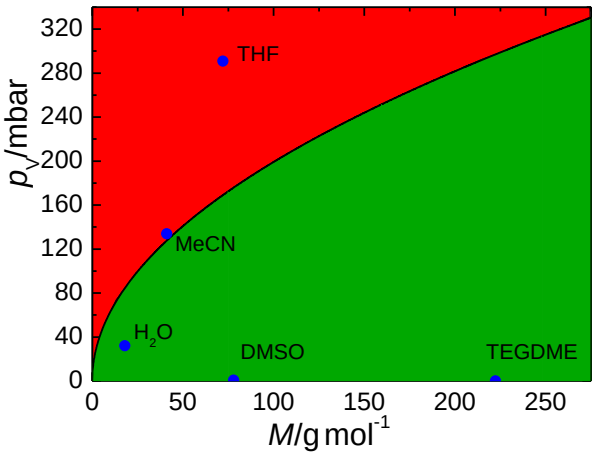

Figure 2.8. Maximum allowable vapour pressure as a function of molar mass. Only solvents in the green area have a sufficiently low vapour pressure. However, the surface tension is even more important property of the solvent and thus, the vapour pressure usually is not that critical.

2.2.5 Vacuum System

The set-up of the vacuum system is shown schematically in Figure 2.9. It comprises two pumping stages which are separated via a circular aperture serving as a differential stage. The first stage contains the ionization chamber and is pumped via a 200 L s^{-1} turbomolecular pump (TPU1), which reduces the pressure close to the ion source to 10^{-5}–10^{-4} mbar, depending on the vapour pressure of the solvent. The second stage, which comprises the analyser (here: quadrupole analyser), is pumped to 10^{-6}–10^{-5} mbar by the second turbomolecular pump (TPU2). Behind the mass filter, a secondary emission multiplier (SEM) is situated amplifying the signals. The overall low pressure in the analyser is required to guarantee a sufficient free mean path for the analyte in the quadrupole. Moreover, residual gas molecules in the secondary electron multiplier (SEM) can be ionized by signal electrons. The ionized gas molecules are then accelerated into the multiplying surface and create further signals, which are not associated with the original process.

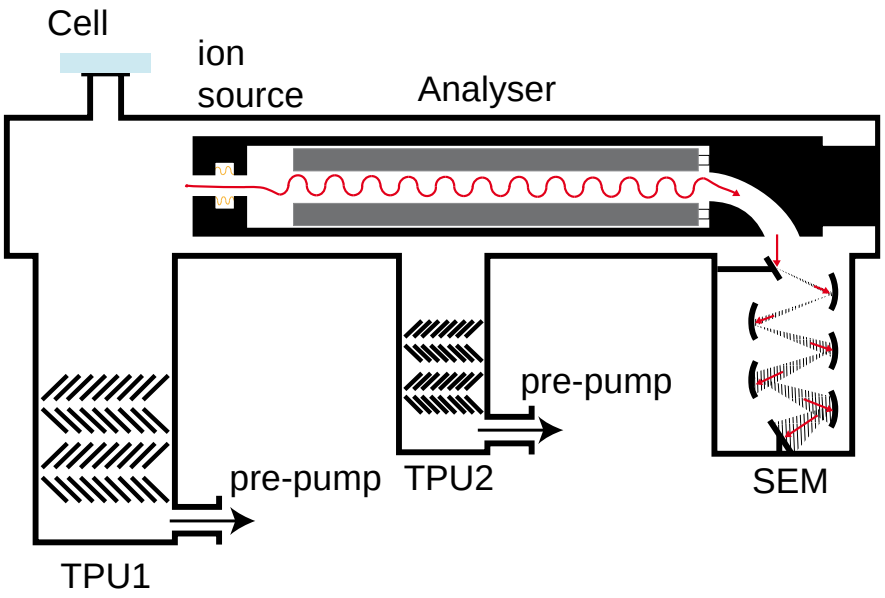

Figure 2.9. Schematic drawing of the vacuum system. TPU: turbomolecular pump, SEM: secondary emission multiplier.

An important aspect for optimizing the mass spectrometer's sensitivity are the settings of the ion source (in this case a cross-beam source equipped with Rhenium filaments). One of these parameters is the acceleration voltage, which determines the energy of the electrons. In the present set-up, an acceleration voltage of 100 V was used, while usual reference spectra are recorded at 70 V. The dependence of the ionization cross section on the energy of the electrons used for ionization is shown in Figure 2.10 a.

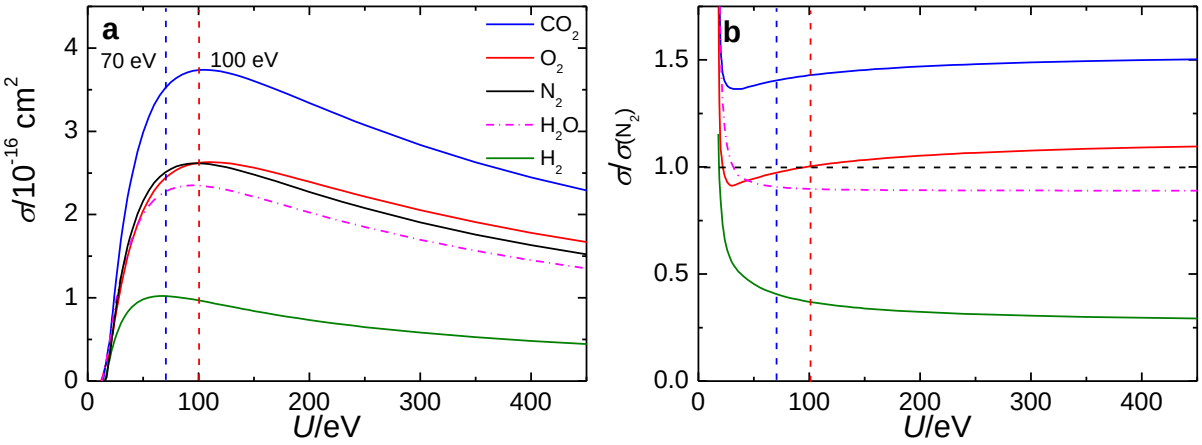

Figure 2.10. Dependence of the ionization cross-section on electron energy. **a**. Absolute cross-section. **b**. Relative cross-section with respect to the cross-section of N2. Data based on the Binary-Encounter-Bethe model[129].

As can be seen, the cross-section sharply increases with electron energy and has a maximum at approximately 100 eV. For all gases shown in Figure 2.10 a, the ionization cross section and thus, ionization probability, is larger at 100 eV as compared to 70 eV, making this ionization energy the optimum choice to maximize sensitivity for small molecules. For larger molecules exhibiting significant fragmentation, the choice of the electron energy is more complicated. The dependence of the ionization probability on the chemical nature of the

analyte is usually expressed by the relative ionization probability with respect to a standard molecule, e.g. N_2. This is shown in Figure 2.10 b. One can clearly observe that also the relative ionization probability is a function of the electron energy.

2.2.6 Calibration of the Mass Spectrometer

While the direct outcome of the mass spectrometer is an ionic current, one usually seeks to correlate this ionic current to the absolute flux of species or partial pressure of the analyte. However, as shown in Figure 2.10, the cross-section for instance, which is directly related to the ionization probability, depends on the nature of the analyte. Moreover, other factors such as the emission current (i.e. the current flow caused by the emission of electrons from the filament) and other settings like the potential in the SEM significantly affect the relation between the flux of species into the MS and the resultant ionic current. Therefore, it is mandatory to calibrate the system for a specific analyte. This is usually done via a calibration leak experiment, where a known flux of the analyte is admitted to the MS and the ionic current is measured [113,123]. The calibration constant of the system, K^o, is then obtained from the ionic current for mass I (I_i) and the flux of species into the mass spectrometer j_i via eq. (2.28):

$$I_i = K^o \cdot \left(\frac{dn_i}{dt} \right) = K^o \cdot j_i \tag{2.28}$$

While eq. (2.28) accounts for all settings in the mass spectrometer, other factors such as the cell geometry and the transfer efficiency N for the transfer of volatile species from the liquid phase to the vacuum are not considered[113]. If the volatile species are produced electrochemically, it is convenient to correlate the ionic current with the Faradaic current I_F, which changes eq. (2.28) to eq. (2.29), where z is the electrochemical valence[113]:

$$I_i = K^o \cdot N \cdot \frac{I_F}{zF} = K^* \cdot I_F / z \tag{2.29}$$

The calibration constant K^* includes properties of the mass spectrometer as well as the transfer efficiency within the cell. However, it is still assumed that the current efficiency, i.e. the share of the faradaic current which flows into the production or consumption of the analyte, is 100%. The calibration constant K^* is determined by using a reaction of known stoichiometry in the electrochemical measurement cell[113]. As the transfer efficiency depends on the flow rate and the cell geometry[130], the calibration reaction has to be carried out under the same experimental conditions. Using the thus obtained calibration constant, the (apparent) flux of species $\dot{n}$ into the mass spectrometer can be calculated according to eq. (2.30):

$$\dot{n} = \frac{I_I}{K * F} \tag{2.30}$$

The flux *j* given in (2.30) is not the *actual* flux of species into the MS, but rather the flux divided by the transfer efficiency as a comparison of eq. (2.28) and (2.29) shows. However, it is useful to report these values as the number of electrons transferred per molecule of analyte can be readily obtained from the ratio between the faradaic current and the flux:

$$z = \frac{I_F}{\dot{n}F} \tag{2.31}$$

2.3 Water Contaminations

Water is a ubiquitous contaminant in non-aqueous solvents and allegedly “dry” salts may still contain a significant amount of residual water. The amount of residual water is usually given as parts per million (ppm) and refers to the ratio of the mass of water $m(H_2O)$ to the mass of the electrolyte ($m(H_2O) + m(\text{Solvent})$).

$$w(H_2O) = \frac{m(H_2O)}{m(H_2O) + m(\text{Solvent})} \tag{2.32}$$

However, due to the low molecular mass of water ($M(H_2O) = 18\ \text{g mol}^{-1}$)[131] and the usually high molar masses of organic electrolytes, even a low mass fraction of water represents a high molar concentration. The relation between the molar concentration of water, $c(H_2O)$ and its mass fraction is given in eq. (2.33), where ρ denotes the density of the solution.

$$c(H_2O) = \frac{w(H_2O) \cdot \rho}{M(H_2O)} \tag{2.33}$$

Assuming that the density of the solution equals the density of the pure solvent at low mass fractions, the molar concentration of water can easily be calculated via eq. (2.33). The corresponding relations between the concentration of water and its mass fraction in ppm are shown in Figure 2.11 for DMSO (black, $\rho(\text{DMSO})$ [132] = 1.094 g cm^{-3}) and tetraglyme (red, $\rho(4G) = 1.007$[133]) as a solvent.

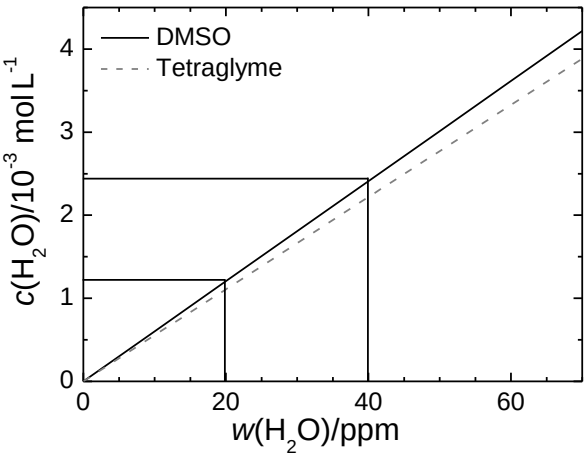

Figure 2.11. Molarity of water as a function of its mass fraction. The red line shows the relation for the solvent tetraglyme, the black line is the analogous line for DMSO.

As can be seen, even at low water contents of 20 ppm, which is a typical value achieved in the experiments, the concentration of water is still of the order of 1 mM. This concentration is in the range of the oxygen concentration (2 mM at 1 bar in DMSO, 4mM in tetraglyme [130]) and therefore might play an important role during the ORR. Markovic *et al.* even claim that the residual amount of water plays the key role in an aprotic electrolyte and that in the total absence of water, no ORR would occur [134]. The authors assume that water is preferentially present in the Helmholtz layer due to its high electric permittivity and that its concentration even at 1 ppm is large enough to saturate the double-layer. The number of surface atoms at polycrystalline platinum is roughly 2.2 nmol cm^{-2} (calculated charge of a monolayer of adsorbed hydrogen, 210 µC cm^{-2}) [135] which means that even for a water fraction of 1 ppm there is a 5000-fold excess of water molecules as compared to surface atoms (assuming a surface area of 0.2 cm^2 and a total electrolyte volume of 35 mL as in a typical experiment). However, investigations of the double-layer at a platinum surface in a mixture of tritium-labelled water and DMSO by Wieckowski *et al*. via radiometry showed the existence of a chemisorbed layer of DMSO on the platinum surface (the pronounced presence of water in the first adsorption layer was excluded due to the high surface activity of DMSO as shown by the effect of small amounts of DMSO added to an aqueous electrolytes) [136]. The second ad layer preferentially contains water molecules and Temkin-adsorption behaviour without potential-dependence of the adsorption process was identified. At a mass fraction of 33 ppm (corresponding to 2 mM or a mole fraction of x = 0.14) the authors observed half a monolayer of water on top of the chemisorbed DMSO layer. At the lowest concentration used in the study (x = 0.04 or 8.5 ppm) the surface coverage only makes up 10% of a monolayer. Thus, at 1 ppm, which is equal to a concentration of 0.06 mM or a mole fraction of 0.004, the becomes essentially zero (in fact, extrapolating Wieckowski's data to this mole fraction yields a value of −0.024 monolayers due to the limited accuracy of the measurement). Water in the double-layer has also been observed via surface-enhanced Raman spectroscopy on silver electrodes in

acetonitrile [137] and propylene carbonate solutions [138] for concentration as low as 0.4 mM. Increasing the water concentration to 9 mM leads to a broadening of the OH-vibration band indicating the formation of hydrogen-bonds within the double-layer.

It is important to note that the solvent itself does not necessarily contain a large amount of water (e.g. 3 ppm for DMSO stored over molecular sieve). Therefore, it is of utmost importance to state the water content of the electrolyte. For instance, preparing a solution of 0.1 M $LiClO_4$ in DMSO increases the water content up to 13 ppm[139]. Moreover, if the experiment is carried out under ambient conditions, i.e. outside of a glovebox, it is most reasonable to also state the water content *after* the experiment to get an estimator for the maximum water content.

It should be noted that the water content of the atmosphere inside of a glovebox is not a good indicator for the overall water content of the experiment as long as it remains in the usual range below (typically less than 1 ppm). Although the value of the amount of water inside the glovebox is also given in *ppm*, it usually refers to the volume instead of mass [140]. Assuming ideal behaviour of the gases this means that at a water content of 0.1 ppm and a box pressure of 1 bar, the partial pressure only equals 10^{-4} mbar. Furthermore, the oxygen used for purging contains a similar amount of water (see below)

A further possible source of water contamination comes from the gases used to saturate or purge the electrolytes: High-purity Argon (Alphagaz 1) usually contains less than 2 ppm (mol) H_2O, while the oxygen used in our Lab (Alphagaz 2) only contains less than 0.5 ppm (mol) H_2O. During an experiment, the solution is purged with argon, oxygen or and argon-oxygen mixture. Let the flow rate be 15 L h^{-1}, then the flow of Argon would be 170 µmol s^{-1} (at 298 K and 1 bar pressure) or 0.3 nmol s^{-1} water. Now, let us assume that the solubility of water in DMSO is infinitely large, i.e. that Henry's constant is infinite (which is certainly not reasonable, but helps to evaluate the worst-case scenario) and that the adsorption of water is also fast. This would mean that the total amount of water of 0.3 nmol s^{-1} is adsorbed by the electrolyte. Inserting the volume of a typical cell (0.035 L) gives us a final increase of the water concentration of 9 nmol L^{-1} s^{-1}. Therefore, even after 10 h of constant flushing, the water content only rises by 0.3 mmol L^{-1} and might be regarded as negligible.

2.4 Digital Data Acquisition and Generation

Nowadays data acquisition is usually fully digitized and implemented into the functionality of the actual measurement device, such as a potentiostat. While this circumstance is appealing in terms of effectivity, as users do not have to operate several separated devices, it also bears the danger of the device being treated as a "black box", which might aggravate trouble shooting. However, in our laboratory, most of the potentiostats are homebuilt and digital data acquisition is mostly achieved via external analog-to-digital converters (ADC). As one of the tasks during the course of this work was to optimize the data acquisition and to also implement options for digital data generation, the following section will be devoted to a short discussion

of digital data acquisition (DAQ) and generation. Due to the large variety of different DAQ systems available, the discussion will focus on the DAQ as it is done in our laboratory. The principal structure of a digital data acquisition system is shown in Figure 2.12.

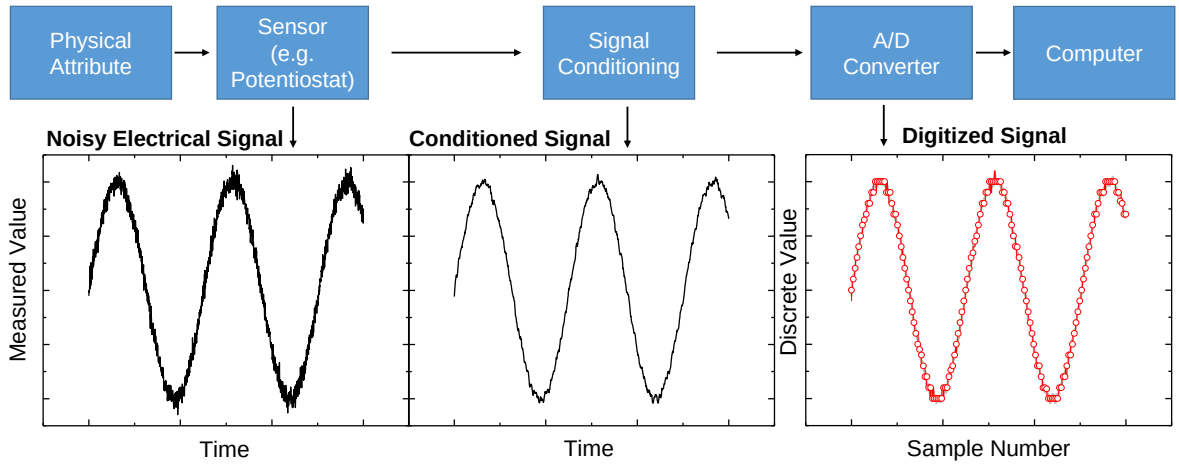

Figure 2.12. Schematic drawing of a digital data acquisition system. The red dots represent the digitized data points.

The physical attribute, e.g. the potential, is first measured by a sensor, which in our case might be the potentiostat. Eventually, the signal is conditioned via an RC-circuit serving as a filter which dampens the random noise. The pre-conditioned signal is then usually amplified and digitized via an ADC, which essentially translate the time-domain into a “sample-domain”, as the previously continuous signal is now represented by discrete values. While the removal of noisy frequencies might be generally desirable, care has to be taken if a high time resolution, for instance for a potential step experiment is needed.

2.4.1 Types of Measurements

The general data flow from the (conditioned) signal to the PC buffer is shown in Figure 2.13. At the first stage, the input signals are distributed successively connected to the instrumentation amplifier. This is necessary as common A/D boards offer more input channels than instrumentation amplifiers and ADCs.

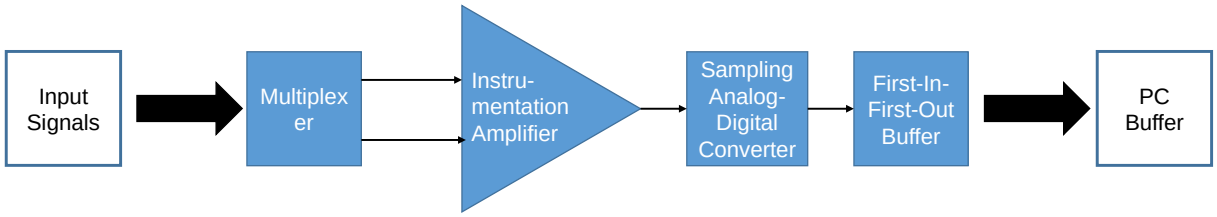

Figure 2.13. Input signal to the PC buffer. Modified according to the schematic drawing given by *National Instruments* [141].

A first consideration for optimizing the measurement is the decision between differential measurements, where two input channels of the A/D board are used to read one signal, and single-ended measurements, in which only one channel is occupied and the signal is measured against the measurement device ground (Figure 2.14). The advantages of

measuring in differential are a more efficient noise reduction as compared to single-ended measurements (noise on both channels is cancelled out) and the avoidance of ground loops. A ground loop affects the measurement if the ground of the signal source is different from the ground of the measurement device and might be a problem when performing single-ended measurements. On the other hand, single-ended measurements only need half as much channels than differential do and therefore are a more cost-effective alternative. However, as one is usually interested in noise reduction, most delicate measurements are operated in differential mode.

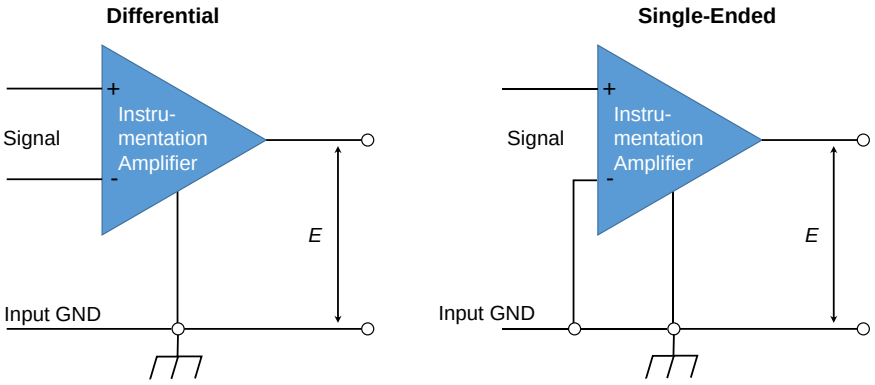

Figure 2.14. Differential vs. single-ended measurement.

2.4.2 Multiplexers

The measurement of more than one signal simultaneously requires either several dedicated instrumentation amplifiers and ADCs or a multiplexer, (MUX) which routes the signals to the instrumentation amplifier. A simplified sketch of a MUX is shown and the connection to the instrumentation amplifier via a switched-capacitor is shown in Figure 2.15.

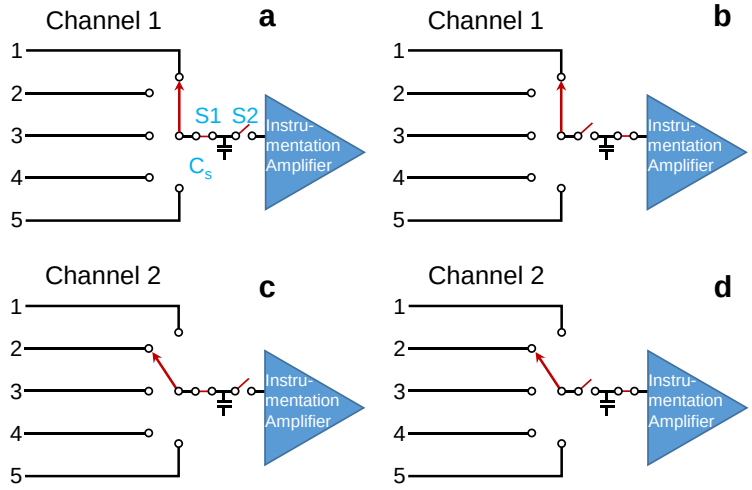

Figure 2.15. Schematic drawing of a multiplexer. **a-d** shows the MUX at different stages of operation. For details refer to the text.

When channel 1 is sampled, switch S1 is closed and the capacitor C_s is charged. In the next step, S1 is opened and S2 is closed. Consequently, the voltage resting on C_s is passed to the instrumentation amplifier. However, if the next sample is sampled, the voltage on C_s induced

by channel 1 is still present and the charge flows backward through channel 2, which is called *ghosting* [142]. The time constant of this leak current is significantly affected by the output impedance of the source. Therefore, if the channels are sampled to fast the signal measured on channel 2 will be affected by the signal of channel 1. The time the ADC has to be connected to each analogue input channel to attain a certain accuracy is called the settling time for multichannel measurements. The typical multichannel settling times of a multichannel measurement with PCI 6221 DAQ-board (National Instruments) are shown in Figure 2.16. For a source impedance below 100 Ω the settling time of a full-scale step with an accuracy of 90 ppm of the step size requires 7 µs to settle, which equals a sampling rate of 143 kHz.

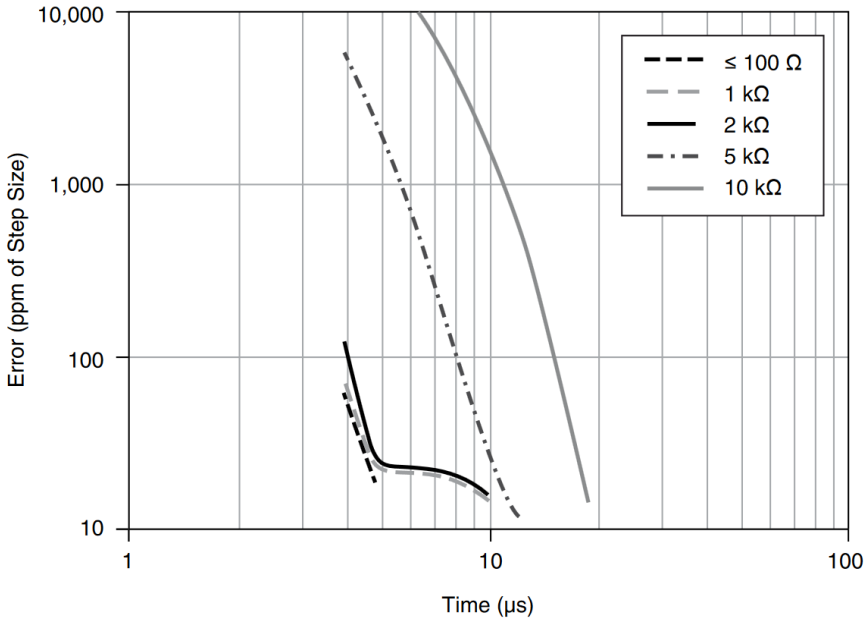

Figure 2.16. Settling times for multichannel measurements. Taken from the datasheet for the NI PCIe 6321 DAQ board [143].

A strategy to avoid ghosting caused by high input impedances and largely varying inputs is to optimize the sequence of channel reading. For instance, grounded channels can be inserted in between two channels to minimize ghosting and furthermore, also to reduce channel cross-talk, which is higher between adjacent channels (−75 dB vs. −90 dB [143]). The latter is especially important for potentiostats offering small maximum output voltages for the current channels. Let us assume that at a potential of 2 V a current of 125 µA flows and the maximum output voltage of the current channel is 0.125 V. Under ideal conditions, the current of 125 µA is exactly translated to the full range potential of 0.125 V. In this case, the error in the current measurement due to cross-talk between the channels carrying a voltage of 2 V would be 0.5%. However, in the more realistic case of a current range of e.g. 500 µA equalling 0.125 V, the error due to cross-talk is already 2%. Using a non-adjacent channel (−90 dB dampening) reduces this error to only 0.2%.

2.4.3 Instrumentation Amplifier

After being routed via the MUX, the signal is amplified via the instrumentation amplifier to ensure that maximum resolution of the ADC is used. An important characteristic of an instrumentation amplifier is its settling time, which is illustrated in Figure 2.17. The settling time is defined as the time it takes the instrumentation amplifier to settle within a certain accuracy. Operating the instrumentation amplifier at very high frequencies might, therefore, result in loss of accuracy as the amplifier does not have enough time so settle to the desired accuracy. However, in a typical measurement a sampling rate of 75 kHz (e.g. 3 channels à 25 kHz), the settling time error is not of great significance (cf. Figure 2.16).

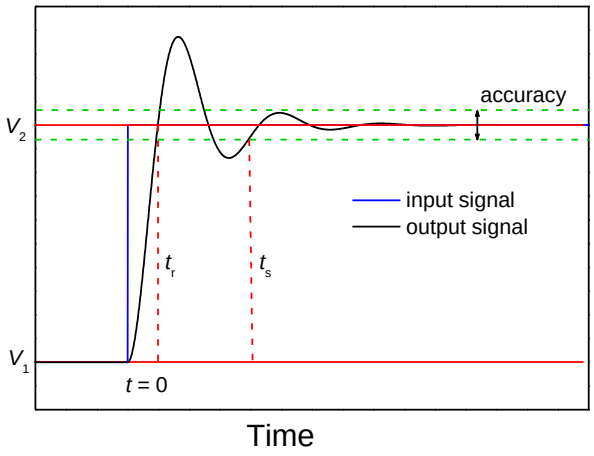

Figure 2.17. Settling time of an instrumentation amplifier. The curve was simulated applying the standard equations for an underdamped vibration.

2.4.4 Analog-to-Digital Converter (ADC)

The amplified signal is finally digitized in the ADC, which writes data to the first-in-first-out (FIFO) buffer. While there are many different technical realisations of ADCs, resolution is always an important parameter as it determines the magnitude of the quantization error and thus, influences the signal-to-noise ratio (SNR). Moreover, the minimum detectable change in, for instance, potential (E_{min}) is directly related to the resolution (Q) and the maximum input range of the ADC (V_{Range}):

$$E_{\mathrm{min}} = \frac{V_{Range}}{2^{Q}} \tag{2.34}$$

For a typical ADC with a resolution of 16 bit and an input range of 20 V (-10 to +10 V), the minimum detectable change equals 0.3 mV and thus, is not of great concern for classical electrochemistry. However, if the maximum output voltage of the current-to-voltage converters is very low and high current ranges are chosen to measure currents, the resolution also plays a role in classical electrochemistry: For an output voltage of 0.125 V and a current range of 1.25 mA the minimum detectable current is 3 µA.

The quantization error due to the finite step-size associated with conversion process is illustrated in Figure 2.18 (note that the finite time resolution of the digitalization process has

been neglected in this figure). As the steps have a finite size (Figure 2.18a), the analog signal has to be rounded. The difference between the signal and the rounded signal is shown in Figure 2.18b and expectedly increases for larger step size, which correlate with a lower resolution.

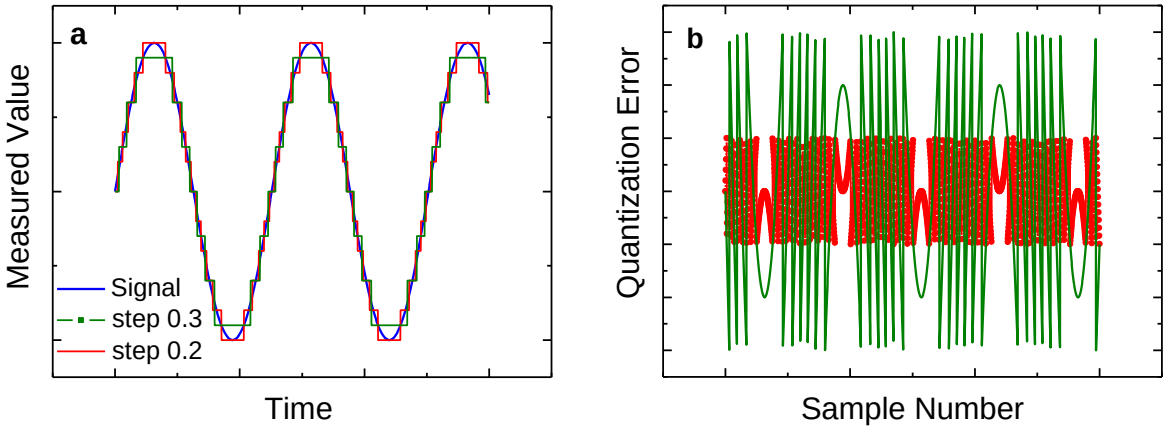

Figure 2.18. Quantization error. **a**. Illustration of the digitization of the signal. **b**. Quantization error for different step sizes calculated as the difference between the signal and the red or green curve.

2.4.5 Clocks

The whole process of analog-to-digital conversion is driven by highly precise clocks: The sample clock and the convert clock. Both clocks are derived from the master time base (20 MHz for PCI 6221 [144]) and therefore, should be integer divisors of the master time base. For a multichannel application with three channels, the timing of data acquisition can be illustrated as shown in Figure 2.19. The sample clock defines when the channels should be sampled. The rate of the sample acquisition is usually directly defined by the user and defines the time resolution of the sampling process. However, for a multichannel acquisition, a second clock is needed, the convert clock. The convert clock causes the AD conversion for each distinct channel and therefore has to operate at a frequency, which is at least three times larger than the rate of the sample clock in this example. The inverse of the conversion frequency gives us the interchannel delay, which gives us the maximum settling time in our multichannel acquisition and also conveys information on how simultaneous the data points from the different channel rally are.

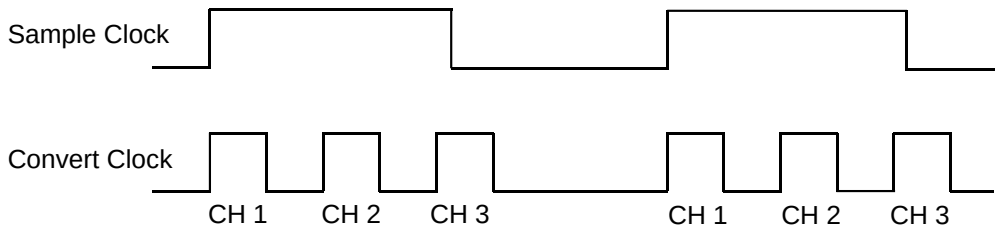

Figure 2.19. Sample clock and convert clock for multichannel data acquisition. The convert clock controls the conversion of a single channel, while the sample clock controls the aggregate.

A typical interchannel delay shall be briefly discussed in an example. For a sampling rate of 25 kHz, the convert clock therefore has to operate at 75 kHz. As 75 kHz is not an integer divisor, which is required by the hardware (as of 20 MHz ($20x10^6$ Hz/$75x10^3$ Hz = 266.67), the actual conversion rate is 75187.97 Hz. The resulting interchannel delay equals 13.3 µs. According to Figure 2.16, this time is sufficient for achieving the maximum accuracy of 15 ppm for a full scale step even if the output impedance of is larger than 5 kΩ. However, if higher sampling rates of 50 kHz are used, the interchannel delay decrease to 6.65 µs, which is insufficient for maximum accuracy. For significantly slower measurements (i.e. 10 kHz per channel) another complication arises: In a normal application, one seeks to sample data from multiple channels simultaneously. However, as long as only one ADC is available, the data has to be sampled sequentially and the interchannel delay gives the time separation between each channel and results in asynchronicity. In the case of 2-channel measurement with a sampling rate of 20 kHz, the interchannel delay is 25 µs, which is more than sufficient in terms of settling time error, but introduces some degree of asynchronous behaviour. Therefore, the standard NI-DAQmx driver, the maximum interchannel delay is set to the minimum interchannel for the specific device (1/250 kHz or 4 µs for PCI 6221 [144]) delay plus 10 µs, resulting in a default delay of 14 µs unless higher rates are required. As the experiments in our laboratory do not require channels to be measured completely simultaneous, the interchannel delay is usually maxed via the software [145].

2.4.6 Onboard First-in-First-Out (FIFO) Buffer and the PC Buffer

The onboard FIFO buffer on the PCI 6221 is a circular buffer which can store up to 4095 samples generated by the ADC [144,146]. Starting the data acquisition task causes the PC to read from the onboard buffer (Figure 2.20). By default, this is done via the direct memory access (DMA) without using the CPU, offering high transfer rates of 20 Mb/s equalling 1.25 MS/s at 16 bit resolution. An *overflow error* will be the result if this transfer is too slow as compared to the sample generation by the ADC [147].

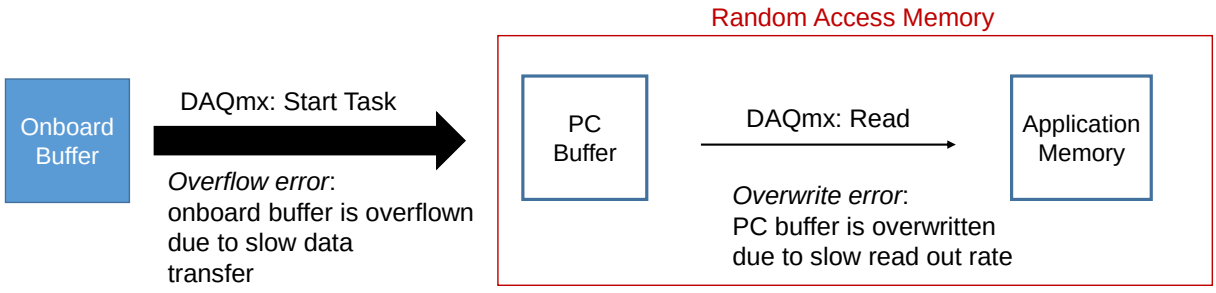

Figure 2.20. Transfer from the onboard buffer to the application memory. As soon as the DAQmx task is started, data is transferred from the onboard buffer to the PC buffer. Only the transfer from the PC buffer to the application buffer is controlled by the program and thus, software-timed.

Via the DAQmx: Read command the samples are transferred from the PC buffer to the application memory, from where the samples can be processed and saved to the hard disk.

Slowly calling the read-function results in an *overwrite error* because the samples are written faster to the PC buffer as they are read. While the *overflow error* is rather uncommon and cannot be solved programmatically, the *overwrite error* has to be avoided in the program structure [147].

2.4.7 Structure of the DAQ-Program

The DAQ-program developed for this work offers a continuous hardware-timed data acquisition. After initializing the hardware, the acquisition task is started in continuous mode, which causes the ADC to continuously convert samples and store them in the onboard FIFO buffer, from where they are transferred via DMA to the PC buffer. All these steps are hardware-timed and depend on speed of the sample clock. To avoid *overwrite errors* the following program has a producer/consumer FIFO queue. The producer's only task is to call the DAQmx Read function at a certain, user-defined rate and to transfer data from the PC buffer to the application buffer. The data is subsequently processed by two consumers. The first consumer averages the data over a certain amount of samples, puts them into an array and finally displays the data as a graph. The speed of this consumer loop is mainly determined by the size of the array where data is temporarily stored. To avoid that the consumer becomes too slow, the number of elements in the array cannot grow infinitely and at some user-defined value, old values are deleted. The second consumer loop is only active on demand and its purpose is to shuffle data from the application memory to the hard disk. To improve SNR, the data is usually averaged (note that the number of averages has to be an integer divisor of the number of samples read per readout by the producer) and then stored in ASCII format. The execution speed of this consumer is mainly given by the time it takes to actually write data to the disk because the file remains opened during the saving process.

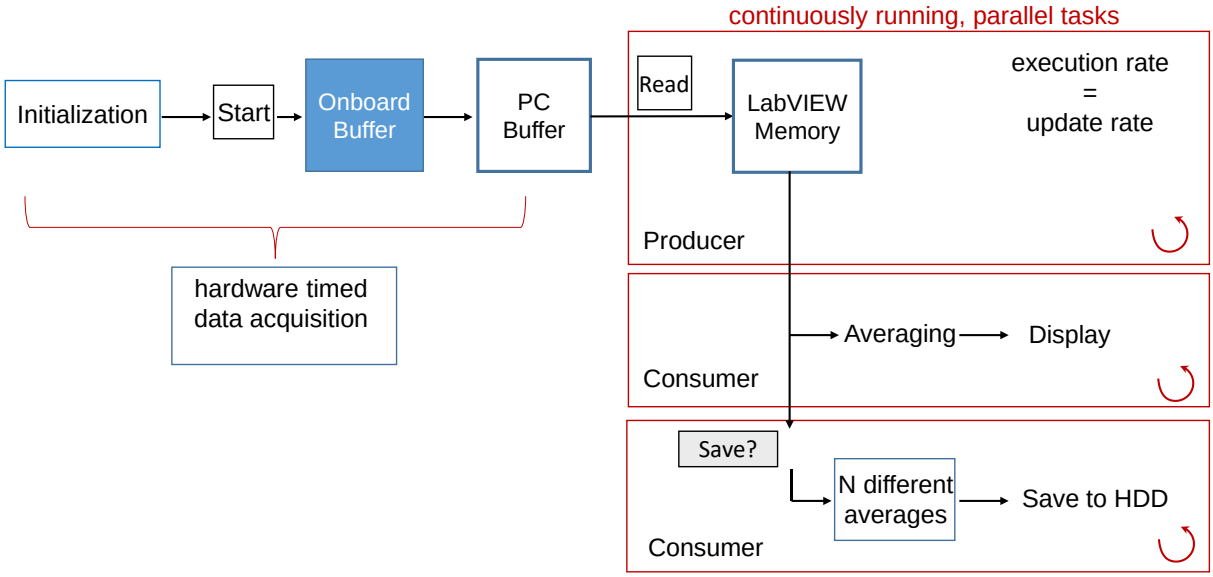

Figure 2.21. Program architecture. The data from the PC buffer is continuously read and distributed via a FIFO-buffered producer-consumer architecture.

2.4.8 Digital Data Generation

Besides data acquisition, the *National Instruments* PCI 6221 can also be used to output (pseudo-) analog data. In combination with digital data acquisition, this offers the opportunity to automatize measurements, such as programmatically switching the sweep rate at a certain potential or to change to rotation rate and much more. An important consideration again is the resolution of the digital-to-analog converter (DAC) as it defines how smooth the analog curves are. For a typical output range of ±5 V and a resolution of 16 bit, the minimum step size is 0.15 mV. An example of the analog curve produced by the DAC as compared to the truly analog curve is shown in Figure 2.22a for a sweep rate of 10 mV s^{-1}. The main problem which arises from the finite step size in an electrochemical experiment is related to the capacity of the electrochemical double layer. To shortly illustrate the problem, the electrochemical cell is represented by the electrolyte's resistance in series with the double layer capacitance, in absence of any charge transfer. Assuming a typical capacity of 20 µF and an electrolyte resistance of 100 Ω the aforementioned step of 0.15 mV results in a current spike of 1.5 µA , which decays with a time constant of 2 ms (Figure 2.22b). In order to maintain a certain sweep rate a minimum output sampling rate of $v_{sample} = v_{sweep}/u_{step}$ is necessary. For the example discussed here, the minimum sample rate for the output is 66.7 S/s and therefore, every step has 15 ms to decay. The charge passed within these 15 ms is 2.99 µC and very close to the 3 µC, which would refer to complete charging. It should be noted that the average charging current is independent of the frequency of potential steps.

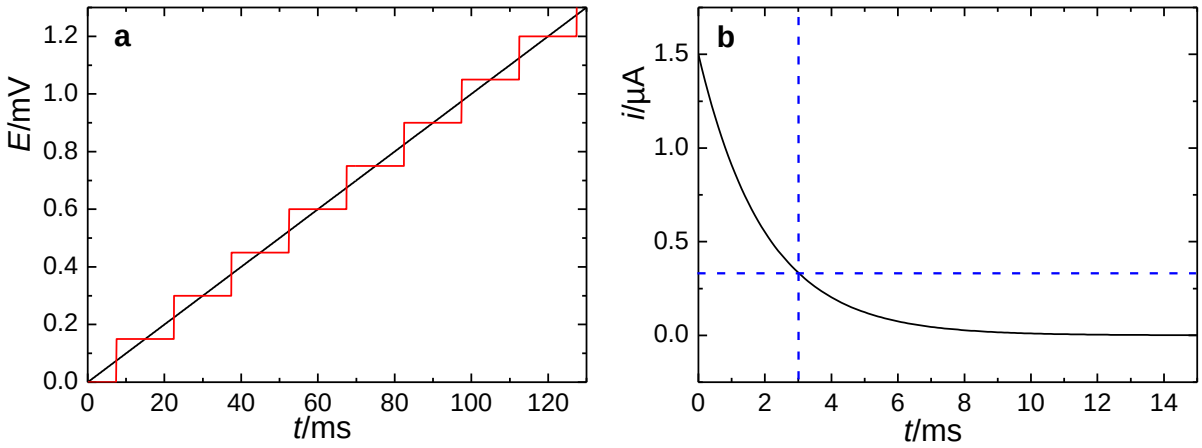

Figure 2.22. Digital data generation. **a**. The black curve shows the analog ramp, while red curve is the digital step-function representing the ramp. **b**. Current answer of a RC-circuit with C = 20 µF and R = 100 Ω to a potential step of 0.15 mV.

For a higher sweep rate of 50 mV s^{-1}, the current step cannot decay completely before a next step occurs. This situation is shown in Figure 2.23 for different resistances, where the blue line shows the current as observed for an analog signal. As can be seen from Figure 2.23 a, for a sweep rate of 10 mV s^{-1} and a resistance of 100 Ω the current decays completely before the next step. However, for higher sweep rates (Figure 2.23 b) or higher resistances, the current

oscillates and increases in the beginning before it oscillates around a limiting value. The lower the resistance, the larger the oscillation is as expected from the small time constants of the electrochemical cell.

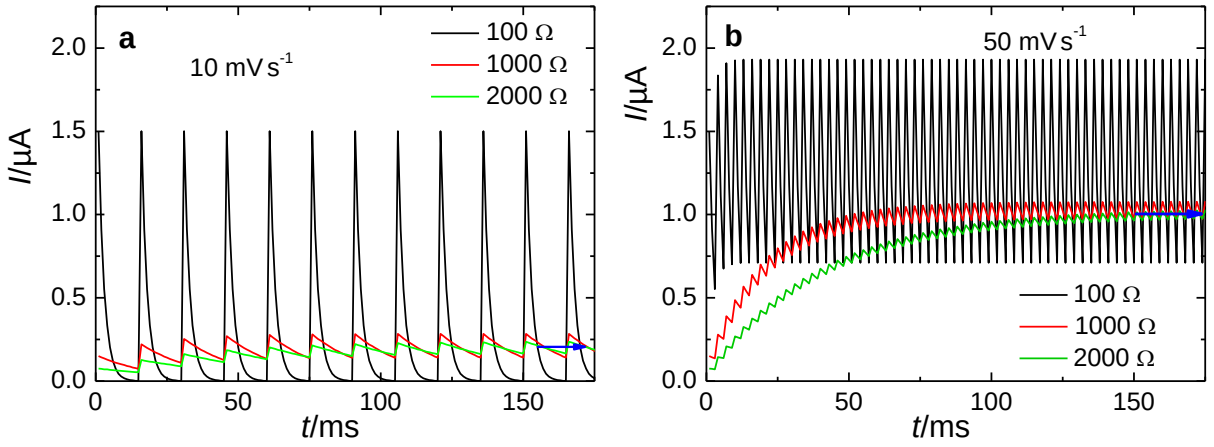

Figure 2.23. Current answer to a digital voltage ramp. a. Current answer for a sweep rate of 10 mV s^{-1} and a step resolution of 0.15 mV. b. Current answer for a sweep rate of 50 mV s^{1} and a step resolution of 0.15 mV.

While Figure 2.23 shows the current answer with a time resolution sufficient to record the maximum current, in an actual data acquisition system the current transient cannot be recorded that exactly. It therefore depends on the time resolution as well as the synchronization between digital data generation and data acquisition, how the recorded capacitive current will appear. If the data collection is, for instance, synchronized in a way that it collects one data point every 14 ms after the potential step, the measured current will almost contain no capacitive current. However, in our case the rate of data acquisition is significantly higher than the rate of steps (e.g. 20 kS/s vs the aforementioned 67 steps/s) so that the current answer is collected with a sufficiently high resolution and the current due to double-layer charging can be measured.

A last practical consideration for data generation, with which the discussion shall be ended, is its responsivity. Usually, the outputted waveform is first written to the FIFO buffer of the DAC. The DAC subsequently starts conversion and the voltage-ramp is produced. To ensure continuous conversion the buffer should never be completely empty. However, in such a buffered architecture, the DAC cannot react immediately to changes in the waveform which are made during operation of the program. This is because the DAC first has to convert samples in the FIFO, which have been stored prior to the change in the waveform. Thus, a compromise between responsivity and the risk of a discontinuity of the conversion is needed. In this work, the issue is addressed in the following way: Most importantly, the task does not allow regeneration to ensure that the output can be changed programmatically. The FIFO buffer retrieves new samples from the program environment every time the buffer is not full anymore. The FIFO size is calculated as the product of the DA sampling rate and a user-defined input delay, which represents the time between the programmatic change of the

waveform and the change of the actual output wave. Moreover, a second buffer in the software is defined, which is only half as large as the onboard buffer. This buffer ensures the software generates the waveform parallel to the DA conversion and minimizes the probability that the onboard buffer runs empty due to temporary loads slowing down the generation of waveforms by the software.

Although the digital function generator certainly has its downsides, it can be exploited to conduct whole series of experiments programmatically (as long as the electrolyte and electrode do not have to be exchanges). For example, a CV, followed by a series of potential steps, then followed by a CV with a lower sweep rate, which ends in a potential stop at a certain potential, can easily be programmed into the function generator without any further user action.

2.5 Infrared Spectroelectrochemistry

It is certainly beyond the goal of this work to give a complete overview of infrared spectroscopy or to discuss the basic mechanisms. Therefore, this section will focus on some aspects related to the combination of *operando* infrared (IR) spectroscopy and electrochemistry. Mainly two principal modes of operation are possible(Figure 2.24): the internal reflection mode, where the IR beam is totally reflected at the boundary between the internal reflection element (e.g. Si, Ge, ZnSe) [148,149] and the external reflection mode[150-152], where the IR beam passes through the boundary but is reflected at the surface of an electrode above the external reflection element (e.g. CaF_2).

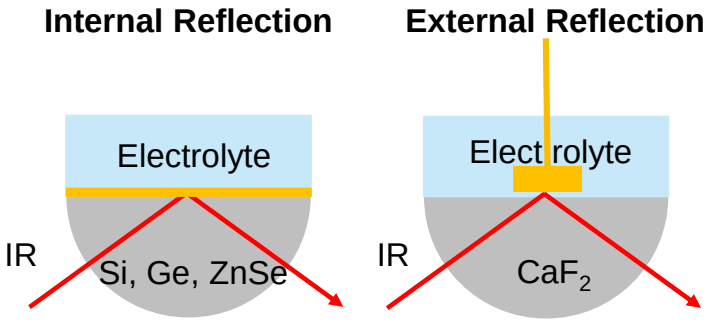

Figure 2.24. Different modes of operation of infrared spectroelectrochemistry. In internal reflection geometry, the IR beam is totally reflected at the boundary between the IR crystals and liquid phase. In external reflection geometry, the IR beam leaves the IR crystal and is reflected at a reflecting surface, which is ideally close to the surface.

The former case is called *attenuated total reflection* (ATR) infrared spectroscopy. In the context of electrochemistry, ATR is often referred to as the Kretschmann configuration [153], who used an arrangement as shown in Figure 2.24 (left) to measure optical constants of metals by the excitation of surface plasmons. In ATR-IR spectroscopy, only a highly attenuated part of the IR beam, the evanescent wave of the reflected IR beam, is used for detection [154]. The situation is additionally acerbated by the metal deposit on the internal reflection element, which prevents investigation of the electrolyte phase if the metal layer is too thick.

On the contrary, the external reflection works with the full intensity of the IR beam, which is reflected by the electrode [150,151]. However, due to the significant infrared absorption of usual solvents such as water the electrode has to be pushed as close as possible to the IR window to reduce absorption by the solvent [150,151]. Due to the very thin electrolyte layer, transport of species to the electrode surface is slow and a high resistances hampers a quick response of the electrode to changes in potential[152]. However, it has been shown in 1 M perchloric acid that the charge balance within the thin-layer can be re-established on timescales below 0.1 s due to migration effects[155,156].

In both cases it has to be kept in mind that for metals the vector of the electric fields is always orthogonal to the surface as any other orientation would be compensated by charge flow. Furthermore, dipoles that are adsorbed parallel to the surface induce a mirror dipole in the metal surface. This mirror dipole has the same dipole moment but of opposite direction and thus, cancels out the dipole moment of the adsorbed species. In contrast to that, the dipole moment of a perpendicularly adsorbed species is reinforced by the mirror dipole. Therefore, only the share of IR radiation, whose electric field vector is oriented perpendicular to the surface (*p*-polarized) can be used for detection [157]. Consequently, the angle of incident beam with respect to the surface normal should be large[152,156].

2.5.1 Historical Background

One of the earliest successful attempts to combine surface sensitive infrared-spectroscopy (IR- spectroscopy) with an electrochemical measurement goes back to 1980, when Bewick *et al*. studied the nitrogen-mediated adsorption of indole from acetonitrile[150] as well as hydrogen adsorption from aqueous solutions of sulfuric acid on platinum electrodes pushed against a Si plate as an external reflection element [150-152,158]. Bewick *et al*. coined the term *Electrochemically Modulated Infrared Spectroscopy* (EMIRS) to differentiate their approach from the simultaneously developed *Infrared Reflection-Absorption Spectroscopy* (IRRAS), which was originally developed to measure the absorption of gaseous molecules on a reflecting surface in ultra-high vacuum [159] and had also been employed to study electrochemical processes by Russel *et al.* [160]. In EMIR spectroscopy, the reflectance at different potentials was measured to investigate the potential-dependent adsorption of species [150-152]. Therefore, the intensities measured have always to be interpreted as relative to the reference potential. The potential at the working electrode is modulated with a square wave and lock-in technique in combination with a grating spectrometer. On the contrary, in IRRA spectroscopy the polarization of the IR beam is used to generate a reference spectrum, thus yielding information on the absolute intensity at a given potential[160,161].

With the advent of Fourier-transform spectrometers a new technique was developed by Pons and coworkers [162-164]. In their new approach, which they named *Subtractively Normalized Interfacial Fourier Transform Infrared Spectroscopy* (SNIFTIRS), first a spectrum was recorded

at the reference potential. Then the potential was stepped to the potential of interest and another spectrum was recorded. This step-sequence was repeated several times to enhance the signal-to-noise ratio and to reduce effects of the baseline drift. The main difference to the EMIRS approach is the significantly lower potential modulation frequency (0.01 Hz instead of 10 Hz) [161,165]. Weaver and co-workers instead coined the term *potential-difference infrared spectroscopy* (PDIRS) to emphasize that a complete normalization of the spectra with respect to the solution phase infrared spectra does not occur in the presence of adsorbing species[165]. As EMIRS, SNIFTIRS or PDIRS require that the process under investigation is essentially reversible, Weaver and co-workers introduced another approach, *single potential alteration infrared spectroscopy* (SPAIRS), where first a reference spectrum is recorded and then several sample spectra at different potentials[166]. This technique was also called *multi-step FTIR spectroscopy* (MS-FTIRS) [167].

An important milestone in the history of surface spectroelectrochemistry was the discovery of markedly enhanced intensities of the IR bands of adsorbed species on electrodes of a special morphology. This was first observed for Raman spectroscopy by Fleischmann *et al*. who studied adsorption of pyridine on silver electrodes [168], but later on also found by Hartstein *et al*. in the context of IR spectroscopy [169]. Important contributions to the understanding of the origin of surface enhancement have been made by Jeanmaire and Van Duyne [170], Albrecht and Creighton [171] as well as Osawa and coworkers, who coined the term *Surface-Enhanced Infrared Absorption Spectroscopy* (SEIRAS) for ATR-IR spectroscopy exploiting surface-enhancement [157,172-174].

2.5.2 Surface Enhanced Infrared Spectroscopy (SEIRAS)

The term surface enhancement refers to the fact that the IR intensities of adsorbates are markedly larger on certain electrodes than on others. The effect of an enhanced IR intensity has been observed and exploited in internal reflection geometry using for instance silver[174-178], gold [174,179-181] and platinum-group metals [181,182] as well as in external reflection geometry using silver [183] and platinum [184,185]. The effect is generally short-ranged and decays within 5 nm [157,173,186]. Moreover, it significantly depends on the characteristics of the metal deposit [173,187].

Today, the mechanism of surface-enhancement is believed to mainly consist of two components: an electromagnetic and a chemical mechanism [157,173,188-190]. The electromagnetic (EM) mechanism arises from the fact that the local field at the electrode's surface is increased due to an interaction of the incident IR radiation and the local plasmonic waves of the electrode [157]. This mechanism strongly depends on the morphology of the surface, where structured surfaces exhibit larger enhancement [157,173,187,191]. The second effect refers to the fact that the vibronic intensity of chemisorbed species is larger than that of

condensed layers or physisorbed species due to larger absorption coefficients[192]. It has been discussed that this might be due to an 'intensity borrowing' from charge-oscillations [157,193].

2.5.3 Attenuated Total Reflection Spectroscopy

A detailed description of the principles of attenuated total reflection (ATR) spectroscopy can be found elsewhere[194]. However, a certain aspect which is important in the context of surface spectroscopy shall be highlighted here, which is the surface sensitivity. When a beam traverses from one transparent medium to another of different refractive index, the beam is refracted according to Snell's law (Figure 2.25):

$$n_1 \sin(\theta_1) = n_2 \sin(\theta_2) \tag{2.35}$$

Assuming that $n_1 > n_2$, the angle of the transmitted ray with respect to the surface normal is larger. However, at a certain angle of incidence, the left-hand side of (2.36) becomes as large as n_2 resulting in a beam that is transmitted parallel to the surface (Figure 2.25, right). This angle is the critical angle θ_c and can be calculated according to eq. (2.36):

$$\theta_c = \arcsin\left(\frac{n_2}{n_1}\right) \tag{2.36}$$

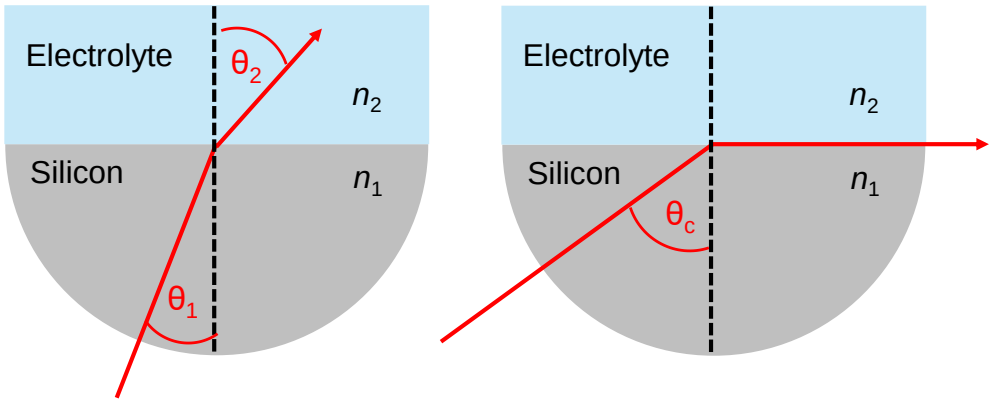

Figure 2.25. Reflection at the boundary between silicon and electrolyte. On the left-hand side the IR beam hits the surface under a small angle and is transmitted. On the right-hand side, the incident beam is reflected horizontally as the angle of incidence equals the critical angle.

Although the beam is reflected at the boundary for angles above the critical angle for total reflection (θ_c), a part of the beam penetrates into the electrolyte, which is the evanescent wave. The intensity of the evanescent wave decays exponentially and thus, one usually defines the penetration-depth d_p as the distance at with the intensity has decreased to 37% of the incoming beam. This penetration depth is dependent on the wavelength λ, the angle of incidence and the refraction indices of the media according to eq. (2.37):

$$d = \frac{\lambda}{2\pi n_1 \sqrt{\sin(\theta)^2 - \left(\frac{n_2}{n_1}\right)^2}} \tag{2.37}$$

The penetration depth as a function of the wavenumber for the boundary between silicon and different solvents is shown in Figure 2.26. As can be seen, the penetration depth at 3500 cm^{-1} is only 1/3 of the penetration depth at 1000 cm^{-1}, but does not vary too much with the solvent. This has to be kept in mind when comparing ATR spectra to transmission spectra. However, for SEIRAS the situation is different as the Si crystal is covered by a thin layer of a metal[149]. Moreover, the enhancement effect is very short-ranged (5 nm[157] and thus, the penetration depth will have a less significant influence on the intensity of the absorption bands.

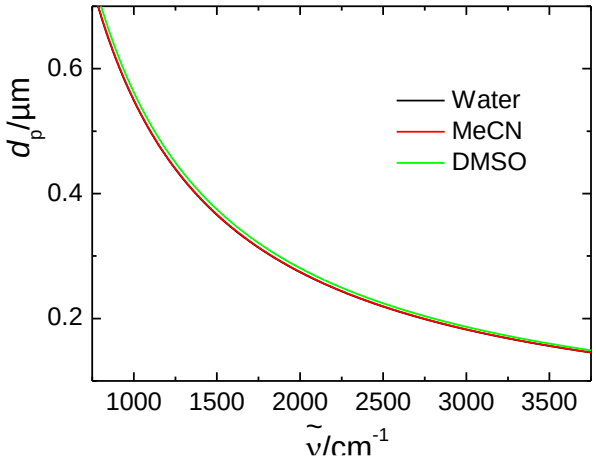

Figure 2.26. Penetration depth of the evanescent wave. Angle of incidence: 60°. Wavelength-dependent refractive index of Si taken from Edwards *et al.*[195]. Refractive index of the solvents: 1.32 (water), 1.33 (MeCN), 1.46 (DMSO) at 1.55 µm [196].

2.6 Fourier-Transform Infrared Spectroscopy

Fourier transform infrared (FTIR) spectrometers have been used already in the early 1980's to study electrochemical processes on surfaces[162,164,197]. The main advantages of a FTIR-spectrometer as opposed to a dispersive spectrometer are the much higher speed of spectrum acquisition, the high throughput and high resolution[194]. The heart of a FTIR-spectrometer is an interferometer, which is comprising of a mirror at a fixed position and a moving mirror and was originally introduced by Michelson[194,198]. In the Michelson interferometer, an incoming beam is divided into two parts by a beam splitter. One half of the beam is reflected under an angle of 90° with respect to the incoming beam and travels a distance which is given by the distance between the beam splitter and the fixed mirror before it is again reflected. The second beam traverses through the beam splitter and is reflected again at the surface of a moving mirror, which changes its distance to the beam splitter. After reflection at the mirrors, the beam recombine again at the beam splitter, where they interfere and are again partially reflected and transmitted.

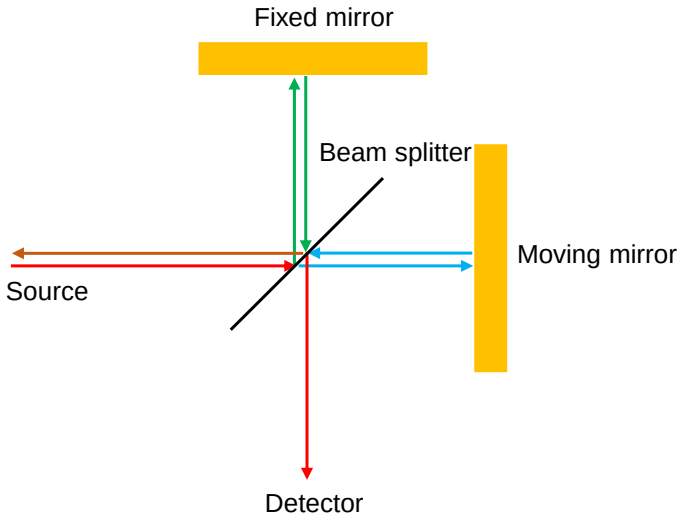

Figure 2.27. Michelson interferometer [194]. The different colours of the beams are used to make differentiation easier although all beams have the same wavelength.

Depending on the difference in path of the beams, the interference is of constructive or destructive nature. It is noteworthy that in the case of destructive interference the main part of the beam travels back to the source and thus, is not measured in a usual single detector set-up. This variation of the intensity (or voltage at the detector) of the IR beam detected by the detector with the variation of the path difference or the moving mirror position (represented by data points) yields the interferogram and contains the full spectral information of a FT-spectrometer (Figure 2.28).

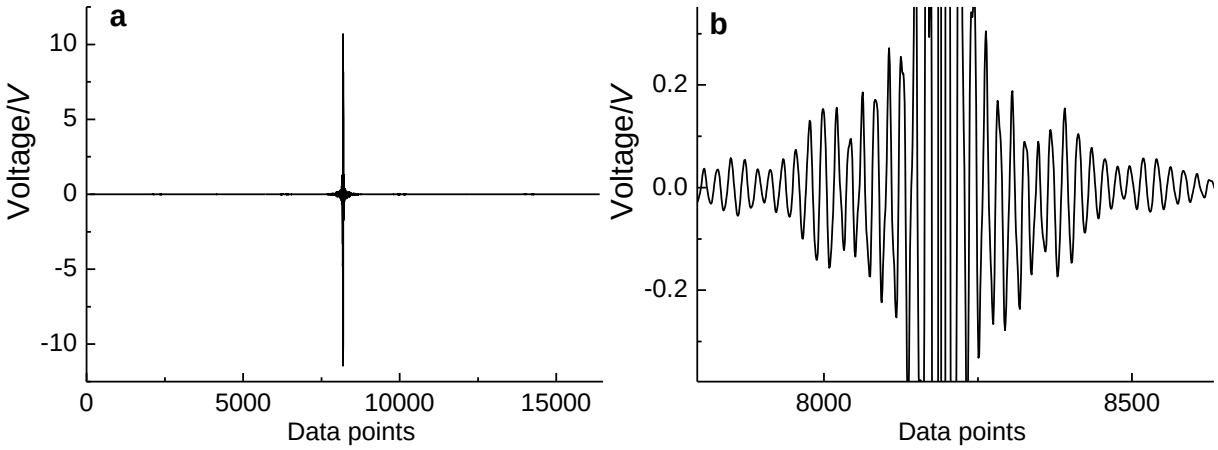

Figure 2.28. Interferogram recorded with the Nicolet iS50. **a**. Interferogram over the whole range. **b**. Close-up of the interferogram at zero path difference. Resolution: 4 cm^{-1}, Mirror speed 1.8988 cm s^{-1}, zero filling level:2.

Acquisition of the interferogram as depicted in Figure 2.28 is achieved by the movement of the moving mirror. Each movement leads to an optical path difference (OPD) or retardation between the two beams of 2-times its displacement as the beam has to travel the distance between beam splitter and moving mirrors twice before it gets reflected again at the beam splitter. The retardation is represented as data points in Figure 2.28. If both mirrors are placed at the same distance to the beam splitter, the beam interfere constructively and maximum

intensity if achieved. This distance is often referred to as zero path difference (ZPD) and is at situated at data point 8192 in Figure 2.28.

The general relation between the intensity *I* at the detector and the retardation δ is given by eq. (2.38), where $\tilde{\nu}$ is the wavenumber of the incident beam:

$$I(\delta) = 0.5 \cdot I(\tilde{\nu})\left(1 + \cos\left(2\pi\tilde{\nu}\delta\right)\right) \tag{2.38}$$

The alternating element in eq. (2.38) is referred to as the interferogram. To obtain the spectrum, which is a representation of the intensity as a function of the frequency (or wavenumber) rather than the time, eq. (2.38) has to be transformed via Fourier-transformation. The cosine Fourier-transform is given as:

$$B(\tilde{\nu}) = \int_{-\infty}^{+\infty} I(\delta)\cos\left(2\pi\tilde{\nu}\cdot\delta\right)d\delta \tag{2.39}$$

Equation (2.39) theoretically allows a conversion of the interferogram at infinite resolution. However, in an actual measurement, the retardation is finite and the interferogram is discretely sampled instead of being continuous. The finiteness of the retardation limits the maximum attainable resolution of the spectrum[194]. The restriction of the retardation can be incorporated in eq. (2.39) by introducing a function which is 0 for all retardations greater than the maximum retardation $\delta_{\max}$ and 1 for $-\delta_{\max} < \delta < +\delta_{\max}$. As can be shown[194], this truncation introduces artificial ripples around the peak. Using weighing functions which do not abruptly change their value between 0 and 1, the ripples can be decreased. This process is called *apodization* and several apodization functions are available. It is noteworthy, that apodization always decreases and broadens also the main peak, effectively reducing the maximum resolution.

Instead of carrying out the integration in eq. (2.39) continuously, the increments in δ are discrete and thus, a discrete Fourier-transformation rather than a continuous Fourier-transformation has to be carried out. To increase performance, a fast Fourier transform (FFT) algorithm is used, which is an efficient way to calculate the discrete Fourier transform of a function. A requirement of the FFT-algorithm is that the number of points in the interferogram is a power of 2. Therefore, prior to FFT, the interferogram is padded with zeros to increase its size to a number that is a power of 2. This method of *zero filling* is not only necessary to enable efficient FFT-algorithm but also increases the number of data points per resolution elements and alleviates distinction between adjacent spectroscopic features. A further step of data treatment is the correction of phase errors introduced by optical path differences in the instrument as well as different low and high pass filters, which is described in detail elsewhere [194] [199]. The final result of the phase-corrected, zero-filled Fourier transform of the interferogram is the *single beam* spectrum, which is a representation of the IR intensity as a function of the wavelength.

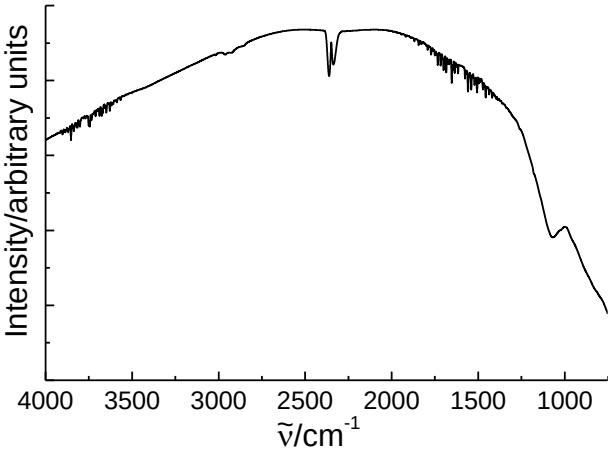

Figure 2.29. Single-beam spectrum. Spectrum recorded with open path under ambient conditions.

3 The Effect of Magnesium Ions on the ORR in DMSO

Philip Reinsberg*, Christoph J. Bondue* and Helmut Baltruschat*

*Institut für Physikalische und Theoretische Chemie, Universität Bonn, Römerstraße 164, D-53117 Bonn, Germany

Received: January 21, 2016
Published online: March 29, 2016

Reprinted (adapted) with permission from
P. Reinsberg, C. J. Bondue and H. Baltruschat, *Electrochim. Acta* **2016**, *200*, 214–221.
 DOI: 10.1016/j.electacta.2016.03.157
A correction to the article is available at: 10.1016/j.electacta.2016.04.149

Comments: The work presented in this article is based on a previous master thesis by P. Reinsberg (P. Reinsberg, *Sauerstoffreduktion in Dimethylsulfoxid unter Verwendung von $Mg(ClO_4)_2$ als Leitsalz* (Master's thesis), **2015**).

Own manuscript contribution:

- design of the experiments
- conducting the experiments
- interpretation of the results
- writing the manuscript

ACKNOWLEDGMENTS

The authors gratefully acknowledge the Federal Ministry of Education and Research for funding this work (03EK3027 A

3.1 Abstract

Mg–O_2 batteries appear to be a promising alternative to Li-O_2 system due to the high abundancy and volumetric energy density of Mg. Although much effort has been put into research on Li-O_2 batteries, little is known about the oxygen reduction and evolution in Mg^{2+}-containing aprotic electrolytes. In this paper, we present a detailed analysis of the ORR in Mg^{2+}-containing DMSO using RRDE and DEMS-techniques and derive a more general reaction mechanism of ORR in aprotic electrolytes using the results for Li^+, Na^+ and K^+-containing DMSO. O_2 first reacts via an initial adsorption step to superoxide which, in the presence of Mg^{2+}, is subsequently reduced to peroxide as the main reaction product. However, this product undergoes further reactions leading to a deactivation of the electrode. Regarding the reversibility, unfortunately no OER was observed and reactivation of the electrode proved difficult.

3.2 Introduction

The world population's increasing demand for energy combined with scarcity of fossil resources requires an alternative energy production, which relies on renewable resources. One of the current issues concerning the efficiency and attractiveness of renewable energies is the energy storage technology. Since Abraham introduced the concept of the lithium-air battery in 1996, research is focused on metal-air batteries in aprotic media as the future in energy technology [13]. The oxygen reduction reaction (ORR) in aprotic media in the presence of divalent cations like Mg^{2+}-ions has attracted little attention [17,200], while there has been a lot of interest in monovalent cations such as Li^+ [21,61,62,123,139,201-207], Na^+ [15,76,77,139], K^+ [32,61,139] and tetrabutylammonium (TBA^+) [61,62,123]. Nevertheless, a reversible Mg-O_2 battery appears attractive due to the high abundancy and volumetric energy density of magnesium as compared to e.g. Li-O_2.

Despite the effort which was put into research on metal-air batteries the exact mechanism of oxygen reduction in aprotic media is still not fully understood. For the ORR in aprotic Li^+ electrolytes, which is probably the best known system regarding ORR in aprotic solvents, it is generally accepted that the final reduction product is Li_2O_2 with the at least intermediate formation of LiO_2 [21,61,62,123,139,203,205,208-211]. In principle two pathways of the formation of Li_2O_2 have been considered: the *direct* pathway including the direct reduction of superoxide to peroxide at the electrode surface and the *indirect* one proceeding via disproportionation of the initially formed superoxide [62,139,201,206,207,212].

Concerning the detailed mechanism of the direct pathway, Lu *et al.* could show a volcano like correlation between the adsorption enthalpy of O_2 at the electrode material and the potential, which has to be applied in Li^+-containing electrolytes to supply a certain current density [213]. This directly implies that the ORR takes places via an inner-sphere reaction. More strikingly, Bondue *et al.* showed for the ORR on boron-doped diamond electrodes that even the initial

reduction step of O_2 to superoxide proceeds via an inner-sphere reaction [139]. Additionally, the cation as well as the electrode material exerts a catalytic effect by shifting the potential of direct peroxide formation by several hundred millivolts [139]. The effect of the cation on peroxide formation can be observed most strikingly when the ORR in the presence of TBA^+ is compared to the ORR in the presence of Li^+: In the former case, peroxide cannot be produced at all [61,62,123] while in the latter case it is a question of the applied potential and electrode material [21,61,62,123,139,201-204,214]. Further kinetic investigations regarding the Tafel-slope in TBA^+- [61] and Li^+-[62,213,215] containing DMSO and MeCN yielded values of about 120 mV/dec suggesting a one-electron transfer as the rate determining step. The only study related to the electrochemical reaction order with respect to O_2 in aprotic solvents supports the assumption that O_2 is adsorbed prior to reduction [213] as the reaction order is in between 0 and 1. However, the determination of the reaction order is flawed as discussed later on.

Preliminary work concerning ORR in Mg^{2+}-containing DMSO has been done by Shiga *et al.* who presumably identified MgO as the main discharge-product in I_2-containing DMSO [17]. Additional mechanistic investigations have been conducted by Vardar *et al*. who could show by examining the thermodynamic potentials that the initial step of the ORR in Mg^{2+}-containing THF involves the intermediate formation of superoxide [200]. Despite the results of Shiga, the authors identified a mixture of 2/3 MgO and 1/3 MgO_2 as the discharge products. However, it remains unclear whether there are possible side-reactions between the electrolyte salt and O_2 and to what extent these reactions could influence the distribution of the products. The aim of the present paper was to elucidate the detailed mechanism of oxygen reduction in DMSO in the presence of Mg^{2+}-ions. Comparison with ORR in the presence of other cations and electrode materials will lead to the derivation of a comprehensive mechanism.

3.3 Experimental Section

3.3.1 Chemical reagents

All electrolytes where prepared and stored under an Ar-atmosphere in an *MBraun* glovebox. The freshly prepared electrolytes contained approx. 40 ppm water. The expected error due to the reaction of DMSO with the *Karl-Fischer*-reagents was previously estimated by adding a water standard and is already included in the presented values [139].

Extra dry DMSO (99.7%, over molecular sieve, *Acros Organics*) was used as received, while magnesium perchlorate (≥ 99%*Sigma-Aldrich*) was dried at 245 °C under reduced pressure (10^{-2} mbar) before usage. Highly pure Argon (*Air Liquid*, 99.999%) and highly pure oxygen (*Air Liquid*, 99.995%) were used to purge the vessels and electrolytes. Most of the measurements were performed using a custom made mixture of Ar and O_2 (80:20 = Ar:O_2) obtained from *Air Liquid*. The different Ar-O_2-mixtures for measuring the oxygen dependence of the current were produced by employing two flowmeters (*Krohne Duisburg*).

3.3.2 Rotating Ring-Disk Electrode (RRDE) Measurements

The RRDE-measurements were performed in a classical H-cell which was continuously purged with an Ar-O_2 mixture to avoid water contamination and keep the electrolyte saturated with O_2. After finishing the RRDE measurement, a sample of the electrolyte within the working compartment was used to determine the water content, which was approximately 60 ppm for a typical measurement.

3.3.3 Differential Electrochemical Mass Spectrometry (DEMS) Measurements

The dual thin-layer cell used in this work consists of an upper compartment, where the working electrode is placed and a lower compartment, which is connected to the mass spectrometer via a porous Teflon membrane pressed on a steel frit. The electrolyte enters the cell at the upper and leaves it at the lower compartment. The reference electrode is placed at the electrolyte inlet while the main counter electrode, which is connected to a resistance of 1 Ω, is placed at the outlet. A second counter electrode connected to a resistance of 1 MΩ is placed at the inlet. This dual counter electrode arrangement suppresses electronic oscillations and the choice of resistances guarantees an optimal current distribution. The dual thin-layer cell used in this work is described in detail in previous papers [112,113]. To correlate faradaic and ionic currents to get information on the number of electrons transferred per oxygen molecule, a calibration of the system is necessary, employing a reaction of known stoichiometry. For this purpose the ORR in $KClO_4$-containing DMSO was used, which is discussed in detail elsewhere [123].

3.3.4 Reference Electrode

A silver wire in a solution of 0.1 M $AgNO_3$ in DMSO was used as a reference electrode. In order to avoid contamination of the working electrolyte with silver-ions during the RRDE-measurement, the reference electrode was connected via a *Luggin* capillary, which had contact to the reference electrolyte through the wet surface of a closed, rough glass stopcock. For the DEMS measurements, the electrolyte contact was established using a Teflon tube which was filled with the reference electrolyte and closed with a rough glass bead. The potential of the reference electrode is calculated to be +0.49 V vs. SHE [216] or +2.8 V vs. Mg^{2+}|Mg. A more detailed description can be accessed elsewhere [139].

3.4 Results and Discussion

3.4.1 Identification of the ORR-products via DEMS

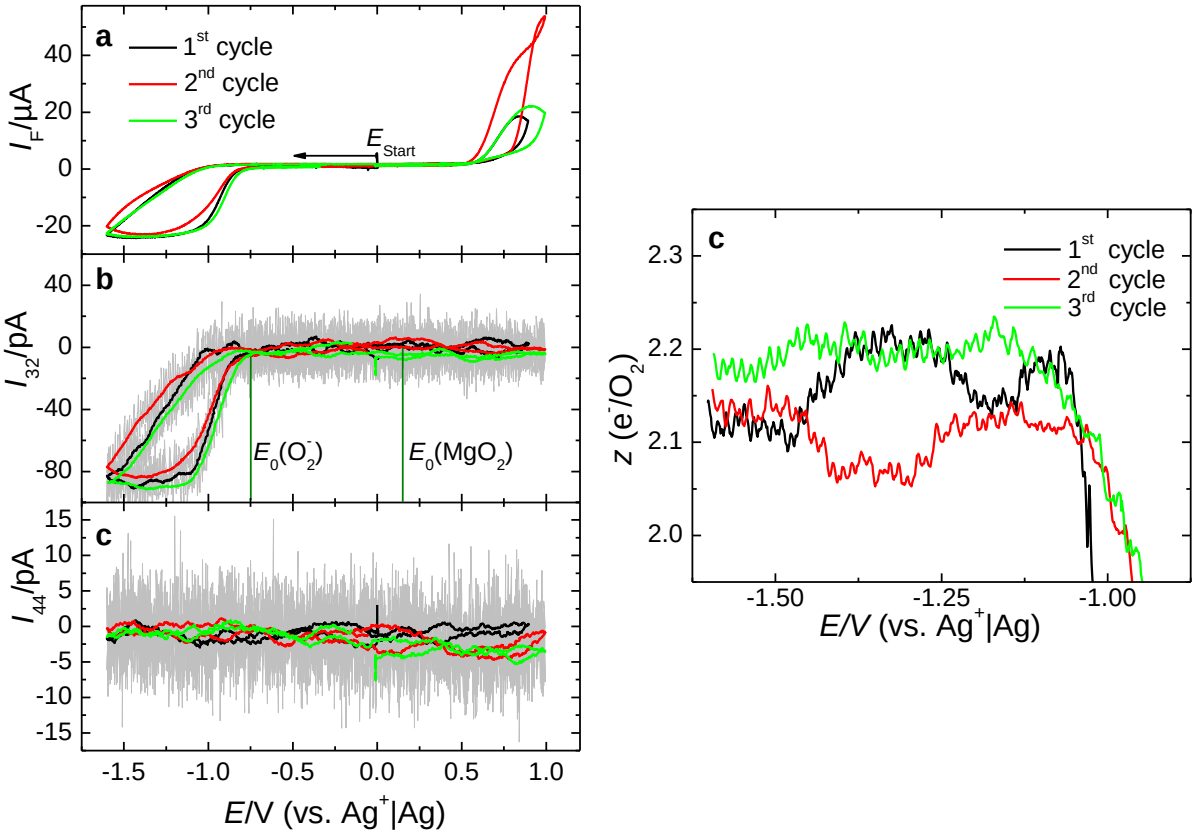

Figure 3.1. Subsequent CV and MSCV of the ORR at a gold electrode. **a**. Subsequent CVs. **b**, **c**. Corresponding MSCV for mass 32 and mass 44 in DMSO containing 0.4 M $Mg(ClO_4)_2$ saturated with a mixture (80:20) of Ar and O_2 at a Pt-electrode. **d**. Number of electrons transferred per oxygen molecule. Flow rate u = 5 µL s−1; sweep rate v = 10 mV s−1; black: first cycle; red: second cycle; blue: third cycle. The arrow indicates the initial sweep direction.

As shown in Figure 3.1, the onset of ORR is at −0.8 V and a constant current is achieved between −1.3 V and −1.6 V. The 2nd cycle shows a slight deactivation of the electrode indicating the partial formation of a solid precipitate on the electrode. However, no oxygen evolution is visible during the anodic sweep although reactivation of the electrode from the 2nd to the 3rd cycle occurs after increasing the anodic potential limit to 1 V. Besides, the anodic currents at 0.7 V do neither correspond to CO_2-evolution as observed in Li^+- and Na^+-containing electrolytes. Using the calibration constant of $K^* = 8x10^{-6}$, the number of electrons z transferred per oxygen molecule can be calculated by correlating the faradaic current I_F to the ionic current I_{32} according to eq. (3.1). As shown in Figure 3.1d z equals 2 within almost the whole potential range.

$$z = \frac{I_F}{I_{32} K^*} \tag{3.1}$$

This indicates that not MgO, but rather MgO_2 or at least a species containing a peroxide anion is the main product of the ORR. Even though MgO is slightly more stable than MgO_2 [14,217], it is not unexpected that MgO_2 is formed as it should be kinetically favoured (no bond-breaking has to occur in the O_2 molecule). The overall amount of reduced oxygen during the first cycle from the MSCV corresponds to a charge of 10 000 pC cm^{-2} (roughness factor R_F = 3.0) related to the true surface area: Given the assumption that each reduced oxygen molecule occupies only one surface site and is reduced by 2 electrons, this equals an amount of 12 nmol cm^{-2} or 6 monolayers (ML). Further investigations on the ORR in Mg^{2+}-containing DMSO at different electrode materials reveals that the ORR proceeds via a two-electron process also at glassy carbon (GC), gold (Au) and ruthenium (Ru) (Figure 3.2). However, for the rhodium electrode the electron numbers are considerably larger and imply at least the partial formation of MgO. Analogous to the Li^+-containing electrolyte the boron-doped diamond electrode exhibited no ORR-activity at all (not shown here), suggesting that the ORR in the presence of Mg^{2+} proceeds via an inner-sphere reaction in accordance to the argumentation of Bondue [139]. As already observed by evaluating the OCP in THF-based electrolytes [200], there is a large discrepancy (~ 1 V) between the onset of the ORR and the thermodynamic redox potential of MgO_2 or MgO (using the free enthalpies of formation $\Delta_f G^o(MgO_2) = -567.8$ kJ mol^{-1} [218] and $\Delta_f G^o(MgO) = -568.9$ kJ mol^{-1} [14], the redox potential is calculated to be +0.16 V versus the employed reference electrode). However, using the data acquired in TBA^+-containing DMSO[62], the onset potential is close to the redox potential of the $O_2|O_2^-$ couple at −1.0 V. The shift of the onset potential in the positive direction, which is also observed in Li^+-containing DMSO[62], can be explained by a thermodynamic stabilization of the superoxide. Coincidentally, the onset potential is also close to the redox potential of the $O_2|O_2^-$ couple at −0.8 V in aqueous solution [217].

The absence of oxygen evolution together with the fact that there is indeed a reactivation of the electrode during the anodic cycle has some implications for the products formed. According to the electron number, peroxo-species should be the final products of the ORR at the electrode surface. Disproportionation of the peroxo-species to oxygen and an oxide, as suggested by Vardar *et al*. [200], will not affect the electron number as long as it is a rather slow process and takes place within the electrolyte so that the evolving oxygen cannot be reduced again. If accordingly MgO_2 is assumed to be the reaction product which deposits on the surface, the evolution of oxygen would be expected upon oxidation of this film as it is unlikely that superoxide will be the final product of oxidation. Thus, the lack of oxygen evolution and the highly irreversible behavior indicate that some kind of chemical reaction occurs which decomposes the products or intermediates of the reaction. However, at this point it remains unclear whether this chemical reaction or rather degradation takes place after the final reduction step or prior to it, as both pathways could be in agreement with a two-electron process and the lack of oxygen evolution.

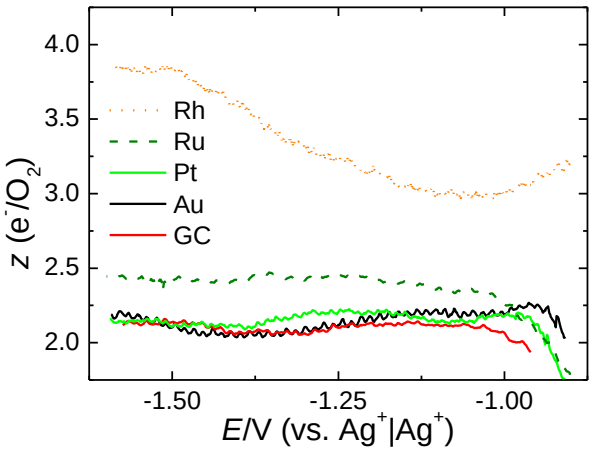

Figure 3.2. Number of electrons *z* transferred per O_2 molecule. Electrolyte: 0.4 M $Mg(ClO_4)_2$ in DMSO with 20% O_2 saturation.

3.4.2 Collection Efficiencies at the RRDE

To further investigate the nature of the products and the kinetic properties of the ORR in Mg^{2+}-containing DMSO RRDE measurements were performed. As shown in Figure 3.3 the oxidation of soluble species at the ring electrode can be observed during ORR. However, the portion of the formed species which can be oxidised at the ring depends strongly on the rotation frequency *f* with a maximum collection efficiency of 35 % of the theoretical value (Figure 3.3 b).The fact that the collection efficiency increases with rotation frequency suggests that the species which can be detected at the ring electrode are unstable. There are two possible explanations for the observed behaviour. Firstly, the species detected at the ring could represent intermediates of the electrochemical reduction process, similar to the alkaline electrolytes, where H_2O_2 can be detected at the ring whereas the final product of oxygen reduction, H_2O, cannot be detected. Secondly, the species formed at the disc electrode could participate in a homogeneous chemical reaction before they reach the ring electrode, which finally leads to products which cannot be oxidised at the ring anymore. If a situation coinciding with the first explanation takes place in the aprotic electrolyte, there should be a competition between the further reduction of the intermediates and the transport of these intermediates to the ring electrode. Consequently, the collection efficiency should increase with the rotation rate at a constant potential since the transport rate of the intermediates is increased whereas the competing rate of the further reduction steps is unaltered by the rotation rate. As has been shown [219], $1/N$ should depend linearly on $f^{-1/2}$ in this particular case which is not the true for the experimental data presented here (Figure 3.3c). Furthermore, it is also expected that the collection efficiency decreases when the disc potential is increased at a constant rotation rate as the rate of the further reduction steps increases while the transport rate remains constant, which again is not the case regarding the experimental results (Figure 3.3c). Therefore, it is probable that a degradation of the products or intermediates via a chemical reaction is involved as this homogeneous reaction within the gap between disc and ring electrode should not be

strongly susceptible to the potential at the disc electrode. Additionally, the plot of $1/N$ vs. $f^{-1/2}$ should not yield a straight line as the assumption made in [219] cannot be applied anymore. The dependence of the collection efficiency on the rotation rate can be easily understood by a competition between the rate of transport and the rate of the chemical reaction. Taking the species present in the system into account, DMSO seems to be the most reasonable to react with the reduced oxygen species.

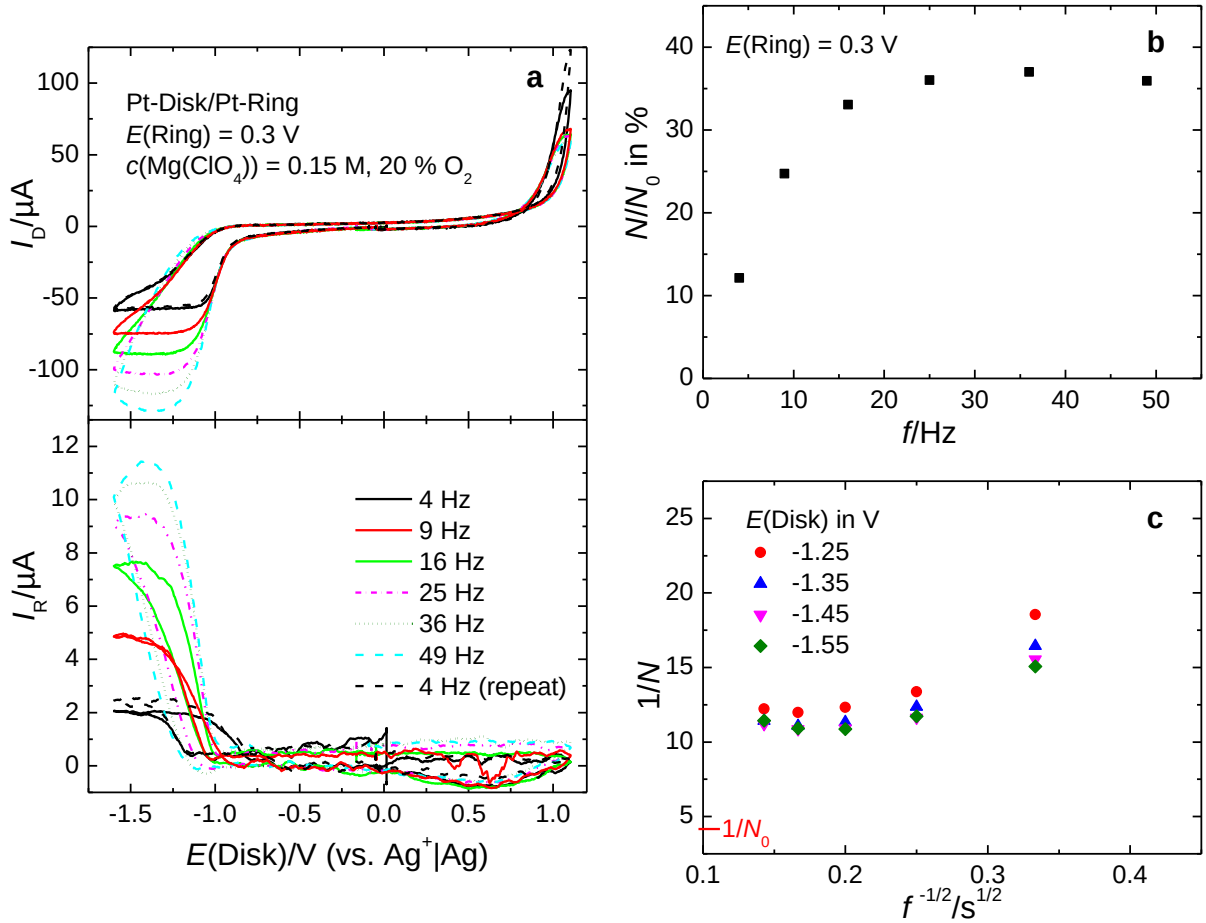

Figure 3.3. CVs at a Pt-Disk/Pt-Ring rotating ring disk electrode. **a**. CVs at a Pt-disk (upper) and corresponding CVs at a Pt-Ring (lower). Electrolyte: 0.1 M $Mg(ClO_4)_2$ in DMSO saturated with 20% O_2. Sweep rate $v = 100\ mV\ s^{-1}$. **b**. Collection efficiencies N with respect to the theoretical efficiency N_0 ($N_0 = 0.25$) as a function of the rotation frequency f. **c**. Variation of $1/N$ with $f^{-1/2}$ at different disc potentials for analysis of the degradation mechanism [219].

3.4.3 Kinetic Investigation of the Disk Currents and Tafel-slope

Investigating the disc currents (I_D), a constant current in the potential range between −1.3 V and −1.6 V can be observed for rotation frequencies up to 16 Hz. For higher rotation frequencies a deactivation within the cycle becomes visible. However, the control measurement at 4 Hz shows that the electrode was fully reactivated during the anodic sweep. The Levich-Koutecký equation (3.2)

$$\frac{1}{I} = \frac{1}{I_K} + \frac{1}{I_{Diff}} = \frac{1}{I_K} + \frac{\nu^{1/6}}{0.62zFAD^{2/3}c\sqrt{2\pi}} f^{-1/2} \tag{3.2}$$

allows the calculation of the number of electrons z transferred per reactant, where I_K denotes the kinetic or rather diffusion-independent part of the current and I_{Diff} the diffusive part. With the kinematic viscosity ν = 0.018 cm²s^{-1} [220], the geometric surface area A = 0.2 cm², the faradaic constant F, the oxygen solubility c = 0.40 mol m^{-3} and a diffusion coefficient of D = 15.8x10^{-5} cm²s^{-1} [130] for oxygen a theoretical slope of 33.7 mA^{-1} s$^{1/2}$ can be calculated for z = 2. The experimental slopes at high overpotentials (Figure 3.4) are in fair agreement with that theoretical value, thus confirming the results of the DEMS-measurement and the formation of peroxide. However, extrapolating the current at a potential, at which diffusion limitation of the currents must be assumed due to the potential-independent currents, the Levich-Koutecký plot exhibits a large intercept which accounts for up to 50 % of the measured currents. Accordingly, another limitation for the current has to be assumed, which is not directly connected to the heterogeneous charge-transfer or the diffusion of the reactants. From Figure 3.5 it seems reasonable to conclude that the additional limitation does not depend on the potential. If the additional limitation depended on the potential, the currents should increase until the experimental current resembles the theoretical diffusion-limited current. As the highest obtained currents are significantly lower than the theoretical diffusion-limited currents (40 % lower at 25 Hz) and do not increase further in the range of −1.2 V to −1.6 V, the additional limitation does not seem to directly depend on the potential (Potential step experiments under convection revealed monotonously decreasing currents for a step potential of −1.3 V. Together with the presented results, this indicates a migration hindrance through a blocking surface layer, which will be discussed in a further publication). To examine the influence of the rotation frequency on this additional limitation, the currents directly connected to the charge-transfer (I_{CT}) were calculated in two different ways. In the first approach, equation (3.3) was used for a rotation frequency of 16 Hz (Figure 3.4b, black) with I_{Diff} as the apparently diffusion-limited current (the additional limitation is contained in I as well as in I_{Diff} in equation (3.3) if the experimental values are used and is cancelled out if it does not greatly vary with the applied potential).

$$I_{CT} = \frac{I \cdot I_{Diff}}{I_{Diff} - I} \tag{3.3}$$

Furthermore, the current due to charge-transfer was calculated using equation (3.4) with I_K as the diffusion-independent current, directly obtained as the ordinate's intercept using the Levich-Koutecký extrapolation and I_A^{-1} as the additional limitation (Figure 3.4b, red). This additional limitation was acquired using the ordinate's intercept of the Levich-Koutecký extrapolation at such high overpotentials that the current does not change with the potential anymore and therefore $1/I_{CT}$ is negligible.

$$\frac{1}{I_{CT}} = \frac{1}{I_K} - \frac{1}{I_A} \tag{3.4}$$

Both methods lead to similar currents and a Tafel-slope of approximately 120 mV/dec as can be seen from Figure 3.4b, which is in agreement with the value observed in Li^+ and TBA^+-containing DMSO [62,213].

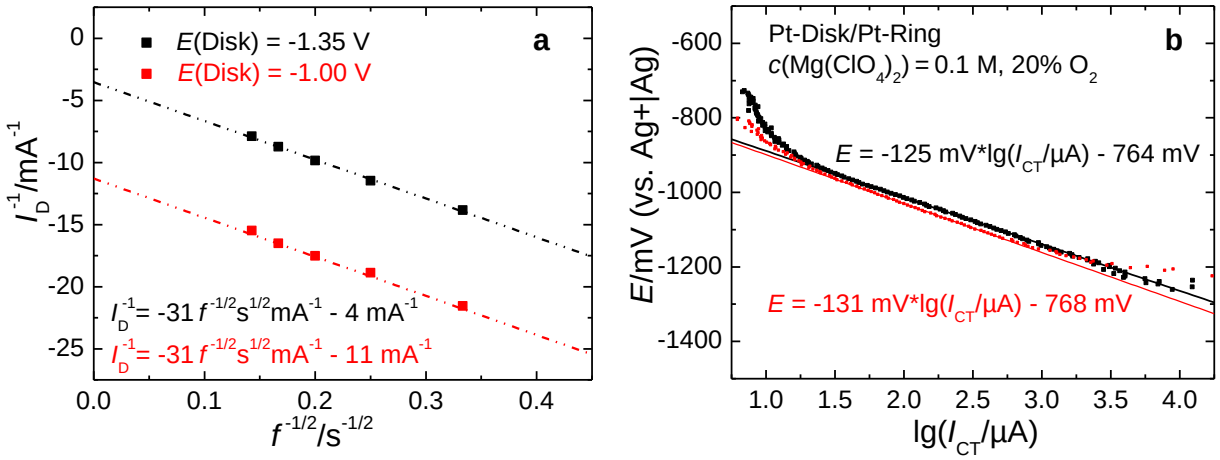

Figure 3.4. Kinetic evaluation of the ORR in Mg^{2+}-containing DMSO. **a**. Levich-Koutecký extrapolation for different disk potentials at a Pt-electrode and 20% O_2-saturation. **b**. Tafel-plot using the currents due to charge-transfer (I_{CT}) calculated via equation (3.3) (black) and at 25 Hz via equation (3.4) (red).

3.4.4 Electrochemical Reaction Order with Respect to O_2

Having verified a method to calculate the kinetic currents, the influence of the oxygen and magnesium-ion concentration on the kinetic current was studied to further elucidate the mechanism. The dependency of the experimental currents on the oxygen concentration is depicted in Figure 3.5a. As expected, the currents increase with increasing oxygen concentration while the collection efficiency remains more or less unchanged. According to the Levich-Koutecký equation (3.2), when a possible dependence of I_A on the concentration is neglected, a plot of I^{-1} vs. c^{-1} should yield a straight line with a slope of 2.5 mol L^{-1} mA^{-1} for f = 25 Hz, which is in fair agreement with the experimental value of 2 mol L^{-1} mA^{-1} (Figure 3.5b) regarding the estimated experimental error of 20% in determining diffusion coefficient. After calculating the kinetic currents according to equation (3.3) or rather (3.4), the electrochemical reaction order with respect to the oxygen concentration can be evaluated using equation (3.5)

$$m(\mathrm{O_2}) = \frac{\partial \ln(I_{CT})}{\partial \ln(c(\mathrm{O_2}))} \tag{3.5}$$

As shown in Figure 3.5c the reaction order is significantly lower than 1, which can only be explained by assuming an adsorption of some (maybe reduced) oxygen species close to saturation. To the authors' best knowledge, the only other reaction order with respect to oxygen for ORR in aprotic electrolytes was reported by Lu *et al.,* who observed a reaction order below 1 in Li^+-containing propylene carbonate on well-defined glassy carbon [221]. However, the

authors mistakenly evaluated the currents at a constant overpotential instead of a constant potential as they neglected the concentration dependence of the exchange current density. Furthermore, the effect of deactivation of the electrode and the electrolyte decomposition remains unclear.

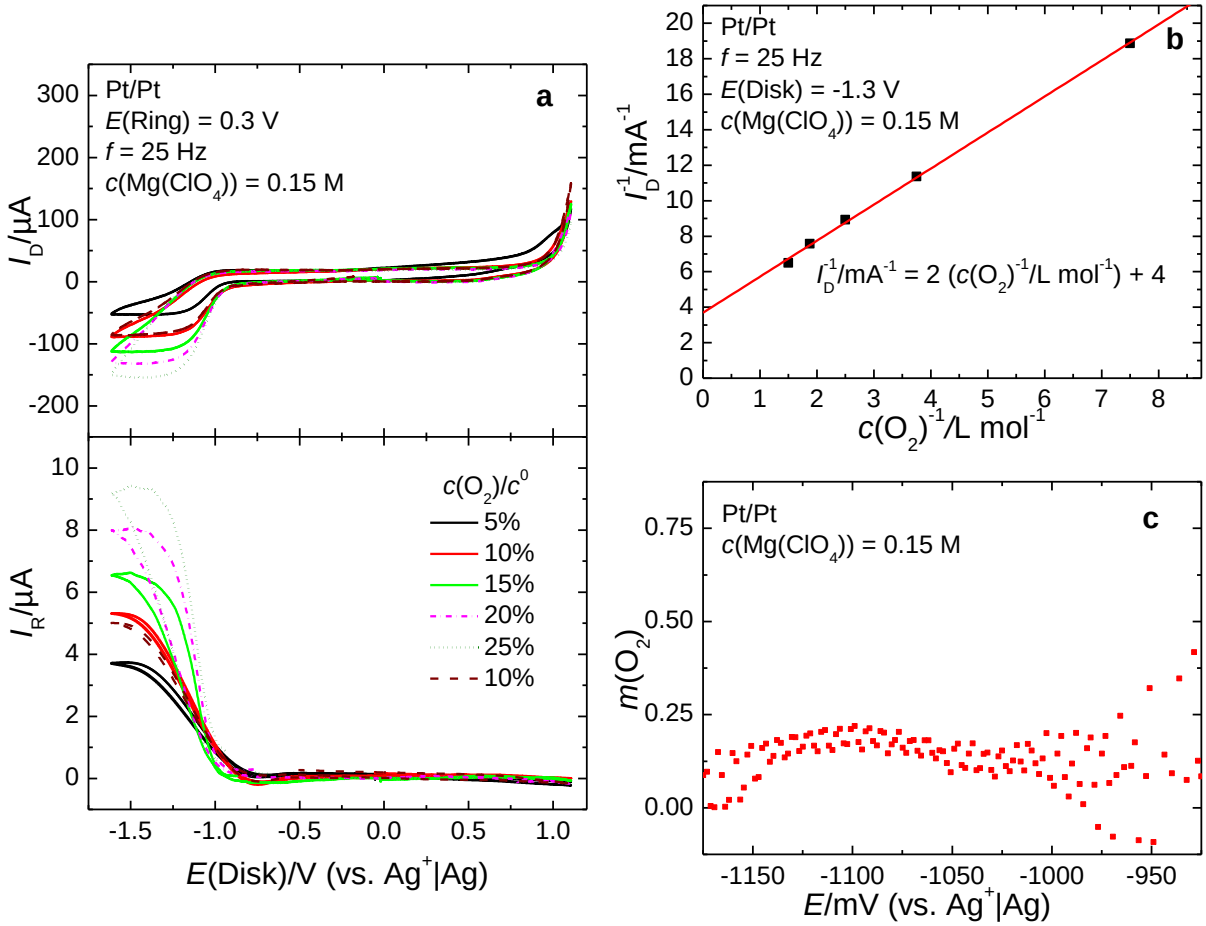

Figure 3.5. Effect of the O_2 concentration on the ORR. **a**. Currents for different oxygen concentrations at f = 25 Hz. **b**. Extrapolation of the apparently diffusion–limited currents with respect to the inverse of O_2-concentration. **c**. Electrochemical reaction order with respect to O_2.

The finding that the oxygen order is less than 1, poses the question on the validity of the Levich-Koutecký equation as its derivation requires a reaction which is first-order with respect to the reactant. In the general case of a reaction order m unequal to 1 the relation between the kinetic current I_K, the measured current I, and the diffusion-limited current I_{Diff} is given by equation (3.6):

$$I_K = I \cdot \left(1 - \left|\frac{I}{I_{Diff}}\right|\right)^{-m} \tag{3.6}$$

Equation (3.6) is similar to equation (3.3) if the latter is divided by I_{Diff}. The main difference lies in the exponent of the denominator. Using equation (3.3) instead of (3.6) provides too high currents, as the term in brackets varies always between 0 and 1 and an exponent of $0 < m < 1$ in this case increases the denominator. Accordingly, the values of m should not be understood

as quantitative, but qualitative values. It should be mentioned that the low reaction order leads to less significance of the diffusive part of the current. Consequently, the rotation frequency's influence for low overpotentials is weaker as compared to the normal case with $m = 1$.

3.4.5 Electrochemical Reaction Order with Respect to Mg^{2+}

Varying the concentration of the involved cation, namely Mg^{2+}, is not as straightforward as varying the oxygen concentration due to secondary effects of the dissolved salts on activity coefficients and the rate constants. Thus, the ionic strength has to be kept constant in order to exclude, or at least minimize, these secondary effects on the kinetics. This was done by the addition of an inert salt ($KClO_4$) which was shown to not greatly affect the ORR [139]. To sum up, the currents do not greatly depend on the Mg^{2+}-concentration within a range of 0.032 M up to 0.150 M (Figure 3.6) and the corresponding reaction order with respect to Mg^{2+} $m(Mg^{2+})$ is close to 0 (Figure 3.6, inset). For lower concentrations the ORR-characteristics change probably due to a change in the reaction mechanism. The ring currents seem to be affected by the Mg^{2+}-concentration, but the trend remains unclear. It is interesting to note that the ORR-characteristics of Mg^{2+}-containing DMSO are still dominant at an excess of a 13-times higher K^+-concentration. The decrease of the apparently diffusion-limited currents with decreasing Mg^{2+}-concentration can be attributed to the decreasing oxygen solubility due to a higher total amount of dissolved species.

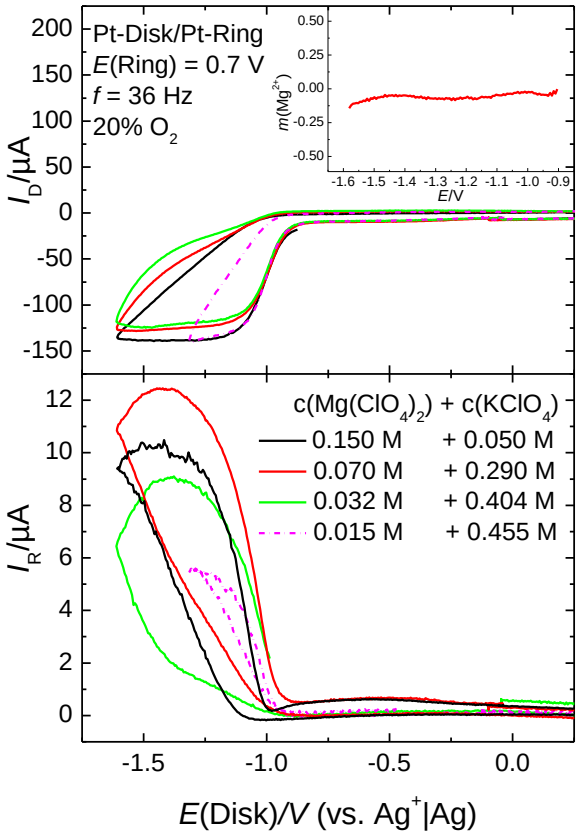

Figure 3.6. Influence of the Mg^{2+}-concentration on the ORR. CVs at a Pt-electrode for different concentrations of Mg^{2+}-ions at 20% O_2-saturation. Rotation frequency f = 36 Hz, sweep rate

v = 100 mV/s. The ionic strength was kept at 0.5 mol L^{-1} in order to exclude secondary effects of changing activity coefficients.

3.4.6 Proposed ORR Mechanism in the Presence of Mg^{2+}

Using the kinetic data and the information given in the introduction, the following mechanism seems to be the most probable mechanism of the ORR in Mg^{2+}-containing DMSO at polycrystalline platinum electrodes:

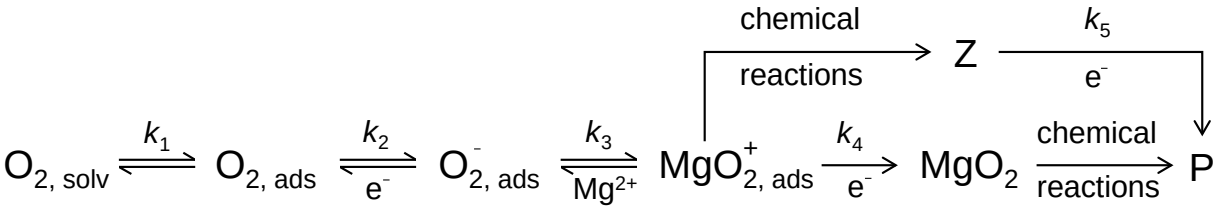

Figure 3.7. Proposed Reaction Mechanism of the ORR at a Pt-Electrode. . k_i is the rate constant of step *i*. A justification is given in the text below. P designates the unknown, final reaction products, whereas Z represents an intermediate.

The first step involves the adsorption of oxygen to the surface and its subsequent (or simultaneous) reduction to superoxide as already stated in the introduction. This is supported by the experimental findings that BDD-electrodes do not exhibit ORR-activity and more concise, by the low reaction order with respect to oxygen. Without any kind of adsorption of an oxygen species a reaction order below 1 could obviously not be understood. It appears improbable that the first step of the ORR is strongly affected by the interaction of the oxygen molecule with cations as the onset of the ORR seems to be uninfluenced by the nature of the cation (considering Bondue's data the onset of ORR remains more or less unchanged for Li^+, Na^+, K^+ and Mg^{2+}-containing DMSO [139]). Nevertheless, in the case of TBA^+-containing DMSO the onset potential is shifted by 200 mV [123], but it remains unclear whether this is a thermodynamic effect (the overall redox-potential of the O_2/O_2^- couple in the presence of TBA^+ seems to be shifted to significantly lower potentials [62]) or a kinetic effect. However, it is hard to imagine that the interaction between a non-charged species like O_2 and a cation is strong enough to detach the latter from its solvation shell (which should be strongly bound to the ion considering the high donor number of DMSO [222]). However, the cation does indeed have a strong impact on the reduction potential from superoxide to peroxide, which was already pointed out in the introduction. This impact can be illustrated by the formation of a hypothetical superoxide-ion-complex (MgO_2^+). Besides, the catalytic effect of the cathode material on the peroxide formation, most strikingly observed in Li^+-containing DMSO [139], suggests that the superoxide-ion-complex is attached to the surface when the second reduction step occurs. This is further underlined by the fact that the reaction order with respect to Mg^{2+} is close to 0. If the formation of the final products took place via a disproportionation within the solution, a dependence of the current on the Mg^{2+}-concentration would be expected (as long as the formation of superoxide itself is not rate determining). The formation of this hypothetical,

adsorbed contact-ion pair is followed by a second reduction step, indicated by the total amount of 2 electrons transferred per oxygen molecule, and probably a chemical reaction, which leads to products (P) that do not evolve oxygen upon oxidation. However, it remains unclear whether the chemical degradation takes place after the second electron-transfer or prior to it (via the intermediate Z) as already stated. Evaluating the rate law of the proposed reaction mechanism and taking the Tafel-slope of 120 mV/dec into account, there are only three possible kinetic conditions which fulfil the experimental observations (assuming that one step can be designated as rate determining).

Table 3.1: Possible rate determining steps in agreement with the experimental results.[a]

case	rds		additional conditions
1	k_2	$K_1 c(O_2) \gg 1$	
2	k_4	$K_{1,2} c(O_2) \gg 1$	$K_3 c(Mg^{2+}) \gg 1$
3	k_4	$K_{1,2} c(O_2) \gg k_4$	k_3: irreversible $k_3 c(Mg^{2+}) \gg k_4$

[a] The column “additional conditions” contains the further requirements to the kinetics. k denotes a rate constant, K an equilibrium constant. $K_{1,2}$ denotes the combined equilibrium constant of step 1 and 2. Rds: rate determining step

The first case implies that the formation of superoxide is the rds and consequently leads directly to a Tafel-Slope of 120 mV/dec and $m(Mg^{2+}) = 0$. However, in this case the saturation of the surface with molecular oxygen would have to be required in order to maintain $m(O_2) \approx 0$. Moreover, the superoxide formation in the presence of K^+-ions has been shown to be reversible and facile [61,139]. The formation of superoxide should also be facile in the presence of Mg^{2+}-ions as the onset potential for the ORR is not changed greatly and is still close to the thermodynamic potential of superoxide formation. Hence, this first case does not seem to be plausible. The remaining two cases, which are in agreement with experimental results, consider the second electron transfer as the rds, but differ in detail. Assuming case 2, the formation of MgO_2^+ is in equilibrium while in case 3 this step is irreversible. However, these cases cannot be distinguished by the experimental data even though the irreversible attachment of an Mg^{2+}-ion to the superoxide ion seems to be more plausible. Again, saturation of the surface is required to maintain $m(Mg^{2+}) = 0$ and $m(O_2) \approx 0$, but now a major contribution of other adsorbed species such as superoxide to the total surface coverage is more likely than in case 1. A high value of $K_1 c(O_2)$ or $K_{1,2} c(O_2)$ is easily achieved if the total number of free Pt-sites is low due to the adsorption of other species.

It is reasonable to have a look at the suggested surface saturation as it is one of the keys to the proposed mechanism. In principle, the strong adsorption of DMSO on metal surfaces has to be considered [223-230]. The maximum surface coverage related to adsorption of DMSO from the gas phase on platinum has been found to be $\theta = 0.25$ [231], which was attributed to a planar adsorption, and is luckily not greatly changed by the presence of water in the solution [136].

Furthermore, Katekaru *et al*. found that the maximum coverage of iodine on a platinum surface, which was first exposed to DMSO, is $\theta = 0.2$ [231]. The fact that iodine can only replace DMSO to a limited extent emphasizes the importance of DMSO adsorption. Additionally, Puglia *et al.* revealed by using UHV-techniques that even at a clean Pt(111) surface the maximum coverage of physisorbed O_2 is only $\theta = 0.3$ indicating side-on adsorption [232]. Therefore, it is reasonable to assume that only a very limited number of free surface sites are available for O_2 adsorption. Consequently, the equilibrium constants K_1 and $K_{1,2}$ in Table 3.1 will be large even if the total amount of oxygen adsorbed to the surface is low related to the total number of surface atoms.

3.5 Conclusions

Employing DEMS and RRDE, the mechanism of ORR in Mg^{2+}-containing DMSO has been elucidated for the first time. Unfortunately with respect to battery research, no OER has been observed, which is probably due to reaction of the reduced oxygen species like MgO_2 with the solvent. The slight deactivation of the electrode and the overall low collection efficiency in RRDE-measurements imply the partial formation of insoluble products. Furthermore, the fact that the collection efficiency increases with respect to the rotation frequency suggests that the soluble proportion of the products is susceptible to chemical decomposition, which leads to non-oxidisable products.

The total number of electrons transferred per oxygen molecule has been found to equal 2, which implies the formation of some kind of peroxide. This was confirmed by using two independent methods (DEMS and RRDE). RRDE-measurements reveal that the kinetic currents are independent of the oxygen concentration as well as the Mg^{2+}-concentration. This is explained by a pre-adsorption step of an oxygen molecule and a corresponding adsorption isotherm which is close to saturation. If any step can be designated as rate determining, the Tafel-slope of 120 mV/dec should signify a one-electron transfer as the rds. Taking the saturation of the surface into account, this rds is expected to be the second electron transfer. The effect of the cathode material and the cations on the peroxide formation potential indicates the formation of a contact ion-pair which is attached to the surface.

Furthermore, an additional limitation of the measurable currents has been identified which is independent of the applied potential. As will be stated elsewhere, this additional limitation is probably related to migration of charged species through an increasing surface film. The investigation of this additional limitation will be subject of a subsequent publication.

4 The Effect of Calcium Ions on the ORR in DMSO

Philip Reinsberg*, Christoph J. Bondue* and Helmut Baltruschat*

*Institut für Physikalische und Theoretische Chemie, Universität Bonn, Römerstraße 164, D-53117 Bonn, Germany

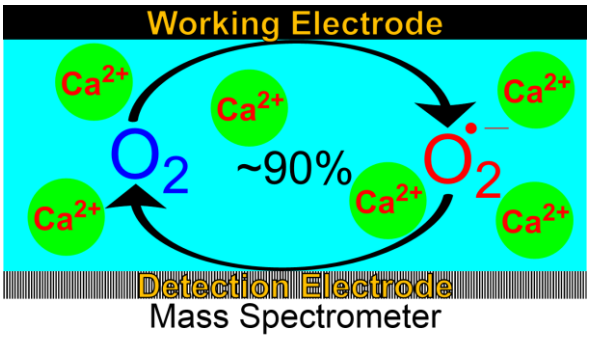

Received: July 4, 2016
Published online: August 30, 2016

Reprinted (adapted) with permission from
P. Reinsberg, C. J. Bondue and H. Baltruschat, *J. Phys. Chem.* C **2016**, *120*, 22179–22185.
 DOI: 10.1021/acs.jpcc.6b06674

Own manuscript contribution:

- design of the experiments
- conducting the experiments
- interpretation of the results
- writing the manuscript

ACKNOWLEDGMENTS

The authors gratefully acknowledge the Federal Ministry of Education and Research for funding this work (03EK3027 A). P.R likes to thank the German National Merit Foundation for financial support

4.1 Abstract

The development of a reversibly working metal–O_2 battery is an ongoing challenge. While lithium and sodium have been extensively used to study the oxygen reduction reaction in aprotic solvents, calcium did not receive attention for use in a metal–O_2 battery. This paper aims at examining the oxygen reduction and evolution reaction in Ca^{2+}-containing dimethyl sulfoxide at different electrode materials via the use of differential electrochemical mass spectrometry and rotating ring disk electrodes. The measurements reveal that superoxide is the main product of the oxygen reduction at various electrode materials. However, at gold electrodes the transfer of two electrons per oxygen molecule is observed. The superoxide is soluble and can be reoxidized almost completely from the solution to evolve oxygen, leading to roughly 90% true Coulombic efficiency. Furthermore, the oxygen evolution from species deposited during the oxygen reduction has been observed resulting in an overall reversibility of 95%. Our results combined with recent advances in the deposition of calcium emphasize the relevance of calcium for use in a future Ca–O_2 battery.

4.2 Introduction

Two decades after the introduction of the concept of a Li–Air battery[13] the development of a highly reversible Metal-oxygen battery remains challenging. While research on the Li–O_2[46,233-236] and Na–O_2[15,237,238] systems is highly advanced by now, other Metal–O_2 system promising high theoretical energy densities like Mg–O_2 [17,200,239] have attracted only little attention. Due to the influence of the cation on the distribution of the products[16,62,240], i.e. mainly the preferred formation of either superoxide or peroxide, and related to that the reversibility of the battery, a larger screening of cations seems promising. However, as the specific energy of the Metal–O_2 battery is inherently coupled to the metal anode, only a few cations derived from low density metals appear to be eligible to outperform conventional Li^+-ion batteries.

Probably a highly promising cation, which has not been subject to any research related with the oxygen reduction reaction (ORR) and oxygen evolution reaction (OER) in aprotic solvents, is the calcium ion. Calcium has a high abundance in the continental's crust (more than 150% of the abundance of sodium and magnesium)[241,242]. This and its low molecular weight of $M = 40.078\ \mathrm{g\ mol^{-1}}$ combined with the low standard potential of −2.368 V for the Ca^{2+}|Ca redox couple in aqueous solution establish calcium as competitive metal for application in metal–O_2 batteries. Adding to this, recent studies have shown that it is indeed possible to deposit Ca from aprotic solvents using simple salts like $Ca(ClO_4)_2$ [243,244]. Besides, Ca-deposition via insertion or alloy formation has been observed[245-247].

Regarding the reactions in an aprotic Ca–O_2 battery, the formation of three major products seem to be plausible. The calculation of the thermodynamically expected cell voltage ΔE^o is described in the text below:

$$Ca(s) + 2\,O_2(g) \rightleftharpoons Ca\left(O_2\right)_2(s) \qquad \Delta E^0 = 3.25\,V \tag{4.1}$$

$$Ca(s) + O_2(g) \rightleftharpoons CaO_2(s) \qquad \Delta E^0 = 3.38\,V \tag{4.2}$$

$$Ca(s) + 0.5\,O_2(g) \rightleftharpoons CaO(s) \qquad \Delta E^0 = 3.13\,V \tag{4.3}$$

Calculations based on the Born-Haber cycle and extrapolations of known properties by Sadhukhan[248] yield a free enthalpy of formation of $Ca(O_2)_2$ of $\Delta_F G^o(Ca(O_2)_2) = -314\ kJ\ mol^{-1}$. $Ca(O_2)_2$ can be prepared by heat-induced disproportionation of $CaO_2 \times 2\,H_2O_2$[249,250]. The finding that $Ca(O_2)_2$ does not undergo further disproportionation to CaO_2 or CaO underlines its kinetic stability. Regarding CaO_2, the free enthalpy of formation was determined experimentally to be $\Delta_F G^o(CaO_2) = -652\ kJ\ mol^{-1}$ ([251] cited in [252]). The formation of CaO is less exergonic $\Delta_F G^o(CaO) = -603.5\ kJ\ mol^{-1}$ [14]. The resulting specific energy, with respect to the mass of the resulting $Ca–O_2$ species, as well as the expected potentials with respect to the reference electrode used in the experiments are listed in Table 4.1. For comparison, corresponding values for the $Na–O_2$ system are included as well.

Table 4.1: Thermodynamically expected parameters of the $Ca–O_2$ and $Na–O_2$ System[a]

	***u*/W h kg^{-1}**	**ΔE^o/V**	***E*^{o} (vs. Ag$^+$|Ag)[a]/V**
$Ca(O_2)_2$	838	3.25	−0.11
CaO_2	2515	3.38	0.02
CaO	2989	3.13	−0.23
NaO_2	1103	2.26	−0.98
Na_2O_2	1595	2.32	−0.91
Na_2O	1683	1.95	−1.29

[a] *u*: Specific energy with respect to the mass of the product of the discharge reaction. ΔE^o: Thermodynamically expected cell voltage. E^o(vs $Ag^+|Ag$): Expected standard potential with respect to the potential of the reference electrode used in this work. The potentials have been calculated using the redox potential of $Ca^{2+}|Ca$ in DMSO (E^o ($Ca^{2+}|Ca$) = −2.93 V vs NHE[253,254] with some uncertainty due to diffusion potentials), the potential of Na/Na+ in DMSO (E^o (Na+|Na) = −2.81 V[216]) and the potential of the $Ag^+|Ag$-electrode in DMSO used as the reference in this work ($E(Ag^+|Ag)$ = 0.43 using the standard potential obtained by Gritzner[216].

In the current work, the oxygen reduction and evolution reaction in Ca^{2+}-containing electrolytes is examined for the very first time. DEMS and RRDE techniques are used to identify relevant products and elucidate the reaction mechanism. Due to the high practical relevance, this work mainly focuses on electrode made of carbon, while noble metal electrodes have been used for comparison.

4.3 Experimental Section

4.3.1 Dual thin-layer cell

The dual thin-layer cell used for DEMS measurements consists of two compartments connected by six capillaries. The flow of electrolyte is maintained by a peristaltic pump. The electrolyte enters the upper compartment, where the working electrode (WE) (A = 0.283 cm^2) is placed and where species can react electrochemically. It then flows through the capillaries to the lower compartment and leaves the cell. The lower compartment is connected to the mass spectrometry (MS) via a porous Teflon membrane resting on a steel frit. Volatile species diffuse through the membrane and thus can be detected by the MS. Using a reaction of known stoichiometry, a calibration constant can be calculated which relates the MS signal to the faradaic current. This allows the calculation of the flow of oxygen $\dot{n}(O_2)$ and finally the determination of the number of electrons z which are transferred per molecule according to the following equation:

$$z = \frac{I_F}{\dot{n}(O_2) \cdot F} \tag{4.4}$$

4.3.2 6-electrode dual thin-layer cell

The geometries of the six-electrode cell and of the dual thin-layer cell are quite similar. However, in the former it is possible to use a metal-sputtered Teflon membrane as a detection electrode in the lower compartment. Hence, intermediates formed at the working electrode in the upper compartment (WE1) (A = 0.283 cm^2) are transported to the lower compartment and can undergo a reaction in the lower compartment (WE2) (A = 0.283 cm^2). This arrangement is reminiscent of an RRDE arrangement but with the possibility to gain information on the nature of the intermediate if it reacts to a volatile species at WE2. Like using RRDE, it is possible to determine from the ratio of the currents at WE1 and WE2 the share of intermediates that are formed at WE1. In addition, it is possible to calculate the number of electrons z that are transferred during the electrochemical reaction at WE1 and WE2 by a calibration similar to that mentioned above. In some cases the reactions at WE1 and WE2 cause an MS signal on the same mass. In this case two experiments are necessary to determine the MS signal due to the reaction at WE2. In one experiment no reaction in the lower compartment is allowed, while in the other a reaction at WE2 takes place. The MS signal due to the reaction at WE2 is determined by subtraction of the MS signals of the individual measurements. All potentials are reported vs $Ag^+|Ag$ in DMSO as the redox potential of $Ca^{2+}|Ca$ in DMSO is subject to some uncertainties. The potential of $Ca^{2+}|Ca$ in DMSO is 3.36 V vs the used reference electrode[216,222,253].

4.4 Results and discussion

4.4.1 ORR in Ca^{2+}-containing DMSO evaluated by DEMS

Some general features of the ORR in $Ca(ClO_4)_2$ containing DMSO are shown in Figure 4.1a. The onset of the ORR is at about −0.8 V vs. $Ag^+|Ag$ and the diffusion-limited current is achieved at −1.2 V. t is remarkable that a deactivation of the electrode as in the case of the use of Li^+ is not occurring. The reduction of oxygen is accompanied by a decrease of the flow of oxygen $\dot{n}(O_2)$ into the MS (Figure 4.1b). This directly proves that it is in fact oxygen which is reduced at the electrode. Figure 4.1c shows that there is no electrolyte decomposition to CO_2. Both at GC and at Au electrodes, the integration of $\dot{n}(O_2)$ for potentials lower than −0.8 V yields a total amount of 20 nmol of reduced oxygen.

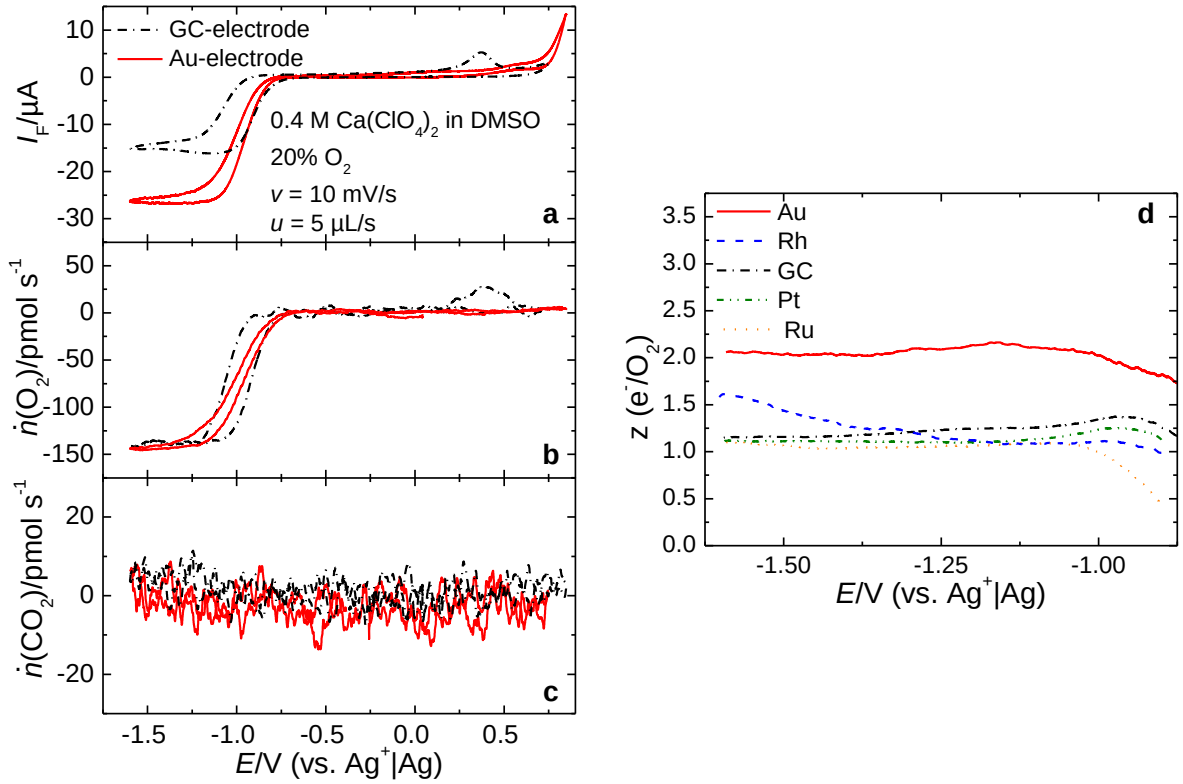

Figure 4.1. DEMS measurements at different electrode materials. **a**. CV at a GC- and an Au-electrode. **b**. flow of oxygen $\dot{n}(O_2)$ after background subtraction. **c**. flow of CO_2 $\dot{n}(CO_2)$ after background subtraction. **d**. corresponding number of electrons z transferred per O_2 molecule calculated according to equation (4.4). Electrolyte: DMSO containing 0.4 M $Ca(ClO_4)_2$ saturated with a mixture (80:20) of Ar and O_2 at. Flow rate u = 5 µL s^{-1}; sweep rate v = 10 mV s^{-1}.

However, in the same potential range less charge is transferred at the GC-electrode (7100 µA cm^{-2}) than at the Au-electrode (11300 µA cm^{-2}). It is evident from Figure 4.1d that this difference is due to a different product distribution: At the Au-electrode oxygen is reduced to peroxide ($z \approx 2$) and at GC to superoxide ($z \approx 1$). The latter is also true for Pt, Rh and Ru. It is interesting to note that a small anodic peak at 0.4 V, which is related to oxygen evolution, is

visible for the GC electrode. The total amount of oxygen evolved in this peak equals 0.9 nmol, which is roughly 5% of the amount of reduced oxygen.

Comparing the experimentally observed onset potential for ORR to the calculated potential in Table 4.1 a large discrepancy becomes obvious. However, as the products of the ORR are in fact soluble, it is implausible to use the standard potential of the formation of *solid* Ca–O_2 species for comparison. In fact, the ORR occurs close to the standard potential of the O_2/O_2^- couple determined in TBA^+-containing DMSO (E^o = −1.0 V vs. $Ag^+|Ag$ in DMSO)[62]. Taking into account that the presence of Li^+, Na^+, K^+ or Mg^{2+}-ions[62,139,239] shifts the onset potential roughly 200 mV into the positive direction, the ORR in Ca^{2+}-ion containing solution takes place via a similar initial step, which is presumably the formation of superoxide. However, the onset potential for ORR is significantly more negative than the standard potential expected for the formation of solid $Ca(O_2)_2$ (Tab. 1). This implies that there is a kinetic barrier like a nucleation barrier which hampers the precipitation of $Ca(O_2)_2$ and thus leads to the preferred formation of dissolved superoxide.

4.4.2 Identifying the soluble products of the ORR using DEMS for Pt

As the amount of oxygen evolved in the subsequent anodic sweep (peak at 0.4 V) only makes up 5% of the reduced oxygen, the fate of the remaining reduced oxygen species is highly interesting. In principle, an RRDE setup could be used in order to investigate the nature of the soluble species. However, the soluble species are expected to be reduced oxygen species. Thus, oxidation of these species should yield oxygen (if the reaction can in fact be reversed). Hence, a direct proof of the reversibility of the ORR can be achieved by the use of MS which detects oxygen evolved upon oxidation. For this reason, a six-electrode dual thin-layer cell employing a second porous working electrode (WE2) close to the MS was used to examine the nature of the soluble species. Due to the porous nature of WE2, volatile species can still enter the MS. From the comparison of $\dot{n}(O_2)$ in the presence of WE2 and in its absence, it can be concluded whether oxygen is evolved upon oxidation at WE2 or not. As already indicated by the electron numbers in Figure 4.1 d and further underlined in the section 4.6, the ORR at platinum and glassy carbon occurs in a very similar manner. Thus, it is believed that the experimental results obtained at the platinum electrode hold as well for the glassy carbon electrode. Later RRDE experiments are presented below using glassy carbon as electrode material.

As can be seen from Figure 4.2 c, the absolute value of $\dot{n}(O_2)$ is significantly lower when an Au-sputtered Teflon membrane (WE2) is placed close to the MS. This means that a lower amount of oxygen is consumed when the Au-sputtered membrane with a positive potential applied to it is present. Since the membrane does not have an influence on the ORR at the working electrode (WE1) in the upper compartment (as can be seen from the faradaic current for WE1), this can only be understood by assuming that the reduced oxygen species are

reoxidized to molecular oxygen at the second working electrode. Thus, the dissolved oxygen species can indeed be reoxidized, and this oxidation product leads to the evolution of oxygen.

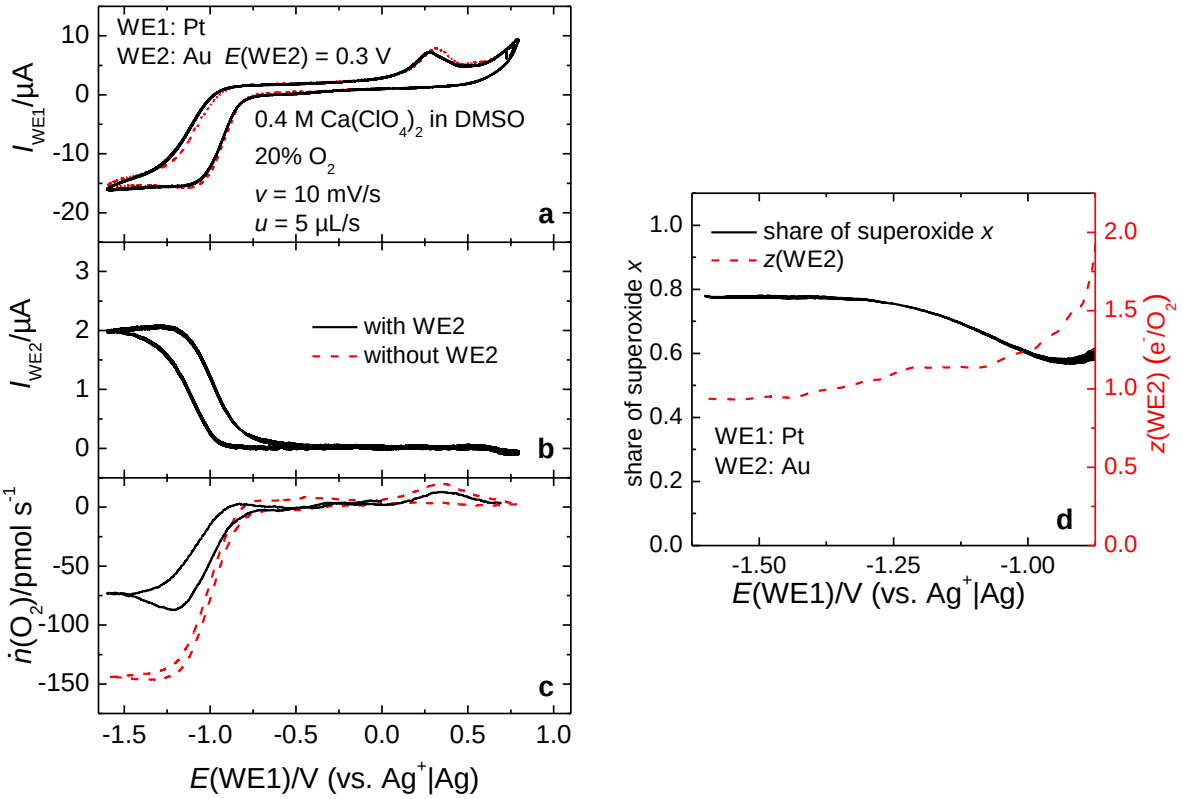

Figure 4.2. Identification of the soluble products via DEMS. **a**. CVs at the Pt-working electrode with (black) and without (red) the use of an Au-sputtered Teflon membrane (E(WE2) = 0.3 V) in the detection compartment. **b**. Faradaic currents at the sputtered Teflon-membrane. **c**. Corresponding flow of oxygen $\dot{n}(O_2)$. **d**. Resulting electron numbers at the second working electrode (black) and share of superoxide x (red) calculated according to equation (4.5) . Electrolyte: DMSO containing 0.4 M $Ca(ClO_4)_2$ saturated with a mixture of 80% Ar and 20% O_2.

The number of electrons transferred at the second working electrode WE2 can be calculated from the ratio of the current at WE2 to the difference of the oxygen flows $\dot{n}(O_2)$ without and with an Au-sputtered membrane. The actual flow $\dot{n}(O_2)$ can be calculated from the MS signal using the corresponding calibration constant K_2* obtained in TBA^+-containing DMSO (see Figure S 4.1). As shown in Figure 4.2d (red Y-scale), the number of electrons at the second working electrode is close to 1, which indicates that the soluble species are indeed related to superoxide. In analogy to RRDE-measurements the share of this soluble superoxide can be calculated according to equation (4.5) once the theoretical collection efficiency N_0^F has been determined by the calibration reaction, where I_{WE1} is the current as the first working electrode and I_{WE2} is the current at the second working electrode.

$$\text{share of superoxide } x = \frac{2I_{WE2}}{N_0^F I_{WE1} + I_{WE2}} \qquad (4.5)$$

As can be seen from Figure 4.2d (black Y-scale), the amount of superoxide oxidized at the second working electrode equals almost 80% of the amount of species generated at the disk

electrode. When adding this to the amount of reduced oxygen species which remains on the surface, a rather high reversibility of 85% is achieved.

4.4.3 Investigations of the ORR in RRDE-measurements

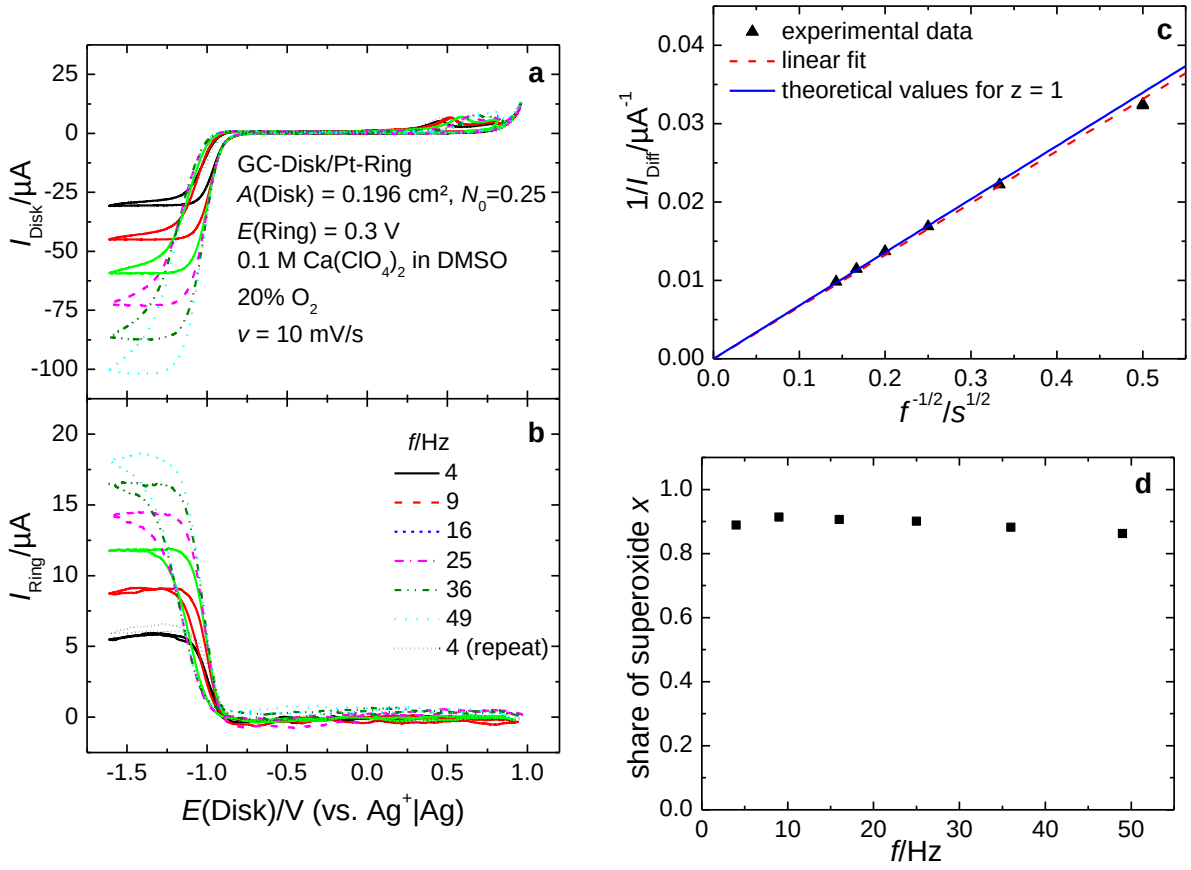

Figure 4.3. Oxygen reduction and evolution at a GC-disk/Pt-ring RRDE-assembly. **a**. CV at a GC-disk at various rotation rates *f*. **b**. corresponding CV at a Pt-ring electrode with a constant ring-potential of *E*(Ring) = 0.3 V. **c**. Comparison of the experimental and theoretical values of the diffusion-limited current I_{Diff}. **d**. Share of superoxide *x* calculated according to equation (4.5) using N_0 = 0.24.in Electrolyte: 0.1 M $Ca(ClO_4)_2$ in DMSO saturated with a mixture (80:20) of Ar and O_2. Sweep rate $v = 10\ mV\ s^{-1}$.

To further investigate the nature and fate of the dissolved superoxide, RRDE-measurements at GC-electrodes have been conducted with different rotation rates and ring potentials. The general behavior of the ORR at a glassy carbon disk-electrode can be seen in Figure 4.3a and Figure 4.3b. I_{Disk} indicates the current obtained at the disk-electrode and I_{Ring} as the ring-current. At potentials lower than −1.3 V diffusion-limited currents I_{Diff} are achieved, which are in excellent agreement (Figure 4.3c) with the theoretical values for a one-electron process. This was calculated using $D(O_2) = 15.8 \times 10^{-6}\ cm^2\ s^{-1}$ and $c(O_2) = 0.4\ mmol\ L^{-1}$ assuming that the solubility and diffusivity of oxygen in a solution of 0.1 M $Ca(ClO_4)_2$ in DMSO is roughly the same as in 0.1 M $Mg(ClO_4)_2$ containing DMSO[130]. Using equation (4.5) and substituting I_{WE1} by I_{Disk}, I_{WE2} by I_{Ring} and N_0^F by N_0 (which is defined by the geometry of the assembly) the share of superoxide *x* can be calculated. The outcome is similar to that of the DEMS-measurements with $x \approx 90\%$ independent of the rotational rate (Figure 4.3d). The Tafel-plot (Figure S4.2) leads

to a slope of 116 mV/dec characteristic for a one-electron process as the rate determining step, which is in accordance with previous observations in DMSO[61,62,213,221].

4.4.4 Potential-dependence of the ring-currents

So far, little attention has been paid to the potential, which has to be applied to the ring electrode (or sputtered Teflon-membrane) in order to oxidize the incoming species. The dependence of the ring currents on the potential applied to the ring-electrode is shown in Figure 4.4. While the disk-currents are unaffected by the ring-potential (Figure 4.4a), the currents at the ring electrode vary greatly from roughly 0 µA to 15 µA (Figure 4.4b). Diffusion-limited oxidation is apparently achieved at a potential of 0.3 V as the ring currents do not increase further when increasing the ring-potential. The experimental collection efficiency N ($N = |I_{Ring}/I_{Disk}|$) divided by the theoretical collection efficiency N_0 is plotted against the ring-potential in Figure 4.4c. It is somewhat astonishing that a minimum potential of −0.3 V has to be applied in order to measure a reasonable current although the ORR starts at significantly lower potentials (−0.8 V) and the soluble product has been identified as superoxide. While significant overpotentials are expected for precipitating species or species, which undergo further chemical reactions, dissolved species as the superoxide usually exhibits a more reversible behavior (as has been observed in TBA^+-containing electrolyte[62,123]).

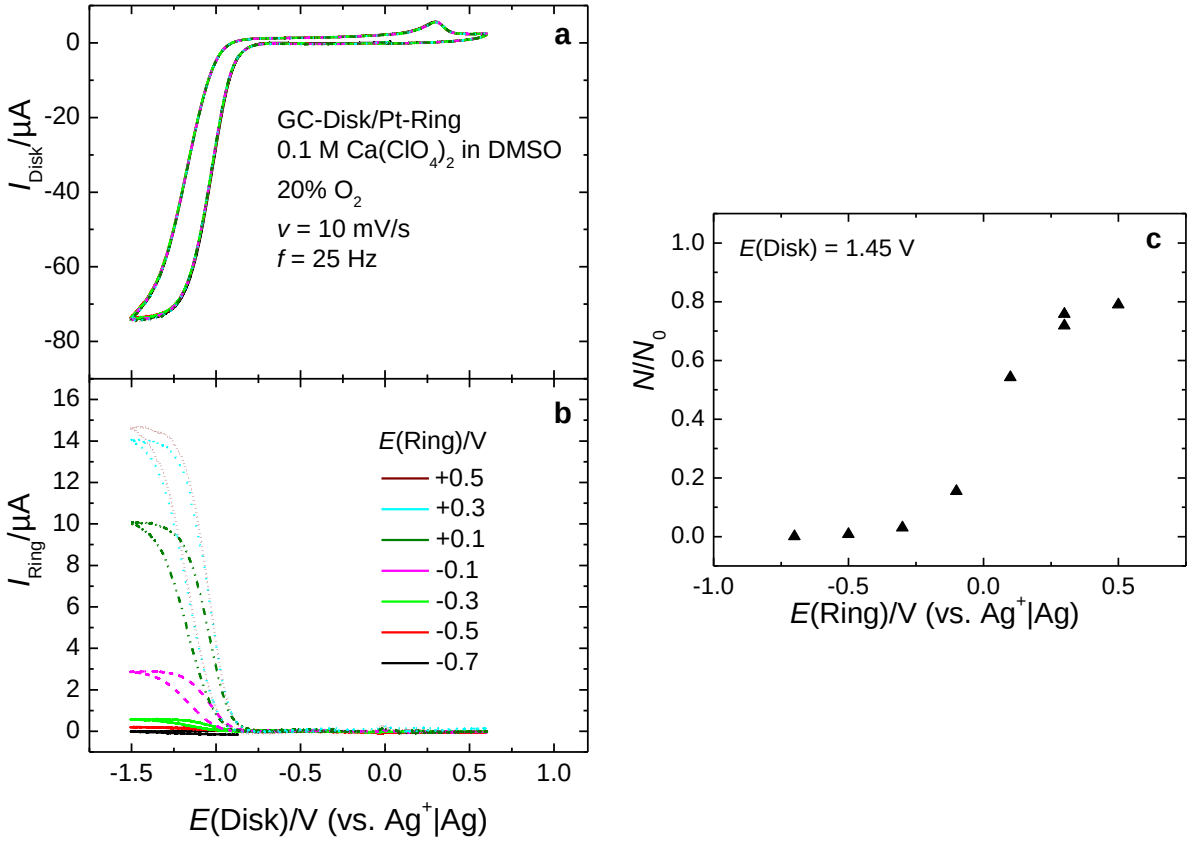

Figure 4.4. Potential dependence of the ring-currents. **a**. CV at the GC-disk. **b**. CV at the Pt-ring electrode, both under variation of the ring-potentials. **c**. Collection efficiencies N divided by the theoretical collection efficiency N_0 with respect to the potential applied to the ring E(Ring) at a constant disk-potential. Electrolyte: 0.1 M $Ca(ClO_4)_2$ in DMSO saturated with a mixture (80:20) of Ar and O_2.

Nonetheless, these rather high overpotentials can be understood if the Ca^{2+}-cations exert a strong effect on the O_2^--anions as it is the case for a contact-ion-pair. A chemical reaction of the superoxide appears to be improbable as the OER was not observed in a similar case ($MgClO_4)_2$ in DMSO), in which peroxide-species presumably reacted with the solvent[239]. Furthermore, some dependence of the collection efficiency on the rotation rate would be expected if the superoxide degraded chemically. Thus, it is plausible to assume the formation of a contact ion-pair. This is further supported by the finding that the presence of Li^+-ions affects the redox potential of the O_2/O_2^- couple which cannot be accounted for by the formation of solid LiO_2 as it is known to be unstable[48,62,255].

4.4.5 ORR and OER without convection

In order to further investigate the oxidation of the soluble products, cyclic voltammograms without convection have been recorded in a classical H-cell (Figure 4.5). As can be seen from Figure 4.5a, a peak is exhibited in the potential range of the ORR. The peaks shift from −0.95 V at v = 10 mV s^{-1} to −1.07 V at v = 200 mV s^{-1}, while the anodic peaks shift in the same direction from −0.02 V to − 0.07 V. This potential is in fair agreement with the formation potential of solid $Ca(O_2)_2$ (Tab. 1). The shift of the anodic peak is probably related to the decreasing ORR charge (430 µC at 10 mV s^{-1} vs. 49 µC at 200 mV s^{-1}).

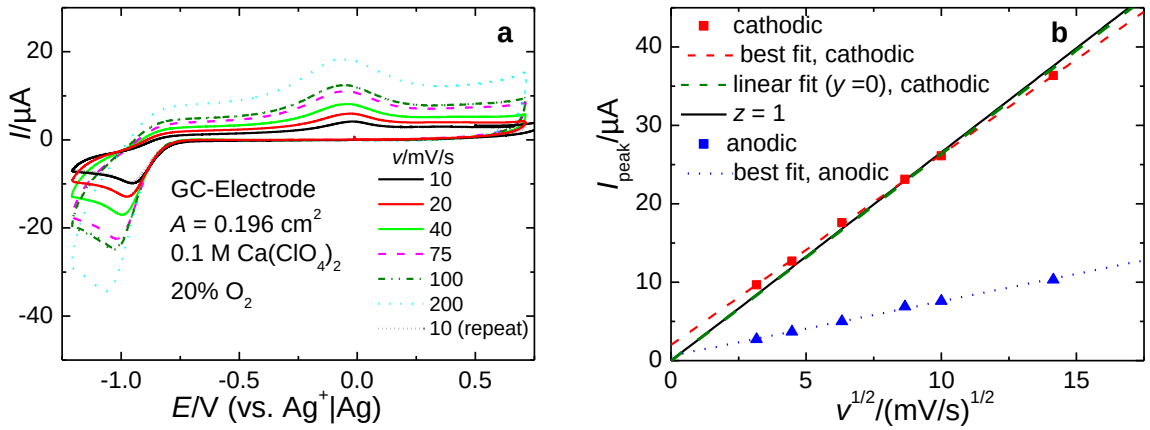

Figure 4.5. Cyclic voltammetry at a GC-electrode. **a**. CVs at a GC-electrode without convection for different sweep rates v. **b**. Randles-Sevcik-plot of the cathodic and anodic peak potentials, where y denotes the ordinate's intercept. Electrolyte: 0.1 M $Ca(ClO_4)_2$ in DMSO saturated with a mixture of (80:20) Ar:O_2.

The large peak separation of almost 1 V again confirms that the soluble species cannot be "free" superoxide, but are either complexed by cations or react in a way that a severe overpotential for the oxidation arises. Plotting the peak currents of the cathodic peak versus the square root of the sweep rate $v^{1/2}$ (Figure 4.5b) reveals again that the experimental data is in very good agreement with the theoretical data for z = 1. The existence of a peak during ORR indicates that there is some kind of diffusion limitation. Thus, the ORR in Ca^{2+}-containing

DMSO appears to be, as expected, a rather facile reaction. The applicability of the Randles–Sevcik eq. (4.6)

$$I_{Peak} = 0.4663zF\left(\frac{zF}{RT}\right)^{1/2} c\left(O_2\right) D_{O_2}^{1/2} v^{1/2} \tag{4.6}$$

suggests that the formation of superoxide is indeed a reversible reaction. However, the high overpotential for the oxidation of superoxide depicted in Figure 4.4 implies that the superoxide undergoes a subsequent reaction (which is presumably the formation of a contact ion-pair). The linear correlation of the anodic peak potential with $v^{1/2}$ is probably related to the fact that the total ORR charge is also proportional to $v^{1/2}$ and thus to the amount of oxidisable species.

4.5 Conclusions

It has been shown via the use of DEMS, RRDE, and simple cyclic voltammetry that the ORR in Ca^{2+}-containing DMSO leads to the almost exclusive formation of superoxide at electrodes made of glassy carbon, platinum, ruthenium, and rhodium. However, the ORR at gold electrodes leads to the formation of peroxide over the whole potential range. Reasons for the unique behaviour of the gold electrode have to be elucidated. The dissolved species, forming at the other electrodes, have been identified as superoxide and have been oxidized to re-evolve oxygen. At glassy carbon electrodes the amount of dissolved, re-oxidisable species corresponds to almost 90% of the amount of reduced oxygen. Additionally, an amount of 5% of insoluble species is formed which as well yields oxygen upon oxidation resulting in an overall reversibility of 95%, which is remarkable for the oxygen reduction reaction in aprotic solvents. The fate of the remaining 5% of the reduced oxygen species remains so far unclear. However, preliminary experiments indicate that the reversibility decreases with increasing water content. Thus, decreasing the water content to a very low degree might increase the reversibility sufficiently. At first glance, the formation of mainly soluble species seems to be disadvantageous for employing Ca in a real life battery. However, it has to be taken into account that in real life batteries only small electrolyte volumes are employed. Hence, the discharge products will be able to precipitate.

However, a significant overpotential was necessary for the reoxidation of the superoxide, which leads to the assumption that even the dissolved superoxide is stabilized by contact-ion interactions with Ca^{2+} ions. Further studies have to be conducted to identify possibilities to reduce the overpotential for the oxidation of the dissolved species.

4.6 Supporting Information

4.6.1 Chemical reagents

Calcium perchlorate tetrahydrate (99%, *Sigma Aldrich*) was repeatedly dried over an extended period of time (8 h) at 250 °C under reduced pressure (10^{-2} mbar) giving a white powder with

a water content below 20 ppm (measured in MeCN). Tetrabutylammonium perchlorate (≥ 99 %, *Sigma Aldrich*) was used as received.

The electrolyte preparation was carried out under an Ar-atmosphere in an *MBraun* glovebox. Extra dry DMSO (99.7%, over molecular sieve, *Acros Organics*) was used as received. The DEMS-measurements were performed using a custom made mixture of Ar and O_2 (80:20 = Ar : O_2) obtained from *Air Liquid*. Oxygen concentrations for the RRDE-measurements were adjusted by mixing highly pure Argon (*Air Liquid*, 99.999%) and highly pure oxygen (*Air Liquid*, 99.995%) using two flowmeters (*Krohne Duisburg*). The accuracy of the flowmeters was verified by measuring the volume expansion of the flowing gases with respect to time.

4.6.2 Rotating-Ring-Disk-Electrode (RRDE) measurements

The RRDE-measurements were performed in a closed H-cell. This H-cell was purged with an Ar-O_2 mixture throughout the experiment to saturate with oxygen and avoid contamination of the electrolyte with water from the ambient air. The water content was determined after the experiment via Karl-Fischer-titration (approx. 40 ppm). A silver wire in a solution of 0.1 M $AgNO_3$ in DMSO was used as reference electrode. To avoid contamination of the working electrolyte with $AgNO_3$ the contact between reference electrode and working compartment was established via the wet surface of a closed glass stopcock. The geometric surface area of the glassy carbon-disk electrode was $A(\mathrm{GC}) = 0.196\ \mathrm{cm^2}$, whereas a different tip (thin-gap) with $A(\mathrm{Pt}) = 0.164\ \mathrm{cm^2}$ was used as the Pt-electrode. The collection efficiency N_0 of the GC-disk and Pt-ring arrangement was calculated to $N_0(\mathrm{GC\text{-}Pt}) = 0.24$. The thin-gap RRDE-tip consisting of a Pt-disk and -ring had a collection efficiency of $N_0(\mathrm{Pt\text{-}Pt}) = 0.22$.

4.6.3 Differential electrochemical mass spectrometry (DEMS) measurements

Two different cells were used in order to carry out the DEMS-measurements. The first cell, the dual thin-layer cell, consists of two compartments. The electrochemical reaction takes place in the upper compartment (working compartment), where the working electrode is placed. The lower compartment (detection compartment), is connected to a mass spectrometer (MS) via a porous Teflon membrane. Both compartments are connected via six capillaries. The porous Teflon membrane rests on a steel frit and allows volatile species to diffuse into the vacuum. However, the solvent itself cannot pass the membrane due to its high surface tension and low vapour pressure. Due to continuous flow, products formed in the upper compartment are transported to the lower compartment where they may evaporate into the vacuum of the mass spectrometer. The simultaneous acquisition of the faradaic current I_F at the working electrode and the ionic current related to the mass z I_z allows a direct identification of (volatile) products and the calculation of the number of electrons transferred per products molecule.

The second cell, the 6-electrode dual thin-layer cell, also consists of two compartments. The major difference to the first cell is that a metal-sputtered membrane can be employed as a detection electrode in the lower compartment. This is not possible in the dual thin layer cell

because the high Ohmic drop inhibits potential control of the detection electrode. This problem was circumvented by employing two distinct sets of three electrode arrangements (one working electrode, one reference electrode and one counter electrode). Each working electrode was controlled by a potentiostat. The potentiostat of the detection electrode was decoupled from ground. The six electrode cell is reminiscent of an RRDE-arrangement: The metal sputtered Teflon membrane is held at a fixed potential at which species formed at the working electrode in the upper compartment can undergo an electrochemical reaction. The advantage of the 6-electrode cell over a conventional RRDE-arrangement is the option to combine a detection electrode with mass spectroscopy. It is, therefore, possible to detect the products of the electrochemical reaction at the working electrode in the lower compartment as well as the products of the electrochemical reaction at the working electrode in the upper compartment.

For both cells a reference electrode consisting of a silver wire in $Ag/AgNO_3$ in DMSO was connected via a Teflon-tube, which was closed by a rough glass bead, to the cell. The ionic current related to mass 32 I_{32} is considered to be the ionic current due to O_2, while I_{44} should resemble the ionic current due to CO_2. Especially the first assumption was further assured by introducing oxygen into the electrolyte and observing the change of I_{32}. All ionic currents presented here have been subject to a background subtraction and a smoothing process. The geometric surface areas of the working electrodes in the upper compartment amounted to $A = 0.283\ cm^2$.

4.6.4 Calibration of the dual thin-layer cell

The number of electrons *z* transferred per oxygen molecule can be calculated according to equation (S 4.1) as the ionic current I_{32} (which is directly measurable) is proportional to the amount of oxygen entering the MS per time and the faradaic current I_F is proportional to the amount of oxygen, which is converted at the electrode, times the number of transferred electrons:

$$z = \frac{I_F}{I_{32}} \cdot K^* = \frac{I_F}{\dot{n}(O_2) \cdot F} \qquad \text{(S 4.1)}$$

To alleviate understanding of the data presented in the main paper, the flow of oxygen $\dot{n}(O_2)$ is plotted in the figures. The mathematical relation between $\dot{n}(O_2)$ and I_{32} is obvious from equation (S 4.1) where *F* denotes Faraday's constant.

In order to determine the calibration constant *K** calibration of the system with a reaction of known stoichiometry (known *z*) is required. For that purpose, the ORR in the presence of $TBAClO_4$ was chosen, which was already reported to yield superoxide quantitatively. *K** does not only contain all the settings of the mass spectrometer that determine its sensitivity but also the probability that a molecule enters the vacuum in the first place. Therefore, *K** is only the proportionality constant that relates the faradaic current at the working electrode in the upper

compartment to the corresponding ionic current. Thus, if *z* is known, equation (S 4.1) can be used to determine *K**.

4.6.5 Calibration of the six-electrode dual thin-layer cell

In order to relate the faradaic current at the detection electrode WE2 to the corresponding ionic current a second calibration constant K_2* is required. K_2* will differ from *K** because the probability of a volatile product to enter the vacuum is larger. That is due to the fact that the detection electrode is placed at the interface between vacuum and electrolyte.

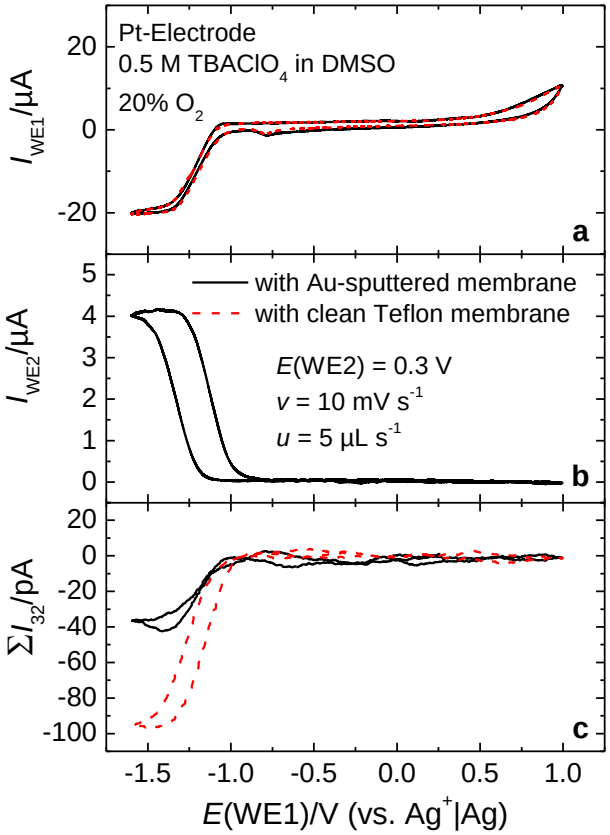

Figure S 4.1. Calibration of the six-electrode dual thin-layer cell at a Pt-electrode **a**. CVs at the working electrode WE1 in the upper compartment. **b**. Currents at the porous Au-electrode in the lower compartment (WE2) at a constant potential of *E*(WE2) = 0.3 V. **c**. Corresponding ionic currents measured. Electrolyte: 0.5 M $TBAClO_4$ in DMSO saturated with 20% O_2 and 80 Ar.

The measurement used for calibration of the six-electrode dual thin-layer cell is shown in Figure S 4.1. K_2* as well as *K** is determined by the reduction of oxygen to superoxide in TBA^+-containing DMSO. In the detection compartment superoxide is re-evolved to oxygen. This is a problem because the MS-signals of both working electrodes overlap: Oxygen is consumed at the working electrode in the upper compartment and oxygen is formed at the detection electrode. Hence, we can only determine the sum of the ionic current $\sum I_{32}$ of both processes. However, in order to determine K_2* we require the ionic current $I_{32,WE2}$ due to the reaction at the detection electrode WE2. The ionic current I_{32} due to the reaction at the working electrode WE1

in the upper compartment equals $\sum I_{32}$ when no reaction takes place in the lower compartment. Therefore, $I_{32,WE2}$ can be determined when I_{32} (no reaction in the lower compartment) is subtracted from the $\sum I_{32}$ (detection reaction in the lower compartment). K_2* is then determined via equation (S 4.2). It is also possible to determine the number of electrons that are transferred during the reaction at the detection electrode via equation (S 4.2) if K_2* is known. Hence, allowing the experimentalist to gather some information on the nature of the intermediate that reacts at the detection electrode.

$$K_2^* = \frac{I_{32,\mathrm{WE2}}}{I_{\mathrm{WE2}}} = \frac{\sum I_{32} - I_{32}}{I_{\mathrm{WE2}}} \qquad \text{(S 4.2)}$$

It might be interesting to evaluate the amount of species, which react at the second working electrode with respect to the total amount of species generated at WE1 (i.e. the share of superoxide *x* in this case). This can be determined from the ratio of the current at the detection electrode I_{WE2} to the current I_{WE1} at the working electrode in the upper compartment. This means that the transfer efficiency (the analogue of the collection efficiency of an RRDE arrangement) is needed. In general, there are also different methods to evaluate the share of superoxide. However, in this publication we shall limit ourselves to the faradaic currents at WE1 and WE2 in order to alleviate the comparability between RRDE and DEMS-experiments. In the case of an RRDE, the maximum share of species, first produced at the disk-electrode and then reacting at the ring-electrode, is defined by the theoretical collection efficiency N_0, which is defined by the geometry of the arrangement. The theoretical collection efficiency can also be measured: In such experiments a reversible redox system is employed and potentials for the disk and ring-electrode are chosen such that the reactions at both electrodes are limited by diffusion. The collection efficiency is then determined from the ratio of the current at the ring electrode to the current at the disk electrode.

Similar to this, a calibration constant which relies on the faradaic currents at WE1 and WE2 can be defined for the 6-electrode dual thin-layer cell. This calibration constant N_0^F (the faradaic transfer efficiency) also represents the maximum share of products that can undergo a reaction at the detection electrode. N_0^F depends on the geometry of the cell, the flow rate *u* and the diffusion coefficient of the species under investigation. According to equation (S 4.3) N_0^F can be determined from the results presented in Figure S 4.1.

$$N_0^F = \left| \frac{I_{WE2}}{I_{WE1}} \right| \qquad \text{(S 4.3)}$$

The calibration constant N_0^F can now be used to calculate the share of superoxide on the total amount of formed species in a manner, which is analogous to the evaluation of RRDE-measurements. If the assumption is made that either superoxide or some small amount of

peroxide is formed at the first working electrode WE1, the total current observed at WE1 can be written as:

$$I_{WE1} = (2 - x) \cdot F \cdot \left(\frac{dn}{dt} \right) \qquad \text{(S 4.4)}$$

x in equation (S 4.4) represents the share of superoxide, *F* is the Faradaic constant and dn/dt is the number of moles reacting per unit of time. At the same time, the current observed at the second working electrode can be written as

$$I_{WE2} = z \cdot F \cdot N_0^F \cdot \left(\frac{dn}{dt} \right) \qquad \text{(S 4.5)}$$

By assuming that only superoxide is oxidised at the ring (which is indeed justified as Figure 4.2 shows), combination and rearrangement of equation (S 4.4) and (S 4.5) leads to:

$$x = \frac{2 \cdot I_{WE2}}{I_{WE1} \cdot N_0^F + I_{WE2}} \qquad \text{(S 4.6)}$$

Equation (S 4.6) resembles the equation used to calculate the share of intermediates for RRDE assemblies.

4.6.6 Tafel-plots at the GC-electrode

The Tafel-plot in Figure S4.2 indicates, in accordance with previous measurements, that a one-electron transfer is the rate determining step for the ORR at glassy carbon.

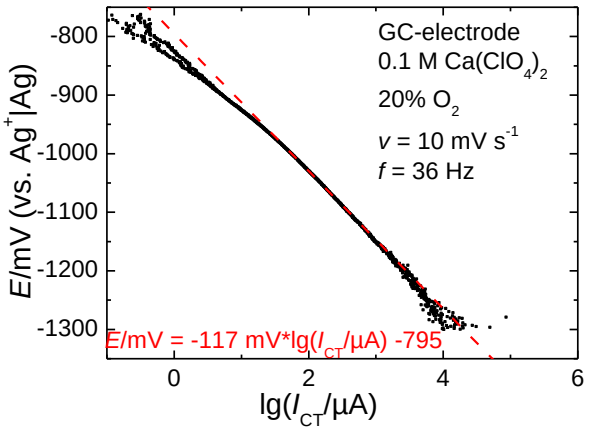

Figure S4.2. Tafel-plot using the data of Figure 4.4. I_{CT} indicates the current due to the charge-transfer without any kind of diffusion overpotential.

4.6.7 Comparison of RRDE experiments at GC- and Pt-electrodes

As already stated in the main section, it is expected from the electron numbers (Figure 4.1 d) that the ORR at GC- and Pt-electrodes is rather similar. To further compare the ORR at GC- and Pt-electrodes, RRDE measurements are presented in Figure S 4.3.

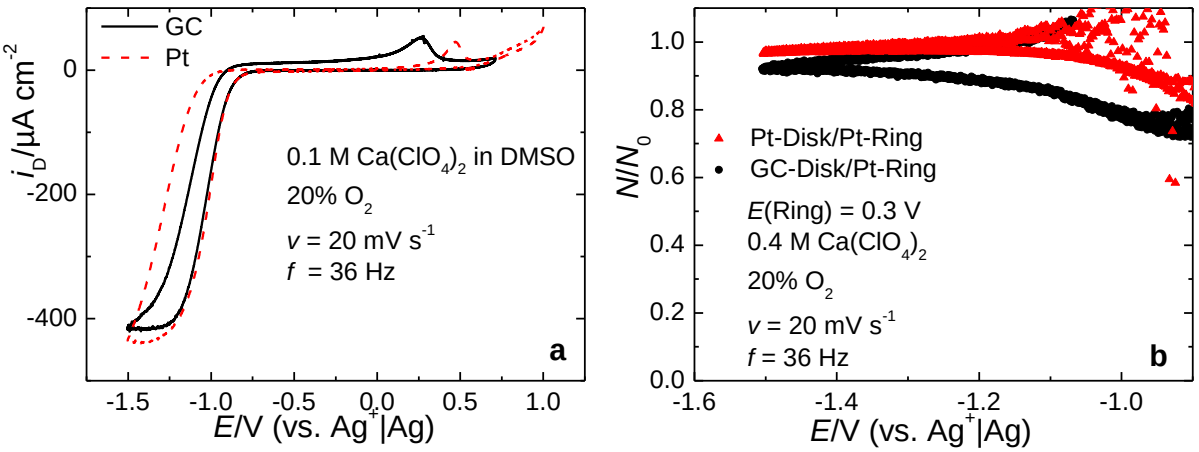

Figure S 4.3. Comparison of the RRDE-measurements at GC- and Pt-disks. **a**. Comparison of the disk-currents at a GC (black)- and Pt-electrode with respect to the geometric surface area. **b**. Comparison of the collection efficiency N with respect to the theoretical collection efficiency N_0 at a ring-potential of 0.3 V.

A Pt ring-electrode was used in each of these different arrangements. Instead of the measured disk-currents the disk-currents with respect to the geometric surface are used, as the Pt-electrode was a preassembled thin-gap electrode with a different geometric area (and a different theoretical collection efficiency of $N_0 = 0.22$). Comparing the diffusion-limited currents between −1.3 V and −1.5 V, the electrodes behave rather similar. Deviations can mainly be attributed to slightly different concentrations of oxygen. The difference in the collection efficiency might be explained by the fact that the Pt-Pt-arrangement is preassembled and thus might be in better agreement with the theoretical value of the collection efficiency than the GC-Pt-arrangement, which is a change-disk assembly.

A difference between GC on the one hand and Pt on the other hand is the hysteresis between anodic and cathodic sweep, which is more pronounced in the case of Pt (Figure S 4.3 a). This is not unexpected regarding the generally weak adsorption observed on GC-electrodes. The anodic peak at the Pt-electrode is shifted into the positive direction, which is in agreement with the larger hysteresis observed. To sum up, GC appears to be the more promising electrode material as compared to Pt.

5 The Effect of Divalent Cations on the ORR

Philip Reinsberg*, Abd-El-Aziz A. Abd-El-Latif*,+ and Helmut Baltruschat*

*Institut für Physikalische und Theoretische Chemie, Universität Bonn, Römerstraße 164, D-53117 Bonn, Germany

+ Permanent address: National Research Centre, Physical Chemistry Dept., El-Bohouth St. Dokki, 12311 Cairo, Egypt.

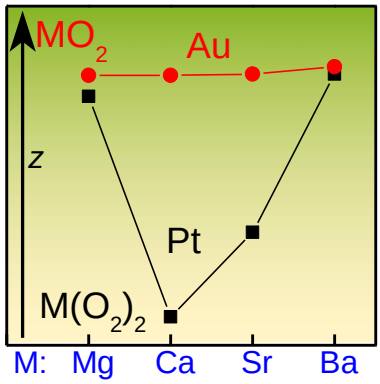

Received: January 18, 2018
Published online: March 21, 2018

Reprinted (adapted) with permission from
P. Reinsberg, A. A. Abd-El-Latif and H. Baltruschat, *Electrochim. Acta* **2018**, *273*, 424–431.
 DOI: 10.1016/j.electacta.2018.03.123

Own manuscript contribution:

- design of the experiments
- conducting the experiments
- interpretation of the results
- writing the manuscript

ACKNOWLEDGMENTS

The authors gratefully acknowledge financial support by the German Federal Ministry of Education in the framework of the Mg–air-(grant number: 03EK3027A) and the MeLuBatt-project (grant number: 03XP0110D).

5.1 Abstract

The resurgence of interest in oxygen reduction in non-aqueous electrolytes makes it necessary to develop a fundamental understanding of the factors influencing its kinetics and reversibility. One of these key factors is the cation of the conducting salt. This study focuses on the influence of the cation by extending research to the field of the alkaline earth cations. At gold electrodes, the main formation of the peroxides is observed for all the different cations. However, the peroxides do not lead to a deactivation of the electrode as opposed to the observations in the presence of lithium ions. Interestingly, at platinum and glassy carbon the cation exerts a more complex influence on the product distribution: The number of electrons transferred per oxygen molecule (z) increases in the order $z(Ca^{2+})<z(Sr^{2+})<z(Ba^{2+})\approx z(Mg^{2+})$. This is in good agreement with the acceptor numbers of the cations, with high acceptor numbers fostering the formation of peroxides. These results add an important aspect in understanding the oxygen reduction in non-aqueous solvents.

5.2 Introduction

Developing an aprotic secondary metal–O_2 battery is an ongoing challenge. The energy-wise most appealing battery, the lithium–O_2 battery, still suffers from insufficient reversibility and low discharge densities[139,202,256-264]. Various research groups attempt to address these issues by using soluble species as redox mediators for the oxygen reduction reaction (ORR) and oxygen evolution reaction (OER) in Li^+-containing electrolytes [75,86,265-271], but alternative cations (with the exception of Na^+[15,76,272-275]) have been investigated only to a minor extent. This is especially true for divalent cations despite their theoretically high specific energies and expected equilibrium potentials (see Table 5.1). Although the ORR in Mg^{2+}-cation containing electrolytes has proven difficult[79,200,239,276,277], the Ca^{2+}-ion facilitates a highly reversible ORR[18]. In battery research, barium has only been used as an additive so far: Matsuda *et al.* added Ba^{2+} to a Li^+-containing solution and found an improved discharge capacity, which they attributed to an incorporation of Ba^{2+} in the Li_2O_2 lattice[278].

Table 5.1. Thermodynamic properties of different alkaline earth metal–O_2 batteries[a]

	u/W h kg^{-1}	ΔE^o/V
MgO_2[218] cited in [279]	2801	2.94
CaO_2[251]	2515	3.38
SrO_2[280]	1431	3.19
BaO_2[280]	1002	3.16

[a]Specific energy u with respect to the mass of the peroxide and expected equilibrium potentials ΔE^o according to the standard free enthalpies of formation of the peroxides given in the references.

In this work, we extend research to the regime of alkaline earth cations using a flow-through cell coupled to differential electrochemical mass spectrometry (DEMS), which has the invaluable advantage of granting direct insight into the consumption and evolution of volatile species such as oxygen or species produced by parasitic reactions. The DEMS-analysis is complemented by electrospray ionization mass spectrometry (ESI-MS), which is used to elucidate the solvation shell of the different cations.

5.3 Experimental Section

5.3.1 Preparation of Electrolytes

Magnesium perchlorate ($Mg(ClO_4)_2$) (≥ 99% *Sigma-Aldrich*), calcium perchlorate tetrahydrate ($Ca(ClO_4)_2x4\ H_2O$) (99%, *Sigma Aldrich*), strontium perchlorate trihydrate ($Sr(ClO_4)_2x3\ H_2O$) (98%, *Alfa Aesar*) and barium perchlorate hydrate ($Ba(ClO_4)_2\ xH_2O$) (≥ 99%, *Fluka Analytical*) were dried under reduced pressure (10^{-2} mbar) at up to 230 °C for 6 h yielding white powders. The temperature was not raised higher to avoid decomposition of the salts. Cloudy solutions or white precipitates in contact with silver-containing solution were indicative of the decomposition of the salt. The residual water content of all salts was tested in acetonitrile via coulometric Karl-Fischer titration (C20 *Metler Toledo*) and was below 20 ppm. The electrolytes were prepared by dissolving the dried salt slowly in extra dry dimethyl sulfoxide (DMSO) (99.7+%, stored under molecular sieve, *Acros Organics*) in an Ar-filled glovebox (*MBraun*). Silver nitrate ($AgNO_3$) (≥ 99%, *ChemPure*) for preparation of the reference electrolyte and tetrabutylammonium perchlorate ($TBAClO_4$) (≥ 99%, *Sigma-Aldrich*) for calibration were used as received.

For the ESI measurements, the corresponding alkaline earth trifluoromethanesulfonates were used instead of the perchlorates due to the corrosive nature of the perchlorate anions in the ESI set-up. Magnesium trifluoromethanesulfonate ($Mg(SO_3CF_3)_2$) (Sigma-Aldrich, ≥ 97%), calcium trifluoromethanesulfonate ($Ca(SO_3CF_3)_2$) *(Sigma-Aldrich,* 99.9%*),* barium trifluoromethanesulfonate ($Ba(SO_3CF_3)_2$) *(Sigma-Aldrich,* 98%*)* and lithium trifluoromethanesulfonate ($Li(SO_3CF_3)_2$) (*Sigma-Aldrich*, 99.95%) were used as received for preparing the electrolyte. Extra dry acetonitrile (*Acros Organics*, 99.9%) was used as received. Highly pure Ar (*Air Liquide*, 99.999%) was used for purging the electrolyte and highly pure nitrogen (*Air Liquide*, 99.995%) was used as auxiliary and sheath gas to facilitate the evaporation of solvents. The solutions used for the measurement had a concentration of 100 µM with respect to the dissolved salt. As solvent pure acetonitrile and mixtures of DMSO and water (1:9 in volume) as well as DMSO and acetonitrile (1:9 in volume) were used. The concentration of DMSO was kept low as it contaminates the vacuum system of the ESI-system and is difficult to remove due to its low vapor pressure.

5.3.2 Setup and Methods

The DEMS set-up used for this work consists of a QMA 430 quadrupole mass spectrometer (*Pfeiffer Vacuum*), which is differentially pumped by two turbomolecular pumps (*Pfeiffer Vacuum*, 200L s^{-1} and 50 L s^{-1}). The dual thin-layer cell employed in this study was made of Kel-F® and consists an upper compartment (working compartment) and a lower compartment (detection compartment). In the working compartment, a thin layer of electrolyte is formed by the working electrode (WE) and two O-Rings (PTFE, inner diameter 6 mm, thickness: 200 µm). Thus, the geometrically available surface of the working electrode equals 0.28 cm^2. The detection compartment is formed by one O-Ring (PTFE, inner diameter 6 mm, thickness: 200 µm) and a porous PTFE membrane (thickness: 50 µm, pore diameter 20 nm) supported by a steel frit, which is in contact with the vacuum system of the mass spectrometer (MS). The connection between working and detection compartment is established via six capillaries in a circular arrangement. The electrolyte, which is saturated with an oxygen-argon mixture (20:80, *Air Liquide*) in a storage flask, enters the cell in the upper compartment, passes through the six capillaries and leaves the cell at the detection compartment. Further information regarding the DEMS-system as well as the cell can be found elsewhere[113].

The reference electrode consists of a silver wire immersed in 0.1 M $AgNO_3$ in DMSO, which gives a potential of 0.43 V versus the normal hydrogen electrode[216]. In order to avoid contamination of the working electrolyte, the connection between reference electrode and the outlet of the cell is established via a PTFE-tube, which was closed by a rough glass bead. A drawing of the reference electrode can be found elsewhere[123]. Two counter electrodes were employed to reduce electronic oscillations owing to the high impedance of the reference. The first one is placed at the inlet of the cell and connected via a low resistance (1 Ω) to the potentiostat, the second one is situated at the outlet of the cell in vicinity of the reference electrode and is contacted via a 1 MΩ resistance to minimize the Ohmic potential drop. The flow rate used for the measurements was 5 µL s^{-1} and the potential sweep rate was 10 mV s^{-1} resulting in a delay of 3.5 s or 35 mV between the electrochemical reaction at the working electrode and the detection via mass spectrometry. The data was corrected for this delay prior to evaluation.

The simultaneous acquisition of the faradaic signal I_F at the working electrode and the ionic current I_x related to mass *x* allows for identification of volatile species produced or consumed during the electrochemical reduction. Furthermore, the relation between I_F and the baseline-corrected values of I_x can be used for the calculation of the number of electrons *z* transferred per molecule according to eq. (5.1)

$$z = \frac{I_F}{I_x} \cdot K^* = \frac{I_F}{\dot{n}(x) \cdot F} \tag{5.1}$$

Where $\dot{n}(x)$ represents the flux of species with mass *x* into the MS, *F* represents the faradaic constant and *K** is the calibration constant taking into account properties of the MS itself (e.g.

ionisation probability) as well as the collection efficiency within the dual thin-layer cell. For evaluation of K^* a reaction of known stoichiometry (and thus known z) is needed. The calculation of from the ionic current is also evident from eq. (5.1). The oxygen reduction reaction in $TBAClO_4$ containing DMSO serves this purpose, which is known to quantitatively yield superoxide [123,281]. Alternatively, the oxygen reduction in $KClO_4$ containing DMSO can also be used for calibration as a more cost-efficient alternative[139].

ESI-MS measurements were performed in the positive electrospray ionization mode on a Finnigan MAT SSQ7000 instrument at 4.5 kV and a capillary temperature of 250°C. The sample solution, stored in a gas-tight syringe (*Hamilton*), was introduced to the ESI system via a 125 µm inner diameter PEEK tube at a flow rate of 20 µL/min using a syringe pump (Syringe Infusion Pump 22, *Harvard Apparatus, Inc.*, Cambridge, MA).

5.4 Results and Discussion

5.4.1 Oxygen Reduction and Evolution at Gold

The oxygen reduction and evolution in the presence of four different alkaline earth cations is shown in Figure 5.1, where data for the Ca^{2+}-containing DMSO was taken from [18]. Figure 5.1 a–b shows the ORR and OER at a gold electrode, the CO_2 signal is displayed in Figure 5.1 c, while the number of electrons transferred per oxygen molecule (z) is displayed in Figure 5.1 d.

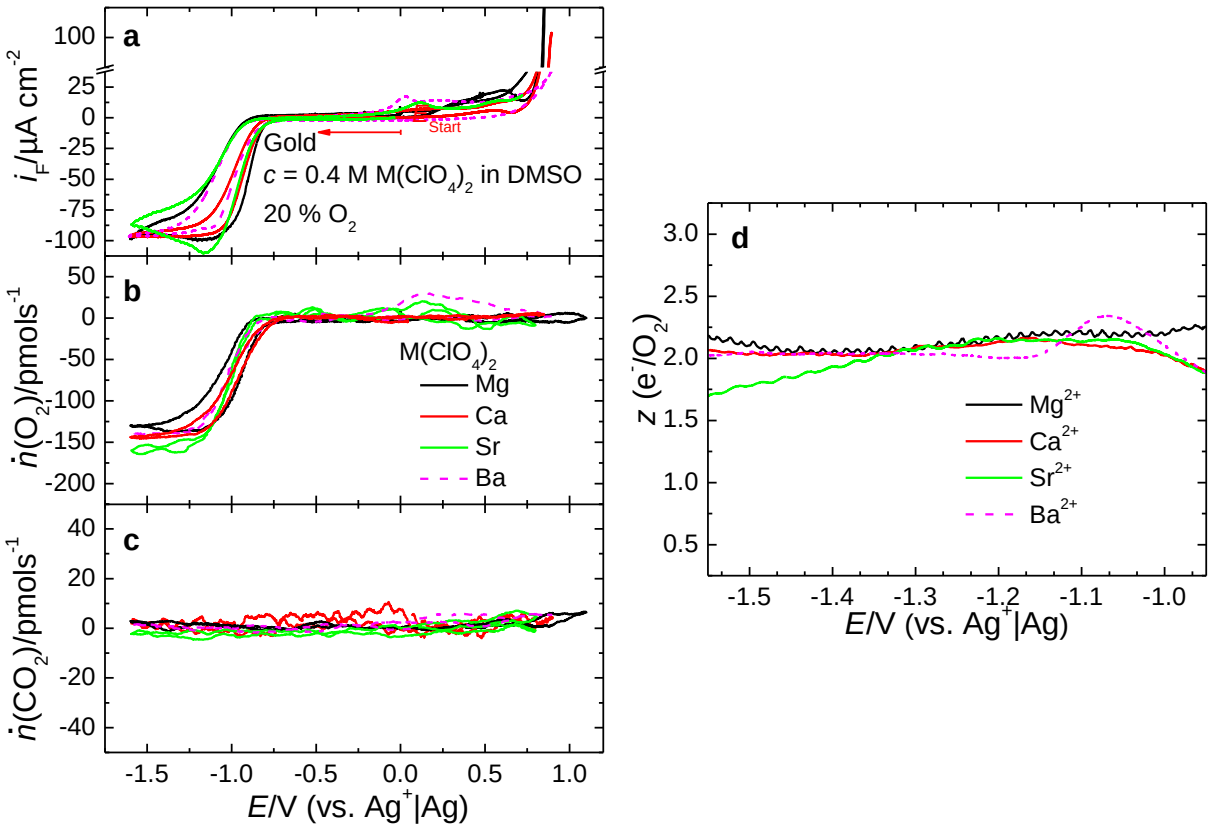

Figure 5.1. ORR and OER for different divalent cations in DMSO at gold **a.** Faradic current density (i_F) of the ORR/OER in the presence of Mg^{2+}, Ca^{2+}, Sr^{2+} and Ba^{2+}. **b–c.**. Simultaneously recorded

consumption and evolution of O_2 and CO_2. **d.** Number of electrons *z* transferred per oxygen molecule. Flow rate: 5 µL s^{-1}.

As can be seen from Figure 5.1 a, the onset of the ORR is similar in the cathodic direction for the four cations. However, while a constant current with a small hysteresis between cathodic and anodic sweep is observed in the presence of Ca^{2+}, this is not true for the other cations, which show larger hysteresis indicating a slight deactivation of the electrode. Nonetheless, the deactivation of the electrode in presence of any of the cations used in this study is not as severe as in the presence of Li^+ in the same experimental set-up, where basically no electrochemical activity for ORR is observed in the anodic sweep [139]. Investigations using the rotating ring-disc electrode imply that the peroxides formed during ORR with divalent cations are at least partially soluble [18,239], which will be further elucidated in an upcoming publication. The weakly deactivating behaviour principally favours high discharge capacities and might be utilized in the development of other metal–air batteries as indicated by Matsuda *et al.* [278]. Interestingly, when using Sr^{2+} or Mg^{2+} there is a peak at a potential of −1.15 V in the faradaic current followed by a constant current in the case of Mg^{2+} and a decreasing current for Sr^{2+}. When using Ba^{2+} in the electrolyte, a small shoulder appears at a similar potential, which is then followed by an increasing current. However, this not reflected in the consumption of oxygen (Figure 5.1 b), which is constant after an initial increase, and is possibly rather due to a shift of the product distribution. The evolution of CO_2, which is usually observed at anodic potentials in the case of Li^+-containing electrolytes[21,256], is absent for the different cations Figure 5.1 c. Comparing the number of electrons per oxygen (Figure 5.1 d) reveals that the peroxide formation is dominant for all alkaline earth metals at the gold electrode. This is different from the observations made using Li^+, Na^+ or K^+ as cations, where a distinct transition from the formation of superoxide to peroxide occurs [120,139,282]. Furthermore, the potential of this transition depends on the (alkali) cation.

In the anodic sweep at around 0 V, a small amount of oxygen evolution can be observed when Sr^{2+} or Ba^{2+} are present in the electrolyte. It has to be kept in mind that due to convection reaction species, which are not adherent to the electrode surface, are transported out of the cell and are therefore not oxidized. Thus, the oxygen evolution has to be due to the oxidation of previously deposited, insoluble species, which are most probably related to peroxide according to the number of electrons transferred per O_2 molecule. However, this deposition of species does not directly lead to a deactivation of the electrode during the ORR, but rather seems to shift the product distribution from mainly peroxide to superoxide as reflected in the electron numbers in Figure 5.1 d. This is similar to Li^+-containing DMSO, where the deposition of peroxide inhibits its own formation, while the superoxide generation is only affected to a lesser degree [282].

5.4.2 Oxygen Reduction and Evolution at Platinum and Glassy Carbon

Not only the cation but also the electrode's material affects the ORR and OER. This is probably due to the different adsorption behaviour of the products and intermediates on the different surfaces. As already known from Li^+-containing electrolytes, gold exhibits a special behaviour for the ORR [139,283,284]: At a certain overpotential, the formation of peroxide occurs via a direct process without the formation of soluble intermediates [282,284]. Thus, it is worthwhile to use other electrocatalysts in order to get a broader understanding of the effect of the cations on the ORR and OER. Figure 5.2 shows the ORR and OER at a platinum electrode.

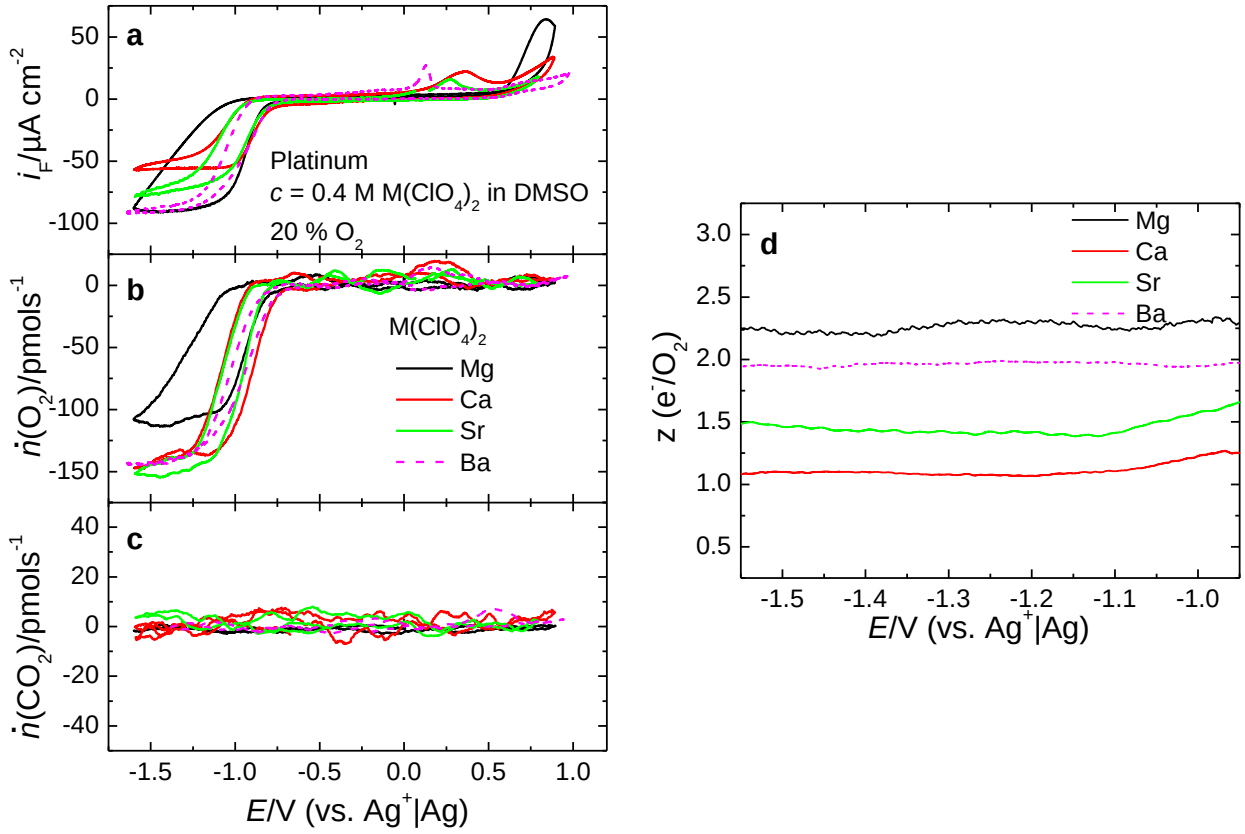

Figure 5.2. ORR and OER for different divalent cations in DMSO at platinum. **a.** Faradic current density of the ORR/OER in the presence of Mg^{2+}, Ca^{2+}, Sr^{2+} and Ba^{2+}. **b–c.**. Simultaneously recorded consumption and evolution of O_2 and CO_2. **d.** Number of electrons ***z*** transferred per oxygen molecule. Flow rate: 5 µL s^{-1}.

While the differences between the voltammograms among the four cations at the gold electrode were mainly restricted to the OER, the faradaic currents at platinum differ greatly for Ca^{2+}, Sr^{2+} and Mg^{2+}/Ba^{2+} (Figure 5.2a). Although the mass transfer limited consumption of oxygen (Figure 5.2 b) is similar for Ca^{2+}, Sr^{2+} and Ba^{2+}, the faradaic currents in case of Ca^{2+} are only half of the currents measured using Mg^{2+} or Ba^{2+} and the current for Sr^{2+} can be found somewhere in between. In the presence of Mg^{2+}, a notable hysteresis between cathodic and anodic sweep is visible, indicating a change in activity of the electrode. Furthermore, the maximum oxygen consumption is significantly lower than for the other cations, implying that

the process is not solely diffusion-limited [239]. Again, no CO_2 formation is observed (Figure 5.2 c). The resulting electron numbers (Figure 5.2 d) increase in the order: $z(Ca^{2+}) < z(Sr^{2+}) < z(Ba^{2+}) \approx z(Mg^{2+})$, implying that mainly superoxide is formed in the presence of Ca^{2+} and exclusively peroxide in the presence of Mg^{2+}. The fact that the electron number in presence of Mg^{2+} is even above 2 indicates that there are either side reactions or the partial formation of MgO. The electron numbers for Ca^{2+} and Sr^{2+} are in agreement with early work of Johnson *et al.*, who concluded from polarographic measurements and the titration of the insoluble products formed during ORR that oxygen is mainly reduced to superoxide in the presence of Ca^{2+} and Sr^{2+} at mercury electrodes [35,36].

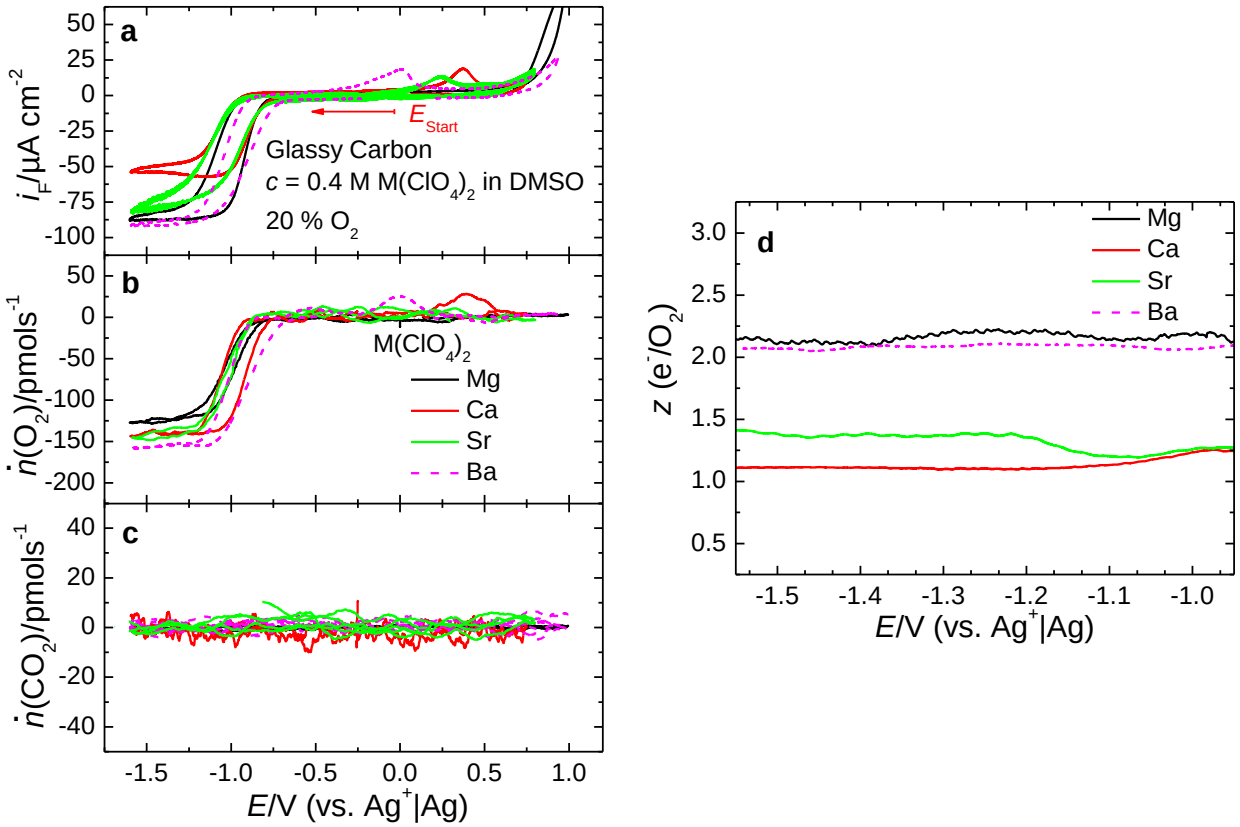

Figure 5.3. ORR and OER using different divalent cations in DMSO at glassy carbon. **a.** Faradic current density of the ORR/OER in the presence of Mg^{2+}, Ca^{2+}, Sr^{2+} and Ba^{2+}. **b–c.**. Simultaneously recorded consumption and evolution of O_2 and CO_2. **d.** Number of electrons *z* transferred per oxygen molecule. Flow rate: 5 µL s^{-1}.

A similar trend as in the case of the platinum electrode can also be observed when using glassy carbon as electrocatalyst (Figure 5.3). The faradaic current in the presence of Ca^{2+} again is the smallest (Figure 5.3 a), while the current in presence of Mg^{2+} and Ba^{2+} are equally large. As the consumption of oxygen is rather similar in all cases (Figure 5.3 b) and no evolution of CO_2 is observed (Figure 5.3 c, indicating a limited amount of side-products), the resulting electron numbers show a similar trend to that observed at platinum, with Ca^{2+} fostering superoxide formation and Ba^{2+} as well as Mg^{2+} peroxide formation (Figure 5.3 d).

As already pointed out, the oxygen evolution is also dependent on the cation present in the electrolyte solution. While no oxygen evolution can be observed in the presence of Mg^{2+} at any of the electrodes, this is not true for the other cations. At glassy carbon and platinum, the potential region in which oxygen evolution occurs is less broad as compared to gold. The half-wave potential of the OER shifts from Ba^{2+} to Sr^{2+} to Ca^{2+} to values that are more positive. This is in qualitative agreement with the expected equilibrium potentials (see Table 1), although Mg^{2+} again behaves special and does not show any OER at all. For Mg^{2+} there are considerably high anodic currents at even more positive potentials, which are not related to oxygen evolution and imply side reactions [239].

5.4.3 Structure of the Solvation Shell

To further elucidate differences between the earth alkaline cations used for this study, their solvation in mixtures of DMSO and acetonitrile (MeCN) as well as pure acetonitrile (MeCN) was investigated via ESI-MS and compared to that of Li^+ (Table 5.2, for an example of the original data please refer to the Supporting Information and already published data[139]). The reason not to use pure DMSO as solvent is related to its low vapor pressure and the contamination of the ESI system. As water is expected to be a ubiquitous contaminant in metal–air batteries, its effect on the solvation was probed by adding water to the organic solvents (up to a ratio of 9:1 in volume (H_2O:DMSO)). The decision whether a contact-ion pair is present in solution or water is present in the solvation shell was made by screening the raw data for any masses corresponding to the contact-ion pairs or complexes containing water.

Table 5.2. Solvation Shell for Different Alkaline Earth Cations and Li^+ in DMSO Containing Water and Pure MeCN.

Salt	Contact-Ion Pair?	Water in the ligand sphere?
$Mg(OTf)_2$ in MeCN	+	-
$Ca(OTf)_2$ in MeCN	+	-
$Ba(OTf)_2$ in MeCN	+	-
LiOTf in DMSO	-	-
$Mg(OTf)_2$ in DMSO	+	-
$Ca(OTf)_2$ in DMSO	+	-
$Ba(OTf)_2$ in DMSO	+	-

As shown in Table 5.2, no water is present in the solvation shell of the electrolytes used for this study. While the absence of water in the solvation shell does not necessarily imply that it cannot accumulate in the double-layer and thus participate in the electrochemical reaction, it has two important consequences: Firstly, the determination of the water content via for instance Karl-Fischer titration should yield reliable results. Secondly, it is likely that a certain amount of

water has the same effect on the electrochemical reaction regardless of the cation present in the solution as long as the reaction mechanism in the absence of water is similar. The formation of associates between the triflate anion and the cation has been observed for every divalent cation, but not for lithium. Only in lithium triflate containing solution, a complete dissociation of the salt was observed[139], while the divalent salts tend to form contact ion-pairs in solution.

5.4.4 The Cation's Complex Influence

The differences among the alkali and alkaline earth cations with respect to the ORR and OER give rise to the question: How do the cations influence the mechanism of oxygen reduction and evolution? A possible answer is given in Figure 5.4, which shows the mechanism suggested for the ORR in an aprotic solvent. The cation does not seem to exert a crucial effect on the reduction of oxygen to superoxide, as can be seen from the only slightly varying onset potentials of the ORR (Figure 5.1–3). However, the varying number of electrons transferred per O_2 molecules shows that the cations indeed have a significant influence on the relative amount of superoxide and peroxide. We suggest that this influence is present at the stage of the superoxide, which is polarized by the cations present in the electrochemical double layer. A strongly polarizing cation withdraws electron density from the superoxide, which is therefore easier to reduce to the corresponding peroxide. Therefore, the overall ratio of peroxide to superoxide, which is mainly determined by the ratio of the rate constant of the second electron transfer to the rate constant of the superoxide diffusion into the bulk solution, is expected to be higher in the presence of strongly polarizing cations. However, an effect of the cation on the mobility of superoxide might also play a role: Lowering the diffusion coefficient of superoxide would also lead to the more pronounced formation of peroxide at a certain potential and thus, at a certain rate of the electron transfer.

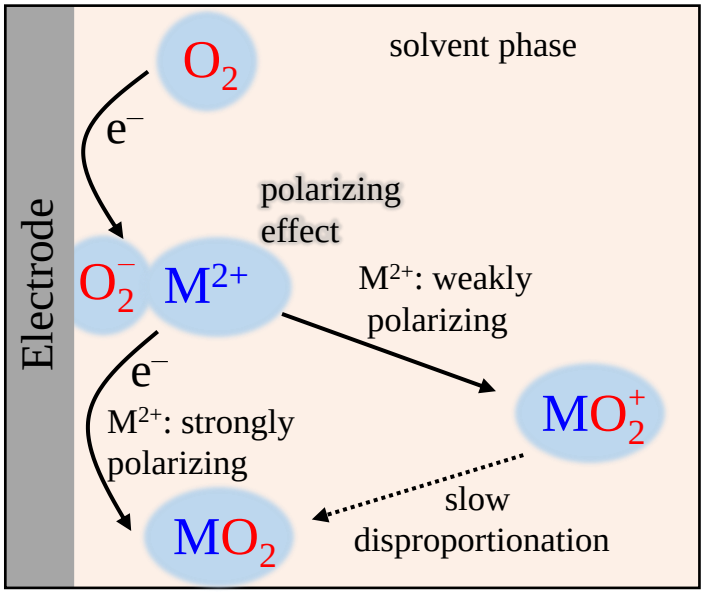

Figure 5.4. Suggested mechanism of the oxygen reduction at platinum. While the reduction of oxygen to superoxide is not greatly affected by the presence of the cation, the superoxide is polarized by the cation. Strongly polarizing cations alleviate the second electron transfer and thus, foster peroxide

formation. In the case of weakly polarizing cations, superoxide can diffuse into the electrolyte prior to the second electron transfer, which can eventually disproportionate.

Having developed a hypothesis for the possible influence of the cations on the overall reaction mechanism, the next goal is to identify a property of the cation, which can help predicting its influence on the ORR. A major problem related to this task is that a parameter has to be defined, which somehow quantifies the cation's influence on the ORR. Bondue proposed to use the potential upon which peroxide formation is observed at gold electrodes and found from the comparison of Li^+, Na^+, K^+ and Mg^{2+} that highly charged cations (calculated from solid state-radii) shift this formation potential into the positive direction [139]. However, this correlation does not seem to be that distinct in other solvents and when more cations are used for comparison [40]. Especially if the alkaline earth metals are included in the comparison with the alkali metals, the cation's influence is indeed not only restricted to its charge density as can be seen from Figure 5.5 a. However, there is a correlation between the so-called *apparent acceptor number* of the cation ($AN_{M+/2+}$, *vide infra*) and the potential ($E_{z=2}$) upon a transition from the superoxide to the peroxide formation occurs. The concept of the apparent acceptor number has been proposed by Linert *et al.* and determined from the solvatochromic shift of the absorption maximum of $Fe(phen)_2(CN)_2$ or $Ru(phen)_2(CN)_2$. Therefore, it is an indicator of the polarizing interaction between the complex and the cation. The high acceptor number of Ba^{2+} for instance, is in good agreement with the finding that Ba^{2+} forms coordination complexes in solution[42]. From comparison with a reference system, which is usually a solvent with low donor and acceptor properties, the apparent acceptor number of the cation $AN_{M+/2+}$ can be evaluated.

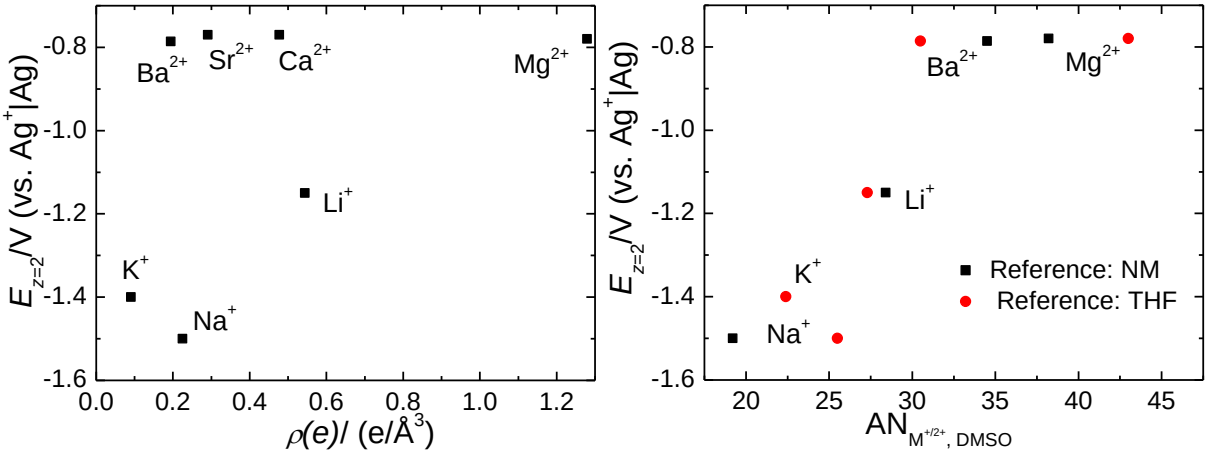

Figure 5.5. Potential $E_{z=2}$ upon which two electrons are transferred at gold. **a.** Plot of $E_{z=2}$ versus the charge density ρ(e) of the cation of the conducting salt. Charge densities were calculated according to Shannon's effective ionic radii [285]. **b.** Plot of $E_{z=2}$ versus the apparent acceptor number of the cation in DMSO obtained from the solvatochromism of $Fe(Phe)_2(CN)_2$ for different reference solvent (NM: nitromethane, THF: tetrahydrofurane) [286].

For high acceptor numbers, which indicate a strong interaction between superoxide and cation, the transition occurs at more positive potentials. However, there seems to be a threshold above acceptor numbers of 30, upon which peroxide is produced from the onset of

the ORR over the whole potential range. It should be noted that *Gutmann*'s concept of donor and acceptor numbers[222] has also been previously evoked in the explanation of the influence of the solvent[93,201,287] and anion[236,288] on the product distribution of the ORR in presence of Li^+. However, Bondue *et al.* showed that the transition potential $E_{z=2}$ more distinctly correlates with the Dimroth-Reichardt coefficient E_T[289,290] of the solvent than it does with its acceptor number[93]. The E_T again reflects the solvatochromism of betaines and can be used as a measurement of polarity of the solvent and therefore is closely related to Linert's apparent acceptor number.

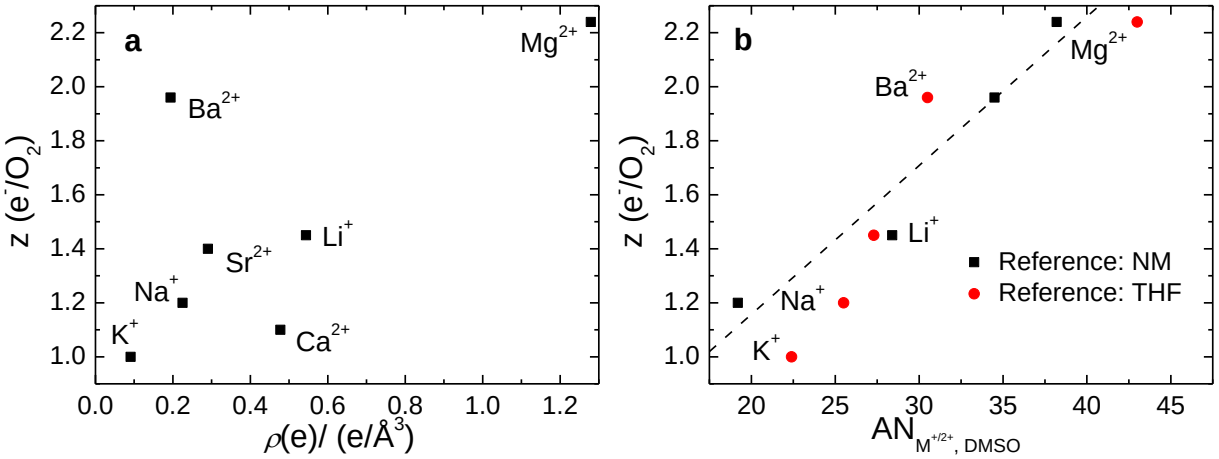

Figure 5.6. Number of electrons *z* at a potential of −1.5 V at platinum electrode. **a.** Plot of *z* versus the charge density ρ(e) of the cation of the conducting salt. Charge densities were calculated according to Shannon's effective ionic radii [285]. **b.** Plot of *z* versus the apparent acceptor number of the cation in DMSO obtained from the solvatochromism of $Fe(Phe)_2(CN)_2$ for different reference solvent (NM: nitromethane, THF: tetrahydrofurane) [286].

As there is no distinct transition from a one-electron to a two-electron process in the case of the earth alkaline cations and at platinum in general, the product distribution (which is represented by the *z* value) at a constant potential at a platinum electrode has been used as another parameter for comparison. Again, there does not seem to be a correlation between the number of electrons per oxygen and the charge density (Figure 5.6 a). However, a correlation between the Linert's apparent acceptor number and the product distribution at platinum electrodes as represented by the *z*-value can be observed (Figure 5.6 b): Cations exhibiting high acceptor numbers seem to foster peroxide formation. This is especially visible for Ba^{2+}, which has a low charge density but a high acceptor number and thus, might polarize the intermediately formed superoxide in order to produce peroxide. Unfortunately, there is no data available on the apparent acceptor number of Ca^{2+} or Sr^{2+} in DMSO. It has to be noted that are some deviations based on the choice of a reference for evaluation of the acceptor numbers (nitromethane vs. tetrahydrofuran (THF), which reflect the uncertainty of the acceptor number.

5.5 Conclusions

The oxygen reduction and evolution in the presence of four different cations from the alkaline earth metals (Mg, Ca, Sr, Ba) has been investigated on different electrode materials via on-line mass spectrometry. From the comparison with the ORR in presence of the alkali metals, it has been concluded that the effect of the cation on the product distribution of the oxygen reduction is not only restricted to its charge density. While for monovalent cations, the tendency to form peroxide seems to increase with charge density of the cation, this is not true for divalent cations. For instance, Ba^{2+}-cations foster peroxide formation while the presence of Ca^{2+}-cations leads to the main formation of superoxide at platinum and glassy carbon electrodes. This behavior can be understood in terms the acceptor number of the cation, which is related to its *Lewis* acidity. It appears that a high acceptor number leads to a shift of the product distribution from superoxide to peroxide, which can be understood by the polarizing influence of the cation on the initially formed superoxide. A highly polarizing cation might accelerate the second electron transfer, while the rate of diffusion of superoxide into the bulk solution remains mostly unaltered or is even lowered due to the interaction with the cation. Thus, the overall product distribution shifts from superoxide to peroxide. With the exception of Mg^{2+}, the experimentally observed oxidation potentials of the earth alkaline metal peroxides correspond well with the trends expected from thermodynamic data. Furthermore, an effect of the electrocatalyst was found: While platinum and glassy carbon foster superoxide or peroxide formation depending on which cation is present, at gold the exclusive formation of peroxide is observed. As compared to Li^{+}-containing electrolytes, only a slight deactivation of the electrodes has been observed in the presence of the divalent cations, indicating the major formation of soluble species. For a final conclusion on the cation’s influence on the ORR, further studies employing different organic solvents as well as additional cations have to be conducted to account for all different effects of the cation and the interplay between cation and solvent.

5.6 Supporting Information

5.6.1 Electrospray Ionisation Mass Spectrometry: Raw Data

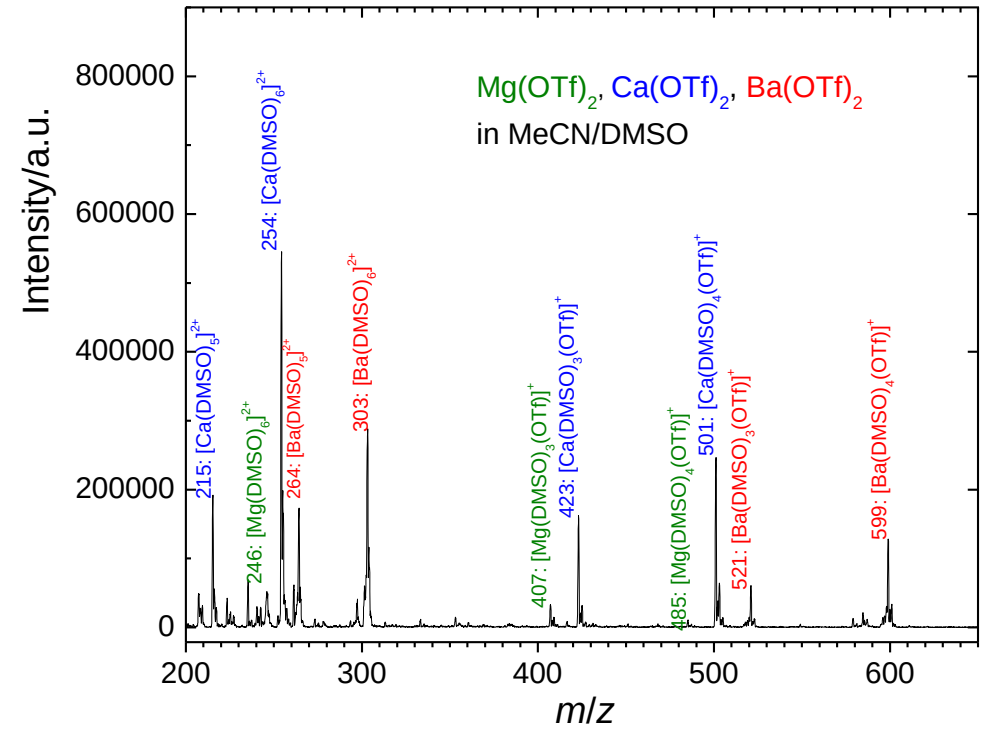

Figure S 5.1. Complex ions in a mixture of 100 µM $Mg(OTf)_2$, $Ca(OTf)_2$ and $Ba(OTf)_2$ in a mixture of MeCN and DMSO (9:1 in volume).

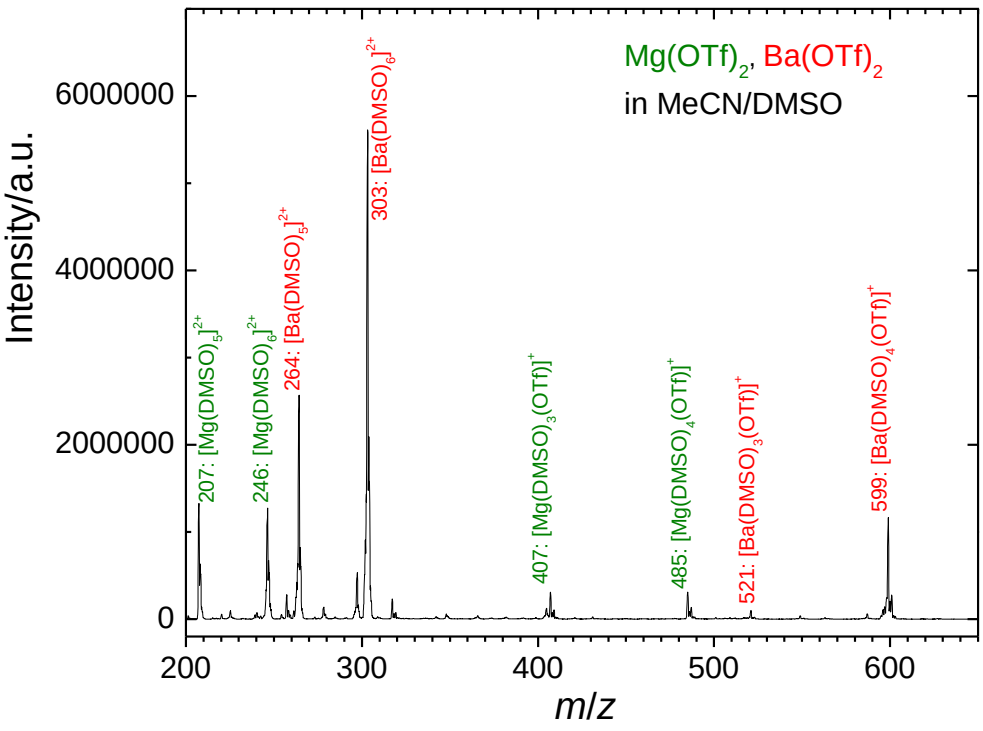

Figure S 5.2. Complex ions in a mixture of 100 µM $Mg(OTf)_2$ and $Ba(OTf)_2$ in a mixture of MeCN and DMSO (9:1 in volume).

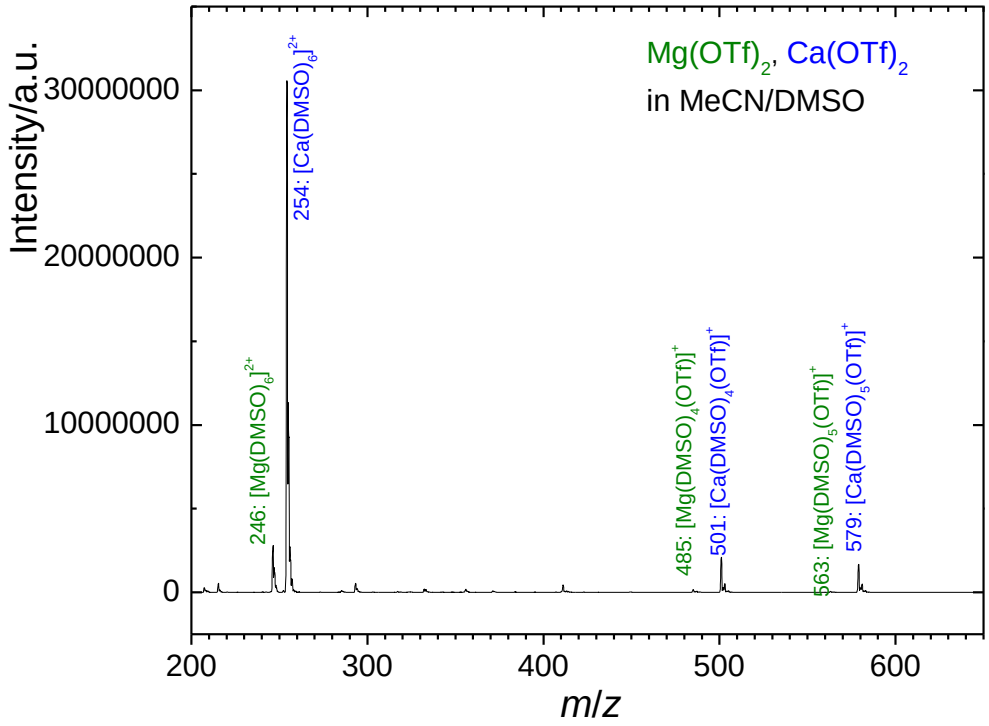

Figure S 5.3. Complex ions in a mixture of 100 µM $Mg(OTf)_2$ and $Ca(OTf)_2$ in a mixture of MeCN and DMSO (9:1 in volume).

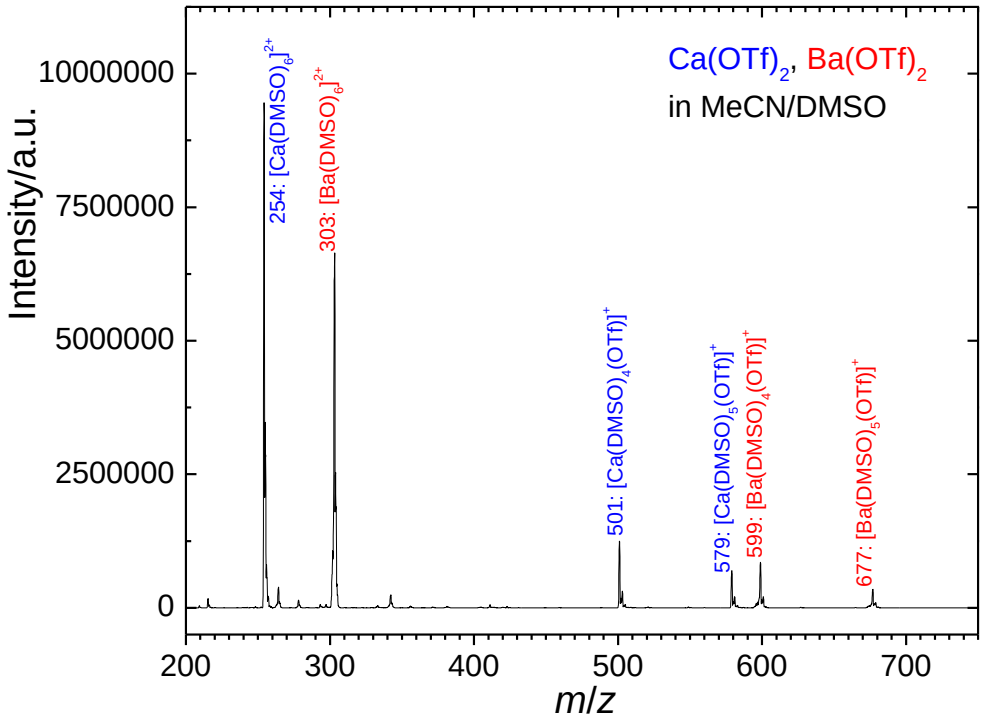

Figure S 5.4. Complex ions in a mixture of 100 µM $Ca(OTf)_2$ and $Ca(OTf)_2$ in a mixture of MeCN and DMSO (9:1 in volume).

6 Reaction Order of the ORR in Li Ion-Containing DMSO

Philip Reinsberg*, Annchristin Weiß*, Pawel Peter Bawol* and Helmut Baltruschat*

*Institut für Physikalische und Theoretische Chemie, Universität Bonn, Römerstraße 164, D-53117 Bonn, Germany

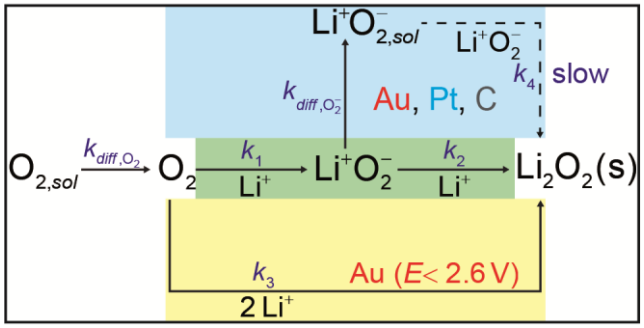

Received: January 19, 2017
Published online: March 20, 2017

P. Reinsberg, A. Weiß, P. P. Bawol and H. Baltruschat, *J. Phys. Chem.* C **2017**, *121*, 7677–7688. Copyright © 2017 American Chemical Society: DOI: 10.1021/acs.jpcc.7b00576

Own manuscript contribution:

- design of the experiments
- supervision of the experiments
- interpretation of the results
- writing the manuscript

ACKNOWLEDGMENTS

The authors gratefully acknowledge the Federal Ministry of Education and Research (FRG) for funding this work. This work is part of the LiBaLu-project in the framework of the “Vom Material zur Innovation”-initiative (03XP0029A).

6.1 Abstract

Understanding the mechanism underlying the oxygen reduction and evolution in aprotic solvents is crucial for developing secondary metal–air batteries. Despite much scientific effort, the mechanism of the oxygen reduction in aprotic solvents in the presence of Li^+ ions is still not fully understood. In this work, rotating ring–disk electrode and differential electrochemical mass spectrometry experiments have been employed to investigate the influence of the oxygen partial pressure on the oxygen reduction and evolution reaction at gold, glassy carbon, and platinum electrodes. A further aim was to elucidate the different pathways leading to peroxide formation and to analyse their importance for the overall reaction. As expected, the electrochemical reaction order for the superoxide formation is unity. Despite that, the reaction order for the reaction path leading to peroxide is below unity, indicating the participation of an adsorption step. This is further indicated by the finding that the amount of peroxide deposited on the surface changes only very slightly upon increasing the oxygen concentration. While the oxygen reduction at glassy carbon and platinum takes place via the parallel formation of superoxide and peroxide, there is a distinct transition between superoxide and peroxide formation at the gold electrode. This transition occurs close to a potential where the rate of superoxide formation is mainly limited by diffusion. By investigating the rotation dependence of the collection efficiency, it can be shown that the peroxide formation at gold indeed proceeds via a direct reduction step without the formation of a soluble intermediate. This finding adds to the current mechanistic picture which only differentiates between the electrochemical and the chemical formation of lithium peroxide. For platinum and glassy carbon, this direct reduction without the formation of soluble intermediates cannot be noted. Based on these observations, a reaction scheme is presented including rate constants for the different reaction pathways.

6.2 Introduction

The concept of lithium–air batteries has drawn much attention during the last two decades due its promising specific energy of 3500 W h kg^{-1} [11,13,22,212,291]. It is generally accepted that the final product of the oxygen reduction reaction (ORR) in the presence of Li^+-ions leads to the formation of insoluble Li_2O_2[11,48,53,61,65,69,139,209,266,283,291,292]. It has also been confirmed that superoxide is an intermediate product[61,120,201,203,233,283,293,294], which can either be electrochemically reduced or disproportionate to Li_2O_2 depending on the electrocatalyst[139,233,295], solvent properties[201,202,283,296], discharge rate[206,257] and electrolyte salt[234,235,288,297]. Regarding the electrocatalyst, gold seems to be of special significance as a distinct transition from the formation of superoxide to the direct formation of peroxide is found[139,283,295]. However, despite of the effort which has been put into understanding the mechanism of the ORR, concentration effects of the conducting salt[234,298] or the partial pressure of oxygen[57,299,300] have been only scarcely investigated. Yang *et al.* found that the discharge capacity increases and the formation of particles is favored at oxygen pressures

higher than 1 atm[299]. On the other hand, Lu and coworkers[57] conducted rotating disk electrode measurements using partial pressures below one atmosphere and found an electrochemical reaction order below one. However, in both studies propylene carbonate-based electrolytes have been used, which are known to be unstable against the products of the ORR by now[21]. Thus, the implications for the actual ORR are not very clear. However, McCloskey's results using dimethoxy ethane as a solvent imply a weak dependence of the current on the oxygen partial pressure for pressures above 1 bar[300].

In this paper, we present a detailed study of the dependence of the ORR and the OER on the partial pressure of oxygen well below 1 bar via the use of rotation ring–disk electrode (RRDE) and differential electrochemical mass spectrometry (DEMS) in DMSO-based electrolytes. Gold (Au), platinum (Pt), and glassy carbon (GC) electrodes have been employed during the measurements. All potentials are reported with respect to the $Ag^+|Ag$ couple in DMSO, which is described in the Experimental Section (6.3).

6.3 Experimental Section

6.3.1 Materials

The preparation of all electrolytes was carried out in an *MBraun* glovebox. Lithium perchlorate ($LiClO_4$, battery grade, *Sigma-Aldrich*), silver nitrate ($AgNO_3$, ≥99%, *ChemPure*), tetrabutylammonium perchlorate ($TBAClO_4$, ≥99%, *Sigma-Aldrich*), and extra dry dimethyl sulfoxide (DMSO, 99.7%, over molecular sieve, *Acros Organics*) were used as received. During the experiments, the electrolytes were purged with different mixtures of highly pure argon (*Air Liquid,* 99.999%) and highly pure oxygen (*Air Liquid*, 99.995%).

6.3.2 Preparation of Oxygen/Argon Mixtures

Argon and oxygen were mixed by using thermal mass flow controllers. For argon, a flow controller by *Bronkhorst* (model: F-201C-UA-22-V) was used, whereas for oxygen a flow controller by *Union Carbide* was employed (model: MFT-V12C). Prior to the experiments, both flow controllers had been calibrated to account for the different heat capacity of the gases. The calibration was carried out using the independence of the volume of an (ideal) gas from its specific properties. For details please refer to the Supporting Information. The estimated calibration factors are in excellent agreement with the theoretical values calculated from the molar heat capacity.

6.3.3 Reference Electrode

A silver wire immersed in 0.1 M $AgNO_3$ in DMSO was used as the reference electrode. In order to avoid contamination, the connection between the working electrolyte and the reference electrode was established via the rough surface of a closed glass stopcock or the

rough surface of a glass bead. The potential of the reference electrode is approximately 3.83 V versus the $Li^+|Li$ couple or 0.43 V versus NHE[216].

6.3.4 Rotating Ring–Disk Electrodes (RRDE)

A gold disk (A = 0.196 cm^2) and a glassy carbon disk (A = 0.196 cm^2) were used together with a glassy carbon ring (AFE6R1GC, Pine Research Instrumentation). The theoretical collection efficiency N_0 in this configuration equals 0.256. For platinum, a thin gap electrode with a fixed geometry (AFE7R8PTPT, Pine Research Instrumentation) with A(disk) = 0.164 cm^2 and N_0 = 0.218 was employed. The experiment itself was carried out in an H-cell which was continuously flushed using a total flow of 15 mL min^{-1} of the argon/oxygen mixture to avoid water contamination and to keep the electrolyte saturated. The water content itself was probed after the experiment via coulometric Karl Fischer titration. A typical water content was 20 ppm.

The apparent collection efficiency N ($N = |I_R / I_D|$, with I_R as the ring current and I_D as disk current) can be used to estimate the proportion of species which can be oxidized at the ring electrode. However, if there are two reaction pathways at the disk, one proceeding via a two-electron process and one via a one-electron process and only the products of the latter are detectable at the ring electrode, the relative amount x of the one-electron product can be calculated using eq. (6.1):

$$x = \frac{2|I_R|}{|I_D N_0| + |I_R|} \tag{6.1}$$

Consequently, the share of peroxide can be calculated by subtracting x from 1.

6.3.5 Differential Electrochemical Mass Spectrometry (DEMS)

The cell used for the DEMS-measurements is a thin-layer cell and similar to a cell described earlier by Hartung and Baltruschat[301]. However, there are some important differences. Firstly, the cell body consist of Kel-F instead of titanium. Furthermore, the working electrode is sputtered onto a Teflon membrane, which is mechanically stabilized by a steel frit and in contact with the vacuum of the mass spectrometer (similar to the case of the traditional cell used with static electrolyte[112,113,302]). The sputtered electrode is electrically contacted via a gold wire (diameter 0.05 mm) with the steel cell holder. The actual thin-layer is formed by 4 O-rings made of Teflon membrane creating a total cell volume of 5.6 µL with a height of 200 µm. The upper part of the cell is closed via another Teflon membrane which again is stabilized by a steel frit. Oxygen supply is established via the upper steel frit, where a specific oxygen pressure can be applied. The thin-layer cell is filled with 0.5 M $LiClO_4$ in DMSO via an inlet capillary which is sealed by a syringe during the experiment. A diagrammatic sketch can be found in the supporting information. Further details will be given in a future publication[122]. The reference electrode consists of a silver wire immersed in 0.1 M $AgNO_3$ in DMSO and is

connected via a Teflon tube which is sealed using a rough glass bead. A detailed description can be found elsewhere[123].

To calculate the flux of oxygen $\dot{n}$ into the mass spectrometer, the calibration constant K^* is needed according to eq. (6.2):

$$\frac{dn}{dt} = \dot{n} = \frac{I_{32}}{K^* \cdot F} \tag{6.2}$$

I_{32} indicates the ionic current due to oxygen after baseline subtraction, F represents the faradaic constant. To determine the calibration constant K* the ORR in $TBAClO_4$ containing DMSO was employed, which is known to yield superoxide [62,120,123].

6.4 Results and Discussion

6.4.1 Rotation Dependence of the ORR at Gold Electrodes

The general behavior of the ORR in Li^+-containing DMSO at an Au disk electrode is shown in Figure 6.1a–b.

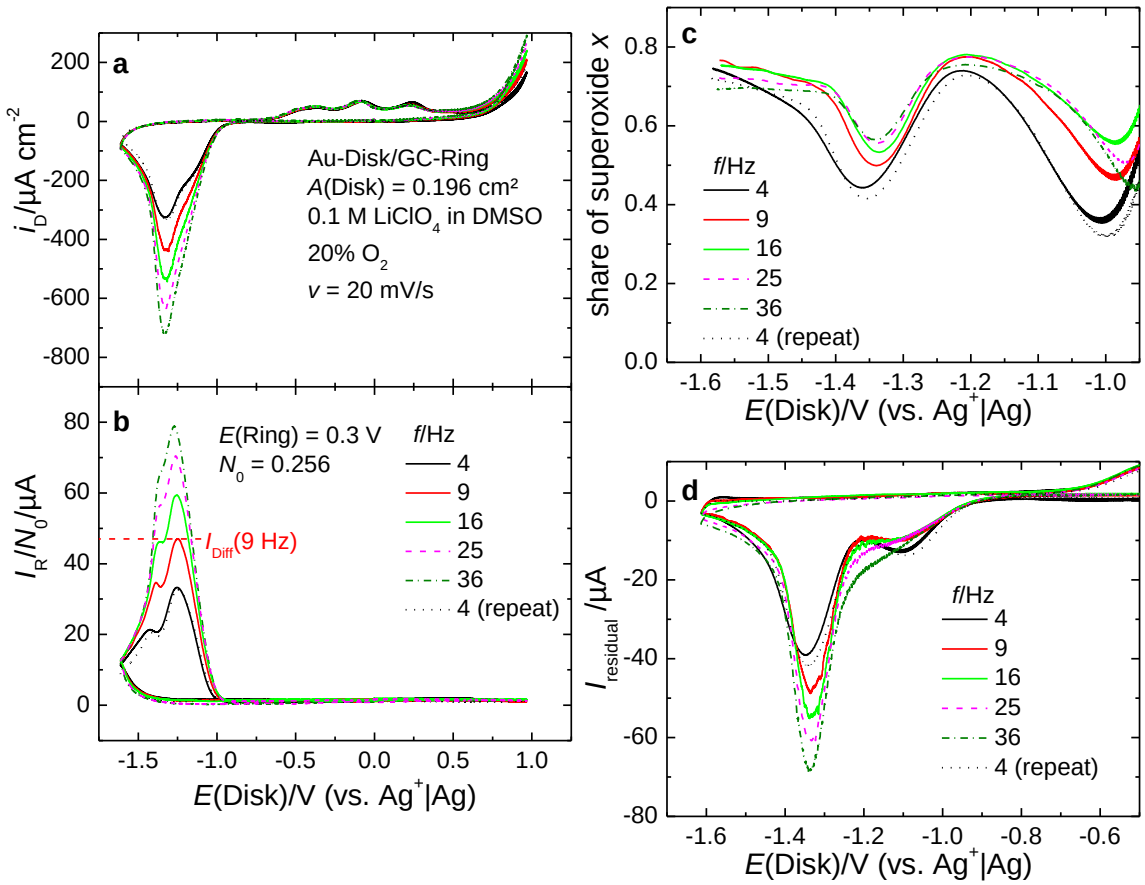

Figure 6.1. Oxygen reduction and evolution at an Au disk/GC ring RRDE assembly. **a**. CV at an Au disk electrode for various rotation rates. **b**. Corresponding CV at a GC ring electrode. The dotted line shows the theoretical diffusion-limited current for a one-electron process at a rotation rate of 9 Hz. **c**. Share of superoxide x for different rotation rates calculated according to eq. (6.1). **d**. Residual current ($I_{residual} = I_D + I_R/N_0$) which cannot be directly explained via the oxidation of superoxide at the ring electrode.

At low rotation rates a shoulder between a potential of −1.1 V to −1.2 V becomes visible. This shoulder has been previously assigned to the transition from direct formation of superoxide to the direct formation of peroxide[139,295]. A sweep rate of 20 mV s^{-1} was used as a compromise: Typically, a sweep rate of 10 mV s^{-1} is used for kinetic measurements to ensure stationary conditions. However, the shoulder, which has a remarkable significance for the ORR at gold, can be observed more distinctly at higher sweep rates (see Figure S 6.1). It probably occurs as the superoxide formation is close to diffusion limitation and thus becomes independent of the potential. In accordance with the Levich-Koutecký equation (6.3), the shoulder disappears at higher rotation rate as the diffusion-limited current increases and thus diffusion-control is shifted to higher overpotentials where the two-electron reduction already has started. In eq. (6.3), i_K denotes the kinetic current density, i_{Diff} the diffusion-limited current density, z the number of electrons, k(E) a potential-dependent rate constant, c_0 the bulk concentration of the reactant, D the diffusion coefficient, ν the kinematic viscosity and ω is the angular frequency.

$$\frac{1}{i} = \frac{1}{i_K} + \frac{1}{i_{Diff}} = \frac{1}{zFk(E)c_0} + \frac{1}{0.62 \cdot zFD^{2/3}\nu^{-1/6}c_0 \cdot \omega^{1/2}} \tag{6.3}$$

The shoulder in the disk current coincides with a peak in the ring current, again substantiating the hypothesis that the shoulder is due to superoxide formation. Furthermore, the height of the peak in the ring current is close to the value of the theoretical diffusion-limited current (as indicated by the dotted line for a rotation rate of 9 Hz) calculated with the solubility and the diffusion coefficient of O_2 obtained by Khodayari *et al.* [130], which supports the idea that the shoulder is correlated to the diffusion-limited superoxide formation. The theoretical value of the diffusion-limited current for 10% O_2 is shown as a red dotted line in Figure 6.1b. However, for higher rotation rates the deviation of the peak from the diffusion-limited current becomes more significant. This can be explained by deactivation of the surface and will be discussed in detail in a later section: The peak in the ring current is followed by a steep decrease. For low rotation rates, a second peak arises at a potential of −1.35 V, whereas for high rotation rates this peak is more like a shoulder in the ring current. The increase of I_R when I_D is decreasing implies that, as the precipitation of Li_2O_2 proceeds, the share of oxygen reduced to superoxide apparently increases again. This has been attributed to a geometric effect of Li_2O_2. [139,283,295].

While the amount of reduced oxygen varies greatly with the rotation rate (5700 µC cm^{-2} at 4 Hz vs 10 200 µC cm^{-2} at 36 Hz), the anodic charge between −0.7 and 0.4 V is more or less constant at 2300 µC cm^{-2}. As shown in Figure 6.1c, the share of superoxide of the total amount of oxygen reduced increases slightly with rotation rate. As will be discussed in more detail when the rate constants are presented, this results from the more efficient transport of superoxide to the solution at high rotation speeds at the expense of a further direct electron transfer. However, for rotation rates above 16 Hz the share of superoxide remains relatively constant. Regardless of the rotation rate, the share of superoxide x is significantly lower than 1 over the whole potential range. At −1.2 V there is a maximum, whereas at −1.4 V there is a

minimum of x. It should be noted that the apparent increase of x for potentials above −1.0 V is an artefact because of the extremely low currents. Subtracting the ring current normalized by the theoretical collection efficiency N_0 from the disk current should yield the residual current due to peroxide current (Figure 6.1d). As can be seen from Figure 6.1d, the peak of the residual current shifts to more positive potentials with increasing rotation rates. As the peak is related to the deactivation of the surface, this is equivalent to the formation of a higher total amount of peroxide (i.e., a higher rate of peroxide formation) at higher rotation rates. Comparing the charge obtained by integrating the residual current to the anodic charge, it seems that the residual charge is up to 20% higher than the anodic charge obtained from integration between −0.6 and 0.2 V. This missing anodic charge can probably be found in the anodic currents starting at roughly 0.75 V, which also slightly increase with increasing rotation rate and, thus, should not only be connected to electrolyte decomposition. The increase of this anodic charge might be in fact related to the total amount of decomposition products depositing on the surface, which should be higher at high rotation rates.

6.4.2 Concentration Dependence of the ORR at Gold Electrodes

The variation of the currents observed with an RRDE at different partial pressures p of O_2 and a constant rotation rate of 25 Hz is shown in Figure 6.2a–b. The shoulder in the disk currents is only visible at a partial pressure of 5% of the atmospheric pressure at this rotation speed.

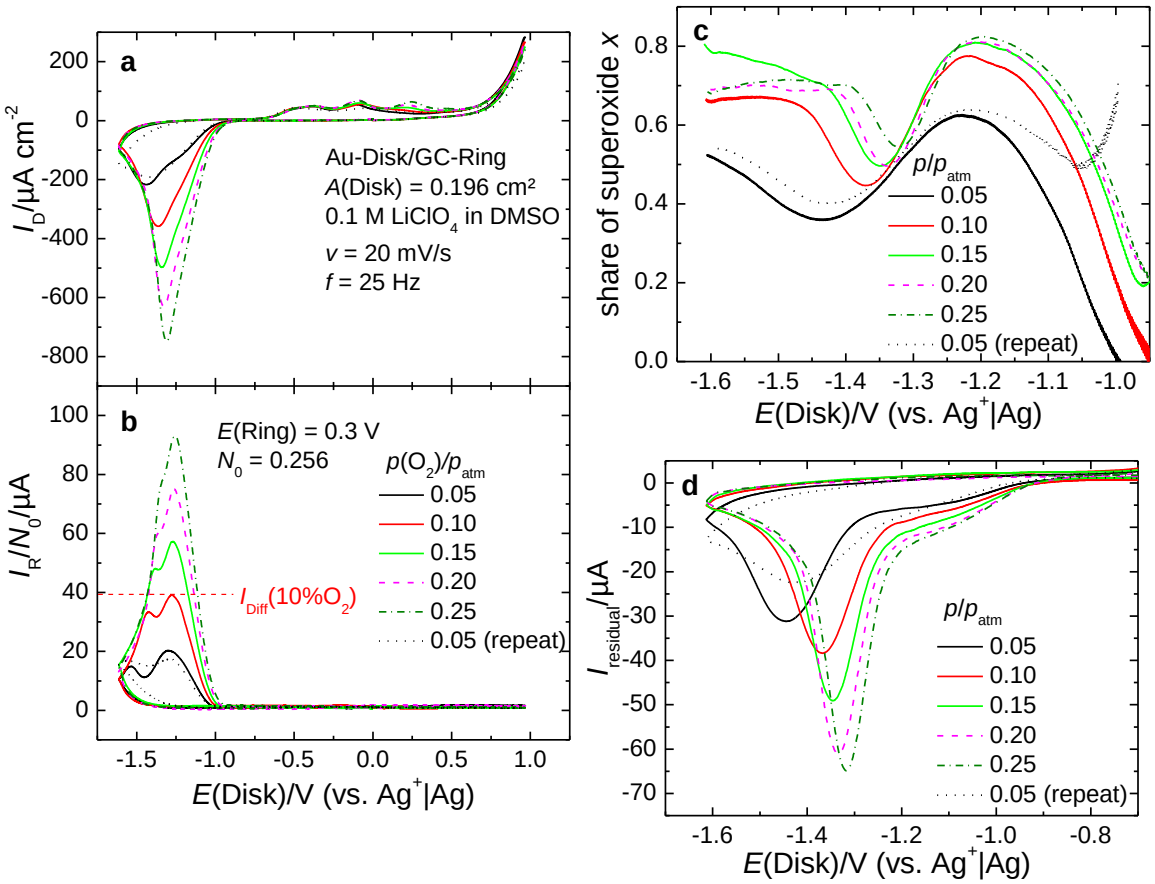

Figure 6.2. Effect of the oxygen concentration at an Au disk/GC ring RRDE assembly. **a**. CVs at an Au disk electrode for different oxygen concentrations. **b**. Corresponding CV at a GC ring electrode held at 0.3 V. The dotted line shows the theoretical diffusion-limited current for a one-electron process at oxygen partial pressure of 0.1 atmospheres. **c**. Share of superoxide under variation of the oxygen concentration calculated using eq. (6.1). **d**. Residual current ($I_{residual} = I_D + I_R/N_0$) which cannot be directly explained via the oxidation of superoxide at the ring electrode.

As can be seen for instance from the ring currents at 10% O_2 (Figure 6.2b, dotted red line), he diffusion-limited current for the formation of superoxide is reached at low O_2 partial pressures. For higher partial pressures, the height of the peak deviates more from the expected diffusion-limited currents. The share of superoxide itself seems to increase with the oxygen concentration, indicating a larger dependence of the superoxide formation on the O_2 partial pressure than that of peroxide (Figure 6.2c). Again, from the subtraction of the disk and ring currents, the residual current due to peroxide can be obtained and only a weak dependence of the current due to peroxide on the oxygen pressure is observed (Figure 6.2d). The peak potential shifts to more positive potentials, as expected and is responsible for the low collection efficiencies at low rotation rates. Obviously, the effect of the concentration on the share of superoxide is more crucial than the effect of the rotation rate.

6.4.3 Rotation Dependence of the ORR at Platinum Electrodes

The general behavior of the ORR at Pt disk can be seen in Figure 6.3a. To alleviate comparison to the results obtained at the gold electrode, a sweep rate of 20 mV s^{-1} was used

for this measurement. The onset of the ORR is close to that observed at the gold electrode. However, the CV of the disk electrode lacks the characteristic shoulder, and the peaks, indicating deactivation of the electrode, are broad.

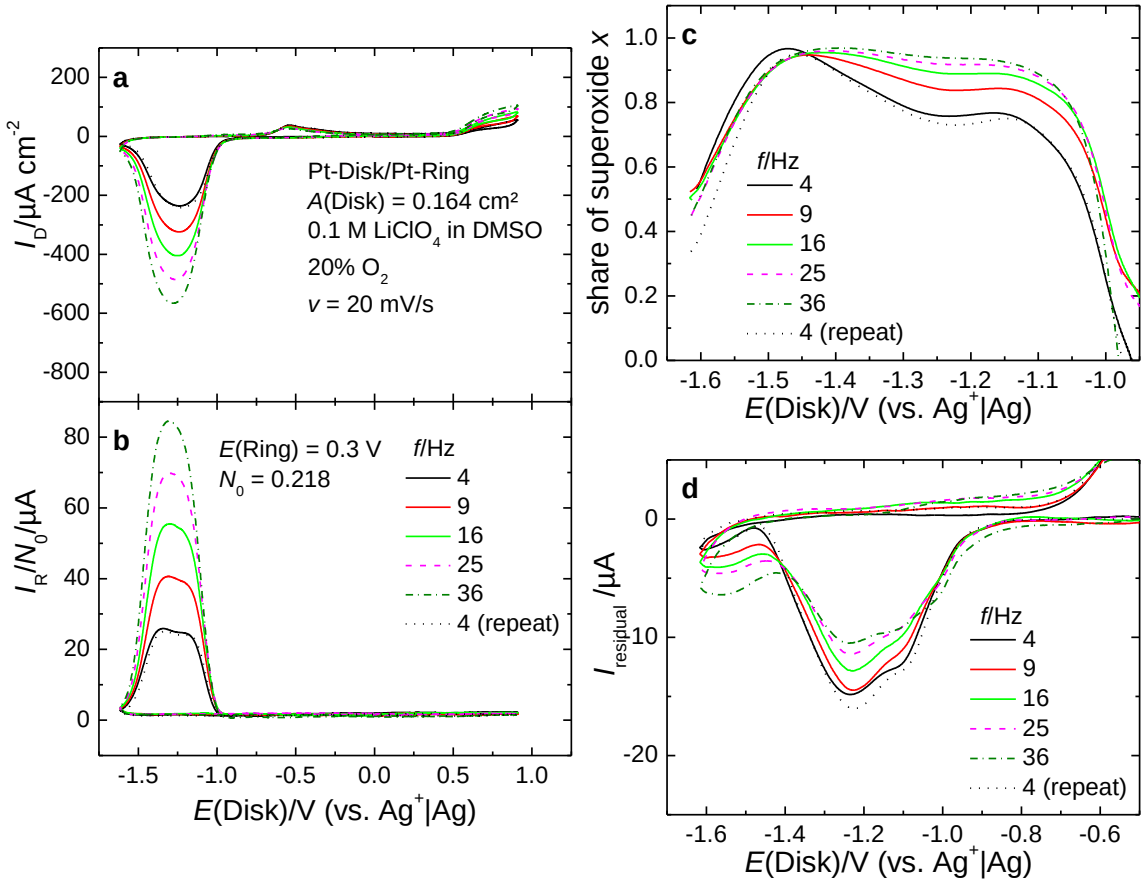

Figure 6.3. Oxygen reduction and evolution at a thin-gap Pt disk/Pt ring RRDE assembly. Note that the sweep rate is 20 mV s^{-1} for this specific measurement. **a**. CV at a Pt disk electrode for various rotation rates. **b**. Corresponding CV at a Pt ring electrode. **c**. Share of superoxide *x* for different rotation rates calculated according to eq. (6.1). **d**. Residual current ($I_{residual} = I_D + I_R/N_0$) which cannot be directly explained via the oxidation of superoxide at the ring electrode.

However, at low rotation rates a shoulder in the ring current can be observed at −1.2 V, where the current remains constant until it increases again beyond −1.25 V. This can be understood in terms of the geometric effect Bondue *et al*. proposed [139]. At the beginning of the ORR, peroxide is formed at a high rate, which then decreases. This effect could lower the apparent collection efficiency at low overpotentials. The amount of oxidisable species deposited on the surface is again more or less independent of the amount of reduced oxygen. Considering Bondue's finding [139] hat a mixed process of the formation of superoxide and peroxide takes place, the less effective deactivation of the Pt electrode as compared to the Au electrode is plausible: While at the Au electrode almost exclusively peroxide is formed from −1.25 V on, the amount of peroxide at the Pt electrode remains relatively low. This is further supported by the observation that the collection efficiency is close to that expected from geometry (Figure 6.3b) and accordingly, the share of superoxide is approximately unity (Figure 6.3c). The share of

superoxide again increases slightly with increasing rotation rate. The residual current (Figure 6.3d), however, remains relatively constant which is in good agreement with the anodic current at −0.5 V.

6.4.4 Concentration Dependence of the ORR at Platinum Electrodes

The oxygen dependence of the disk and ring currents is shown in Figure 6.4a and b. Again, the anodic currents do not vary much with the oxygen concentration. For the lowest oxygen concentrations (5% and 10%), a broad plateau is exhibited which is in good agreement with the theoretically expected diffusion-limited current (red, dotted line in Figure 6.4b). Similar to the observations at the gold electrode, the share of superoxide (Figure 6.4c) slightly increases with the oxygen concentration. Since the ring currents are close to the theoretically expected ones, the residual currents (Figure 6.4d) do not appear reliable as they are rather small and thus susceptible to small baseline errors or the collection efficiency. Note that the difference between the measurements using 20% O_2 in Figure 6.4 and Figure 6.3 is related to the different sweep rate.

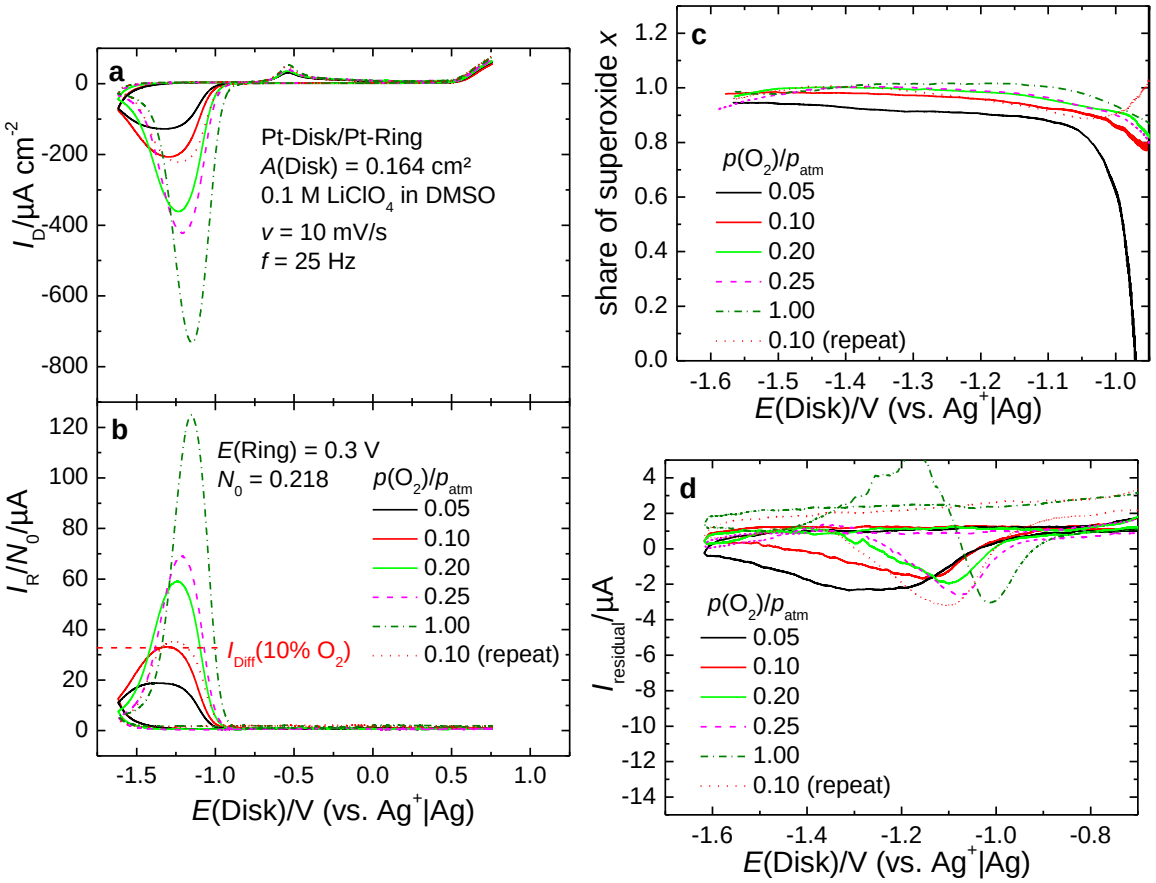

Figure 6.4. Effect of the oxygen concentration at a Pt disk/Pt ring RRDE assembly. **a**. CVs at a Pt disk electrode for different oxygen concentrations. **b**. Corresponding CV at a Pt ring electrode held at 0.3 V. The dotted line shows the theoretical diffusion-limited current for a one-electron process at oxygen partial pressure of 0.1 atmospheres. **c**. Calculated share of superoxide under variation of the oxygen concentration. **d**. Residual current ($I_{residual} = I_D + I_R/N_0$) which cannot be directly explained via the oxidation of superoxide at the ring electrode.

6.4.5 Rotation Dependence of the ORR at Glassy Carbon Electrodes

When using a GC disk electrode, the current minima become much broader indicating a less effective deactivation (Figure 6.5a and b). In the ring current, again a small maximum is visible although no shoulder is visible in the disk CV. At low oxygen concentrations and low rotation rates, even two maxima in the ring current are visible (Figure S 6.8) similar to the ring currents observed at the gold electrode. The anodic currents again do not vary significantly with rotation rate. The share of superoxide (Figure 6.5c) increases with rotation rate, but is generally lower than in the case of the platinum disk. Finally, the residual current in Figure 6.5d only slightly increases with rotation rate.

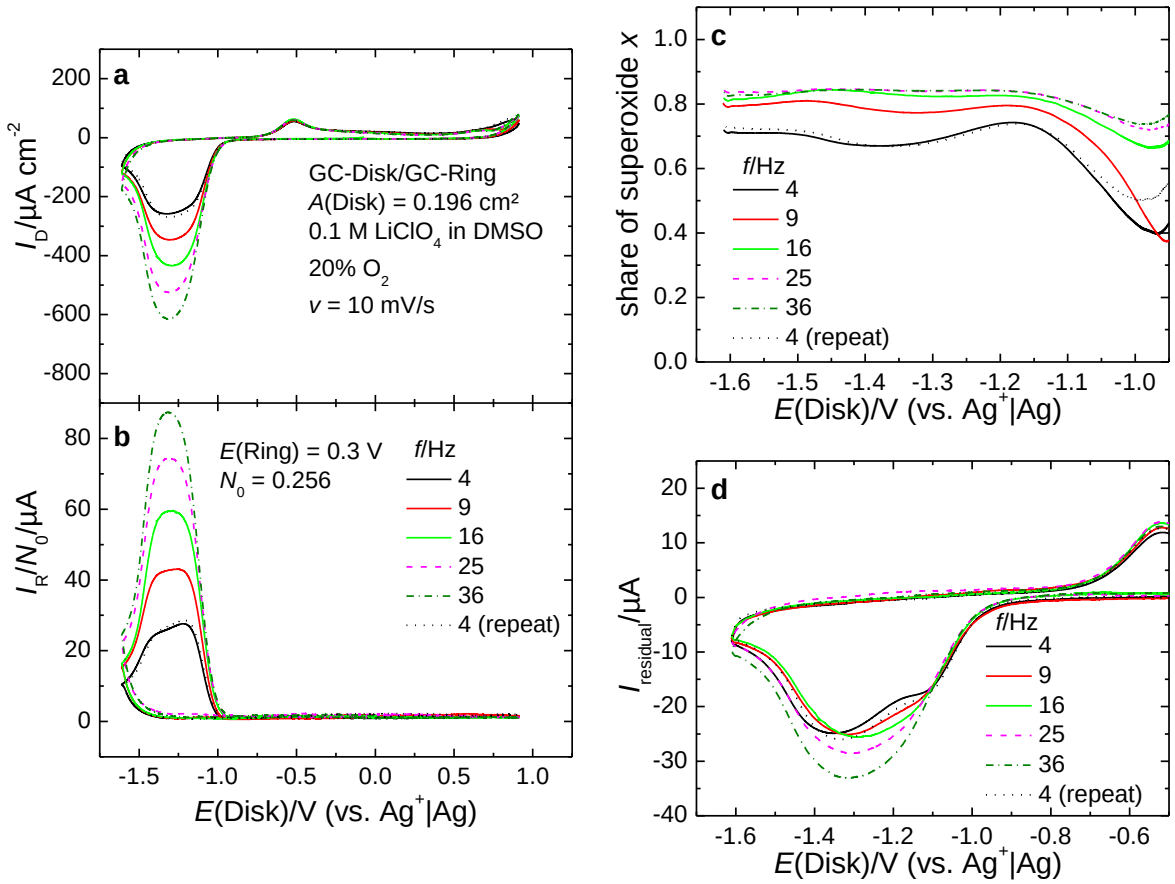

Figure 6.5. Oxygen reduction and evolution at a GC disk/GC ring RRDE assembly. **a**. CV at a GC disk electrode for various rotation rates. **b**. Corresponding CV at a GC ring electrode. **c**. Share of superoxide *x* for different rotation rates calculated according to eq. (6.1). **d**. Residual current ($I_{residual} = I_D + I_R/N_0$) which cannot be directly explained via the oxidation of superoxide at the ring electrode.

6.4.6 Concentration Dependence of the ORR at Glassy Carbon Electrodes

The concentration dependence of the disk and ring currents at a glassy carbon electrode is shown in Figure 6.6a and b. or the partial pressures of 5% and 10% of the atmospheric pressure, broad, more or less potential independent plateaus are exhibited in the ring currents, which are close to the theoretical diffusion-limited currents (red, dotted line in Figure 6.6b). However, at e.g. a rotation rate of 4 Hz, the ring-currents in fact show two maxima (Figure

S 6.8b). These two peaks can be observed indirectly, but more evidently in Figure 6.6c, where the share of superoxide is shown. Again, the share of superoxide increases with increasing oxygen concentration. The residual current (Figure 6.6d) slightly increases with the oxygen concentration.

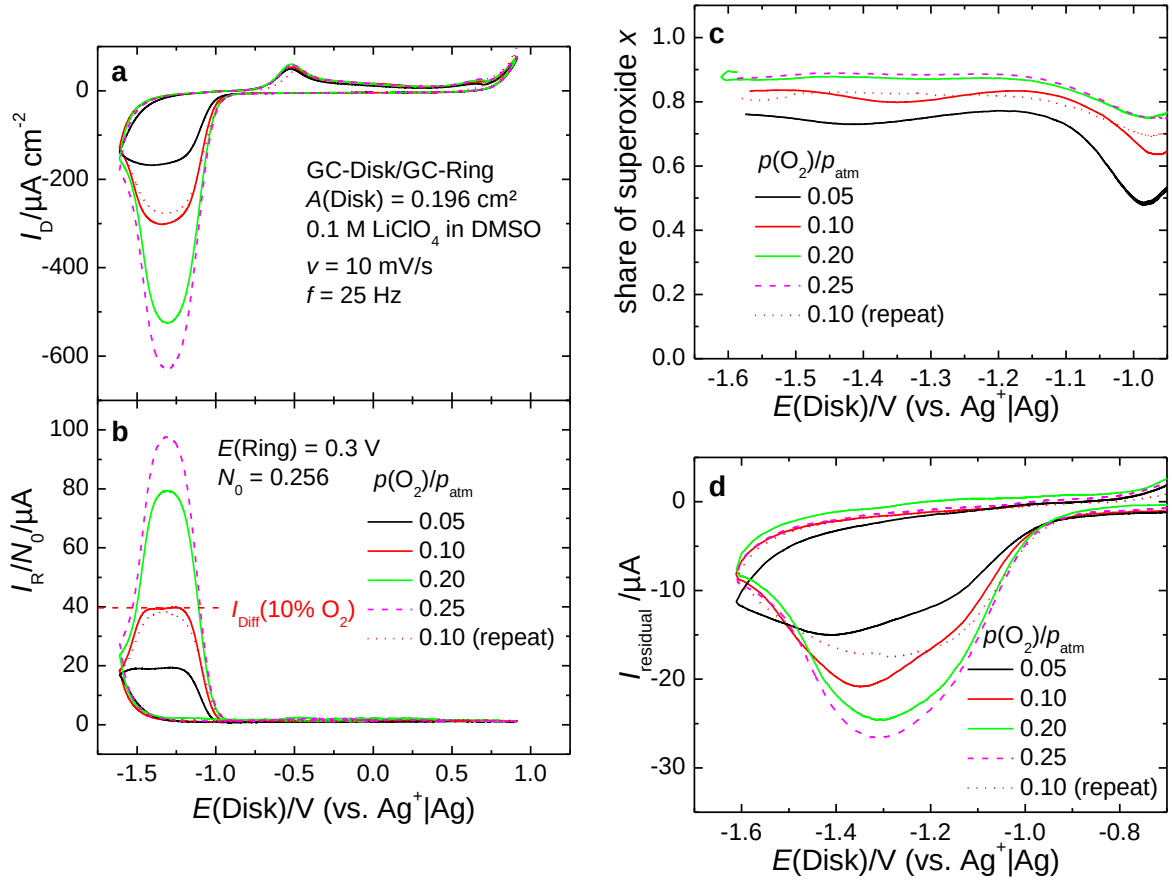

Figure 6.6. Effect of the oxygen concentration at a GC disk/GC ring RRDE assembly. **a**. CVs at a GC disk electrode for different oxygen concentrations. **b**. Corresponding CV at a GC ring electrode held at 0.3 V. The dotted line shows the theoretical diffusion-limited current for a one-electron process at oxygen partial pressure of 0.1 atmospheres. **c**. Calculated share of superoxide under variation of the oxygen concentration. **d**. Residual current ($I_{residual} = I_D + I_R/N_0$) which cannot be directly explained via the oxidation of superoxide at the ring electrode.

6.4.7 Tafel-Plots of the ORR at Gold, Platinum and Glassy Carbon

While the diffusion of oxygen within the solution is independent of the electrode material, the actual kinetics of the ORR is not. To investigate the effect of the electrode material and the oxygen concentration on the kinetics, the currents which are occurring solely due to charge transfer have to be extrapolated using the experimental currents. Per eq. (6.3), this can either be done via an extrapolation of $1/I$ vs $1/\omega^{-1/2}$ or, if the diffusion-limited current is known, directly calculated at a certain rotation frequency (eq. (6.4)):

$$|I_K| = \frac{I \cdot I_{diff}}{I - I_{diff}} \tag{6.4}$$

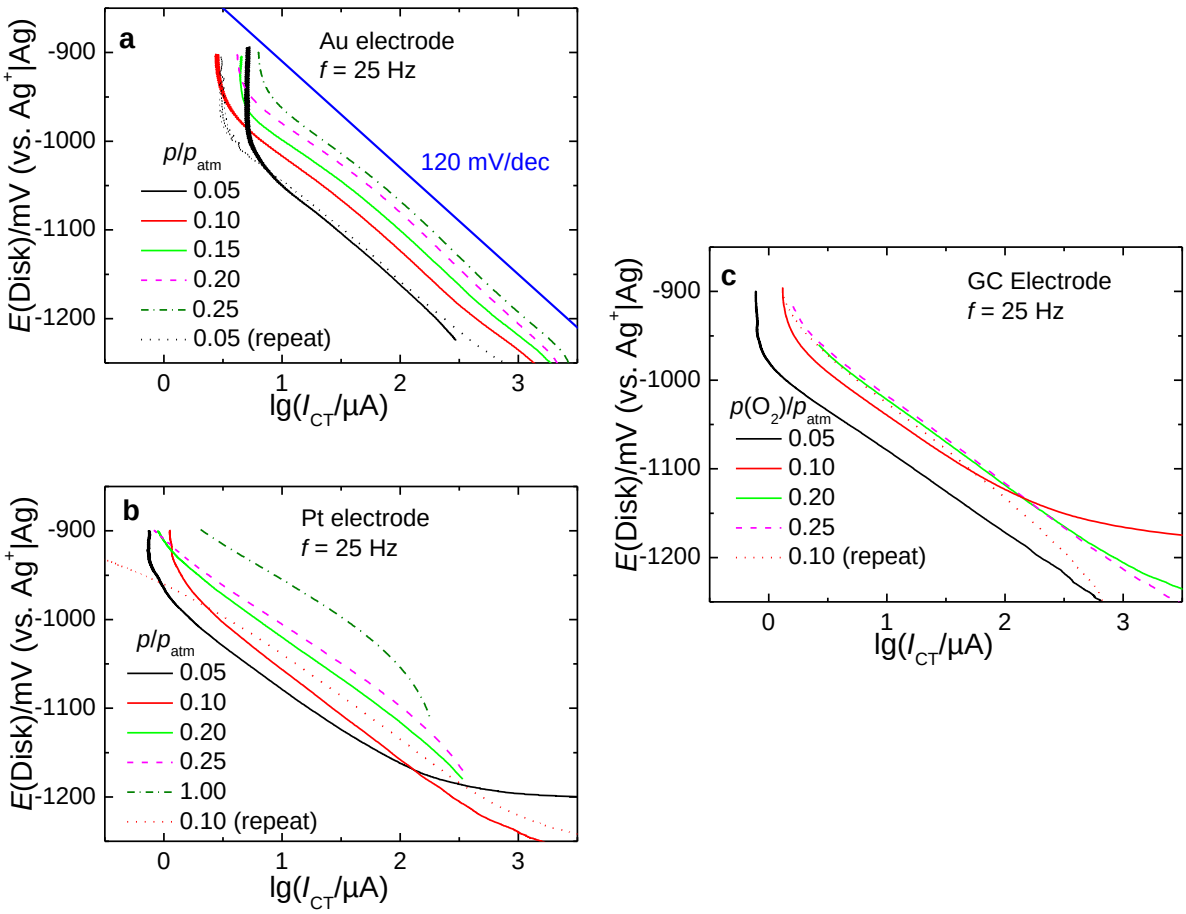

Figure 6.7. Tafel-plots for different electrode materials and partial pressures of oxygen. **a**. Tafel-plots at the gold electrode. **b**. Tafel-plots at the platinum electrode. **c**. Tafel-plots at the glassy carbon electrode. Calculated from the ring currents at a rotation rate of 25 Hz.

However, the analysis of the currents proves more difficult than usual as two species are generated simultaneously and the ratio of their formation rates might be potential dependent (at least at gold this is obvious). Fortunately, the peroxide is insoluble and thus cannot be detected at the ring electrode. Consequently, the ring currents can be used to investigate the current, which is only due to superoxide formation. The Tafel plots in Figure 6.7 have been calculated applying eq. (6.4) to the ring currents at a rotation rate of 25 Hz. Equation (6.4) was preferred over eq. (6.3) as the deactivation of the electrode changes with potential and rotation speed. This will finally affect the extrapolated currents. The Tafel slopes for the different electrode materials as well as different partial pressures are similar and close to 120 mV/dec, as can be seen from the comparison with the blue line in Figure 6.7a. This implies that a one-electron step is the overall rate-determining step. However, for overpotentials more positive than −1200 mV the Tafel-slope at glassy carbon (Figure 6.7b) and platinum (Figure 6.7c) seems to be smaller as compared to gold or platinum. For an oxygen partial pressure of 5% of the atmospheric pressure a Tafel-slope of 90 mV/dec is obtained. From a potential of −1200 mV on (coinciding with the end of the shoulder observed in the disk current), the Tafel-slope at the gold electrode decreases as well to a value of 90 mV/dec (for 5%, 10% and 15% O_2). This

might imply the (partial) influence of a potential-controlled adsorption process, which was also considered by Yu *et al.*[283] or a non-symmetric transmission coefficient α, being larger than 0.5[211]. However, the slightly anomalous Tafel-behavior might be absent at higher O_2 concentrations which might explain the different Tafel-slopes observed by Laoire and Viswanathan[62],[303].

6.4.8 Electrochemical Reaction Order with Respect to Oxygen

Having calculated the currents due to charge transfer, these currents have to be evaluated according to eq. (6.5) to determine the reaction order *m* with respect to oxygen:

$$\left(\frac{\partial \ln(i_{CT})}{\partial \ln(c(\mathrm{O_2}))} \right)_E = m \tag{6.5}$$

Fortunately, uncertainties regarding the theoretical collection efficiency N_0 or Henry's constant for oxygen (and thus its absolute concentration) do not influence the reaction order as these are not dependent on the oxygen concentration. The reaction order obtained by this procedure using the ring currents is presented inFigure 6.8a. Furthermore, the reaction order calculated from the disk currents is plotted in Figure 6.8b to show the consistency between the different extrapolations. The additional measurements which have been used for the evaluation of the electrochemical reaction order can be found in Figure S 6.2 and Figure S 6.3 for Au, Figure S 6.6 and Figure S 6.7 for Pt and Figure S 6.8 and Figure S 6.9 for GC.

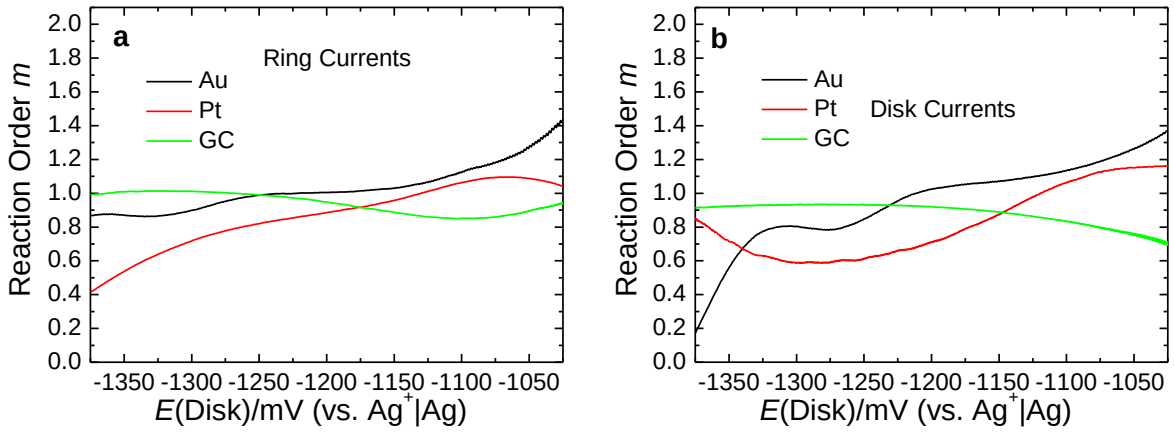

Figure 6.8. Electrochemical reaction order *m* with respect to the oxygen. **a**. Reaction order extrapolated using the ring currents. **b**. Reaction order extrapolated using the disk currents. The values at very low or very high overpotentials, at which deactivation occurs, are not reliable because of the low currents.

As can be seen from Figure 6.8a and b, the reaction order for the gold electrode is close to unity as well using the ring current as the disk current for extrapolation. However, from a potential of −1200 mV the reaction order using the disk currents of the gold electrode (black curve) significantly drops, which is probably related to the peroxide formation. The reaction order using the ring currents remains constant until a potential of −1250 mV, where it also starts to decrease. This is most likely due to the deactivation of the electrode, which is more severe for higher oxygen concentration leading to artificially lowered currents at higher oxygen

concentrations. In the case of the platinum electrode (red curve), the reaction order is also close to unity at low overpotentials whereas there is a decrease of the reaction order at high overpotentials, which is probably also related to the deactivation of the electrode. At glassy carbon, the reaction order remains close to unity even at relatively high overpotentials reflecting the less effective deactivation already observed in the CV.

While the reaction order for superoxide can be determined using the ring currents, the determination of the reaction order for peroxide is not as straightforward. In principle, the concentration dependence of the "residual" currents can be used although these currents are not necessarily only kinetically limited. The resultant plots using the currents presented in Figure 6.2d for the gold electrode are shown in Figure 6.9a and b. Obviously, the reaction order for the peroxide formation is below unity, which is typical for a surface-limited process. The hypothesis of a surface-limited process is supported by the finding of a nucleation hindrance of the ORR on gold, which has been shown recently via potential step experiments [263,304]. The finding of adsorbed superoxide on gold supports this idea further [283]. At gold and platinum, it can directly be seen from the plots in Figure 6.4d and Figure 6.6d that the electrochemical reaction order is below unity.

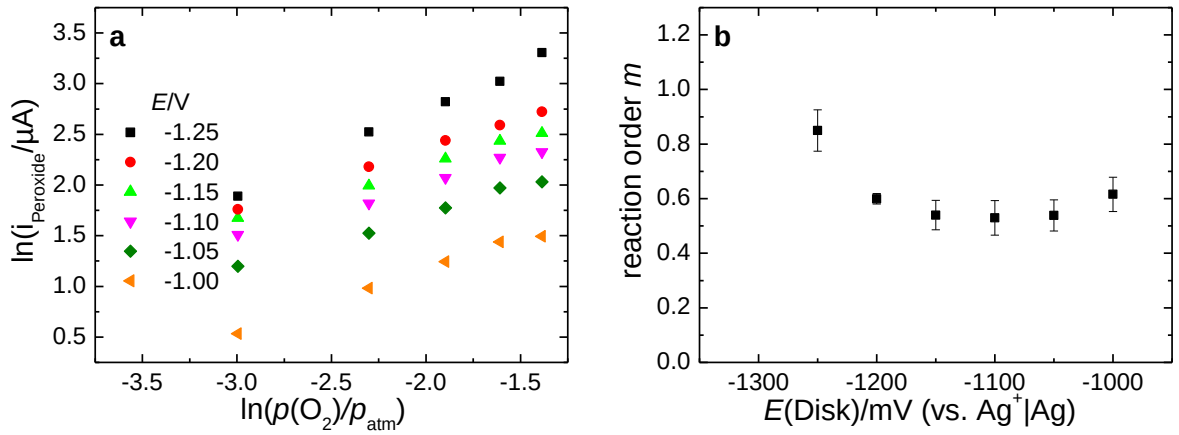

Figure 6.9. Electrochemical reaction order of peroxide at a gold electrode. **a**. Double-logarithmic plots at different potentials. **b**. Corresponding reaction order.

6.4.9 Electrochemical Reaction Order Determined via DEMS

While RRDE studies are in general an excellent way to acquire kinetic data and therefore electrochemical reaction orders due to the well-defined convection, the occurrence of side reactions affecting the currents and, thus, the reaction order cannot be fully excluded. Via the use of DEMS, the consumption of oxygen can be directly measured, and thus a very direct approach to evaluate the electrochemical reaction order with respect to oxygen is possible (Figure 6.10a and b). It is noteworthy that the electrode used for this DEMS measurement is a porous electrode. The faradaic current density i_F referred to geometric surface area is shown in Figure 6.10a, while the rate of oxygen consumption is contained in Figure 6.10b. It is remarkable that a truly constant rate of oxygen consumption is exhibited between −1.2 V and −1.5 V even at a partial pressure of 200 and 400 mbar. This can be attributed to the overall

lower current density as compared to the RRDE measurements as well as to the significantly larger surface area: While the geometric area of the sputtered electrode is only larger by a factor of 1.5, the real surface area is 8 times larger as determined by charge related to the reduction of gold oxide.

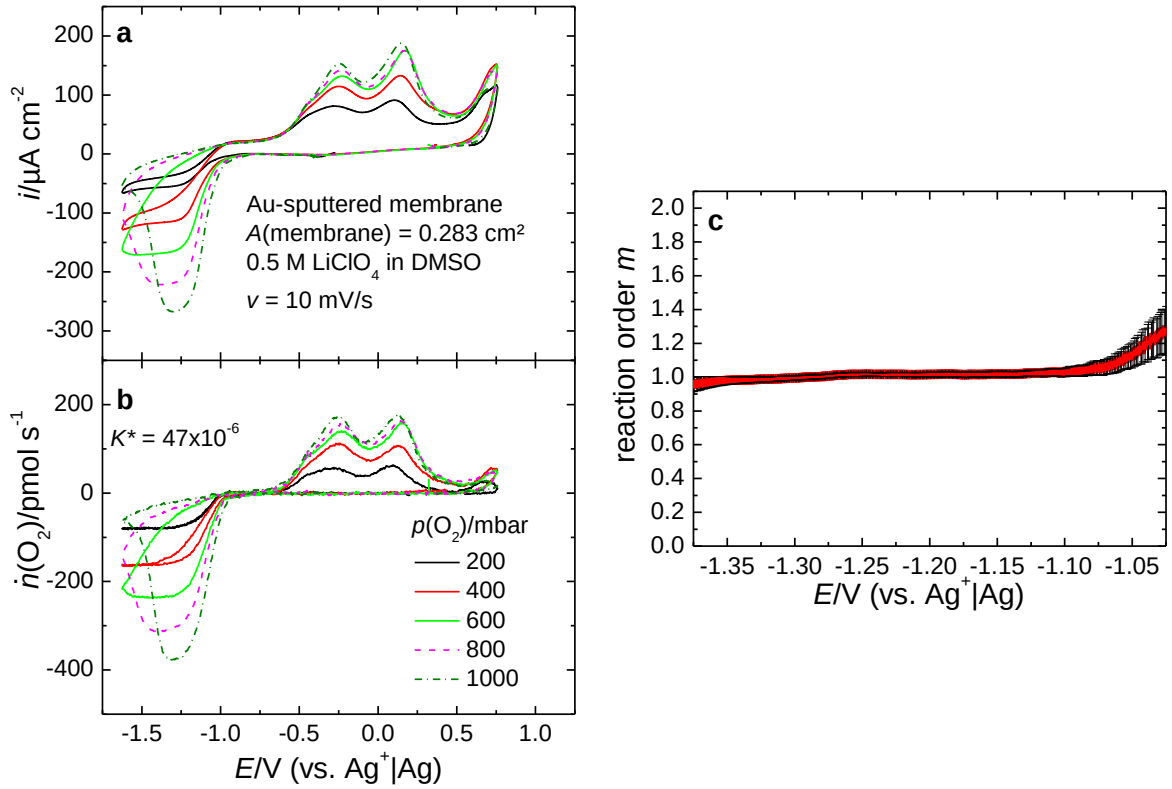

Figure 6.10. DEMS measurements using different O_2 partial pressures. **a**. Faradaic current density. **b**. Consumption of oxygen per second. **c**. Electrochemical reaction order using the consumed oxygen. The black error bars indicate the standard error of the slope at the 95% confidence level. Electrode: Sputtered gold.

For higher oxygen pressures, a significant deactivation becomes visible followed by anodic currents. From 200 to 600 mbar the anodic currents increase with increasing oxygen partial pressure. However, for higher oxygen pressures the anodic currents do not increase further due to the deactivation of the surface similar to the RRDE measurements. The reaction order with respect to oxygen is shown in Figure 6.10c. For low overpotentials the reaction order is slightly above unity, but rises to a value close to it. The reaction order remains 1 for a potential range of roughly 300 mV and then decreases due to the deactivation of the electrode which is more severe at higher oxygen partial pressures.

6.4.10 Determination of the Rate Constants of the Peroxide Formation

The next step in understanding the ORR in the presence of Li^+ is to develop a model mechanism and to test its applicability to the observations. The mechanism which shall be used for the further treatment is depicted in Figure 6.11, where the index *sol* indicates species within the bulk solution and *surf* denotes species close to the surface. It should be noted that

the oxygen ions are not bare ions but connected to Li^+ ions. Especially for the peroxide it is assumed that this is in fact Li_2O_2. Although the possibility of a disproportionation of superoxide has been discussed[201,202], it is neglected for this treatment due to the short transition times in the RRDE assembly (at maximum 300 ms for 4 Hz) and assumingly rather slow reaction kinetics.

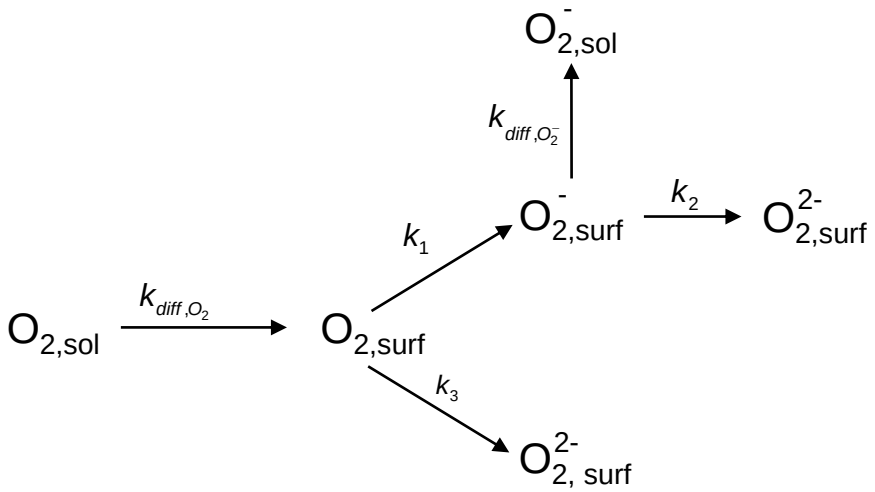

Figure 6.11. Reaction scheme for the oxygen reduction reaction. The index *sol* denotes species within the bulk solution, whereas *surf* indicates that the molecule is close to the surface of the electrode. The cation Li^+ has been omitted for the sake of simplicity.

In principle, the rate of peroxide formation is proportional to the concentration of superoxide close to the surface $\left[O_2^-\right]$, where k_2 contains the roughness factor of the electrode:

$$\left(\frac{dn(O_2^{2-})}{dt}\right)\cdot\frac{1}{A} = k_2[O_2^-] + k_3[O_2] \tag{6.6}$$

Starting from eq.(6.6) a rate law for the peroxide formation can be established using the rate law for superoxide formation as well as assuming stationary conditions(section 6.6.6). The final expression for the rate of peroxide formation is given in eq. (6.7), where $c(O_2)$ denotes the bulk concentration of oxygen and the other symbols have the same meaning as in:

$$\left(\frac{dn(O_2^{2-})}{dt}\right) = \frac{0.62\cdot A\cdot D(O_2)^{2/3}\nu^{-1/6}[O_2]*\left(k_1k_2 + k_2k_3 + 0.62k_3\cdot D(O_2^-)^{2/3}\omega^{1/2}\nu^{-1/6}\right)}{k_1k_2\omega^{-1/2} + k_2k_3\omega^{-1/2} + 0.62k_1\cdot D(O_2^-)^{2/3}\nu^{-1/6} + 0.62k_3\cdot D(O_2^-)^{2/3}\nu^{-1/6}} \tag{6.7}$$

It should be noted that the effect of the deactivation on the rate of peroxide formation has been neglected at this point to alleviate analytical treatment. Thus, eq. (6.7) only holds for potentials at which the overall deactivation is negligible. For highly cathodic potentials the value of k_2 increases, which thus accelerates the rate of peroxide formation as expected. For the limiting case $k_2 = 0$ and $k_3 = 0$, the rate of peroxide formation drops to zero as expected.

The rate of peroxide formation increases with increasing oxygen concentration (e.g. Figure 6.2d). An increasing rotation rate leads to a decreasing denominator due to the inverse scaling of the denominator with $\omega^{-1/2}$. This finally leads to a higher rate of peroxide formation, which

can be directly seen from e.g. Figure 6.1d. Furthermore, the overall charge transferred up to a certain potential is higher for high rotation rates as compared to low rotation rates finally resulting in an earlier deactivation. This deactivation on the other hand lowers the rate constants due to the decreasing surface (formally resulting in roughness factors below 1).

Equation (6.7) also implies that the peroxide current is more susceptible to changes in the oxygen concentration than changes in the rotation rate due to the different scaling. Qualitatively, this can be understood as follows: When the concentration is doubled, the total peroxide current will be doubled as more oxygen is available for reduction. An increase of the rotation rate on the other hand leads to a faster mass transport and thus accelerates the oxygen reduction as well. However, as the main proportion of oxygen is reduced via superoxide as an intermediate, it also has to be taken into account that the higher rotation rate also fosters diffusion of superoxide into the solution prior to further reduction. Consequently, the rate of peroxide formation increases due to the faster transport of oxygen to the electrode, but suffers from the faster diffusion of superoxide to the solution. This can be confirmed from the comparison of Figure 6.1d and Figure 6.2d. Equation (6.7) can also be used to explain the behavior of the shoulder in the disk current in Figure 6.2a. While the disappearance of the shoulder at higher rotation rates could be understood via eq. (6.3) in terms of higher diffusion-limited currents, this explanation cannot be transferred directly to the concentration dependence. Even though the theoretical diffusion-limited current increases, the kinetic current as well increases with concentration. As long as the electrochemical reaction order is close to unity, these two effects cancel out each other. However, if the deactivation is considered, the vanishing of the shoulder in the disk current for higher O_2 partial pressures can be understood. For higher concentrations, the electrode is already deactivated at lower overpotentials as implied by the increasing peroxide current in eq. (6.7). As the disk current is the sum of the current due to peroxide as well as the current due to superoxide, both dependent on the state of deactivation of the surface, this leads to the disappearance of the shoulder.

Rigorous treatment of the kinetic laws also allows to find an expression for the collection efficiency *N* (which is proportional to the share of superoxide):

$$\frac{I(\mathrm{Ring})}{I(\mathrm{Disk})\cdot N_0} = \frac{k_1}{k_1 + 2k_3 + 3.22D(\mathrm{O_2^-})^{-2/3}\omega^{-1/2}\nu^{1/6}\left(k_1k_2 + k_2k_3\right)} \tag{6.8}$$

Equation (6.8) predicts an increase of the collection efficiency (and thus the share of superoxide) with the rotation rate, which is experimentally observed (e.g. Figure 6.1c). Qualitatively, this can be understood as follows: With increasing rotation rate superoxide is transported to the ring electrode more efficiently. As the rate constant of the further reduction of superoxide to peroxide (k_2) is unaffected by the rotation rate, this means that overall larger collection efficiencies can be observed. However, if a parallel reaction (k_3) is assumed, it does not reach the maximum value N_0 even at high rotation rates. This is because the parallel reaction lacks a soluble intermediate and the rate constant of the competing reaction (reduction

of O_2 to superoxide) is independent of the rotation rate as well. Therefore, varying the rotation rate will not affect the ratio between the superoxide and the direct peroxide formation. This seems to be true for the gold electrode, but not for glassy carbon and platinum. To quantify the rate constant k_2,eq. (6.8) must be rearranged to eq. (6.9):

$$\frac{I(\text{Disk})}{I(\text{Ring})} = \frac{1+\frac{2k_3}{k_1}}{N_0} + \frac{1.61D(O_2^-)^{-2/3}\nu^{1/6}k_2\left(\frac{2k_3}{k_1}+2\right)}{N_0\omega^{1/2}} \qquad (6.9)$$

If eq. (6.9) is compared to Damjanovic's diagnostic equation[219], it has to be considered that the ratio x between the current due to direct peroxide formation to the current due to superoxide formation is equal to $2k_3/k_1$.

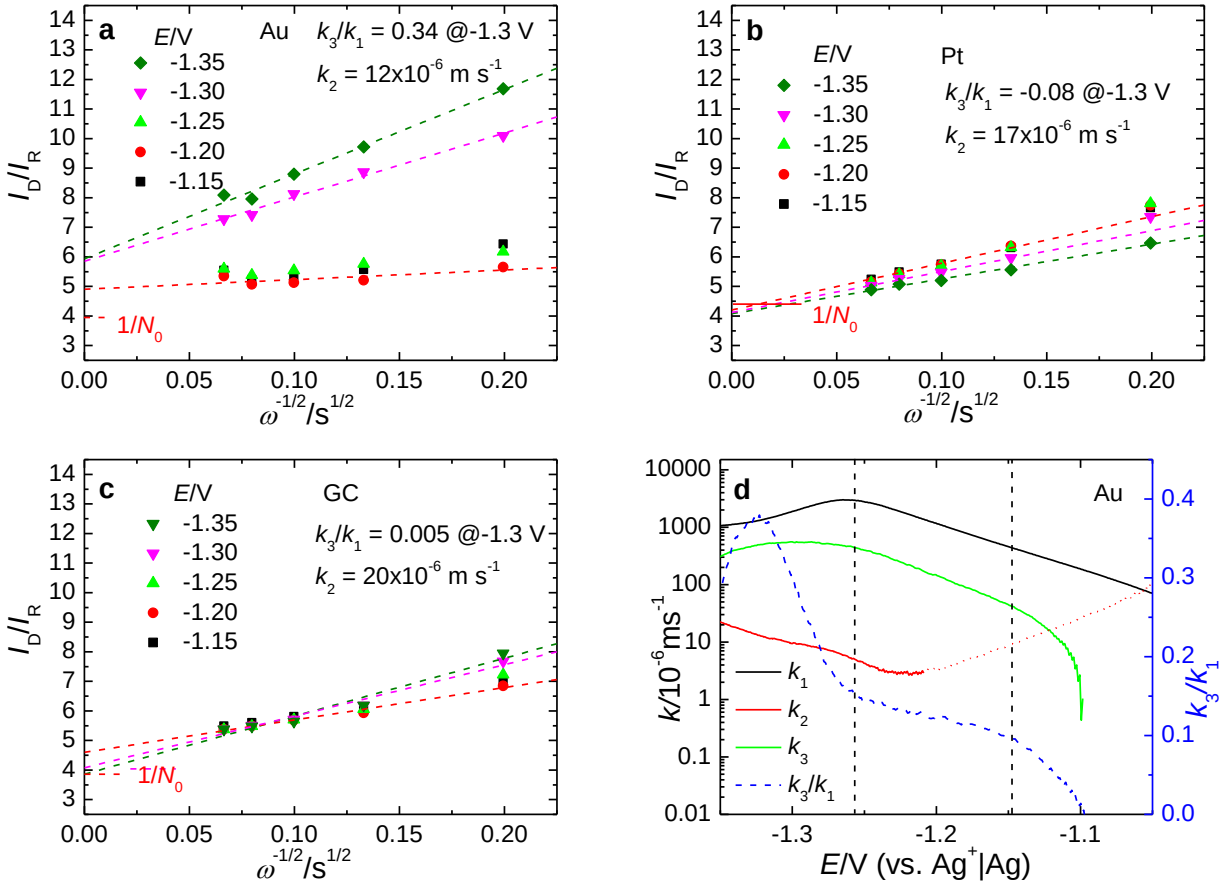

Figure 6.12. Determination of the rate constants at a potential of −1.2 V. **a**. Plots for the gold electrode according to eq. (6.9). **b**. Plots for the platinum electrode. **c**. Plots for the glassy carbon electrode. d. Rate constants at the gold electrode. The region within the dotted lines designates the potential range of the shoulder observed in the disk current. The decrease of k_2 between −1.2 V and −1.05 (red, dotted line) is probably related to an artifact and is explained in the text. For definition of the rate constants see Figure 6.11. Data for a–c was taken from Figure 1–3. k_1 was calculated from the Tafel-plot in Figure 6.7a.

Plots according to eq. (6.9) using data of Figure 6.1, Figure 6.3 and Figure 6.5 are shown in Figure 6.12a–c. Apparently, only for the gold electrode there is a significant contribution of a direct reduction of oxygen to peroxide via reaction path 3 indicated by the deviation of the intercept from $1/N_0$. The plausibility of such a direct reduction step is further supported by the

finding of adsorbed superoxide an Au-electrodes[283]. However, as pointed out by the authors, in the presence of Li+ the signals related to adsorbed superoxide are not visible, which is probably due to the facile further reduction of the adsorbed superoxide. The rate constants k_2 for the further reduction of superoxide to peroxide are in the range of 10^{-5} m s^{-1} for all electrode materials. Finally, rate constants for the different reduction steps at gold are presented in Figure 6.12d. The rate constant k_1 was calculated from the Tafel-plot in Figure 6.7a. Due to the deactivation of the electrode, k_1 seems to decrease from −1.25 V on. The dotted black lines designate the potential region of the shoulder observed at during the ORR at gold electrodes. Apparently, the ratio between k_3 and k_1 increases sharply directly before the shoulder appears. As the slope of the plots for low overpotentials is low, the resulting value of k_2 is susceptible to errors which might be the reason for its apparent decrease between −1.0 V and −1.2 V.

It has to be noted that no disproportionation of soluble superoxide has to be taken into account to explain the experimental observations. In fact, it is arguably if the disproportionation of superoxide in the presence of Li^+-ions takes place at all on the time scale of an experiment. For instance, Yu *et al.* showed using UV-Vis spectroscopy that the amount of superoxide in TBA^+-containing DMSO remains constant for at least 15 min after addition of Li^+ [283], which was further supported by atomic force microscopy measurements[305]. Contrary to this, Johnson *et al.* have found a decrease of the UV-vis absorption at 300 nm when adding Li^+ to a solution of KO_2 in DMSO[287]. However, the decrease of the absorption apparently follows first-order kinetic, which seems hard to believe for a homogenous disproportionation reaction. If one still trusts the rate constants for disproportionation obtained by fitting cyclic voltammograms at different sweep rates (0.03 s^{-1}), only 1 % of the superoxide generated at the disk electrode would disproportionate before reaching the ring electrode at a rotation rate of 4 Hz.

6.5 Conclusions

The electrochemical reaction order with respect to oxygen and the rate constants for different reaction pathways of the ORR at gold, glassy carbon, and platinum electrodes have been investigated employing RRDE and DEMS measurement and varying the concentration of oxygen within the solution. At glassy carbon and platinum electrodes, the ORR yields the formation of superoxide as well as peroxide. Evaluating the dependence of the experimental collection efficiency on the rotation rate, it is plausible to assume that the formation of peroxide proceeds via a direct reduction rather than a homogeneous disproportionation of intermediately formed superoxide. This is further supported by the finding that at gold electrodes there is the sole formation of superoxide up to a potential of −1.2 V. Assuming a homogeneous disproportionation, the electrocatalyst should not have an impact on the amount of peroxide formed. However, homogeneous disproportionation might still occur on longer time scales than the experiment's one (at maximum 300 ms). Using the dependence of the inverse of the collection efficiency on inverse square root of the rotation rate, the rate constant of the

further, direct reduction has been calculated to be of the order of 10^{-5} m s^{-1}. At the gold electrode, a further, parallel reduction step has to be taken into account starting at −1.1 V. As indicated by the noni deal intercepts of the $1/N$ vs $\omega^{-1/2}$, this parallel reduction step does not involve the formation of insoluble intermediates. At a potential of −1.3 V, 30% of oxygen is reduced to peroxide via a direct reduction step.

Regardless of the oxygen concentration, the Tafel slope for all electrode materials under investigation remains close to 120 mV/dec, implying that a one-electron transfer is the rate-determining step. The electrochemical reaction order with respect to oxygen is close to unity regarding the overall current as the sum of superoxide and peroxide current as could be shown using a DEMS setup. However, separating the contribution of superoxide and peroxide via the use of an RRDE assembly, the evaluation leads to a reaction order significantly below one for the peroxide formation. This has been attributed to an adsorption isotherm of superoxide. For high overpotentials the reaction order with respect to oxygen drops due to the deactivation of the electrode, which is more severe at higher oxygen concentrations. Finally, a reaction scheme has been proposed and applied to the experimental observations. Additional spectroscopic studies would help further understanding the reaction pathways.

6.6 Supporting Information

6.6.1 CV for Different Sweep Rates at a Constant Rotation Rate and Oxygen partial Pressure at Gold and Platinum.

Figure S 6.1 shows CV for different sweep rates at a constant rotation rate and constant oxygen concentration for a gold disk electrode (a–b) and a platinum disk electrode (c–d).

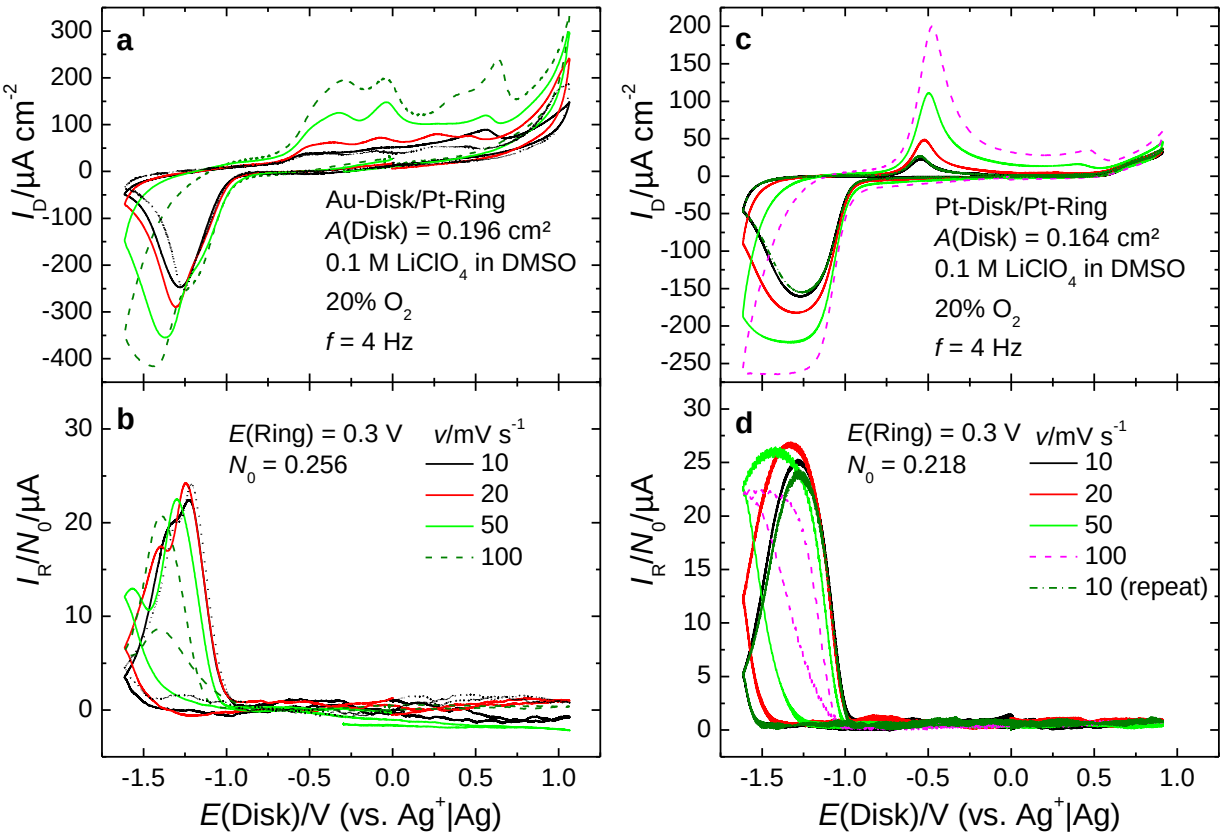

Figure S 6.1. Subsequent CV for different sweep rates at a rotation rate of 4 Hz and an oxygen partial pressure of 20%. **a**–**b**. Disk and ring currents at an Au disk/GC ring assembly. **c**–**d**. Disk and ring currents at an Pt disk/Pt ring assembly.

As can be seen from Figure S 6.1 a, the currents at the onset potential of approx. −0.8 V are quite the same for the different sweep rates. However, the occurrence of the shoulder at −1.2 V is hardly visible at 10 mV s^{-1} and becomes more distinct for higher sweep rates. Furthermore, the peak, signifying deactivation of the electrode, shifts to higher overpotentials the higher the sweep rate is. This and the fact that the currents increase for higher sweep rate are related to the surface deactivation, which is expected to be less severe at higher sweep rates due to the lower ORR charge. Additionally, a larger proportion of O_2 is expected to be reduced to peroxide at high sweep rates, which are resulting in a less effective deactivation of the surface.

The sweep rate also affects the ring currents shown in Figure S 6.1 b. For the measurements at high sweep rates a large hysteresis of the potential can be observed, which is due to the time it takes products to diffuse from the disk to the ring electrode. For instance, at 100 mV s^{-1} the second peak in the ring current arises in the anodic direction. Therefore, a kinetic evaluation of the ring currents proves difficult. Nonetheless, again the transition from one to two electron reduction is more distinct for higher sweep rates. Furthermore, the ring currents are generally lower for higher sweep rates suggesting an increase of the relative amount of peroxide formed during the ORR. To find a compromise between the hysteresis of the potential and the distinguishability of the one and two electron process, a sweep rate of 20 mV s^{-1} was for the kinetic investigation at the gold electrode.

At the platinum electrode, the sweep rate affects the CV in a similar way (Figure S 6.1 c–d). For large overpotentials, the currents are higher for increased sweep rates due to less effective deactivation of the surface. Again, this effect is of twofold nature: Firstly, less deactivation means that a larger proportion of the surface is still available for reduction at high overpotentials. Secondly, the surface deactivation affects the peroxide pathway more strongly than the superoxide pathway. Thus, a lower deactivation entails a higher relative amount of peroxide formation resulting in larger currents. This is also reflected by the lower ring currents. However, as platinum lacks a separation between one and two electron process, a sweep rate of 10 mV s^{-1} was chosen to ensure applicability of the equations used for evaluation.

6.6.2 CV for Different Rotation Rates and Oxygen Pressures at Gold

Additional CV for oxygen partial pressures of 5% and 10% of the atmospheric pressure are shown in Figure S 6.2. Figure S 6.3 shows measurements for an oxygen partial pressure of 15% and 25% O_2 and the final control measurement for 5% oxygen pressure. The expression "x% O_2" always indicates that the partial pressure of oxygen equals x percent of the atmospheric pressure (which was approx. 1 bar).

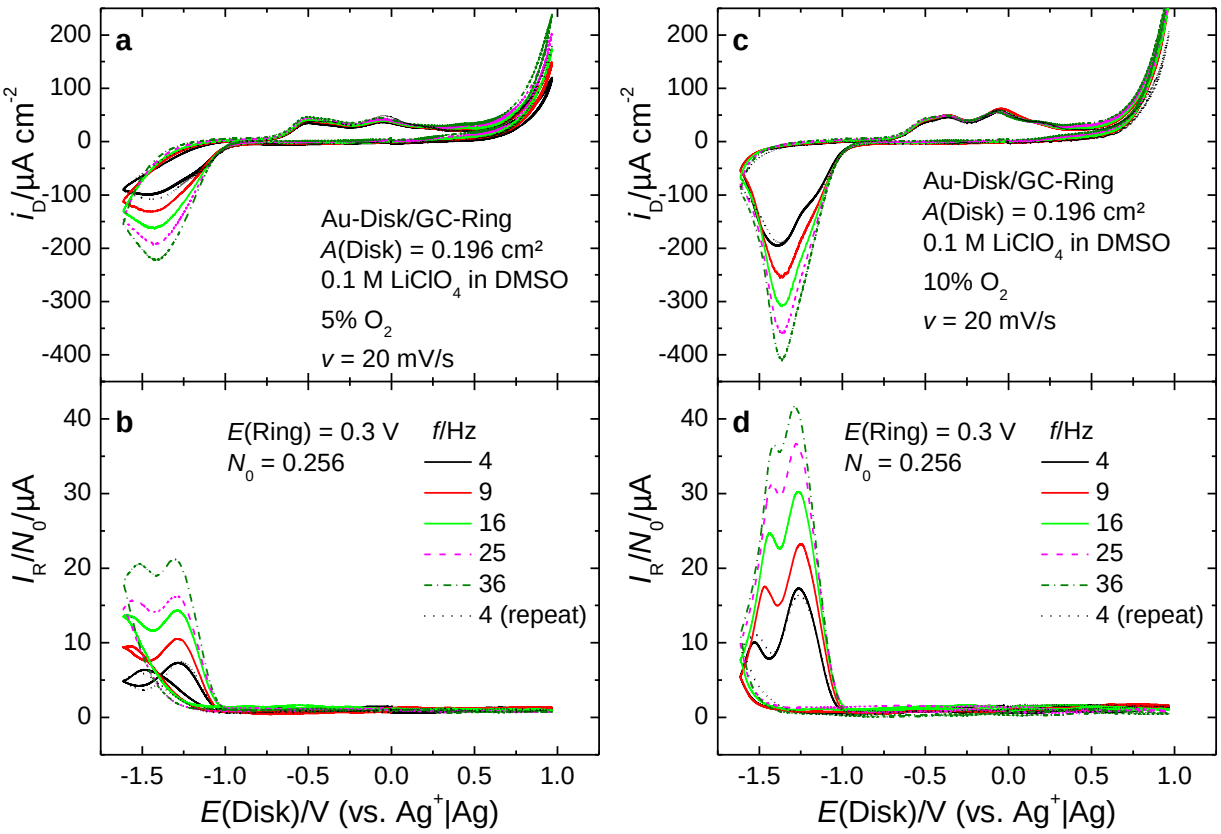

Figure S 6.2. Subsequent CV for different rotation rates at an Au disk/GC ring RRDE assembly. **a**–**b**. Disk and ring currents for 5% O_2 **c**–**d**. Disk and ring currents for 10% O_2.

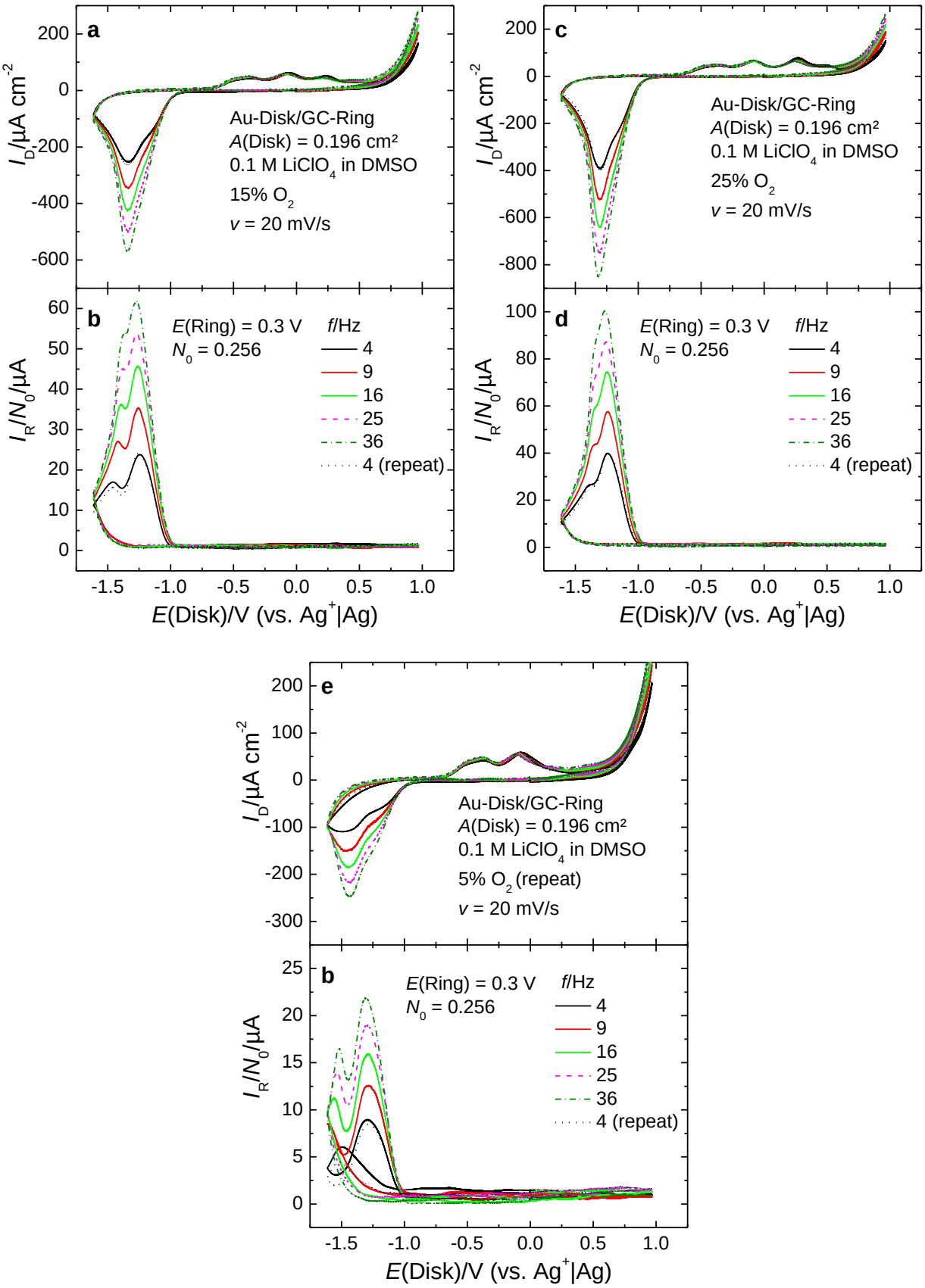

Figure S 6.3. Subsequent CV for different rotation rates at an Au disk/GC ring RRDE assembly. **a**–**b**. Disk and ring currents for 15% O_2. **c**–**d**. Disk and ring currents for 25% O_2. **e**–**f**. Control measurement with disk and ring currents for 5% O_2.

6.6.3 CV for Different Rotation Rates and Oxygen Pressures at Platinum for a Sweep Rate of 20 mV s^{-1}

Additional CV for oxygen partial pressures of 5% and 10% of the atmospheric pressure are shown in Figure S 6.4. The oxygen concentrations 15%, 20%, 25% as well as the control measurement at 20% O_2 are shown in Figure S 6.5. The expression "x% O_2" always indicates that the partial pressure of oxygen equals x percent of the atmospheric pressure. The order of experiments was: 20%, 5%, 10%, 15%, 25% and finally 20% (repeat).

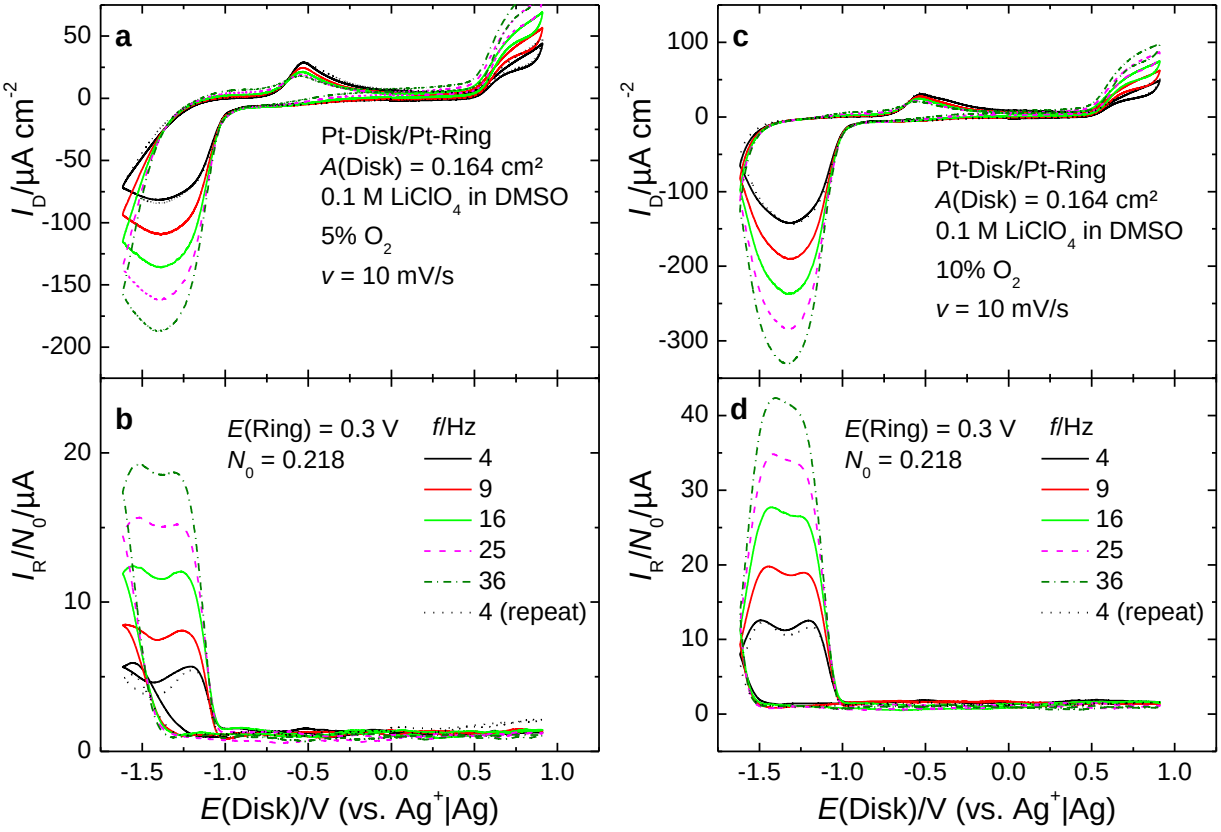

Figure S 6.4. Subsequent CV for different rotation rates at a Pt disk/Pt ring RRDE assembly. **a**–**b**. Disk and ring currents for 5% O_2. **c**–**d**. Disk and ring currents for 10% O_2.

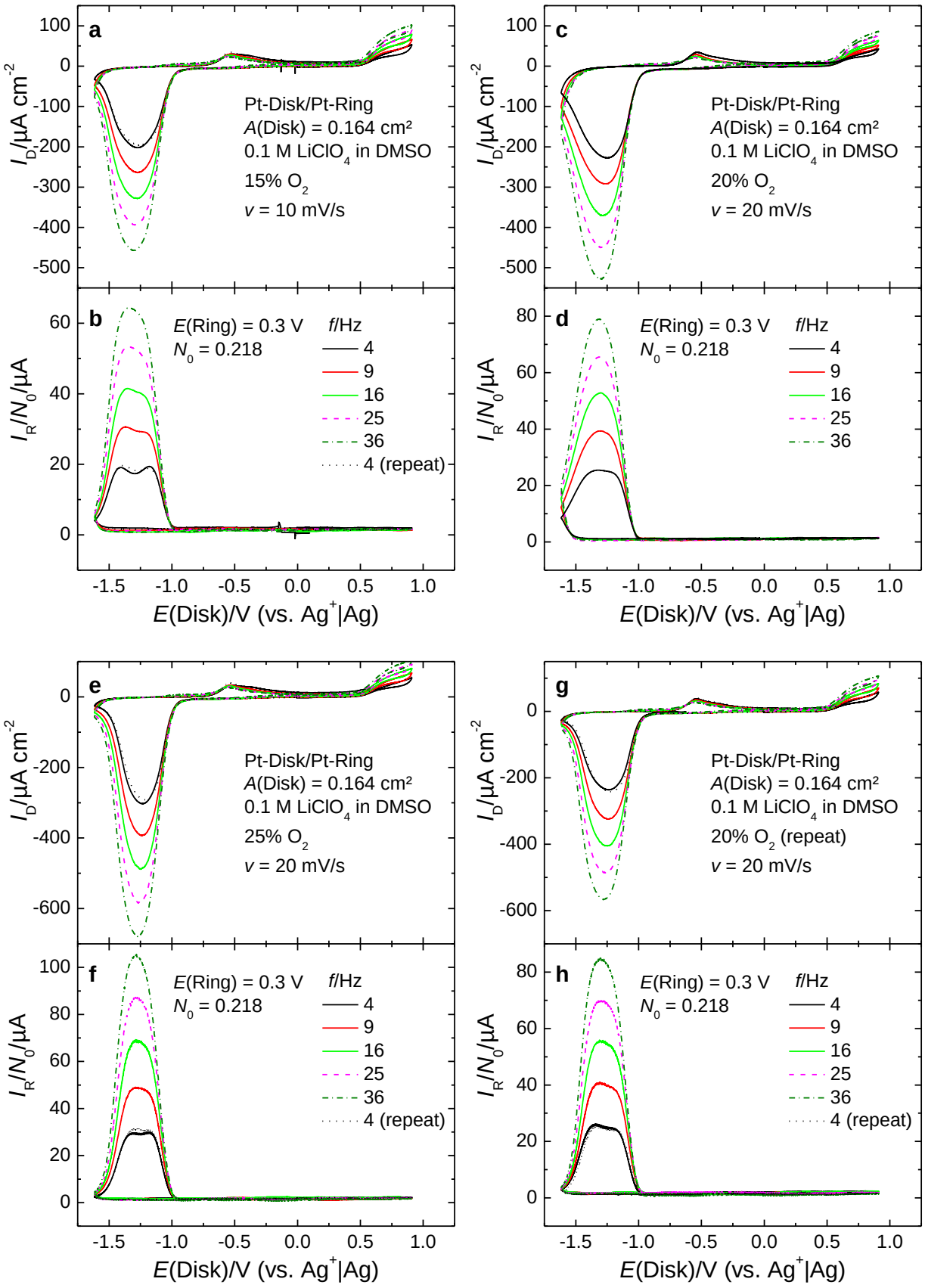

Figure S 6.5. Subsequent CV for different rotation rates at a Pt disk/Pt ring RRDE assembly. **a**–**b**. Disk and ring currents for 15% O_2. **c**–**d**. Disk and ring currents for 20% O_2 **e**–**f**, Disk and ring currents for 25% O_2. **g**–**h**. Control measurement with disk and ring currents for 20% O_2.

6.6.4 CV for Different Rotation Rates and Oxygen Pressures at Platinum for a Sweep Rate of 10 mV s^{-1}

Additional CV for oxygen partial pressures of 5% and 10% of the atmospheric pressure are shown in Figure S 6.6. The oxygen concentrations 20%, 25%, 100% as well as the control measurement at 10% O_2 are shown in Figure S 6.7. The expression "x% O_2" always indicates that the partial pressure of oxygen equals x percent of the atmospheric pressure. The order of experiments was: 10%, 5%, 20%, 25%, 100% and finally 10% (repeat).

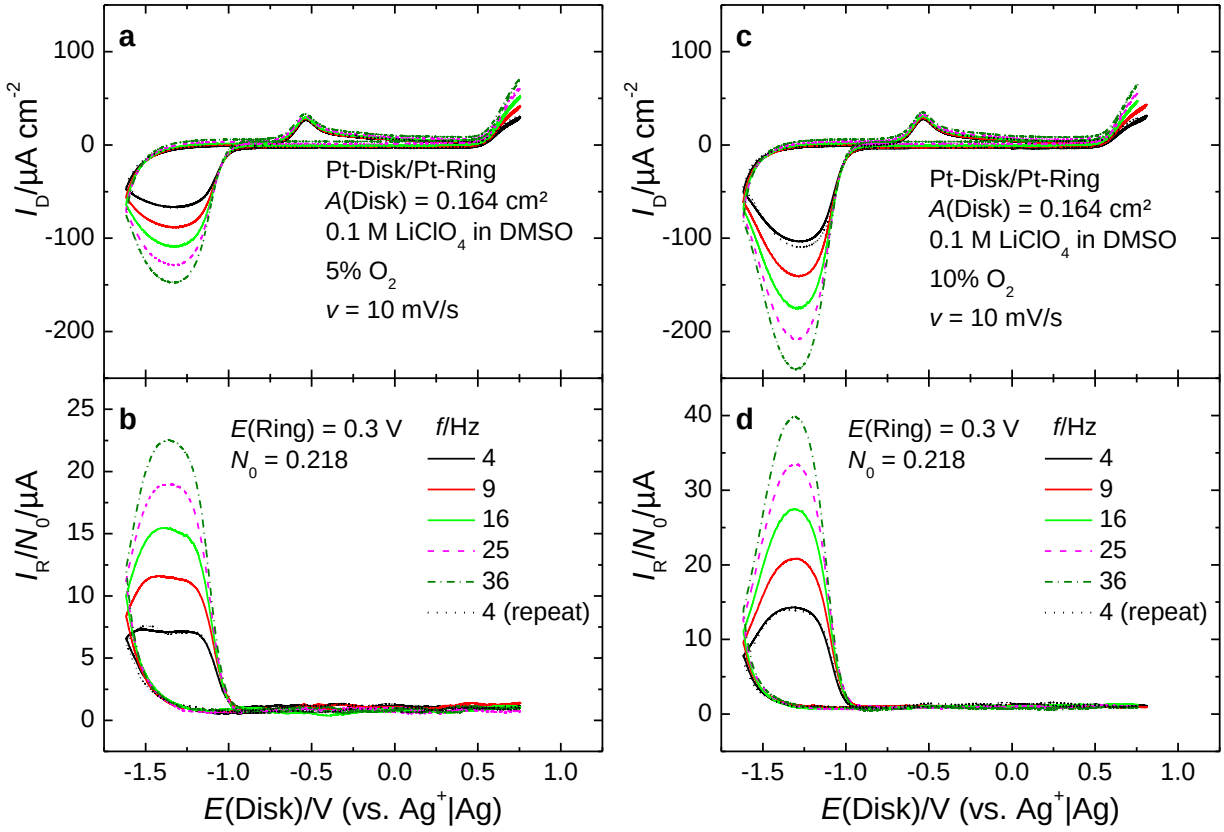

Figure S 6.6. Subsequent CV for different rotation rates at a Pt disk/Pt ring RRDE assembly. **a**.–**b**. Disk and ring currents for 5% O_2. **c**.–**d**. Disk and ring currents for 10% O_2.

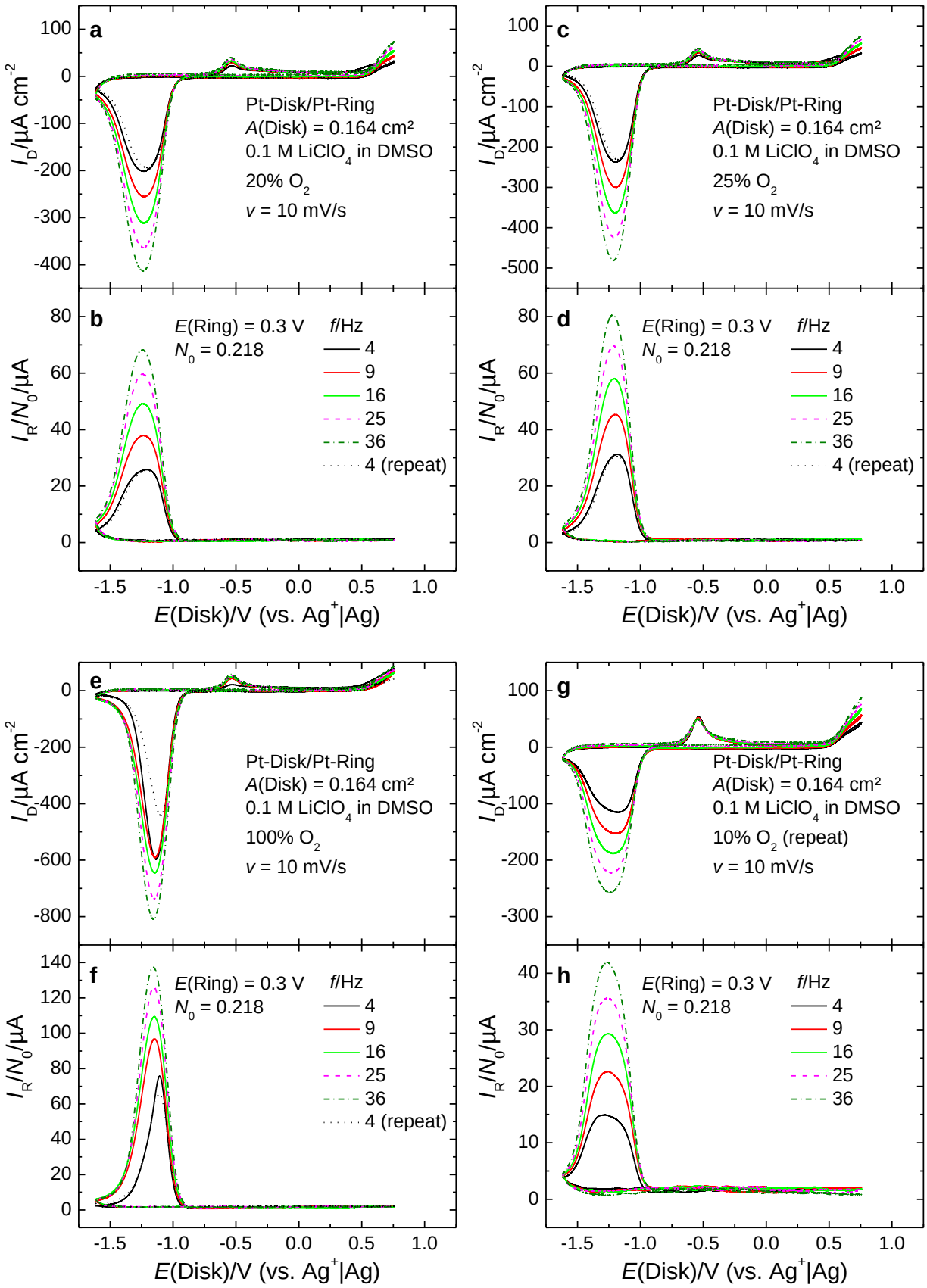

Figure S 6.7. Subsequent CV for different rotation rates at a Pt disk/Pt ring RRDE assembly. **a**–**b**. Disk and ring currents for 20% O_2. **c**–**d**. Disk and ring currents for 25% O_2 **e**–**f**. Disk and ring currents for 100% O_2. **g**–**h**. Control measurement with disk and ring currents for 20% O_2.

6.6.5 CV for Different Rotation Rates and Oxygen Pressures at Glassy Carbon for a Sweep Rate of 10 mV s^{-1}

Additional CV for oxygen partial pressures of 5% and 10% of the atmospheric pressure are shown in Figure S 6.8. The oxygen concentrations 20%, 25%, 100% as well as the control measurement at 10% O_2 are shown in Figure S 6.9. The expression "x% O_2" always indicates that the partial pressure of oxygen equals x percent of the atmospheric pressure. The order of experiments was: 10%, 5%, 20%, 25%, 100% and finally 10% (repeat).

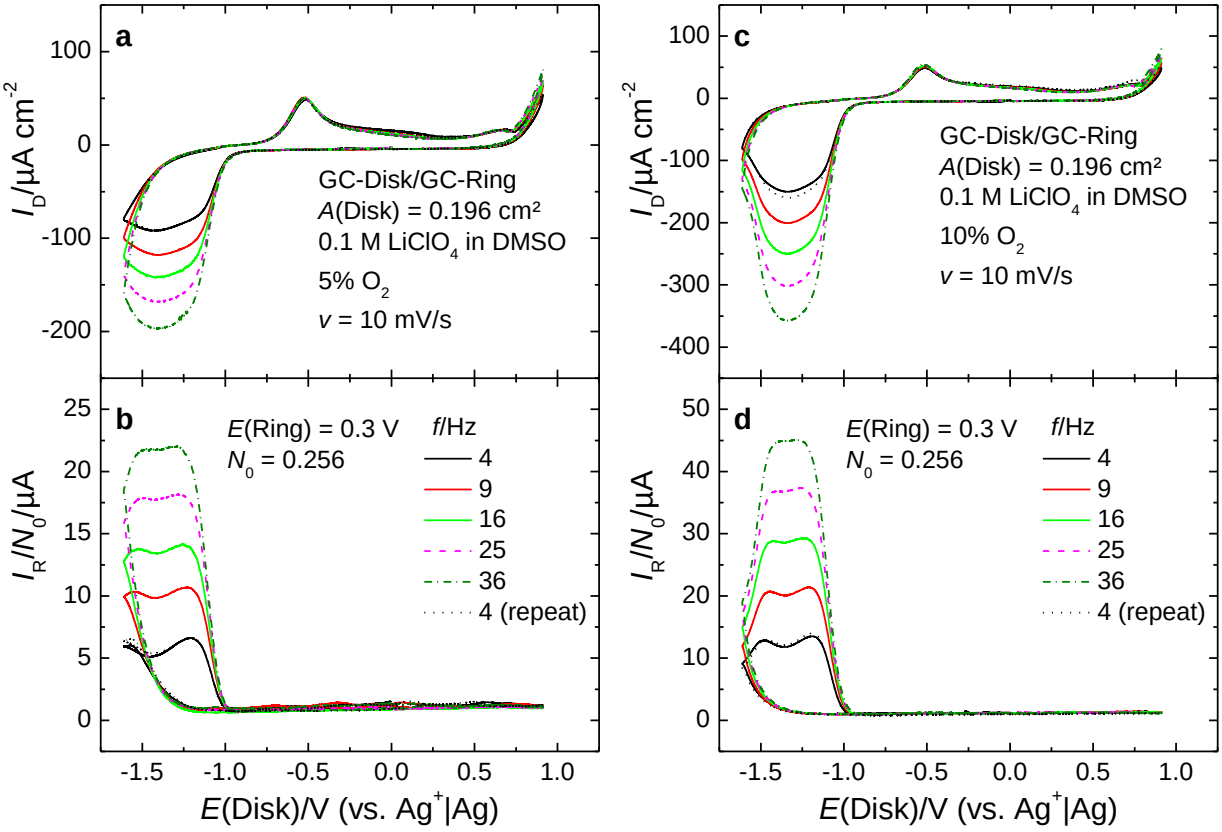

Figure S 6.8. Subsequent CV for different rotation rates at a GC disk/GC ring RRDE assembly. **a**–**b**. Disk and ring currents for 5% O_2. **c**–**d**. Disk and ring currents for 10% O_2.

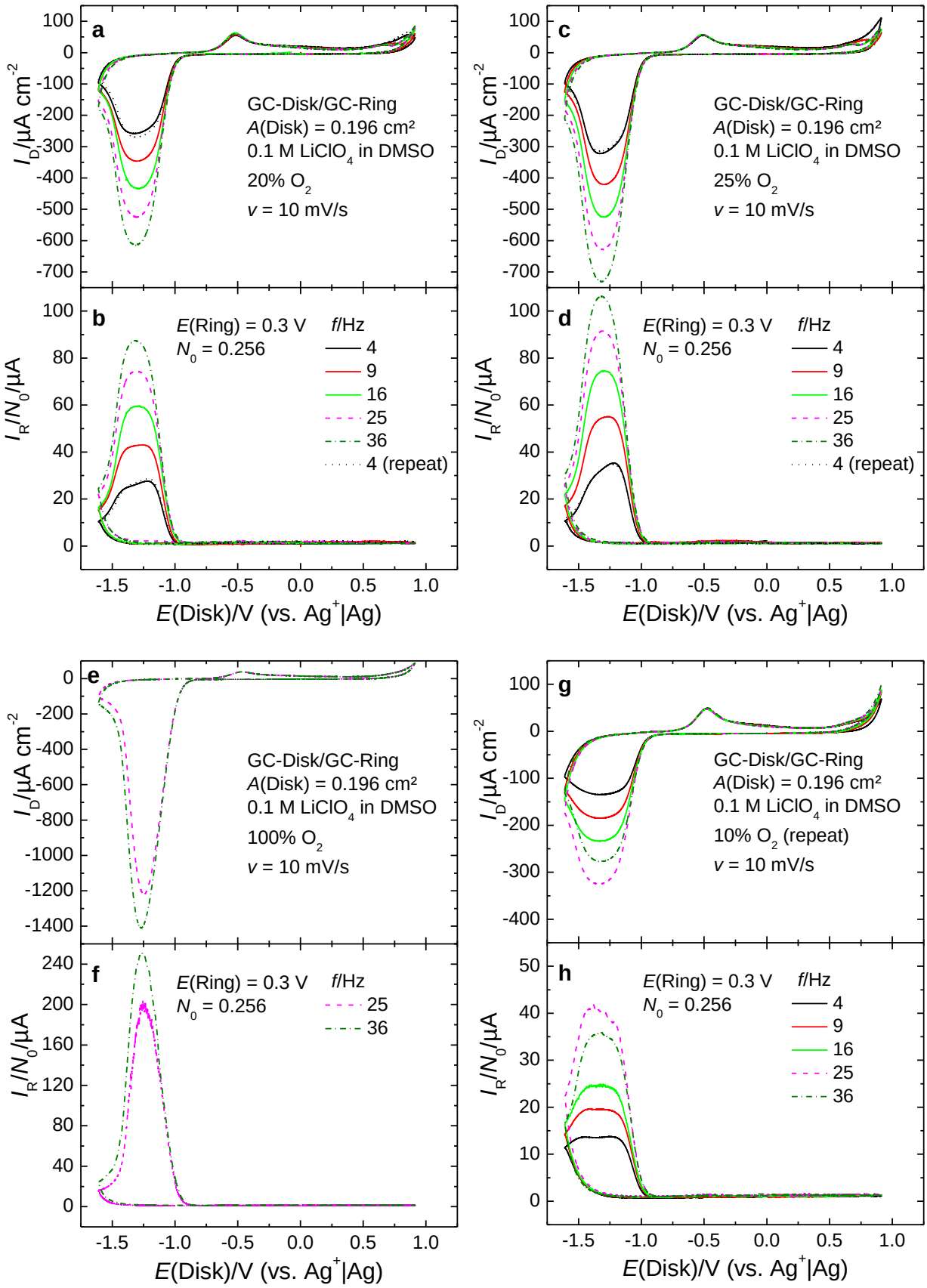

Figure S 6.9. Subsequent CV for different rotation rates at a GC disk/GC ring RRDE assembly. **a**–**b**. Disk and ring currents for 20% O_2. **c**–**d**. Disk and ring currents for 25% O_2. **e**–**f**. Disk and ring currents for 100% O_2. **g**–**h**. Control measurement with disk and ring currents for 10% O_2.

6.6.6 Theoretical Treatment of the Proposed Mechanism

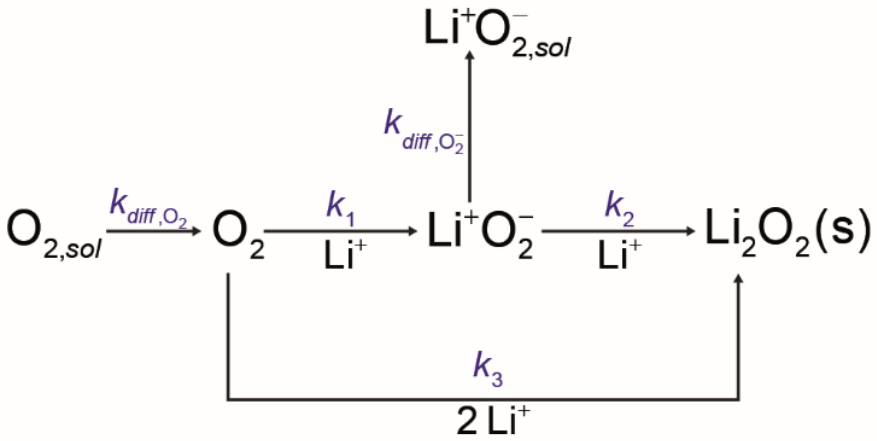

Figure S 6.10. Possible reaction pathways of the formation of superoxide and peroxide. The index *sol* designates species within the bulk solution.

Although there are already many treatments of the theoretical currents expected for an RRDE assembly for different reaction mechanisms [105-108,219,306,307], it might be helpful to derive explicit expressions for the reactions under investigation. In order to derive a rate law for the currents observable at an RRDE, the following assumptions shall be made:

1) The reactions occur under stationary conditions, i.e. the change of the surface concentrations of oxygen and superoxide with time is 0.
2) The bulk concentration of superoxide is 0 due to the high electrolyte volume.
3) The concentration of Li^+ is high with respect to the concentration of oxygen, thus leading to a constant Li^+ concentration.
4) The homogeneous disproportionation of superoxide is rather slow and does not occur on the time scale of the experiment.

The general rate law of the peroxide formation is presented in eq. (S 6.1):

$$\left(\frac{dn(O_2^{2-})}{dt}\right)\cdot\frac{1}{A} = k_2[O_2^-] + k_3[O_2] \qquad \text{(S 6.1)}$$

Square brackets designate concentrations, A is the geometric surface area. Unless otherwise stated, the concentrations in the rate laws always represent surface concentrations. It is important to note that the rate constants k_2 and k_3 contain the roughness factor which is defined as the ratio of the real surface area to the geometric surface area. As the surface concentration of superoxide and oxygen is unknown, it is necessary to correlate these concentrations to the bulk concentration of oxygen [O_2*]. Equation (S 6.2) describes the rate law for superoxide, while eq. (S 6.3) contains an expression for the surface concentration of superoxide under the assumption of stationary conditions:

$$\left(\frac{dn(O_2^-)}{dt}\right)\cdot\frac{1}{A} = k_1[O_2] - k_2[O_2^-] - k_{diff,O_2^-}[O_2^-] \qquad \text{(S 6.2)}$$

$$[O_2^-] = \frac{k_1 \cdot [O_2]}{k_2 + k_{diff,O_2^-}} \qquad \text{(S 6.3)}$$

Note that the roughness factor is again contained in k_1, but *not* in k_{diff,O_2^-} as the diffusion only depends on the geometric surface area with a microscopic surface roughness.

The surface concentration of oxygen can be related to its bulk concentration via eq. (S 6.4) and (S 6.5):

$$\left(\frac{dn(O_2)}{dt}\right) \cdot \frac{1}{A} = k_{diff,O_2}[O_2{*}] - k_1[O_2] - k_3[O_2] \qquad \text{(S 6.4)}$$

$$[O_2] = \frac{k_{diff,O_2}[O_2{*}]}{k_1 + k_3} \qquad \text{(S 6.5)}$$

This results in an expression for the surface concentration of superoxide in relation to the bulk concentration of oxygen:

$$[O_2^-] = \frac{k_1 k_{diff,O_2}[O_2{*}]}{\left(k_2 + k_{diff,O_2^-}\right)\left(k_1 + k_3\right)} \qquad \text{(S 6.6)}$$

As eq. (S 6.6) appears to be rather complex expression for the surface concentration of superoxide, it might be helpful to make have some qualitative thoughts on it. For the limiting case that there is no peroxide formation at all (k_2 and k_3 equal 0), eq. (S 6.6) converges to eq. (S 6.7), which is the normal relation expected for a simple reaction without parallel or following reactions:

$$[O_2^-] = \frac{k_{diff,O_2}[O_2{*}]}{k_{diff,O_2^-}} \qquad \text{(S 6.7)}$$

Increasing k_2 or leads to a lower value of, which is also expected. The equations (S 6.5) and (S 6.7) can now be used to substitute the surface concentrations in eq. (S 6.3) and (S 6.4). Before that is done, general expression for the disk and ring currents shall be derived.

The disk current density *i*(*Disk*) related to the surface area consists of three contributions: formation of superoxide (k_1), further reaction to peroxide (k_2) and direct reduction of oxygen to peroxide (k_3). Considering the number of electrons transferred during each step and Faraday's constant *F*, this leads to eq. (S 6.8)

$$\begin{aligned} i(Disk) &= Fk_1[O_2] + Fk_2[O_2^-] + 2Fk_3[O_2] && (a)\\ &= Fk_1 \cdot \frac{k_{diff,O_2}[O_2{*}]}{k_1 + k_3} + Fk_2 \cdot \frac{k_1 k_{diff,O_2}[O_2{*}]}{\left(k_2 + k_{diff,O_2^-}\right)\left(k_1 + k_3\right)} + 2Fk_3 \cdot \frac{k_{diff,O_2}[O_2{*}]}{k_1 + k_3} && (b)\\ &= Fk_{diff,O_2}[O_2{*}] \frac{2k_1k_2 + k_1k_{diff,O_2^-} + 2k_2k_3 + 2k_3k_{diff,O_2^-}}{\left(k_2 + k_{diff,O_2^-}\right)\left(k_1 + k_3\right)} && (c) \end{aligned} \qquad \text{(S 6.8)}$$

Given that only superoxide can be oxidized at the ring electrode, the ring current is directly proportional to the share of superoxide, which diffuses away prior to further reaction (N_0 designates the theoretical collection efficiency due to geometry, A describes the geometric surface area of the *disk electrode*):

$$\begin{aligned} \frac{I(Ring)}{N_0} &= F \cdot A \cdot k_{diff,O_2^-}[O_2^-] && (a) \\ &= F \cdot A \cdot k_{diff,O_2^-} \frac{k_1 k_{diff,O_2}[O_2{*}]}{\left(k_2 + k_{diff,O_2^-}\right)\left(k_1 + k_3\right)} && (b) \end{aligned} \qquad \text{(S 6.9)}$$

Having developed two equations describing the disk and ring current, an expression for the collection efficiency N, which is defined as the modulus of the ratio of the ring current to the disk current, can be derived (eq. (S 6.10)):

$$\frac{I(Ring)}{I(Disk) \cdot N_0} = Fk_{diff,O_2^-} \frac{k_1 k_{diff,O_2}[O_2{*}]}{\left(k_2 + k_{diff,O_2^-}\right)\left(k_1 + k_3\right)} \cdot \frac{1}{Fk_{diff,O_2}[O_2{*}]} \cdot \frac{\left(k_2 + k_{diff,O_2^-}\right)\left(k_1 + k_3\right)}{2k_1k_2 + k_1k_{diff,O_2^-} + 2k_2k_3 + 2k_3k_{diff,O_2^-}} \qquad \text{(S 6.10)}$$

Reduction of the fraction leads to eq. (S 6.11):

$$\frac{I(Ring)}{I(Disk) \cdot N_0} = \frac{k_1 k_{diff,O_2^-}}{2k_1k_2 + k_1k_{diff,O_2^-} + 2k_2k_3 + 2k_3k_{diff,O_2^-}} \qquad \text{(S 6.11)}$$

Again, in the absence of parallel or further reactions, eq. (S 6.11) converges to unity, as expected. The last expression needed for interpretation of the experimental data is the current due to peroxide formation:

$$\begin{aligned} i(O_2^{2-}) &= Fk_2[O_2^-] + 2Fk_3[O_2] && (a) \\ &= Fk_2 \cdot \frac{k_1 k_{diff,O_2}[O_2{*}]}{\left(k_2 + k_{diff,O_2^-}\right)\left(k_1 + k_3\right)} + 2Fk_3 \frac{k_{diff,O_2}[O_2{*}]}{k_1 + k_3} && (b) \\ &= Fk_{diff,O_2}[O_2{*}] \frac{k_1k_2 + 2k_2k_3 + 2k_3k_{diff,O_2^-}}{\left(k_2 + k_{diff,O_2^-}\right)\left(k_1 + k_3\right)} && (c) \end{aligned} \qquad \text{(S 6.12)}$$

For the final discussion, eq. (S 6.11) and (S 6.12) have to be written in a more explicit form, substituting the rate constant of diffusion and using Levich's formula for the Nernstian diffusion layer ((S 6.13)):

$$\delta_N = 1.61 \cdot D(O_2)^{1/3} \nu^{1/6} \omega^{-1/2} \qquad \text{(S 6.13)}$$

$$\begin{aligned} k_{diff,O_2} &= \frac{D(O_2)}{\delta_N} = 0.62 \cdot D(O_2)^{2/3} \nu^{-1/6} \omega^{1/2} && (a) \\ k_{diff,O_2^-} &= \frac{D(O_2^-)}{\delta_N} = 0.62 \cdot D(O_2^-)^{2/3} \nu^{-1/6} \omega^{1/2} && (b) \end{aligned} \qquad \text{(S 6.14)}$$

Substituting eq. (S 6.14) b into eq. (S 6.11) leads to eq. (S 6.15):

$$\frac{I(Ring)}{I(Disk)\cdot N_0} = \frac{0.62\cdot D(O_2^-)^{2/3}\omega^{1/2}\nu^{-1/6}k_1}{2k_1k_2 + 0.62\cdot D(O_2^-)^{2/3}\omega^{1/2}\nu^{-1/6}\left(k_1+2k_3\right)+2k_2k_3} \quad (a)$$

$$= \frac{k_1}{k_1+2k_3+3.22\cdot D(O_2^-)^{-2/3}\omega^{-1/2}\nu^{1/6}\left(k_1k_2+k_2k_3\right)} \quad (b) \qquad \text{(S 6.15)}$$

As can be seen from eq. (S 6.15), the experimental collection efficiency increases with increasing rotation frequency. Furthermore, higher values of or lead to a decrease of the collection efficiency. For the limiting case eq. (S 6.15)converges to eq.(S 6.16):

$$\lim_{\omega\to\infty}\left(\frac{I(Ring)}{I(Disk)\cdot N_0}\right) = \frac{k_1}{k_1+2k_3} \qquad \text{(S 6.16)}$$

This means that even at very high rotation rates the collection efficiency will not equal the theoretical value, which is in agreement with Damjanovic's diagnostic equation [219]. Moreover, the occurrence of a parallel reaction (i.e.) decreases the slope of a plot of *N* versus $\omega^{-1/2}$.
As the current due to peroxide formation is directly related to the deactivation of the surface, it might be interesting to investigate its concentration and rotation dependence. Substituting (S 6.14) a and b into eq. (S 6.12) leads to eq. (S6.17):

$$i(O_2^{2-})$$

$$= 0.62F\cdot D(O_2)^{2/3}\omega^{1/2}\nu^{-1/6}[O_2{}^*]\frac{k_1k_2+2k_2k_3+1.24k_3D(O_2^-)^{2/3}\omega^{1/2}\nu^{-1/6}}{\left(k_2+0.61D(O_2^-)^{2/3}\omega^{1/2}\nu^{-1/6}\right)\left(k_1+k_3\right)} \quad (a)$$

$$= \frac{0.62F\cdot D(O_2)^{2/3}\omega^{1/2}\nu^{-1/6}[O_2{}^*]\left(k_1k_2+2k_2k_3+1.24k_3\cdot D(O_2^-)^{2/3}\omega^{1/2}\nu^{-1/6}\right)}{k_1k_2+k_2k_3+0.62k_1\cdot D(O_2^-)^{2/3}\omega^{1/2}\nu^{-1/6}+0.62k_3\cdot D(O_2^-)^{2/3}\omega^{1/2}\nu^{-1/6}} \quad (b) \qquad \text{(S6.17)}$$

$$= \frac{0.62F\cdot D(O_2)^{2/3}\nu^{-1/6}[O_2{}^*]\left(k_1k_2+2k_2k_3+1.24k_3\cdot D(O_2^-)^{2/3}\omega^{1/2}\nu^{-1/6}\right)}{k_1k_2\omega^{-1/2}+k_2k_3\omega^{-1/2}+0.62k_1\cdot D(O_2^-)^{2/3}\nu^{-1/6}+0.62k_3\cdot D(O_2^-)^{2/3}\nu^{-1/6}} \quad (c)$$

As can be seen from eq. (S6.17), the peroxide current increases with increasing rotation rate as well as increasing oxygen concentration $[O_2]^*$. This should in general lead to a faster deactivation of the electrode.

6.6.7 DEMS-Set up

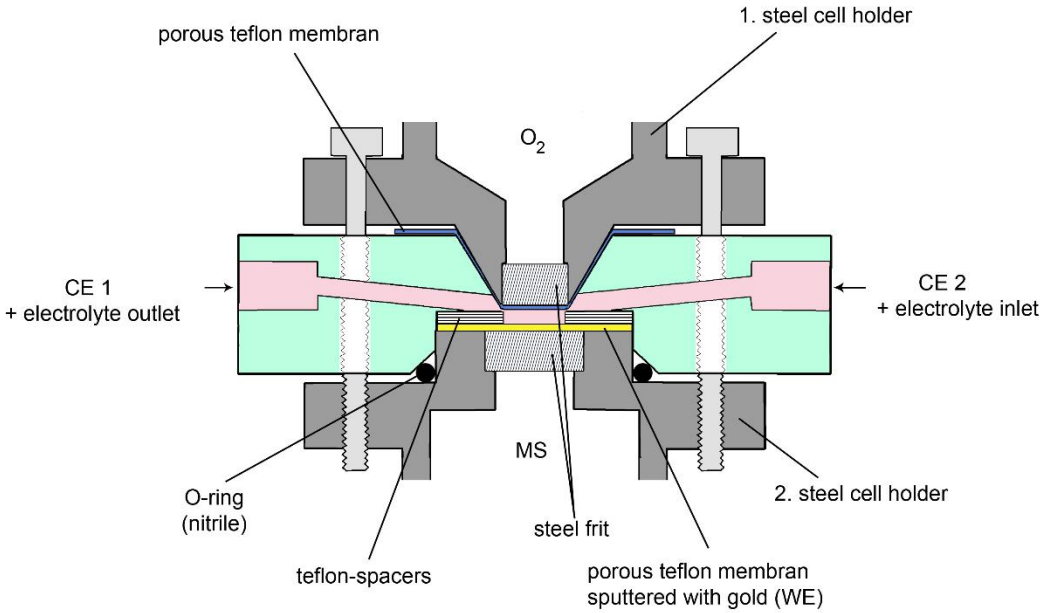

Figure S 6.11. Diagrammatic sketch of the DEMS-cell. The cell volume is confined via 4 PTFE-spacers with an inner diameter of 6 mm, porous Teflon-membrane resting a steel frit filled with O_2 and a gold-sputtered membrane resting on another steel frit which connects the cell to the vacuum of a mass spectrometer. The height of each spacer is 50 µm. Adapted from [122].

A diagrammatical sketch of the DEMS-set up adapted from Bawol [122] is shown in Figure S 6.11. The actual working compartment is defined by two steel frits covered with a Teflon membrane and four Teflon O-rings with an inner diameter of 6 mm and a thickness of 50 µm per O-ring, resulting in a total cell volume of 5.6 µL. The electrochemical reaction takes place on a porous Teflon-membrane sputtered with gold which separates the solution phase from the vacuum of the mass spectrometer. At the other end, the cell is sealed via another porous Teflon-membrane which is in contact with a steel holder filled with an adjustable amount of oxygen. Two counter electrodes and one reference electrode are connected to the working compartment via capillaries. Experimental details and performance tests will be given in a future publication [122].

7 Reversible Peroxide Formation in Presence of Potassium Ions

Philip Heinrich Reinsberg*, Andreas Koellisch Pawel Peter Bawol* and Helmut Baltruschat*

*Institut für Physikalische und Theoretische Chemie, Universität Bonn, Römerstraße 164, D-53117 Bonn, Germany

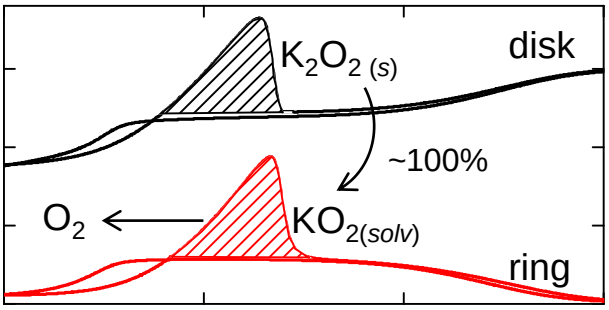

Received: October 12, 2018
Published online: January 25, 2019

Reprinted (adapted) with permission from the PCCP Owner Societies from
P. H. Reinsberg, A. Koellisch, P. P. Bawol and H. Baltruschat, *Physical Chemistry Chemical Physics*, **2019**, *21*, 4286–4294. DOI: 10.1039/C8CP06362A

Own manuscript contribution:

- design of the experiments
- supervision of the experiments
- interpretation of the results
- writing the manuscript

ACKNOWLEDGMENTS

The authors gratefully acknowledge financial support by the German Federal Ministry of Education via the LiBaLu-project in the framework of the "Vom Material zur Innovation"-initiative (03XP0029A). P. H. R. wishes to thank the German National Merit Foundation for a PhD-scholarship. The authors thank Dr. R. Weisbarth for help with the determination of the solubility of KO_2.

7.1 Abstract

Since the advent of the lithium–air battery, researchers have focused on understanding the underpinning mechanisms of the oxygen reduction and evolution reaction in aprotic solvents. In this work, the oxygen reaction in presence of potassium ions in dimethyl sulfoxide as exploited as a model system to refine the present mechanistic picture of the oxygen reduction in aprotic environments. In a combined approach utilizing differential electrochemical mass spectrometry in a generator-collector arrangement as well as classical electrochemical techniques, the reversible formation of insoluble peroxide as well as of slightly soluble superoxide is shown. Opposed to other peroxides in other non-aqueous metal–oxygen systems, potassium peroxide can be re-oxidized to superoxide with an overpotential as little as 100 mV. The investigation of the effect of the oxygen partial pressure between 0 and 1 atmosphere demonstrates how the precipitation of superoxide increases the oxidation overpotential of the peroxide and establishes a link between this work and other studies, in which the reversibility of the peroxide formation has not been identified.

7.2 Introduction

Secondary potassium–oxygen batteries have received much attention since the first report of a rechargeable potassium–oxygen battery based on superoxide as a product by Ren et al. [16,78,308-312]. The main advantage of the K–O_2 battery as compared to the even more popular Li–O_2 analogue is the significantly higher reversibility as well as the much lower oxidation-overpotential of the oxygen redox reaction[16,313]. As opposed to the oxygen reduction in the presence of Li^+, KO_2 has been identified as the main product of the ORR in dimethoxy ethane [16,309,314], diethylene glycol diethyl ether [310] and dimethyl sulfoxide (DMSO) [311,315]. Depending on the experimental conditions, such as the potential applied, a mixed process of superoxide and peroxide formation has been observed [61,311,315] similarly to the Na–O_2 system [238,316]. Despite that, mainly the superoxide has been investigated so far [311,315]. For instance, Wang *et al*. found a second reduction peak on glassy carbon via cyclic voltammetry, which they attributed to the formation of K_2O_2 [311]. Employing the rotating ring-disk electrode, the authors show that K_2O_2 cannot be oxidized at the ring electrode, possibly due to its insolubility. More recently, Sankarasubramanian and Ramani also observed the formation of K_2O_2 following the formation of KO_2 during the ORR in DMSO [315]. As opposed to Wang *et al*., who show two cathodic peaks but only one large anodic peak, the authors show two pairs of redox peaks, referring to the superoxide and peroxide formation and re-oxidation on glassy carbon [315]. Apart from using a different anion, the experimental conditions in both cases were similar, which gives rise to the question, why the observations are so different. Moreover, Sankarasubramanian et al. found indications for a surface confined follow-up reaction of KO_2, which the authors attribute to a surface-disproportionation at low overpotentials. However, the authors do not comment on the fate of the oxygen evolved during the disproportionation, which

should be readily reduced as it is produced close to the surface. As this would mean that ultimately two electrons are transferred per O_2 molecule, it is unclear how such a surface-disproportionation could be differentiated from a direct reduction step as observed in the presence of Li^+ [282] in a rotating ring-disk set up.

While previous work focused almost exclusively on the oxygen-potassium superoxide redox couple in several solvents, the reversibility of the peroxide formation is elucidated in this work. Moreover, the effect of the partial pressure of oxygen on the ORR is investigated and the importance of the limited solubility of potassium superoxide on the overall reaction is highlighted. Mechanistic investigations were carried out by differential electrochemical mass spectrometry (DEMS) in a specially designed generator-collector arrangement [120] and the use of rotating-ring disk electrodes (RRDE).

7.3 Experimental

7.3.1 Materials

Potassium perchlorate ($KClO_4$, EMSURE® ACS, *Merck*) was dried at 160 °C at reduced pressure (10^{-2} mbar) for two days. Dimethyl sulfoxide (DMSO, 99.7+ %, stored under molecular sieve, *Acros Organics*) was used as received. All electrolytes were prepared in a *GS* glovebox with a water content below 0.5 ppm. Silver nitrate ($AgNO_3$, ≥ 99 %, *ChemPure*) was used for preparation of the reference electrode, which was a silver wire immersed in 0.1 M $AgNO_3$ in DMSO. All electrolytes were purged either with a custom mixture of argon and oxygen (80:20, *Air Liquide*) or with other mixtures prepared from highly pure oxygen (99.9995%, Alphagaz 2, *Air Liquide*) and highly pure argon (99.9999%, Alphagaz 2, *Air Liquide*) using electrical flow meters (F-201C-UA-22-V, *Bronkhorst*, MFT-V12C *Union Carbide*). The flow meters have been calibrated for the specific gases.

The potential of the reference electrode was calibrated using decamethylferrocene ($Me_{10}Fc$, 97%, *Sigma Aldrich*) as solvent-independent redox system [317] in 0.1 M $KClO_4$ in DMSO. The resultant potential of the reference electrode is +0.340 V vs. $Me_{10}Fc^+|Me_{10}Fc$. The quality of $Me_{10}Fc$ as a solvent-independent redox system was confirmed by the nearly identical diffusion coefficients of the neutral and oxidized form in the working electrolyte ($D = 5.9 \times 10^{-6}$ cm^2s^{-1}). To alleviate comparison to other studies, it is helpful to reference the results also to the $K^+|K$ redox couple. Using the standard potential of the $K^+|K$ redox couple reported by Gritzner ($E^o(K^+|K) = -2.86$ vs. standard hydrogen) and the potential of the reference electrode employed in this work ($E^o(Ag^+|Ag) = 0.49$, $c(Ag^+) = 0.1$ M) a potential of $E(Ag^+|Ag) = 3.29$ V vs $K^+|K$ is obtained. This value is very close to the value of 3.39 V, which can be calculated from the potential of $K^+|K$ (3.4 V vs. $Ag^+|Ag$ in acetonitrile, $c(Ag^+)$ = 0.01 M) measured in diglyme as reported by Wang *et al*. [311]. However, the value of 3.29 V was used for conversion as this was determined from data in DMSO.

7.3.2 Cyclic Voltammetry and Rotating Ring-Disk Electrode

The cyclic voltammetry and rotating ring-disk electrode measurements have been conducted in a classical H-cell with a *Luggin* capillary. The counter electrode was a gold sheet. Electrical contact of the electrolyte to the silver reference electrode was established via the rough surface of a closed glass stopcock, which prevented contamination of the working electrolyte with the reference electrolyte (0.1 M $AgNO_3$ in DMSO). The typical electrolyte resistance as determined by electrochemical impedance spectroscopy was in the range of 3 Ω cm. A thin-gap electrode with a gold-ring and a gold-disk (AFE7R8AUAU, *Pine Research Instrumentation*) and a change-disk electrode with a gold-ring (E6R1AU, *Pine Research Instrumentation*) and a glassy carbon-disk were used as working electrodes. A schematic drawing of the RRDE is given in the Supporting Information. Gold as a ring material was chosen instead of platinum as DMSO is not expected to chemically adsorb on gold [318]. The thin-gap electrode has a theoretical collection efficiency of $N_0 = 0.22$ and the surface of the disk is $A = 0.164$ cm^2, while the change disk electrode has $N_0 = 0.25$ and $A = 0.196$ cm^2. All disk currents are referred to the geometrical surface of the disk electrode, while the ring currents are referred to the theoretical collection efficiency. The share of superoxide (x) can be calculated from the ring current I_R and the disk current I_D according to eq. (7.1) assuming that only superoxide and peroxide are formed as a product:

$$x = \frac{2 \cdot I_R}{\left| I_D / N_0 \right| + I_R} \tag{7.1}$$

In the RRDE and CV-measurements, a rather low concentration of 0.1 M $KClO_4$ was used for two reasons: The maximum achievable solubility of superoxide is expected to be higher at low concentrations of K^+ (see below), which helps separating the peroxide formation from the superoxide formation. Moreover, as the salt is the main source of water, even though it has been dried, a low salt concentration leads to a low amount of water in the electrolyte.

7.3.3 Differential Electrochemical Mass Spectrometry

A detailed description of the DEMS set-up can be accessed elsewhere [113,125] and a sketch of the cell is shown in the Supporting Information. In short, the flow-through cell used in this study consists of two thin-layers: an upper compartment, where the first working electrode (WE1) is situated and the electrolyte enters the cell and a lower compartment, which is connected to the vacuum of a mass spectrometer (MS) via a gold-sputtered porous Teflon-membrane, which serves as the second working electrode (WE2). By choosing appropriate potentials for both electrodes, the working electrodes can work in a generator-collector arrangement. For more details on the set up refer to the Supporting Information and see Bondue *et al.* [120]. The thickness of the two thin-layers is 200 µm each and the geometric area of the electrode confined by Teflon O-Rings is 0.28 cm^2. The concentration of $KClO_4$ in the DEMS-cell was 0.5 M $KClO_4$ to avoid an unfeasibly high iR-drop associated with the high

resistances in the thin-layer geometry. The effect of the K^+-concentration on the ORR in DMSO is subject of a soon appearing publication.

The flux of oxygen into the mass spectrometer can be calculated using an externally determined calibration constant K_1 using a reaction of known stoichiometry (here: the ORR in tetrabutylammonium perchlorate-containing DMSO):

$$\frac{dn}{dt} = \frac{I_I}{K_1 \cdot F} \tag{7.2}$$

The number of electrons per O_2 molecule transferred at WE1 (z_1) can subsequently be determined from the ratio of the faradaic current and the flux of oxygen [113]. In order to calculate the number of electrons transferred at WE2 (z_2), which serves as the collector electrode, a second calibration constant K_2 has to be determined, which is defined by eq. (7.3) [120]:

$$z_2 = \frac{I_{F,2}}{\Delta I_I} \cdot K_2 \tag{7.3}$$

In eq.(7.3), $I_{F,2}$ is the faradaic current measured at WE2 and ΔI_I is the difference of the ionic current in presence and absence of a reaction at WE2. In this case, WE2 was either kept at +0.3 V, where superoxide is quantitatively oxidized to oxygen, or at open circuit potential, where no reaction occurs. The latter was confirmed by exchanging the gold-sputtered membrane for a pristine membrane and comparing the MS signals. Once K_2 is known, the number of electrons at WE2 can be calculated. Moreover, it is possible to calculate the share of intermediates formed at WE1 from the currents measured at WE1 and WE2 similar to the RRDE.

7.4 Results and Discussion

7.4.1 Reversibility of the Peroxide Formation

A sophisticated way to investigate the ORR is to utilize differential electrochemical mass spectrometry, which yields insights into the true reversibility as well as product distribution of the reaction. As the formation of soluble KO_2 is expected, a dual thin-layer flow-through cell working in a generator-detector arrangement[120] has been employed to study the processes. The results are shown in Figure 7.1, where the Faradaic currents at the generator electrode (WE1, gold) are shown in Figure 7.1 a and the currents at the detector electrode (WE2, gold) for a potential of 0.3 V(black) and at OCP (red, dotted) are displayed in Figure 7.1 b. Note that WE2 is a gold-sputtered, porous PTFE-membrane, which allows for the evaporation of volatile species into the vacuum of the MS. The baseline-corrected flux of oxygen into the MS is shown in Figure 7.1 c, where a negative flux represents a consumption of oxygen. First of all, we shall discuss the results if WE2 is at OCP (red, dotted line). As shown in Figure 7.1 a and c, the ORR starts at −0.9 V and reaches a plateau starting at −1.3 V. The number of electrons transferred per oxygen molecule (z) in this potential window is close to one which indicates the formation of superoxide (Figure 7.1 d, the initially higher z-value is an artefact resulting from the delay-correction between faradaic and ionic current[113,120,125]). From a potential of −1.55 V on, the currents at WE2 further decrease and the *z*-value increases, implying the formation of peroxides. In the anodic sweep, a narrow oxidation peak is observed starting at −1.5 V (Figure 7.1 a, peak a2), which is tentatively attributed to the highly reversible re-oxidation of insoluble peroxide (soluble species would be swept out of the cell due to the electrolyte flow). It is noteworthy that in the case of lithium the re-oxidation peak for the peroxide is shifted by 600 mV relative to its formation potential[139] and that the overpotential in battery-environments has been reported to be as large as 1.2 V [273]. A second anodic peak is found at −0.7 V and is ascribed to the oxidation of partially insoluble superoxide (due to the broadness of the peak, the oxygen evolution related to that peak can best be visualized on a time-axis, Figure S1). The difference between the electron number in the cathodic and anodic sweep is mainly related to the re-oxidation of the insoluble peroxide: While in the cathodic sweep, the whole faradaic current is due to the reduction of oxygen (either to superoxide or to peroxide), in the anodic sweep also the oxidation of the previously deposited peroxide contributes to the current. As the anodic current conventionally has a positive sign, the resulting current is less negative as compared to the ORR in absence of the oxidation process. However, the re-oxidation of the peroxide apparently (as will be discussed below) does not directly lead to the formation of oxygen and thus, the oxygen consumption in the anodic sweep is similar to the oxygen consumption in the cathodic sweep. Overall, the faradaic current in the anodic sweep is less negative than in the cathodic sweep, but the oxygen consumption is similar, which results in smaller, apparent electron numbers.

To gain further insights and to prove the hypotheses stated above, the situation for the case that a potential of 0.3 V is applied to WE2 will be discussed now (black lines). Parallel to the plateau ranging from −1.3 V to −1.55V, anodic currents are observed at WE2 (Figure 7.1 b) indicating the re-oxidation of soluble superoxide. From the comparison of the oxygen consumption for E(WE2) = 0.3 V and E(WE2) = OCP in Figure 7.1 c it is obvious that less oxygen is consumed if a potential is applied to WE2. This unambiguously shows that the reduced, soluble oxygen species can indeed be re-oxidized leading to the evolution of oxygen at the interface between vacuum of the mass spectrometer and the electrolyte (it should be noted that due to the efficiency of the cell, which is below unity, no complete reoxidation of the superoxide occurs). The number of electrons transferred at WE2 is calculated from the faradaic current at WE2 and the difference in the oxygen flux when WE2 is at OCP or WE2 is a 0.3 V according to eq. (7.3). The fact that this electron number is unity shows that it is indeed the superoxide, which is re-oxidized (Figure 7.1e).

Interestingly, for potentials below −1.5 V at WE1, the current at WE2 decreases (Figure 7.1 b) and the oxygen consumption in presence of an oxidizing potential at WE2 approaches the oxygen consumption for WE2 at OCP (Figure 7.1 c). This means that no O_2 is evolved at WE2 anymore. Together with the aforementioned increasing number of electrons at WE1, this is an indicator for the formation of insoluble K_2O_2 at WE1. Furthermore, in the anodic scan, the peak a2 at WE1 is accompanied by a corresponding peak at WE2 (Figure 7.1 b), which is also reflected in the oxygen signal (Figure 7.1 c). This directly shows that insoluble K_2O_2, which is formed for potential below −1.55 V, is re-oxidized at WE1 in the anodic scan, yielding superoxide, which is subsequently oxidized to oxygen at the second working electrode. As opposed to the electron numbers at WE1 (Figure 7.1 d), the electron numbers in the cathodic and anodic sweep at WE2 are very similar. This is because the situation at WE2 is very different from the situation at WE1: At WE2, only soluble, superoxide species are present, which are subsequently oxidized to O_2. While in the anodic sweep at WE1, insoluble peroxide is oxidized to superoxide (which does not generate a signal in the MS) and is transported to WE2, the oxidation of this superoxide at WE 2 leads to the formation of O_2, which can be detected in the MS. Therefore, the peak in the faradaic current at WE2 resulting from the oxidation peak a2 at WE1 is accompanied by a peak in the MS signal and thus, the electron number remains one.

Rationalizing the results shown above, the following reaction equation is designated to the redox processes c1 and a1:

$$K^+ + O_2 + e^- \rightleftharpoons KO_2(solv) \tag{7.4}$$

Equation (7.4) takes into account that the superoxide is partially soluble depending on the concentration of the conducting salt as well as the concentration of oxygen. The second redox process c2 and a2 is symbolized by eq. (7.5):

$$2K^+ + O_2^- + e^- \rightleftharpoons K_2O_2(s) \qquad (7.5)$$

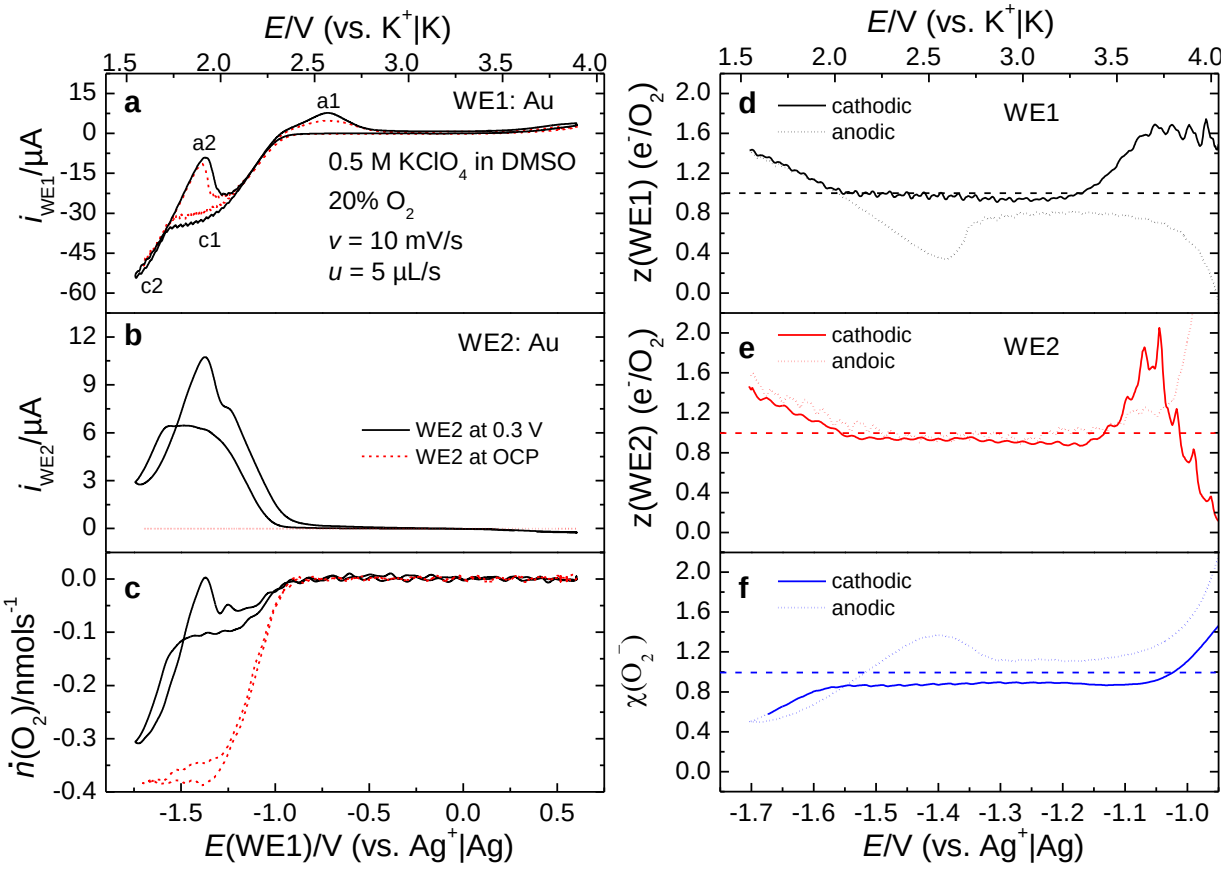

Figure 7.1. DEMS-measurements employing a 6-electrode dual thin-layer flow cell. The two working electrodes work in a generator-collector arrangement. **a**. Faradaic currents at the generator electrode (WE1). c1 and c2 denote two different cathodic processes, formation of superoxide and peroxide. The corresponding peaks a1 and a2 indicate the reoxidation of insoluble superoxide and peroxide. **b.** Faradaic currents at the collector electrode (WE2) for a potential of *E*(WE2) = 0.3 V (solid, black) and at open circuit potential (red, dotted). **c**. Corresponding flux of oxygen (baseline-corrected) for different potentials applied to WE2 (note that the oxygen consumption does not drop to zero if a potential is applied to WE2 because of the non-unity transfer efficiency). **d**. Number of electrons per O_2 at WE1 during cathodic (solid) and anodic sweep (dotted). **e**. Number of electrons per O_2 at WE2 for a potential of *E*(WE2) = 0.3 V. **f.** Share of superoxide $\chi(O_2^-)$ according to the faradaic currents at WE1 and WE2 and a potential of *E*(WE2) = 0.3 V. The potential on a scale vs $K^+|K$ is given at the top x-axis.

Finally, the share of superoxide $\chi(O_2^-)$ (Figure 7.1 f), calculated in analogy to RRDE measurements, substantiates the previously discussed findings and shows an average share of superoxide close to unity, leaving no doubts about the reversibility of the ORR in DMSO in the presence of K^+. No indication of a nucleation hindrance of the process could be identified by chronoamperometry (Figure S 7.2) before the transition to the peroxide formation.

7.4.2 Concentration and Diffusion Coefficient of Electrochemically Generated Superoxide

As indicated above, KO_2 is only slightly soluble in DMSO which has certain mechanistic and practical implications: For instance, the overpotential for reoxidation of solid KO_2 particles is expected to be higher as compared to dissolved KO_2 because KO_2 is a poor conductor [312,319,320]. Moreover, pore clogging might be avoided by influencing the precipitation behaviour of KO_2. Thus, in this section and the following section, we will elucidate the role of the superoxide solubility. Via the application of inductively-coupled plasma optical emission spectroscopy the saturation concentration of KO_2 in pure DMSO at 25°C has been determined as 6.77 mM (see section 7.6.3). As KO_2 is a 1:1-electrolyte, this means that the solubility product K_L is 45.8x10^{-6} mol^{2}L^{-2} ($K_L = c_{eq}(K^+)$x $c_{eq}(O_2^-)$). Aside from the solubility product, only the concentration of potassium ions in solution is necessary to calculate the maximum allowable concentration of superoxide ($c_{eq}(O_2^-)$). The concentration of K^+ in the electrolyte is typically in the range of 100 mM to 500 mM (and might be significantly higher in battery-related environments), which leads to a maximum achievable concentration of superoxide of 0.09 mM (500 mM $KClO_4$) or 0.46 mM (100 mM $KClO_4$).

In a usual cyclic voltammetry or RRDE-experiment, it is assumed that the flux of electroactive reactants is balanced by the flux of the products according to Fick's first law of diffusion. This equality in the case of pure diffusion-limitation is shown in eq. (7.6), where $c_{x=0}(O_2^-)$ indicates concentration of superoxide at the electrode surface, $c_0(O_2)$ is the bulk concentration of oxygen, D is the diffusion coefficient of the respective species and y is a constant, which depends on the hydrodynamic conditions of the experiment (y = ½ for a CV experiment, y = 2/3 at the RRDE; for a comparison and a derivation of the equation refer to the section 7.6.7) [96]:

$$c_{x=0}(O_2^-) = c_0(O_2) \cdot \left(\frac{D(O_2)}{D(O_2^-)} \right)^y \qquad (7.6)$$

While usually the assumption is made that the diffusivity of the reactant and product is equal, it is not expected to be true in this case: Differences between the diffusivity of oxygen and superoxide up to a factor of 10 have been reported in DMSO-based electrolytes and a significant dependence of the diffusivity of superoxide on the conducting salt has been identified [321,322]. Thus, it is necessary to determine the diffusion coefficients in presence of K^+, which can conveniently be done performing potentials steps at the RRDE. While the potential of the ring is kept at a constant value, where the oxidation of superoxide proceeds without kinetic limitations (in this case: E(Ring) = 0.3 V), the potential of the disk electrode is suddenly stepped from a potential where no reaction occurs (−0.75 V for 20 s) to a potential where superoxide is formed (−1.10 V for 45 s). Consequently, the superoxide produced at the disk will diffuse towards the ring and will lead to an increase of the ring current. From the time delay

between disk and ring (t_s), the diffusion coefficient of superoxide can be evaluated according to eq. (7.7) [111]:

$$t_s = 4.51\left[\log\left(\frac{r_2}{r_1}\right)\right]^{2/3} \cdot \left(\frac{\nu}{D(O_2^-)}\right)^{1/3} \cdot \omega^{-1} \qquad (7.7)$$

In eq. (7.7), r_2 is the inner radius of the ring electrode, r_1 is the radius of the disk, ν is the kinematic viscosity, $D(O_2^-)$ is the diffusion coefficient of superoxide and ω is the angular frequency in s^{-1}. To avoid accumulation of insoluble species, the disk potential was stepped to 0.3 V for 20 s after each step to -1.1 V to dissolve eventually precipitated K_2O_2 or KO_2. The step program as well as the normalized disk and ring currents are shown Figure 7.2 a and b. The determination of t_s is elucidated in Figure 7.2 c and d. The dashed line represents a tangent of the turning point of the ring transient and the intercept of the time-axis with the tangent gives the value for t_s at a specific rotation rate. As a last point, a plot of the rotation-dependent transition time t_s is shown in Figure 7.3. From the slope of the plot and the kinematic viscosity of pure DMSO at 25°C (ν = 0.0186 cm^2s^{-1} [220]) a diffusion coefficient of $D(O_2^-)$ = 2.13 x 10^{-6} cm^2s^{-1} is calculated. This diffusion coefficient is similar to the diffusion coefficient of superoxide in the presence of 0.1 M $TBAClO_4$ in DMSO ($D(O_2^-)$ = 4.68 x 10^{-6} cm^2s^{-1})[321] or 0.1 M LiTFSI in DMSO ($D(O_2^-)$ = 2.06 x 10^{-6} cm^2s^{-1})[322].

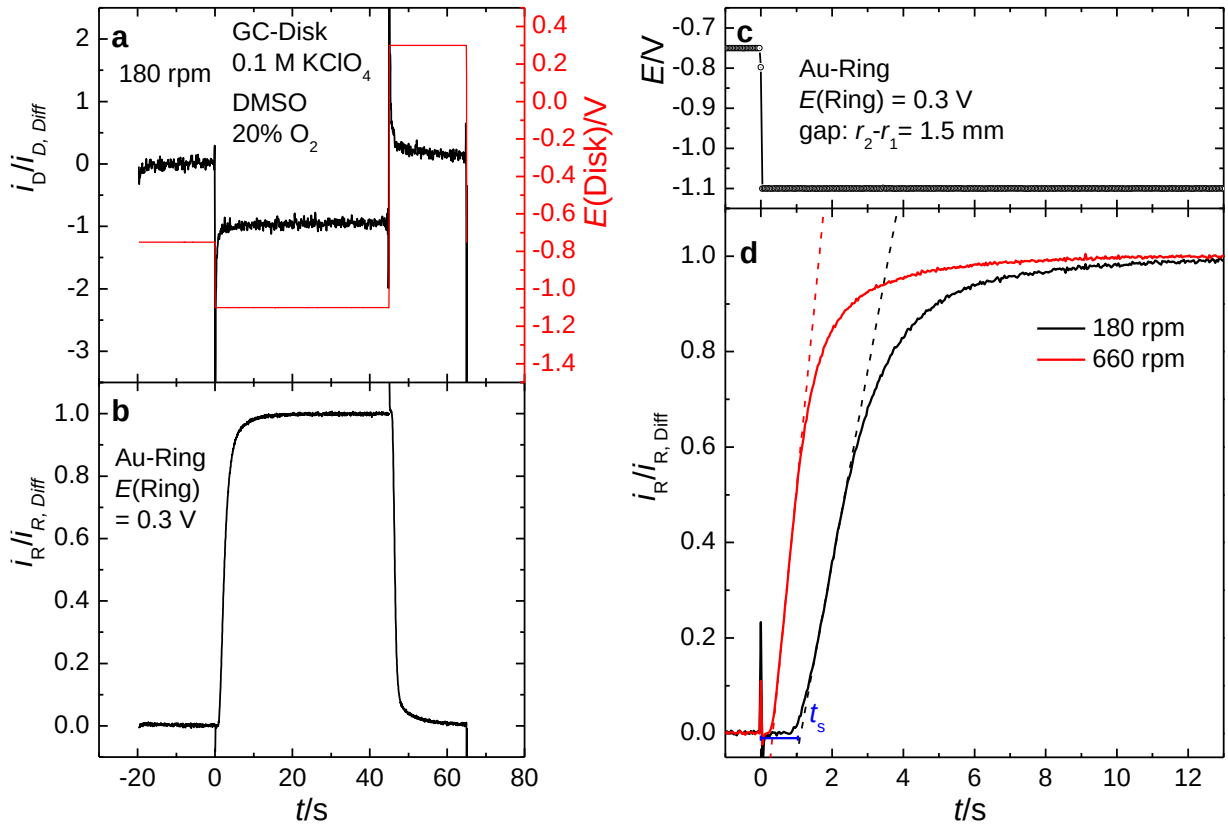

Figure 7.2. Transients at a glassy carbon disk- and gold ring-electrode. **a.** Disk currents normalized to the constant current in the plateau and the potential applied to the disk (red). **b**. Ring currents normalized to the constant current in the plateau. **c**. Magnification of the potential programme. **d**. Normalized ring

transients for a rotation rate of 180 rpm (black) and 660 rpm (red). Electrolyte: 0.1 M $KClO_4$ in DMSO saturated with 20% O_2.

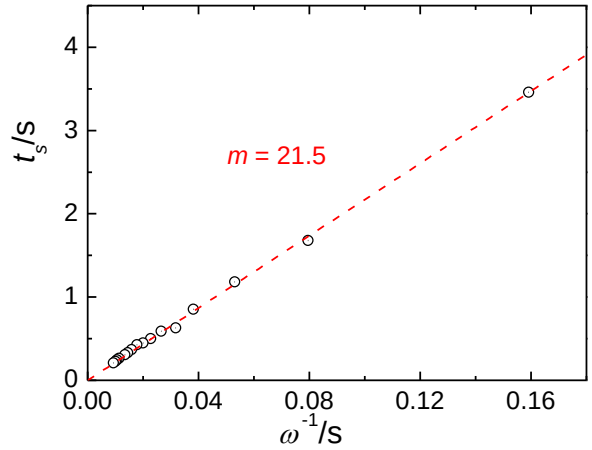

Figure 7.3. Determination of the diffusion coefficient of superoxide.

Inserting the diffusion coefficient of oxygen ($D(O_2) = 24.1 \times 10^{-6}$ cm²s^{-1}) [323] and superoxide ($D(O_2^-) = 2.13 \times 10^{-6}$ cm^{2}s^{-1}) as well as the bulk concentration of oxygen ($c_0(O_2) = 2.03$ mM) at 1 atm[323] into eq. (7.6), a hypothetical concentration of 6.8 mM of superoxide is obtained in a typical CV experiment. In the RRDE experiment, the concentration of superoxide even reaches a value of 10 mM due to the different hydrodynamic conditions as stated above and summarized in section 7.6.7.

7.4.3 Influence of the Oxygen Pressure on the ORR/OER

As shown above, the concentration of superoxide very much depends on the bulk concentration of oxygen. Therefore, the influence of the oxygen concentration on the ORR in a pressure region from 0.2 atm to 1 atm was investigated. The CVs recorded under stagnant conditions at gold and glassy carbon are shown in Figure 7.4. The lower potential limit was adjusted slightly negative of the peak potential c2 to avoid accumulation of K_2O_2, which might affect subsequent cycles due to the formation of minor amounts of side products. As expected, the peak currents increase with increasing oxygen pressure (Figure 7.4 a and b). Moreover, the peak c2 shifts to less negative potentials upon increasing the oxygen concentration. This shift with partial pressure can be understood by the more efficient deactivation of the electrode due to a higher, absolute charge passed into the formation of K_2O_2. Moreover, this shift implies that the peak c2 actually is not due to diffusion-limitation but rather due to surface deactivation.

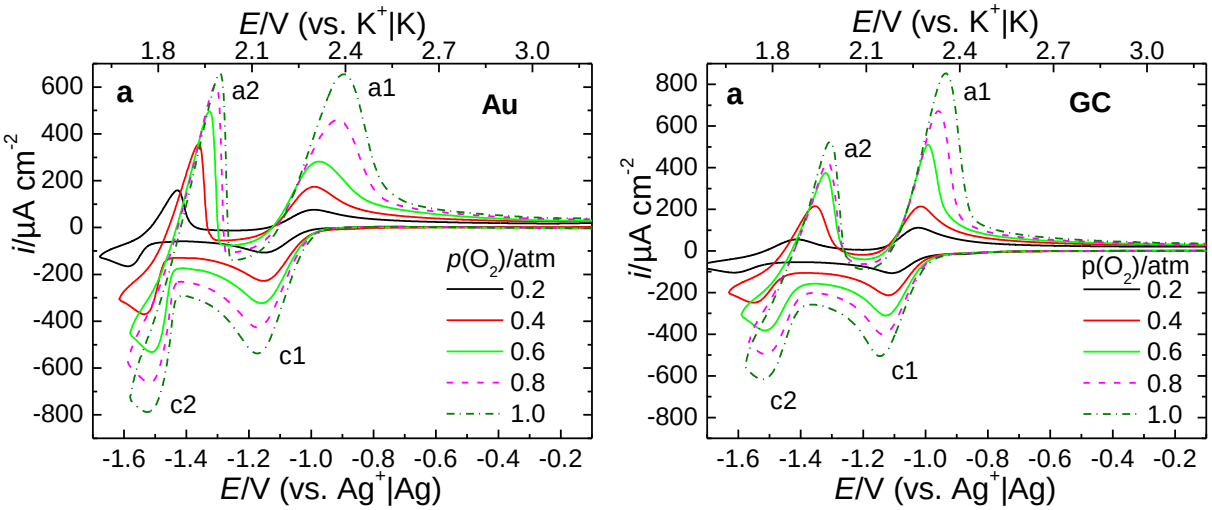

Figure 7.4. Cyclic voltammetry at gold for different oxygen saturations. **a.** Cyclic voltammograms for a fixed sweep rate of 50 mV s^{-1} at gold. **b**. Corresponding CVs at glassy carbon. Electrolyte: 0.1 M $KClO_4$ in DMSO. c1 and c2 denote the formation of superoxide and of peroxide. The corresponding peaks a1 and a2 indicate the reoxidation of superoxide and peroxide.

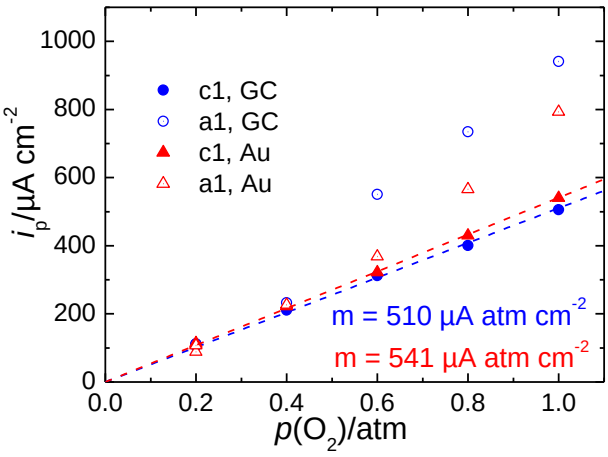

Figure 7.5. Dependence of the peak current on the partial pressure of O_2. Sweep rate of 50 mV s^{-1}.

However, the oxygen concentration also affects the superoxide formation in a non-expected way: As shown in Figure 7.5, the anodic peak a1 starts to exceed c1 for an oxygen saturation above 60%. Whilst the slope for c1 is close to the theoretically expected 598 µA atm^{-1} cm^{-2} for a sweep rate of 50 mV s^{-1} (calculated from the oxygen solubility c derived from Henry's law and diffusivity D according to the Randles-Sevcik equation, $i_{peak} = 0.4463\, z^{3/2}F^{3/2}R^{-1/2}T^{-1/2}v^{1/2}\, c\, D^{1/2}$, with v as the sweep rate), the average slope for a1 is significantly larger. It is intriguing to note that the transition from the "normal" behaviour of a1 to significantly increased values occurs at an oxygen saturation of 60%, at which the superoxide concentration at the electrode surface equals 4 mM (60% of 6.8 mM, according to eq. (7.6), see above). However, considering that the solubility of KO_2 product is only 45.8x10^{-6} mol^2L^{-2} and that the electrolyte contains 0.1 M $KClO_4$ the expected equilibrium concentration of superoxide is only 0.46 mM. This means that a pronounced precipitation only occurs in significantly supersaturated solutions (the concentration of superoxide apparently can be up to 9-times larger than the saturation

concentration before precipitation occurs). Due to the precipitation of superoxide the peak a1 is not solely-diffusion limited anymore. Therefore, KO_2 can accumulate on the surface and add up to the oxidative currents in a1. Using electrolytes with higher K^+-concentrations aggravates the situation and leads to more pronounced deposition of superoxide, which is reflected by the DEMS measurements in Figure 7.1, where superoxide already precipitates at an oxygen saturation of 20%.

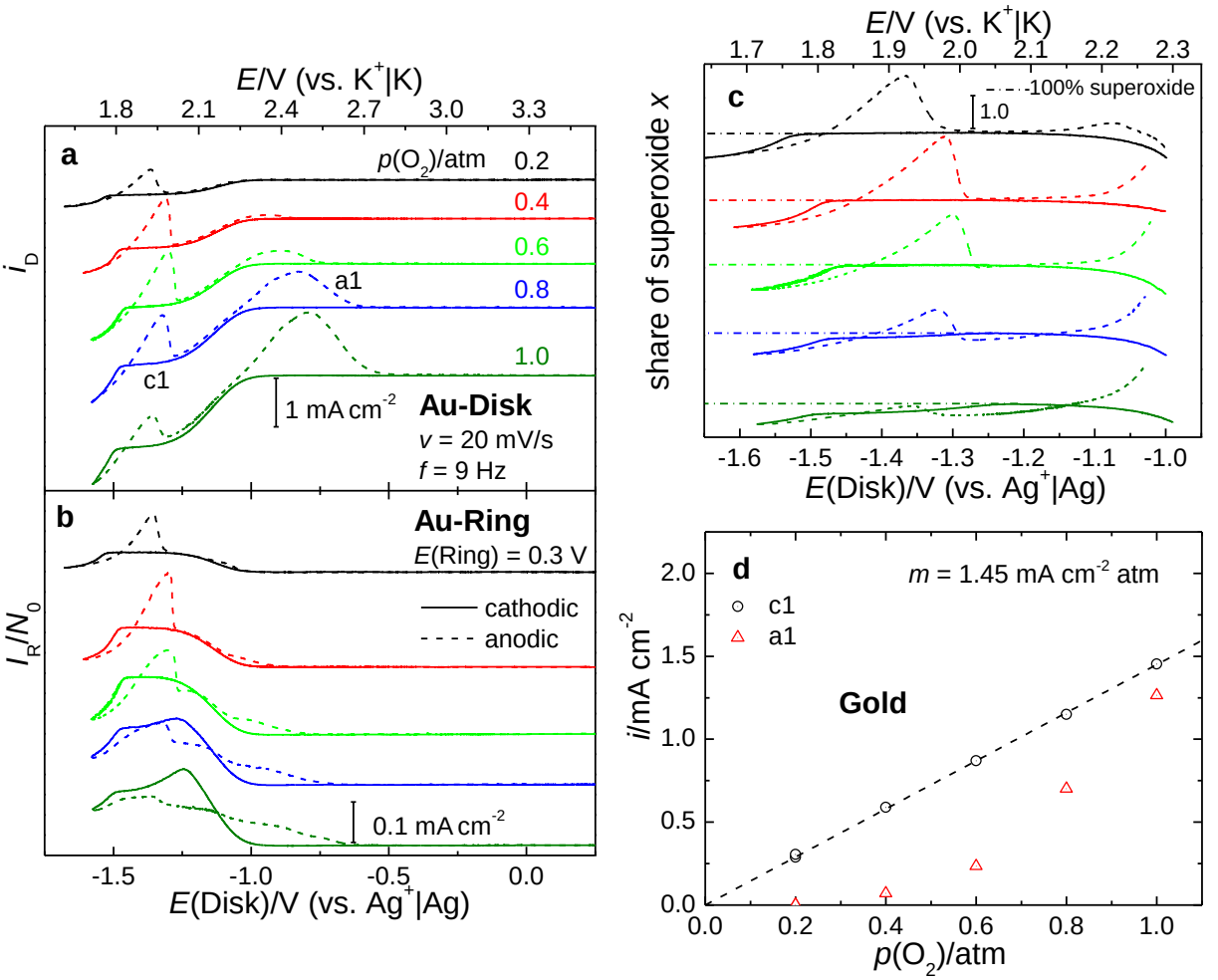

Figure 7.6. CVs at an Au-disk/Au-ring electrode for different O_2 saturations. **a.** Disk currents for a fixed rotation rate of 9 Hz and a sweep rate of 20 mV s^{-1}. **b**. Corresponding ring currents. The dashed lines represent the anodic sweep direction. **c**. Share of superoxide. The dashed lines represent the anodic sweep, while the dashed-dotted line corresponds to a share of superoxide of 100%. **d**. Plot of the diffusion limited current (c1, black circles) and the peak current (a1, red triangles) vs the oxygen pressure. Electrolyte: 0.1 M $KClO_4$ in DMSO.

The partial insolubility of KO_2 can be also observed in RRDE experiments (Figure 7.6 for gold and Figure 7.7 for glassy carbon). As can be seen in Figure 7.6 a (red, dotted-line), a broad re-oxidation peak with its maximum at −1.0 V starts to appear at an oxygen saturation of 40% of the atmospheric pressure. It is very interesting to note that the expected superoxide concentration at 40% O_2 saturation is again 4 mM due to the different scaling of the diffusion coefficients as compared to the CV without rotation (y = 2/3 with rotation vs. y = ½ without rotation in eq. 6). The accordance of these transitions under different conditions is a very

distinct indicator that the transition is indeed related to precipitation of superoxide. Furthermore, the partial solubility of superoxide shows up in the diffusion-limited plateau in the ring-currents for 80% and 100% O_2 (Figure 7.6 b), which decrease in the cathodic sweep although the currents at the disk remain constant. This behaviour is also reflected by the share of superoxide (Figure 7.6 c) which significantly decreases at higher oxygen concentrations. However, the ring currents also indicate that at a potential of −1.0 V soluble superoxide is generated, which originates probably from either the partial oxidation of K_2O_2 or detachment of superoxide particles associated with its oxidation.

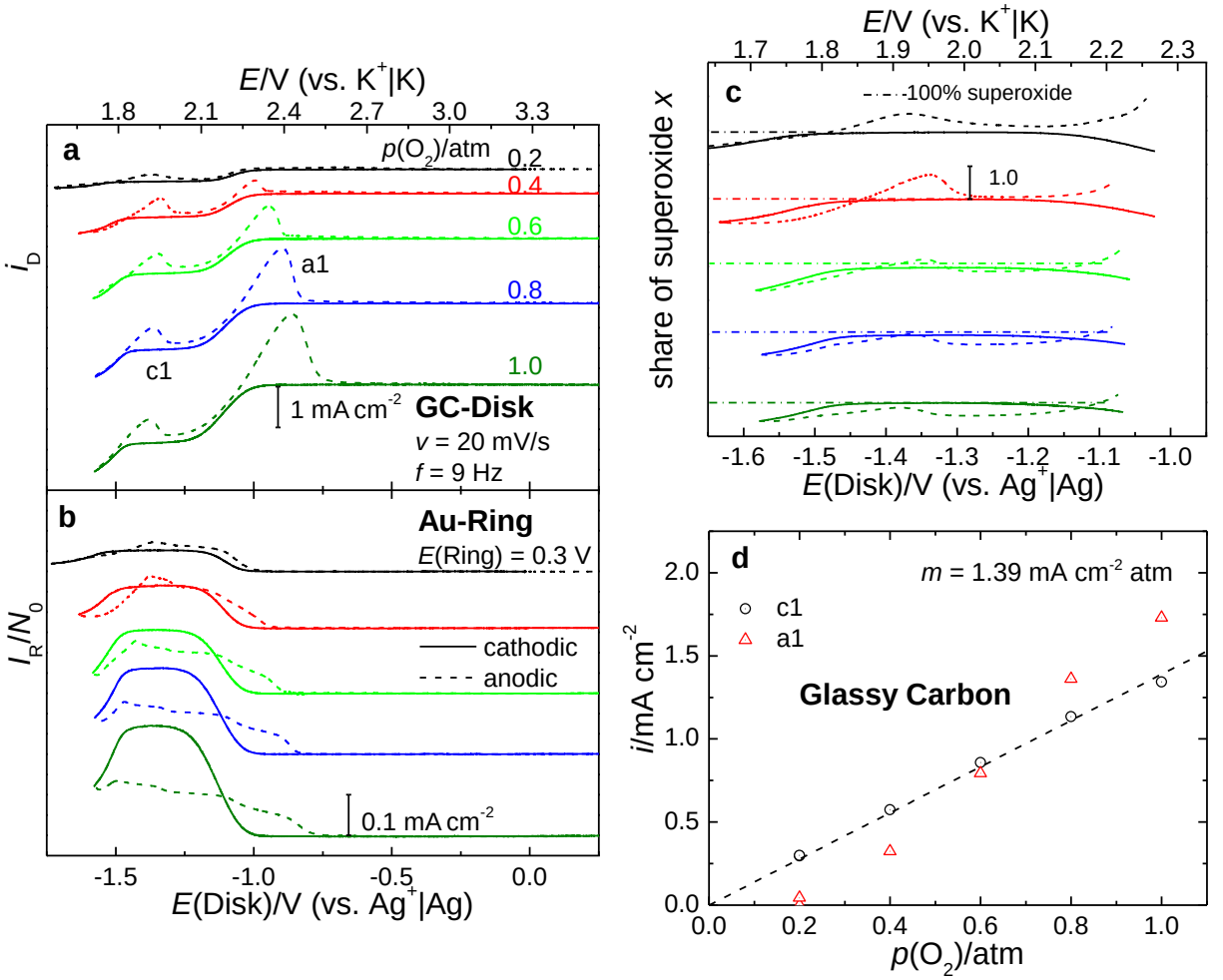

Figure 7.7. CVs at glassy carbon for different oxygen saturations. **a.** Disk currents at a fixed rotation rate of 9 Hz and a sweep rate of 20 mV s^{-1}. **b**. Corresponding ring currents. The dashed lines represent the anodic sweep direction. **c.** Share of superoxide. The dashed lines represent the anodic sweep, while the dashed-dotted line corresponds to a share of superoxide of 100% **d.** Plot of the diffusion limited current (c1, black circles) and the peak current (a1, red triangles) vs the oxygen pressure. Electrolyte: 0.1 M $KClO_4$ in DMSOs.

Overall, the ratio between the charge passed at the disk and detected at the ring electrode is independent of the oxygen concentration and close to 95%. This implies that the main effect of the increased O_2-concentration is a shift of the product distribution from soluble superoxide to insoluble KO_2 and K_2O_2, which can only be oxidized in the anodic sweep. The dependence of the peak current a1 on the O_2-pressure shows a non-linear behaviour owing to the limited

solubility of the superoxide (Figure 7.6 d), while the slope of the diffusion-limited currents at −1.3 V with O_2 concentration (Figure 7.6 d) is in very close agreement with the theoretical one (1.46 mA cm^{-2}atm as calculated from the Levich-Koutecký equation). This effect is also present at the glassy carbon electrode, where the peak current a1 even exceeds the diffusion-limited current (Figure 7.7 c).

As shown above, higher O_2 pressures shift the product distribution towards insoluble KO_2 and K_2O_2 and apparently make the peroxide formation less reversible. This might be attributed to the co-deposition of KO_2, which generally has a more positive redox potential than K_2O_2. Moreover, the reversibility of the oxygen-superoxide couple is not greatly affected by the O_2 partial pressure (note that the reversibility is indicated by the onset of a1 rather than its peak position, which is related to the absolute amount of deposited KO_2). However, the fact that the peroxide reoxidation is shifted to more positive potentials with an increasing amount of KO_2 deposited on the surface helps to understand the differences to the works of other authors, who either use higher O_2 pressures, higher salt concentrations or work with cells of a significantly lower ratio between electrolyte volume and electrode surface. In all the aforementioned cases, the precipitation of KO_2 is more likely and thus, the reoxidation of the peroxide is shifted to more positive potentials, eventually merging with the superoxide reoxidation peak. Apart from helping to understand the different observations for different electrolyte compositions and cell geometries, the partial pressure might be used in a real battery cell with a porous gas-diffusion electrode to influence the position, where KO_2 precipitates in the cell and thus, to avoid pore clogging.

7.5 Conclusions

The oxygen reduction and evolution in $KClO_4$-containing DMSO has been investigated in detail employing a combined approach differential electrochemical mass spectrometry as well as classical electrochemical methods. The main outcomes are summarized as follows:

1) Oxygen is initially reduced to soluble superoxide, which can be quantitatively re-oxidized to oxygen.
2) Superoxide can be reduced to solid K_2O_2 in a second reduction step. Despite its solid nature, K_2O_2 undergoes facile reoxidation with a small overpotential of 100 mV.
3) The limited solubility of superoxide (7 mM) leads to the precipitation of solid KO_2 at high partial pressures of oxygen and is a key factor regarding the reversibility of the peroxide formation. The solubility of superoxide is of utmost importance when comparing the electrochemical responses under different conditions.

Overall, the K–O_2 system is a promising model system for future non-aqueous metal–oxygen and could help answering open questions regarding the general mechanism of the ORR/OER in non-aqueous solvent.

7.6 Supporting Information

7.6.1 Visualization of the Peroxide Oxidation in the Six-Electrode Flow-Through Cell

To visualize the oxidation of the peroxide at a potential of around −1.0 V, two subsequent cycles of the ORR in the dual thin-layer six electrode cell are shown in Figure S 7.1 on a time-scale. The dashed red line in Figure S 7.1 c serves as a guide to the eye and designates to baseline of the experiment.

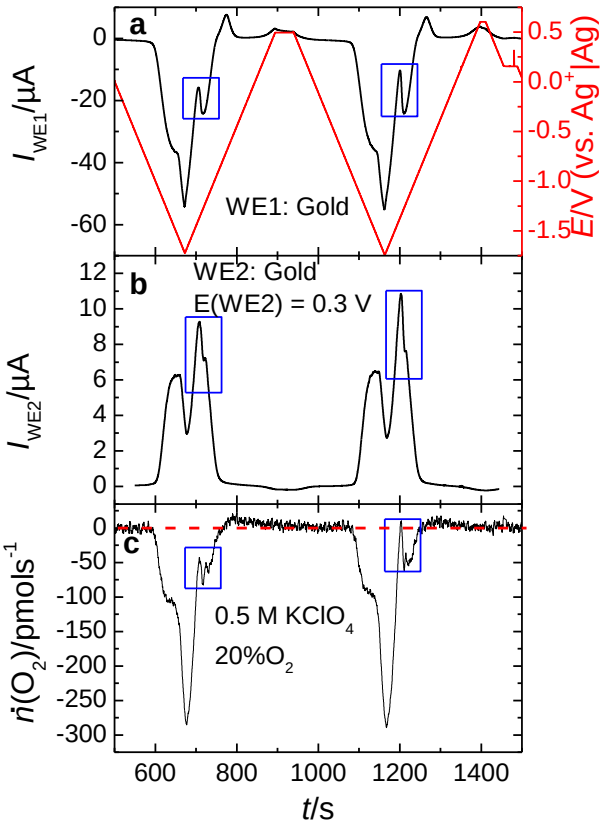

Figure S 7.1. DEMS-measurements employing a dual thin-layer flow cell with two gold working electrodes in a generator-collector arrangement. **a**. Faradaic currents at the generator electrode (WE1) and potentials applied to WE1. **b.** Faradaic currents at the collector electrode (WE2) for a potential of E(WE2) = 0.3 V. **c**. Corresponding flux of oxygen (baseline-corrected). Electrolyte: 0.5 M $KClO_4$ saturated with 20% O_2. Flow rate 5 µL s^{-1}, sweep rate 10 mV s^{-1}. The blue rectangles indicate the oxidation of the peroxide to superoxide and its subsequent oxidation to oxygen at the ring as well as the MS-signal corresponding to this O_2 evolution.

7.6.2 Chronoamperometry in the Flow-Through Cell

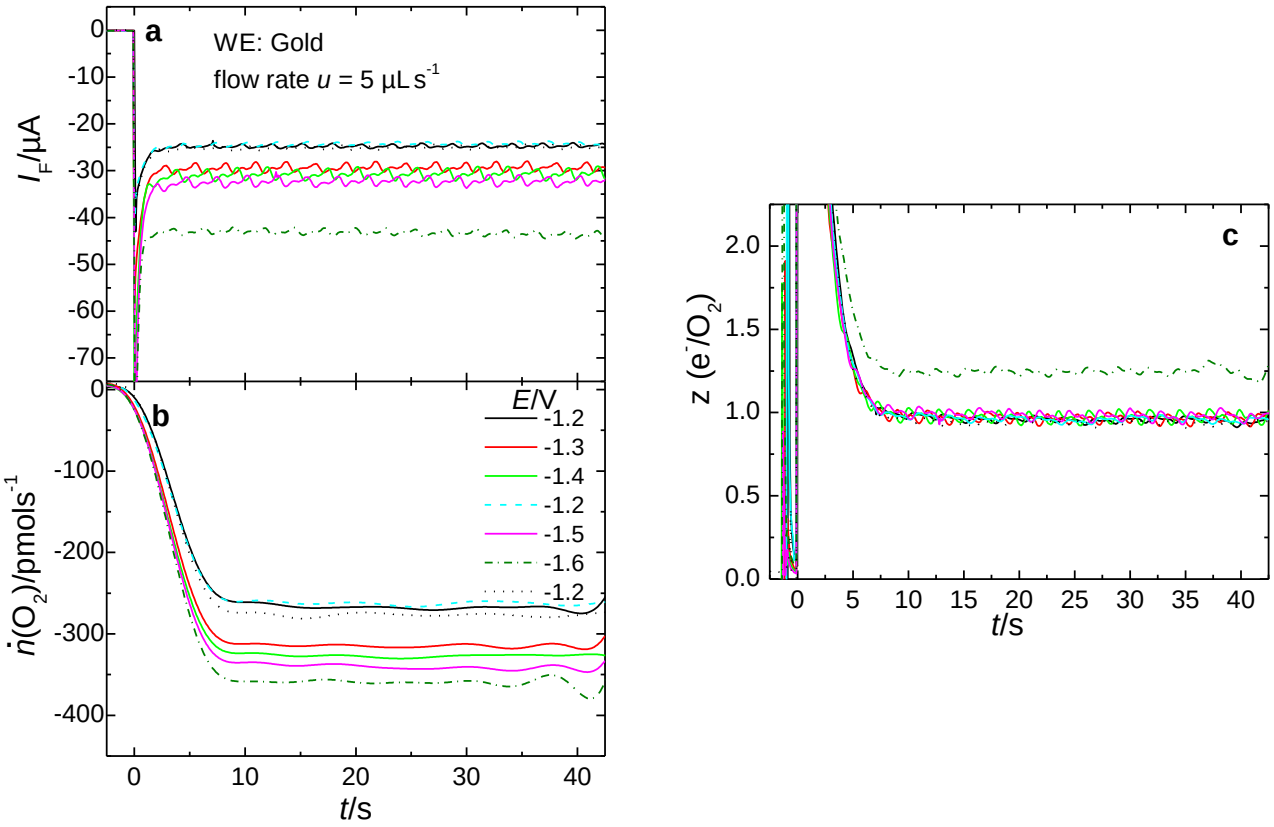

Figure S 7.2. Potential step experiments in a dual thin-layer flow through cell at a gold electrode. **a**. Faradaic currents at the gold electrode. **b**. Corresponding (baseline-corrected) oxygen signal. **c**. Number of electrons transferred per O_2 molecule. Note that the rhythmic noise is due to the peristaltic pump used to maintain electrolyte flow.

From the transients shown Figure S 7.2 no nucleation behaviour is evident, neither for the superoxide nor for the peroxide. Even at a potential of −1.5 V still only one electron is transferred under these experimental conditions.

7.6.3 Determination of the Saturation Concentration of Potassium Superoxide

To determine the saturation concentration of KO_2 in DMSO, two different stock solutions have been prepared. Each solution was produced by adding excess KO_2 to DMSO in an Ar-filled glovebox (*GS Glovebox*) to yield a saturated solution in equilibrium with solid KO_2. Solution *A* was stirred for 1 day at the glovebox temperature (typically 25–27°C) and solution *B* was stirred for 1 day at 40 °C. Each solution was left without stirring for half a day to ensure that the solid particles in the solution precipitate. After that, a fraction of the clear solution was extracted using a syringe with a syringe filter (0.2 µm). To investigate a possible time-effect (due to reaction with trace-amounts of water) on the concentration, solution *B* was stirred for additional 3 days after the extraction and subsequently, an additional fraction was extracted (solution *C*)

The actual determination of the saturation concentration of KO_2 in DMSO was conducted via inductively coupled plasma optical emission spectroscopy (ICP-OES, *PerkinElmer Optima* 8300). Calibration of the instrument was achieved using a multi cation standard (*Merck Certipur* IV, 1000 mg L^{-1}) in four different dilutions (100 µg L^{-1}, 250 µg L^{-1}, 500 µg L^{-1}, 1000 µg L^{-1}) using the K-line at 766 nm (axial detection). The stock solutions *A*–*C* were diluted by a factor of 1000 and 500 to ensure that the measured intensities were within the range of the calibration curve. From the intensities, the saturation concentrations have been calculated (Table S 7.1).

Table S 7.1. Saturation Concentration of K–O_2 in DMSO[a]

	c(O_2^-)(1:1000)/mM	**Δc/c in %**	**c(O_2^-)(1:500)/mM**	**Δc/c in %**
Solution A	6.34	0.21	6.96	0.16
Solution B	6.87	0.08	6.84	0.18
Solution C	6.89	0.13	6.89	0.14

[a]The saturation concentration has been calculated from the dilution factor. Δc/c represents the relative standard deviation of a series of 6 (1:1000) or 3 (1:500) measurements.

The uncertainty of the values (Δc/c) are given in terms of the relative standard deviation of 6 (1:1000) or 3 (1:500) repeated measurements. As can be seen from Table S 7.1, the saturation concentrations for solutions A–C agree well which each other. No pronounced time- or temperature effect can be observed. From the different measurements a saturation concentration of $c(O_2^-) = 6.77 \pm 0.24 \times 10^{-3}$ mol L^{-1} is calculated and the corresponding solubility constant therefore equals 45.8×10^{-6} mol^2 L^{-2}. Consequently, the saturation concentration of superoxide in a 0.1 M K^+-containing solution equals 0.458 mM (which is well below the saturation concentration of oxygen at atmospheric pressure) or 0.09 mM in a 0.5 M K^+-solution.

7.6.4 Calibration of the Reference Electrode

Due to the presence of diffusion potentials and the fact that the activity coefficient of the silver cations does not equal unity the calculation leading to the values of E^{o}(vs $Ag^{+}|Ag$) is not exact.

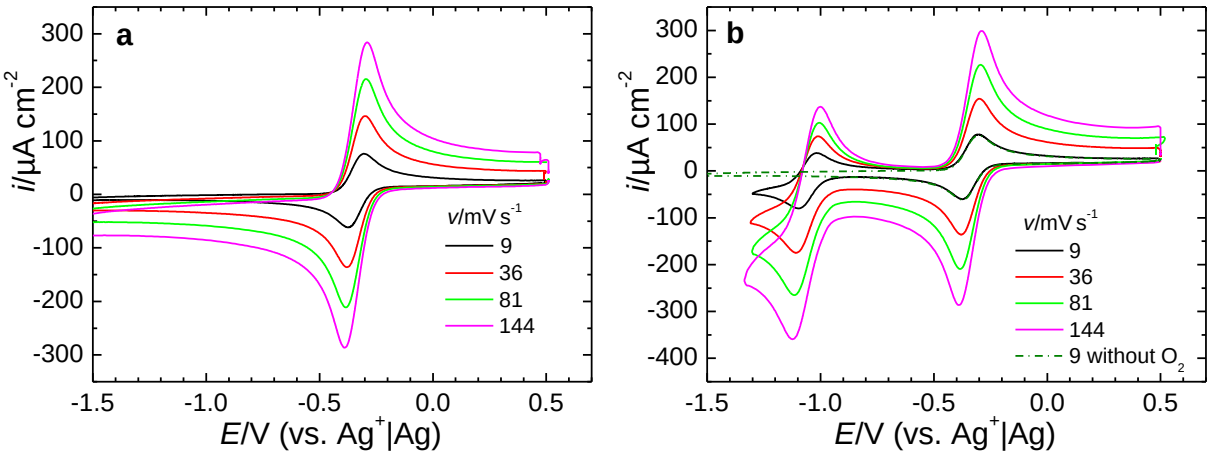

Figure S 7.3. Cyclic voltammetry of the $Me_{10}Fc^{+}|Me_{10}Fc$ redox couple on a GC electrode. . **a**. In the absence of oxygen. **b**. In the presence of 20% oxygen. For comparison, the CV in the absence of oxygen at a sweep rate of 9 mV s^{-1} is shown in dark green. Electrolyte: 0.1 M $KClO_4$ in DMSO at a glassy carbon electrode

To enhance accuracy as well as comparability to other studies decamethylferrocene was used as a solvent-independent reference. Cyclic voltammograms at a glassy carbon electrode in the absence (Figure S 7.3 a) and presence of O_2 (Figure S 7.3 b) reveal that the $Me_{10}Fc|Me_{10}Fc^{+}$ expectedly does not depend on the oxygen content. The half-wave potential of the decamethylferrocene couple was determined by averaging the cathodic and anodic peak potential ($E_{1/2} = (E_c+E_a)/2$). The resultant half-wave potential is −0.340 V vs. $Ag^{+}|Ag$.

7.6.5 Determination of the Diffusion Coefficient of $Me_{10}Fc$ and $Me_{10}Fc^{+}$

The diffusion coefficient $Me_{10}Fc$ and $Me_{10}Fc^{+}$ can conveniently be determined performing potential steps at an RRDE: The diffusion coefficient of $Me_{10}Fc^{+}$ is determined by holding the ring potential at −0.6 V where the reduction of the oxidized species occurs while the disk electrode is suddenly stepped from a potential where no reaction occurs (−0.5 V, 5 s) to a potential where $Me_{10}Fc$ is oxidized (−0.2 V, 11 s). Consequently, the $Me_{10}Fc^{+}$ produced at the disk will diffuse towards the ring and will lead to reduction current at the ring. From the time delay between disk and ring (t_s), the diffusion coefficient of $Me_{10}Fc^{+}$ can be evaluated according to eq.(S 7.1) [111], where t_s is in seconds and W^{-1} in rounds per minute:

$$t_s = 43.1\left[\log\left(\frac{r_2}{r_1}\right)\right]^{2/3}\cdot\left(\frac{\nu}{D}\right)^{1/3}\cdot W^{-1} \qquad \text{(S 7.1)}$$

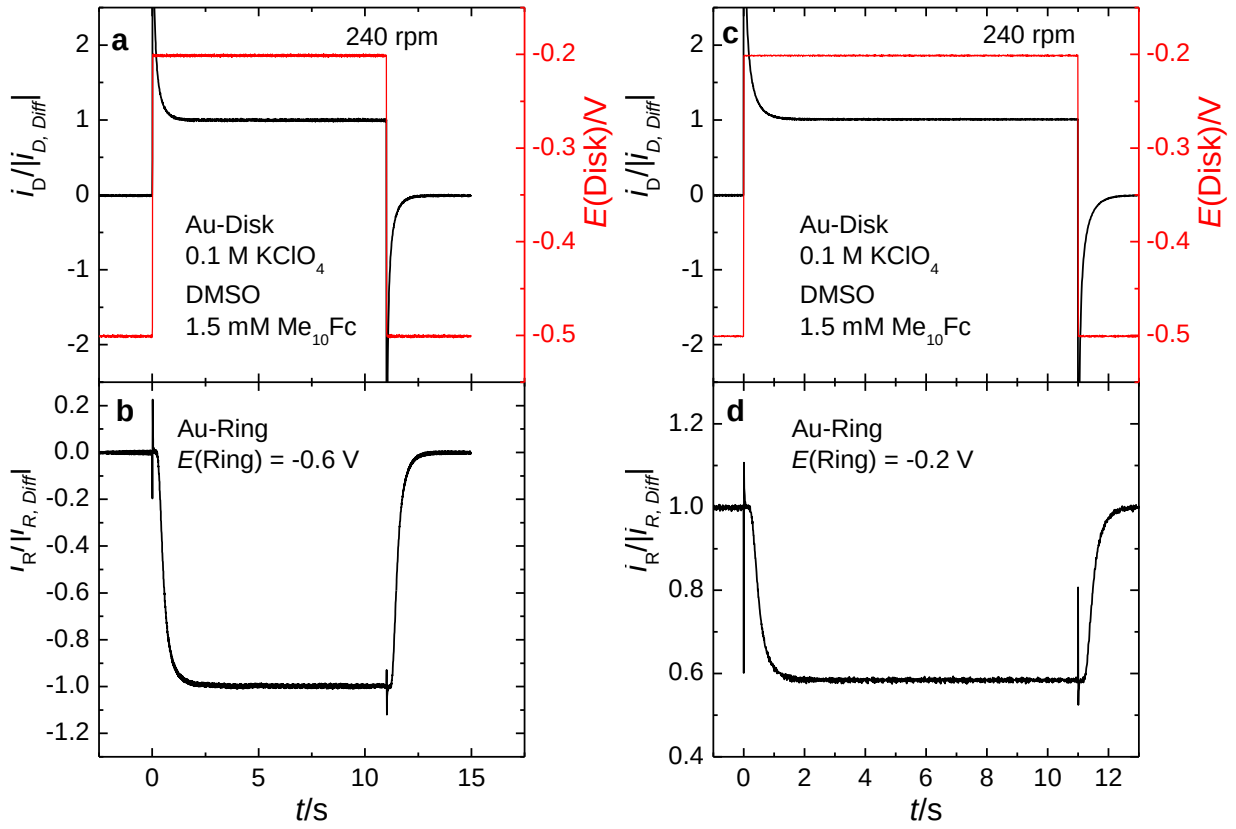

Figure S 7.4. Transients of the ferrocene redox couple at a thin-gap gold disk- and gold ring-electrode. **a**. Disk currents normalized to the constant current in the plateau and the potential applied to the disk (red). **b**. Ring currents normalized to the constant current in the plateau for a ring potential of −0.6 V, where $Me_{10}Fc^+$ is reduced. **c**. Disk currents normalized to the constant current in the plateau and the potential applied to the disk (red). d. Normalized ring current for a ring potential of −0.2 V where $Me_{10}Fc$ is oxidized. Electrolyte: 0.1 M $KClO_4$ in DMSO containing 1.5 mM $Me_{10}Fc$.

In eq. (S 7.1), r_2 is the inner radius of the ring electrode, r_1 is the radius of the disk, ν is the kinematic viscosity, D is the diffusion coefficient of $Me_{10}Fc^+$ and W is the rotation frequency in rounds per minute. The step program as well as the normalized disk and ring currents are shown Figure S 7.5 a and b. The determination of the diffusion coefficient of the neutral species, $Me_{10}Fc$, is carried out via a shielding experiment: A potential of −0.2 V is applied to the ring which leads to an oxidation of $Me_{10}Fc$. The disk potential is stepped from −0.5 V, where no reaction occurs, to −0.2 V and subsequently, $Me_{10}Fc$ is oxidized at the disk electrode. The oxidation of $Me_{10}Fc$ at the disk electrode results in a decrease of the ring current as less $Me_{10}Fc$ is available for oxidation at the ring. From the time delay between disk and ring current, the diffusion coefficient of $Me_{10}Fc$ can be determined according to eq. (S 7.1). The determination of t_s is elucidated in Figure S 7.5 a and b. The dashed line represents a tangent of the turning point of the ring transient and the intercept of the time-axis with the tangent gives the value for t_s at a specific rotation rate. A plot according to eq. (S 7.1) is shown in Figure S 7.5 c.

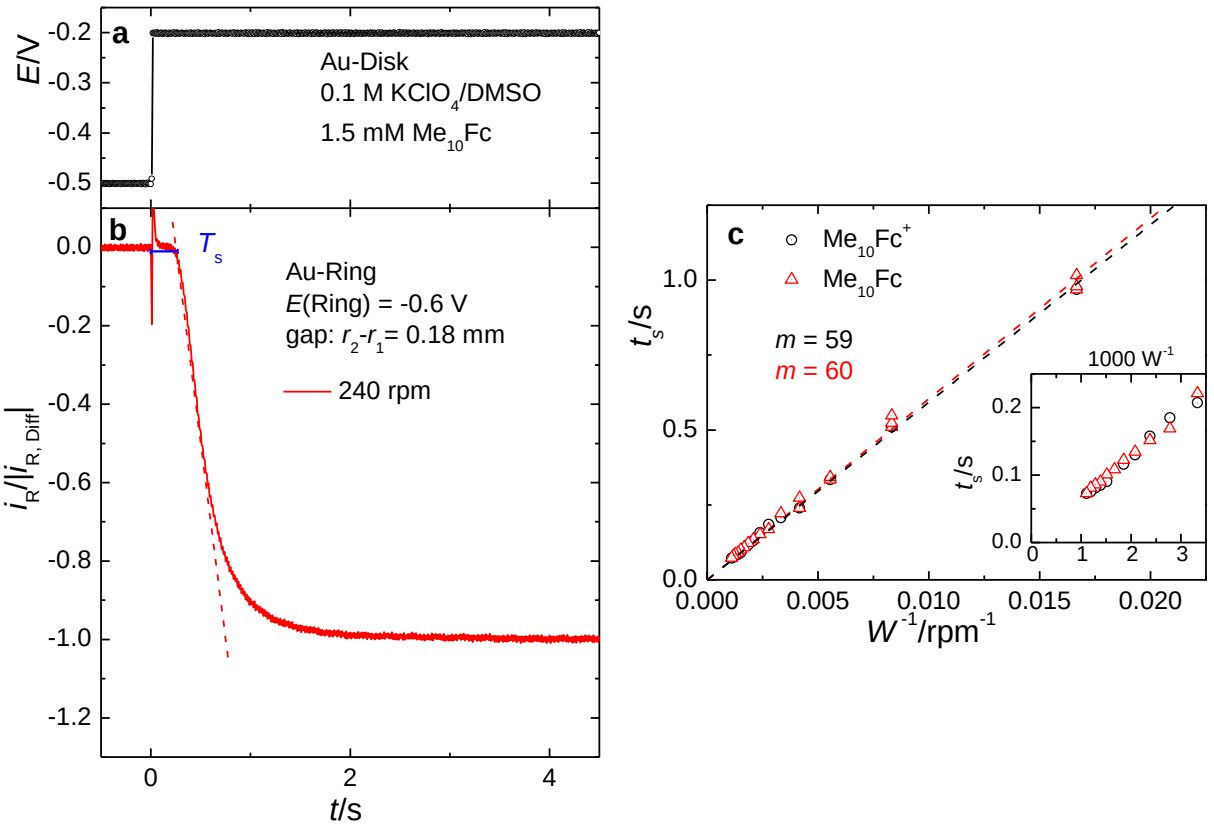

Figure S 7.5. Determination of the transient time t_s. **a**. Magnification of the potential programme. **b**. Normalized ring transients for a rotation rate of 240rpm. **c**. Determination of the diffusion coefficient according to eq. (S 7.1) for $Me_{10}Fc^+$ (black) and $Me_{10}Fc$ (red).

The deviation between the two slopes is well within the experimental error signifying that the diffusion coefficient of both species is identical as expected for a solvent-independent redox system.

7.6.6 Comparison of the Set Ups

The DEMS set up is schematically shown Figure S 7.6. The electrolyte enters the cell at the upper compartment, where the working electrode 1 (WE1) is placed. The electrolyte then leaves the upper compartment through six, centro-symmetrically aligned capillaries and enters the lower compartment, where a connection to the vacuum of the mass spectrometer (MS) is established via a porous, gold-sputtered Teflon membrane, which serves as the second working electrode (WE2). The electrolyte leaves the cell via a channel connected to the lower compartment. Due to the high electrolyte resistance a set of two reference electrodes (RE) as well as counter electrodes (CE) is necessary. For details refer to Bondue et al. [120]. The time delay between the faradaic current measured at WE1 and the faradaic current at WE2 as well as the signal of the MS is influenced by the thickness of the thin-layer, the length of the capillaries and the flow rate (other factors also play a role but cannot be changed for a given system). Due to the generally high resistances associated with the thin-layer geometry, highly concentrated electrolytes have to be used.

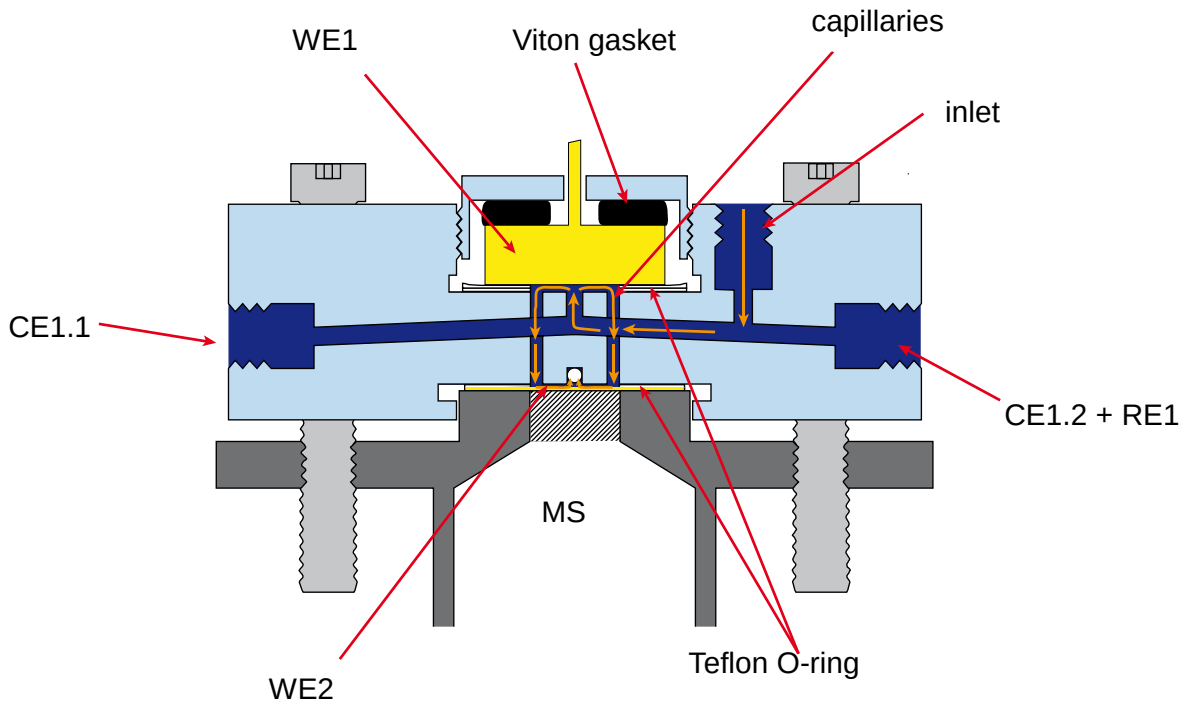

Figure S 7.6: Six electrode dual thin-layer flow through cell.For a detailed description of the cell, refer to the text. Modified after Bondue et al. [120].

A diagrammatic sketch an RRDE set up is shown in Figure S 7.7. The RRDE consist of a disk electrode, which is separated via an insulating O-ring from the ring electrode. Both electrodes are mounted into a chemically inert shroud. During an experiment, the whole assembly including the shroud rotates at a rotational frequency ω. The rotational movement of the disk drags the fluid toward its surface. In radial direction, the fluid is pushed from the centre of the disk to the ring electrode. The RRDE set up can also be used for recording simple CVs if the rotation rate is stopped.

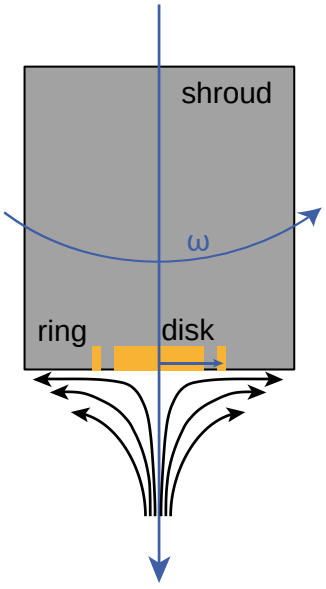

Figure S 7.7: Schematic drawing of the rotating ring-disk electrode. The disk and ring electrode are mounted into non-conducting, chemically inert polytetrafluoroethylene.

For a better understanding of the implications of the different set ups, important parameters are given in Table S 7.2. The hypothetical concentration of superoxide close to the surface, $c_{x=0}(O_2^-)$, has been calculated according to eq.(S 7.2) , which is the same as eq. (7.6) in the main paper.

$$c_{x=0}(O_2^-) = c^0(O_2) \cdot \left(\frac{D(O_2)}{D(O_2^-)} \right)^y \qquad \text{(S 7.2)}$$

The coefficient *y* reflects the hydrodynamic conditions and is ½ for the CV measurements[96], and 2/3 in the case of RRDE[96] and DEMS[130] due to the laminar flow conditions. For a derivation of the equation see below.

Table S 7.2. Comparison of different parameters for the different set ups[a]

	***c*(KClO₄)/M**	**τ/s**	$c_{sat}(O_2^-)$	$c_{x=0}(O_2^-)$	$c_{x=0}(O_2^-) / c_{sat}(O_2^-)_t$
DEMS	0.5	2.5	0.09	2.0	22
RRDE	0.1	0.4 (9 Hz)	0.46	2.0	4.5
CV	0.1	NA	0.46	1.4	3.0

[a] $c(KClO_4)$; concentration of $KClO_4$ in the bulk, τ: transfer time between the two working electrodes, $c_{sat}(O_2^-)$: saturation concentration of superoxide calculated from the solubility product of KO_2 ($K_L = 45.8 \times 10^{-6}$ mol²L⁻²), $c_{x=0}(O_2^-)$: concentration at the electrode surface calculated according to eq. (S 7.2) for an oxygen partial pressure of 0.2 bar.

7.6.7 Derivation of Equation (7.6)/(S 7.2)

Equation (7.6) or rather (S 7.2) can be derived from the law of mass conservation. In order to conserve mass, the flux of the reactant (R) towards the electrode has to equal the negative flux of the product (P) [96]:

$$J_P(0,t) = -J_R(0,t) \qquad \text{(S 7.3)}$$

Using Fick's first law of diffusion eq. (S 7.3) can be rewritten using the diffusion coefficients and concentration gradients at the electrode surface:

$$D_P \left[\frac{\partial C_P(x,t)}{\partial x} \right]_{x=0} + D_R \left[\frac{\partial C_R(x,t)}{\partial x} \right]_{x=0} = 0 \qquad \text{(S 7.4)}$$

Usually, the concentration gradient in front of the electrode is linearly approximated, which leads to the following expression, where δ_P denotes the thickness of the diffusion layer of the product:

$$D_P \frac{c_{x=0}(P) - c_0(P)}{\delta_P} + D_R \frac{c_{x=0}(R) - c_0(R)}{\delta_R} = 0 \qquad \text{(S 7.5)}$$

In the case of diffusion limitation and the initial absence of the product, eq. (S 7.5)simplifies to eq.(S 7.6):

$$D_P \frac{c_{x=0}(P)}{\delta_P} + D_R \frac{-c_0(R)}{\delta_R} = 0 \tag{S 7.6}$$

Now, only an expression for the thickness of the diffusion-layer is needed. In the case of the RRDE, the diffusion-layer thickness is given by:

$$\delta_P = 1.61 D_P^{1/3} \omega^{-1/2} v^{1/6} \tag{S 7.7}$$

In eq.(S 7.7), ω is the angular frequency and *v* is the kinematic viscosity. Substituting eq. (S 7.7) into eq. (S 7.6) yields:

$$\begin{aligned} & D_P \frac{c_{x=0}(P)}{1.61 D_P^{1/3} \omega^{-1/2} v^{1/6}} + D_R \frac{-c_0(R)}{1.61 D_R^{1/3} \omega^{-1/2} v^{1/6}} = 0 \\ & D_P \frac{c_{x=0}(P)}{D_P^{1/3}} = D_R \frac{c_0(R)}{D_R^{1/3}} \\ & c_{x=0}(P) = c_0(R) \cdot \left(\frac{D_R}{D_P} \right)^{2/3} \end{aligned} \tag{S 7.8}$$

Comparing eq. (S 7.8) to eq. (S 7.2), with O_2^- = P and O_2 = R, shows that *y* =2/3.

Using the definition of the diffusion-limited current, I_{Diff} = zFDc$_0$/δ and the Cottrell-equation (I_{Diff} = zFD$^{1/2}$c$_0$/π$^{1/2}$ t$^{1/2}$), the thickness of the diffusion-layer for semi-infinite diffusion (which is applicable to normal cyclic voltammetry) is given by:

$$\delta_P = \sqrt{\pi D_P t} \tag{S 7.9}$$

Substitution into eq. (S 7.6) and rearrangement leads so the final expression:

$$c_{x=0}(P) = c_0(R) \cdot \left(\frac{D_R}{D_P} \right)^{1/2} \tag{S 7.10}$$

Thus, the exponent *y* equals ½.

Lastly, the expression for the diffusion-limited current in the DEMS-cell at a flow rate *u* of 5 µL s^{-1} (laminar flow) and a geometric factor *g* is given by[130]:

$$I_{Diff} = zF \cdot g \cdot u^{1/3} \cdot c_0 D^{2/3} \tag{S 7.11}$$

Accordingly, the diffusion-layer thickness can be expressed as:

$$\delta_P = D_P^{1/3} u^{-1/3} g^{-1} \tag{S 7.12}$$

Substituting this equation into eq. (S 7.2) again leads to the same expression obtained for the RRDE:

$$c_{x=0}(P) = c_0(R) \cdot \left(\frac{D_R}{D_P} \right)^{2/3} \qquad \text{(S 7.13)}$$

The similarity between the results for the RRDE and the DEMS originates from the fact that in both cases laminar flow conditions are fulfilled.

8 Ion Pairs and the Effect of Water in Potassium Ion-Containing DMSO

Philip Heinrich Reinsberg*, Andreas Koellisch and Helmut Baltruschat*

*Institut für Physikalische und Theoretische Chemie, Universität Bonn, Römerstraße 164, D-53117 Bonn, Germany

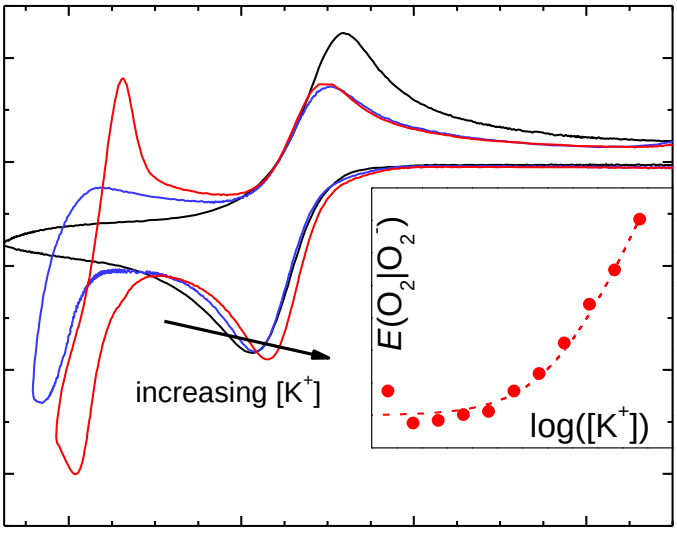

Reprinted (adapted) from an article submitted to *Electrochimica Acta*, title: *On the Importance of Ion-Pair Formation and the Effect of Water in Potassium–Oxygen Batteries*.

Own manuscript contribution:

- design of the experiments
- supervision of the experiments
- interpretation of the results
- writing the manuscript

ACKNOWLEDGMENTS

The authors gratefully acknowledge financial support by the German Federal Ministry of Education via the LiBaLu-project in the framework of the "Vom Material zur Innovation"-initiative (03XP0029A). P. H. R. wishes to thank the German National Merit Foundation for a PhD-scholarship.

8.1 Abstract

Oxygen reduction in the presence of potassium ions has been identified as a promising candidate for the cathode reaction in aprotic metal–air batteries due to its inherent reversibility. Here, we explore the kinetics of the oxygen reduction reaction in a dimethyl sulfoxide-based electrolyte using rotating ring-disk electrode measurements as well as differential electrochemical mass spectrometry. Thorough kinetic analysis reveals that the oxygen reduction in presence of K^+ behaves like an ideal model system and that the usual relationships for reversible reactions are applicable. From the comparison of different electrode materials it has been concluded that the electrode material has an influence on the kinetics of the reduction of oxygen to superoxide, which challenges the picture of a simple outer-sphere mechanism. In fact, the reduction of oxygen to superoxide is most facile at glassy carbon electrodes, whereas it is significantly lower at gold electrodes. Adding potassium perchlorate to an inert, tetrabutylammonium-containing electrolyte showed a significant stabilization of the superoxide via a shift of the half-wave potentials of the reduction to more positive potentials. This stabilization of superoxide by potassium as compared to tetrabutylammonium shows that the current interpretation of the cation's effect via Pearson's acid-base (HSAB) concept has to be used with great caution. From a detailed analysis of the effect of K^+, the constant of ion-pairing between superoxide and K^+ has been determined as 725 L mol^{-1}. Using isotopically labelled $H_2{}^{18}O$ it has been shown that the formation of potassium peroxide is alleviated in the presence which is attributed to a further reaction of the peroxide with water. This in contrast to Li^+-containing electrolytes, where water has the opposite effect and prevents peroxide formation. Finally, the unexpected consumption of oxygen has been observed during the oxidation of species deposited onto the surface of the electrode, which has been correlated to the amount of CO_2 evolution.

8.2 Introduction

The oxygen reduction and evolution in aprotic electrolytes has been investigated in different electrolytes [15,16,18,61,80,125,139,266,276,294,324]. Among the different systems under investigation, potassium-ion containing electrolytes have been shown to be very promising as potassium superoxide, which is the main product of the reduction reaction, can be reversibly re-oxidized [16,309-311,314,315,325]. What renders the oxygen reaction in presence of potassium unique among other metal–oxygen systems are the thermodynamics of the superoxide and peroxide formation. Using the standard free reaction enthalpies of formation at 25 °C for KO_2 ($\Delta_F G$ = −241 kJ mol^{-1})[14] and K_2O_2 ($\Delta_F G$ = −430 kJ mol^{-1})[14] the reaction enthalpy $\Delta_R G$ for the disproportionation reaction (eq. (8.1)) equals +52 kJ mol^{-1}, making it thermodynamically unfeasible (although it should be noted that solvation of the different species affects all enthalpies):

$$2\,KO_2(s) \rightarrow K_2O_2(s) + O_2(g) \qquad \Delta_R G = +52\,kJ\,mol^{-1} \qquad (8.1)$$

As opposed to that, the disproportionation enthalpy for the Na-analogue of eq. (8.1) is exergonic with a value of $-13\,kJ\,mol^{-1}$ ($\Delta_F G(NaO_2) = -218\ kJ\,mol^{-1}$, $\Delta_F G(Na_2O_2) = -449\ kJ\,mol^{-1}$[14]) and is observed experimentally in low-donating solvents [326]. For the case of LiO_2, the situation is even worse: LiO_2 has only been observed in the gas phase at low temperatures so far[255] and in solution, a fast and efficient disproportionation of the superoxide to peroxide is observed[45,46]. A further implication of the enthalpies of formation is that KO_2 would be generated 0.27 V positive of K_2O_2, which in fact has been observed in dimethyl sulfoxide-based electrolytes [311,315,325] This is in contrast to Li^+-containing electrolytes, where the superoxide is only observed due to kinetic limitations of the peroxide formation, such as crystallization overpotentials [139,263,304]. The oxide would be observed at potentials 0.83 V more negative (see Table S1), which is in excellent agreement with experimental observations on mercury[40].

Although the aforementioned thermodynamic consideration is of fundamental importance, the reaction is often limited by the kinetics of the reaction and the solvation of the reactants and products have to be considered. In K^+-containing acetonitrile, for instance, a mixed process of KO_2 and K_2O_2 and a significant deactivation of the surface have been observed [61,312]. Despite its stability towards the products of the oxygen reduction reaction (ORR) [327,328], acetonitrile (MeCN) is not the best solvent for mechanistic investigations as the intermediates of the ORR undergo facile further reduction and soluble intermediates cannot be detected employing the usual techniques [293,312,326,329]. In contrast to that, dimethyl sulfoxide (DMSO) has been shown to dissolve superoxide species and thus, enables distinction between the superoxide and peroxide formation [211,282,294,312,315,325,329,330].

So far, two reduction processes have been identified in K^+-containing DMSO, that have been attributed to the formation of (sparingly) soluble KO_2 and insoluble K_2O_2 [311,315,325]. While Wang et al. do not find reversible reoxidation of insoluble K_2O_2 [311], Sankarasubramanian and Ramani observed a re-oxidation peak [315] and Reinsberg et al. were able to show the reversible re-oxidation of the peroxide via the superoxide to oxygen using differential electrochemical mass spectrometry (DEMS) [325]. Employing rotating-ring disk studies, the surface-confined reduction of O_2 to peroxide has been identified, although the author's interpretation of the result as a surface-confined disproportionation reaction is questionable [315]. Firstly, a surface disproportionation should lead to the formation of O_2 close to the surface, which is subsequently reduced leading to a two-electron process, which the authors explicitly exclude. Furthermore, it is hard to believe that a surface-disproportionation occurs without participation of the electrons of the metal surface. In our recent work on the ORR in K^+-containing DMSO, we highlighted the importance of the limited solubility of KO_2 and showed how high oxygen pressures lead to a pronounced precipitation of KO_2 and also alleviate the formation of the peroxide [325].

In this work we investigate the oxygen reduction reaction in $KClO_4$-containing DMSO in detail using classical cyclic voltammetry (CV), rotating ring-disk electrodes (RRDE) and differential electrochemical mass spectrometry (DEMS) in a thin-layer geometry[122]. While our previous work focused on the influence of the O_2 partial pressure and the pathway of K_2O_2 re-oxidation, the role of the ion-pairing between K^+ and O_2^- is elucidated in this article and a detailed kinetic characterisation of the system is given and compared to the appropriate literature. Moreover, the influence of water on the reaction is investigated as it is a ubiquitous contamination, which has been shown to affect the ORR in aprotic solvent [134,139,304,331].All CVs in the main part of the paper have been recorded at gold, while analogous measurements at glassy carbon and platinum can be found in the Supporting Information.

8.3 Experimental

8.3.1 Materials

All electrolytes have been prepared in a *GS* glovebox. Potassium perchlorate ($KClO_4$, EMSURE® ACS, *Merck*) has been dried under reduced pressure (10^{-2} mbar) at 160 °C for two days. Dimethyl sulfoxide (DMSO, 99.7+ %, stored under molecular sieve, *Acros Organics*) has been used as received. The as-prepared electrolyte typically had a water content of 20 ppm as determined via coulometric Karl-Fischer analysis. A silver wire immersed in 0.1 M $AgNO_3$ ($AgNO_3$, ≥ 99 %, *ChemPure*) in DMSO was used as a reference. The potential of the reference electrode is +0.340 V vs. $Me_{10}Fc^+|Me_{10}Fc$ [325]. All electrolytes were purged with custom mixture of argon and oxygen (80:20, *Air Liquide*) at least 20 min before the experiment.

8.3.2 Cyclic Voltammetry and Rotating Ring-Disk Electrode

Cyclic voltammetry and rotating ring-disk electrode measurements have been conducted in classical H-cells with a *Luggin* capillary using a thin-gap electrode with a gold-ring and a gold-disk (surface $A = 0.164$ cm^2, theoretical collection efficiency $N_0 = 0.22$), a thin-gap electrode with a platinum-ring and platinum-disk ($A = 0.164$ cm^2, $N_0 = 0.22$) as well as a change-disk electrode with a gold-ring ($N_0 = 0.25$) and a glassy carbon-disk ($A = 0.196$ cm^2). All disk currents are referred to the geometrical surface of the disk electrode, while the ring currents are referred to the theoretical collection efficiency. The typical electrolyte resistance as determined by electrochemical impedance spectroscopy was in the range of 3 Ω cm².

8.3.3 Differential Electrochemical Mass Spectrometry

A detailed description of the DEMS set-up can be accessed elsewhere [113,125]. The thin-layer cell consists of only one compartment confined by a porous PTFE-membrane (*Goretex*, thickness 50 µm, pore diameter 0.02 µm) which connects the cell to a gas reservoir, four PTFE O-Rings of a total thickness of 200 µm and a porous gold-sputtered Teflon-membrane, which connects the cell to the vacuum of a (MS) and serves as working electrode. An advantage of

the thin-layer cell is the high ratio of the surface area to the electrolyte volume simulating battery-like conditions as well as the high sensitivity of the mass spectrometric detection. For details see Bawol *et al.* [122]. Using the calibration constant *K* of the mass spectrometer as determined in an external calibration experiment of known stoichiometry (e.g. the ORR in the presence of $TBAClO_4$ [123,283]), the flux of oxygen (dn/dt) and the number of electrons transferred per O_2 molecule (*z*) can be calculated according to eq. (8.2), where I_F denoted the Faradic current measured at the working electrode.

$$\frac{dn}{dt} = \frac{I_I}{K \cdot F}$$
$$z = \frac{I_F}{F} \cdot \left(\frac{dn}{dt} \right)^{-1} \tag{8.2}$$

8.4 Results and Discussion

8.4.1 Introducing the Effect of K^+ on the ORR in DMSO

The effect of the concentration of K^+ on the ORR kinetics is elucidated in Figure 8.1. In the absence of K^+, a single redox process (c1 and a1) is exhibited due to the formation of superoxide (Figure 8.1 a), which is in accordance with previous results [123,283]:

$$K^+ + O_2 + e^- \rightleftharpoons KO_2(solv) \tag{8.3}$$

In the RRDE set-up, this leads to a plateau in the disk current which is accompanied by a plateau in the ring current, if the ring current is held at a potential sufficiently positive to oxidize superoxide (Figure 8.1 b and c). Increasing the concentration of K^+ shifts the potential of superoxide formation to positive potentials and leads to the occurrence of a second reduction peak (c2) and a corresponding oxidation peak (a2) (Figure 8.1 a), which are attributed to formation and reversible oxidation of K_2O_2 in accordance with our previous DEMS-investigations [325] and RRDE-investigations by Sankarasubramanian [315]:

$$2K^+ + O_2^- + e^- \rightleftharpoons K_2O_2(s) \tag{8.4}$$

Remarkably, the anodic peak (a2) for the re-oxidation of the peroxide is shifted by only 100 mV into the positive direction, rendering the ORR in the presence of K^+ unique: The overpotentials associated with the re-oxidation of, for instance, Li_2O_2 normally lie in the range of 600 mV[139,266,313]. Measurements under forced convection in the same electrolyte (Figure 8.1 b and c) reveal that the product of the second reduction step, K_2O_2, has a very limited solubility as indicated by the persistence of the oxidation peak a2. Moreover, from the corresponding oxidation peak in the ring currents during the anodic sweep it can be deduced that K_2O_2 is only partially oxidised to superoxide at a potential of −1.4 V as expected for a well-behaved redox system, which we recently confirmed via DEMS-measurements[325].

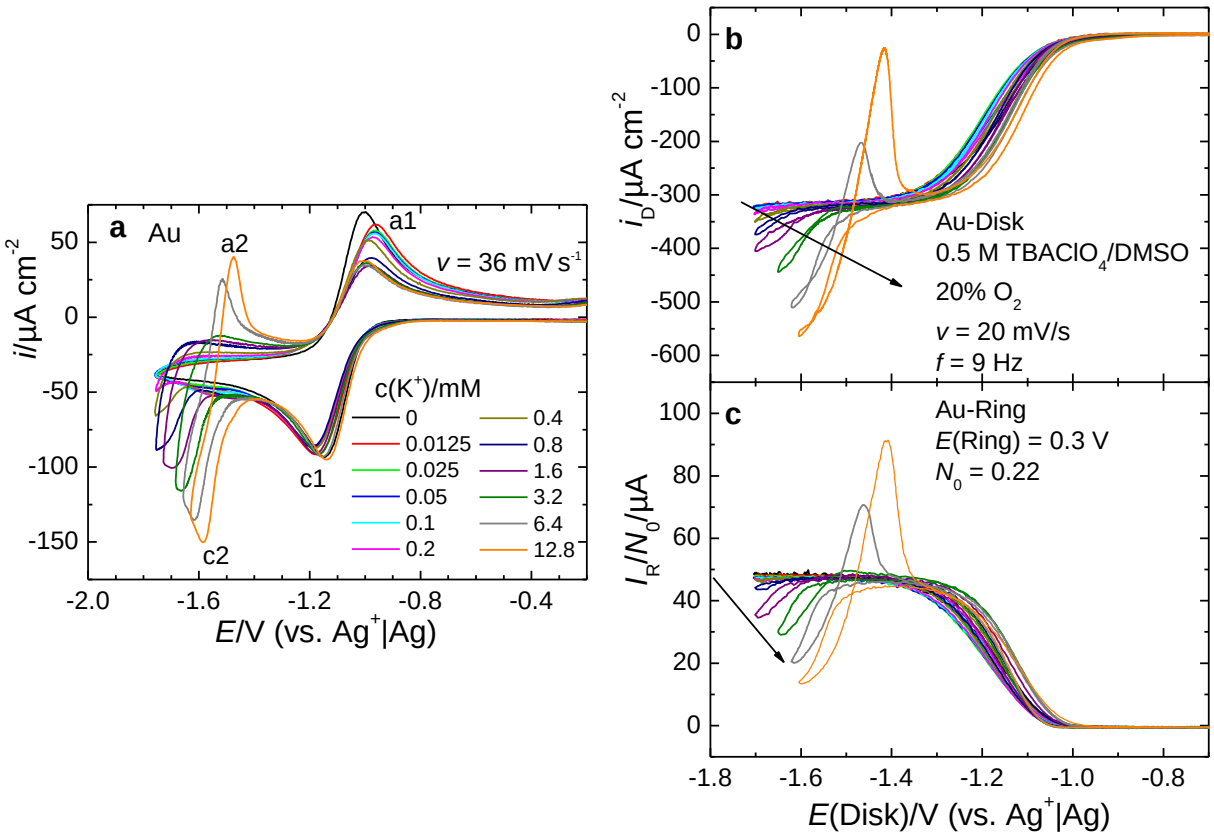

Figure 8.1: Cyclic voltammetry at a gold for different concentrations of K^+. **a**. Cyclic voltammograms under stagnant conditions. **b**. Disk-currents at an Au-disk/Au-ring RRDE set-up for a rotation rate of 9 Hz. **c.** Corresponding ring currents held at a potential sufficiently positive to oxidize superoxide. Electrolyte: 0.5 M $TBAClO_4$ in DMSO saturated with 20% O_2.

Before discussing the effect of K^+ on the ORR in detail, a brief overview of the current understanding of the effect of the solvent and cation on the ORR shall be given here. Concepts which are often invoked in this context are Pearson's hard and soft acid base (HSAB) theory [91] and Gutmann's concept of donor and acceptor numbers[222]. For instance, Abraham and co-workers, used these concepts to explain the higher stability of superoxide in DMSO as compared to MeCN[62]. This has been invoked many times since then [211,287,311,315,329,332]. The authors argue that the solvation of the strong solvation of the cation by DMSO renders the cation (e.g. Li^+) soft and leads to a *stabilizing* interaction between *soft* superoxide and the *soft* solvated cation [62,87,311]. Furthermore, similar arguments are used to explain the effect of the cation [87]. However, there seems to be the widespread misconception that interaction between soft bases and acids are always stronger than interactions between soft bases and hard acids[93]. This is because concept of hardness/softness of an ion does not replace the concept of weak and strong acids[333] (for a complete discussion of this misconception see Bondue et al., Supporting Information [93]). For instance, the interaction between H^+ and S^{2-} is certainly stronger than the interaction between H^+ and Cl^- despite the former being a hard–soft acid–base pair and the latter being hard–hard. As tetraalkylammonium-ions are usually considered *weak* Lewis-acids a strong interaction with superoxide is unlikely and should ultimately result

in precipitation of e.g. $TBAO_2$ similar to the precipitation of AgI from aqueous electrolytes. Moreover, if only the softness of the ions played a role, why would the Li^+, which is rendered soft by DMSO, not strongly interact with the soft ClO_4^-, PF_6^- or OTf^--anion and thus, lead to a precipitation of the salts? We therefore proposed that alternative way of explaining the role of the solvent and the cation: Initially, the largest interaction exists between the cation and the solvent. Once O_2 is reduced to superoxide, a *strong* Lewis base is present in the electrolyte. If the conducting salt contains Li^+, which represents a *strong* Lewis acid, the strong interaction between O_2^- and Li^+ leads to disproportionation of the superoxide (one could argue that the Li^+ actually *destabilizes* the O_2^-). In contrast to that, the interaction between the *weak* Lewis acid TBA^+ and O_2^- is much weaker and thus, O_2^- is not as much destabilized as in the case of Li^+. It is important to note that the main difference between our approach and Abraham's so far is that we propose a destabilizing interaction via a strong base, whereas Abraham proposes a stabilizing interaction via a soft/weak base. The effect of the solvent can now be understood in terms of the solvation of the cation and superoxide. For strongly solvation solvents such as DMSO, the Lewis acidity and basicity of the cation and anion are lowered, resulting in a lower interaction energy and thus, an increasing lifetime of the superoxide [93].

Having discussed the current concepts, we can now rationalize the effect of K^+ on the ORR as follows: The interaction energy between potassium ions and soluble superoxide is larger than between TBA^+-ions and superoxide, which leads to a shift in the half-wave potential to more positive values (Figure 8.2). Mathematically, this ion-pairing effect is described by eq. (8.5), where E^o represents the standard potential in TBA^+-containing solution, p is the number of K^+-ions interacting with the oxygen species and $E_{1/2}^{K^+}$ is the half-wave potential in the presence of K^+ [334]:

$$E_{1/2}^{K^+} = E^0 + \frac{RT}{F}\ln\left(1 + K_{ion}\cdot c^p\left(\mathrm{K^+}\right)\right) - \frac{RT}{F}\ln\left(\left(\frac{D(\mathrm{O_2})}{D(\mathrm{O_2^-})}\right)^y\right) \qquad (8.5)$$

Note that due to the largely different diffusion coefficients of oxygen and superoxide (factor of 10[323,325]) the deviation between half-wave potential and standard potential has to be taken into account. The exponent y depends on the hydrodynamic conditions and equals ½ for cyclic voltammetry under stagnant conditions and 2/3 for RRDE-measurements[325]. The corresponding plot for the superoxide couple is shown in Figure 8.2 a, where the dotted line is the simulated curve for E^o = 1137 mV and K_{ion} = 725 L mol^{-1}. Note that the difference between half-wave potentials obtained from RRDE and CV data is close to the 10 mV expected from the different values for y, which again shows how well the system behaves. The shift of the half-wave potential of the superoxide formation to more positive potentials with increasing concentration of K^+ can be used as a direct proof that the "current" interpretation of the HSAB-concept by Abraham and co-workers is flawed: K^+ is certainly a *harder* acid than TBA^+, but still exerts a stronger stabilizing effect (reflected by the shift of the half-wave potential to more

positive potentials) on the superoxide. If the interaction between TBA^+ and superoxide was of particular strength, the addition of small amounts of K^+ should not shift the half-wave potential of the superoxide formation.

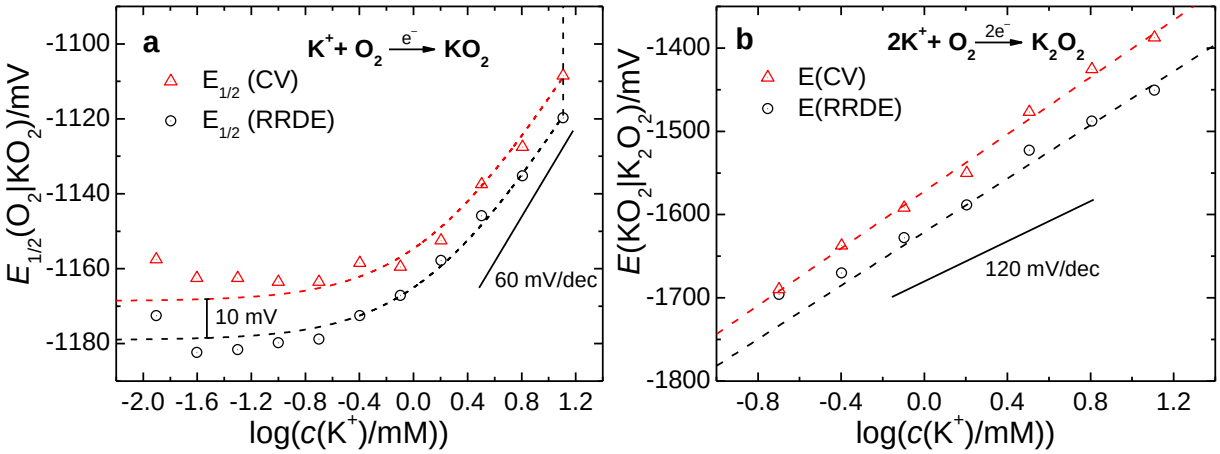

Figure 8.2: Characteristic potentials of the ORR in presence of K^+ **a.** Half-wave potential of the superoxide formation as well as simulated curves according to eq. (8.5) for $E^o = 1137$ mV and $K = 725$ L mol^{-1}. Half-wave potentials of the CV have been calculated from the peak potentials by adding 28.5 mV [96] **b.** Potential where the current exceeds the diffusion-limited current for superoxide formation by more than a factor of 1.05 or a slope of 0 is achieved in the CV with respect to the logarithm of the K^+-concentration.

As in total two K^+-ions are necessary to form K_2O_2 the slope in (8.5) changes by a factor of two, giving a final value of 120 mV/dec when plotted versus the decadic logarithm. The corresponding plots of the peroxide formation potentials are shown in (Figure 8.2 b), which again agree very well with theory. In contrast to the superoxide couple, the equilibrium constant of the reaction is so large that truly linear behaviour is observed.

8.4.2 Effect of the Electrocatalyst on the Superoxide Formation

As the solubility and diffusivity of oxygen and superoxide in K^+-containing DMSO will be used throughout the next sections to compare experimental to theoretically expected data, the respective values are given here:

- $c(O_2) = 2\text{x}10^{-3}$ mol L^{-1}, $D(O_2) = 24.1\text{x}10^{-6}$ cm^{2}s^{-1} [325]
- $c(O_2^-) = 6.77\text{x}10^{-3}$ mol L^{-1}, $D(O_2^-) = 2.13\text{x}10^{-6}$ cm^{2}s^{-1} [325]

For the kinematic viscosity of the K^+-containing DMSO the kinematic viscosity of pure DMSO ($\nu = 0.01816$ cm²s^{-1}) [220] has been used.

An elucidation of the influence of the electrocatalyst on the ORR in K^+-containing DMSO is shown in Figure 8.3 a. The peak positions c1 and a1 as well as the peak currents observed in the CV are very similar for platinum and glassy carbon, whereas the peak separation at gold is significantly larger and the peak currents are smaller. This indicates a less reversible behaviour of the superoxide formation at the gold electrode. A control experiment using the gold electrode in the very same solution directly after the measurements with the glassy carbon

(Figure 8.3 a, dotted line) gave similar results as before and underlines that the difference observed between Pt and GC on the one hand and Au on the other hand is indeed real. As can be seen in Figure 8.3 b, the slope of a plot of the peak current versus square root of the sweep rate (for the corresponding CVs see Figure 8.4 and Figure S 8.1 to Figure S 8.3) is smallest for the gold electrode, which is again expected from the less reversible behaviour[335]. For glassy carbon, the slope (m_{exp}=16.1 µA cm^{-2}(s/mV)$^{1/2}$) is close to that one expected by the Randles-Sevcik equation (m_{RS}=16.7 µA cm^{-2}(s/mV)$^{1/2}$). Moreover, comparison with the data reported by Wang *et al.* [311] for a glassy carbon electrode shows astonishing agreement with the data reported in this work and further stresses that the less reversible behaviour of the gold electrode is indeed significant and not within the margin of the experimental uncertainty. It should be noted that indications for the adsorbing behaviour of superoxide and deviations from a purely outer-sphere mechanism have been also found in the presence of Li^+[56,139,282,283,284] Na^+ [238] and recently also in the presence of K^+ [315]. Moreover, Markovic and co-workers found a surface-sensitivity of the ORR in presence of Li^+ on single crystalline gold electrode, which they attributed to the presence of water [134]. The special behaviour of gold towards the ORR has also been previously highlighted [18,263,282,284] and thus, it is not unexpected that gold behaves differently from platinum and glassy carbon. In contrast these results, Trahan et al. [329] claimed that the inner sphere reaction is only active in solvents with a low donor number. This was concluded from the existence of a pre-peak of the ORR; which was attributed to the adsorption of oxygen. However, while the pre-peaks are less visible in the case of DMSO, a small peak can in fact be observed at the gold electrode, whereas it is not visible at carbon or platinum [329]. Due to the complex structure of the CV in Li^+-containing electrolytes (significant deactivation, rather unstable superoxide as compared to KO_2), it is not possible to conduct the same experiments as in the K^+-containing electrolytes. Therefore, we cannot make a final conclusion at this point. No pre-peaks are present for the superoxide formation in presence of K^+, which is in agreement with the results by Trahan et al. However, the question is whether this pre-peak really is an appropriate indicator for the existence of an inner- or outer-sphere mechanism.

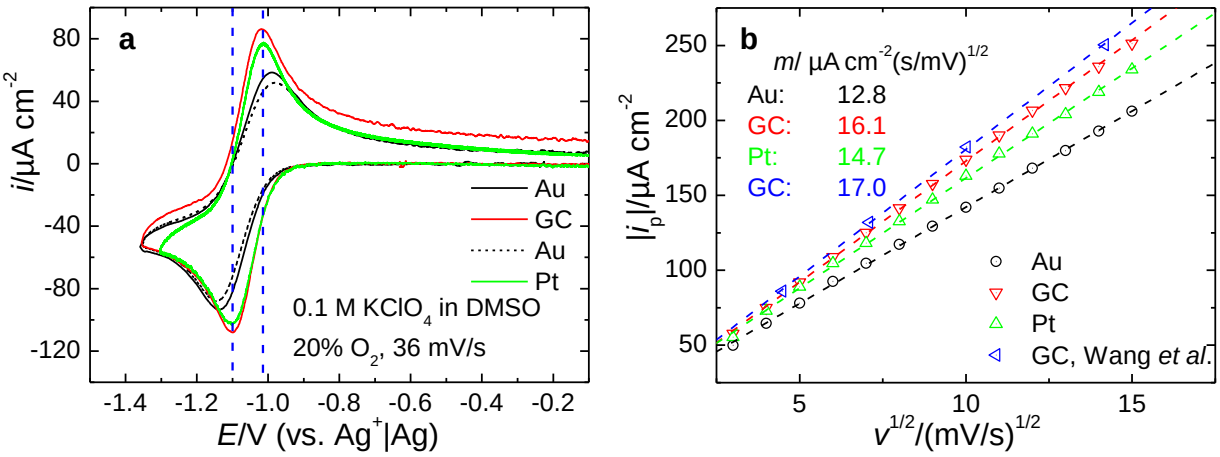

Figure 8.3. Cyclic voltammetry at gold, glassy carbon and platinum. **a.** Cyclic voltammograms for a fixed sweep rate of 36 mV s^{-1}. **b**. Sweep rate dependence of the peak current. The blue data points are taken from Wang et al. and have been adjusted to the O_2-concentration used in this study[311].Electrolyte: 0.1 M $KClO_4$ in DMSO, saturated with 20% O_2.

8.4.3 Kinetic Analysis of the Oxygen–Superoxide and Superoxide–Peroxide Couples

For the kinetic analysis, exemplarily cyclic voltammograms (CV) of the oxygen reduction at a gold electrode in K^+-containing DMSO saturated with 20% O_2 are shown in Figure 8.4.

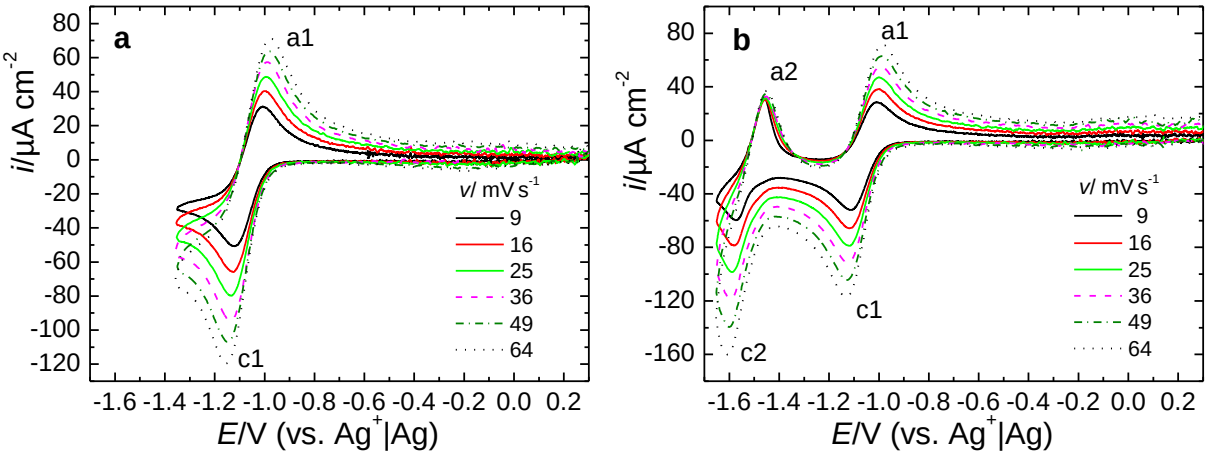

Figure 8.4. Cyclic voltammograms for different sweep rates at a gold electrode. **a**. Lower potential limit is -1.35 V. **b.** Lower potential limit extended to −1.65 V. Electrolyte: 0.1 M $KClO_4$ in DMSO saturated with 20% O_2.

The redox couple designated by c1 and a1 in Figure 8.4 a can be used for the evaluation of kinetic parameters of the oxygen–superoxide redox pair. For evaluation of the standard rate constants, the peak separation ΔE in mV is converted to the unit-less ψ-function using the simulated fitting curve obtained by Lavagnini[336] based on the data of Nicholson[335]:

$$\Psi = \frac{\left(-0.6288 + 0.0021 \cdot \Delta E\right)}{\left(1 - 0.017 \cdot \Delta E\right)} \tag{8.6}$$

Having calculated the corresponding ψ-values, the standard rate constant k_0 can be evaluated from a plot of ψ vs. $\nu^{-1/2}$ according to eq. (8.7) [335]:

$$\Psi = k_0 \left(\frac{D_O}{D_R} \right)^{\alpha/2} \sqrt{\frac{RT}{\pi z F D_O}} \cdot \frac{1}{\sqrt{\nu}} \tag{8.7}$$

In eq. (8.7) D_O is the diffusion coefficient of the oxidized species (oxygen), D_R the one of the reduced species (superoxide), ν is the sweep rate, α the transfer coefficient and the other symbols have the usual meaning. The plots corresponding to eq. (8.6) and eq. (8.7) are shown in Figure 8.5 based on the data given in Figure 8.4 and Figure S 8.1 to Figure S 8.3.

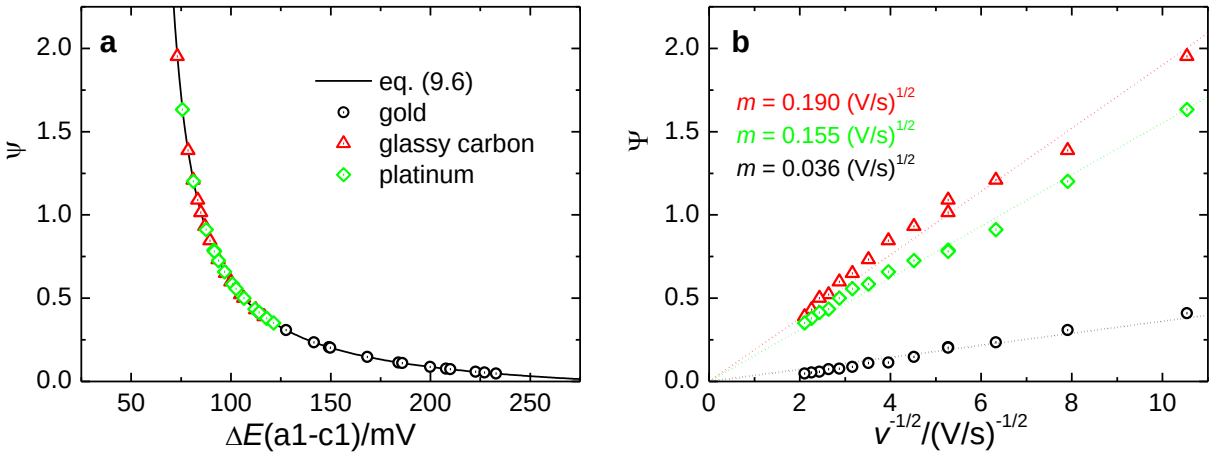

Figure 8.5. Graphical representation of the evaluation of the standard rate constant. **a.** Correlation between ψ and the peak separation Δ*E*. **b.** Evaluation of the standard rate constant from the ψ-function and the inverse square root of the sweep rate.

For the final calculation of the standard rate constant the transfer coefficient α has to be evaluated. Although the exact determination of the transfer coefficient for a quasi-reversible reaction cannot be done analytically (for a truly reversible reaction there is no transfer coefficient), it can be estimated from the shift of the peak potential with the sweep rate assuming irreversible conditions at higher sweep rates. For a totally irreversible reaction, the peak potential E_{Peak} shifts with the sweep rate according to eq.(8.8) [96]:

$$E_{Peak} = E^0 - \frac{RT}{2\alpha F} \ln(\nu) - \frac{RT}{\alpha F} \left[0.780 + \ln\left(\frac{D_O^{1/2}}{k^0} \right) + \ln\left(\frac{\alpha F}{RT} \right) \right] \tag{8.8}$$

Thus, a plot of the peak potential versus the decadic logarithm of the sweep rate should yield a straight line with a slope of 30 mV/α at 25 °C. A graphical representation corresponding to eq. (8.8) using the cathodic peak c1 for the gold electrode (Figure 8.4) is shown in Figure 8.6.

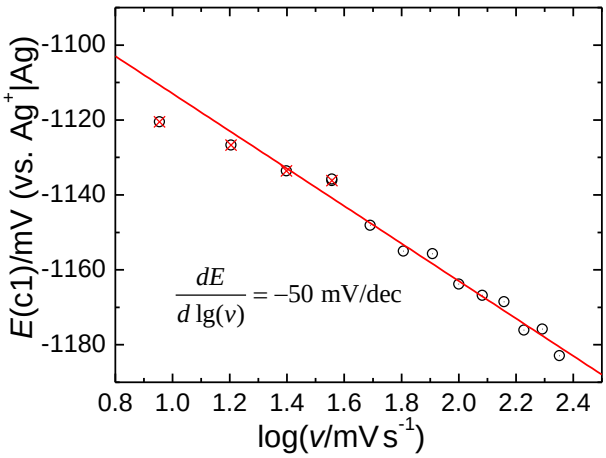

Figure 8.6. Graphical representation of the evaluation of the transfer coefficient α. Evaluation according to eq. (8.8) using the cathodic peak potential c1 obtained at the gold electrode.

The transfer coefficient obtained from the slope gives a value of 0.6. For glassy carbon and platinum an alpha of 0.5 has been due to the non-linearity of the plot of E_{c1} vs log(v) . The standard rate constant at gold gives a value of $k_0(O_2|O_2^-) = 0.94 \times 10^{-3}$ cm s^{-1}, at glassy carbon it is 4.98×10^{-3} cm s^{-1} and at platinum it gives a similar value of 4.06×10^{-3} cm s^{-1}. It is interesting to note that the standard rate constant obtained by Wang *et al*. for a glassy carbon electrode in 0.5 M KPF_6 saturated with oxygen is very similar to the one obtained at gold in this study ($k_0 = 1.57 \times 10^{-3}$ cm s^{-1}, assuming equal diffusion coefficients) [311]. However, a major problem in the evaluation of the standard rate constant in 0.5 M K^+-containing solution saturated with oxygen at atmospheric pressure might be related to the precipitation of the superoxide. This problem becomes obvious from the relative magnitude of the cathodic and anodic peaks (only −0.05 mA for cathodic peak, but 0.13 mA for the corresponding anodic peak[311]), implying that the anodic peak they used for the evaluation comprises insoluble superoxide as well as the peroxide and is therefore not purely limited by diffusion. If insoluble species as well as the presence of K_2O_2 are taken into account, only a mixed standard rate constant can be obtained, which is likely to be lower than the standard rate constant of the pure, soluble superoxide and might explain the deviation.

The evaluation of the standard rate constant for the superoxide-peroxide couple has been carried out in a similar fashion (section 8.6.3). Signifying the reversibility of the peroxide formation, the standard rate constants of the superoxide–peroxide couple are of the same order of magnitude as the standard rate constants for the oxygen–superoxide couple: $k_0(O_2^-|O_2^{2-}) = 0.89 \times 10^{-3}$ cm s^{-1} for glassy carbon and $k_0(O_2^-|O_2^{2-}) = 0.69 \times 10^{-3}$ cm s^{-1} for gold (the calculation assumes equal diffusion coefficients for super- and peroxide due to lack of data for the peroxide).

8.4.4 Analysis of the Oxygen–Superoxide Couple using Forced Convection

To further substantiate the kinetic analysis, measurements with the rotating ring-disk electrode have been conducted using a gold-disk/gold-ring arrangement (Figure 8.7, corresponding data for the GC electrode is shown in Figure S 8.7).

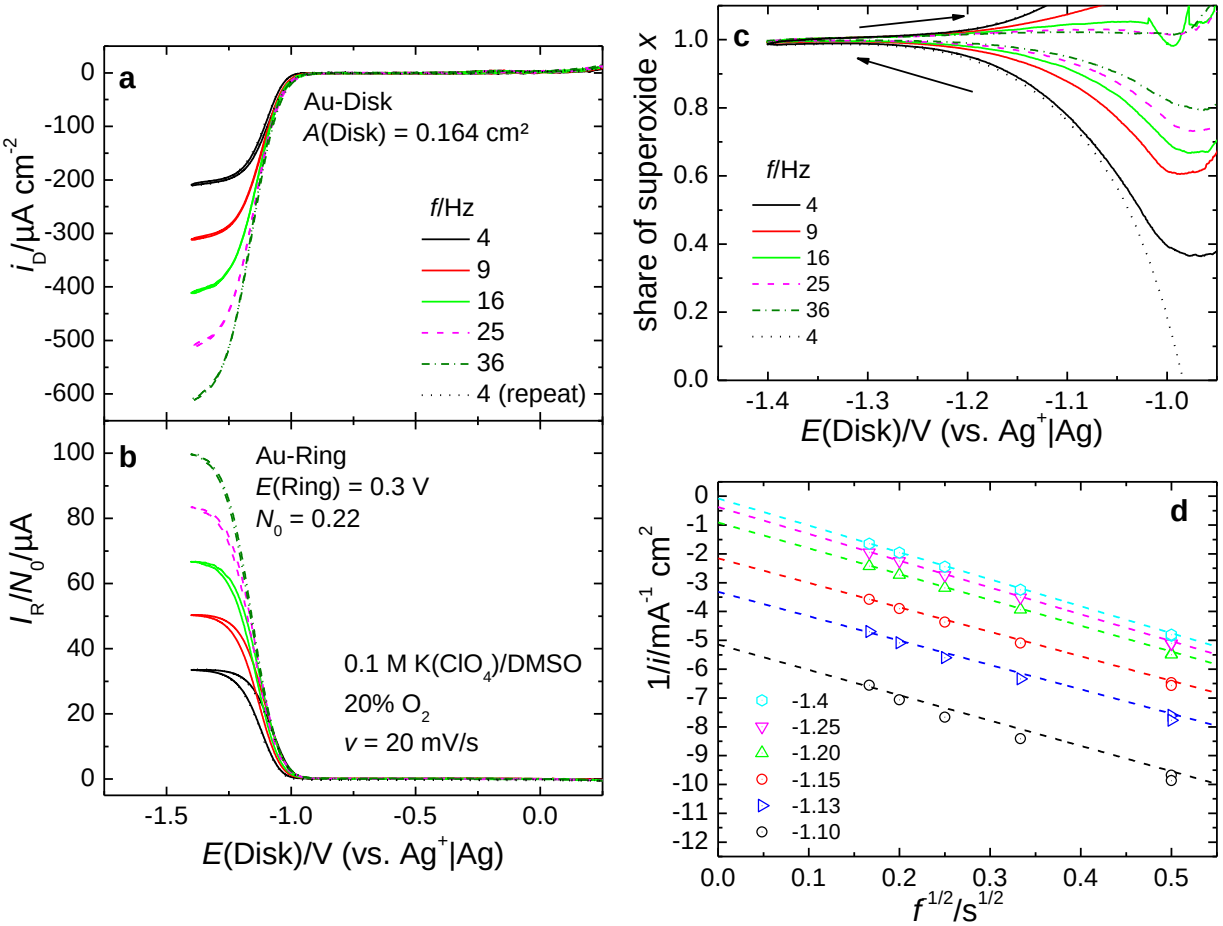

Figure 8.7. RRDE measurements of the ORR using an Au-disk/Au-ring assembly. **a.** Currents at the gold disk. **b.** Corresponding currents at a gold ring electrode. **c**. Share of superoxide *x* according to eq. (8.9). **d**. Koutecký-Levich plots according to eq. (8.10) for different potentials at the disk electrode. Electrolyte: 0.1 M $KClO_4$ in DMSO saturated with 20% O_2

As can be seen from Figure 8.7 a and b, down to a potential of −1.4 V there is no indication of electrode deactivation in accordance with the formation of soluble superoxide. With assumption that only superoxide and peroxide are formed (i.e. a one or two electron process is observed) the share of superoxide *x* of the total amount of species can be calculated from the ring current I_R and the disk current I_D:

$$x = \frac{2 \cdot I_R}{\left| I_D / N_0 \right| + I_R} \tag{8.9}$$

Equation (8.9) follows from simple mass balances at the disk and ring electrode. As expected, the share of superoxide is close to unity (Figure 8.7 c). The initially lower values at potentials around −1.0 V are most probably artifacts due to the slight delay of the ring current with respect

to the disk current (for a rotation rate of 4 Hz, the expected, average time delay is 800 ms[111], which is translated to 16 mV at 20 mV/s). While the overall observed current density is limited by kinetics as well as diffusion, only the kinetic part is influenced by the electrode and contains information about the reaction mechanism. To obtain the part of the current density which is only limited by the charge-transfer kinetics (i_{CT}), the Koutecký-Levich equation[96] can be used, if the reverse reaction is ignored (which is only valid at large overpotentials):

$$\begin{aligned}\frac{1}{i} &= \frac{1}{i_{CT}} + \frac{1}{i_{Diff}} \\ &= \frac{1}{zFk_{CT}(E)c(\mathrm{O_2})} + \frac{\nu^{1/6}}{0.62zFD_O^{2/3}c(\mathrm{O_2})\sqrt{2\pi f}}\end{aligned} \tag{8.10}$$

In eq. (8.10) i_{Diff} denotes the diffusion-limited current, z is the number of electrons transferred, $k_{CT}(E)$ is the potential-dependent rate constant, ν is the kinematic viscosity, $c(O_2)$ is the oxygen concentration, D_O its diffusivity and f is the rotation rate in revolutions per second. As expected from eq. (8.10) parallel, linear plots are obtained with potential-dependent intercepts (Figure 8.7 d). The current density due to charge transfer can now be used to gain further mechanistic insights. A diagnostic criterion for the rate-determining step (if any step can be signified as rate-determining) is the Tafel-slope b which is defined according to eq. (8.11) (although usually the overpotential η with $\eta = E - E_{eq}$ instead of the potential E is used), where a is a constant and contains information about the exchange current density:

$$E = a - b\log\left(i_{CT}\right) \tag{8.11}$$

The corresponding Tafel-plots are shown in Figure 8.8 a. Two distinct regions of different slope can be identified, one giving a slope of 66 mV/dec in a potential window between −900 mV and −1000 mV and the other giving a Tafel-slope of 130 mV/dec between −1050 mV and −1300 mV. While a Tafel-slope of 120 mV/dec is indicative of a one-electron transfer as the rate-determining step and has been observed for the ORR in TBA^+-[61] and Li^+-containing DMSO[282], a “Tafel”-slope of 60 mV/dec is obtained for highly reversible, electrochemical reaction and has been observed for the ORR in TBA^+-containing DMSO [32] and propylene carbonate [68] as well as K^+-containing DMSO at glassy carbon [311]. For a fully reversible system, a plot according to eq. (8.12) should yield a straight line[96] with an intercept equaling the half-wave potential $E_{1/2}$:

$$E = E_{1/2} + \frac{RT}{F}\ln\left(\frac{i_{Diff} - i}{i}\right) \tag{8.12}$$

Thus, a plot of the potential versus the decadic logarithm of the kinetic current should yield a straight line with a slope of 59 mV at 25 °C. The corresponding plot at a rotation rate of 36 Hz is shown in Figure 8.8 b. The similarity of the slopes of the two plots is evident from the comparison of the current due to charge transfer (i_{CT}) as described by eq. (8.10) and the expression in the logarithm in eq. (8.12):

$$\ln\left(i_{CT}\right) = \ln\left(\frac{i_{Diff}\cdot i}{i_{Diff}-i}\right) = \ln\left(i_{Diff}\right) - \ln\left(\frac{i_{Diff}-i}{i}\right) \tag{8.13}$$

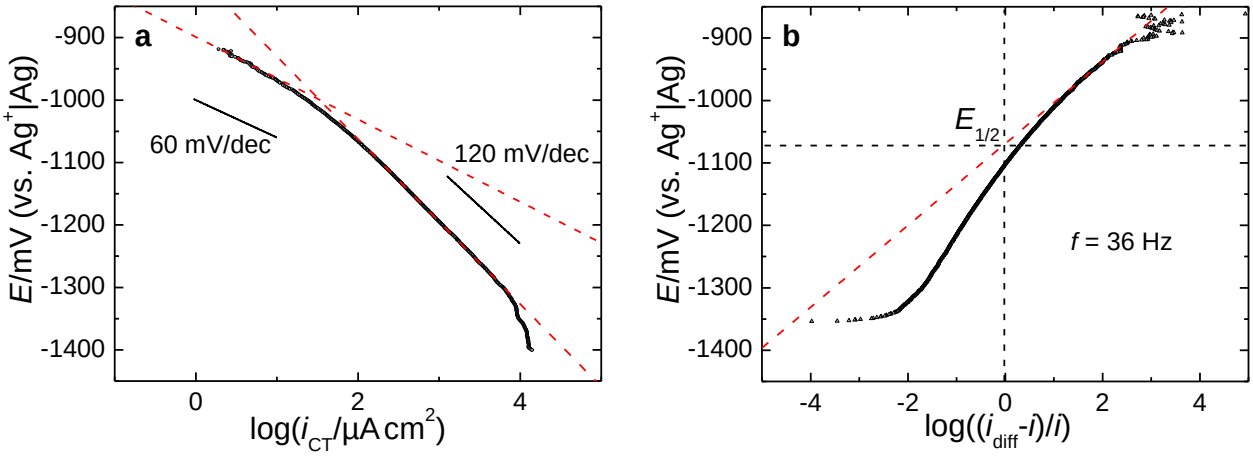

Figure 8.8. Evaluation of the ORR currents obtained at a rotating ring-disk electrode. **a.** Tafel-plots (eq. (8.11)) according using the kinetic currents evaluated according to Figure 8.7 d. **b.** Determination of the half-wave potential according to eq. (8.12) using the currents obtained at a rotation rate of 36 Hz. Electrolyte: 0.1 M $KClO_4$ in DMSO saturated with 20% O_2.

8.4.5 Evaluation of the Formal Potential of the O_2–O_2^- Redox Couple

The formal potential can conveniently be determined from cyclic voltammetry as well as methods under forced convection [96]. While rate constant of the superoxide formation might depend on the electrode material being a kinetic parameter, the formal potential is independent from kinetics and a purely thermodynamic parameter. However, the usual methods for evaluation of the formal potential rely on the reversibility of the reaction as otherwise kinetic correction have to be taken into account [96]. Therefore, we chose the ORR at the glassy carbon as the model system to determine the formal potential of the oxygen–superoxide couple $E^o(O_2|O_2^-)$ in the presence of K^+. At the lowest sweep rate 9 mV s^{-1}, reversibility is the highest and a half-peak potential of −1.031 V is obtained, which corresponds very well with the half-peak potential at platinum of −1.030 V (for comparison the value for gold is −1.046 V from Figure 8.4 a). The half-peak potential $E_{p/2}$ can be transformed to the half-wave potential $E_{1/2}$ according to eq. (8.14), where the number of electrons z equals one:

$$E_{p/2} = E_{1/2} + 1.09\cdot\frac{RT}{zF} \tag{8.14}$$

The half-wave potential is directly related to the formal potential via the ratio of the diffusion coefficients of oxygen D_O to the diffusion coefficient of superoxide D_R:

$$E_{1/2} = E_0 - \frac{RT}{F} \ln\left(\left(\frac{D_O}{D_R}\right)^{1/2}\right) \tag{8.15}$$

The resulting formal potential for the superoxide couple is $E^o(O_2|O_2^-) = -1.028$ V at glassy carbon, −1.027 V at platinum and −1.043 V at gold. From the peak potential c2 (Figure 8.4 b) at a sweep rate of 9 mV s^{-1} a half-wave potential of $E_{1/2}(O_2^-|O_2^{2-}) = -1.54$ V is obtained for gold.

Alternatively, the formal potential can be evaluated from the measurements using the rotating electrode. The half-wave potential at the gold electrode $E_{1/2}$ equals −1069 mV and is connected to the formal potential E^o according to eq. (8.16).

$$E_{1/2} = E^0 - \frac{RT}{F} \ln\left(\left(\frac{D(O_2)}{D(O_2^-)}\right)^{2/3}\right) \tag{8.16}$$

The formal potential gives a final value of $E^o = -1027$ mV. The same evaluation of the currents at the glassy carbon electrode (Figure S 8.7) shows that at glassy carbon the reversible behavior of the ORR is exhibited in a much broader potential window of 200 mV (a rotation rate of 4 Hz was chosen in this case as the diffusion-limited current is most clearly visible at this rate). The half-wave potential determined from Figure S 8.7 c has a value of −1060 mV and thus, translates to a formal potential of −1018 mV, which is in satisfying agreement with the values obtained from cyclic voltammetry and the data obtained at the gold electrode.

8.4.6 The Effect of Water Contaminations on the ORR/OER

As water is a nearly ubiquitous contaminant and is especially of concern if air is used as an oxygen supply, the final paragraph shall be devoted to the elucidation influence of water on the oxygen reduction. As can be seen from Figure 8.9 a, increasing the water content leads to a shift of the transition from the one-electron process to the two-electron process to more positive potentials. Moreover, the current exceeds the currents expected for a two-electron reduction from a water content of 100 ppm on, while the current for the one-electron remains unaffected, implying that the presence of water has little to no effect on the superoxide formation, which is also obvious from the share of superoxide (Figure 8.9 c). It is noteworthy that the re-oxidation peak of the peroxide in the anodic scan increases with increasing water content, implying that even in the presence of water mainly insoluble peroxide is formed at potentials below −1.4 V. However, the absolute height of the peak is also influenced by the choice of the lower potential relative to the transition potential and therefore, is difficult to compare. The ratio between the re-oxidation peak and the cathodic reduction charge below the peroxide-formation potential, as indicated by the share of superoxide (Figure 8.9 c) stays constant for 40 and 100 ppm, but decreases for higher water contents indicating the formation of side products, which can also be seen by the anodic currents arising at −0.6 Vs.

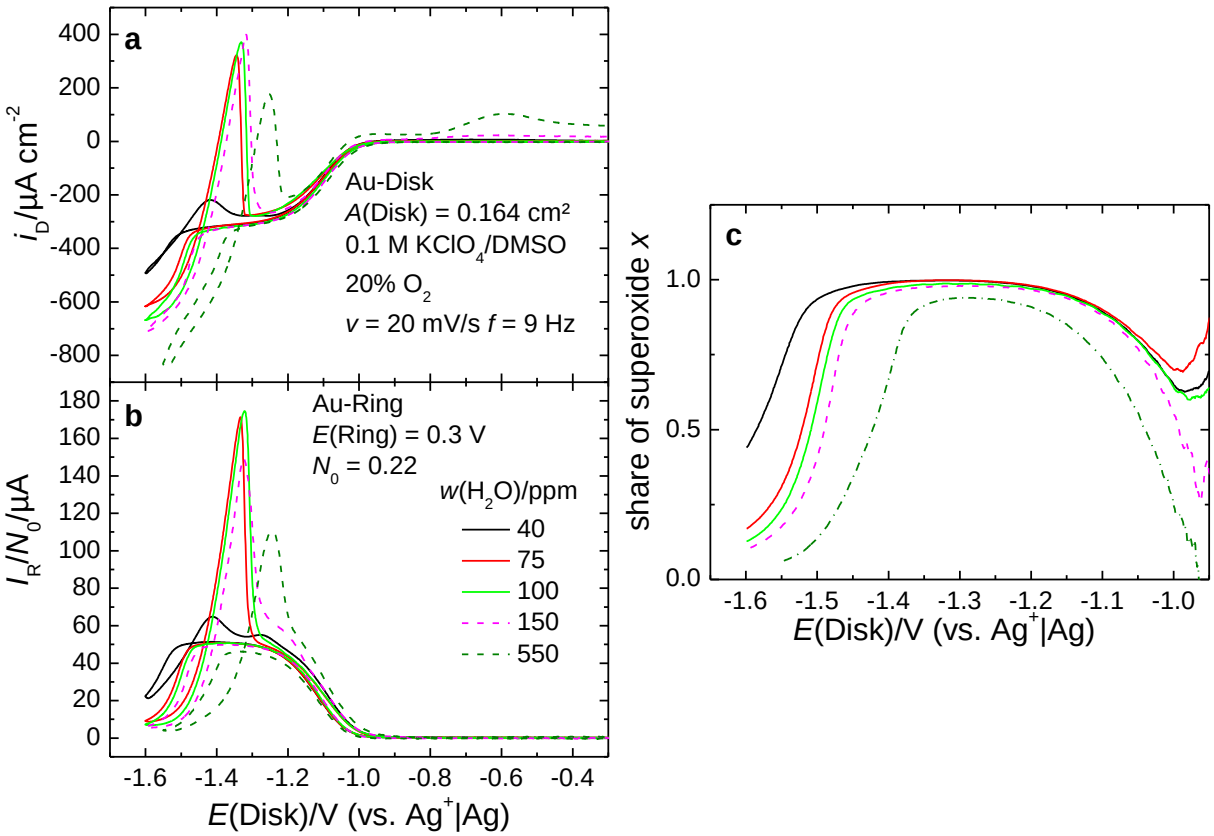

Figure 8.9. CVs at a gold-disk/gold-ring electrode for different concentrations of water. **a.** Disk currents for a fixed rotation rate of 9 Hz and a sweep rate of 20 mV s^{-1} (for clarity of presentation the measurement with a water content of 300 ppm is omitted). **b**. Corresponding ring currents. **c**. Share of superoxide. Electrolyte: 0.1 M $KClO_4$ in DMSO, saturated with 20% O_2.

The fact that the transition from the one-electron to the two or many-electron process shifts to positive potentials has an important implication: While the peroxide formation in the absence of water is a rather reversible process (as shown above), the equilibrium is disturbed by the presence of water, which presumably reacts with the peroxide. Therefore, the half-wave of the reduction potential is shifted to more positive values (Figure 8.10 a) with increasing water content. Unfortunately, the determination of the half-wave potential proves difficult as for water contents above 100 ppm the contribution of a more-electron process becomes more significant, shifting the apparent half-wave potential of the peroxide formation to even more positive values, which complicates quantitative evaluation. Quantitatively, the influence of a homogenous reaction with the rate constant *k* following a (quasi)-reversible, electrochemical reaction is described by eq. (8.17) [337] (assuming that *k* is large as compared to the rotation rate):

$$E_{1/2} = E^0 - \frac{RT}{zF}\ln\left(1.61D^{-1/6}\nu^{1/6}\right) + \frac{RT}{2zF}\ln\left(\frac{k}{2\pi f}\right) \qquad (8.17)$$

Therefore, a plot of the half-wave potential versus the decadal logarithm of the rate constant should yield a straight line with a positive slope of 30 mV/dec for a one-electron process at

25°C. Note that the rate constant of the homogeneous reaction, namely the reaction of the peroxide with water, might be interpreted as a pseudo first-order rate constant if the water concentration is treated as constant (which is only justified for concentration significantly much larger than 0.4 mM, which is the concentration of O_2 in this electrolyte [325]). On the contrary, the corresponding plot of the half-wave potential versus the rotation frequency would yield a straight line with a negative slope of −30 mV/dec. Plots according to eq. (8.17) are shown in Figure 8.10 (the data was evaluated from Figure 8.9, Figure S 8.8 and additional CVs, which are not shown). While the dependence on the water content does not follow eq. (8.17), the dependence on rotation rate is very well followed as shown in Figure 8.10 b.

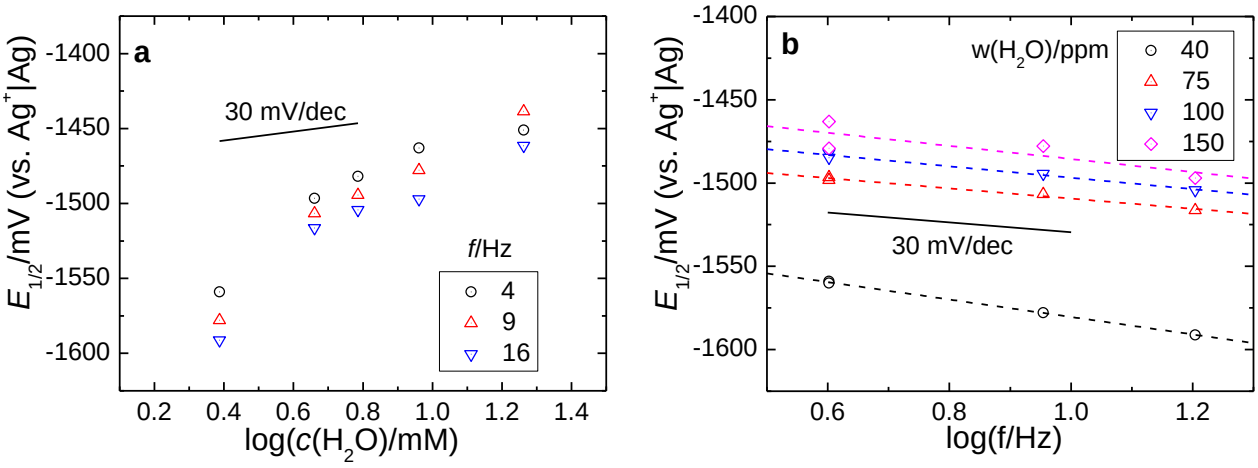

Figure 8.10. Evaluation of the half-wave potential of peroxide formation. **a.** Dependence on the water content. **b**. Dependence on the rotation rate. Data was taken from Figure 8.9, Figure S 8.8 and additional CVs which are not shown. Evaluation according to eq. (8.17).

Reasons for the significant deviations with respect to the water concentration might be associated to the uncertainty of the starting water content as well as the fact that initially, the water concentration is not much higher than the oxygen concentration and therefore cannot be treated as constant. However, the larger slope might also imply that the water concentration does not enter the rate law in a simple linear manner but in a quadratic fashion, giving rising to a theoretical slope of 60 mV/dec. Similar plots using the half-wave potential for the superoxide formation are shown in Figure S 8.9. The fact that the half-wave potential for the superoxide actually shifts with a slope of 30 mV/dec as expected from eq. (8.17) shows that superoxide also reacts with water although the influence of water on the peroxide formation is larger. It is noteworthy that the rate constant of the reaction between water and superoxide in DMSO, which is reported in literature ($k = 1.2 \times 10^{-4}\ M^{-1}s^{-1}$ [338], translating to a pseudo-first order rate constant of $0.3 \times 10^{-6}s^{-1}$ to $8 \times 10^{-6}s^{-1}$ in the experiment), is small as compared to the rotation frequency. However, for the validity of eq. (8.17) the rate constant of the homogenous reaction has to be significantly larger than the rotation frequency. Thus, in light of these results, we propose that the actual rate constant of the decomposition reaction is much larger than reported.

Finally, the formation of side products in the presence of water has been investigated using isotopically labelled water ($H_2{}^{18}O$) in a highly sensitive thin-layer DEMS cell with a gold electrode under stagnant conditions [122] (Figure 8.11). The high ratio of the real surface area (2.8 cm^2) to the small electrolyte volume (5.6 µL) confined in a thin-layer helps simulating battery-like conditions. As shown in Figure 8.11 a, a distinct transition in the faradaic current is not visible, although a slight change in the slope at a potential of −1.2 V still indicates the presence of two processes. Parallel to that, the oxygen consumption remains constant indicating a diffusion-limited process (Figure 8.11 b). A significant difference to the other measurements is that a high concentration of superoxide is established during the reaction (up to 15 mM as calculated from the overall charge passed) fostering a pronounced precipitation and alleviating peroxide formation[325].

As shown in Figure 8.11 c, the signal for $H_2{}^{18}O$ decreases from a potential of −1.2 V on substantiating the hypothesis of a fast reaction between peroxide and water, while the reaction with superoxide does not seem to be that facile. The evolution of CO_2 is observed in the anodic scan between 0 and 0.5 V, which is tentatively attributed to the oxidation of carbonates produced by side reactions of the reactive oxygen species with the solvent[339]. Astonishingly, the evolution of CO_2 is not only not accompanied by an evolution of O_2, as expected in the case of Li_2CO_3 [339], but corresponds to a *consumption* of oxygen (Figure 8.11 b, inset). Note that the formation of singlet oxygen would not explain a consumption of oxygen, but only the absence of an evolution. However, during oxidation of the insoluble species reactive intermediates might form which react with oxygen as has been previously reported in e.g. aqueous electrolytes [340]. Considering the 1.4-times higher relative ionization probability of CO_2 to O_2 one oxygen molecule is consumed for every CO_2 evolved. Increasing the water content leads to a decrease of the overall evolution of CO_2 (Figure 8.11 d). No significant indication for the evolution of isotopically labelled CO_2 has been identified.

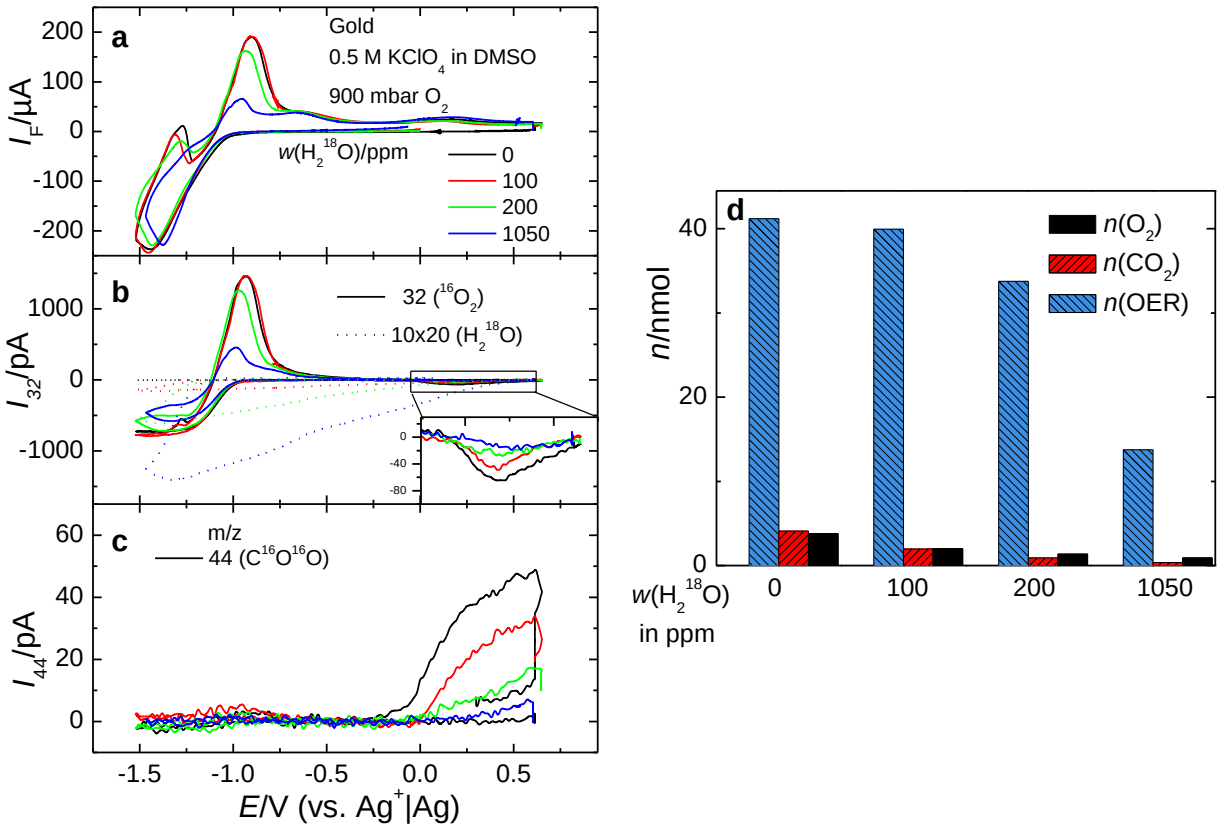

Figure 8.11. Influence of $H_2{}^{18}O$ on the ORR and OER in a thin-layer cell. **a**. CV for different fractions of $H_2{}^{18}O$. **b**. Corresponding MSCV on mass 32 (O_2) and 20 (dotted, $H_2{}^{18}O$). The inset shows a magnification of the oxygen consumption at anodic potentials between 0.25 V and 0.75 V **c.** Corresponding signals for masses 44 (solid, CO_2). **d.** Amounts of consumed species obtained from integration of the MSCV. $Q(O_2)$ denotes the amount of oxygen consumption between 0.25 and 0.75 V.

The findings might be rationalized as follows. The first reaction step involves a reaction between the peroxide and water, which is first order with respect to water.

$$K_2{}^{16}O_2 + H_2{}^{18}O \rightarrow K^{16}O^{16}OH + K^{18}OH \tag{8.18}$$

KOOH has been hypothesized in the past to oxidize DMSO to dimethyl sulfone[341]:

$$K^{16}O^{16}OH + (CH_3)_2S^{16}O \rightarrow K^{16}OH + (CH_3)_2S^{16}O_2 \tag{8.19}$$

The corresponding $DMSO_2$ only contains ^{16}O and is speculated to be the main source of the CO_2 in the anodic sweep (no indications for $C^{18}O_2$ or $C^{18}O^{16}O$ have been identified). It should be noted that the large currents in the RRDE measurements in Figure 8.9 indicate that the ORR in the presence of high amounts of water does not stop at the stage of peroxide, but direct formation of KOH, which would inhibit a reaction according to eq. (8.18) might also be possible. This would eventually lead to a decrease of the CO_2 signal as observed in the experiment. The oxygen consumption during the CO_2 evolution might be understood in analogy to previous observations [340]. Although the mixture of KOH/DMSO is used as a superbase in organic synthesis[342], the formation of DMSO radicals in the presence hydroxide has been

reported [343]. A similar hypothesis has been given by Yang et al. [344], which would explain that one molecule of oxygen is consumed per CO_2:

$$\begin{aligned} K_2CO_3 &\rightarrow CO_2 + 2K^+ + O_2^- \\ O_2^- + O_2 + \text{electrolyte} &\rightarrow \text{products} \end{aligned} \tag{8.20}$$

It is noteworthy that the absence of oxygen evolution in the case of Li^+-containing electrolytes has been attributed to the formation of highly reactive singlet oxygen[339] and would also explain the observed absence of any O_2 evolution during carbonate oxidation as observed by Yang et al. However, in the present case, oxygen is actually consumed, which might imply a reaction according to eq. (8.20), but does not exclude formation of singlet oxygen.

8.5 Conclusions

By investigating the kinetics of the oxygen reduction in $KClO_4$-containing DMSO it has been shown that the K–O_2 system is a well-behaved system, which make it an attractive system for further, battery-related research although stability issues of K-metal with DMSO will have to be addressed, e.g. via an K^+-conducting membrane which protects the potassium metal anode from the solvent and oxygen cross-over. Utilizing gold, platinum and glassy carbon as electrode materials a dependence of the reversibility of the oxygen–superoxide couple on the electrocatalyst has been identified, with gold being the worst electrocatalyst regarding the kinetics of the superoxide formation. While this does not preclude that parts of the reaction proceed via an outer-sphere mechanism, this shows that at least some kind of adsorption is involved in the reaction. The results of the kinetic analysis are summarized Table 8.1. Interestingly, kinetics are most facile at glassy carbon, which is pleasant from a practical point of view.

Table 8.1: Standard rate constants of the superoxide couple k_1^0 (eq. (8.3)), standard rate constant of the peroxide couple k_2^0 (eq. (8.4)), the formal potential of the oxygen–superoxide couple in presence of K^+ $E^{o\prime}$ and the mass-corrected "Tafel-slope" b as determined from RRDE measurements[a]

Electrode	**10^3 k_1^0/cm s^{-1}**	**10^3 k_2^0/cm s^{-1}**	**$E^{o\prime}$/V**	**b/mV/dec**
Gold	0.94	0.69	−1.035	60–120
Glassy Carbon	4.98	0.89	−1.023	67
Platinum	4.06		−1.027	

[a] The transfer coefficient determined at gold equals 0.6. Electrolyte: 0.1 M $KClO_4$, saturated with 20% O_2.

Moreover, from the addition of small amounts of potassium perchlorate to a tetrabutyl-ammonium perchlorate solution significant ion-pairing between superoxide and K^+ has been shown, which leads to a shift of the half-wave potential to more positive potentials. The ion-pairing constant has been evaluated as $K_{ion} = 7.25 \times 10^2$ mol L^{-1}. Due to the very efficient ion-pairing between peroxide and K^+ the relevant equilibrium constant could not be evaluated. The

positive shift of the half-wave potential in presence of K^+ as compared to TBA^+ shows that the interaction between K^+ and superoxide is actually stronger than the interaction between TBA^+ and superoxide. This is direct evidence against the current misconception of the HSAB-theory in the field of metal–air batteries, which states that the interaction between the *soft* Lewis acid TBA^+ and the *soft* superoxide is of particular strength and leads to a stabilization of the superoxide. Our results show that the acid *strength* of the ions cannot be neglected (K^+ is a *hard*, but relatively *strong* Lewis acid) and that the overall interaction between TBA^+ and O_2^- is weak as compared to K^+ and O_2−. In other words, stronger Lewis acids like K^+ and Li^+ interact more strongly with O_2^-, which eventually leads to disproportionation, while TBA^+ only weakly interacts with O_2^-.

The addition of water alleviates both, the formation of K_2O_2 and KO_2, which has been interpreted in terms of a subsequent reaction. However, the effect of water on the peroxide formation is much more pronounced as compared to the effect on the superoxide formation. Moreover, CO_2 evolution at anodic potentials is inhibited in the presence of larger amounts of water and does not directly originate from water contaminations in the electrolyte as shown by the use of isotopically labelled water. The unexpected consumption of oxygen, which occurs in parallel to CO_2 evolution, has to be further investigated with prospects of valuable insights into decomposition reactions related to superoxide and peroxides in general.

8.6 Supporting Information

8.6.1 Thermodynamic Considerations on different K_xO_y Species and KOH

As pointed out in the introduction of the main paper, the K–O_2 system exhibits a special thermodynamic behavior as compared to Li–O_2, Na–O_2 or Mg–O_2. Thermodynamically expected properties as well as the expected standard potentials in the experiment for different oxygen-containing potassium species are listed in Table S 8.1. Note that the free standard enthalpies refer to the solid states of the K–O_2 species, while during the experiments mostly soluble superoxide forms, which additionally is stabilized by solvation. This might be a reason why Fujinaga *et al*. actually observed a potential shift of 0.51 V between the half-wave potentials of KO_2 and K_2O_2 [40], while the potential shift between K_2O_2 and K_2O is 0.55 V which fits very well with the expected shift of 0.56 V. For sake of simplicity and clarity, inclusion of activity coefficients into the equations is neglected in the further discussion and formal potential will be used instead of standard potentials.

Table S 8.1 Thermodynamically Expected Parameters of the K–O_2 System[a]

	$\Delta_F G$/kJ mol^{-1}	ΔE^o/V	u/W h kg^{-1}	E^o (vs Ag^+|Ag)/V
KO_2	−240.589	2.49	940	−0.96
K_2O_2	−429.758	2.23	1083	−1.22
K_2O	−322.094	1.67	950	−1.78
KOH	−378.899	/	/	/

[a] $\Delta_F G$: Free enthalpy of formation taken from Chase *et al*. [14]. ΔE^o: Thermodynamically expected cell voltage. u: Specific energy with respect to the mass of the product. E^o (vs Ag^+|Ag): Expected standard potential with respect to the silver/silver nitrate electrode in DMSO used in this work. The standard potentials E^o (vs Ag^+|Ag) have been calculated using the potential of the K|K^+ redox couple in DMSO (-3.02 V vs the standard hydrogen electrode (SHE) [216]) and the formal potential of the reference electrode, which is 0.43 V vs SHE, using the standard potential of 0.49 V reported by Gritzner[216].

8.6.2 Evaluation of the Standard Rate Constants of Superoxide Formation

Additional cyclic voltammograms at different sweep rates used for the evaluation of the standard rate constants of the superoxide are shown in this section. Figure S 8.1 a contains additional CVs at the gold electrode, while the peak separation with respect to the logarithm of the sweep rate is shown in Figure S 8.1 b, including data from Figure 1 of the main paper. Note that it was not necessary to correct for the Ohmic potential drop due to the very small currents and the low resistance (typically around 3.3 Ω cm² as determined via impedance spectroscopy), leading to a maximum correction of less than 1 mV in the peak.

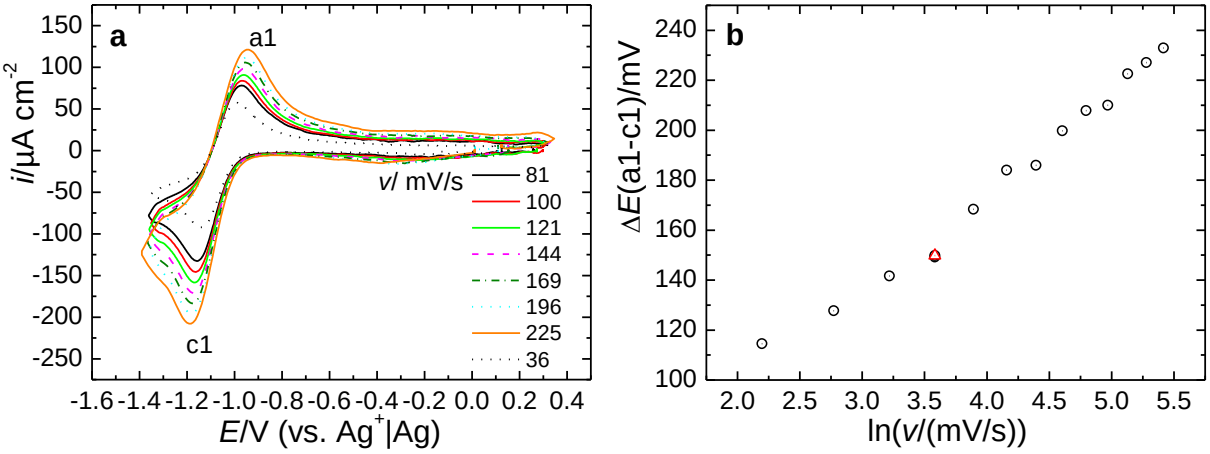

Figure S 8.1. Cyclic voltammetry of the ORR at gold. **a.** Additional cyclic voltammograms at higher sweep rates. **b**. Potential separation of the peaks a1 and c1 versus the logarithm of the sweep rate (including data from Figure 8.4). The red triangle indicates the repeated measurement for 36 mV s^{-1}. Electrolyte: 0.1 M $KClO_4$ in DMSO saturated with 20% O_2

Cyclic voltammograms at the glassy carbon electrode are shown in Figure S 8.2 a. Note that only every second CV is shown for clarity of presentation. The peak separation versus the logarithm of sweep rate is shown in Figure S 8.2 b.

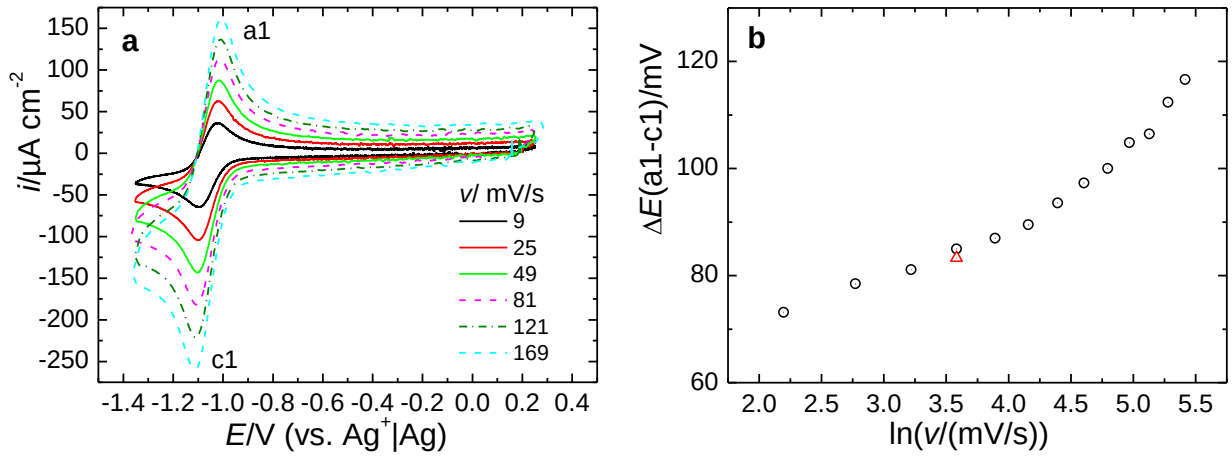

Figure S 8.2. Cyclic voltammetry of the ORR at glassy carbon. **a.** CVs for different sweep rates (for clarity, only every second CV is shown). **b**. Potential separation of the peaks a1 and c1 versus the logarithm of the sweep rate. The red triangle indicates the repeating measurement for 36 mV s^{-1}. Electrolyte: 0.1 M $KClO_4$ in DMSO saturated with 20% O_2

Finally, the CVs at a platinum electrode are presented in Figure S 8.3 a (only second CV is shown) and the peak separation versus the logarithm of the sweep rate is depicted in Figure S 8.3 b. Note the similar peak separations for the platinum and glassy carbon electrode as opposed to gold, implying a surface sensitivity of the superoxide formation and therefore, a mechanism probably deviating from a simple outer-sphere reaction.

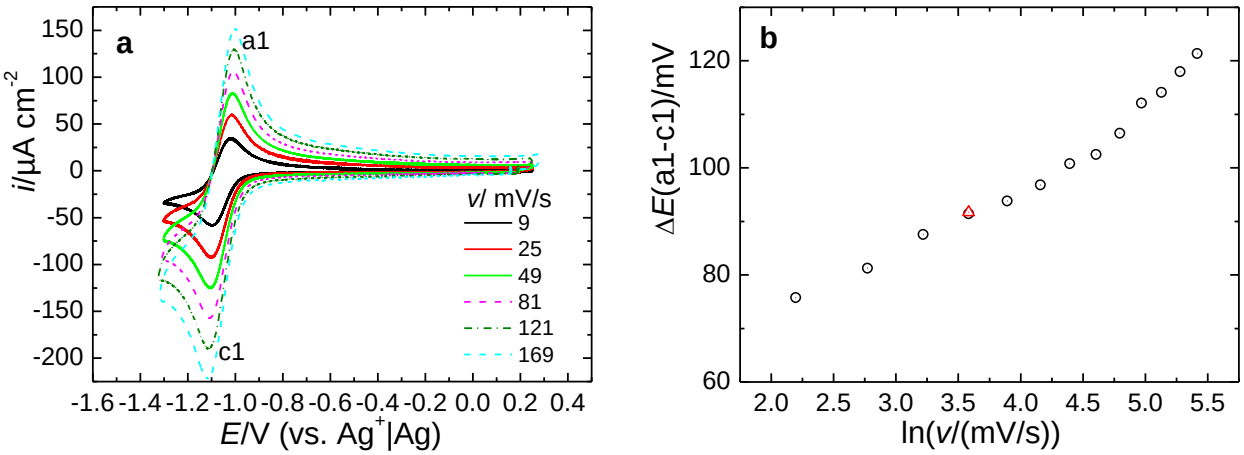

Figure S 8.3. Cyclic voltammetry at platinum. **a.** CVs for different sweep rates (for clarity, only every second CV is shown). **b**. Potential separation of the peaks a1 and c1 versus sweep rate. The red triangle indicates the repeating measurement for 36 mV s^{-1}. Electrolyte: of the ORR in 0.1 M $KClO_4$ in DMSO saturated with 20% O_2.

8.6.3 Evaluation of the Standard Rate Constant for Peroxide Formation at Gold

In contrast to the superoxide formation the reduction of superoxide to peroxide leads to insoluble species creating certain obstacles for the evaluation of the standard rate constant as the anodic peak a2 is not purely diffusion-limited anymore. However, to get an approximate idea of the rate constant, the same evaluation method as for the superoxide has been applied.

Additional CVs for the gold electrode are shown in (Figure S 8.4 a), while a plot of the peak separation versus the logarithm of the sweep rate is shown in Figure S 8.4 b.

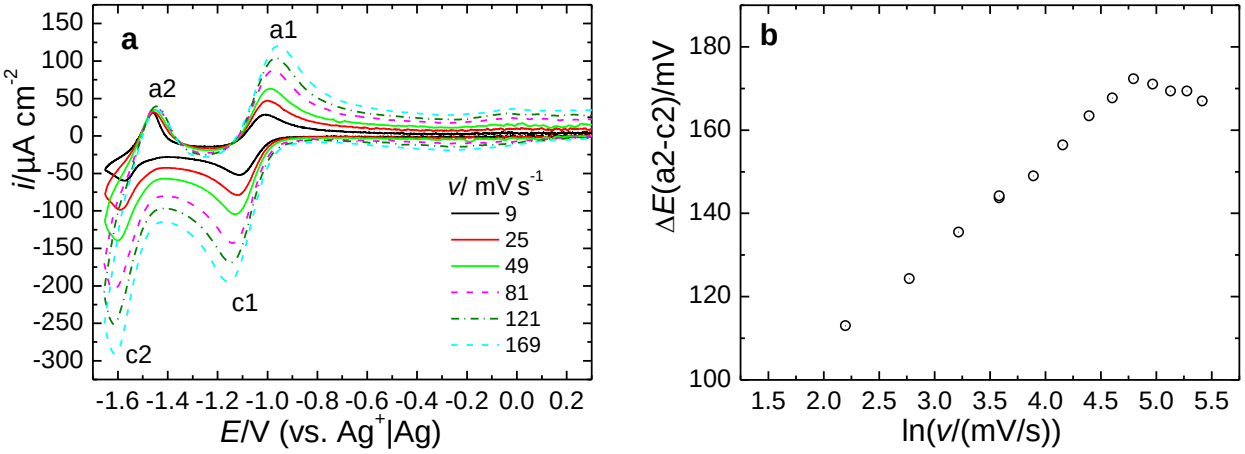

Figure S 8.4. Cyclic voltammetry of the ORR at gold up to a lower limit of −1.6 V. **a.** Additional cyclic voltammograms at higher sweep rates. **b**. Potential separation of the peaks a1 and c1 versus sweep rate (including data from Figure 8.4). The red triangle indicates the repeating measurement for 36 mV s^{-1}. Electrolyte: of the ORR in 0.1 M $KClO_4$ in DMSO saturated with 20% O_2.

Related data for the glassy carbon electrode is shown in Figure S 8.5 a and b. Note that only every second CV is shown for clarity of presentation. The corresponding values of the ψ-function are shown in Figure S 8.6 a and the final evaluation is presented in Figure S 8.6 b. In the case of the gold electrode significant deviations from a linear behaviour are discernible for sweep rates above 100 mV s^{-1}, while for glassy carbon the plot is only linear for sweep rates which are greater than 49 mV s^{-1}. The latter might be understood in terms of deactivation of the electrode surface which is more significant at lower sweep rates. The actual evaluation of the slope has only been carried out in the respective, linear range of sweep rates mentioned above.

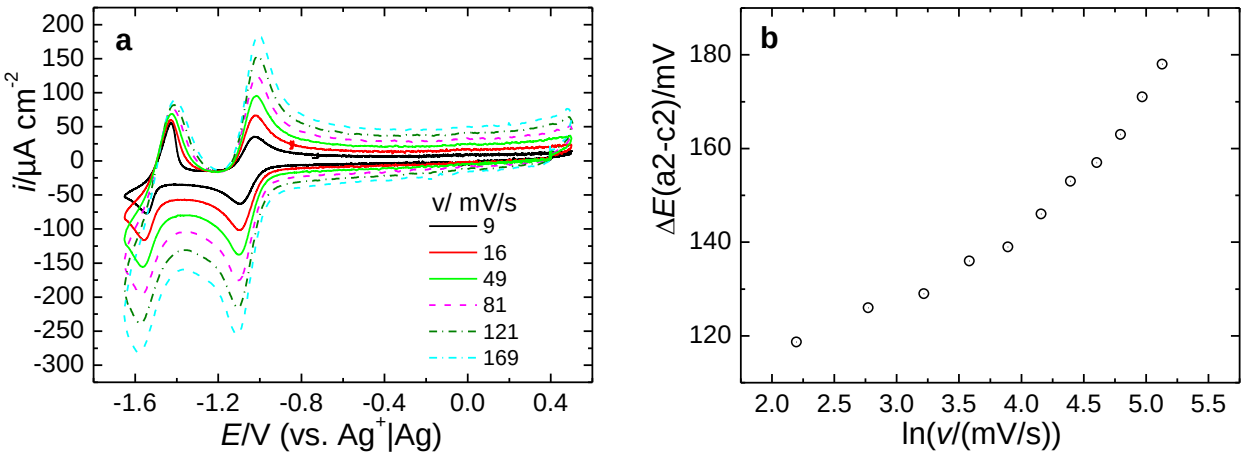

Figure S 8.5. Cyclic voltammetry of the ORR at glassy carbon up to a lower limit of −1.6 V. **a.** Cyclic voltammograms for different sweep rates (for clarity, only every second CV is shown). **b**. Potential separation of the peaks a1 and c1 versus logarithm of sweep rate. Electrolyte: of the ORR in 0.1 M $KClO_4$ in DMSO saturated with 20% O_2.

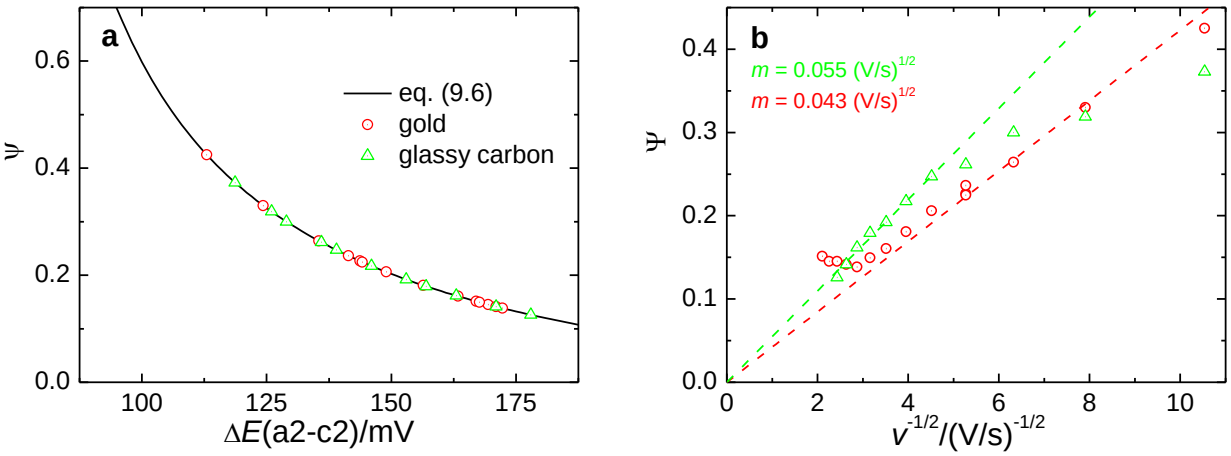

Figure S 8.6. Graphical representation of the evaluation of the standard rate constant from the peak separation Δ*E*. **a.** Correlation between ψ and the peak separation Δ*E*. **b.** Evaluation of the standard rate constant from the ψ-function and the inverse square root of the sweep rate.

8.6.4 Analysis of the Oxygen–Superoxide Couple using Forced Convection

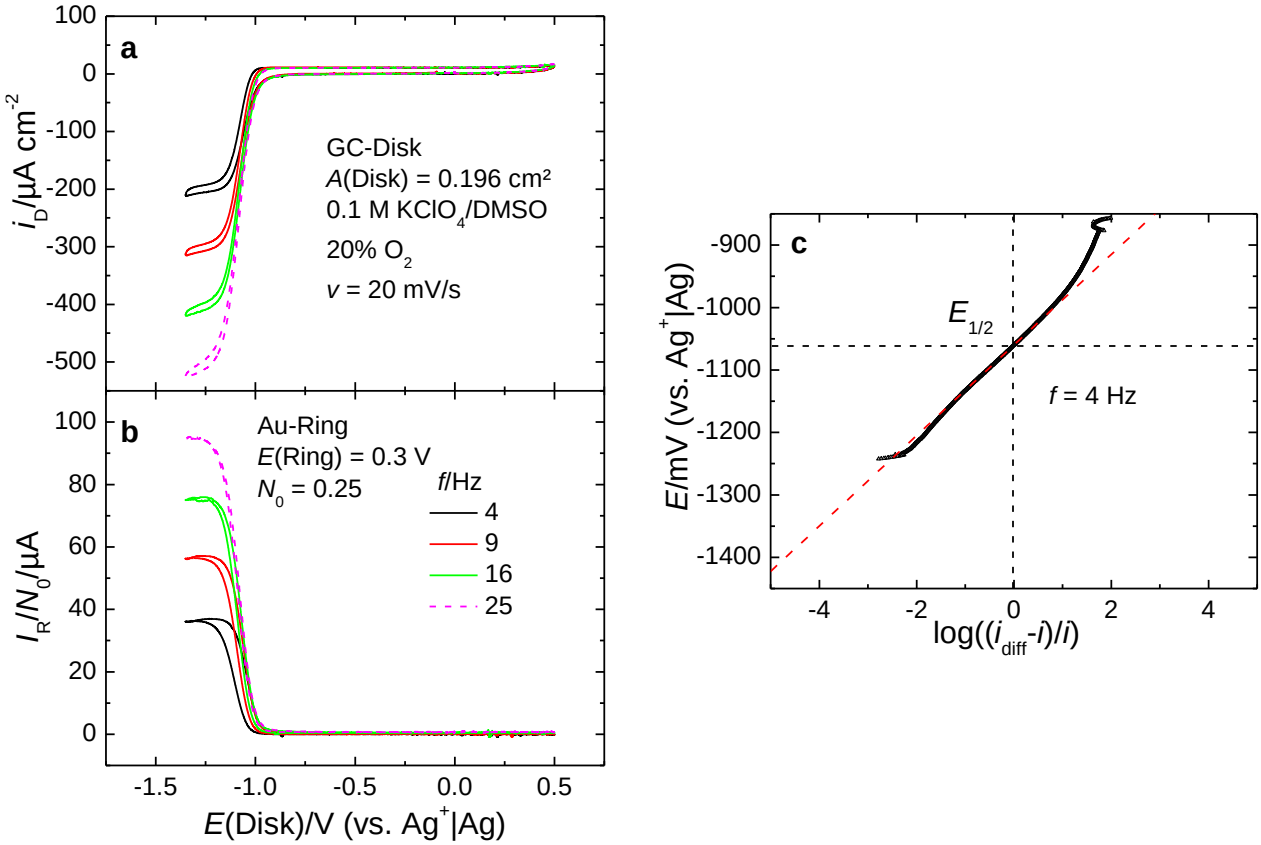

Figure S 8.7. Rotating ring-disk electrode measurements of the ORR using a GC-disk/Au-ring assembly. **a.** Currents at the glassy carbon disk. **b.** Corresponding currents at a gold ring electrode. **c**. Determination of the half-wave potential using the currents obtained at a rotation rate of 4 Hz. Electrolyte: of the ORR in 0.1 M $KClO_4$ in DMSO saturated with 20% O_2..

8.6.5 Influence of Water Contaminations on the ORR/OER

As shown in Figure S 8.8 a and b, the increasing water content leads to a higher peak of a2, but does not directly affect the total share of superoxide (Figure S 8.8 c) or the reaction kinetics (Figure S 8.8 d).

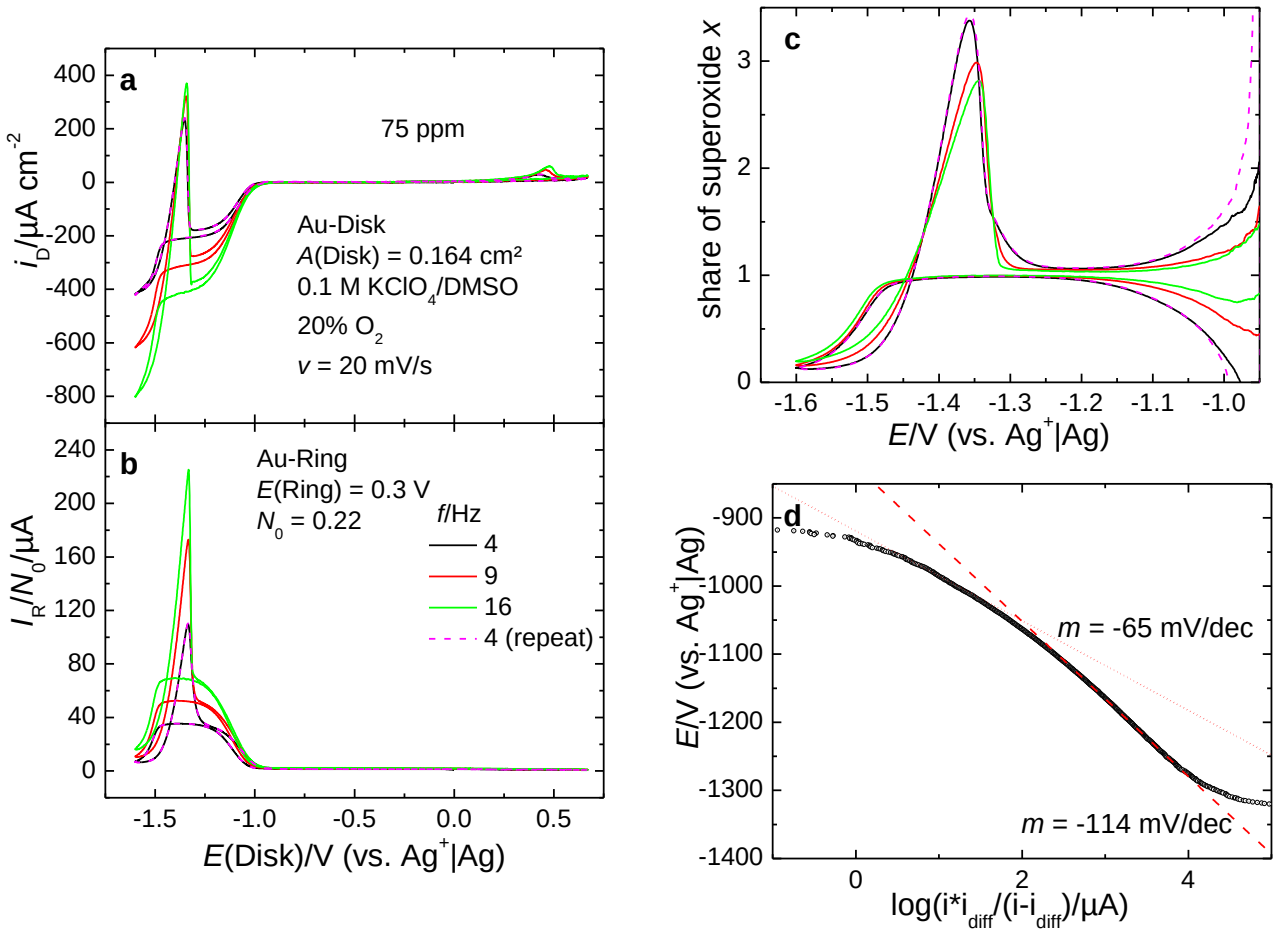

Figure S 8.8. Rotating ring-disk measurements at glassy gold electrode for different rotation rates. **a.** Current densities obtained at the disk electrode. **b**. Corresponding ring currents normalized to the geometric collection efficiency N_0. **c**. Share of superoxide. **d.** Tafel-plot using the current densities obtained at 4 Hz. Electrolyte: 0.1 M $KClO_4$ in DMSO saturated with 20% O_2.

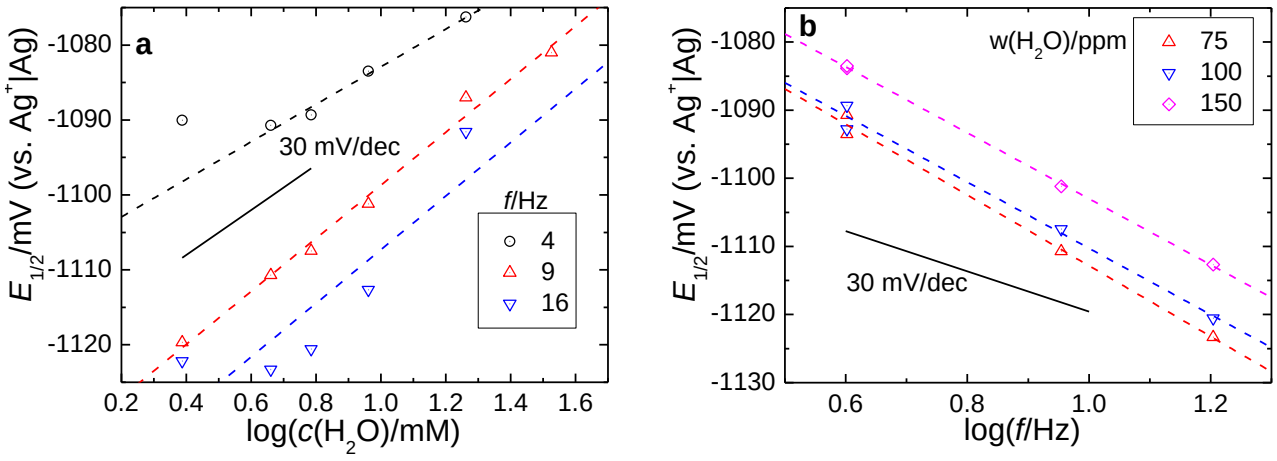

Figure S 8.9. Evaluation of the half-wave potential of peroxide formation according to eq. (8.17) in the main article. **a.** Dependence on the water content. **b**. Dependence on the rotation rate. Data was taken from Figure 8.9, Figure S 8.8 and additional CVs which are not shown.

9 O_2 Solubility and Diffusivity in DMSO-based Electrolytes

Philip Heinrich Reinsberg*, Pawel Peter Bawol*, Elke Thome* and Helmut Baltruschat*

*Institut für Physikalische und Theoretische Chemie, Universität Bonn, Römerstraße 164, D-53117 Bonn, Germany

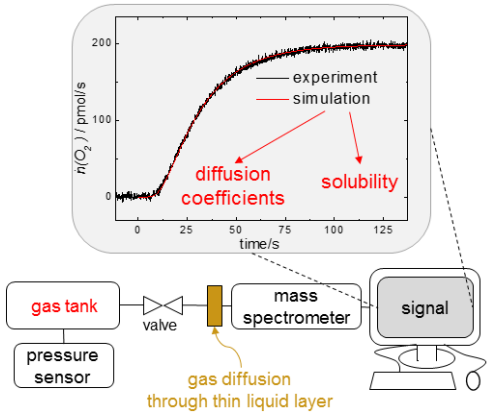

Received: September 21, 2018
Published online: November 9, 2018

Comments: The paper presented here has a companion paper, in which the experimental details are described (DOI: 10.1021/acs.analchem.8b04319). The whole project was realized in close collaboration with Pawel Peter Bawol and a German patent application has been filed (DE 10 2017 128 269.6).

Own manuscript contribution:

- design of the experiments
- supervision of the experiments
- interpretation of the results
- writing the manuscript

ACKNOWLEDGMENTS

The authors gratefully acknowledge financial support by the German Federal Ministry of Education in the framework of the LiBaLu-project (grant number: 03XP0029A), which is part of the “Vom Material zur Innovation”-initiative and the MeLuBatt-project (grant number: 03XP0110D).

9.1 Abstract

A new method for simultaneously determining gas diffusivities and solubilities in liquids was presented and discussed in detail in Part I of this series. In this part of the series, the new measurement cell was employed to determine oxygen solubilities and diffusivities in 20 different dimethyl sulfoxide-based electrolytes. In addition, a comparison to values available in literature was made. From the temperature dependence of the diffusivity between 20 and 40 °C an activation barrier of 19 kJ mol^{-1} for the diffusion of oxygen in pure dimethyl sulfoxide was found. Moreover, qualitative agreement between Jones–Dole viscosity coefficients and the dependence of the diffusivity on the electrolyte concentration was confirmed. The temperature-dependent solubility measurements revealed an unexpected increase of the oxygen solubility for temperatures above 30 °C. While the oxygen solubility in the case of the alkali-perchlorates decreases with increasing electrolyte concentration, a pronounced salting-in effect for lithium bis(trifluoromethane)sulfonimide was observed.

9.2 Introduction

In the first part of this series, a new method for simultaneous determination of gas diffusivities and solubilities in liquids was presented. In this part, the method is employed to determine oxygen solubilities and diffusion coefficients in pure dimethyl sulfoxide (DMSO) as well as in different alkali perchlorate and lithium bis(trifluoromethane)sulfonimide (LiTFSI)-based electrolytes at different temperatures. Moreover, the influence of the temperature on the characteristics of electrolytes is investigated, illustrating fundamental differences between aqueous and non-aqueous electrolytes.

9.3 Experimental

9.3.1 Materials

H Highly pure oxygen (99.995%, *Air Liquide*) was used to saturate the electrolytes. Electrolytes were prepared in a Glovebox Systemtechnik (*GS*) glovebox with a water content below 1 ppm and an oxygen content below 0.1 ppm. Lithium perchlorate ($LiClO_4$, battery grade, *Sigma-Aldrich*), tetrabutylammonium perchlorate ($TBAClO_4$, for electrochemical analysis, ≥99%, *Sigma-Aldrich*), and extra dry DMSO (99.7%, over molecular sieve, *Acros Organics*) were used as received. LiTFSI (99%, *abcr* GmbH), sodium perchlorate ($NaClO_4$, p.a., *Fluka*), potassium perchlorate ($KClO_4$, 99%, *Sigma-Aldrich*), rubidium perchlorate ($RbClO_4$, 99.9%, *abcr*), and cesium perchlorate ($CsClO_4$, 99.9%, *abcr*) were dried at reduced pressure at elevated temperatures up to 180 °C for 2 d. Usually, a pressure of 900 mbar of highly pure oxygen (99.999%, *Air Liquide*) was applied to the cell during the measurement. The reported values of solubility are extrapolated to a pressure of 1 bar applying Henry's law.

9.4 Results and Discussion

9.4.1 Diffusion Coefficients and Concentrations

The experimentally obtained diffusivities and solubilities for oxygen in different DMSO-based electrolytes are shown in Table 9.1. The uncertainty of the diffusivity and solubility refers to the standard error of mean as determined from multiple pressure-jump experiments employing the same electrolyte. In addition to that, the experiments in pure DMSO were repeated on several days, as they served as an internal reference for the calibration constant of the mass spectrometer. A major reason for the deviations between repeating measurements is probably related to the constancy of the temperature as well as residual oxygen from previous pressure-jump experiments.

Table 9.1. Diffusion coefficients ($D(O_2)$) and solubilities of oxygen ($c(O_2)$) in different DMSO-based electrolytes at variable temperatures and an oxygen pressure of 1 bar[a]

Electrolyte	T/K	$D(O_2)/10^{-6}$ cm^{2}s^{-1}	c(O_2)/ mM
DMSO	292.1	21.2±0.1	2.11±0.04
	297.1	24.3±0.3	2.04±0.04
	302.2	28.1±0.1	2.31±0.03
	306.9	31.9±0.6	2.32±0.11
	311.9	33.4±0.8	2.53±0.08
	319.1	39.2±0.8	2.58±0.08
	321.6	43.8±1.4	2.57±0.16
0.5 M LiTFSI/DMSO	292.3	19.1±0.2	2.37±0.02
	297.0	21.3±0.3	2.66±0.07
	303.0	23.7±0.7	2.53±0.08
	311.5	26.8±1.5	2.90±0.27
1.0 M LiTFSI/DMSO	292.6	15.6±0.1	2.40±0.12
	297.5	17.3±0.3	2.40±0.08
	302.1	18.7±0.3	2.51±0.02
	311.8	25.8±0.5	2.40±0.17
2.0 M LiTFSI/DMSO	292.6	14.3±0.3	2.49±0.01
	297.4	15.4±0.1	2.44±0.24
	301.7	15.8±0.6	2.51±0.04
	311.7	16.3±0.2	2.63±0.10
3.0 M LiTFSI/DMSO	292.2	9.3±0.4	2.73±0.21
	297.5	9.8±0.1	2.77±0.03
	301.9	10.3±0.1	2.79±0.02

	311.5	11.2±0.1	2.87±0.08
0.1 M $LiClO_4$/DMSO	297.1	23.5±0.1	2.02±0.01
0.5 M $LiClO_4$/DMSO	293.4	17.0±0.4	1.79±0.04
	297.2	19.1±0.4	1.78±0.10
	301.9	20.0±0.6	1.76±0.07
	311.8	23.1±0.8	1.92±0.01
1.0 M $LiClO_4$/DMSO	297.0	15.7±1.4	1.56±0.04
1.5 M $LiClO_4$/DMSO	297.1	11.9±0.4	1.45±0.06
2.0 M $LiClO_4$/DMSO	297.0	8.2±0.3	1.33±0.03
0.1 $TBAClO_4$/DMSO	292.2	21.9±0.2	1.95±0.03
	297.5	24.7±0.4	1.97±0.03
	302.2	30.7±0.5	2.02±0.05
	311.6	35.6±1.0	2.23±0.07
0.5 M $TBAClO_4$/DMSO	293.1	21.3±0.2	1.81±0.07
	297.5	23.0±0.7	1.90±0.02
	302.1	25.2±0.1	2.08±0.03
	312.0	30.7±0.3	2.40±0.07
0.1 M $NaClO_4$/DMSO	297.0	23.8±2.1	1.85±0.02
0.5 M $NaClO_4$	297.0	21.3±0.1	1.69±0.04
0.1 M $KClO_4$/DMSO	292.4	22.6±0.2	1.90±0.03
	297.1	24.1±0.1	2.00±0.05
	302.3	25.7±0.7	2.27±0.05
	311.8	31.0±0.4	2.42±0.01
0.5 M $KClO_4$/DMSO	292.7	16.9±0.5	1.68±0.05
	297.2	20.5±0.1	1.64±0.02
	303.1	21.6±0.4	1.64±0.04
	311.6	24.8±0.7	1.85±0.05
0.1 M $RbClO_4$/DMSO	293.2	23.5±0.7	2.14±0.06
	297.8	26.4±0.9	2.31±0.17
	302.5	30.8±0.2	2.14±0.34
0.5 M $RbClO_4$/DMSO	292.4	18.6±0.5	2.38±0.12
	297.5	22.0±0.5	2.07±0.15
	303.0	25.7±0.2	2.14±0.07
0.1 M $CsClO_4$/DMSO	292.5	24.5±0.5	1.69±0.02
	297.3	26.5±0.4	1.79±0.10

	301.8	30.2±0.7	1.67±0.07
0.5 M $CsClO_4$/DMSO	292.8	21.0±0.5	1.56±0.11
	297.4	23.8±0.4	1.82±0.12
	302.2	26.7±0.7	1.7±0.10

[a] The uncertainty of temperature is estimated to be ±0.5 K by comparison with an external mercury thermometer at the different measurement temperatures. The uncertainties of the diffusion coefficients and solubilities correspond to the standard error of mean in a 95% confidence interval.

9.4.2 Comparison to Values Reported in Literature

An overview of the solubility and diffusivity of oxygen in DMSO as reported in literature is given in Table 9.2 and shall serve as a preliminary basis for discussion of results obtained in this work.

Table 9.2. Comparison of the solubility and diffusivity data in this work to the data given in literature at 1 bar†

Electrolyte	***ϑ*/°C**	***D*(O_2)/10^{-6} cm^2s^{-1}**	**c(O_2)/ mM**	**Reference**
Pure DMSO	24	**24.3**[n]	**2.04**[n]	
	22		2.25[n, r]	[332]
	25±2	18	2.47[n, r]	[130]
	21±1		2.56[n, r]	[345]
	25		1.85[n, r]	[346]
	25±2		1.59[n, r]	[347]
	25		2.1[n, r]	[348]
	25		2.21[n, r]	[349]
0.1 M $TBAClO_4$	24	**24.7**[n]	**1.97**[n]	
	RT	32.2[e]		
	RT	9.75[e]		
	20	19.3[e]	1.8[e]	[350]
	RT	23[e]	2.96[e]	[321]
0.1 M $TEAClO_4$	25	20.8[e]	2.24[e]	[351]
	25		2.07[e]	[43]
	RT	27.6[e]	2.12[e]	[39]
	25		2.1[e]	[38]
	RT	28.2[e]	1.65[e]	[35]

0.2 M $TEAClO_4$	RT	21.6[e]		
0.1 M LiTFSI	22	12.8[e]	2.06[e]	[322]
0.5 M LiTFSI	24	**21.3**[n]	**2.66**[n]	
	22±1		2.5[n]	[352]
	22	14.0[e]	1[e]	[322]
	22		2.49-2.58[n]	[332]
1.0 M LiTFSI	24	**17.3**[n]	**2.4**[n]	
	22±1		2.82[n]	[352]
	22	10.9[e]	1.2[e]	[322]
0.1 M $LiClO_4$	24	**23.5**[n]	**2.02**[n]	
	25	17[n]	2.04[n]	[130]
0.5 M $LiClO_4$	24	**19.1**[n]	**1.78**[n]	
	22±1		2.00[n]	[352]
0.1 M $KClO_4$	24	**24.1**[n]	**2.00**[n]	
	25	18-20[n]	2[n]	[130]

† Temperatures as specified by the authors. If no temperature was specified, the term RT is used. The number after the solubility or diffusivity indicates the reference. Values obtained in this work are **bold**. Letter assignment: *e*: electrochemical measurement, *n*: non-electrochemical measurement, *r*: value recalculated by the author according to the definitions given by Battino[353].

For comparison, values obtained in this work are listed at the beginning of the list for each electrolyte and are marked bold. The expression RT denotes room temperature and is used when no temperature was specified by the authors. Recalculation of the Ostwald and Bunsen-coefficients (for the definition of these, see Battino[353]) as well as the mole fraction to a concentration was done assuming ideal gas behaviour and using the density of pure DMSO at 25 °C ($\rho = 1.096$ g cm^{-3}) [132].

The solubility of oxygen in pure DMSO lies well within the range of the reported values. Especially agreement with Achord[348] is good. The only diffusion coefficient of oxygen in pure DMSO reported in the literature is from our own lab [130]. However, we recommend to use the diffusion coefficient reported in this work, as the new measurement cell has a higher accuracy and has a temperature control, which was not present in the previous study and might be a reason for the low diffusion coefficient. Theoretical predictions of the diffusivity based on simple equations such as the Stokes–Einstein equation (eq. (9.1)) give the correct order of magnitude for the diffusivity, but only Scheibel's equation (eq. (S 9.7))[354] seems to yield a value of $19.7 \times 10^{6} cm^{2-1}$, which is comparable to that one obtained in this study (Table S 9.1).

$$D = \frac{k_b T}{6\pi\eta R_s} \tag{9.1}$$

In equation 1, k is Boltzmann's constant, T denotes the temperature, η is the dynamic viscosity of the solvent and R_S is the solvated radius of the diffusing molecule.

The oxygen solubility in electrolyte solutions has usually been determined via electrochemical methods (these are marked with an *e* in Table 9.2), such as chronoamperometry or electrodes under forced convection [35,37,62,321,322,350,351,355]. A disadvantage common to all these methods is that knowledge of the number of electrons transferred per oxygen molecule is essential for obtaining the correct solubility, which acerbates the evaluation for ill-defined systems. That said, the mean solubility of oxygen in 0.1 M $TBAClO_4$ or tetraethylammonium perchlorate ($TEAClO_4$) containing DMSO is 2.07 ± 0.07 if the two extreme values are excluded. This value is in very good agreement with the one obtained in this study. Interestingly, the solubility data on the LiTFSI electrolytes obtained by Lindberg *et al*. [352] agrees qualitatively as the authors show a significant salting-in effect, which has been also found in LiTFSI-containing tetraglyme [356]. As opposed to that, Gittleson *et al*. do not find a net salting-in effect, but only find a smaller salting-out effect as compared to $LiClO_4$ [322]. However, a problem in electrochemical determination of the oxygen solubility in presence of Li^+ is the deactivation of the electrode and the fact that at glassy carbon the number of electrons transferred per oxygen is not simply one or two, but rather something between one and two [139,282]..

Comparison of the diffusivity of oxygen in 0.1 M $TBAClO_4$, 0.1 M $TEAClO_4$ and 0.2 M $TEAClO_4$ gives a mean value of 24×10^{-6} $cm^2\,s^{-1}$ if the extreme values reported by Laoire [62] and Sawyer[37] are excluded, which again agrees very well with the value of 24.7×10^{-6} $cm^2\,s^{-1}$ reported herein. The diffusivity in LiTFSI-containing DMSO by Gittleson *et al*. is approximately 1.5-times lower than the value measured with our new set-up and is generally very low if compared to the other electrolytes. A possible explanation besides the deactivation of the electrode might be that geometric constant for the transfer from disk to ring in the set-up has not been calibrated[322]. As pointed out for example by Herranz *et al*. the real geometric constant might significantly deviate from the ideally expected constant [68].

9.4.3 Temperature Dependence of the Diffusion Coefficient

The temperature-dependent diffusion coefficients *D* of oxygen obtained in pure DMSO are displayed in Figure 9.1.

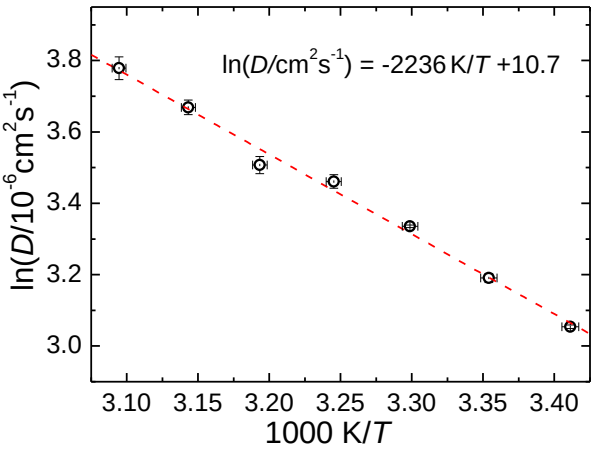

Figure 9.1. Temperature dependence of the O_2 diffusion coefficient in DMSO.

As expected, the diffusion coefficient increases with temperature. The dependence of the diffusion coefficient is usually expressed by an Arrhenius-like equation, with k_1 as the (constant) pre-exponential factor and E_D symbolizing the activation barrier of the diffusion process (for more details, refer to the section 9.6):

$$D = k_1 \exp\left(-E_D / RT\right) \tag{9.2}$$

From the slope a diffusion barrier of 18.6 kJ mol^{-1} can be calculated which is very close to the value of 18.7 kJ mol^{-1} obtained for O_2 in water by Ferrell and Himmelblau[357]. Bennion *et al.* report a value of 14 kJ mol^{-1} as the activation energy obtained from temperature-dependent viscosity measurements in DMSO[358]. However, as the friction coefficient as well as solvation of the diffusing species contributes to the activation barrier of diffusion, the value obtained from viscosity and diffusivity measurements are not expected to be identical.

9.4.4 Dependence of the Diffusion Coefficients on the Electrolyte Concentration c_{EL}

Changing the concentration c_{EL} of the electrolyte has a major consequence for the diffusion coefficient of dissolved gas: The dynamic viscosity of the solution changes due to local disturbances in the solvent structure. This change in viscosity with the concentration of the electrolyte is usually described in terms of eq. (9.3)[359,360] (for more details refer to section 9.6):

$$\eta_r = 1 + A\sqrt{c_{EL}} + Bc_{EL} \tag{9.3}$$

The coefficient *B* is called the (viscosity) Jones-Dole coefficient [359,361] and is normally positive, implying an increase of the viscosity with increasing concentration of the electrolyte and thus, a structuring effect of the ion. As the viscosity has a reciprocal influence on the diffusion coefficient of species in the solution (e.g., see equation eq. (9.1)), the Jones-Dole coefficients

A and *B* can be used to predict diffusivities of gases in electrolyte solutions (see Supporting Information).

Alternative approaches for describing the electrolyte's influence on the diffusivity rely on empirical relationships, which directly relate diffusivity and electrolyte concentration. Although there are different equations to correlate the diffusivity of a gas with the concentration of an (inert) electrolyte, we will restrict the evaluation to one of the simpler equations [353,362,363]:

$$D = D_0\left(1 - k' c_{EL}\right) \tag{9.4}$$

In eq. (9.4) *k*' is a constant, c_{EL} denotes the concentration of the inert electrolyte and D_0 denotes the diffusion coefficient of the gas in the pure solvent. As the viscosity as described in eq. (9.3) has a reciprocal influence on the diffusivity (eq. (9.1)), it is clear that eq. (9.3)and eq. (9.4) are somehow correlated and that *k*' is correlated to *B*.

A fit according to eq. of for LiTFSI and $LiClO_4$ is shown in Figure 9.2a. The slope is negative, indicating a decrease of diffusivity and thus, structuring effect of LiTFSI on the solvent. As shown in Figure 9.2b, a similar structuring effect is also exhibited for the alkali perchlorates. Moreover, as expected, there is a correlation of the constant *k*' (eq. (9.4)) and the Jones-Dole coefficient *B*, which has been previously shown by Hung *et al.* [364].

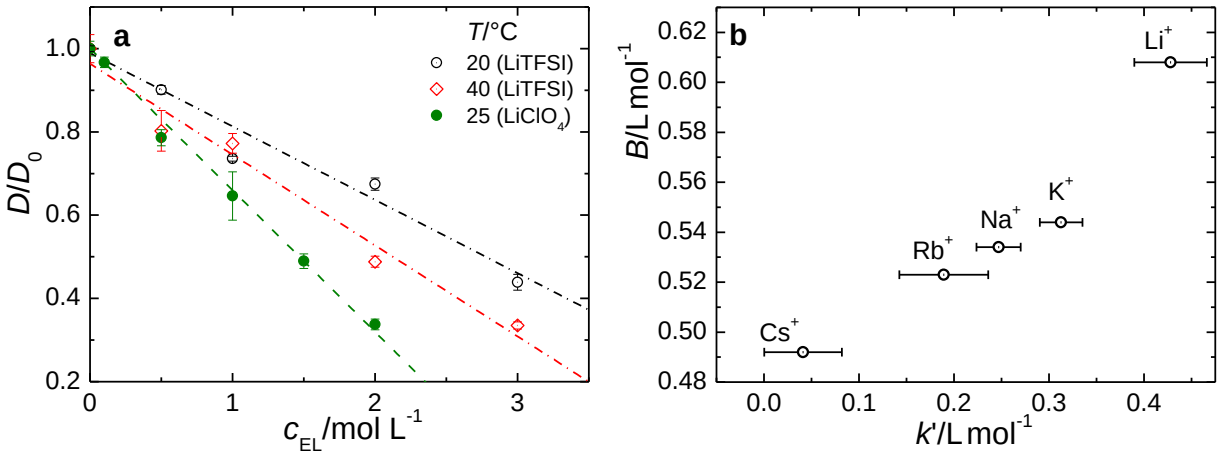

Figure 9.2. Concentration dependence of the O_2 diffusion coefficient D. **a**. Dependence of *D* on the concentration of LiTFSI and $LiClO_4$ (circles, dark green) at different temperatures. **b** Correlation of (viscosity) Jones-Dole coefficient *B* with the constant *k*' in eq. (9.4) for different alkali perchlorates at a concentration of 0.5 M and a temperature of 24 °C.

The temperature-dependence of the constant *k*' as defined in eq. (9.4) is shown in Figure 9.3. The negative slope implies that the decrease of diffusivity with electrolyte concentration is more pronounced at higher temperatures. Considering that the effect of the alkali cation concentration on the viscosity and, thus, diffusivity is less pronounced at higher temperatures (see Supporting Information, especially. Table S 9.3), it must be the TFSI-anion that causes the effect to increase with temperature. A similar behaviour has been observed for the perchlorate or sulphate anion in water, and the size of these effects exceeds that one on the Li^+ cation. [359]. Similarly, the *k*' values for 0.5 M $LiClO_4$, $KClO_4$ and $TBAClO_4$ decrease with

temperature, although for $RbClO_4$ and $CsClO_4$ a positive temperature coefficient is discernible (Figure S 9.2).

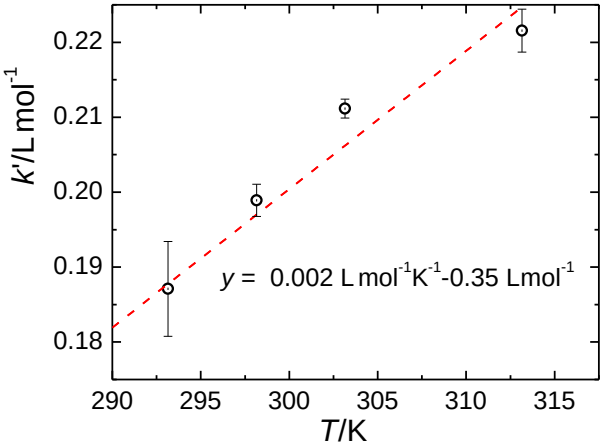

Figure 9.3. Temperature-dependence of the constant *k*' for O_2 in 3 M LiTFSI in DMSO.

Alternatively one can use eq.(9.2) to describe the temperature dependence of the diffusivity. Plots according to eq. (9.2) can be found in the Supporting Information (Figure S 9.3). The major outcome of this is that the activation barrier decreases from 18.6 to 11 kJ mol^{-1} in the presence of LiTFSI as compared to pure DMSO.

9.4.5 Temperature Dependence of the Oxygen Solubility

Temperature-dependent solubilities of oxygen in pure DMSO, 0.5 M $KClO_4$, 0.1 M TBAClO4 and 2 M LiTFSI are shown in Figure 9.4a. As can be seen, the concentration slightly increases at higher temperatures. Although this might appear counterintuitive at first glance and in the light of our experience with aqueous solutions, this behaviour is not that uncommon and can even be observed for the oxygen solubility in water at temperatures above 100 °C[365]. The observation of a solubility minimum has been made for several gases and several solvents, for instance noble gases in water[366].

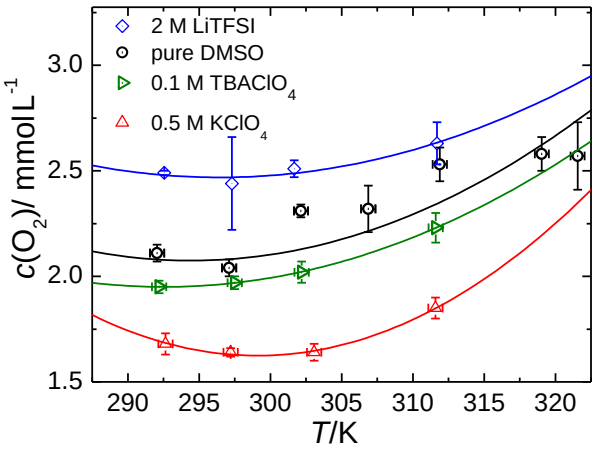

Figure 9.4. Temperature dependence of the O_2 solubility. The solid lines serve as a guide to the eye.

9.4.6 Dependence of O_2 Solubility on Electrolyte Concentration

The concentration dependence of the oxygen solubility on the electrolyte concentration for $LiClO_4$ and LiTFSI is shown in Figure 9.5. While in $LiClO_4$ solution the solubility of oxygen deceases, it increases in the presence of the $TFSI^-$-anion, implying a significant salting-in effect. This is in good agreement with the findings of Lindbergh *et al.* who observe significant salting-in in the presence of LiTFSI [352]. On the contrary, Gittleson *et al*. indeed observe a lesser degree of salting-out in the presence of $TFSI^-$ as compared to BF_4^- or ClO_4^-, but do not observe actual salting-in [322]. The salting-in effect of $TFSI^-$ can be attributed to the polarizability and large dispersion effects of the large $TFSI^-$-anion.

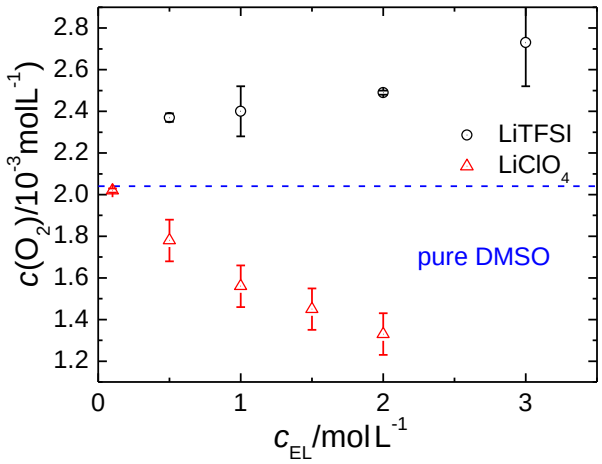

Figure 9.5. Oxygen solubilities as a function of the electrolyte concentration. Temperature for LiTFSI: 20 °C. Temperature for $LiClO_4$: 24 °C.

9.4.7 Dependence of the Oxygen Transmissibility on the Electrolyte Concentration

As shown above, the presence of a dissolved salt in the liquid phase affects the solubility and diffusivity. Instead of analysing the effects separately, Ho *et al*. [367] have shown that one can also directly investigate the electrolyte's influence on the oxygen transmissibility ($D(O_2)$x$c(O_2)$). Based on the works of Van Krevelen and Hoftijzer [368] as well as Gubbins *et al*. [362], Ho derived the following relation between the oxygen transmissibility and the electrolyte concentration:

$$\log\left(\frac{D_0 \cdot c_0}{D \cdot c}\right) = \alpha \cdot c_{EL} \tag{9.5}$$

The index 0 denotes the properties of oxygen in the pure solvent, while α is a constant. Plots according to eq. (9.5) are shown in Figure 9.6 using the data for $LiClO_4$- and LiTFSI-containing DMSO at different temperatures. Especially the transmissibility data in presence of $LiClO_4$ seems to follow eq. (9.5) very well.

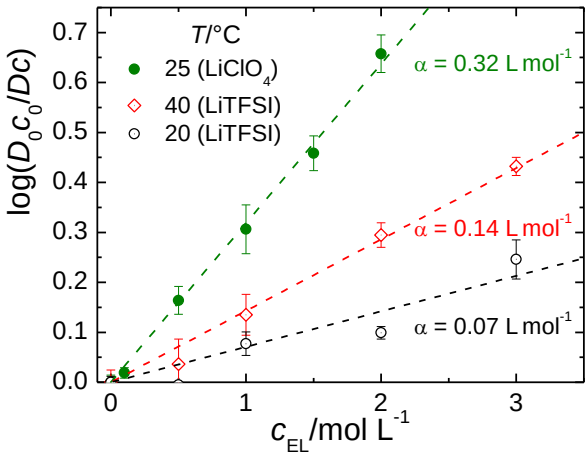

Figure 9.6. Concentration dependence of the relative O_2 transmissibility. Electrolytes: LiTFSI and $LiClO_4$ at the temperatures indicated in the Figure.

9.5 Conclusions

Employing the method presented in Part I of this series, the diffusivity and solubility of oxygen in a large set of different DMSO-based electrolytes have been determined. Comparison to values obtained in the literature verifies the accuracy of the method presented in this work. While different alkali perchlorates lead to the usual salting-out of oxygen, LiTFSI salts cause an increase of the oxygen concentration. For most of the electrolytes used in this study, a slight increase of the oxygen solubility with temperature has been observed. The diffusivity of oxygen in different electrolyte solutions has been found to decrease with increasing salt concentration, which has been attributed to the increase in dynamic viscosity. From the temperature dependence of the diffusion coefficients in pure DMSO a mean activation barrier for the diffusion of oxygen of 18.6 kJ mol^{-1} has been calculated.

9.6 Supporting Information

9.6.1 Theoretical Prediction of the Diffusion Coefficient

Predicting the diffusion coefficient *D* of a solute in a solvent is most easily done using equations derived by Einstein[369] and Sutherland[370] based on the works of Stokes. The general equation is displayed in eq. (S 9.1) [370]:

$$D = \frac{k_B T}{6\pi\eta R_s}\left(\frac{1+3\eta/\beta R_s}{1+2\eta/\beta R_s}\right) \qquad \text{(S 9.1)}$$

D describes the diffusion coefficient of a solute within a solvent, k_B represents Boltzmann's constant, η is the dynamic viscosity, R_S is the solvated radius of the solute and β is the sliding-friction coefficient (although in the limiting case of a no-slip conditions β is rather the coefficient of static friction) between solute and solvent. Equation (S 9.1) assumes the validity of van-t'-Hoff's equation for the osmotic pressure and that the driving force of diffusion is given by the osmotic pressure, implying dilute solutions with no interaction between the solute molecules. Further assumptions are continuous, laminar flow conditions and a spherical shape of the

solute molecules. [371]. In the limit of a no-slip condition (i.e. the fluid molecules close to the solute stick to the solute and thus, $\beta \to \infty$) eq. (S 9.1) converts to the well-known Stokes-Einstein equation (9.1)[369].

The latter assumption is the main reason why the Stokes-Einstein equation cannot accurately predict diffusivities of solutes which are smaller than the solvent molecules as several large solvent molecules cannot be attached to the smaller solute molecules[370]. For small solute one might think of the solute moving through the gaps between the solvent molecules and thus, experiencing slipping. This condition translates to a negligible coefficient of sliding friction (i.e. $\beta \to 0$) and one obtains the Sutherland equation via substituting and rearranging eq.(S 9.1), [370]:

$$\begin{aligned}\lim_{\beta\to 0}(D) &= \lim_{\beta\to 0}\left(\frac{k_B T}{6\pi\eta R_s}\left(\frac{1+3\eta/\beta R_s}{1+2\eta/\beta R_s}\right)\right)\\ &= \lim_{\beta\to 0}\left(\frac{k_B T}{6\pi\eta R_s}\left(\frac{3\eta/\beta R_s}{2\eta/\beta R_s}\right)\right)\\ &= \frac{k_B T}{6\pi\eta R_s}\cdot\frac{3}{2}\\ &= \frac{k_B T}{4\pi\eta R_s}\end{aligned} \qquad \text{(S 9.2)}$$

Recent work of D'Agostino shows that the truth lies somewhere in between the two equations for a liquid-liquid diffusion [372]. Semi-empirical modifications of the Stokes-Einstein relation have been implemented by Wilke and Chang yielding eq.(S 9.3), which is mostly used for small solutes in solvents of a low molecular weight at low concentrations [373]:

$$D = 7.4\cdot 10^{-8}\frac{(\phi M)^{1/2}\,T}{\eta V_A^{\,0.6}} \qquad \text{(S 9.3)}$$

M denotes the molecular weight of the solvent in g mol^{-1}, V_A is the molar volume of the solute at its boiling point in cm^3 mol^{-1} ϕ is an empirical parameter reflecting the association within the solvent. For non-associating solvents ϕ is 1. However, for DMSO as a solvent the formation of weak h-bonds has been observed [374].To overcome the problems arising from the associative parameter ϕ in eq.(S 9.3), Scheibel gave an alternative relation[354]:

$$D = 8.2\cdot 10^{-8}\frac{T}{\eta}\frac{1+\left(\frac{3V_B}{V_A}\right)^{2/3}}{V_A^{1/3}} \qquad \text{(S 9.4)}$$

In eq. (S 9.4) the subscripts A denotes the solute, whereas B denotes the solvent. The relation between eq. (9.1) and (S 9.2) as well as (S 9.3) and (S 9.4) is visualized when the radius of the solvent is expressed by its molar volume:

$$R_S = \left(\frac{3 \cdot V_A}{4\pi N_A} \right)^{1/3} \tag{S 9.5}$$

Substituting into eq. (9.1) gives:

$$D = \frac{k_b T}{6\pi\eta \left(\frac{3 \cdot V_A}{4\pi N_A} \right)^{1/3}} \tag{S 9.6}$$

Finally, substituting the constants an using the same units as in eq. (S 9.3) yields eq. (S 9.7), which for very large volumes of the solute approximates the equation given by Scheibel:

$$D = 9.96 \cdot 10^{-8} \frac{T}{\eta} \cdot \frac{1}{V_A^{1/3}} \tag{S 9.7}$$

Theoretical estimations for the diffusivity based on the different equations mentioned above are shown in Table S 9.1. While the Stokes-Einstein and Sutherland equation greatly underestimate the diffusion coefficient, theoretical prediction of the diffusivity apparently is most accurate using the empirical Scheibel (eq.(S 9.7)), [354]). However, due to the relatively small size of O_2 molecule as compared to DMSO it is unlikely that the no-slip condition underlying the Stokes-Einstein equation holds in this case. Furthermore, it is unclear what the radius of oxygen in its solvated state in DMSO is.

Table S 9.1. Oxygen diffusivity in DMSO at 19°C in 10^6 cm^2s^{-1}.[a]

Exp.	Stokes-Einstein	Sutherland	Wilke-Chang	Scheibel
21.2	6.15	9.22	11.9	19.7

[a] Values used for the different equations: η =2.291 mPa s (extrapolated using the data of Tsierkezos *et al.*[375]), M = 78.13 g mol^{-1}, V_A = 25.6 $cm^3 mol^{-1}$ [373]), V_B = 82.68 cm^3 mol^{-1} (calculated from the density 0.945 g cm^{-3} at the boiling point of DMSO[376]) and the van-der-Waals radius of O_2 R = 152 pm.

9.7 Prediction of the Temperature Dependence of the Diffusion Coefficient

Although it might be tempting to use equations (S 9.1) to (S 9.4) for predicting the temperature dependence of the diffusion coefficient, the temperature dependence of the viscosity cannot be neglected. The temperature dependence of the viscosity is usually given by the Andrade-equation[371], where *A* and *b* are empirical constants:

$$\eta = A \cdot e^{\frac{b}{T}} \tag{S 9.8}$$

Experimental data for the temperature dependence of the viscosity of DMSO and the plot corresponding to eq. (S 9.8) are displayed in Figure S 9.1.

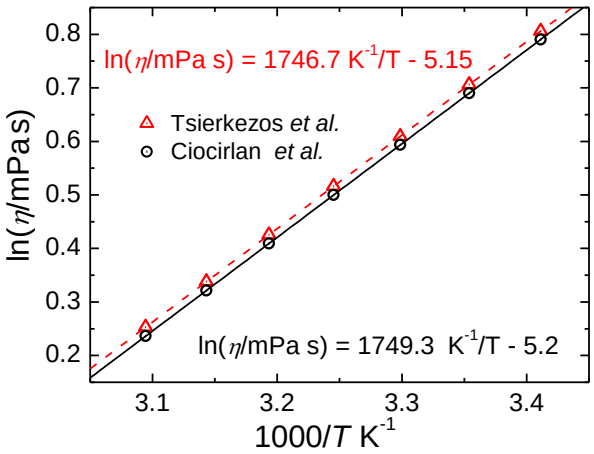

Figure S 9.1.Temperature dependence of the viscosity of pure DMSO. The red triangles refer to experimental data taken from Tsierkezos *et al*. [375], the black circles refer to experimental data taken from Ciocirlan *et al*. [377].

As the diffusion coefficient is inversely correlated to the viscosity, an increase of the diffusion coefficient with increasing temperature is expected. While an Arrhenius-like behavior is often invoked for quantitative description of the diffusion coefficient and yields reasonable linearity over a narrow temperature range, treatment based on Eyring's absolute rate theory also accounts for the temperature dependence of the pre-exponential factor in the Arrhenius equation:

$$D = k_3 \cdot T \cdot \exp\left(-E_D^* / RT\right) \qquad \text{(S 9.9)}$$

The activation barrier for diffusion, E_D*, is directly correlated to the empirical constant *b* in the Andrade-equation (S 9.8). As shown by Simons *et al.* the applicability of these two equation cannot be differentiated easily due to the small change of *RT* with the temperature.

9.8 Jones-Dole *B*-Coefficients

Adding a solute to a solvent influences the solvent structure and therefore, influences its viscosity η or fluidity φ ($\varphi = \frac{1}{\eta}$). One of the first attempts to correlate the fluidity φ of a solution with the concentration of a solute c_{EL} was given by Jones and Dole[361], where φ_0 is the fluidity of the pure solvent:

$$\frac{\varphi}{\varphi_0} = \varphi_r = 1 + A'\sqrt{c_{EL}} + B'c_{EL} \qquad \text{(S 9.10)}$$

The parameter *A'* reflects the ion-ion interaction and can be derived theoretically if the equivalent conductivities of the constituent ions are known[378], while the parameter *B'* includes solvent-solute interactions. Equation (S 9.10) is nowadays usually inverted and written in terms of the dynamic viscosities (eq. (S 9.11)[359,360]:

$$\eta_r = 1 + A\sqrt{c_{EL}} + Bc_{EL} \quad \text{(S 9.11)}$$

The coefficient *B* is usually called the (viscosity) Jones-Dole *B* coefficient. Although the Jones-Dole coefficient *B* is usually a salt-dependent parameter, it can be partitioned into ionic contributions by assuming that for a specific salt, anion and a cation contribute equally to the *B*-coefficient due to their similar size and charge density. Yao and Bennion assumed this equality for iPe_3BuN^+ and BPh_4^- in DMSO[358]. The ionic Jones-Dole *B* coefficients of the ions relevant to this study are listed in the Table S 9.2. The *B* coefficients of the anions in DMSO are generally (unless very bulky cations such as iPe_3BuN^+ are used for comparison) lower reflecting the weaker interaction of the DMSO molecule with the anion as compared to the interaction with the cation [374].

Table S 9.2. Literature values for the ionic Jones-Dole coefficients in L mol^{-1} in DMSO at 25 °C[a]

Ion	25°C	35°C	45°C
Li^+ [374]	0.608	0.586	0.565
Na^+ [374]	0.534	0.509	0.484
K^+ [374]	0.544	0.522	0.502
Rb^+ [374]	0.523	0.505	0.489
Cs^+ [374]	0.492	0.474	0.459
Bu_4N^+ [379]	0.614	0.609	0.583
ClO_4^- [358]	0.260	0.260	0.270

[a] The data given by Bicknell and Bennion is based on the assumption that the *B*-coefficients of the triisopentybutyllammonium cation (iPe_3BN^+) and the tetraphenylborate anion (BPh_4^-) are the same due to their equal, spherical shape in DMSO. The *B*-coefficient of the Bu_4N^+-ion has been derived using the *B*-value for Br^- as reported by Lawrence [380].

9.9 Temperature-Coefficients of the Ionic *B*-Coefficients

The temperature dependence of the diffusivity of an inert solute in an electrolyte solution is affected by two factors. Firstly, the viscosity of the solvent is a function of the temperature as discussed above. Secondly, the influence of the electrolyte on the viscosity, namely the Jones-Dole coefficient, is a function of the temperature as the strength of the interaction between solvent and electrolyte is affected by the temperature. The usually assumed equation for the temperature dependence of *B* is given by eq. (S 9.12)[359]:

$$B = a + b \cdot (T - 273) \quad \text{(S 9.12)}$$

The Jones-Dole coefficients for the alkali metal cations decrease with temperature, implying a negative value for *b* (Table S 9.3). This can qualitatively be understood by assuming that the structuring effect caused by the ion-dipole interactions between the ion and the solvent is weakened by the increased fluctuations of the solvent molecules at higher temperatures. In

that case, it would be expected that the diffusion coefficient in the solution increases with increasing temperature and approximates that in the pure solvent. However, as indicated by Davis *et al.* the change in viscosity cannot fully account for the change in diffusivity, which is why the above said can only be qualitatively adapted [381].

Table S 9.3. Literature values for temperature coefficient of the ionic *B*-coefficient in DMSO L mol^{-1} K^{-1} taken from [379]

Salt	d*B*/d*T*
Li^+[379]	−0.0022
Na^+	−0.0025
K^+	−0.0021
Rb^+	−0.0017
Cs^+	−0.0017
TBA^+	−0.0016

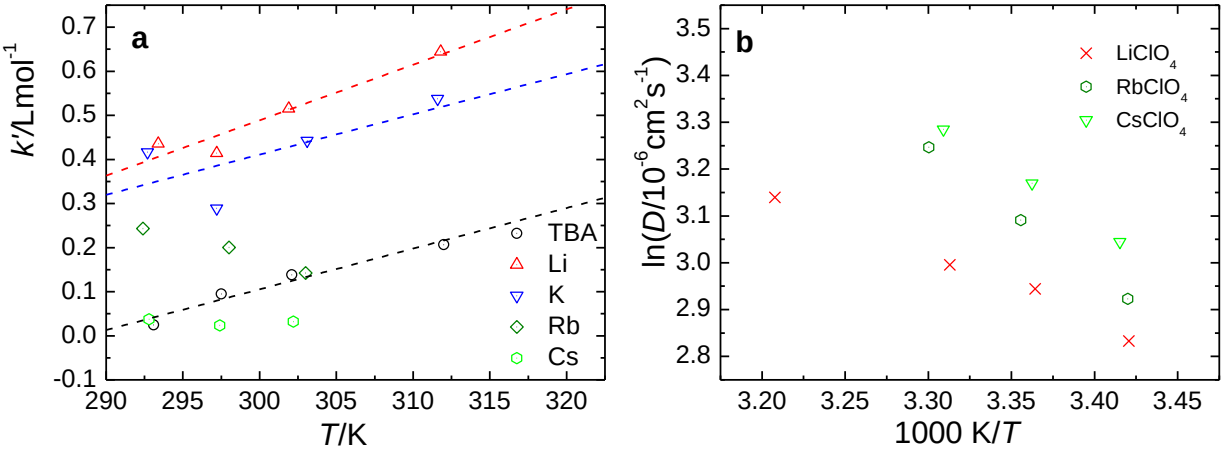

Figure S 9.2. Temperature dependence of the diffusion coefficient. **a**. Normalized diffusion coefficient versus the temperature. **b**. Evaluation of the activation barrier of diffusion.

9.10 Dependence of the Activation Barrier for Diffusion on the Salt Concentration

An alternative approach for the description of the dependence of the diffusivity on the temperature is based on the usual Arrhenius-equation. The corresponding Arrhenius-like plots for the different LiTFSI-solutions are shown in Figure S 9.3a. From the slope of the lines activation barriers of 13 kJ mol^{-1} at 0.5 M LiTFSI, 14 kJ mol^{-1} at 1 M, 5 kJ mol^{-1} at 2 M and 7 kJ mol^{-1} at a concentration of 3 M LiTFSI are obtained. The non-monotonous behaviour of the activation barrier might be understood by the solvation of the LiTFSI: At 0.5 M the ratio of solvent molecules to ions is 14, indicating a sufficient solvation. However, at 2 M this ratio already decreases to 3.5, which means that only 3-4 solvent molecules are available per ion.

As can be seen from Figure S 9.3b, the activation barrier in the presence of potassium is similar to that one of TBA^+, but higher than that of Li^+.

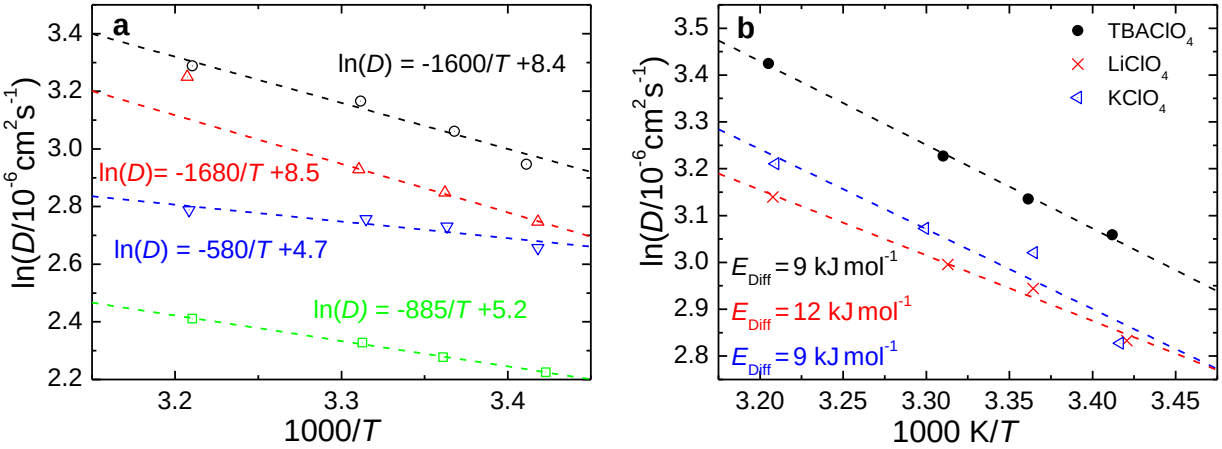

Figure S 9.3. Evaluation of the activation barrier for diffusion. **a**. Different LITFSI-containing solutions: black, 0.5 M, red: 1 M, blue: 2 M, green: 3 M. **b**. 0.5 M perchlorate solutions.

10 Spectroscopic Investigation of the Electrochemical Double-Layer

In contrast to chapters 3–9, the results presented in this chapter have not been published yet. Rather than directly investigating the ORR, the electrochemical double-layer and the adsorption of cyanide and carbon monoxide are studied in this chapter. This is mostly because the ORR products cannot be observed on a silicon as an internal reflection element, which is used in this work [284].

10.1 Introduction

Spectroelectrochemistry has been widely used to study reactions at the electrode surface and the structure of the electrochemical double layer in non-aqueous electrolytes [137,138,150,151,163,382-394]. One of the most widely used non-aqueous solvent for electrochemistry is acetonitrile (MeCN) [137,395-397]. Investigations on platinum [397] and silver electrodes [137,395] showed the partial decomposition of MeCN to cyanide-anions adsorbed to the surface. Furthermore, trace amounts of water have been found to be present close to the electrode surface. More fundamental investigations on single-crystalline platinum electrodes helped elucidating the dissociative adsorption of MeCN from aqueous solutions by identifying reaction intermediates [394,398]. Moreover, the adsorption of cyanide from MeCN solutions has been found to be hindered in the presence of other adsorbing species like pyridine or iodide[396]. Measurements in the external reflection geometry conducted by Pons and Davidson using platinum as a working electrode showed a pronounced adsorption of MeCN and ClO_4^- or BF_4^- anions when shifting the potential positive of their reference potential (−0.5 V vs $Ag^+|Ag$ in MeCN) [163]. Furthermore, the authors found an increase of the water concentration following the increase of the anion concentration in the thin electrolyte layer.

Reorientation of adsorbed, aprotic solvents has also been subject to observation via surface vibrational spectroscopy. Shen and Pemberton found that dimethyl sulfoxide (DMSO) adsorbs on silver electrodes via the oxygen atom at positive potentials (with respect to the point of zero charge), but via sulfur at negative potentials. [388,389] Investigations of the adsorption of pyridine from DMF on silver electrodes imply that the solvent has a crucial effect on the reorientation of the adsorbed species [399].

Fundamental studies using carbon monoxide (CO) (or rather $V(CO)_6$) as a precursor) have been carried out by Pons and coworkers, who found a less pronounced dependence of the vibration of CO adsorbed on platinum in dichloroethane and MeCN as compared to water [382]. The lifetime of the CO vibration in acetonitrile has been determined via infrared sum frequency generation spectroscopy to be in the range of picoseconds [400]. A comparison of the effect of different solvents and conducting salts on CO-adsorption on polycrystalline Pt, Pt(110), Pt(111), and Rh (111) stressed that the surface potential, which is also affected by the solvent

and ions in solution, influences the structure and bonding of CO adsorbates [384-387]. Different researchers showed by the comparison of alkylammonium perchlorates with alkali metal perchlorates that the cations effect on the CO stretching frequency ν_{CO} is manifold[383,385,387]: While the potential dependence of ν_{CO} increases with decreasing size of the tetraalkylammonium cation due to the larger outer Helmholtz plane , the presence of alkali cations leads to the formation of a new absorption band at 1700 cm^{-1} at cathodic potentials. This is attributed to the formation of a 2-fold bridging coordination of CO, which does only occur to a minor extent in aqueous solutions, where strong solvation presumably renders cations less active [401]. The influence of the non-aqueous solvents on CO-adsorption on Pt(111) was found to be less important than the influence of the cation. By comparison of the potential dependent CO-vibration in the presence of TBA^+ and TEA^+, the point of zero charge could be estimated, once again proving surface vibrational spectroscopy to be a powerful technique in determining fundamental properties of the electrode/electrolyte surface.

10.2 Experimental Section

10.2.1 Materials

All electrolytes were prepared in a *Glovebox Systemtechnik* glovebox. Lithium perchlorate ($LiClO_4$, battery grade, Sigma-Aldrich), silver nitrate ($AgNO_3$, ≥99%, *ChemPure*), potassium hexafluorophosphate (KPF_6, ≥99%, *Sigma-Aldrich*), extra dry acetonitrile (MeCN, 99.9%, over molecular sieve, *Acros Organics*), extra dry dimethyl sulfoxide (DMSO, 99.7%, over molecular sieve, Acros Organics) and propylene carbonate (PC, 99.7% anhydrous, *Sigma-Aldrich*) were used as received. Sodium perchlorate (p.a., *Fluka*) and calcium perchlorate tetrahydrate ($Ca(ClO_4)_2x4\ H_2O$ 99%, *Sigma-Aldrich)* were dried for 1 day at 180 °C or rather 250 °C under reduced pressure (10^{-2} mbar). During the experiments, the electrolytes were purged with different mixtures of highly pure argon (Ar, 99.9999%, Alphagaz 2, *Air Liquide*).

10.2.2 Reference Electrode

For the measurements in the aqueous electrolyte, the reversible hydrogen electrode (RHE) was employed. The RHE was filled with the working electrolyte and the hydrogen necessary for a stable reference potential was prepared via electrolysis. For the non-aqueous electrolyte, a silver-wire immersed in a 0.1 M $AgNO_3$ MeCN-electrolyte was used in the reference compartment and the connection between the working electrolyte and the reference electrode was established via the rough surface of a closed glass stopcock. For the working electrolytes containing DMSO as the solvent, the reference electrolyte was also prepared in DMSO instead of MeCN. The potential of the reference electrode in DMSO is approximately 0.43 V versus NHE[216], while the reference electrode in MeCN has a potential of 0.5 V[216].

10.2.3 Spectrometer

The FT-IR spectrometer used for this work is a Nicolet iS50 (*Thermo Scientific*) equipped with a DLaTGS and a nitrogen-cooled MCT-A detector (11700–600 cm^{-1}) and a Germanium beam splitter. The bell-shaped single-beam spectrum resulting from the interplay between the Polaris™ light source and the MCT-A detector is shown in Figure 10.1. Note that the spectrum was recorded in an open beam configuration and therefore, had to be attenuated to prevent saturation of the MCT detector. As can be seen, the maximum intensity is obtained between 2700 cm^{-1} and 2000 cm^{-1}, whereas a significant loss in intensity is observed for wavenumbers below 1300 cm^{-1}. The characteristic absorption bands at 3600 cm^{-1} and 1600 cm^{-1} are due to the rotational-vibrational spectra related to atmospheric water vapour, whereas the double band at 2300 cm^{-1} refers P and Q-branch of the asymmetric stretch vibration of CO_2, which cannot be resolved due to the small rotational constant of CO_2 ($B_0(CO_2) = 0.39\ cm^{-1}$[402] vs $B_0(H_2O) = 27.9$, 14.5 and 9.3 cm^{-1}[403]).

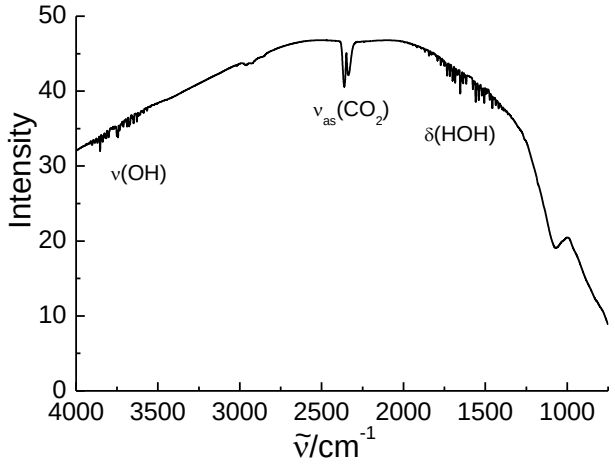

Figure 10.1. Bell-shaped single-beam spectrum in an open path arrangement. The absorption bands of H_2O and CO_2 are visible as ambient air is in the open beam path.

10.2.4 Mirror Accessory and Measurement Cell

The home-build mirror accessory and the measurement cell mounted into the spectrometer are shown in Figure 10.2. The IR beam originating from the source enters the accessory on the right, where it is reflected by a gold mirror under an angle of 75° with respect to the surface normal of the mirror or 30° with respect to the optical axis of the system. This leads to an angle of incidence of 60° (with respect to the surface normal) at the plane side of the silicon hemisphere, which is sufficient to fulfil the criterion of total reflection(θ_c= 17° for the interface between Si and air with n(Si) = 3.429 [195]). After being reflected at the Si hemisphere, the IR beam is reflected on a second mirror and leaves the mirror accessory parallel to the optical axis.

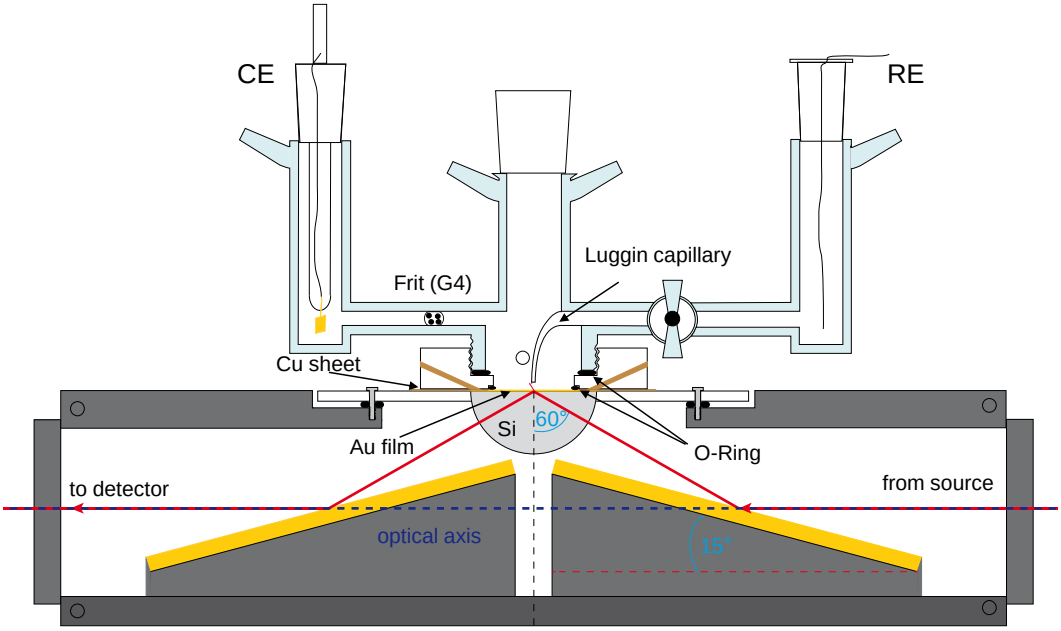

Figure 10.2. Mirror accessory and measurement cell for ATR measurements. The IR beam enters the accessory from the right and leaves at the left-hand side. For a full description refer to the text.

To guarantee optimum reflectivity, first-surface gold mirrors are used (*Edmund optics* 48456, 50x75 mm, protected gold, surface flatness: 4-6 λ at 633 nm), which offer a reflectivity of 96% in a range of wavelength between 700 and 10000 nm [404]. A monocrystalline Si hemisphere (*Tydex*, $r = 12.5$ mm, surface flatness: 2 λ@633 nm, deviation from ideal sphere: ±0.01 mm) was used instead of a prism to reduce reflective losses as the IR beam is always orthogonal to the spherical surface of the crystal if the focus of the IR lies in the centre of the crystal. To reduce absorption due to interstitial oxygen in the crystal, float-zone silicon was preferred over Czochralski silicon, which shows absorption bands at 2500 cm^{-1} [405]. The single beam spectrum using the mirror accessory and Si as an internal reflection element is shown in Figure 10.3. As opposed to the spectrum in Figure 10.1, the intensity decrease sharply at around 1500 cm^{-1} and shows several absorption bands down to 600 cm^{-1}. These absorption bands result from multiphonon absorption of the Si-lattice which result from the anisotropy of the crystal[405].

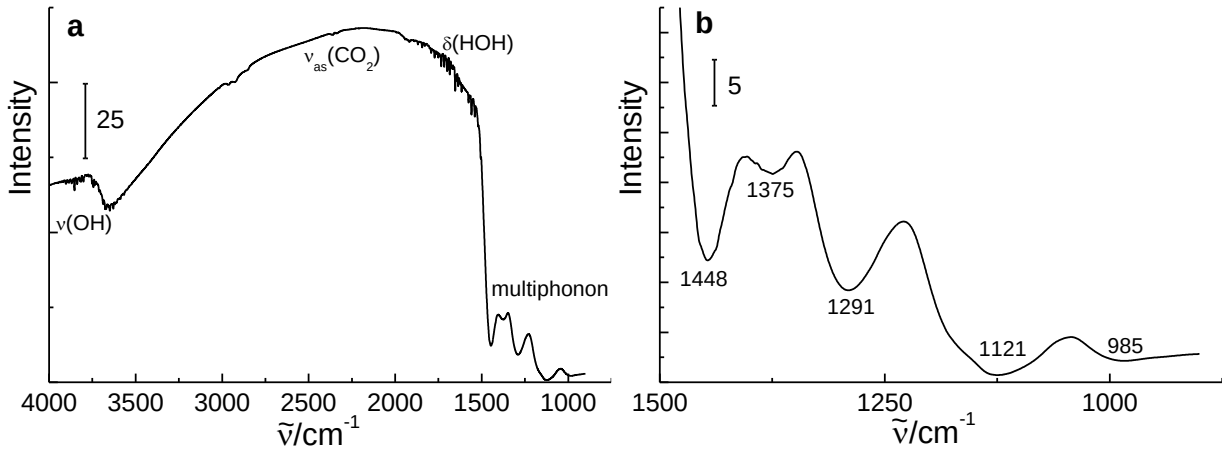

Figure 10.3. Bell-shaped single-beam spectrum of a hemispherical silicon crystal. **a**. Single-beam spectrum at full range. **b**. Close-up of the single-beam spectrum in the region of phonon absorption.

The Si hemisphere is mounted into a holder plate made from polyvinylidene fluoride (PVDF) with is screwed into the outer housing of the mirror accessory. Soft nitrile rubber O-rings (inner diameter: 2.79 mm, thickness: 1.02 mm, hardness: 70 Shore-A) are used between PVDF plate and housing to allow for tilt-correction of the plate. The measurement cell made from glass is screwed into a Teflon transition piece, which has a groove, where a perfluoroelastomer O-Ring (*DTH-Dichtungstechnik GmbH*, 16x1 mm, FFKM: DTH-16028) is situated to prevent electrolyte leakage. Electrical contact to the gold thin-film on the Si hemisphere is ensured via a copper foil (*Schreiber Farb- und Antikglas*, thickness: 0.02 mm) which is pressed onto the gold film by four copper rods. The glass cell is connected to the Teflon transition piece via a GL 25 screw-thread, which is made tight via a flat seal (*DuPont*, Kalrez® 6375, thickness: 2mm, ID = 19 mm, OD =25 mm). The glass cell itself has three compartments: The counter electrode compartment (CE) is separated via a porous glass frit (porosity 4) from the working electrode compartment, which is separated from the third compartment via a closed stopcock to prevent contamination of the working electrolyte with the reference electrolyte. Electrical contact is established via the wetted surface of the rough glass stopcock. To remove ambient moisture from the air inside the cell, the cell was thoroughly flushed with argon gas and the electrolyte was added in the argon counterflow.

10.2.5 Preparation of Electrodes for Use in SEIRAS

In early approaches, the metal thin films used for SEIRAS have been deposited by the evaporation technique [176,177]. However, as an evaporation chamber is a rather costly device, other methods have been used, such as a chemical deposition [180]. This chemical deposition technique is also the method used in this work.

Prior to the deposition, the flat surface of the Si hemisphere was pre-polished with a 1 µm polycrystalline diamond suspension (*Cloeren Technology*, CT DiaTwin May Poly 1 µm) on a medium-hard polishing cloth (*Cloeren Technology*, PT Silk 200). The fine polishing was done using an alkaline silica suspension (*Cloeren Technology*, OxyPol007, 0.2 µm) on a soft

synthetic cloth (*Cloeren Technology*, PT Chem 200). To remove any residues of the polishing steps, the crystal was ultra-sonicated twice for 15 min in isopropanol and twice in ultrapure water (Millipore, 18.2 MΩ cm). After ultrasonication, the crystal was cleaned following the RCA (*Radio Corporation of America*) procedure, which is a standard set of wafer cleaning steps in semiconductor manufacturing[406]: as follows: 5 parts (with respect to volume) of water and 1 part of NH_4OH were heated up to 80 °C, then 3 parts of H_2O_2 were added giving a mixture of 5:3:1 with respect to H_2O:H_2O_2:NH_4OH. Then the crystal was put in the hot solutions for 20 min. After these 20 min, the glass vessels containing the crystals and solution were removed from the heating plate and were overflown with water for about 1 minute to remove the contaminated RCA-solution and to prevent re-adsorption of any organic contamination. The remaining solution was removed via a stopcock at the bottom of the cleaning vessel.

The clean crystals were then transferred to a small chamber made of acrylic glass flushed with argon gas using a self-made tweezer with 3 gripper arms. Subsequently, 1 mL of an aqueous 40% NH_4F solution was pipetted onto the flat surface of the hemisphere to remove SiO_2 according to eq. (10.1):

$$SiO_2 + 6\,NH_4F \rightarrow SiF_6^{2-}(aq) + 6\,H_3O^+ + 6\,NH_4^+ \qquad (10.1)$$

Aside from removing SiO_2, the treatment also leads to an H-termination of the surface [407-410]:

$$\equiv Si - SiF_3 + NH_4F \rightarrow \equiv SiH + SiF_4 \qquad (10.2)$$

After approximately 5 min, the surface is hydrophobic as indicated by the formation of a large droplet of the solution with a high contact angle. After removal of the solution via a pipette, 1 mL of a plating solution[180] (*vide infra*) was pipetted onto the surface. The crystal remained in the Argon-filled chamber during the whole process of H-termination and gold plating. After roughly 3 min (indicated by the change from a yellow to a reddish colour), the gold plating solution was removed and the surface was cleaned with excess of ultrapure water. The gold plating solution was prepared as follows: First a solution of 378 mg Na_2SO_3, 248 mg $Na_2S_2O_3x5\,H_2O$ and 54 mg NH_4Cl was dissolved in deionized water. One mL of this solution was added to a Teflon beaker and mixed with 1 mL of a 30 mM $NaAuCl_4$ solution, 1 mL of 3% HF solution and 1 mL of 20% NH_4F solution. The Teflon beaker was stored in an Argon-filled chamber and was stirred, to remove residual oxygen from the solutions.

The presence of F^--ions in the plating solution decreases the redox potential of silicon via complexation:

$$Si^0(s) + 6\,F^-(aq) \rightarrow SiF_6^{2-}(aq) + 4\,e^- \qquad (10.3)$$

Having reduced the redox potential, the $AuCl_4^-$ complex can be reduced and gold deposits as a metal[180]:

$$AuCl_4^-(aq) + 3\,e^- \rightarrow Au^0(s) + 4\,Cl^-(aq) \qquad (10.4)$$

The solution comprising Na_2SO_3, $Na_2S_2O_3$ and NH_4Cl serves as a pH-puffer ensuring that a sufficient concentration of available F^--ions.

10.3 Results and Discussion

The infrared spectra in this section are reported as absorbance, i.e. $\log(I_0/I)$, where I_0 and I are the single beam spectra at the reference potential and the sample potential. Using this definition, increased absorption of species results in peaks pointing up, whereas a depletion of the species results in peaks pointing down. All spectra reported in this section have been recorded with a resolution of 4 cm^{-1} if not stated otherwise.

10.3.1 Characterisation of the Gold Electrode and CO-Adsorption

A typical CV of the gold electrode in diluted sulfuric acid is shown in Figure 10.4a, where the formation of the gold oxide can be observed starting from a potential of 1.1 V. However, due to the limited stability of the gold film, anodic potentials above 1.3 V have to be avoided as otherwise the gold film will detach from the silicon surface. In the cathodic sweep, the reduction of the gold oxide proceeds as expected. The absence of large, negative currents for potentials below 0.4 V indicates the absence of oxygen in the solution and shows that the argon purging is efficient.

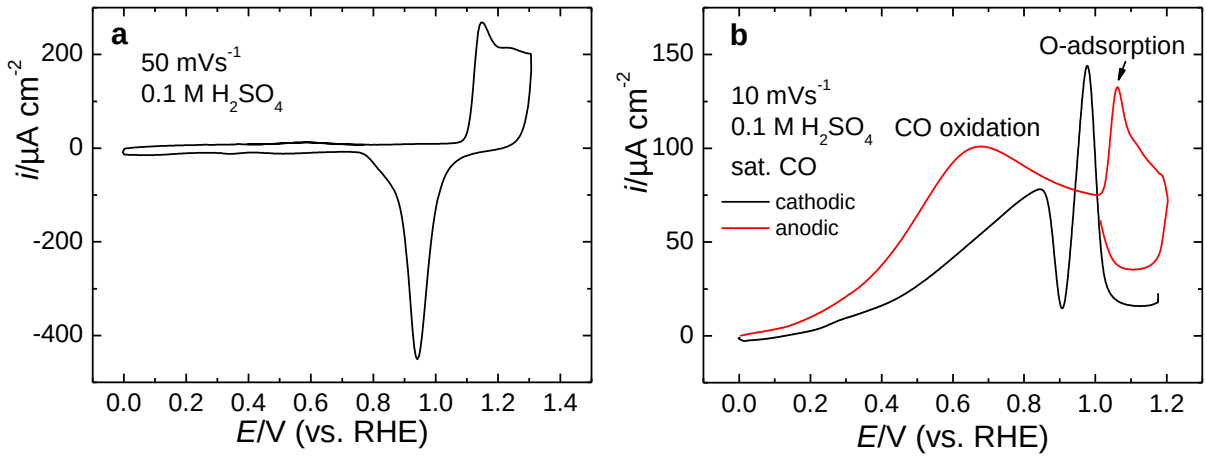

Figure 10.4. Typical CV of the ATR-SEIRAS gold electrode. **a**. CVs in oxygen-free 0.1 M H_2SO_4. **b**. CVs in CO-saturated solution.

After recording CVs in the base electrolyte, the solution in the measurement cell was saturated with carbon monoxide (CO) to investigate the surface enhancement of the gold film. The CV of the CO-saturated solution is shown in Figure 10.4b. Although the formation and reduction of the gold oxide is still present, the CV looks very different from the one shown in Figure 10.4a, which is because of the superimposed oxidation of CO. The IR spectra corresponding to the CV in CO-saturated solution are shown in Figure 10.5. The reference spectrum was recorded at 1.2 V, where a complete desorption of CO is expected due to the formation of the gold oxide [411]. Each spectrum is the average of 4 interferograms corresponding to a time resolution of 2.41 s. As the spectra were recorded during the linear

sweep, this means that each spectrum represents the average of a potential range of 24 mV. As can be seen from Figure 10.5a, an absorption band appears at a potential of 0.5 V with a peak position of 2150 cm^{-1}, which refers to linearly adsorbed CO [411]. As the potential is swept to the negative direction, the peak height increases due to the adsorption of CO and the peak position shifts to smaller wavenumber. Upon reverting the potential sweep (Figure 10.5b), the peak becomes smaller again and is shifting to larger wave number signifying the reproducibility of the measurement.

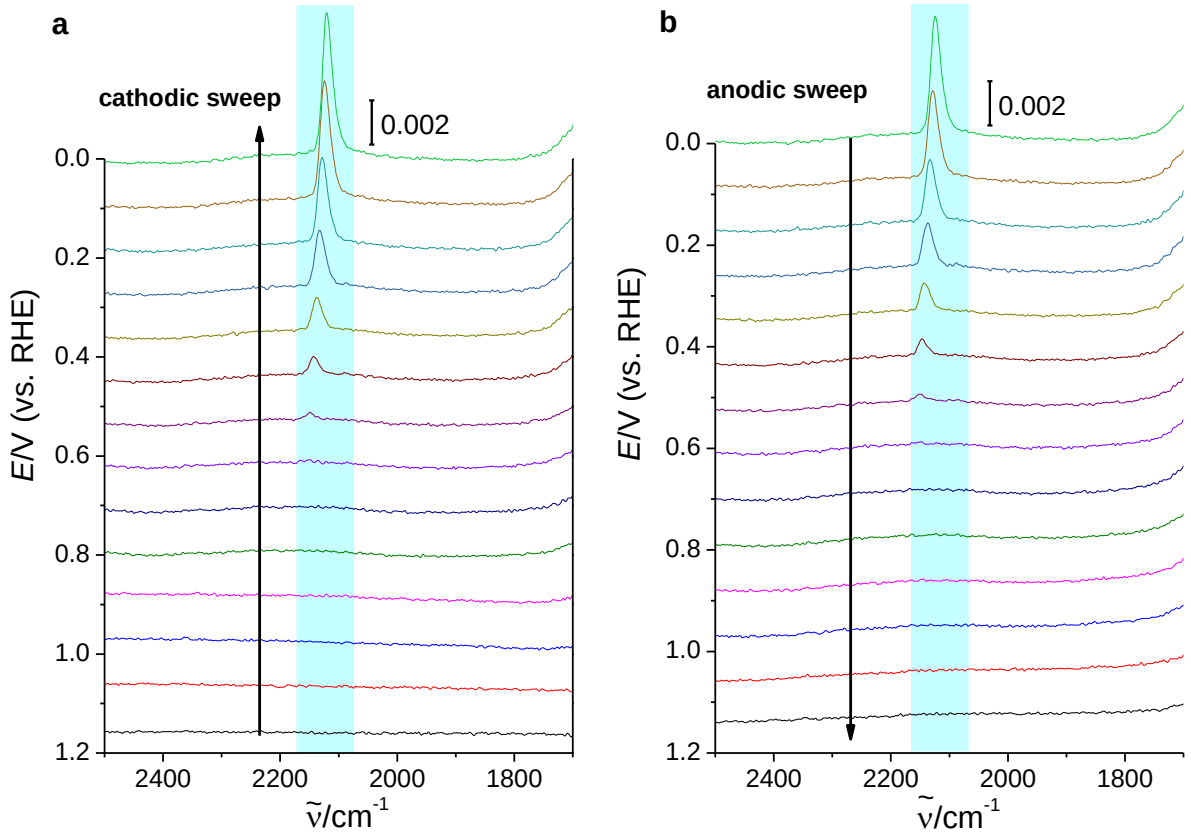

Figure 10.5. Typical ATR-SEIRAS of linearly bonded CO on Gold. **a**. Cathodic sweep starting from 1.2 V. **b**. Anodic sweep starting from 0.0 V. Reference spectrum taken at 1.2 V. The bar indicates the absorbance. The spectra have been offset to enhance clarity.

The shift of the peak position with the electrode potential (the Stark-shift) is displayed in Figure 10.6. The Stark-shift of 50 $cm^{-1}V^{-1}$ agrees well with the values reported in literature (~50 $cm^{-1}V^{-1}$ [412] 46 $cm^{-1}V^{-1}$ [411] reported in literature for CO-saturated perchloric acid). The shift between cathodic and anodic sweep results from the limited time resolution and the fact that the intensity of the CO-band varies with the potential.

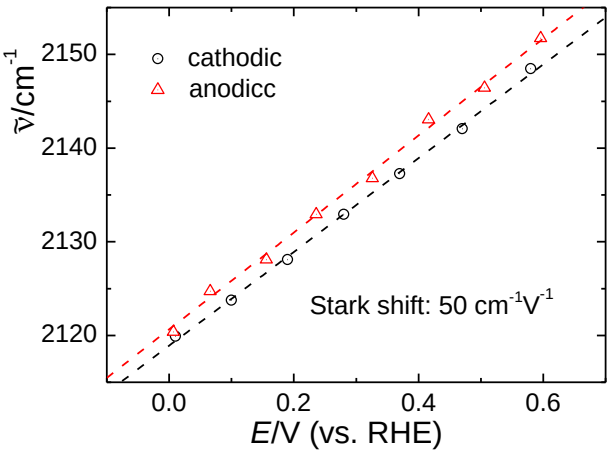

Figure 10.6. Stark-shift of linearly adsorbed CO. .

10.3.2 Cyanide-Adsorption from DMSO

Using non-aqueous electrolytes makes it necessary to remove ambient moisture as shown above. However, it is not feasible to purge a CO-saturated solution with argon. Therefore, cyanide was chosen to probe the interface between the gold electrode and DMSO. The CV of the KCN-containing solution is shown in Figure 10.7. The anodic currents for potential positive of −1.4 V indicate the partial dissolution of the gold film as the standard potential E^o of gold is significantly reduced due to the presence of CN^- (1.69 V vs. NHE for $Au^+|Au$ in absence of CN^- vs. −0.57 V in its presence [413], although the low concentration of KCN makes the shift of the actual redox potential less severe).

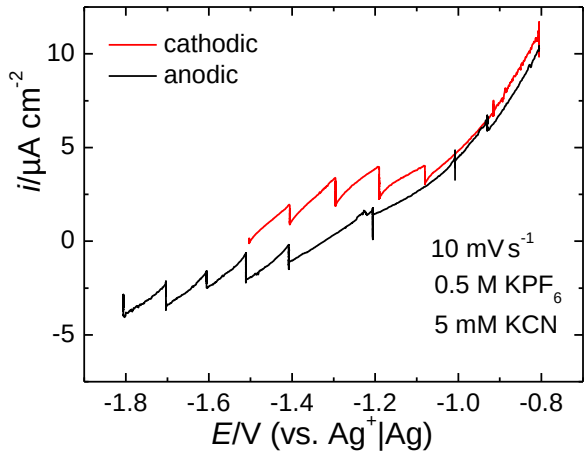

Figure 10.7. CV of the cyanide adsorption in DMSO.

The IR-spectra corresponding to the CVs in Figure 10.7 are shown in Figure 10.8. The main feature of the IR-spectrum is an absorption band at ~2100 cm^{-1}, which corresponds well with the wavenumber reported for adsorbed CN^- on gold as obtained by surface-enhanced Raman-spectroscopy (SERS) in aqueous electrolytes[414], but is somewhat different to the wavenumber 2140 cm^{-1} as determined via SNIFTIRS in DMSO-based electrolytes [392,393]. The reason for the latter might be related to the fact that Alwis *et al*. used a rather positive potential for the reference spectrum (−0.8 V vs. AgCl|Ag which is roughly −1.0 V vs. the reference electrode in

this work, neglecting liquid junction potentials) and generally examined the spectra at potentials positive of the reference potential. Therefore Au is dissolving significantly as $[Au(CN)_2^-]$ and the vibration of this complex in the solution is measured instead of the vibration on the surface, which would also explain the absence of a potential shift of this band.

As opposed to the spectra shown in Figure 10.5, the absorption band is bipolar, i.e. it comprises a minimum and a maximum in intensity. This behaviour generally occurs if the species responsible for the absorption band is still adsorbed at the reference potential and its peak shifts with potential [161,415]. Altering the potential to more positive potentials, the intensity of the minimum and maximum both increase (Figure 10.8a). However, after holding the potential at −0.8 V, significant dissolution of gold is visible (Figure 10.7) and the bipolar band changes to a simple, negative peak in the subsequent cathodic sweep. This signifies the apparent complete desorption of CN^- which occurs due to the dissolution of the gold surface.

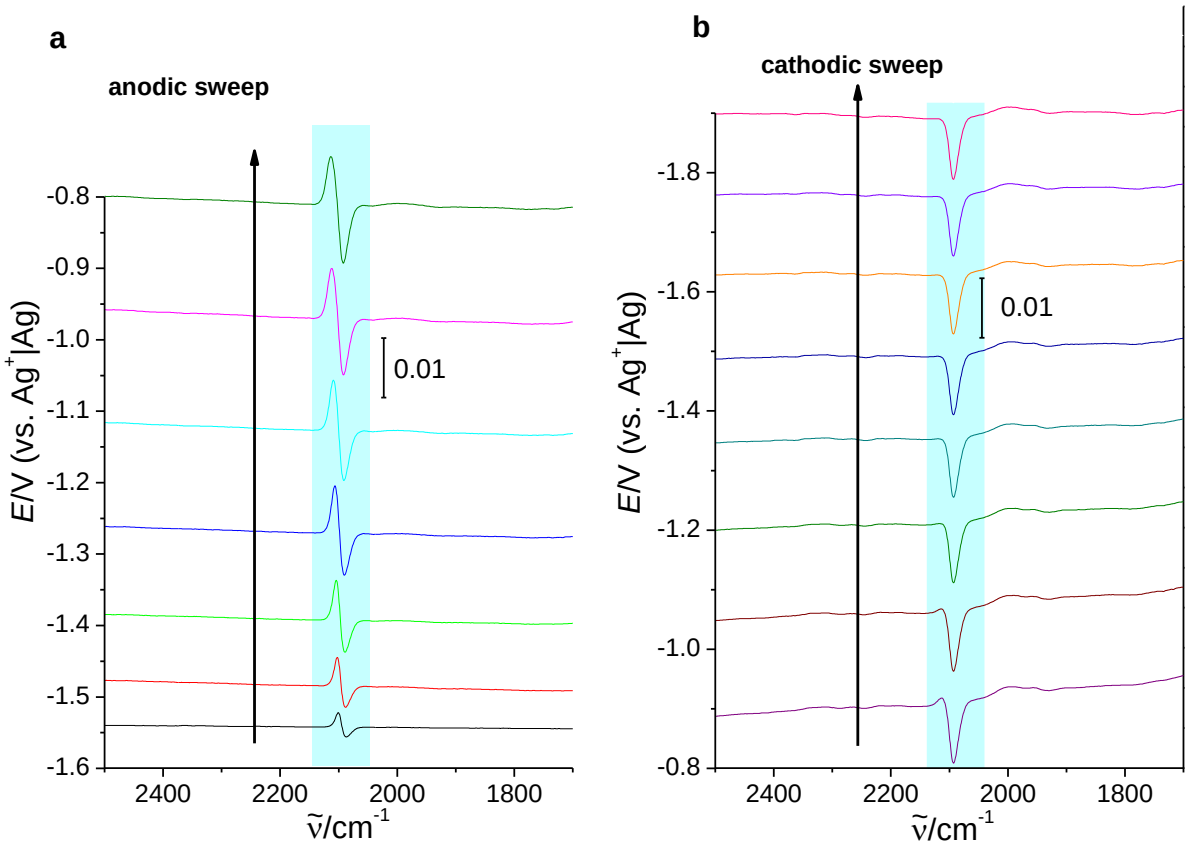

Figure 10.8. IR-spectra of cyanide adsorbed on gold. **a**. Anodic sweep starting from −1.6 V. **b**. Cathodic sweep from −0.8 V. Reference spectrum taken at −1.6 V. The bar indicates the absorbance. The spectra have been offset to enhance clarity. The potential was kept at a constant potential while acquisition of each spectrum. Electrolyte: 0.5 M KPF_6 and 5 mM KCN in DMSO.

Using the last spectrum of the cathodic sweep as a reference, “absolute” spectra can be calculated, resulting in less complex absorption peaks (Figure 10.9a). These spectra can be used to calculate the Stark-shift of the adsorbed CN^-(Figure 10.9b), while the bipolar bands might give erroneous values as the peak position is not only directly affect by the potential but also indirectly due to a changing relative intensity of the two peaks. The resulting Stark-shift

from the “absolute” spectra is 31 $cm^{-1}V^{-1}$, while the one calculated from the bipolar bands is 30% smaller. The value obtained in aqueous electrolytes via SERS is 40 $cm^{-1}V^{-1}$[414]. Although the results shown in Figure 10.8 and Figure 10.9 are promising in principle as they show adsorbed species in non-aqueous electrolytes, the limited potential window and instability of the gold film prevented further experiments. Moreover, the solubility of salts containing cyanide in solvents relevant for this work other than water or DMSO is very limited[416]. The adsorption of CN^- from PC was not successful.

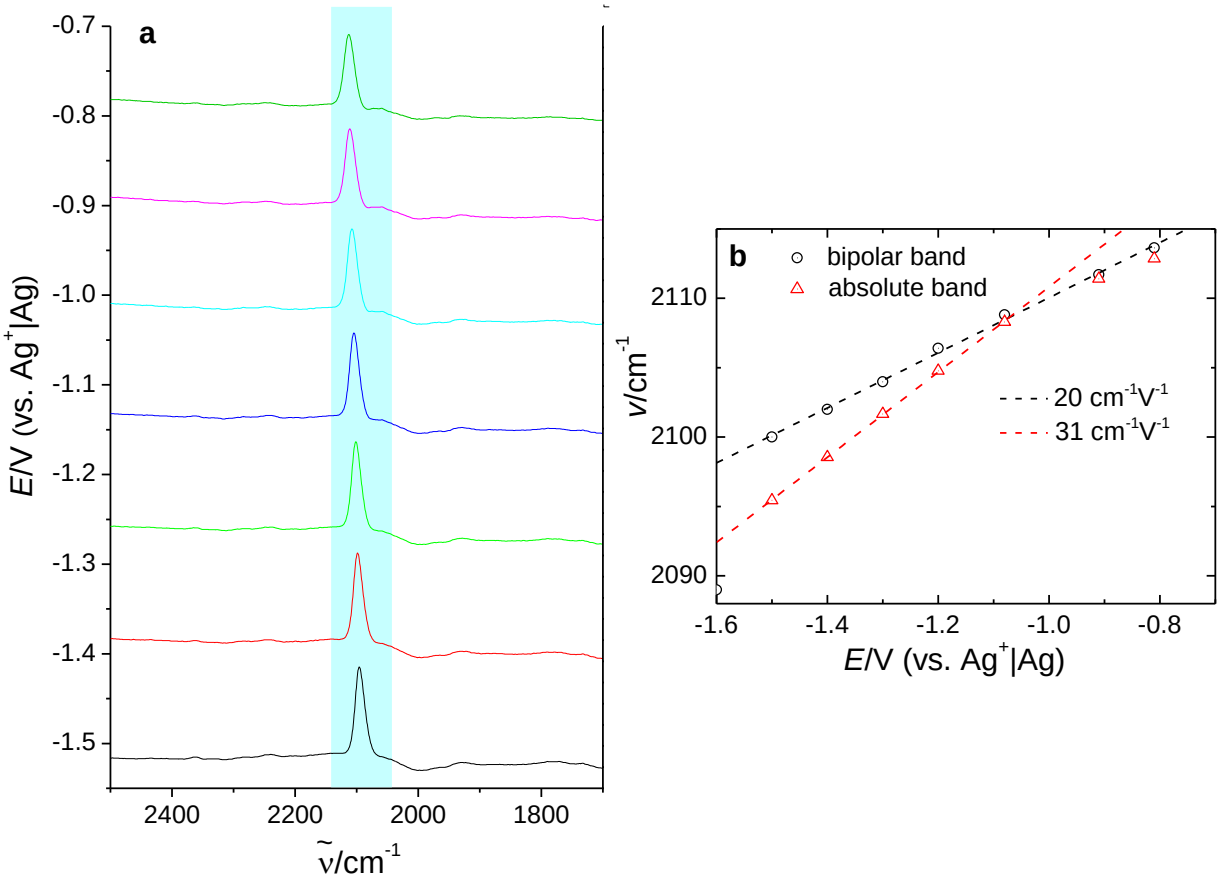

Figure 10.9. Absolute IR-spectra of cyanide adsorbed on gold. **a**. Absolute spectra calculated via subtraction of the spectrum at −1.9 V of Figure 10.8b as a reference. **b**. Shift of the wavenumber with the applied potential. The black circles represent the intensity maxima of the bipolar band, while the red triangles are the positions of the absolute peaks. Electrolyte: 0.5 M KPF_6 and 5 mM KCN in DMSO.

10.3.3 Electrochemical Double Layer: Propylene Carbonate

While CN^- or CO-adsorption could not be observed reproducibly during this work, the adsorption of the solvent itself is shown in Figure 10.10, with the reference spectrum taken at +0.5 V. Going to more negative potentials, a bipolar band at around 1800 cm^{-1} arises with the maximum shifting to lower wavenumbers. This band fits well to the C-O-vibration reported on silver electrodes from SERS measurements in the presence of sodium iodide[138]. Apparently, the process can be reverted. The corresponding CV is relatively featureless with the exception of a broad, weak peak at −0.3 V.

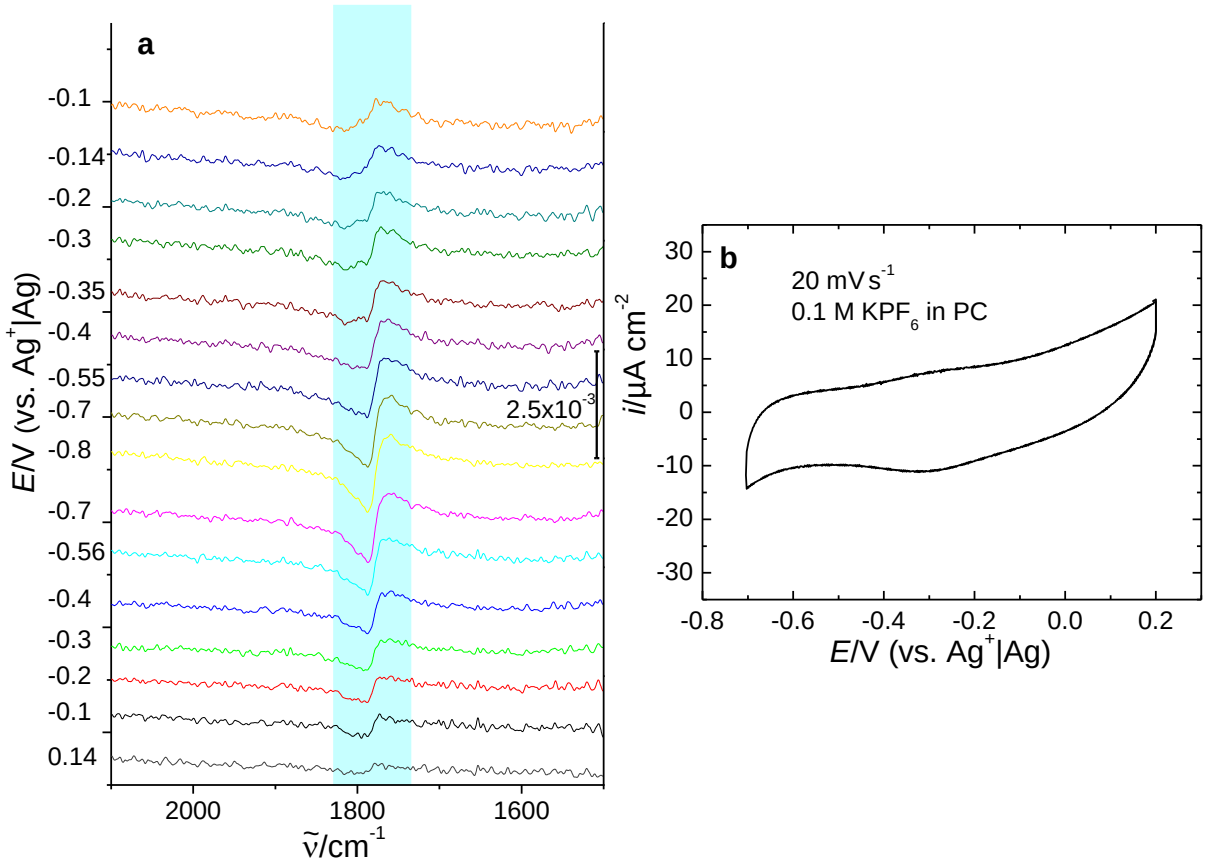

Figure 10.10. IR-spectra of propylene carbonate adsorbed on gold. **a**. IR-Spectra consisting of 8 interferograms with a total time resolution of 1.88 s. Reference spectrum collected at +0.5 V (not shown) **b**. Corresponding CV. Electrolyte: 0.1 M KPF_6 in PC.

Adding small amounts of water significantly affects the IR spectra. Generally, an increase in the absorption intensity is observed for a given potential (Figure 10.11a). However, as shown from a plot of the intensity versus time (Figure 10.11b) this effect does not seem to be an effect of co-adsorption, but is rather related to the properties of the gold film. For a given water content, the overall intensity increases over time or rather cycling. Upon addition of water, there is no discontinuous behaviour, but the slope of the curve increases. Moreover, reducing the water content afterwards by diluting the electrolyte in a separate experiment using MeCN as a solvent (not shown here) did not lead to a decrease of the intensity, which is a very good indication that the effect of water is irreversible and thus, connected to the properties of the gold film.

While the irreversibility of the effect of water and the presence of a time effect makes a quantitative evaluation of the intensity impossible, the water effect can still be exploited to gain insights into the potential-dependence of the propylene carbonate adsorption. Although the spectra for low water contents show bipolar bands, the spectra for high water contents are not bipolar anymore. This is because the overall intensity of the peaks increased so much that the residual intensity of adsorbed PC at the reference spectrum can be neglected. The resulting intensity of the peak at 1800 cm^{-1} are shown in Figure 10.11c. Although a time-effect is present, it can be clearly seen that PC adsorbs preferentially at negative potentials and desorbs at

positive potentials. This might be related to the fact that PC strongly solvates cations via its carbonyl group and therefore, co-adsorbs with the cations[417]. Using the spectra recorded with a water content of 1650 ppm, the shift of the C-O-band with potential can be illustrated (Figure 10.12). The resulting Stark-shift is ~9 $cm^{-1}V^{-1}$. The above-mentioned irreversibility of the water effect indicates that water rather changes the gold film's properties (e.g. its thickness) and thus, has an indirect effect on the PC spectra.

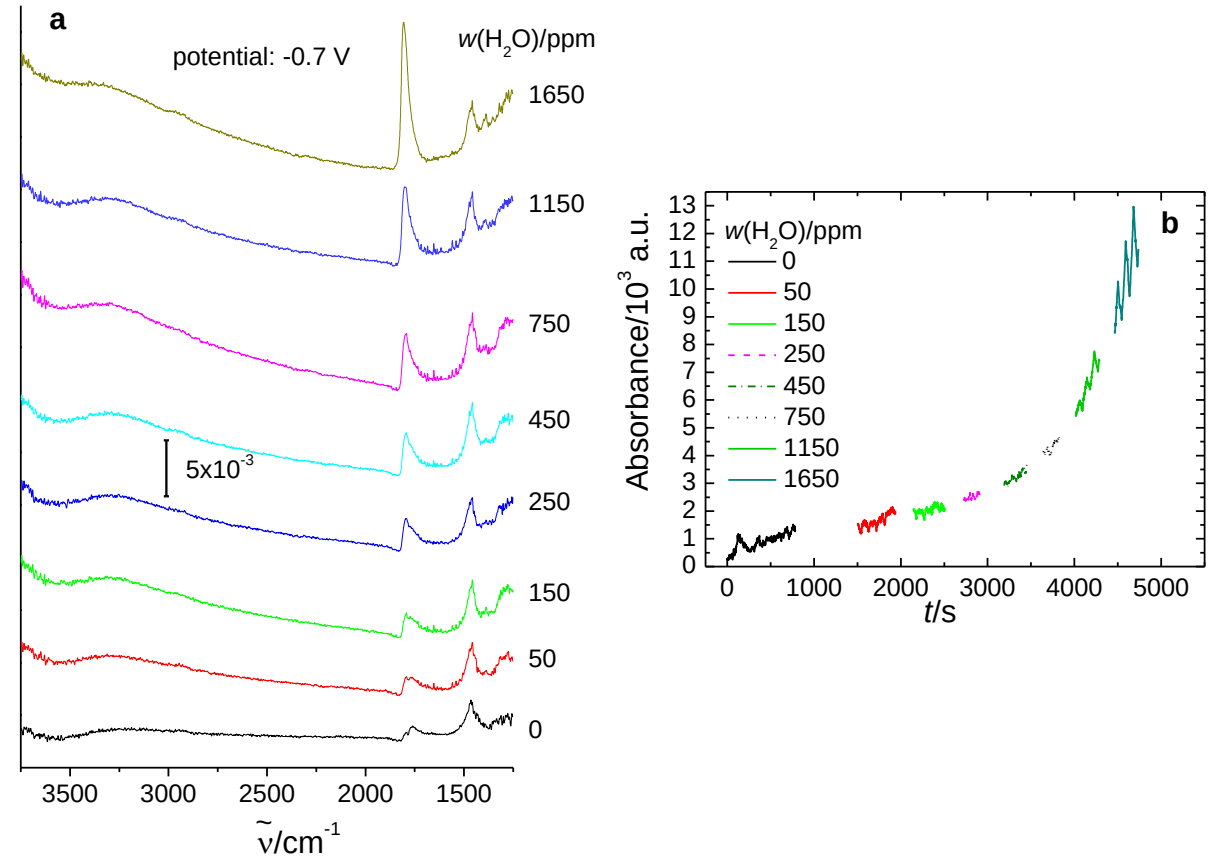

Figure 10.11. Effect of water on the IR-spectra of propylene carbonate. **a**. IR-Spectra consisting of 8 interferograms with a total time resolution of 1.88 s. Reference spectrum collected at +0.5 V in the absence of water. **b**. A plot of the peak intensity versus time. The different colours indicate a different water content. Electrolyte: 0.1 M KPF_6 in PC.

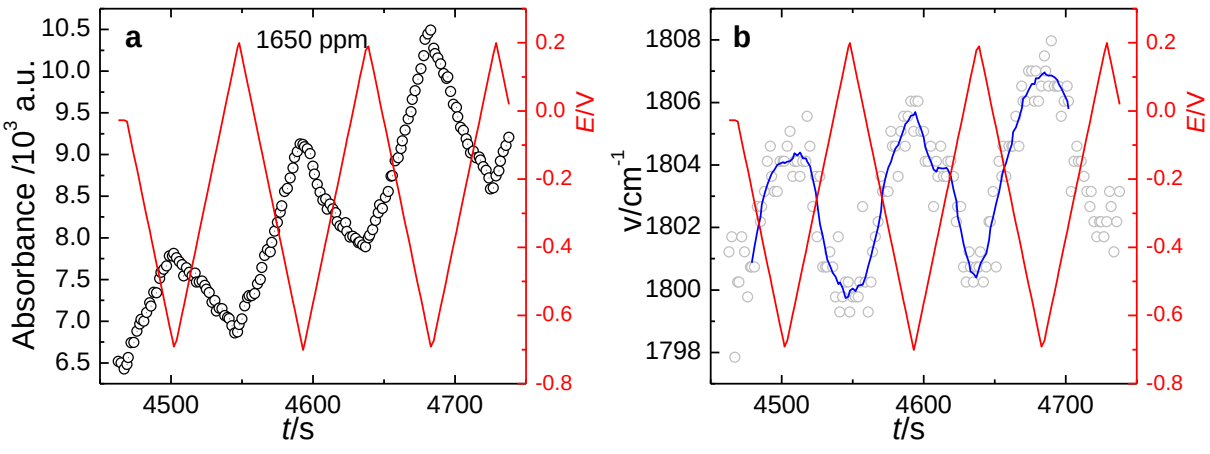

Figure 10.12. Correlation of the CO-band of PC with the potential. **a**. Absorbance of the band at 1800 cm^{-1} for a water content of 1650 ppm as a function of time and potential (right axis, red) without

baseline-correction. **b.** Shift of the CO-band of PC with the potential applied to the gold electrode. Electrolyte: 0.1 M KPF_6 in PC.

10.3.4 Electrochemical Double Layer: Acetonitrile

Another solvent promising intense IR-absorption is acetonitrile. The symmetric stretch vibration of the CN-group is usually observed at 2250–2260 cm^{-1}[418,419], which is very well within the detectable range. The IR-spectra of acetonitrile containing 0.1 M $LiClO_4$ are shown in Figure 10.13. The assignment of the bands for acetonitrile accords to Parellada *et al.* [418] and Irish *et al.* [137].

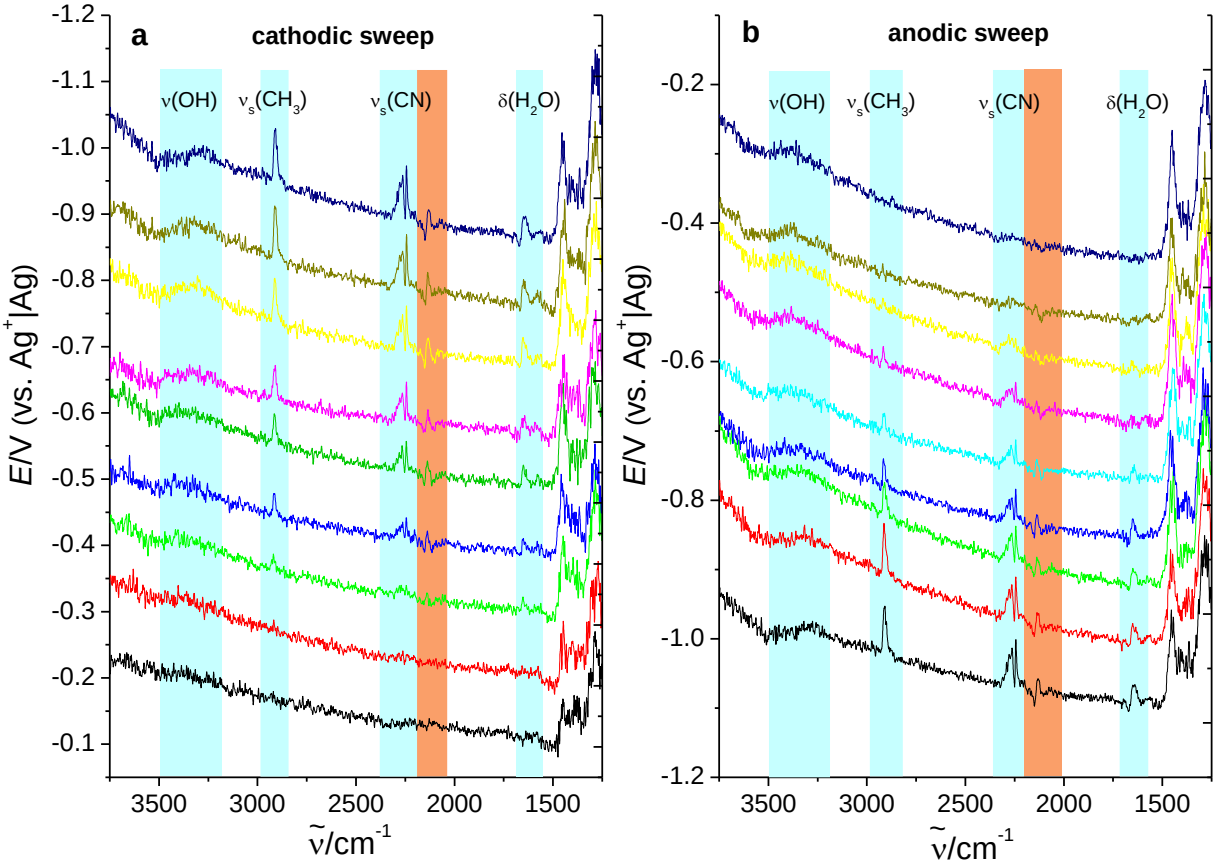

Figure 10.13. IR-spectra of acetonitrile adsorbed on gold. **a**. Cathodic sweep starting from -0.2 V. **b**. Anodic sweep. Each spectrum consist of 8 interferograms with a total time resolution of 1.88 s. Reference spectrum collected at −0.2 V (not shown). Sweep rate: 10 mV s^{-1}. Electrolyte: 0.1 M $LiClO_4$ in MeCN.

As can be seen from Figure 10.13a, several absorption bands are visible upon cycling the potential in the negative direction. Most peaks, with the exception of the broad contribution of the OH-stretching vibration from residual water disappear, when the potential is swept back the reference potential. The band at 2910 cm^{-1} is tentatively attributed to the symmetric CH_3-stretch vibration, although it is significantly red-shifted compared to the reported values of 2945 cm^{-1} for non-adsorbed acetonitrile[418] or 2924 cm^{-1} for adsorbed acetonitrile coordinated by Li^+ on a iodide-covered silver electrode as observed via SERS[137]. This red-shift indicates a significant weakening of the C-H-bonds, which has to be elucidated further. The dependence

of the (baseline-corrected) absorbance of the peak at 2910 cm^{-1} on the potential is displayed in Figure 10.14a, while Figure 10.14b shows the dependence of the peak position on the potential. Due to desorption of acetonitrile at positive potentials, the peak position cannot be determined in a reliable way for potentials above −0.4 V. The overall Stark-shift of the CH_3-stretching vibration is 14 $cm^{-1}V^{-1}$ and shows that the peak is due to an adsorbed species.

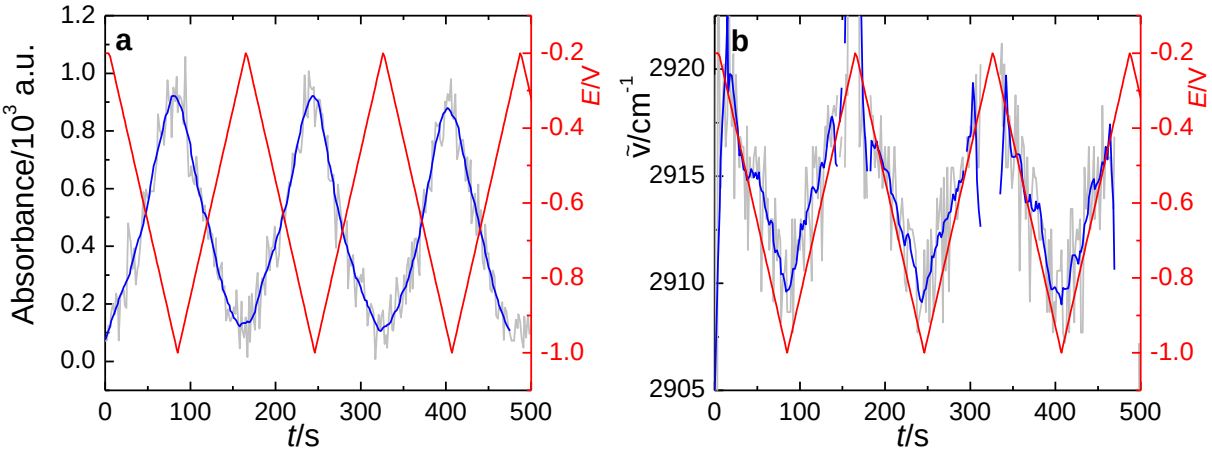

Figure 10.14. Stretching-vibration of the methyl-group of acetonitrile on gold. **a.** Absorbance and potential as a function of time. **b**. Peak position and potential as a function of time. The absorbance and peak position were determined from maximum value between 2900 and 3000 cm^{-1} taking the mean intensity between 2500 and 2750 cm^{-1} as baseline.

Another region which shall be discussed here are the wavenumbers at around 2100 to 2300 cm^{-1} and a magnification of this region is shown in Figure 10.15, where Figure 10.15a is just one single spectrum in almost the full range and Figure 10.15b is the close-up between 2100 and 2300 cm^{-1}. The absorption band at 2130 cm^{-1} is far away from the wavenumbers usually reported for the CN-stretching vibration of acetonitrile [137,418] and is rather attributed to cyanide adsorbed to the surface, which has also been observed via SERS on silver[137,395] and platinum [397].

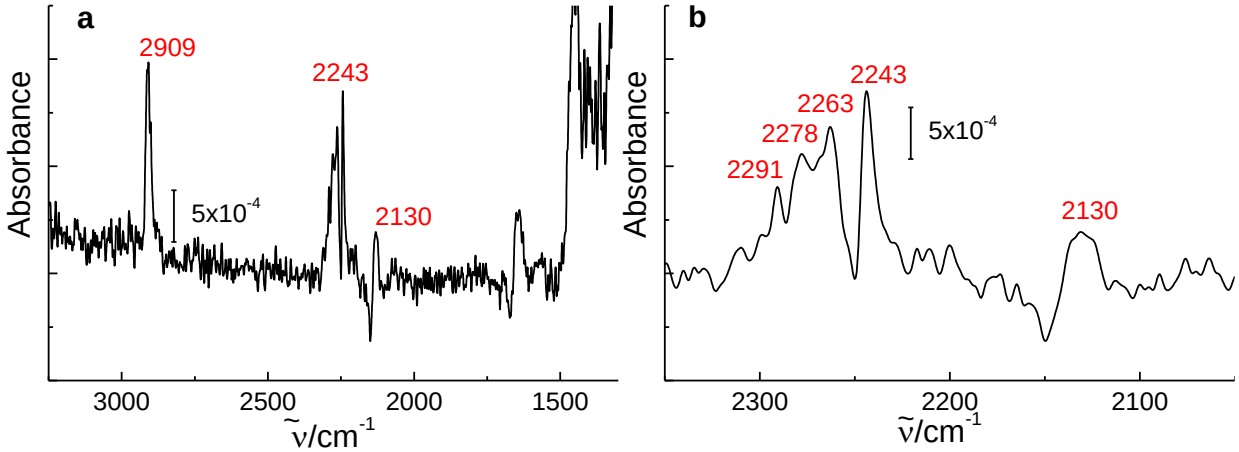

Figure 10.15. Magnification of the SEIRAS of acetonitrile on gold. **a.** Magnification including the C-H-vibration and the H_2O deformation vibration. **b.** Close up on the CN-stretching region. Sample potential: −1 V.

The vibration band of the cyanide resulting from the decomposition of acetonitrile at 2130 cm^{-1} again has a bipolar nature, which results from the fact that some cyanide was probably present when the background spectrum was collected. Regardless of the bipolar nature, the absorbance and the position of the peak in positive direction have been determined and correlated with the potential (Figure 10.16). As can be seen from Figure 10.16a, the cyanide anion is adsorbed at anodic potentials and desorbed at cathodic potentials. The wavenumber changes with a slope of 20 $cm^{-1}V^{-1}$ which is in principle agreement with the results obtained for the bipolar band in DMSO (Figure 10.9). The significant blue-shift of almost 20 cm^{-1} might results from the generally more positive potentials in this measurement and the difficulties of determining a reliable peak position at −1.0 V.

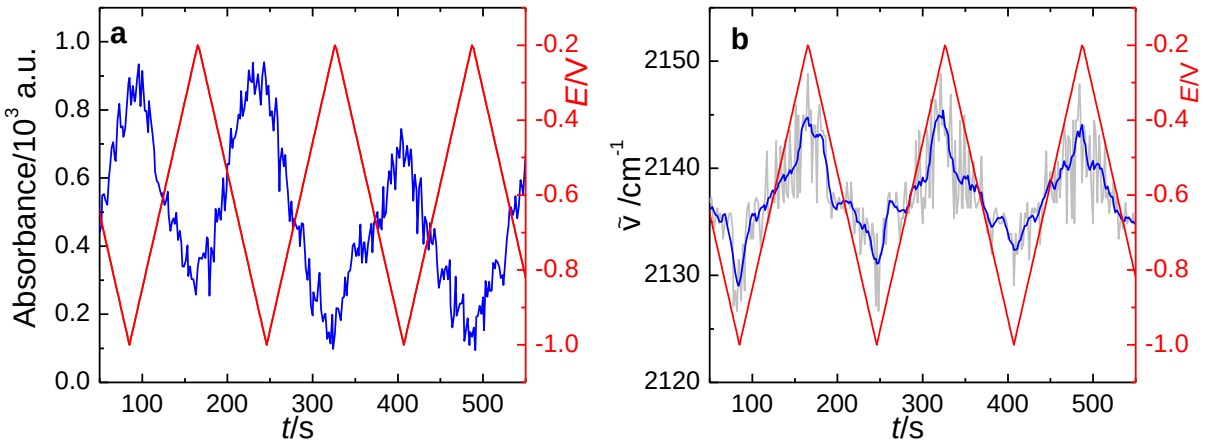

Figure 10.16. Absorbance and position of the CN-Band of decomposed acetonitrile. **a**. Absorbance and potential as a function of time **b**. Peak position and potential as a function of time. The peak position and absorbance were determined from the maximum absorbance between 2100 and 2150 cm^{-1} without baseline correction.

In the following paragraph, the series of peaks attributed to acetonitrile itself shall be discussed. The peak at 2243 cm^{-1}, which is tentatively attributed to the CN-stretching vibration of acetonitrile, is slightly redshifted with reference to the SER spectra obtained on silver(2248 cm^{-1} in presence of LiI [137] and 2253 cm^{-1} in presence of $LiClO_4$ [395]) and platinum Pt (2254 cm^{-1} [397]). The peak only very weakly depends on the potential (Figure 10.17a) with a slope of 2.5 $cm^{-1}V^{-1}$, which is already at the limit of resolution as can be seen from the "steps" in the graph (the resolution after zero-filling (see chapter 2.6) is 4cm^{-1}/8=0.5 cm^{-1}). The fact that this peak depends so weakly on the potential, might imply that it is either from non-adsorbed acetonitrile or that acetonitrile is actually adsorbed via the CH_3-group at this potential (the point of zero charge is 0.07 V [420]), which therefore shows a significant dependence on the applied potential (Figure 10.14b). In fact, it has been hypothesized by Tian and co-workers that the peak at 2254 refers to "bulk" acetonitrile [395], while Irish *et al*. assign the bands at around 2250 cm^{-1} to the solvent at the electrode surface [137]. It is noteworthy that Cao *et al*. only observe a single absorption band at 2254 cm^{-1} instead of three bands as in the present

study or shown in the work of Irish *et al*.. As Irish *et al*. showed that the three bands eventually merge into a single band at 2254 cm^{-1} if the water content is above 20 mM and thus, the presence of water might be the reason for the deviation of Cao's work from ours and Irish's.

The peak at 2291 cm^{-1} can be attributed to the combinational band of the C-C-stretching and the CH_3 symmetric bending vibration[137]. Neither for this peak, nor for the peak at 2263 cm^{-1} a significant potential dependence is observed (Figure 10.17b), which is in contrast to the results obtained by Irish *et al*, who found Stark-shifts of the order of 10 $cm^{-1}V^{-1}$. However, the absorbance is significantly affected by the potential, which shows that the vibration belongs to an adsorbed molecule. The absence of a Stark shift for both bands implies that the peak at 2263 cm^{-1} is also related to the combinational band of the C-C-streatching and CH_3 symmetric bending vibration.

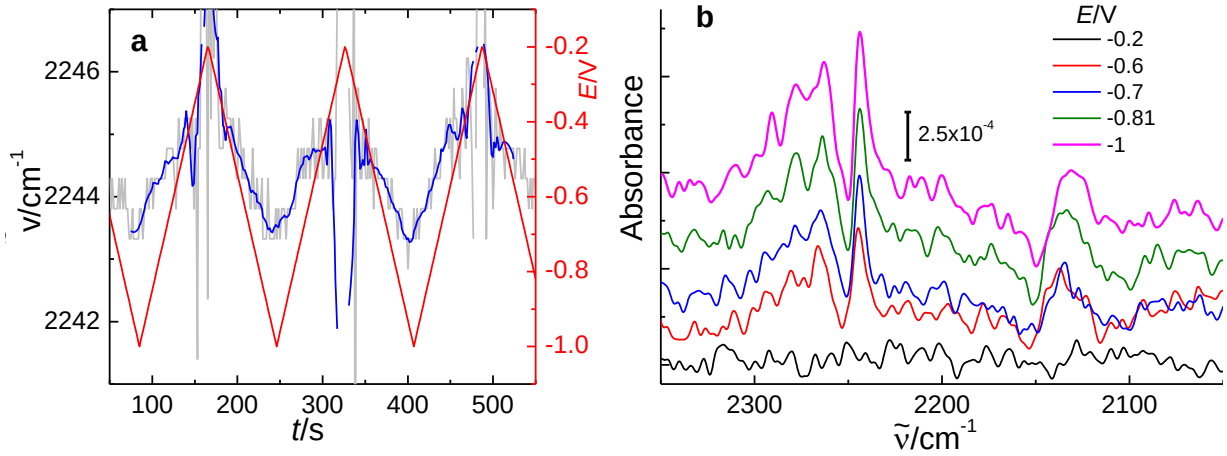

Figure 10.17. Position of the CN-bands of acetonitrile. **a**. Peak position and potential as a function of time. The peak position was determined from the maximum absorbance between 2230 and 2250 cm^{-1} without baseline correction. **b**. Close-up on the CN-stretching region for different potentials. Electrolyte: 0.1 M $LiClO_4$ in acetonitrile.

Preliminary results on the effect of the cation on the absorption bands of MeCN are shown in Figure 10.18. The experiments shown in Figure 10.18 a and b have been recorded using different gold electrodes, which have been prepared in the same way. However, the actual structure of the gold film and its surface-enhancement is difficult to control. To account for effects related to the different structure of the gold film, the measurements have been repeated using the very same gold film in a series of subsequent measurements, starting with Ca^{2+}, followed by Na^+ and ending with Li^+ (Figure 10.18 c and d). As can be seen, the presence of Ca^{2+} causes a significant blueshift of the CH-stretching vibration as compared to Li^+ and Na^+, which have a similar effect on the CH-vibration. The invariance of the symmetric CH-vibration in the presence of either Na^+ or Li^+ has also been reported by Irish *et al*. [137]. In the CN-region of the spectrum, the effect of the cations are more pronounced. In the presence of Li^+, three peaks are observed for wavenumbers above 2260 cm^{-1} although the two peaks at around 2270 cm^{-1} are not resolved in the repeating measurement (Figure 10.18 d). In contrast to that,

for Na^+ and Ca^{2+}, there is a pair of two peaks for wavenumbers *below* 2260 $cm^{-1}$and just a single vibration band at 2283 cm^{-1}. The independence of the vibration band at 2245 cm^{-1} and 2283 cm^{-1} indicate that these band are related to adsorbed MeCN, which does not directly interact with the cation. For further elucidation of the adsorption structure of MeCN and assignment of the vibration bands, the spectra will be simulated. However, the results of these simulation will be part of a future work.

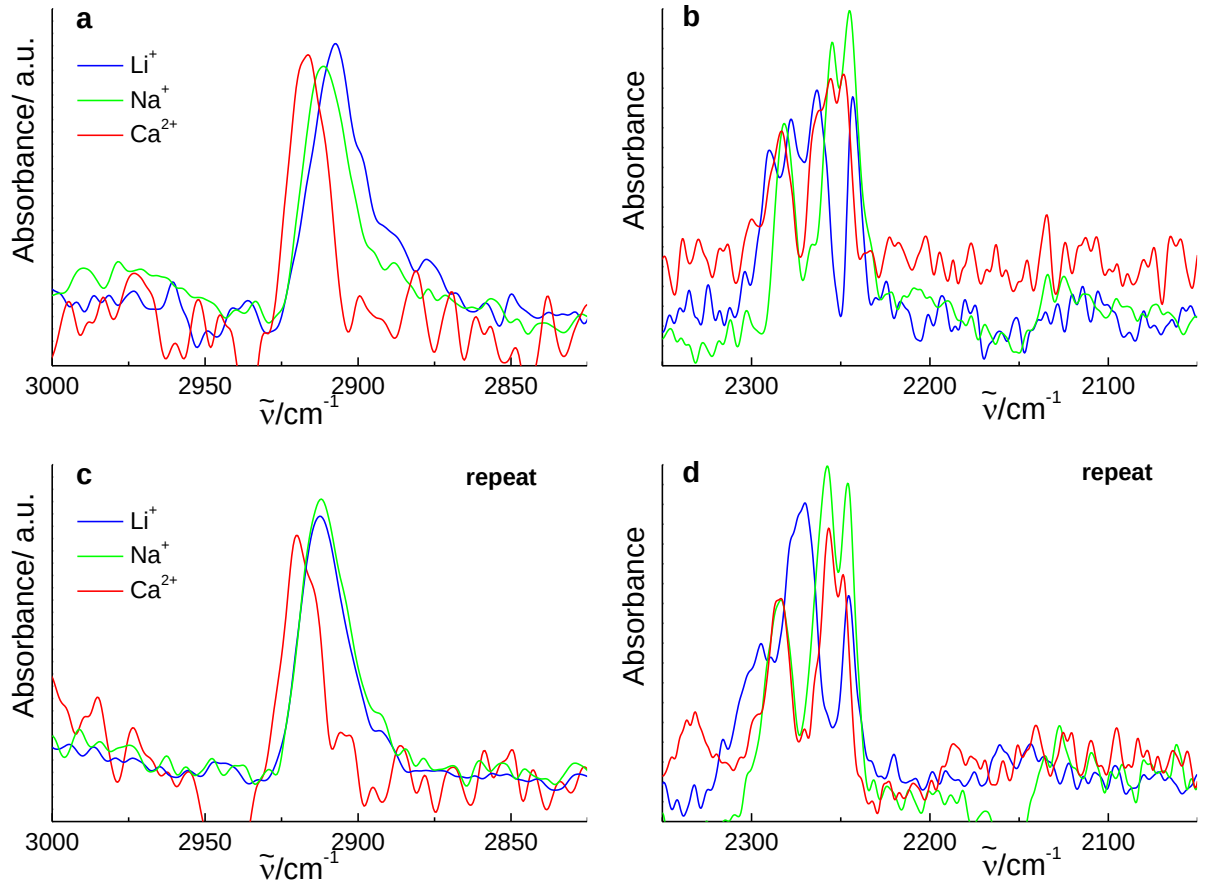

Figure 10.18. Effect of the cation on the absorption bands of acetonitrile. **a, c**. Effect on the CH-vibration band. **b, d**. Effect of the cation in the CN-stretching. The spectra shown in the upper row have been recorded using different gold electrodes. The spectra in the lower row have been recorded on the very same gold electrode on subsequent days. All spectra have been recorded at −1.0 V and consist of 32 interferograms. The background spectrum was recorded at −0.2 V. The absorbances have been multiplied by different factors to alleviate comparison between the measurements. Electrolyte: 0.1 M solutions of the metal perchlorates in acetonitrile.

10.4 Conclusions

Surface-enhanced infrared spectroscopy has been utilized to investigate the interface between the electrified surface of a gold electrode and the electrolyte. The adsorption of carbon monoxide has been observed in propylene carbonate-based electrolytes. The shift of the wavelength with the potential (50 $cm^{-1}V^{-1}$) is similar to the shift observed in aqueous electrolytes and indicates that the CO molecules are linearly adsorbed. Moreover, the

adsorption of cyanide in a DMSO-based electrolyte has been investigated. Although the Stark-shift is only 2/3 of the Stark-shift observed in an aqueous environment, a pronounced effect of the potential on the band position has been determined ($30\,cm^{-1}V^{-1}$). Unfortunately, the investigation of the adsorption of cyanide proved difficult due to the limited stability of the thin-film gold electrode.

The investigation of the effect of water on the adsorption spectra of propylene carbonate showed that great care has to be taken with interpretation as the addition of water led to an irreversible increase in the adsorption intensity, probably related to irreversible changes of the thickness or morphology of the gold film. SEIRA-spectra obtained in Li^+-containing acetonitrile were in excellent accordance with SER spectra under similar conditions. By the comparison to different results in the literature, a solvent-coordinated as well as a cation-coordinated, adsorbed acetonitrile have been identified. Moreover, the reductive decomposition of acetonitrile to adsorbed cyanide has been observed, which has also been found in different SERS measurements. However, it is unlikely that this decomposition is due to a photochemical reaction as proposed by the authors of a SERS study because of the use of low-energy IR radiation as opposed to the use of a high-energy laser radiation as in SERS. From the comparison of different electrolytes, cation-dependent and cation-independent absorption bands have been identified.

11 Summary and Outlook

In this thesis, several effects with focus on the oxygen reduction reaction in non-aqueous electrolytes, in particular DMSO, have been elucidated. In chapter 3, the effect of a divalent cation, namely Mg^{2+}, on the ORR has been investigated via DEMS for the first time. Although the two-electron reduction dominates the ORR, no reoxidation of oxygen could be observed as opposed to the ORR in presence of monovalent cations [123,311,421]. This is especially astonishing as there was evidence for the deposition of insulating species on the electrode, which might be expected to be related to the peroxide. Moreover, the charge passed into this insulating layer was significantly larger than the two monolayers usually observed in Li^+-containing DMSO under similar experimental conditions[139].

To better understand the effects of a divalent cation, a study on the ORR in presence of another earth alkaline metal, namely calcium, has been presented in chapter 4. Similar to the results obtained in Mg^{2+}-containing DMSO, a two-electron process has been observed at gold electrodes. However, neither significant deactivation of the surface nor the evolution of oxygen has been observed under flow conditions (see A 1 for additional results on the ORR and also OER at gold). While we initially believed that this could be attributed to the formation of soluble, reduced oxygen species, RRDE-measurements do not show significant amounts of re-oxidisable species during ORR (see section A 1). Moreover, the RRDE-measurements revealed that there is in fact a transition from the two- to the one-electron process, probably attributable to some kind of surface blocking. In contrast to the ORR at the gold electrode, on glassy carbon and platinum a highly reversible one-electron process was observed. Despite the significantly higher charge density of Ca^{2+} as compared to Na^+ or K^+ [285], no transition from the one- to the two-electron process was observed, which challenged our previous hypothesis of a correlation between charge density of the cation and the relative amount of peroxide formed at a given potential [139].

So far, Ca^{2+} was just an exception to the series of TBA^+, Li^+, Na^+, K^+ and Mg^{2+}-containing electrolytes, which showed a linear relationship between the potential upon a two-electron process was observed at gold and the charge density of the cation of the conducting salt. Therefore, we also investigated the ORR in Sr^{2+} and Ba^{2+}-containing electrolytes on different electrocatalysts in chapter 5 (additional RRDE measurements are shown in section A 2). Again, the almost exclusive formation of peroxide was observed at the gold electrodes, while the number of electrons per oxygen varied at glassy carbon and platinum. Instead of correlating the product distribution to the charge density of the cation, derived from the Shannon radii in the crystal lattice, we introduced another parameter to describe the cation's influence, which should also contain some information on the solvation of the cation: the acceptor number of the cation reflecting the interaction of the cation with a bidentate iron complex as defined by

Linert *et al*. (see Figure 5.6)[286]. As only a small number of acceptor numbers are available, a final conclusion is difficult at this point.

A graphical summary of the effect of the cation on the product distribution at gold is shown in Figure 11.1, including unpublished results in Na^+-, Rb^+- and Cs^+-containing DMSO (appendix A 3 for details on Na^+, Rb^+ and Cs^+). As can be seen from Figure 11.1a, the linear correlation between the potential at which a transition from the one-electron to the two-electron process occurs ($E_{transition}$) and the charge density of the cation is valid for all alkali-cations. However, the invariance of the transition potential in the case of the alkaline earth cations shows that the effect of the cation is not restricted to its charge density. Moreover, comparing the relative stabilities of the superoxides and peroxides (Figure 11.1b) indicates that the effect of the cation is not only a thermodynamic effect. In the case of barium, for instance, the formation potential of the superoxide ($E^o(M(O_2)_x)$) and peroxide ($E^o(M_xO_2)$ are very close to each other and thus, would be expected to behave similar to Na^+. Nonetheless, exclusive formation of BaO_2 is observed, while there is a distinct transition from the formation of NaO_2 to Na_2O_2.

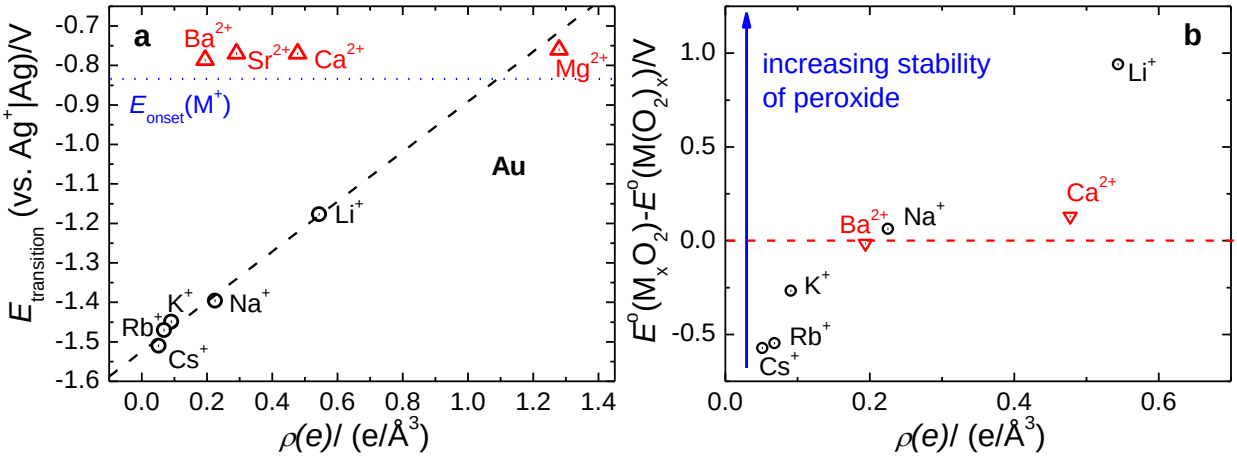

Figure 11.1. Effect of the cation on the product distribution of the ORR. **a**. Potential at which a transition from superoxide to peroxide formation occurs as a function of the charge density of the cation of the conducting salt as calculated from the ionic radii[285]. The potential was derived from RRDE-measurements. The blue, dotted-line indicates the onset of the ORR for the monovalent cations. **b**. Relative stability of the metal peroxides calculated as the difference between the formation potential of the peroxide and the superoxide. The formation potentials have been calculated from the standard enthalpies of formation of the oxides if available [280].

Further elucidation of the ORR in DMSO was presented in chapter 6, where the effect of the oxygen concentration and the electrocatalyst has been addressed in detail. While the electrochemical reaction order with respect to oxygen in presence of Mg^{2+} was close to zero, the reaction order in Li^+-containing DMSO is unity. Moreover, the comprehensive kinetic study allowed us to calculate rate constants and refine the mechanistic picture. Via application of different kinetic models, we were able to identify a surface-confined reaction pathway at gold, which directly leads to the formation of the peroxide and renders the gold electrode unique as compared to the other electrodes under investigation. Indications for this surface-confined

reaction and the presence of adsorbed superoxide has also been found spectroscopically[283,284]. While the reoxidation of Li_2O_2 requires an overpotential of nearly 600 mV, the overpotential for reoxidation of K_2O_2 is only 100 mV as shown in chapter 7. Via the application of a DEMS-cell employing a generator-collector arrangement of the electrodes, it was shown that the peroxide is initially reoxidized to superoxide, which can be further oxidized to oxygen. Moreover, we showed that increasing the oxygen partial pressure leads to a pronounced precipitation of KO_2, which fosters the subsequent formation of K_2O_2. In chapter 8, the ion pair formation between K^+-ions and superoxide was investigated. From the comparison to TBA^+-containing electrolyte, it was concluded that K^+ stabilizes the superoxide in solution. The stabilization of superoxide by K^+ revealed the current misconception of Pearson's HSAB (hard and soft acid base)-theory, which is often invoked in the context of non-aqueous metal-air batteries. The authors usually state that TBA^+-cations stabilize superoxide due to the *softness* of the TBA^+ cation as compared to Li^+ [62,87,311]. However, K^+ is *harder* than TBA^+, but at the same time it is also a stronger acid, which makes the interaction between superoxide and K^+ favorable. The refined mechanistic picture is exemplarily shown in Figure 11.2 for monovalent cations. Evidence for the surface confined mechanism has only been found in the presence of Li^+ at gold electrodes so far. The potentials associated with the two-electron process are given in Figure 11.1. The disproportionation is not active in presence of K^+ (and presumably also not in the presence of Rb^+ and Cs^+), but plays an important role in Li–O_2 electrochemistry.

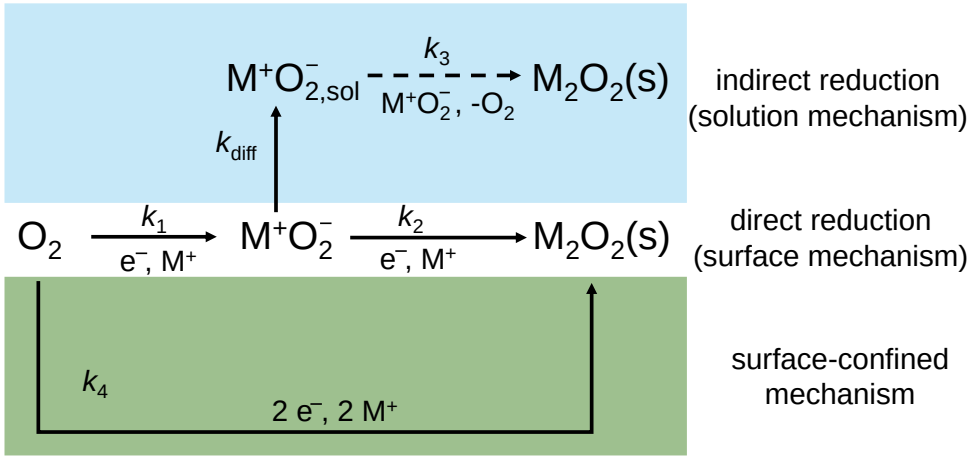

Figure 11.2. Refined mechanism of the ORR for monovalent cations. The surface confined mechanism is only active for large at very negative potentials and has only been observed at gold electrodes.

To also address indirect effects of the cation of the conducting salt on the ORR, we constructed a measurement cell for diffusivities and solubilities of volatile species in liquids and presented a series of measurements and effects in chapter 9. The pronounced effects of the different cations on the solubility have to be taken into account for calculation of theoretical values like the diffusion-limited current. Moreover, as shown in chapter 6, the absolute concentration of oxygen in the electrolyte also might have an important effect on the appearance of certain features, such as the transition from superoxide to peroxide formation.

From a practical point of view, especially the effect of the anion, which was exemplarily elucidated comparing $LiClO_4$ and LiTFSI, is interesting because the cation of the conducting salt is usually corresponding to the metal anode in a metal–air battery. The significant salting-in effect of LiTFSI, which also has been reported by Lindberg *et al*. [352], might foster higher discharge rates and discharge capacities. Fortunately, highly-concentrated LiTFSI electrolytes also seem to be advantageous with respect to the metal deposition[422].

Finally, the adsorption of different species on gold electrodes in a non-aqueous environment has been elucidated in chapter 10. The pronounced effect of the potential on the adsorption of the solvent has mainly been attributed to the adsorption of the cation due to the non-adsorbing nature of the perchlorate. The investigation of carbon monoxide and cyanide adsorption show many parallels to the aqueous system. However, while water contaminations can be kept low, they cannot be fully excluded as the potential-dependent appearance of absorption bands due to water in the different spectra show. As shown by the investigation of the water effect in propylene carbonate, great care has to be taken when interpreting the effect of water as it irreversibly increases SEIRAS-intensities, probably by affecting the gold-film. Despite this result, it was possible to use SEIRAS to study the adsorption of acetonitrile in detail and to extract fundamental adsorption properties by comparison to SERS measurements on silver electrodes. By the comparison of different conducting salts, the effect of the cation on the acetonitrile adsorption has been elucidated.

In this work, the role of the cation and other fundamental details of the ORR have been addressed and elucidated. While especially the underlying mechanisms for Li^+- and K^+-electrolytes have been investigated and discussed in great detail, the mechanism in the presence of divalent cations still has to be further refined. From the comparison of different divalent cations we concluded that for instance the acceptor number of the cation should be rather used as a parameter to predict the cation's influence on the product distribution. However, the fundamental reasons for the different behaviour of the monovalent and divalent cations remain elusive. Using the acceptor number instead of the charge density as a predictor would shift the problem from the prediction of the product distribution to the prediction of the acceptor number, or directly speaking: Why does the acceptor number not depend monotonously on the charge density? Answers to this question might be chelating effects of the divalent cation, but the connection to the ORR cannot be directly drawn. An important aspect aggravating the discussion of the cationic effect is the complexity of the overall reaction mechanism and the presence of a homogenous reaction, the disproportionation. So far, mainly the disproportionation in Li^+-containing DMSO has been investigated [45,46] and it has been proposed that the reaction is first order with respect to superoxide as well as Li^+, although the reaction order of superoxide has only been determined from the time-dependent UV-vis signal and it is difficult to imagine how a reaction that requires the interaction of two molecules of superoxide should be a first-order reaction [423]. However, as for divalent cations there is no

study of the disproportionation kinetics (preliminary results in our lab show that there is disproportionation of superoxide in the presence of Mg^{2+} and Ca^{2+}), it might be very important to investigate the homogeneous reaction. As only one metal cation is needed to form the peroxide, the kinetics might be significantly different and thus, partially responsible for the observed behaviour of the divalent cations (as the different behaviour of gold and platinum/glassy carbon shows, the problem is more complex than a simple, homogeneous reaction).

To close the gap between fundamental and applied research, the effect of the electrocatalyst and its morphology have to be further addressed. While theoretical chemists calculate properties of single crystalline surface, experimental chemists, working in fundamental science, employ smooth, polycrystalline electrodes and researcher working in the more applied fields utilize porous or very rough electrodes. Therefore, the exploration of the effect of the morphology is of utmost importance to enable efficient cooperation within the science community and ultimately, develop a secondary battery addressing all issues related to electromobility.

References

1. Moss, R. H.; Edmonds, J. A.; Hibbard, K. A.; Manning, M. R.; Rose, S. K.; van Vuuren, D. P.; Carter, T. R.; Emori, S.; Kainuma, M.; Kram, T.; Meehl, G. A.; Mitchell, J. F. B.; Nakicenovic, N.; Riahi, K.; Smith, S. J.; Stouffer, R. J.; Thomson, A. M.; Weyant, J. P.; Wilbanks, T. J. *Nature* **2010**, *463*, 747.
2. Oreskes, N. *Science* **2004**, *306*, 1686-1686.
3. John, C.; Dana, N.; Sarah, A. G.; Mark, R.; Bärbel, W.; Rob, P.; Robert, W.; Peter, J.; Andrew, S. *Environmental Research Letters* **2013**, *8*, 024024.
4. Clark, P. U.; Shakun, J. D.; Marcott, S. A.; Mix, A. C.; Eby, M.; Kulp, S.; Levermann, A.; Milne, G. A.; Pfister, P. L.; Santer, B. D.; Schrag, D. P.; Solomon, S.; Stocker, T. F.; Strauss, B. H.; Weaver, A. J.; Winkelmann, R.; Archer, D.; Bard, E.; Goldner, A.; Lambeck, K., et al. *Nature Climate Change* **2016**, *6*, 360.
5. Figueres, C.; Schellnhuber, H. J.; Whiteman, G.; Rockström, J.; Hobley, A.; Rahmstorf, S. *Nature News* **2017**, *546*, 593.
6. Hoffert, M. I.; Caldeira, K.; Jain, A. K.; Haites, E. F.; Harvey, L. D. D.; Potter, S. D.; Schlesinger, M. E.; Schneider, S. H.; Watts, R. G.; Wigley, T. M. L.; Wuebbles, D. J. *Nature* **1998**, *395*, 881.
7. Ellabban, O.; Abu-Rub, H.; Blaabjerg, F. *Renewable and Sustainable Energy Reviews* **2014**, *39*, 748-764.
8. Deane, J. P.; Ó Gallachóir, B. P.; McKeogh, E. J. *Renewable and Sustainable Energy Reviews* **2010**, *14*, 1293-1302.
9. Yang, C.-J. *Chapter 2 - Pumped Hydroelectric Storage*; Elsevier: Oxford, 2016, p 25-38.
10. Toyota, *Toyota Launches Production Model "Sora" FC Bus* (14.09.2018), **2018**, http://newsroom.toyota.co.jp/en/corporate/21863761.html.
11. Girishkumar, G.; McCloskey, B.; Luntz, A. C.; Swanson, S.; Wilcke, W. *J. Phys. Chem. Lett.* **2010**, *1*, 2193-2203.
12. Padbury, R.; Zhang, X. *J. Power Sources* **2011**, *196*, 4436-4444.
13. Abraham, K. M.; Jiang, Z. *J. Electrochem. Soc.* **1996**, *143*, 1-5.
14. Chase, M. W. *Journal of Physical and Chemical Reference Data, Monograph 9*, 4 ed., 1998; Vol. Monograph 9, p 1510.
15. Hartmann, P.; Bender, C. L.; Vračar, M.; Dürr, A. K.; Garsuch, A.; Janek, J.; Adelhelm, P. *Nat. Mater.* **2013**, *12*, 228-232.
16. Ren, X.; Wu, Y. *J. Am. Chem. Soc.* **2013**, *135*, 2923-2926.
17. Shiga, T.; Hase, Y.; Kato, Y.; Inoue, M.; Takechi, K. *Chem. Commun. (Cambridge, U. K.)* **2013**, *49*, 9152-9154.
18. Reinsberg, P.; Bondue, C. J.; Baltruschat, H. *J. Phys. Chem. C* **2016**, *120*, 22179-22185.
19. Gu, P.; Xu, Y.; Zhao, Y.; Liu, W.; Xue, H.; Pang, H. *Advanced Materials Interfaces* **2017**, *4*, 1700589.
20. Placke, T.; Kloepsch, R.; Dühnen, S.; Winter, M. *J. Solid State Electrochem.* **2017**, *21*, 1939-1964.
21. McCloskey, B. D.; Bethune, D. S.; Shelby, R. M.; Girishkumar, G.; Luntz, A. C. *J. Phys. Chem. Lett.* **2011**, *2*, 1161-1166.
22. Freunberger, S. A.; Chen, Y.; Peng, Z.; Griffin, J. M.; Hardwick, L. J.; Barde, F.; Novak, P.; Bruce, P. G. *J. Am. Chem. Soc.* **2011**, *133*, 8040-8047.
23. Bryantsev, V. S.; Giordani, V.; Walker, W.; Blanco, M.; Zecevic, S.; Sasaki, K.; Uddin, J.; Addison, D.; Chase, G. V. *J. Phys. Chem. A* **2011**, *115*, 12399-12409.
24. Yeager, E. *J. Mol. Catal.* **1986**, *38*, 5-25.
25. Anastasijević, N. A.; Vesović, V.; Adžić, R. R. *Journal of Electroanalytical Chemistry and Interfacial Electrochemistry* **1987**, *229*, 305-316.
26. Tong, Y. J. *Chem. Soc. Rev.* **2012**, *41*, 8195-8209.
27. Greeley, J.; Markovic, N. M. *Energy Environ. Sci.* **2012**, *5*, 9246-9256.

28. Ge, X.; Sumboja, A.; Wuu, D.; An, T.; Li, B.; Goh, F. W. T.; Hor, T. S. A.; Zong, Y.; Liu, Z. *ACS Catalysis* **2015**, *5*, 4643-4667.
29. Coetzee, J.; Kolthoff, I. *J. Am. Chem. Soc.* **1957**, *79*, 6110-6115.
30. Kolthoff, I.; Reddy, T. *J. Electrochem. Soc.* **1961**, *108*, 980-985.
31. Knecht, L.; Kolthoff, I. *Inorg. Chem.* **1962**, *1*, 195-203.
32. Maricle, D. L.; Hodgson, W. G. *Anal. Chem.* **1965**, *37*, 1562-1565.
33. Peover, M.; White, B. *Chemical Communications (London)* **1965**, 183-184.
34. Peover, M. E.; White, B. S. *Electrochim. Acta* **1966**, *11*, 1061-1067.
35. Johnson, E. L.; Pool, K. H.; Hamm, R. E. *Anal. Chem.* **1966**, *38*, 183-185.
36. Johnson, E. L.; Pool, K. H.; Hamm, R. E. *Anal. Chem.* **1967**, *39*, 888-891.
37. Sawyer, D. T.; Roberts, J. L. *Journal of Electroanalytical Chemistry (1959)* **1966**, *12*, 90-101.
38. Goolsby, A. D.; Sawyer, D. T. *Anal. Chem.* **1968**, *40*, 83-86.
39. Fujinaga, T.; Izutsu, K.; Adachi, T. *Bull. Chem. Soc. Jpn.* **1969**, *42*, 140-145.
40. Fujinaga, T.; Sakura, S. *Bull. Chem. Soc. Jpn.* **1974**, *47*, 2781-2786.
41. Sawyer, D. T.; Valentine, J. S. *Acc. Chem. Res.* **1981**, *14*, 393-400.
42. Sawyer, D. T.; Gibian, M. J. *Tetrahedron* **1979**, *35*, 1471-1481.
43. Sawyer, D. T.; Chiericato, G.; Angelis, C. T.; Nanni, E. J.; Tsuchiya, T. *Anal. Chem.* **1982**, *54*, 1720-1724.
44. Aurbach, D.; Daroux, M.; Faguy, P.; Yeager, E. *Journal of Electroanalytical Chemistry and Interfacial Electrochemistry* **1991**, *297*, 225-244.
45. Black, R.; Oh, S. H.; Lee, J.-H.; Yim, T.; Adams, B.; Nazar, L. F. *J. Am. Chem. Soc.* **2012**, *134*, 2902-2905.
46. Zhang, Y.; Zhang, X.; Wang, J.; McKee, W. C.; Xu, Y.; Peng, Z. *J. Phys. Chem. C* **2016**, *120*, 3690-3698.
47. Ohsaka, T.; Tsushima, M.; Tokuda, K. *Bioelectrochemistry and Bioenergetics* **1993**, *31*, 289-300.
48. Ogasawara, T.; Débart, A.; Holzapfel, M.; Novák, P.; Bruce, P. G. *J. Am. Chem. Soc.* **2006**, *128*, 1390-1393.
49. Debart, A.; Bao, J.; Armstrong, G.; Bruce, P. G. *J. Power Sources* **2007**, *174*, 1177-1182.
50. Kowalczk, I.; Read, J.; Salomon, M. *Pure Appl. Chem.* **2007**, *79*, 851-860.
51. Zhang, T.; Imanishi, N.; Hasegawa, S.; Hirano, A.; Xie, J.; Takeda, Y.; Yamamoto, O.; Sammes, N. *J. Electrochem. Soc.* **2008**, *155*, A965-A969.
52. Andrei, P.; Zheng, J. P.; Hendrickson, M.; Plichta, E. J. *J. Electrochem. Soc.* **2010**, *157*, A1287-A1295.
53. Bryantsev, V. S.; Blanco, M.; Faglioni, F. *The Journal of Physical Chemistry A* **2010**, *114*, 8165-8169.
54. Eswaran, M.; Munichandraiah, N.; Scanlon, L. G. *Electrochemical and Solid State Letters* **2010**, *13*, A121-A124.
55. Tran, C.; Yang, X. Q.; Qu, D. Y. *J. Power Sources* **2010**, *195*, 2057-2063.
56. Lu, Y.-C.; Xu, Z.; Gasteiger, H. A.; Chen, S.; Hamad-Schifferli, K.; Shao-Horn, Y. *J. Am. Chem. Soc.* **2010**, *132*, 12170–12171.
57. Lu, Y. C.; Gasteiger, H. A.; Crumlin, E.; McGuire, R.; Shao-Horn, Y. *J. Electrochem. Soc.* **2010**, *157*, A1016-A1025.
58. Xu, W.; Xu, K.; Viswanathan, V. V.; Towne, S. A.; Hardy, J. S.; Xiao, J.; Hu, D.; Wang, D.; Zhang, J.-G. *J. Power Sources* **2011**, *196*, 9631-9639.
59. Xu, W.; Viswanathan, V. V.; Wang, D.; Towne, S. A.; Xiao, J.; Nie, Z.; Hu, D.; Zhang, J.-G. *J. Power Sources* **2011**, *196*, 3894-3899.
60. Veith, G. M.; Dudney, N. J.; Howe, J.; Nanda, J. *J. Phys. Chem. C* **2011**, *115*, 14325-14333.
61. Laoire, C. O.; Mukerjee, S.; Abraham, K. M.; Plichta, E. J.; Hendrickson, M. A. *J. Phys. Chem. C* **2009**, *113* 20127-20134.
62. Laoire, C. O.; Mukerjee, S.; Abraham, K. M.; Plichta, E. J.; Hendrickson, M. A. *J. Phys. Chem. C* **2010**, *114*, 9178-9186.

63. Li, F.; Ohnishi, R.; Yamada, Y.; Kubota, J.; Domen, K.; Yamada, A.; Zhou, H. *Chem. Commun. (Cambridge, U. K.)* **2013**, *49*, 1175-1177.
64. Marinaro, M.; Theil, S.; Jörissen, L.; Wohlfahrt-Mehrens, M. *Electrochim. Acta* **2013**, *108*, 795-800.
65. Xu, D.; Wang, Z.-l.; Xu, J.-j.; Zhang, L.-l.; Zhang, X.-b. *Chem. Commun. (Cambridge, U. K.)* **2012**, *48*, 6948-6950.
66. Peng, Z.; Freunberger, S. A.; Chen, Y.; Bruce, P. G. *Science* **2012**, *337*, 563-566.
67. De Giorgio, F.; Soavi, F.; Mastragostino, M. *Electrochem. Commun.* **2011**, *13*, 1090-1 093.
68. Herranz, J.; Garsuch, A.; Gasteiger, H. A. *J. Phys. Chem. C* **2012**, *116*, 19084-19094.
69. McCloskey, B. D.; Bethune, D. S.; Shelby, R. M.; Mori, T.; Scheffler, R.; Speidel, A.; Sherwood, M.; Luntz, A. C. *The Journal of Physical Chemistry Letters* **2012**, *3*, 3043-3047.
70. Wang, H.; Xie, K.; Wang, L.; Han, Y. *J. Power Sources* **2012**, *219*, 263-271.
71. Barde, F.; Chen, Y.; Johnson, L.; Schaltin, S.; Fransaer, J.; Bruce, P. G. *J. Phys. Chem. C* **2014**, *118*, 18892-18898.
72. Suo, L.; Borodin, O.; Wang, Y.; Rong, X.; Sun, W.; Fan, X.; Xu, S.; Schroeder, M. A.; Cresce, A. V.; Wang, F. *Advanced Energy Materials* **2017**, *7*.
73. Wu, S.; Qiao, Y.; Yang, S.; Tang, J.; He, P.; Zhou, H. *ACS Catal.* **2018**, 1082-1089.
74. Lacey, M. J.; Frith, J. T.; Owen, J. R. *Electrochem. Commun.* **2013**, *26*, 74-76.
75. Chen, Y.; Freunberger, S. A.; Peng, Z.; Fontaine, O.; Bruce, P. G. *Nat. Chem.* **2013**, *5*, 489-494.
76. Sun, Q.; Yang, Y.; Fu, Z.-W. *Electrochem. Commun.* **2012**, *16*, 22-25.
77. Kim, J.; Lim, H.-D.; Gwon, H.; Kang, K. *Phys. Chem. Chem. Phys.* **2013**, *15*, 3623-3629.
78. Ren, X.; Lau, K. C.; Yu, M.; Bi, X.; Kreidler, E.; Curtiss, L. A.; Wu, Y. *ACS Appl. Mater. Interfaces* **2014**, *6*, 19299-19307.
79. Shiga, T.; Hase, Y.; Yagi, Y.; Takahashi, N.; Takechi, K. *J. Phys. Chem. Lett.* **2014**, *5*, 1648-1652.
80. Vardar, G.; Sleightholme, A. E. S.; Naruse, J.; Hiramatsu, H.; Siegel, D. J.; Monroe, C. W. *ACS Appl. Mater. Interfaces* **2014**, *6*, 18033-18039.
81. Clarivate Analytics, (18.09.2018), **2018**, http://clarivate.com/products/web-of-science/.
82. Matsuda, S.; Hashimoto, K.; Nakanishi, S. *J. Phys. Chem. C* **2014**, *118*, 18397-18400.
83. Gao, X.; Chen, Y.; Johnson, L.; Bruce, P. G. *Nat. Mater.* **2016**, *15*, 882-888.
84. Gao, X.; Chen, Y.; Johnson, L. R.; Jovanov, Z. P.; Bruce, P. G. **2017**, *2*, 17118.
85. Matsuda, S.; Kubo, Y.; Uosaki, K.; Nakanishi, S. *The Journal of Physical Chemistry Letters* **2017**, *8*, 1142-1146.
86. Landa-Medrano, I.; Olivares-Marín, M.; Bergner, B.; Pinedo, R.; Sorrentino, A.; Pereiro, E.; Ruiz de Larramendi, I.; Janek, J.; Rojo, T.; Tonti, D. *J. Phys. Chem. C* **2017**, *121*, 3822-3829.
87. Allen, C. J.; Hwang, J.; Kautz, R.; Mukerjee, S.; Plichta, E. J.; Hendrickson, M. A.; Abraham, K. M. *J. Phys. Chem. C* **2012**, *116*, 20755-20764.
88. Bañares, M. A.; Guerrero-Pérez, M. O.; Fierro, J. L. G.; Cortez, G. G. *J. Mater. Chem.* **2002**, *12*, 3337-3342.
89. Renziehausen, Ursula, *Lateinische Grammatik* (04.12.2018), **1998**, http://www2.uni-erfurt.de/renzi/latein/ZKONLINE/grammar/nd.htm.
90. Kremser, Franz, *Lingua Latina!* (04.12.2018), **2018**, http://members.aon.at/latein/Gerabl.htm.
91. Pearson, R. G. *J. Am. Chem. Soc.* **1963**, *85*, 3533-3539.
92. Abraham, K. M. *J. Electrochem. Soc.* **2015**, *162*, A3021-A3031.
93. Bondue, C. J.; Bawol, P. P.; Abd-El-Latif, A. A.; Reinsberg, P.; Baltruschat, H. *J. Phys. Chem. C* **2017**, *121*, 8864–8872.
94. Levich, B. *Discussions of the Faraday Society* **1947**, *1*, 37-49.
95. Albery, W. *Transactions of the Faraday Society* **1966**, *62*, 1915-1919.
96. Bard, A. J.; Faulkner, L. R. *Electrochemical Methods: Fundamentals and Applications*, 2nd ed.; John Wiley & Sons Inc.: New York, Weinheim, 2001, p 339.

97. Dalton, F. *The Electrochemical Society Interface* **2016**, *25*, 50-59.
98. Cochran, W. In *Mathematical Proceedings of the Cambridge Philosophical Society*; Cambridge University Press, 1934, pp 365-375.
99. Kármán, T. V. *ZAMM - Journal of Applied Mathematics and Mechanics / Zeitschrift für Angewandte Mathematik und Mechanik* **1921**, *1*, 233-252.
100. Levich, V. G. **1962**.
101. Koutecky, J.; Levich, B. G. e. In *Dokl. Akad. Nauk SSSR*; Russian Academy of Sciences, 1957, pp 441-444.
102. Frumkin, A.; Nekrasov, L.; Levich, B.; Ivanov, J. *J. Electroanal. Chem.* **1959**, *1*, 84-90.
103. Bruckenstein, S.; Nagai, T. *Anal. Chem.* **1961**, *33*, 1201-1209.
104. Albery, W.; Bell, R.; Royal Soc Chemistry Thomas Graham House, Science Park, Milton Rd, Cambridge, England, 1963, pp 169-182.
105. Albery, W. J.; Bruckenstein, S.; Napp, D. T. *Transactions of the Faraday Society* **1966**, *62*, 1932-1937.
106. Albery, W. J.; Bruckenstein, S. *Transactions of the Faraday Society* **1966**, *62*, 1920-1931.
107. Albery, W. J.; Hitchman, M. L.; Ulstrup, J. *Transactions of the Faraday Society* **1968**, *64*, 2831 - 2840
108. Albery, W. J.; Bruckenstein, S. *Transactions of the Faraday Society* **1966**, *62*, 1946-1954.
109. Newman, J. *The Journal of Physical Chemistry* **1966**, *70*, 1327-1328.
110. Koutecky, J.; Levich, B. *Zh. Fiz. Khim.* **1958**, *32*, 1565-1575.
111. Bruckenstein, S.; Feldman, G. A. *Journal of Electroanalytical Chemistry (1959)* **1965**, *9*, 395-399.
112. Baltruschat, H. In *Interfacial Electrochemistry*, Wieckowski, A., Ed.; Marcel Dekker, Inc.: New York, Basel, 1999, pp 577- 597.
113. Baltruschat, H. *J. Am. Soc. Mass Spectrom.* **2004**, *15*, 1693-1706.
114. Wolter, O.; Heitbaum, J. *Berichte der Bunsengesellschaft für Physikalische Chemie* **1984**, *88*, 2-6.
115. Bruckenstein, S.; Gadde, R. R. *J. Am. Chem. Soc.* **1971**, *93*, 793-794.
116. Wolter, O.; Heitbaum, J. *Berichte der Bunsengesellschaft für physikalische Chemie* **1984**, *88*, 6-10.
117. Baltruschat, H.; Schmiemann, U. *Berichte der Bunsengesellschaft für physikalische Chemie* **1993**, *97*, 452-460.
118. Hartung, T.; Baltruschat, H. *Langmuir* **1990**, *6*, 953-957.
119. Jusys, Z.; Massong, H.; Baltruschat, H. *J. Electrochem. Soc.* **1999**, *146*, 1093-1098.
120. Bondue, C. J.; Königshoven, P.; Baltruschat, H. *Electrochim. Acta* **2016**, *214*, 241–252.
121. Tegtmeyer, D.; Heitbaum, J.; Heindrichs, A. *Berichte der Bunsengesellschaft für physikalische Chemie* **1989**, *93*, 201-206.
122. Bawol, P. P.; Reinsberg, P.; Bondue, C. J.; Abd-El-Latif, A. A.; Koenigshoven, P.; Baltruschat, H. *Phys. Chem. Chem. Phys.* **2018**, *20*, 21447–21456.
123. Bondue, C. J.; Abd-El-Latif, A. A.; Hegemann, P.; Baltruschat, H. *J. Electrochem. Soc.* **2015**, *162*, A479-A487.
124. Vargaftik, N.; Volkov, B.; Voljak, L. *J. Phys. Chem. Ref. Data* **1983**, *12*, 817-820.
125. Reinsberg, P.; Abd-El-Latif, A. A.; Baltruschat, H. *Electrochim. Acta* **2018**, *273*, 424–431.
126. Edelmann, C. *Vakuumphysik: Grundlagen, Vakuumerzeugung und-messung, Anwendungen*; Spektrum, Akad. Verlag, 1998.
127. Wexler, A. *J. Res. Natl. Bur. Stand. A* **1976**, *80*, 775-785.
128. Trimarco, D. B.; Scott, S. B.; Thilsted, A. H.; Pan, J. Y.; Pedersen, T.; Hansen, O.; Chorkendorff, I.; Vesborg, P. C. K. *Electrochim. Acta* **2018**, *268*, 520-530.
129. Kim, Y.; Irikura, K.; Rudd, M.; Ali, M.; Stone, P.; Chang, J.; Coursey, J.; Dragoset, R.; Kishore, A.; Olsen, K.; National Institute of Standards and Technology: Gaithersburg, MD, 2004.
130. Khodayari, M.; Reinsberg, P.; Abd-El-Latif, A.-E.-A. A.; Merdon, C.; Fuhrmann, J.; Baltruschat, H. *ChemPhysChem* **2016**, *17*, 1647-1655.

131. Vocke, R. D. *Pure Appl. Chem.* **1999**, *71*, 1593-1607.
132. Nikam, P. S.; Jadhav, M. C.; Hasan, M. *J. Chem. Eng. Data* **1996**, *41*, 1028-1031.
133. Henni, A.; Tontiwachwuthikul, P.; Chakma, A. *J. Chem. Eng. Data* **2004**, *49*, 1778-1781.
134. Staszak-Jirkovský, J.; Subbaraman, R.; Strmcnik, D.; Harrison, K. L.; Diesendruck, C. E.; Assary, R.; Frank, O.; Kobr, L. s.; Wiberg, G. K. H.; Genorio, B.; Connell, J. G.; Lopes, P. P.; Stamenkovic, V. R.; Curtiss, L.; Moore, J. S.; Zavadil, K. R.; Markovic, N. M. *ACS Catal.* **2015**, *5*, 6600-6607.
135. Biegler, T.; Rand, D. A. J.; Woods, R. *Journal of Electroanalytical Chemistry and Interfacial Electrochemistry* **1971**, *29*, 269-277.
136. Wieckowski, A.; Szklarzyk, M.; Sobkowski, J. *Journal of Electroanalytical Chemistry and Interfacial Electrochemistry* **1980**, *113*, 79-87.
137. Irish, D.; Hill, I.; Archambault, P.; Atkinson, G. *J. Solution Chem.* **1985**, *14*, 221-243.
138. Hill, I.; Irish, D.; Atkinson, G. *Langmuir* **1986**, *2*, 752-757.
139. Bondue, C.; Reinsberg, P.; Abd-El-Latif, A. A.; Baltruschat, H. *Phys. Chem. Chem. Phys.* **2015**, *17*, 25593–25606.
140. MBraun Inertgas-Systeme GmbH, *MB-MO-SE1 Datasheet* (25.01.2019), **2018**, h ttps://www.mbraun.com/images/05292013_MB-MO-SE1_rev2.pdf.
141. National Instruments, *Is Your Data Inaccurate Because of Instrumentation Amplifier Settling Time?* (04.12.2018), **2013**, http://www.ni.com/white-paper/2825/en/.
142. National Instruments, *DAQ M Series Manual* (04.12.2018), **2016**, http://www.ni.com/pdf/manuals/371022l.pdf.
143. National Instruments, *Device Specifications NI 6321* **2015**, http://www.ni.com/pdf/manuals/374461b.pdf.
144. National Instruments, *Device Specifications NI 6221* **2016**, http://www.ni.com/pdf/manuals/375303c.pdf.
145. National Instruments, *Increasing Interchannel Delay on DAQ Devices for Longer Settling Times* (04.12.2018), **2018**, http://knowledge.ni.com/KnowledgeArticleDetails?id=kA00Z0000019NFQSA2&l=de-DE.
146. National Instruments, *DAQmx Timing and Sample Rates* (04.12.2018), **2018**, http://knowledge.ni.com/KnowledgeArticleDetails?id=kA00Z000000P7KdSAK&l=de-DE.
147. National Instruments, *Understanding and Avoiding NI-DAQmx Overwrite and Overflow Errors* (04.12.2018), **2018**, http://knowledge.ni.com/KnowledgeArticleDetails?id=kA00Z000000PAraSAG&l=de-DE.
148. Lange, P.; Glaw, V.; Neff, H.; Piltz, E.; Sass, J. *Vacuum* **1983**, *33*, 763-766.
149. W. Johnson, B.; Bauhofer, J.; Doblhofer, K.; Pettinger, B. *Electrochim. Acta* **1992**, *37*, 2321-2329.
150. Bewick, A.; Kunimatsu, K.; Stanley Pons, B. *Electrochim. Acta* **1980**, *25*, 465-468.
151. Bewick, A.; Kunimatsu, K. *Surf. Sci.* **1980**, *101*, 131-138.
152. Bewick, A.; Kunimatsu, K.; Pons, B. S.; Russell, J. W. *Journal of Electroanalytical Chemistry and Interfacial Electrochemistry* **1984**, *160*, 47-61.
153. Kretschmann, E. *Zeitschrift für Physik A Hadrons and nuclei* **1971**, *241*, 313-324.
154. Harrick, N. J. *Internal Reflectance Spectroscopy*; Interscience: New York, 1967, p 13-66.
155. Iwasita, T.; Nart, F. *Journal of electroanalytical chemistry and interfacial electrochemistry* **1990**, *295*, 215-224.
156. Iwasita, T.; Nart, F. *Prog. Surf. Sci.* **1997**, *55*, 271-340.
157. Osawa, M. In *Near-Field Optics and Surface Plasmon Polaritons*, Kawata, S., Ed.; Springer Berlin Heidelberg: Berlin, Heidelberg, 2001, pp 163-187.
158. Beden, B.; Lamy, C.; Bewick, A.; Kunimatsu, K. *Journal of Electroanalytical Chemistry and Interfacial Electrochemistry* **1981**, *121*, 343-347.
159. Golden, W.; Dunn, D. S.; Overend, J. *J. Catal.* **1981**, *71*, 395-404.
160. Russell, J. W.; Overend, J.; Scanlon, K.; Severson, M.; Bewick, A. *The Journal of Physical Chemistry* **1982**, *86*, 3066-3068.

161. Christensen, P. A. In *Encyclopedia of Electrochemistry*, 2007.
162. Davidson, T.; Pons, B. S.; Bewick, A.; Schmidt, P., Vibrational Spectroscopy of the Electrode-Electrolyte Interface. Use of Fourier Transform Infrared Spectroscopy; ALBERTA UNIV EDMONTON DEPT OF CHEMISTRY1981.
163. Pons, S.; Davidson, T.; Bewick, A. *Journal of Electroanalytical Chemistry and Interfacial Electrochemistry* **1982**, *140*, 211-216.
164. Pons, S. *Journal of Electroanalytical Chemistry and Interfacial Electrochemistry* **1983**, *150*, 495-504.
165. Corrigan, D. S.; Weaver, M. J. *The Journal of Physical Chemistry* **1986**, *90*, 5300-5306.
166. Corrigan, D. S.; Leung, L. W. H.; Weaver, M. J. *Anal. Chem.* **1987**, *59*, 2252-2256.
167. Lin, W.-f.; Sun, S.-g. *Electrochim. Acta* **1996**, *41*, 803-809.
168. Fleischmann, M.; Hendra, P. J.; McQuillan, A. J. *Chem. Phys. Lett.* **1974**, *26*, 163-166.
169. Hartstein, A.; Kirtley, J. R.; Tsang, J. C. *Phys. Rev. Lett.* **1980**, *45*, 201-204.
170. Jeanmaire, D. L.; Van Duyne, R. P. *Journal of Electroanalytical Chemistry and Interfacial Electrochemistry* **1977**, *84*, 1-20.
171. Albrecht, M. G.; Creighton, J. A. *J. Am. Chem. Soc.* **1977**, *99*, 5215-5217.
172. Osawa, M.; Kuramitsu, M.; Hatta, A.; Suetaka, W.; Seki, H. *Surface Science Letters* **1986**, *175*, L787-L793.
173. Osawa, M.; Ikeda, M. *The Journal of Physical Chemistry* **1991**, *95*, 9914-9919.
174. Osawa, M.; Ataka, K.-I.; Ikeda, M.; Uchihara, H.; Nanba, R. *Anal. Sci.* **1991**, *7*, 503-506.
175. Hatta, A.; Chiba, Y.; Suetaka, W. *Surf. Sci.* **1985**, *158*, 616-623.
176. Hatta, A.; Suzuki, Y.; Suëtaka, W. *Applied Physics A* **1984**, *35*, 135-140.
177. Hatta, A.; Ohshima, T.; Suetaka, W. *Applied Physics A* **1982**, *29*, 71-75.
178. Hatta, A.; Chiba, Y.; Suëtaka, W. *Appl. Surf. Sci.* **1986**, *25*, 327-332.
179. Ataka, K.-i.; Yotsuyanagi, T.; Osawa, M. *The Journal of Physical Chemistry* **1996**, *100*, 10664-10672.
180. Miyake, H.; Ye, S.; Osawa, M. *Electrochem. Commun.* **2002**, *4*, 973-977.
181. Yan; Li, Q.-X.; Huo, S.-J.; Ma, M.; Cai, W.-B.; Osawa, M. *J. Phys. Chem. B* **2005**, *109*, 7900-7906.
182. Miki, A.; Ye, S.; Osawa, M. *Chem. Commun. (Cambridge, U. K.)* **2002**, 1500-1501.
183. Kamata, T.; Kato, A.; Umemura, J.; Takenaka, T. *Langmuir* **1987**, *3*, 1150-1154.
184. Lu, G.-Q.; Sun, S.-G.; Chen, S.-P.; Cai, L.-R. *J. Electroanal. Chem.* **1997**, *421*, 19-23.
185. Lu, G.-Q.; Sun, S.-G.; Cai, L.-R.; Chen, S.-P.; Tian, Z.-W.; Shiu, K.-K. *Langmuir* **2000**, *16*, 778-786.
186. Johnson, E.; Aroca, R. *The Journal of Physical Chemistry* **1995**, *99*, 9325-9330.
187. Nishikawa, Y.; Nagasawa, T.; Fujiwara, K.; Osawa, M. *Vib. Spectrosc.* **1993**, *6*, 43-53.
188. Suzuki, Y.; Osawa, M.; Hatta, A.; Suëtaka, W. *Appl. Surf. Sci.* **1988**, *33*, 875-881.
189. Osawa, M.; Ataka, K.-I.; Yoshii, K.; Nishikawa, Y. *Appl. Spectrosc.* **1993**, *47*, 1497-1502.
190. Osawa, M. *Bull. Chem. Soc. Jpn.* **1997**, *70*, 2861-2880.
191. Alonso-González, P.; Albella, P.; Neubrech, F.; Huck, C.; Chen, J.; Golmar, F.; Casanova, F.; Hueso, L. E.; Pucci, A.; Aizpurua, J. *Phys. Rev. Lett.* **2013**, *110*, 203902.
192. Dumas, P.; Tobin, R.; Richards, P. *Surf. Sci.* **1986**, *171*, 555-578.
193. Krauth, O.; Fahsold, G.; Pucci, A. *The Journal of chemical physics* **1999**, *110*, 3113-3117.
194. Griffiths, P. R.; De Haseth, J. A. *Fourier transform infrared spectrometry*; John Wiley & Sons, 2007; Vol. 171.
195. Edwards, D. F.; Ochoa, E. *Appl. Opt.* **1980**, *19*, 4130-4131.
196. Saunders, J. E.; Sanders, C.; Chen, H.; Loock, H.-P. *Appl. Opt.* **2016**, *55*, 947-953.
197. Pons, S.; Davidson, T.; Bewick, A. *J. Am. Chem. Soc.* **1983**, *105*, 1802-1805.
198. Michelson, A. A. *The London, Edinburgh, and Dublin Philosophical Magazine and Journal of Science* **1891**, *31*, 256-259.
199. Mertz, L. *Infrared Phys.* **1967**, *7*, 17-23.
200. Vardar, G.; Nelson, E. G.; Smith, J. G.; Naruse, J.; Hiramatsu, H.; Bartlett, B. M.; Sleightholme, A. E. S.; Siegel, D. J.; Monroe, C. W. *Chem. Mater.* **2015**, *27*, 7564-7568.

201. Aetukuri, N. B.; McCloskey, B. D.; García, J. M.; Krupp, L. E.; Viswanathan, V.; Luntz, A. C. *Nat Chem* **2015**, *7*, 50-56.
202. Schwenke, K. U.; Metzger, M.; Restle, T.; Piana, M.; Gasteiger, H. A. *J. Electrochem. Soc.* **2015**, *162*, A573-A584.
203. Cao, R.; Walter, E. D.; Xu, W.; Nasybulin, E. N.; Bhattacharya, P.; Bowden, M. E.; Engelhard, M. H.; Zhang, J.-G. *ChemSusChem* **2014**, *7*, 2436-2440.
204. McCloskey, B. D.; Scheffler, R.; Speidel, A.; Bethune, D. S.; Shelby, R. M.; Luntz, A. C. *J. Am. Chem. Soc.* **2011**, *133*, 18038-18041.
205. Hummelshøj, J. S.; Blomqvist, J.; Datta, S.; Vegge, T.; Rossmeisl, J.; Thygesen, K. S.; Luntz, A. C.; Jacobsen, K. W.; Nørskov, J. K. *J. Chem. Phys.* **2010**, *132*, 071101.
206. Adams, B. D.; Radtke, C.; Black, R.; Trudeau, M. L.; Zaghib, K.; Nazar, L. F. *Energy Environ. Sci.* **2013**, *6*, 1772-1778.
207. Black, R.; Adams, B.; Nazar, L. F. *Advanced Energy Materials* **2012**, *2*, 801-815.
208. Debart, A.; Paterson, A. J.; Bao, J.; Bruce, P. G. *Angewandte Chemie-International Edition* **2008**, *47*, 4521-4524.
209. Xu, D.; Wang, Z.-l.; Xu, J.-j.; Zhang, L.-l.; Wang, L.-m.; Zhang, X.-b. *Chem. Commun. (Cambridge, U. K.)* **2012**, *48*, 11674-11676.
210. Xu, W.; Hu, J.; Engelhard, M. H.; Towne, S. A.; Hardy, J. S.; Xiao, J.; Feng, J.; Hu, M. Y.; Zhang, J.; Ding, F.; Gross, M. E.; Zhang, J.-G. *J. Power Sources* **2012**, *215*, 240-247.
211. Trahan, M. J.; Mukerjee, S.; Plichta, E. J.; Hendrickson, M. A.; Abraham, K. M. *J. Electrochem. Soc.* **2013**, *160*, A259-A267.
212. Luntz, A. C.; McCloskey, B. D. *Chem. Rev. (Washington, DC, U. S.)* **2014**, *114*, 11721-11750.
213. Lu, Y.-C.; Gasteiger, H. A.; Shao-Horn, Y. *J. Am. Chem. Soc.* **2011**, *133*, 19048-19051.
214. Peng, Z.; Freunberger, S. A.; Hardwick, L. J.; Chen, Y.; Giordani, V.; Bardé, F.; Novák, P.; Graham, D.; Tarascon, J.-M.; Bruce, P. G. *Angewandte Chemie International Edition* **2011**, *50*, 6351-6355.
215. Lu, Y.-C.; Gasteiger, H. A.; Shao-Horn, Y. *Electrochem. Solid-State Lett.* **2011**, *14*, A70-A74.
216. Gritzner, G. *J. Mol. Liq.* **2010**, *156*, 103-108.
217. Wood, P. M. *Biochem. J.* **1988**, *253*, 287-289.
218. Coughlin, J. P. *US Bur. Mines Bull.* **1954**, *542*.
219. Damjanovic, A.; Genshaw, M. A.; Bockris, J. M. *The Journal of Chemical Physics* **1966**, *45*, 4057-4059.
220. LeBel, R. G.; Goring, D. A. I. *J. Chem. Eng. Data* **1962**, *7*, 100-101.
221. Lu, Y.-C.; Gasteiger, H. A.; Parent, M. C.; Chiloyan, V.; Shao-Horn, Y. *Electrochem. Solid-State Lett.* **2010**, *13*, A69-A72.
222. Gutmann, V. *Coord. Chem. Rev.* **1976**, *18*, 225-255.
223. Borkowska, Z.; Stafiej, J. *Journal of Electroanalytical Chemistry and Interfacial Electrochemistry* **1987**, *226*, 283-293.
224. Trasatti, S. *Journal of Electroanalytical Chemistry and Interfacial Electrochemistry* **1983**, *150*, 1-15.
225. Payne, R. *J. Am. Chem. Soc.* **1967**, *89*, 489-496.
226. Taraszewska, J. *Journal of Electroanalytical Chemistry and Interfacial Electrochemistry* **1981**, *121*, 215-230.
227. Si, S. K.; Gewirth, A. A. *The Journal of Physical Chemistry B* **2000**, *104*, 10775-10782.
228. Ikemiya, N.; Gewirth, A. A. *The Journal of Physical Chemistry B* **2000**, *104*, 873-877.
229. Safonov, V. A.; Komissarov, L. Y.; Petrii, O. A. *Electrochim. Acta* **1997**, *42*, 675-687.
230. Petrii, O. A.; Khomchenko, I. G. *Journal of Electroanalytical Chemistry and Interfacial Electrochemistry* **1980**, *106*, 277-286.
231. Katekaru, J. Y.; Garwood Jr, G. A.; Hershberger, J. F.; Hubbard, A. T. *Surf. Sci.* **1982**, *121*, 396-410.
232. Puglia, C.; Nilsson, A.; Hernnäs, B.; Karis, O.; Bennich, P.; Mårtensson, N. *Surf. Sci.* **1995**, *342*, 119-133.
233. Qiao, Y.; Ye, S. *J. Phys. Chem. C* **2016**, *120*, 8033-8047.

234. Markus, I. M.; Jones, G.; García, J. M. *J. Phys. Chem. C* **2016**, *120*, 5949-5957.
235. Scheers, J.; Lidberg, D.; Sodeyama, K.; Futera, Z.; Tateyama, Y. *Phys. Chem. Chem. Phys.* **2016**, *18*, 9961-9968.
236. Sharon, D.; Hirsberg, D.; Salama, M.; Afri, M.; Frimer, A. A.; Noked, M.; Kwak, W.; Sun, Y.-K.; Aurbach, D. *ACS Appl. Mater. Interfaces* **2016**, *8*, 5300-5307.
237. Schröder, D.; Bender Conrad, L.; Pinedo, R.; Bartuli, W.; Schwab Matthias, G.; Tomovic, Z.; Janek, J. *Energy Technology* **2016**, *5*, 1242-1249.
238. Xia, C.; Black, R.; Fernandes, R.; Adams, B.; Nazar, L. F. *Nat. Chem.* **2015**, *7*, 496-501.
239. Reinsberg, P.; Bondue, C.; Baltruschat, H. *Electrochim. Acta* **2016**, *200*, 214-221.
240. Moshkovich, M.; Gofer, Y.; Aurbach, D. *J. Electrochem. Soc.* **2001**, *148*, E155-E167.
241. Taylor, S. R. *Geochim. Cosmochim. Acta* **1964**, *28*, 1273-1285.
242. Hans Wedepohl, K. *Geochim. Cosmochim. Acta* **1995**, *59*, 1217-1232.
243. Ponrouch, A.; Frontera, C.; Barde, F.; Palacin, M. R. *Nat. Mater.* **2016**, *15*, 169-172.
244. See, K. A.; Gerbec, J. A.; Jun, Y. S.; Wudl, F.; Stucky, G. D.; Seshadri, R. *Advanced Energy Materials* **2013**, *3*, 1056-1061.
245. Shiga, T.; Kondo, H.; Kato, Y.; Inoue, M. *J. Phys. Chem. C* **2015**, *119*, 27946-27953.
246. Newhouse, J. M.; Poizeau, S.; Kim, H.; Spatocco, B. L.; Sadoway, D. R. *Electrochim. Acta* **2013**, *91*, 293-301.
247. Downey, S. B.; Devereux, O. F. *J. Electrochem. Soc.* **1992**, *139*, 3129-3135.
248. Sadhukhan, P.; Bell, A. T. *J. Solid State Chem.* **1979**, *29*, 97-100.
249. Brosset, C.; Vannerberg, N.-G. *Nature* **1956**, *177*, 238-238.
250. Ballou, E. V.; Wood, P. C.; Spitze, L. A.; Wydeven, T. *Industrial & Engineering Chemistry Product Research and Development* **1977**, *16*, 180-186.
251. Vedeneev, A. V.; Kazarnovkaya, L. I.; Kazarnovskii, I. A. *Zh, Fiz. Khim* **1952**, *26*, 1808-1813.
252. Wriedt, H. A. *Bulletin of Alloy Phase Diagrams* **1985**, *6*, 337-342.
253. Chaudhry, M.; Kinjo, Y.; Persson, I. *J. Chem. Soc., Faraday Trans.* **1994**, *90*, 2683-2689.
254. Gutmann, V.; Schöber, G. *Fresenius' Zeitschrift für analytische Chemie* **1959**, *171*, 339-343.
255. Andrews, L. *The Journal of Chemical Physics* **1969**, *50*, 4288-4299.
256. McCloskey, B. D.; Speidel, A.; Scheffler, R.; Miller, D. C.; Viswanathan, V.; Hummelshøj, J. S.; Nørskov, J. K.; Luntz, A. C. *The Journal of Physical Chemistry Letters* **2012**, *3*, 997-1001.
257. Horstmann, B.; Gallant, B.; Mitchell, R.; Bessler, W. G.; Shao-Horn, Y.; Bazant, M. Z. *The Journal of Physical Chemistry Letters* **2013**, *4*, 4217-4222.
258. Grande, L.; Paillard, E.; Hassoun, J.; Park, J.-B.; Lee, Y.-J.; Sun, Y.-K.; Passerini, S.; Scrosati, B. *Adv. Mater. (Weinheim, Ger.)* **2015**, *27*, 784-800.
259. McCloskey, B. D.; Burke, C. M.; Nichols, J. E.; Renfrew, S. E. *Chem. Commun. (Cambridge, U. K.)* **2015**, *51*, 12701-12715.
260. Wang, Y.; Liang, Z.; Zou, Q.; Cong, G.; Lu, Y.-C. *J. Phys. Chem. C* **2016**, *120*, 6459-6466.
261. Vivek, J. P.; Berry, N.; Papageorgiou, G.; Nichols, R. J.; Hardwick, L. J. *J. Am. Chem. Soc.* **2016**.
262. Mozhzhukhina, N.; Tesio, A. Y.; Leo, L. P. M. D.; Calvo, E. J. *J. Electrochem. Soc.* **2017**, *164*, A518-A523
263. Bondue, C. J.; Reinsberg, P.; Baltruschat, H. *Electrochim. Acta* **2017**, *245*, 1035-1047.
264. Belova, A. I.; Kwabi, D. G.; Yashina, L. V.; Shao-Horn, Y.; Itkis, D. M. *J. Phys. Chem. C* **2017**.
265. Bergner, B. J.; Schürmann, A.; Peppler, K.; Garsuch, A.; Janek, J. *J. Am. Chem. Soc.* **2014**, *136*, 15054-15064.
266. Qiao, Y.; Ye, S. *J. Phys. Chem. C* **2016**, *120*, 8044-8047.
267. Zhu, Y. G.; Jia, C.; Yang, J.; Pan, F.; Huang, Q.; Wang, Q. *Chem. Commun. (Cambridge, U. K.)* **2016**, *51*, 9451-9454.
268. Yao, K. P. C.; Frith, J. T.; Sayed, S. Y.; Barde, F.; Owen, J. R.; Shao-Horn, Y.; Garcia-Araez, N. *J. Phys. Chem. C* **2016**, *120*, 16290-16297.

269. Zhang, J.; Sun, B.; Zhao, Y.; Kretschmer, K.; Wang, G. *Angew. Chem.* **2017**, *129*, 8505-8509.
270. Park, J.-B.; Lee, S. H.; Jung, H.-G.; Aurbach, D.; Sun, Y.-K. *Adv. Mater. (Weinheim, Ger.)* **2017**, 1704162.
271. Torres, W. R.; Davia, F.; del Pozo, M.; Tesio, A. Y.; Calvo, E. J. *J. Electrochem. Soc.* **2017**, *164*, A3785-A3792.
272. Peled, E.; Golodnitsky, D.; Mazor, H.; Goor, M.; Avshalomov, S. *J. Power Sources* **2011**, *196*, 6835-6840.
273. McCloskey, B. D.; Garcia, J. M.; Luntz, A. C. *J. Phys. Chem. Lett.* **2014**, *5*, 1230-1235.
274. Schröder, D.; Bender, C. L.; Osenberg, M.; Hilger, A.; Manke, I.; Janek, J. *Scientific Reports* **2016**, *6*, 24288-24294.
275. Aldous, I. M.; Hardwick, L. J. *Angewandte Chemie International Edition* **2016**, *55*, 8254-8257.
276. Law, Y. T.; Schnaidt, J.; Brimaud, S.; Behm, R. J. *J. Power Sources* **2016**, *333*, 173-183.
277. Fischer, P.; Schwarz, R. M.; Marinaro, M.; Wachtler, M.; Jörissen, L. *ECS Trans.* **2017**, *75*, 3-12.
278. Matsuda, S.; Uosaki, K.; Nakanishi, S. *J. Power Sources* **2017**, *353*, 138-143.
279. Smith, J. G.; Naruse, J.; Hiramatsu, H.; Siegel, D. J. *Chem. Mater.* **2016**, *28*, 1390-1401.
280. Vol'nov, I. y. I. *Peroxides, Superoxides, and Ozonides of Alkali and Alkaline Earth Metals*, 1 ed.; Springer US: Boston, MA, 1966, p 146.
281. Vasudevan, D.; Wendt, H. *J. Electroanal. Chem.* **1995**, *392*, 69-74.
282. Reinsberg, P.; Weiss, A.; Bawol, P. P.; Baltruschat, H. *J. Phys. Chem. C* **2017**, *121*, 7677–7688.
283. Yu, Q.; Ye, S. *J. Phys. Chem. C* **2015**, *119*, 12236-12250.
284. Vivek, J. P.; Berry, N. G.; Zou, J.; Nichols, R. J.; Hardwick, L. J. *J. Phys. Chem. C* **2017**.
285. Shannon, R. *Acta Crystallographica Section A* **1976**, *32*, 751-767.
286. Linert, W.; Jameson, R. F.; Bauer, G.; Taha, A. *J. Coord. Chem.* **1997**, *42*, 211-229.
287. Johnson, L.; Li, C.; Liu, Z.; Chen, Y.; Freunberger, S. A.; Ashok, P. C.; Praveen, B. B.; Dholakia, K.; Tarascon, J.-M.; Bruce, P. G. *Nat. Chem.* **2014**, *6*, 1091-1099.
288. Burke, C. M.; Pande, V.; Khetan, A.; Viswanathan, V.; McCloskey, B. D. *Proc. Natl. Acad. Sci. U. S. A.* **2015**, *112*, 9293-9298.
289. Reichardt, C. *Chem. Rev. (Washington, DC, U. S.)* **1994**, *94*, 2319-2358.
290. Dimroth, K.; Reichardt, C.; Siepmann, T.; Bohlmann, F. *Justus Liebigs Annalen der Chemie* **1963**, *661*, 1-37.
291. Read, J. *J. Electrochem. Soc.* **2002**, *149*, A1190-A1195.
292. Zhang, T.; Imanishi, N.; Shimonishi, Y.; Hirano, A.; Takeda, Y.; Yamamoto, O.; Sammes, N. *Chem. Commun. (Cambridge, U. K.)* **2010**, *46*, 1661-1663.
293. Calvo, E. J.; Mozhzhukhina, N. *Electrochem. Commun.* **2013**, *31*, 56-58.
294. Torres, W.; Mozhzhukhina, N.; Tesio, A. Y.; Calvo, E. J. *J. Electrochem. Soc.* **2014**, *161*, A2204-A2209.
295. Bondue, C. J.; Hegemann, M.; Molls, C.; Thome, E.; Baltruschat, H. *J. Electrochem. Soc.* **2016**, *163*, A1765-A1775.
296. Meini, S.; Solchenbach, S.; Piana, M.; Gasteiger, H. A. *J. Electrochem. Soc.* **2014**, *161*, A1306-A1314.
297. Elia, G. A.; Park, J.-B.; Sun, Y.-K.; Scrosati, B.; Hassoun, J. *ChemElectroChem* **2014**, *1*, 47-50.
298. del Pozo, M.; Torres, W. R.; Herrera, S. E.; Calvo, E. J. *ChemElectroChem* **2016**, *3*, 1537-1540.
299. Yang, X.-h.; Xia, Y.-y. *J. Solid State Electrochem.* **2010**, *14*, 109-114.
300. McCloskey, B. D.; Scheffler, R.; Speidel, A.; Girishkumar, G.; Luntz, A. C. *J. Phys. Chem. C* **2012**, *116*, 23897-23905.
301. Hartung, T.; Baltruschat, H. *Langmuir* **1990**, *6*, 953-957.

302. Abd-El-Latif, A. A.; Baltruschat, H. In *Encyclopedia of Applied Electrochemistry*, Kreysa, G.; Ota, K.-i.; Savinell, R., Eds.; Springer New York Dordrecht Heidelberg London, 2014, pp 507 - 516.
303. Viswanathan, V.; Nørskov, J. K.; Speidel, A.; Scheffler, R.; Gowda, S.; Luntz, A. C. *The Journal of Physical Chemistry Letters* **2013**, *4*, 556-560.
304. Kwabi, D. G.; Batcho, T. P.; Feng, S.; Giordano, L.; Thompson, C. V.; Shao-Horn, Y. *Phys. Chem. Chem. Phys.* **2016**, *18*, 24944-24953.
305. Liu, C.; Ye, S. *J. Phys. Chem. C* **2016**.
306. Wroblowa, H. S.; Razumney, G. *Journal of Electroanalytical Chemistry and Interfacial Electrochemistry* **1976**, *69*, 195-201.
307. Hsueh, K. L.; Chin, D. T.; Srinivasan, S. *Journal of Electroanalytical Chemistry and Interfacial Electrochemistry* **1983**, *153*, 79-95.
308. Ren, X.; He, M.; Xiao, N.; McCulloch, W. D.; Wu, Y. *Advanced Energy Materials* **2016**, 1601080.
309. Xiao, N.; Ren, X.; He, M.; McCulloch, W. D.; Wu, Y. *ACS Appl. Mater. Interfaces* **2017**, *9*, 4301-4308.
310. Yu, W.; Lau, K. C.; Lei, Y.; Liu, R.; Qin, L.; Yang, W.; Li, B.; Curtiss, L. A.; Zhai, D.; Kang, F. *ACS Appl. Mater. Interfaces* **2017**, *9*, 31871-31878.
311. Wang, W.; Lai, N.-C.; Liang, Z.; Wang, Y.; Lu, Y.-C. *Angew. Chem.* **2018**, *130*, 5136–5140.
312. Chen, Y.; Jovanov, Z. P.; Gao, X.; Liu, J.; Holc, C.; Johnson, L. R.; Bruce, P. G. *J. Electroanal. Chem.* **2018**, *819*, 542–546.
313. Aurbach, D.; McCloskey, B. D.; Nazar, L. F.; Bruce, P. G. *Nat. Energy* **2016**, *1*, 16128.
314. Xiao, N.; Rooney, R. T.; Gewirth, A. A.; Wu, Y. *Angew. Chem.* **2017**, n/a-n/a.
315. Sankarasubramanian, S.; Ramani, V. *J. Phys. Chem. C* **2018**, *122*, 19319-19327.
316. Bender, C. L.; Schröder, D.; Pinedo, R.; Adelhelm, P.; Janek, J. *Angewandte Chemie International Edition* **2016**, *55*, 4640-4649.
317. Noviandri, I.; Brown, K. N.; Fleming, D. S.; Gulyas, P. T.; Lay, P. A.; Masters, A. F.; Phillips, L. *The Journal of Physical Chemistry B* **1999**, *103*, 6713-6722.
318. Mozhzhukhina, N.; Méndez De Leo, L. P.; Calvo, E. J. *J. Phys. Chem. C* **2013**, *117*, 18375-18380.
319. Khan, A. U.; Mahanti, S. *The Journal of Chemical Physics* **1975**, *63*, 2271-2278.
320. Gerbig, O.; Merkle, R.; Maier, J. *Adv. Funct. Mater.* **2015**, *25*, 2552-2563.
321. Gunasekara, I.; Mukerjee, S.; Plichta, E. J.; Hendrickson, M. A.; Abraham, K. M. *J. Electrochem. Soc.* **2014**, *161*, A381-A392.
322. Gittleson, F. S.; Jones, R. E.; Ward, D. K.; Foster, M. E. *Energy Environ. Sci.* **2017**, *10*, 1167-1179.
323. Reinsberg, P. H.; Bawol, P. P.; Thome, E.; Baltruschat, H. *Anal. Chem.* **2018**, *90*, 14150-14155.
324. Freunberger, S. A.; Chen, Y.; Drewett, N. E.; Hardwick, L. J.; Barde, F.; Bruce, P. G. *Angewandte Chemie-International Edition* **2011**, *50*, 8609-8613.
325. Reinsberg, P. H.; Koellisch, A.; Bawol, P. P.; Baltruschat, H. **2019**.
326. Chuanchao, S.; Fengjiao, Y.; Yuping, W.; Zhangquan, P.; Yuhui, C. *Angewandte Chemie International Edition* **2018**, *0*.
327. Bryantsev, V. S.; Uddin, J.; Giordani, V.; Walker, W.; Addison, D.; Chase, G. V. *J. Electrochem. Soc.* **2013**, *160*, A160-A171.
328. Younesi, R.; Norby, P.; Vegge, T. *ECS Electrochemistry Letters* **2014**, *3*, A15-A18.
329. Trahan, M. J.; Gunasekara, I.; Mukerjee, S.; Plichta, E. J.; Hendrickson, M. A.; Abraham, K. M. *J. Electrochem. Soc.* **2014**, *161*, A1706-A1715.
330. Sankarasubramanian, S.; Seo, J.; Mizuno, F.; Singh, N.; Prakash, J. *J. Phys. Chem. C* **2017**, *121*, 4789-4798.
331. Liu, T.; Frith, J. T.; Kim, G.; Kerber, R. N.; Dubouis, N.; Shao, Y.; Liu, Z.; Magusin, P. C. M. M.; Casford, M. T. L.; Garcia-Araez, N.; Grey, C. P. *J. Am. Chem. Soc.* **2018**.
332. Lindberg, J.; Wickman, B.; Behm, M.; Cornell, A.; Lindbergh, G. *J. Electroanal. Chem.* **2017**, *797*, 1-7.
333. Pearson, R. G. *J. Chem. Educ.* **1968**, *45*, 581.

334. Saveant, J.-M. *The Journal of Physical Chemistry B* **2001**, *105*, 8995-9001.
335. Nicholson, R. S. *Anal. Chem.* **1965**, *37*, 1351-1355.
336. Lavagnini, I.; Antiochia, R.; Magno, F. *Electroanalysis* **2004**, *16*, 505-506.
337. Tong, L. K. J.; Liang, K.; Ruby, W. R. *Journal of Electroanalytical Chemistry and Interfacial Electrochemistry* **1967**, *13*, 245-262.
338. Arudi, R. L.; O Allen, A.; HJ Bielski, B. *FEBS Lett.* **1981**, *135*, 265-267.
339. Mahne, N.; Renfrew, S. E.; McCloskey, B. D.; Freunberger, S. A. *Angewandte Chemie International Edition* **2018**, *57*, 5529-5533.
340. Kapalka, A.; Lanova, B.; Baltruschat, H.; Fóti, G.; Comninellis, C. *Electrochem. Commun.* **2008**, *10*, 1215 - 1218.
341. Choban, A.; Yurchuk, I.; Lyavinets, A. *Russ. J. Gen. Chem.* **2008**, *78*, 2071-2074.
342. Kawabata, T.; Moriyama, K.; Kawakami, S.; Tsubaki, K. *J. Am. Chem. Soc.* **2008**, *130*, 4153-4157.
343. Øpstad, C. L.; Melø, T.-B.; Sliwka, H.-R.; Partali, V. *Tetrahedron* **2009**, *65*, 7616-7619.
344. Yang, S.; He, P.; Zhou, H. *Energy Environ. Sci.* **2016**, *9*, 1650-1654.
345. Read, J. *J. Electrochem. Soc.* **2006**, *153*, A96-A100.
346. Read, J.; Mutolo, K.; Ervin, M.; Behl, W.; Wolfenstine, J.; Driedger, A.; Foster, D. *J. Electrochem. Soc.* **2003**, *150*, A1351-A1356.
347. Franco, C.; Olmsted, J. *Talanta* **1990**, *37*, 905-909.
348. Achord, J. M.; Hussey, C. L. *Anal. Chem.* **1980**, *52*, 601-602.
349. Dymond, J. H. *The Journal of Physical Chemistry* **1967**, *71*, 1829-1831.
350. Tissot, P.; Yadav, A. K. *Electrochim. Acta* **1986**, *31*, 71-77.
351. Tsushima, M.; Tokuda, K.; Ohsaka, T. *Anal. Chem.* **1994**, *66*, 4551-4556.
352. Lindberg, J.; Endrődi, B.; Åvall, G.; Johansson, P.; Cornell, A.; Lindbergh, G. *J. Phys. Chem. C* **2018**, *122*, 1913–1920.
353. Battino, R. *Solubility Data Series, Vol. 7 Oxygen and Ozone*; Pergamon: New York, 1981.
354. Scheibel, E. G. *Industrial & Engineering Chemistry* **1954**, *46*, 2007-2008.
355. Wadhawan, J. D.; Welford, P. J.; Maisonhaute, E.; Climent, V.; Lawrence, N. S.; Compton, R. G.; McPeak, H. B.; Hahn, C. E. *The Journal of Physical Chemistry B* **2001**, *105*, 10659-10668.
356. Messaggi, F.; Ruggeri, I.; Genovese, D.; Zaccheroni, N.; Arbizzani, C.; Soavi, F. *Electrochim. Acta* **2017**, *245*, 296-302.
357. Ferrell, R. T.; Himmelblau, D. M. *J. Chem. Eng. Data* **1967**, *12*, 111-115.
358. Bennion, D. N.; Yao, N.-P. *The Journal of Physical Chemistry* **1971**, *75*, 1727-1734.
359. Jenkins, H. D. B.; Marcus, Y. *Chem. Rev. (Washington, DC, U. S.)* **1995**, *95*, 2695-2724.
360. Waghorne, W. E. *Philosophical Transactions of the Royal Society of London A: Mathematical, Physical and Engineering Sciences* **2001**, *359*, 1529-1543.
361. Jones, G.; Dole, M. *J. Am. Chem. Soc.* **1929**, *51*, 2950-2964.
362. Gubbins, K. E.; Bhatia, K. K.; Walker, R. D. *AIChE J.* **1966**, *12*, 548-552.
363. Tham, M. J.; Walker Jr, R. D.; Gubbins, K. E. *The Journal of Physical Chemistry* **1970**, *74*, 1747-1751.
364. Hung, G. W.; Dinius, R. H. *J. Chem. Eng. Data* **1972**, *17*, 449-451.
365. Pray, H. A.; Schweickert, C.; Minnich, B. H. *Industrial & Engineering Chemistry* **1952**, *44*, 1146-1151.
366. Morrison, T.; Johnstone, N. *Journal of the Chemical Society (Resumed)* **1954**, 3441-3446.
367. Ho, C. S.; Ju, L.-K.; Baddour, R. F.; Wang, D. I. *Chem. Eng. Sci.* **1988**, *43*, 3093-3107.
368. Van Krevelen, D.; Hoftijzer, P. *Chimie et Industrie: Numéro spéciale du XXIe congrès internationale de chimie industrielle, Bruxelles* **1948**.
369. Einstein, A. *Annalen der Physik* **1905**, *322*, 549-560.
370. Sutherland, W. *The London, Edinburgh, and Dublin Philosophical Magazine and Journal of Science* **1905**, *9*, 781-785.
371. Glasstone, S.; Laidler, K. J.; Eyring, H. *The Theory of Rate Processes*; McGraw-Hill Book Compandy: Princeton, 1941.

372. D'Agostino, C. *RSC Advances* **2017**, *7*, 51864-51869.
373. Wilke, C.; Chang, P. *AIChE J.* **1955**, *1*, 264-270.
374. Bicknell, R. T.; Lawrence, K. G.; Feakins, D. *Journal of the Chemical Society, Faraday Transactions 1: Physical Chemistry in Condensed Phases* **1980**, *76*, 637-647.
375. Tsierkezos, N. G.; Kelarakis, A. E.; Palaiologou, M. M. *J. Chem. Eng. Data* **2000**, *45*, 395-398.
376. Campbell, A. N. *Can. J. Chem.* **1979**, *57*, 705-707.
377. Ciocirlan, O.; Iulian, O. *J. Serb. Chem. Soc.* **2009**, *74*, 317-329.
378. Falkenhagen, H.; Vernon, E. *The London, Edinburgh, and Dublin Philosophical Magazine and Journal of Science* **1932**, *14*, 537-565.
379. Das, S.; Hazra, D. K.; Lahiri, S. C. *Z. Phys. Chem. (Muenchen, Ger.)* **1983**, *138*, 185-198.
380. Lawrence, K. G.; Sacco, A. *Journal of the Chemical Society, Faraday Transactions 1: Physical Chemistry in Condensed Phases* **1983**, *79*, 615-624.
381. Davis, R.; Horvath, G.; Tobias, C. *Electrochim. Acta* **1967**, *12*, 287-297.
382. Anderson, M. R.; Blackwood, D.; Pons, S. *Journal of Electroanalytical Chemistry and Interfacial Electrochemistry* **1988**, *256*, 387-395.
383. Anderson, M. R.; Huang, J. *Journal of Electroanalytical Chemistry and Interfacial Electrochemistry* **1991**, *318*, 335-347.
384. Chang, S. C.; Jiang, X.; Roth, J. D.; Weaver, M. J. *The Journal of Physical Chemistry* **1991**, *95*, 5378-5382.
385. Roth, J. D.; Weaver, M. J. *Langmuir* **1992**, *8*, 1451-1458.
386. Roth, J. D.; Chang, S.-C.; Weaver, M. J. *Journal of Electroanalytical Chemistry and Interfacial Electrochemistry* **1990**, *288*, 285-292.
387. Jiang, X.; Weaver, M. J. *Surf. Sci.* **1992**, *275*, 237-252.
388. Shen, A.; Pemberton, J. E. *J. Electroanal. Chem.* **1999**, *479*, 21-31.
389. Shen, A.; Pemberton, J. E. *J. Electroanal. Chem.* **1999**, *479*, 32-42.
390. Alwis, L.; Mucalo, M. R.; Ingham, B. *J. Electrochem. Soc.* **2013**, *160*, H803-H812.
391. Alwis, K. H. K. L.; Mucalo, M. R. *J. Electrochem. Soc.* **2014**, *161*, H738-H750.
392. Alwis, K. H.; Mucalo, M. R.; Lane, J. R. *RSC Advances* **2015**, *5*, 31815-31825.
393. Alwis, L.; Mucalo, M. R. *Electrocatalysis* **2016**, *7*, 104-114.
394. Morin, S.; Conway, B. E.; Edens, G. J.; Weaver, M. J. *J. Electroanal. Chem.* **1997**, *421*, 213-220.
395. Cao, P.; Gu, R.; Qiu, L.; Sun, R.; Ren, B.; Tian, Z. *Surf. Sci.* **2003**, *531*, 217-225.
396. Cao, P.; Sun, Y. *J. Phys. Chem. B* **2003**, *107*, 5818-5824.
397. Gu, R. A.; Cao, P. G.; Sun, Y. H.; Tian, Z. Q. *J. Electroanal. Chem.* **2002**, *528*, 121-126.
398. Morin, S.; Conway, B. E. *J. Electroanal. Chem.* **1994**, *376*, 135-150.
399. Hutchinson, K.; McQuillan, A. J.; Hester, R. E. *Chem. Phys. Lett.* **1983**, *98*, 27-31.
400. Peremans, A.; Tadjeddine, A.; Zheng, W. Q.; Le Rille, A.; Guyot-Sionnest, P.; Thiry, P. A. *Surf. Sci.* **1996**, *368*, 384-388.
401. Chang, S.-C.; Weaver, M. J. *Surf. Sci.* **1990**, *238*, 142-162.
402. Herzberg, G.; Herzberg, L. *JOSA* **1953**, *43*, 1037-1044.
403. Hall, R. T.; Dowling, J. M. *The Journal of Chemical Physics* **1967**, *47*, 2454-2461.
404. Edmund Optics, *50x75 mm Protected Gold* (04.12.2018), **2018**, https://www.edmundoptics.com/p/50-x-75mm-protected-gold-4-6lambda-mirror/8702/.
405. Materials, T. S. **2013**.
406. Kern, W. *J. Electrochem. Soc.* **1990**, *137*, 1887-1892.
407. Ubara, H.; Imura, T.; Hiraki, A. *Solid State Commun.* **1984**, *50*, 673-675.
408. Burrows, V.; Chabal, Y.; Higashi, G.; Raghavachari, K.; Christman, S. *Appl. Phys. Lett.* **1988**, *53*, 998-1000.
409. Chabal, Y.; Higashi, G.; Raghavachari, K.; Burrows, V. *Journal of Vacuum Science & Technology A: Vacuum, Surfaces, and Films* **1989**, *7*, 2104-2109.
410. Higashi, G.; Chabal, Y.; Trucks, G.; Raghavachari, K. *Appl. Phys. Lett.* **1990**, *56*, 656-658.
411. Jusys, Z.; Behm, R. J. *J. Electroanal. Chem.* **2017**, *800*, 60-76.
412. Sun, S.-G.; Cai, W.-B.; Wan, L.-J.; Osawa, M. *J. Phys. Chem. B* **1999**, *103*, 2460-2466.

413. Nicol, M.; Fleming, C.; Paul, R. In *The Extractive Metallurgy of Gold*, Stanley, G. C., Ed., 1987, pp 831-905.
414. Baltruschat, H.; Heitbaum, J. *Journal of Electroanalytical Chemistry and Interfacial Electrochemistry* **1983**, *157*, 319-326.
415. Russell, A. E.; Pons, S.; Anderson, M. R. *Chem. Phys.* **1990**, *141*, 41-49.
416. Blandamer, M. J.; Burgess, J.; Duffield, A. J. *Journal of the Chemical Society, Dalton Transactions* **1980**, 1-6.
417. Yeager, H. L.; Fedyk, J. D.; Parker, R. J. *The Journal of Physical Chemistry* **1973**, *77*, 2407-2410.
418. Parellada, R.; Perez-Peña, J.; Arenas, J. F. *J. Mol. Struct.* **1979**, *51*, 1-7.
419. Pace, E.; Noe, L. J. *The Journal of Chemical Physics* **1968**, *49*, 5317-5325.
420. Elshatla, A. S.; Baltruschat, H. *in preparation*.
421. Hartmann, P.; Bender, C. L.; Sann, J.; Durr, A. K.; Jansen, M.; Janek, J.; Adelhelm, P. *Phys. Chem. Chem. Phys.* **2013**, *15*, 11661-11672.
422. Pranay Reddy, K.; Fischer, P.; Marinaro, M.; Wohlfahrt-Mehrens, M. *ChemElectroChem* **2018**, *5*, 2758-2766.
423. Kern, D.; Orlemann, E. *J. Am. Chem. Soc.* **1949**, *71*, 2102-2106.

A Appendix

A 1 ORR in $Ca(ClO_4)_2$/DMSO

This section of the appendix is an addendum to chapter 4. The ORR at a gold electrode in 0.1 M $Ca(ClO_4)_2$ is shown in Figure A 1.1. After a rise in current, a plateau is observed for a rotation rate of 4 Hz, which is close to the diffusion-limited current for a two-electron reduction of oxygen[3] and thus, agrees well with the observations made in the DEMS flow-through cell (Figure 4.1). However, after a charge of 8200 µC cm^{-2}, the current starts to become less negative at a potential of −1.29 V and reaches a second plateau, which corresponds well with the diffusion-limited current of the one-electron process and is also reflected in the share of superoxide (Figure A 1.1c). This is in principle reminiscent of the ORR in Li^+-containing DMSO chapter 6, where a transition to superoxide formation was observed after the electrode was partially blocked by Li_2O_2 (Figure 6.1). However, a major difference between these measurements is the large charge which can be passed before this transition occurs: Even if the charge detected at the ring electrode is subtracted (2500 µC cm^{-2}), the remaining charge is still 5700 µC cm^{-2} and thus, in the order of several monolayers.

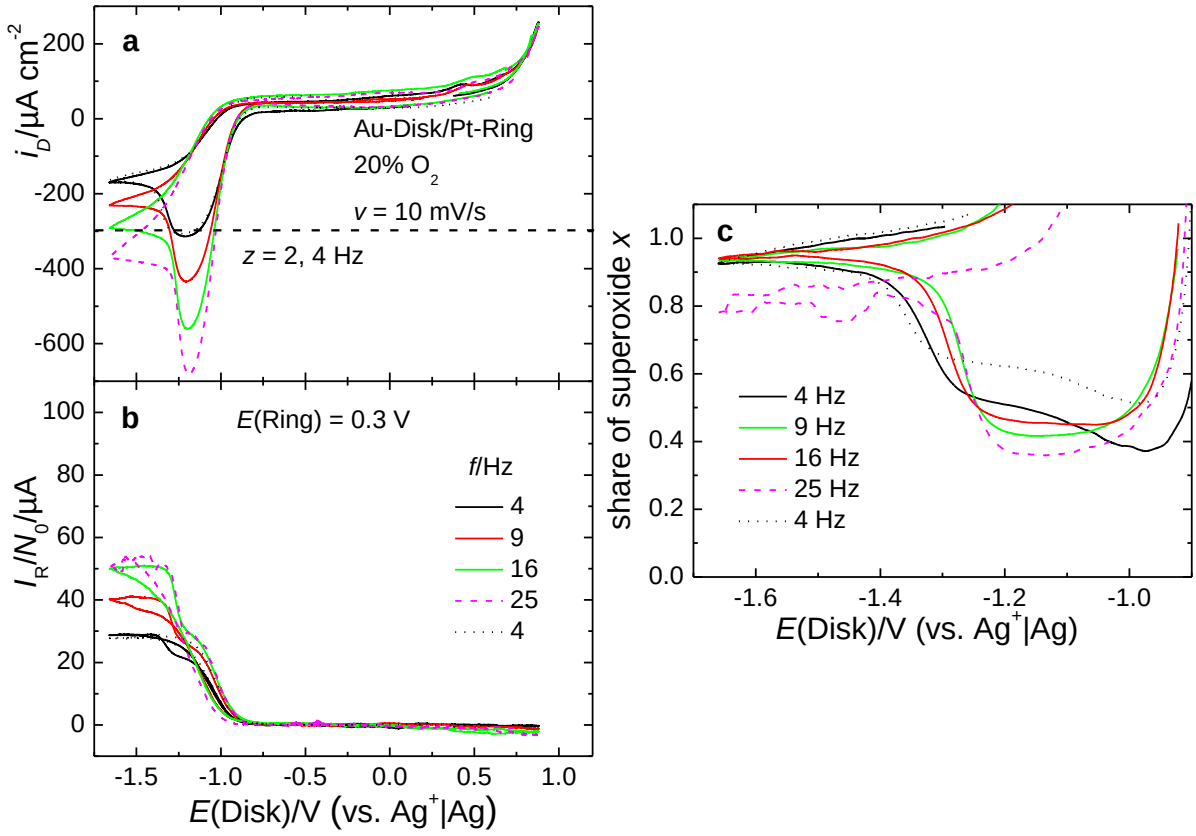

Figure A 1.1. ORR in presence of Ca^{2+} at a gold-RRDE. **a.** Currents at the gold-disk. **b**. Corresponding currents at a platinum-ring. **c**. Share of superoxide. Electrolyte: 0.1 M $Ca(ClO_4)_2$ in DMSO. A(Disk) = 0.196 cm^2, N_0 = 0.25. The dashed line indicates the expected, diffusion-limited current for z = 2.

[3] The diffusion-limited current equals 295 µA cm^{-2}, assuming that the solubility and diffusivity of oxygen in presence of $Ca(ClO_4)_2$ are similar to the $Mg(ClO_4)_2$-containing solution[130].

The fact that a charge of several monolayers can be transferred prior to the transition to the superoxide might also be responsible for the different behaviour of the RRDE- and the DEMS-electrode. In the cathodic sweep in the DEMS-measurement (chapter 4, Figure 4.1) a charge of 6000 µC cm^{-2} is transferred, which is significantly smaller than the charge passed at the RRDE-electrode (note that this refers to the 8200 µC cm^{-2}). Taking into account that the DEMS-electrodes are usually somewhat rougher than the RRDE-electrodes, it is understandable why only slight deactivation is visible in the anodic sweep.

While reasons for the different behaviour as opposed to the Li^+-containing solution are elusive without an elucidation of the morphology, an interesting observation is presented in Figure A 1.2, where disk and the corresponding ring currents are shown for a constant rotation rate under variation of the ring potential. From Figure A 1.2b and c a pronounced dependence of the ring currents and share of superoxide on the ring potential can be seen. While for ring potentials below −0.3 V almost no ring current is visible within the plateau of the two-electron process (e.g. −1.25 V), the current significantly increases up to a potential of 0.7 V. On the other hand, the ring currents in the superoxide-regime (E(Disk) = −1.4 to −1.6 V) are only changing slightly between 0.0 V and 0.7 V (taking into account the uncertainty of the measurement as indicated by the comparison between black and brown).

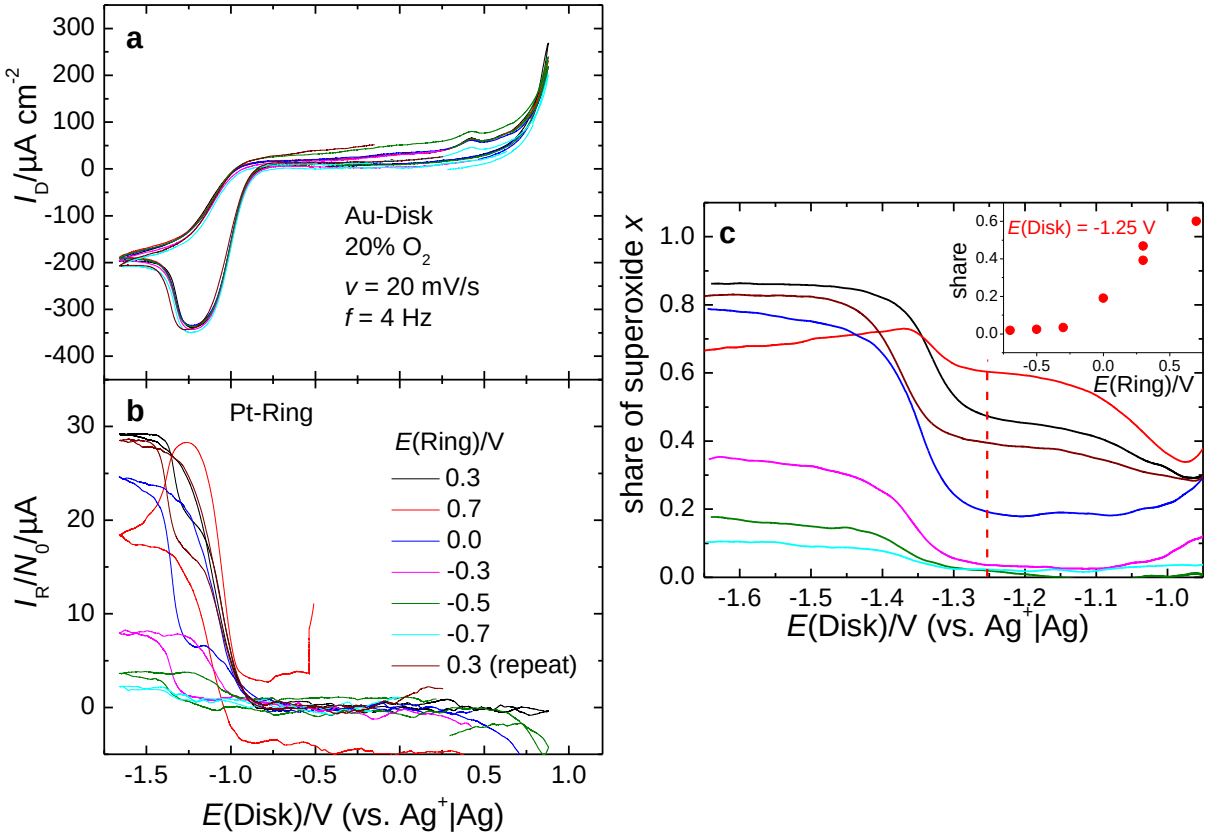

Figure A 1.2. Effect of the ring-potential on the ORR in presence of Ca^{2+} at a gold-RRDE. **a.** Currents at the gold-disk. **b**. Corresponding currents at a platinum-ring. **c**. Share of superoxide. The inset shows the share of superoxide as a function of the ring potential at E(Disk) = -1.25 V. Electrolyte: 0.1 M $Ca(ClO_4)_2$ in DMSO. A(Disk) = 0.196 cm^2, N_0 = 0.25.

The fact that the ring current in the superoxide-regime even decreases at a ring potential of 0.7 V implies a deactivation of the ring electrode at this potential, which is possibly induced by the oxidation of reduced species. Summarising, the results presented in Figure A 1.2 indicate that there are not only superoxide-species, which can be reoxidized, but maybe also peroxide species.

Further evidence for the general re-oxidizability of the peroxide is given in Figure A 1.3, where oxygen evolution is observed, which corresponds to a two-electron process. The major difference of this measurement as compared to the DEMS-measurement with the flow-through cell (chapter 4, Figure 4.1) is the high surface area of the electrode and the high oxygen concentration. To probe for soluble, reduced oxygen species, the experiment was carried out as follows: First, the potential was swept to −1.5 V, where it was kept for 500 s and roughly 170 nmol of O_2 were reduced. Then, the electrolyte was exchanged and the potential was stepped to −0.5 V, before it was cycled to 0.75 V. The amount of O_2 evolved during this measurement is only 1.5 nmol. In contrast to this, the amount of O_2 reduced without a potential stop is 42 nmol and the amount evolved is 12 nmol. The large discrepancy between OER and ORR charge in the case of electrolyte exchange implies that the peroxide-species (as indicated by the two-electron process during reduction as well as oxidation) are at least partially soluble.

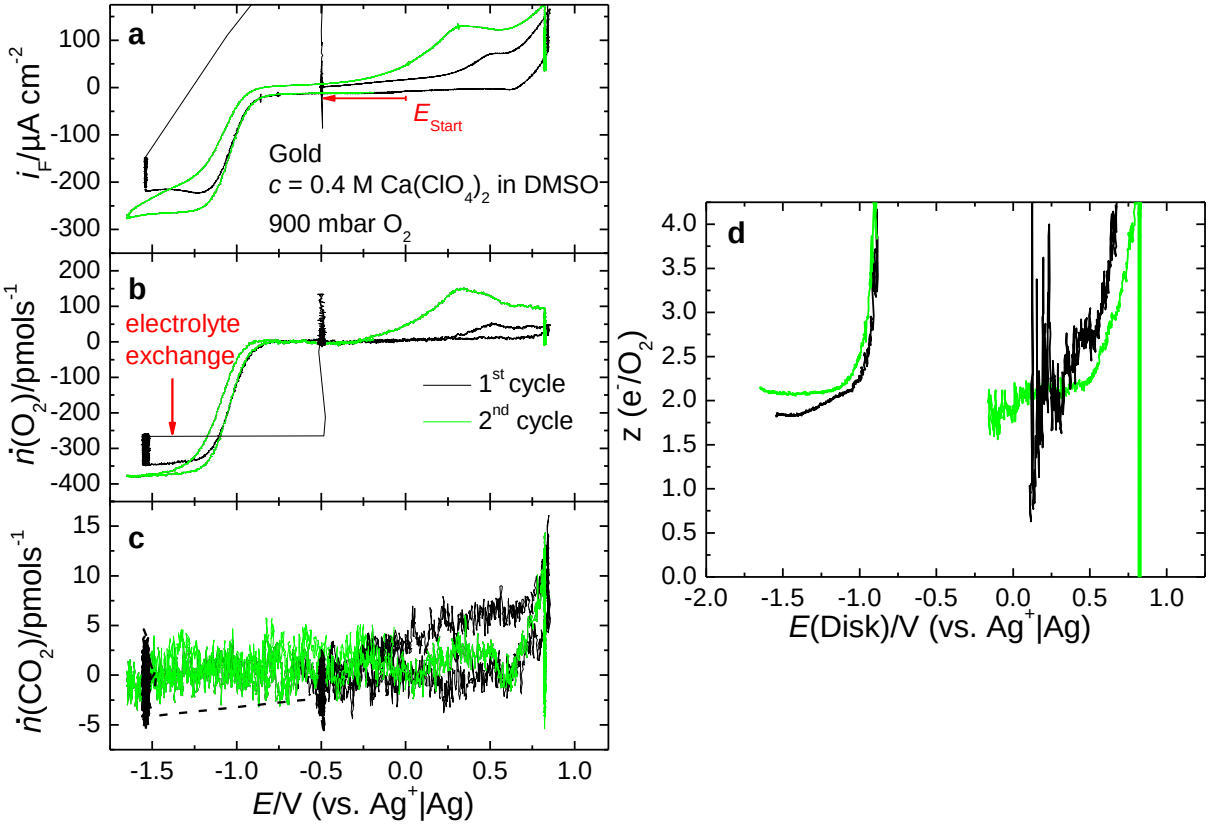

Figure A 1.3. Thin-layer DEMS-measurement of ORR in presence of Ca^{2+}. **a.** Currents at the gold working electrode. **b**. Corresponding flux of oxygen. **c**. Corresponding flux of CO_2. **d**. Number of electrons transferred per reduced and evolved molecule of O_2. After holding the potential for 500 s at

−1.5 V, the electrolyte was exchange under potential control and then stepped to −0.5 V before continuing cycling. Electrolyte: 0.4 M $Ca(ClO_4)_2$ in DMSO, 900 mbar O_2.

A 2 ORR in $Sr(ClO_4)_2$ and $Ba(ClO_4)_2$/DMSO

Adding to the DEMS-measurements presented in chapter 5, RRDE measurements at gold electrodes are presented in Figure A 3.2. For $Sr(ClO_4)_2$ a peak similar to the one observed in Ca^{2+}-containing DMSO is observed, although significantly more narrow. In contrast to that, there is only a shoulder followed by a steep increase in current in the case of $Ba(ClO_4)_2$.

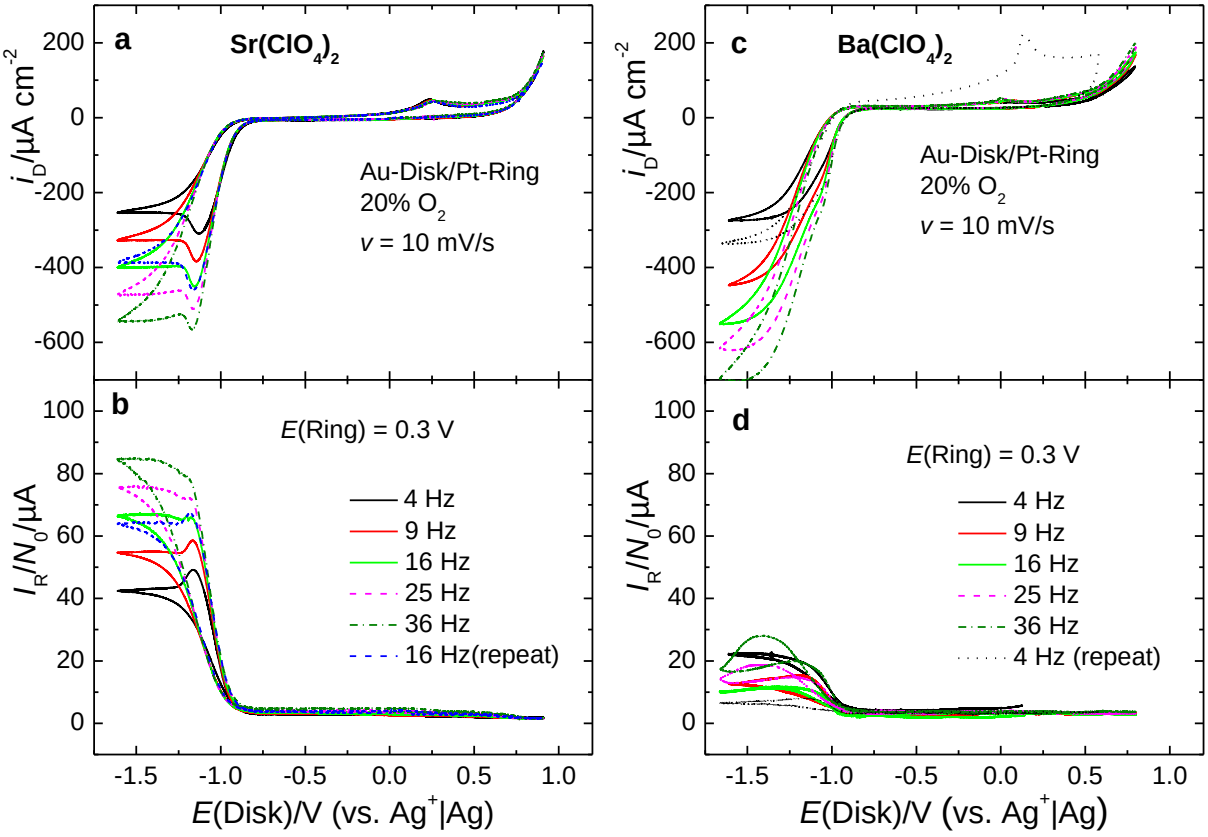

Figure A 2.1. ORR in presence of Sr^{2+} and Ba^{2+} at a gold-RRDE. **a.** Currents at the gold-disk in a Sr^{2+}-containing electrolyte. **b**. Corresponding currents at a platinum-ring. **c**. Currents at the gold-disk in a Ba^{2+}-containing Electrolyte. **d**. Corresponding ring currents at a platinum ring. Electrolyte: 0.1 M $M(ClO_4)_2$ in DMSO. A(Disk) = 0.164 cm², N_0 = 0.22.

A 3 ORR in $NaClO_4$, $RbClO_4$ and $CsClO_4$/DMSO

The ORR in DMSO in presence of Na^+ at a gold Figure A 3.1. Similar to Li^+-containing DMSO, a shoulder in the disk current can be observed at around −1.1 V, which corresponds to high ring currents (Figure A 3.1 b) and therefore, is related to superoxide. At around −1.35 V, a transition to the two-electron process occurs leading to decreasing ring currents and a lower share of superoxide (Figure A 3.1 c). Similar to the ORR in presence of Li^+, the peroxide formation leads to a deactivation of the electrode and the product distribution is shifted back to the superoxide (Figure A 3.1 d).

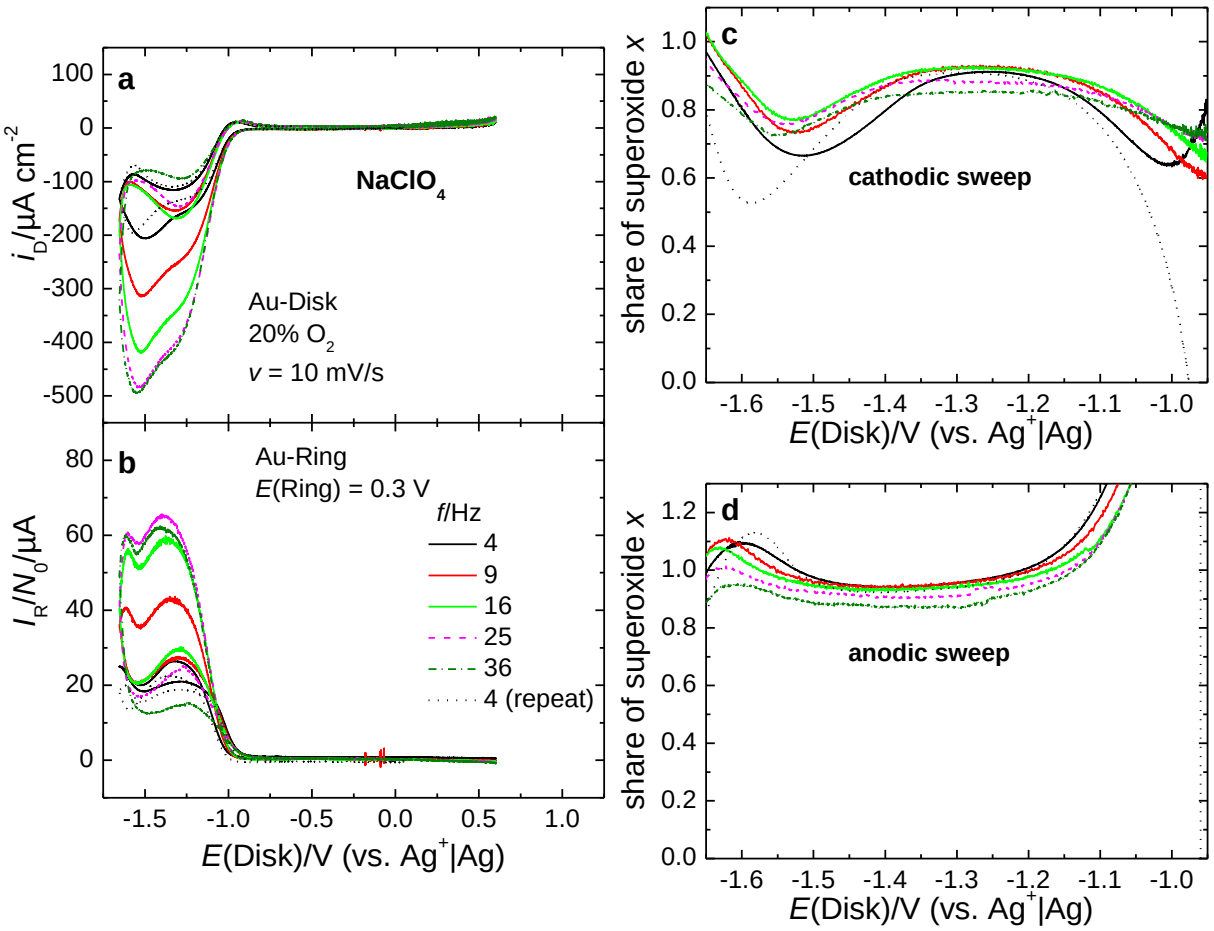

Figure A 3.1. ORR in presence of Na^+ at a gold-RRDE. **a.** Currents at the gold-disk. **b**. Corresponding currents at a gold-ring. **c**. Share of superoxide in the cathodic direction. **d**. Share of superoxide in the anodic direction. Electrolyte: 0.1 M $NaClO_4$ in DMSO. A(Disk) = 0.196 cm^2, N_0 = 0.25.

The ORR in DMSO in presence of Rb^+ at a gold RRDE is shown in Figure A 3.2. As can be seen from Figure A 3.2a, after a rotation-dependent shoulder at −1.0 V, a plateau between −1.2 V and −1.5 V is exhibited in the disk current. However, the current is larger than the 240 µA cm^{-2} expected for the one-electron process ($c(O_2)$ = 2.31 mM, $D(O_2)$ = 26.4x10^{-6} cm^2s^{-1}). Moreover, the ring-currents (Figure A 3.2b) are rather small, resulting in a low share of superoxide (Figure A 3.2c–d). Nonetheless, the overall process appears to operate over superoxide, which is further reduced to peroxide, but side-reactions are present. In the anodic sweep a small re-oxidation peak is observed at a potential of around −1.5 V, indicating the re-oxidation of insoluble peroxide. The resulting superoxide is also found as a peak in the ring current.

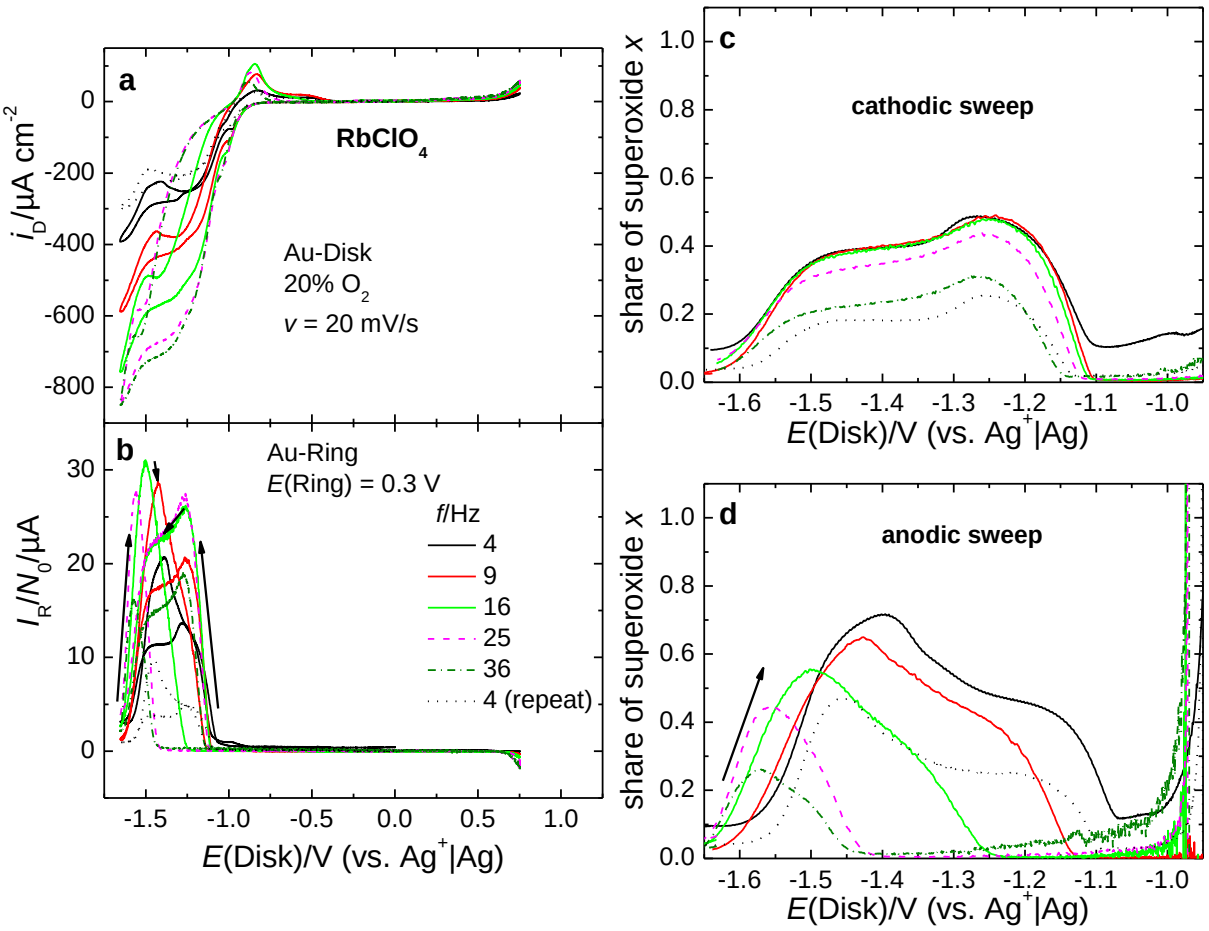

Figure A 3.2. ORR in presence of Rb^+ at a gold-RRDE. **a.** Currents at the gold-disk. **b**. Corresponding currents at a gold-ring. **c**. Share of superoxide in the cathodic direction. **d**. Share of superoxide in the anodic direction. Electrolyte: 0.1 M $RbClO_4$ in DMSO. A(Disk) = 0.164 cm², N_0 = 0.22.

CVs under stagnant conditions are shown in Figure A 3.3. Similar to the observations in K^+-containing electrolytes, two pairs of corresponding peaks are visible. However, a third pre-peak is distinguishable close to the onset of the ORR in agreement with the RRDE-measurements.

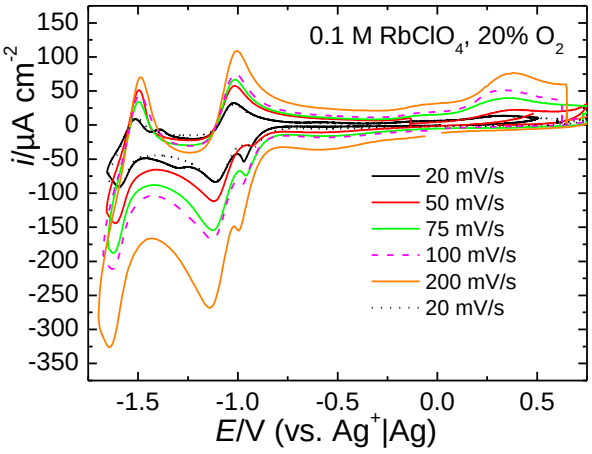

Figure A 3.3. ORR in presence of Rb^+ at a gold-electrode under stagnant conditions. Electrolyte: 0.1 M $RbClO_4$. A = 0.164 cm².

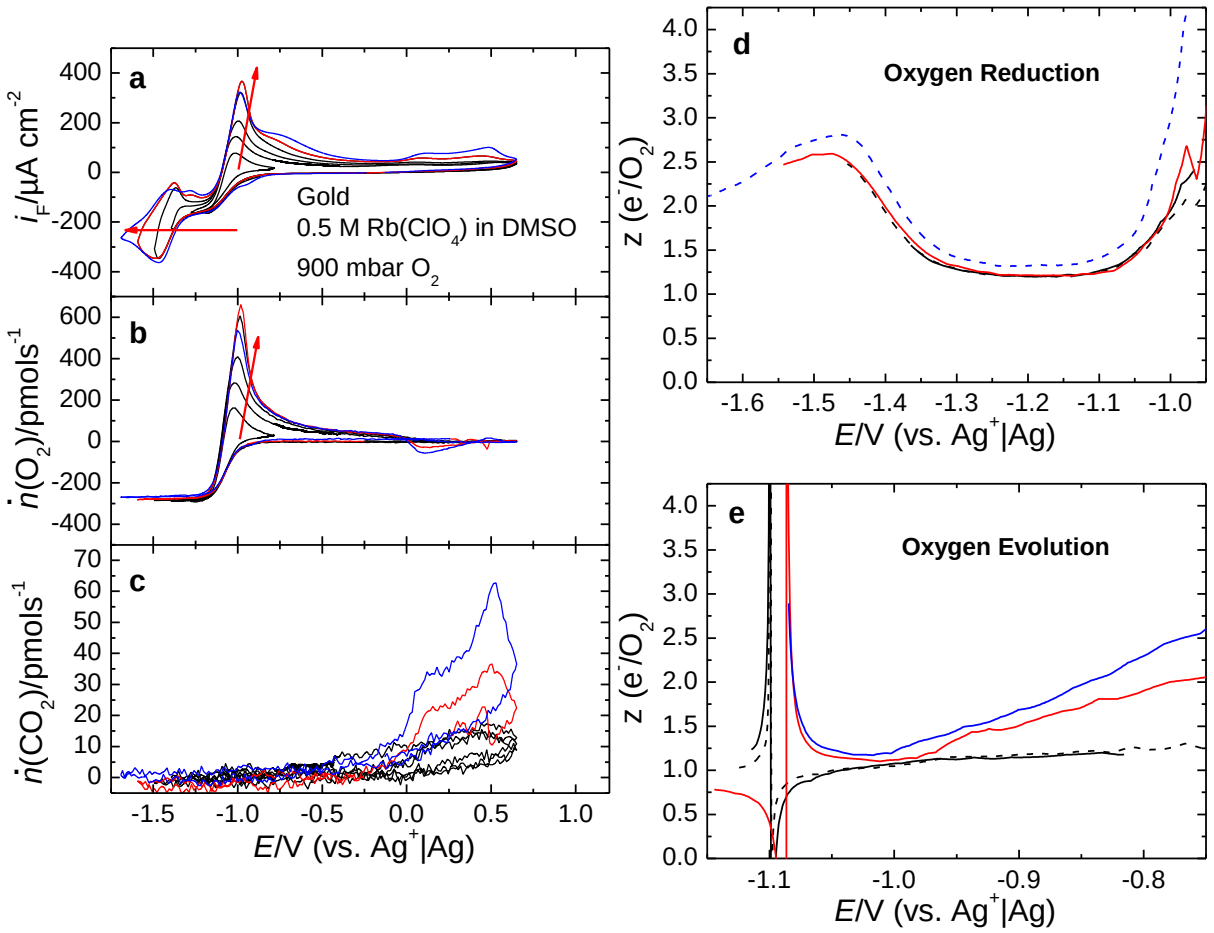

Figure A 3.4. Thin-layer DEMS-measurement of ORR in presence of Rb^+. **a.** Currents at the gold working electrode. **b**. Corresponding flux of oxygen. **c**. Corresponding flux of CO_2. **d**. Number of electrons transferred per reduced molecule of O_2. **e**. Number of electrons transferred per reduced molecule of O_2. The lower potential limit was shifted more negative for subsequent cycles, leading to a larger ORR-charge. Electrolyte: 0.5 M $RbClO_4$ in DMSO, 900 mbar O_2. Notice the oxygen consumption at around 0 V.

The DEMS-measurements in the thin-layer cell under stagnant conditions in Figure A 3.4 prove that the processes are actually related to oxygen reduction and evolution and also show a significant amount of side-reactions (Figure A 3.4c). While the number of electrons per O_2 during the ORR implies a mixed process between −1.1 V and −1.3 V rather than the sole formation of superoxide, the number of electrons from the OER are very close to 1 and show that mainly superoxide is re-oxidised (Figure A 3.4e). Summarizing the different results it seems likely that in Rb^+-containing DMSO initially superoxide is produced, but a side-reaction occurs in parallel, leading to too large currents. However, the general process can still be envisioned as the initial formation of superoxide and the subsequent formation of peroxide, which deposits as a re-oxidisable species.

The ORR in DMSO in presence of Cs^+ at a Gold-RRDE is shown in Figure A 3.5. A distinct transition from a plateau to a more negative current is observed in the disk and corresponding

ring currents. The share of superoxide as well as the occurrence of two reduction peaks (Figure A 3.5c–d) indicate the formation of superoxide within a broad potential window.

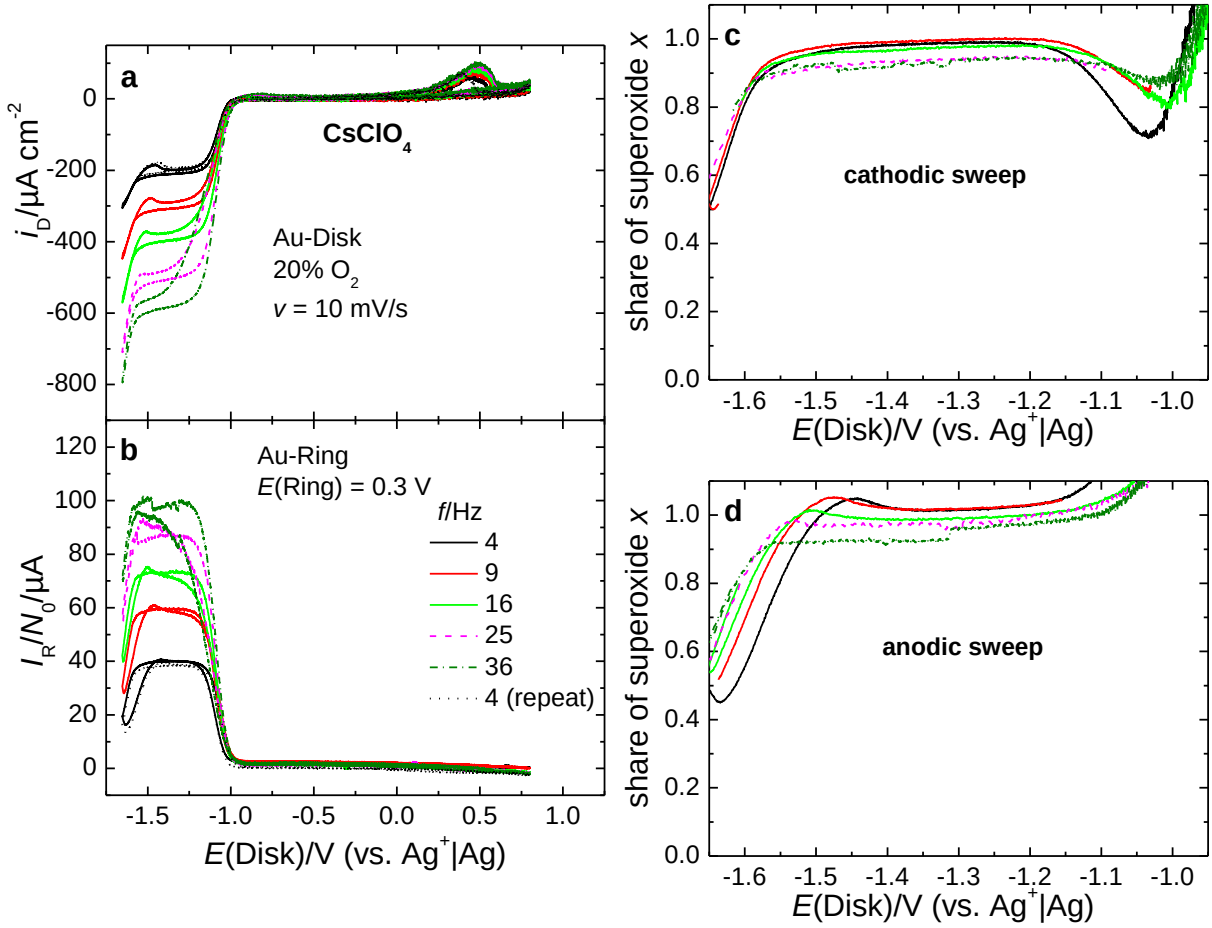

Figure A 3.5. ORR in presence of Cs^+ at a gold-RRDE. **a.** Currents at the gold-disk. **b**. Corresponding currents at a gold-ring. **c**. Share of superoxide in the cathodic direction. **d**. Share of superoxide in the anodic direction. 0.1 M $CsClO_4$ in DMSO. A(Disk) = 0.196 cm², N_0 = 0.25.

CVs under stagnant conditions are shown in Figure A 3.6. Similar to the observations in K^+- and Rb^+-containing electrolytes, two pairs of corresponding peaks are visible.

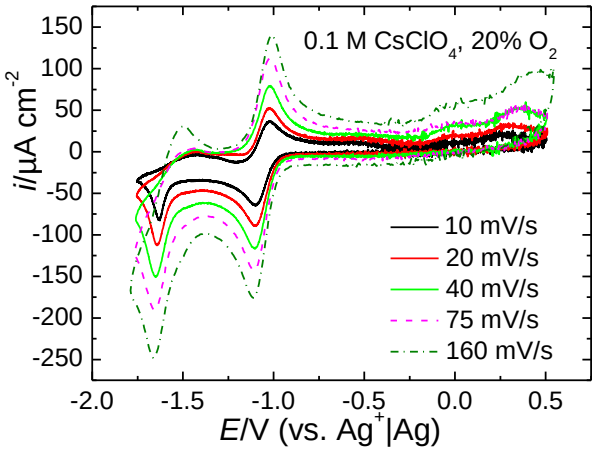

Figure A 3.6. ORR in presence of Cs^+ at a gold-electrode under stagnant conditions. Electrolyte: 0.1 M $CsClO_4$. A = 0.196 cm².

The transition from the one- to the two-electron process is also confirmed by the thin-layer

DEMS-measurement shown in Figure A 3.7.

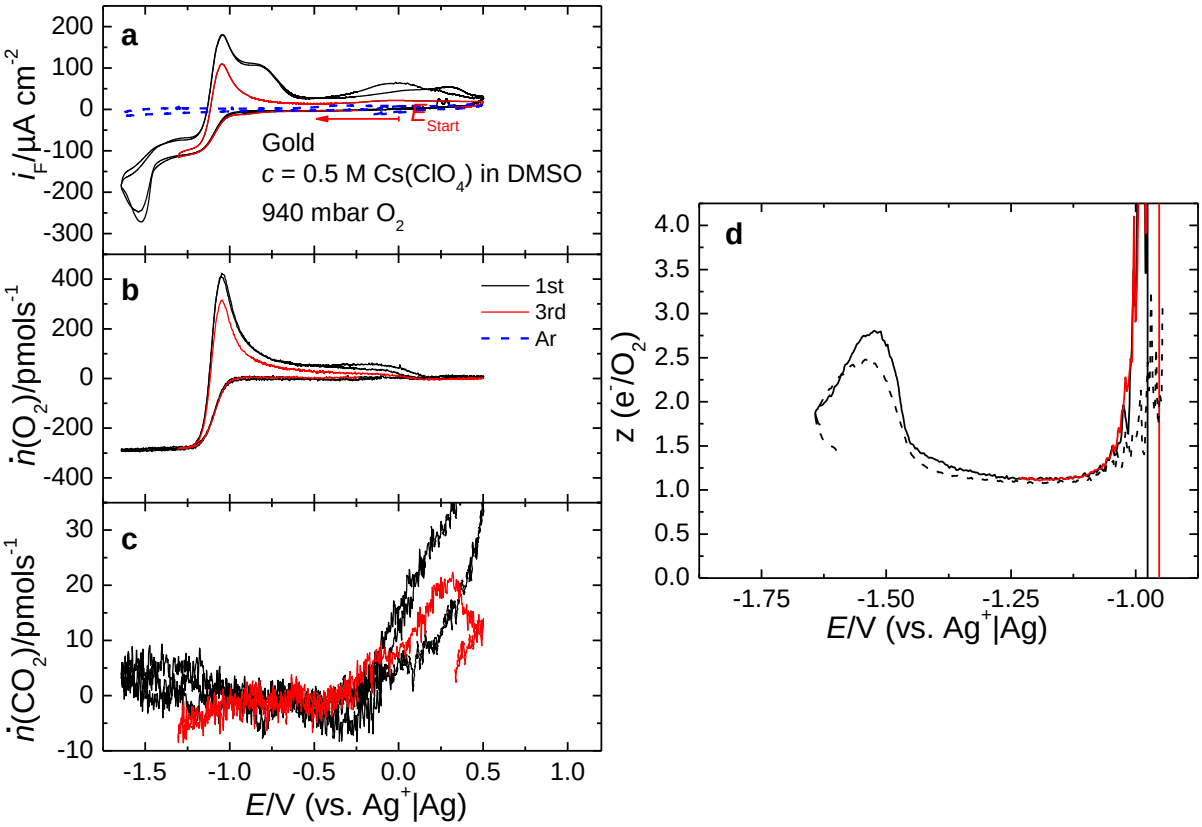

Figure A 3.7. Thin-layer DEMS-measurement of ORR in presence of Cs^+. **a.** Currents at the gold working electrode. **b**. Corresponding flux of oxygen. **c**. Corresponding flux of CO_2. **d**. Number of electrons transferred per reduced molecule of O_2. The lower potential limit was shifted more negative for subsequent cycles, leading to a larger ORR-charge. Electrolyte: 0.5 M $CsClO_4$ in DMSO, 940 mbar O_2.

A 4 Oxygen Consumption at Anodic Potentials

Similar to the observations in K^+-containing DMSO, the consumption of O_2 at anodic potentials can also be observed in Rb^+-containing solution (Figure A 3.4) Cs^+-containing electrolytes and is accompanied by anodic currents (Figure A 4.1)

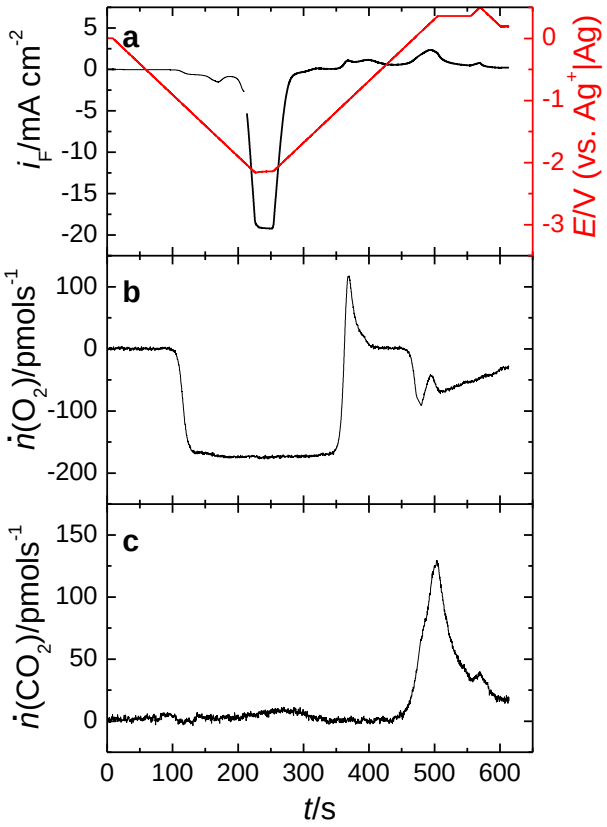

Figure A 4.1. Anodic oxygen consumption in the presence of Cs^+. **a.** Currents at the gold working electrode. **b**. Corresponding flux of oxygen. **c**. Corresponding flux of CO_2. **d**. Number of electrons transferred per reduced molecule of O_2. The lower potential limit was shifted more negative for subsequent cycles, leading to a larger ORR-charge. Electrolyte: 0.5 M $CsClO_4$ in DMSO, 940 mbar O_2.

A 5 Effect of Water in the Presence of Cs^+

An example of the effect of water on the ORR in Cs^+-containing DMSO is shown in Figure A 5.1. The major effect of the water is to shift the onset for peroxide into positive direction, which agrees with the results obtained in K^+-containing electrolyte. Moreover, the OER region becomes more complicated and the amount of oxygen consumption at anodic potentials increases with an increasing water content.

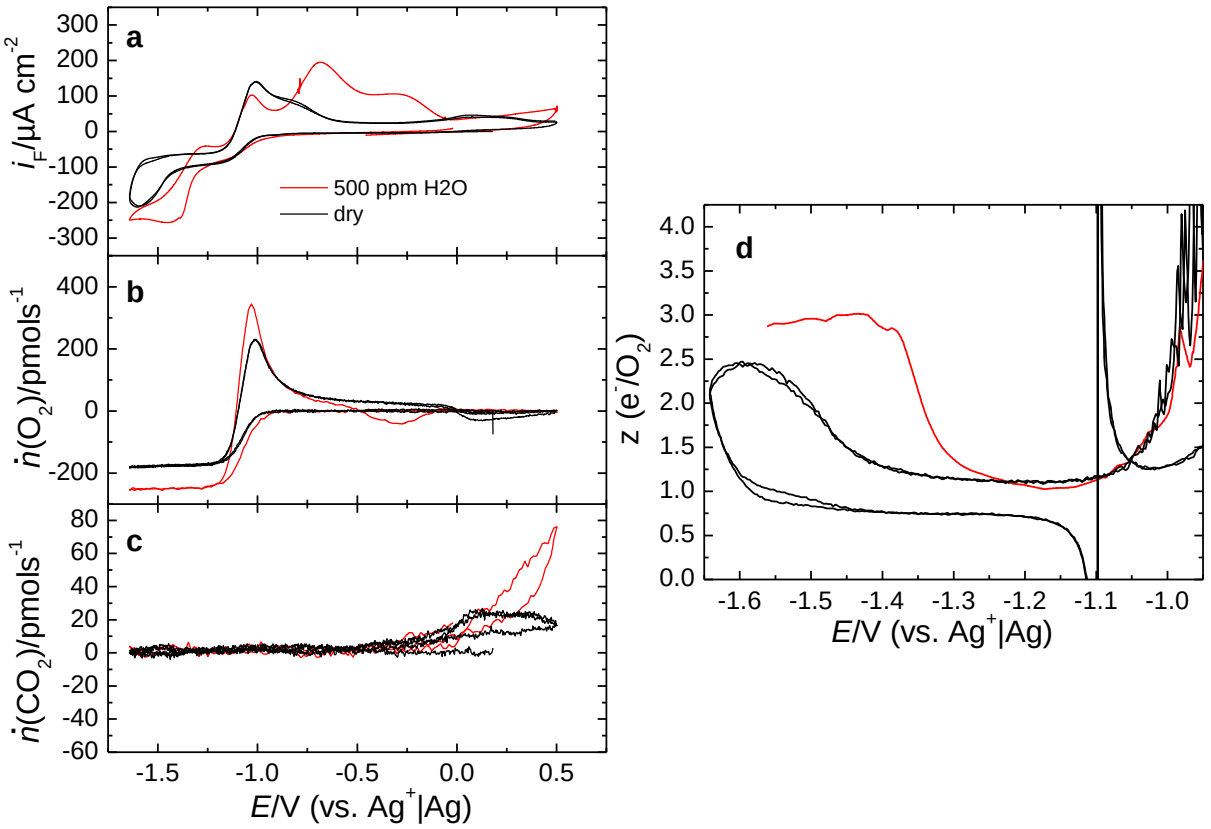

Figure A 5.1. Effect of water on the ORR in presence of Cs^+. **a.** Currents at the gold working electrode for two water contents. **b**. Corresponding flux of oxygen. **c**. Corresponding flux of CO_2. **d**. Number of electrons transferred per reduced molecule of O_2. Electrolyte: 0.5 M $CsClO_4$ in DMSO. 940 mbar O_2, water content as indicated.

A 6 Deactivated Gold-Electrodes and the ORR in $CsClO_4$/DMSO

For Li^+-containing electrolytes, two transition at gold electrodes have been reported in chapter 6. Initially superoxide is formed, which is then followed by peroxide formation from a potential of −1.3 V on. However, the peroxide blocks the surface leading again to a shift of the product distribution back to superoxide. A similar behaviour can be observed also in Cs^+-containing DMSO (Figure A 6.1) under certain experimental conditions. Initially, the exclusive formation of superoxide is observed and a transition to the peroxide formation is visible at −1.6 V. If the sweep rate is small enough (5 mV s^{-1}) and the lower potential limit is sufficiently negative, a deactivation of the gold electrode is visible. Then, at a potential of −1.67 V, the reductive current at the disk electrode rises again and a corresponding current appears in the ring current, indicating the formation of superoxide. It is noteworthy that this behaviour is somewhat different from the behaviour observed in Li^+-containing electrolyte. In the case of Li^+, the reductive current drops to zero after deactivation of the electrode and the formation of superoxide is only visible in the ring currents. In the case of Cs^+, the current first drops, but then increases again.

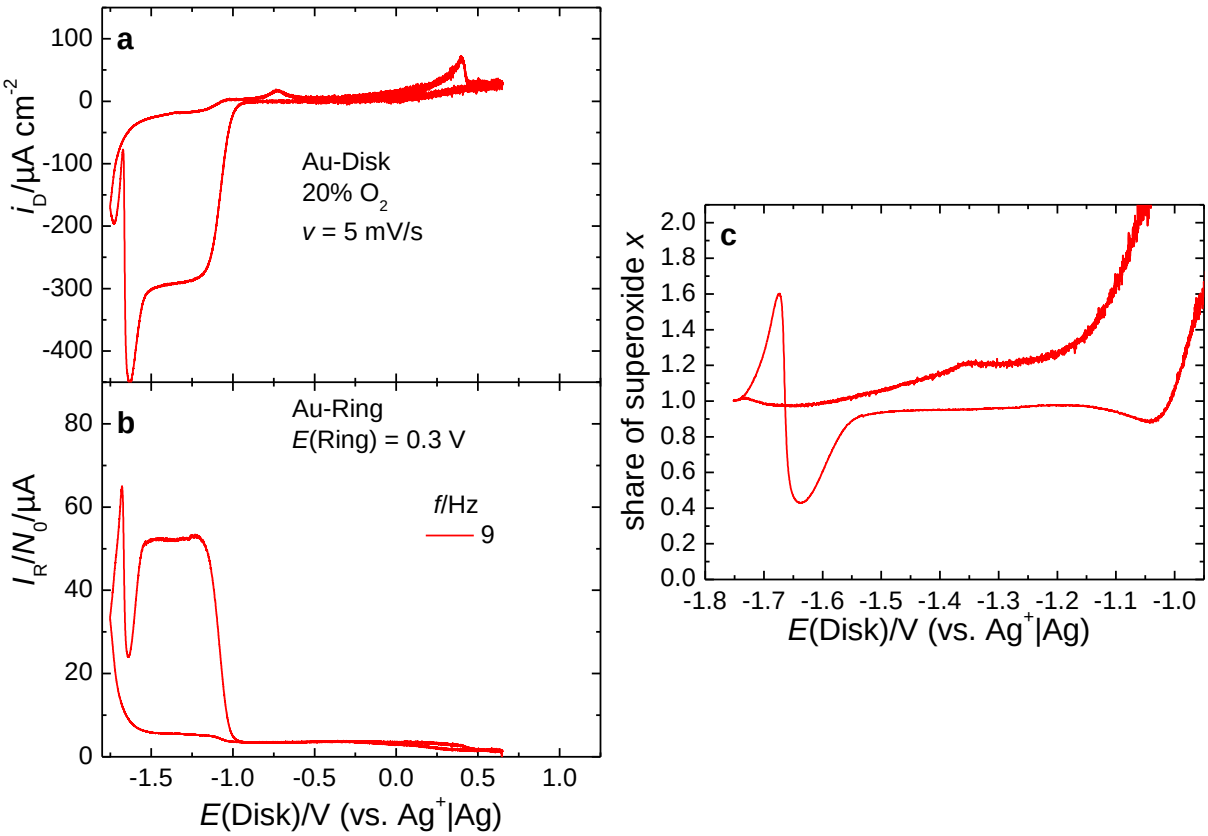

Figure A 6.1. Deactivated gold electrode in Cs^+-containing DMSO. **a.** Currents at the gold disk electrode. **b**. Corresponding currents at a gold ring electrode. **c**. Share of superoxide. Electrolyte: 0.1 M $CsClO_4$ in DMSO. A(Disk) = 0.196 cm^2, N_0 = 0.25.